The Numerical Evaluation of Multi-Piece Crankshafts

A Thesis Submitted to the College of

Graduate Studies and Research

In Partial Fulfillment of the Requirements for the

Degree of Doctor of Philosophy

in the Department of Mechanical Engineering at the

University of Saskatchewan

Saskatoon, Saskatchewan, Canada

by

Jeffrey Allan King

Keywords: finite element method, multi-piece crankshaft, press-fit, sub-surface stress

Permission to Use

In presenting this thesis in partial fulfilment of the requirements for a Postgraduate degree from the University of Saskatchewan, I agree that the Libraries of this University may make it freely available for inspection. I further agree that permission for copying of this thesis in any manner, in whole or in part, for scholarly purposes may be granted by the professor or professors who supervised my thesis work or, in their absence, by the Head of the Department or the Dean of the College in which my thesis work was done. It is understood that any copying or publication or use of this thesis or parts thereof for financial gain shall not be allowed without my written permission. It is also understood that due recognition shall be given to me and to the University of Saskatchewan in any scholarly use which may be made of any material in my thesis.

Requests for permission to copy or to make other use of material in this thesis in whole or part should be addressed to:

Head of the Department of Mechanical Engineering

University of Saskatchewan

57 Campus Drive

Saskatoon, Saskatchewan, Canada

S7N 5A9

ACKNOWLEDGMENTS

The author would like to thank his wife Michelle and his sons Bennett and Louden for their support, patience, and encouragement. Also much thanks goes to our extended family which without their help when needed, the completion of this challenge would not be possible. Thank you to my parents Eugene and Betty King for the encouragement and support from the start. Walerian Szyszkowski, thank you for the knowledge, guidance, and mentoring over the last 20 years. Thanks to all those at Polaris which have provided support in many ways; time, flexibility, hardware, software, and a great group of peers to work and foster this knowledge with.

ABSTRACT

This work develops a methodology for the FEM simulation of a multi-piece crankshaft. Various simulation models that include press-fit joint contact conditions and complex meshing schemes are examined in order to accurately capture details of the stress fields present at the stress concentration area (labeled as the SCA) on the edge of the press-fit. The maximum stress components are demonstrated to be of limited values (non-singular) and Hertzian in nature. To obtain the stress convergence sufficiently small elements, which can be determined using a 2-D axisymmetric model, are required at the vicinity of the SCA. The same level of mesh refinement is then used for large 3-D FEM models of the crankshaft geometry, to study the resulting behavior of the press-fit joint for the dynamic operating loads. However, it may not always be possible or practical, as some limits on the mesh refinement have to be imposed to obtain a reasonable computational time to run such models. Less complex 'equivalent' symmetrical FEM models are investigated to determine if these models can provide a sufficient level of accuracy at an acceptable computational effort. Such models may be useful as practical design tools, producing data to speed up the decision making process. The simulation results are compared to some test data for the stress state monitored in real crankshafts under operating conditions. 'Intuitive' design sensitivities to various crankshaft parameters are examined as well. The numerical tools and engineering rules developed in the thesis may be applied to systematically improve the design by extending the joint's life and/or load carrying capability.

Table of Contents

List of Figures

List of Symbols

and

Nomenclature Used

HP	horsepower, a unit of power
SCA	stress concentration at location A
big end	the crankshaft end of the connecting rod, which is largest
FEM	finite element method
2-D	two dimensional
3-D	three dimensional
FEA	finite element analysis
CAE	computer aided engineering
CVT	continuously variable transmission
PTO	power take-off, the engine crankshaft end which delivers torque
MAG	magneto, or the end of the engine which houses the magneto
m	mass
ω	rotational velocity
F	force
MBD	multi-body dynamics
rpm	rotations per minute
CAD	computer aided design
α	angle
δ	radial interference of the press-fit
σ	stress
τ	shear stress
u	displacement
TDC	top dead center, the highest rotational position of the crankshaft
ATDC	after top dead center, a rotational position of the crankshaft
BDC	bottom dead center, the lowest rotational position of the crankshaft
r	radial direction in a cylindrical co-ordinate system
CS	co-ordinate system
θ	hoop direction in a cylindrical CS
z	axial direction in a cylindrical CS
σ_{VM}	Von Mises equivalent stress
P	Hertzian load parameter on a cylinder / flat plate arrangement
D	diameter
p_o	maximum Hertzian surface contact stress
b	Hertzian contact patch width
E	modulus of elasticity
h	defining unit length of a square FEM element
UTS	ultimate tensile strength
S_{YS}	yield strength
Sn	fatigue strength
HRC	Rockwell C hardness
LC	load case

P1	maximum principal stress
P3	minimum principal stress
throw	the crankpin axis radial offset to the crankshaft main shaft axis
με	micro-strain
ID	internal diameter
OD	outer diameter
r_{SH}	radius of the shoulder feature
t_{SH}	thickness of the shoulder feature
r_{UC}	radius of the undercut feature
t_{UC}	thickness of the undercut feature
NS	no spin loading or no rotational inertial velocity loading

1 Introduction To Multi-Piece Crankshaft Analysis Methods

1.1 Introduction

Multi-piece crankshafts are prevalent in 2-stroke engines used throughout the recreational vehicle market, and in particular for snowmobiles. This type of crankshaft is also used in 4-stroke engines, but is not nearly as widely employed. The research effort will focus on certain challenges present in the computer simulation and design of a durable multi-piece crankshaft for application in the high performance snowmobile market.

The snowmobile performance segment of the market requires engines of high horsepower and high specific performance. Knowledgeable customers who purchase performance snowmobiles are typically aggressive drivers and are very demanding of the engine. The engine use in performance snowmobiling could be best compared to a race track environment in the automotive world. Therefore the design of a durable engine for the performance snowmobile customer is a challenge.

Low overall vehicle mass is very desirable to the snowmobiling customer; the floatation of the vehicle on softly packed snow is a basic engineering concept, determined by the distributed mass on a set vehicle footprint. Thus, there is a fundamental desire to keep the overall ratio of mass to footprint constant for good flotation. This creates difficult engineering challenges since the customer continuously demands greater engine and vehicle performance; the engine typically makes up around 20 to 25 percent of the overall vehicle mass. Therefore the engine and crankshaft mass is highly scrutinized, as the cranktrain system is considered the heart of the engine, and fundamentally it is important to the overall engine dimension and mass. Note also the ride and handling of a snowmobile responds poorly to an over-weight engine, which also very un-desirable.

A typical multi-piece crankshaft for use in a high performance 2-stroke engine as developed by *Polaris* is shown in Fig. 1.1.1. The 2-stroke twin cylinder engine is to provide 110 HP from a 600 cc capacity, which is a specific performance of over 175 HP / litre. For comparison, performance engines in sports car applications range in output from 80 to 125 HP / litre, and in

race motorcycles sit near 150 HP / litre. Engines with higher specific performance require challenging design trade-offs to manage both mass and durability.

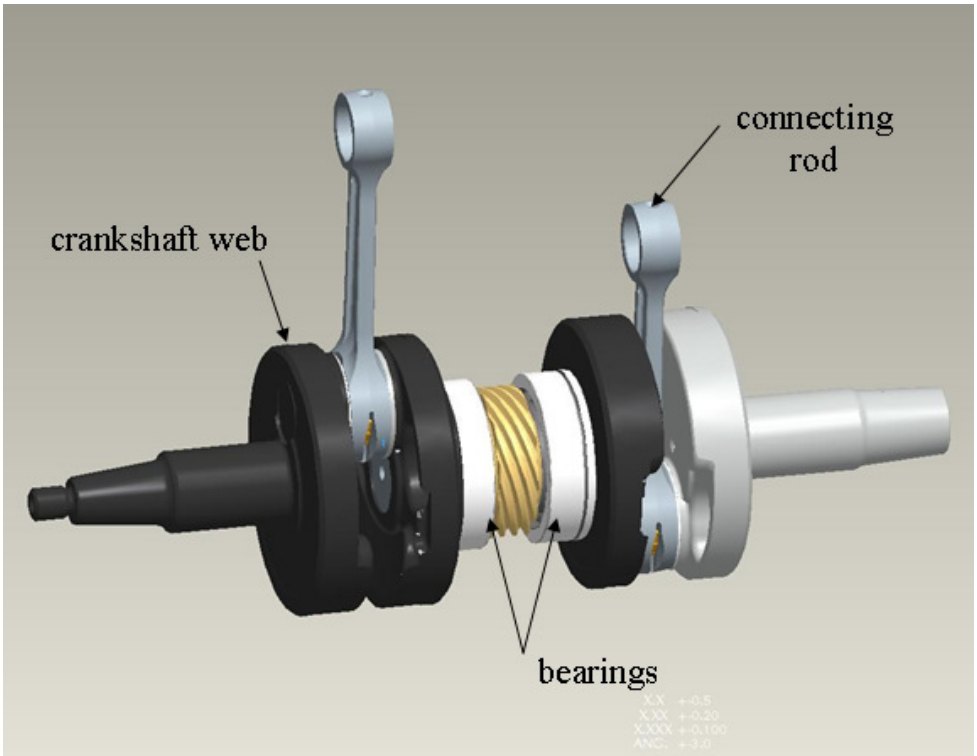

Figure 1.1.1 An assembled multi-piece crankshaft for a twin cylinder engine.

A multi-piece crankshaft uses a press-fit joint construction style to connect all the required pieces together. For each cylinder of the engine the crankshaft consists of a non-integral web and an integral web plus crankpin, as shown in Fig.1.1.2. Note that the integral web refers to a pin that is integral to the web or is one continuous piece. The crankpin is held by the cylindrical hole in the non-integral web through a positive cylindrical interference or press-fit.

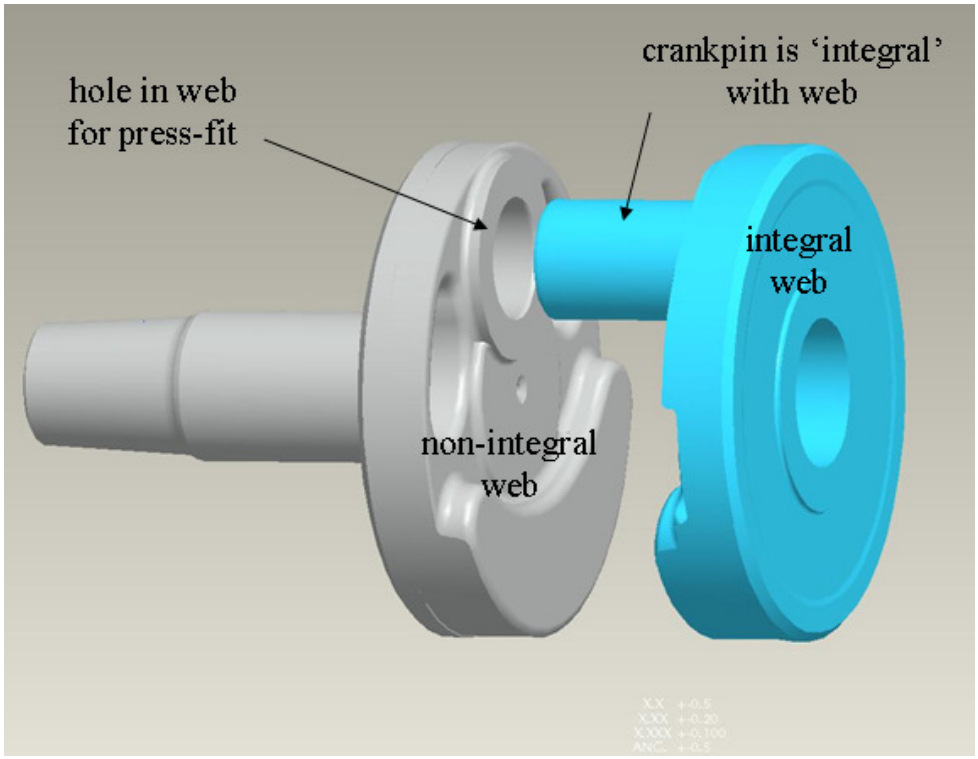

Figure 1.1.2 Components of a multi-piece crankshaft in an exploded view.

Generally, the press-fit interference is sized to adequately transmit the torque from the combustion events in the engine. The press-fit introduces stress concentrations in the pin and non-integral web which compromises the joint's durability. Both engineering logic and durability testing indicate that the design's weakest point is at the press-fit interface of location *A* as indicated in Fig. 1.1.3, and is referred to as the SCA point. The stress concentration there seems to be crucial to selecting the proper geometry that would secure adequate durability and torque retention.

Understanding the stress/strain fields in the vicinity of SCA during the phases of assembling and normal engine operation poses a challenge. Computer simulation models that include sophisticated meshing control, contact conditions, complex load instances, etc need to be considered to improve the performance of multi-piece crankshafts. The employed numerical methods have to be verified by carefully designed experimental techniques to measure the structural behavior of the crankshaft. The computer simulation may then be viewed as a reliable design tool, which is the key to developing improved and optimized crankshaft designs.

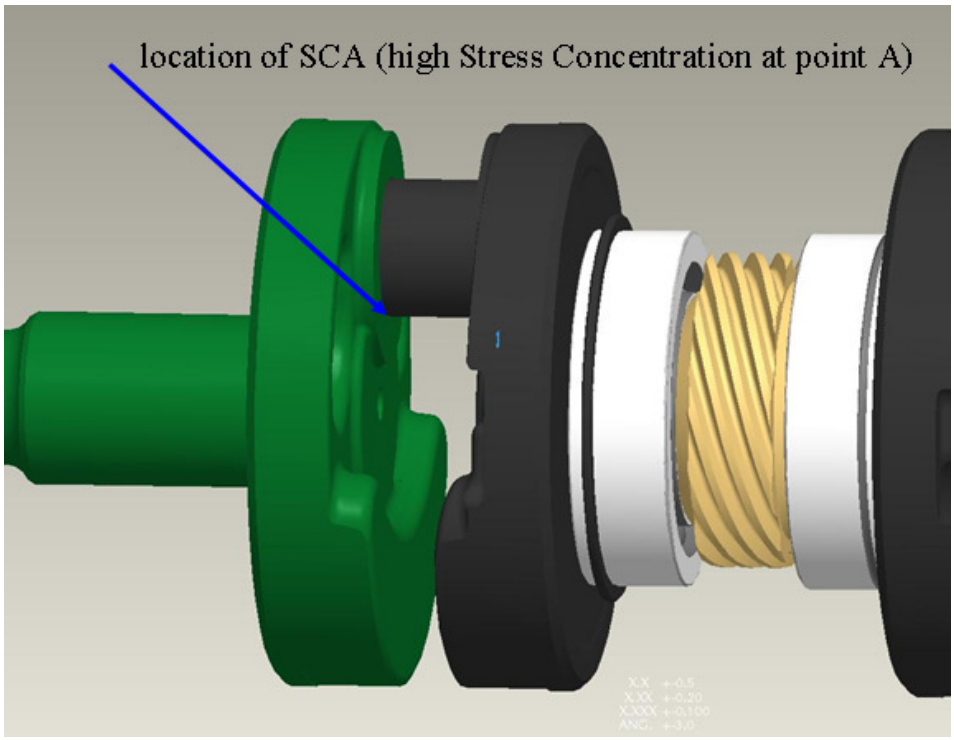

Figure 1.1.3 Components of a multi-piece crankshaft in an assembled state.

Finally, as the overall design and development process matures, the complex computer simulations may grow into easy to use design tools facilitating the design process (especially in the earliest phases). Still though, balancing the tradeoff between higher performing engines with higher output torque and the life requirements of such a multi-piece crankshaft remains a very difficult task. The requirement to be as light as possible and carry high loads for a high number of cycles only adds to the crankshaft's design challenges.

1.2 Objectives

1.2.1 General Objectives

Multi-piece crankshafts are presently of great interest to industry because of manufacturing and packaging advantages over a one-piece forged crankshaft. It allows the design of the connecting rod to be one piece, and will slip onto the integral crankpin before it is pressed into the web's cylindrical hole. A single piece crankshaft requires that this 'big end' of the connecting rod be split into two pieces, and bolted together around the crankpin. The orbital path of the 1-piece connecting rod during crankshaft rotation is much smaller than a comparable 2-piece bolted design. This allows a smaller engine case design envelop, which offers the best solution from a mass optimization perspective.

The over-reaching objective of this research is to enhance the application of numerical tools used in industry to further the durability and application of engines with multi-piece crankshaft construction. (Objective 1, minor significance) Lightweight and efficient engine design is one of the most exciting and challenging engineering problems throughout the snowmobile industry.

Historically one-piece crankshafts were designed based on the mixture of experiments and engineering formulas derived from simplified and intuitive models with high stress concentrators resulting in fatigue being the main concern. Such simplified models are not enough for the design of modern high-output engines, and so advanced numerical tools and processes have evolved to promote these designs, which may be commonly found in technical journals.

However, since the application of multi-piece crankshafts is somewhat limited in industry, there is also a lack of technical guidelines and published research on their design. In particular, design details which describe how to handle the high stress condition due to the press-fit interference are not covered adequately in the literature. Historically the press-fit was sized using the so-called Lame solution, but the stress concentration point SCA was somewhat ignored since there was a lack of understanding of the detailed stress field present. A second broad objective in this research is to assemble the engineering process and tools to calculate accurately the detailed stress field present on the press-fit joint for assembly and engine operating conditions (Objective

2, novel significance). From the start of the research project, all facets of this body of work were developed from a very limited knowledge base.

As stated previously, the design of weight efficient crankshafts necessitates more sophisticated models, which nowadays can be obtained by employing FEM (finite element method). Current methods in place for a one-piece crankshaft construction must be considered, but also these numerical methods must extend to accurately calculate the physical behavior at the press-fit joint. Contact algorithms used in the FEM model are used to capture the non-linear interaction at the press-fit joint, which require many equilibrium iterations, and do not allow the linear assumptions prevalent in the current methods.

1.2.2 Definition of Stress Field Characteristics

It is virtually impossible to create numerical tools to accurately represent a physical problem if the details of that problem are not well understood. The assembly problem including the stress concentration point SCA was first examined using commercial FEM software to understand the characteristics of a stress concentration at the press-fit. A critical objective identified here is to build the FEM model capable of handling the high stress gradient at the SCA (Objective 3, novel significance).

1.2.3 Mesh Refinement Objective Based On The Assembly State

The finite element method represents the behavior of a large object or domain by using a collection of small discrete units or elements with repetitive mathematical formulas employed throughout the entire domain. If the elements are larger than a feature in the domain, then that behavior in that feature of the domain will be lost.

Consider the press-fit joint, and the web stretching around the pin at the end of the joint at location A. The press-fit condition on the pin suddenly changes from press-fit to no press-fit, and the pin is free to expand in the radial direction. As described above, if the element size at the SCA is not refined to a point to capture this detail the stress field present there will not be calculated properly. Only an expert will not to miss these details! Since the stress gradient at the

SCA is very sharp, and occurs over a very small distance, proper judgment in model construction, mesh refinement, and convergence checking would be required in conjunction a good working knowledge of error in FEM solution. In fact early on in this research, mesh sensitivity testing was not carried out to a degree to determine convergence because such high mesh refinement was required.

Actual fatigue failures from testing may alert an engineer that the SCA point is a durability concern, while failures are common in this general location for one-piece crankshafts as well, and so this would be expected. If the assembly stress state is ignored in the FEM model, and the multi-piece geometry is considered one continuous volume, the stress state in the pin is also high when this rudimentary approach is used.

The examination of the press-fit joint assembly stresses using a 2-D axisymmetric FEM model show that the stress field at location *A* is sensitive to mesh size, to a point. If the elastic 2-D assembly solution is singular, convergence will never be achieved because the stress tends to infinity with decreasing mesh size, and elasto-plastic models are needed to get more realistic results. If the solution is not singular, then the results should be mesh-independent or converged but will only suffice if the stress is below the yield point. An objective of the research is to define the mesh sensitivity and refinement that is required for acceptable accuracy (Objective 4, minor significance). High sub-surface stress values at the stress concentration need to be understood and explained also (Objective 5, novel significance).

1.2.4 Objectives Based On 3-D Models Under Operating Loads

So far the discussion has covered only the 2-D axisymmetric solution for the assembly problem. The overall FEM analysis of the multi-piece crankshaft is organized in this research to examine both the press-fit assembly phase and the engine operating condition, which requires 3-D geometry based FEM models as well (Objective 6, minor significance).

Overall, there are three different 3-D models used in this research. First a 30 degree symmetrical slice that is consistent geometry-wise to the 2-D model was created to examine the assembly solution differences between the exact same 2-D and 3-D geometry. Next a ‘bench test’ model

using symmetry assumptions on the 3-D crankshaft geometry was created to minimize solution size. This model was created for ease of use to accelerate the numerical studies, which is also a practical requirement for any of the numerical design tools that are produced by this research effort. Finally the full 3-D geometry of crankshaft was examined with a 3-D FEA model for assembly and operating loads.

The 2-D determined mesh refinement required to predict the accurate stress fields at the SCA creates a very large 3-D model size. Since the press-fit interference between the pin and web is handled with contact algorithms, many equilibrium iterations are required with the large models to solve the difficult non-linear interaction between the pin and web. The high number of equilibrium iterations coupled with a large mesh makes only static solutions realistic for evaluation of the full crankshaft assembly under operating conditions.

To minimize model size and solution time, sophisticated meshing strategies are demonstrated at the SCA to obtain accurate and uniform results. The meshing strategies consider uniformity control for solution accuracy at the SCA, contact algorithm best practices, as well as minimization of the overall mesh size. Meshing strategy was the single biggest roadblock to complete this research. The most successful meshing strategies will be presented along with some that were not as successful (Objective 7, minor significance).

The behavior of the 3-D press-fit joint under operating loads will be defined and discussed, including the details at the SCA, in a similar fashion to the 2-D assembly data (Objective 8, minor significance). Any implications of mesh refinement on stress local maximums are detailed as well. Maximum pin stress locations at the SCA, which matched with historical fatigue failures are also tracked and discussed for several operating conditions.

Practical model size limitations for the 3-D models do not allow a mesh refinement that is present in the 2-D solution. The accuracy of the 3-D model mesh discretization will be defined for some practical limitations in the solution size. A practical real world goal for solution time is 48 hours for all 3-D models; solution times greater than this may inhibit the usage of the numerical design tools and may not add value to the design process. Detailed 2-D axisymmetric

solutions with a highly refined mesh at the SCA are extended to the 3-D domain for press-fit assembly (Objective 9, minor significance).

As described above, the model size required for an accurate solution at the SCA is simply un-usable in the time domain, and so methods must rely on a static numerical approach. To guard from potential problems caused by examination of the problem only in the static domain, steps must be taken to ensure good correlation exists with experimental data, and that the crankshaft also does not show any heightened response due to the excitation of natural frequencies. If modal excitation exists and the static solution is no longer valid, sub-modeling techniques may be employed at the press-fit joint, using inputs from a crudely meshed continuous FEM dynamic solution. (The topic of sub-modeling is only covered briefly in the discussion, and is not the focus of this research effort).

1.2.5 Model Reliability Objectives

The crankshaft is usually a high technical risk in a performance engine program, and could be a very expensive warranty issue also creating low customer satisfaction. It is an objective of the research process to develop good reliability in the overall application of CAE tools to design multi-piece crankshafts (Objective 10, minor significance). All Computer Aided Engineering (CAE) processes should have matching test components so that good confidence will be present for the CAE tasks. Numerical and experimental tools will be combined to grow confidence in crankshaft analysis.

The benefit of good CAE model reliability is extremely important to modern engineering design practice. If the FEM analysis/simulation is found sufficiently accurate/reliable then it can be treated as a virtual experiment. Such computer experiment may be done quickly and may substantially reduce the number of costly physical experiments. They allow investigating 'invisible' details and 'non-measurable' effects (such as stresses in locations inaccessible for strain gauges or under the surface). Design's weak points can be identified early and possibly removed prior to building and testing the prototype.

1.2.6 Objectives Relating To Design Rules and Tool

Modern design and development programs also require shortcuts where possible to facilitate increased design iterations to create a higher quality product for the customer. Lengthy numerical processes are condensed into ‘virtual bench tests’ so that easy to apply numerical tools may drive product design. In particular for the multi-piece crankshaft research effort, geometry symmetry assumptions are used to reduce model effort, size, solution time, and data post-processing (Objective 11, minor significance). The behavior of a press-fit joint design may be quickly evaluated with an analysis template (Objective 12, minor significance). These simplified models may be used for design studies, creation of bench tests, and optimization.

As the stress details at the press-fit SCA become well understood, geometry parameters and historical engine designs are evaluated to determine rules of thumb for application early in design. In particular design rules are also created for assembly stresses at the SCA, as an aid in fast upfront design (Objective 13, novel significance). By interpolating/extrapolating the results from such models obtained for a range of parameters some simple but accurate 'engineering' formulas (to be used as 'quick' design tools) can be derived.

1.2.7 Design Optimization Objectives

Finally, the improved understanding of the press-fit joint and the overall crankshaft behavior is leveraged to study design improvements (Objective 14, novel significance). Geometry modifications on the pin and web at the SCA are evaluated and optimized to reduce assembly and operating condition stresses. The optimization routines are made possible because of the reduced effort required to evaluate such problems since virtual bench tests, meshing regimes, and mesh size sensitivity knowledge is in place. The primary focus of the optimization in this research effort is reduction in the assembly stress at the SCA.

2 Multi-Piece Crankshaft Background Information

Basic information on crankshaft design is provided in this chapter, first beginning with some general vehicle information.

2.1 Engine–Vehicle Integration

Performance oriented snowmobiles currently have similar design architectures regardless of the manufacturer. The engine must be designed to interface with the vehicle chassis, intake, exhaust, cooling, drivetrain, and electrical systems. Figure 2.1.1 shows a typical 2-stroke engine in place in a sectioned engine compartment, detailing some of the major engine interfaces.

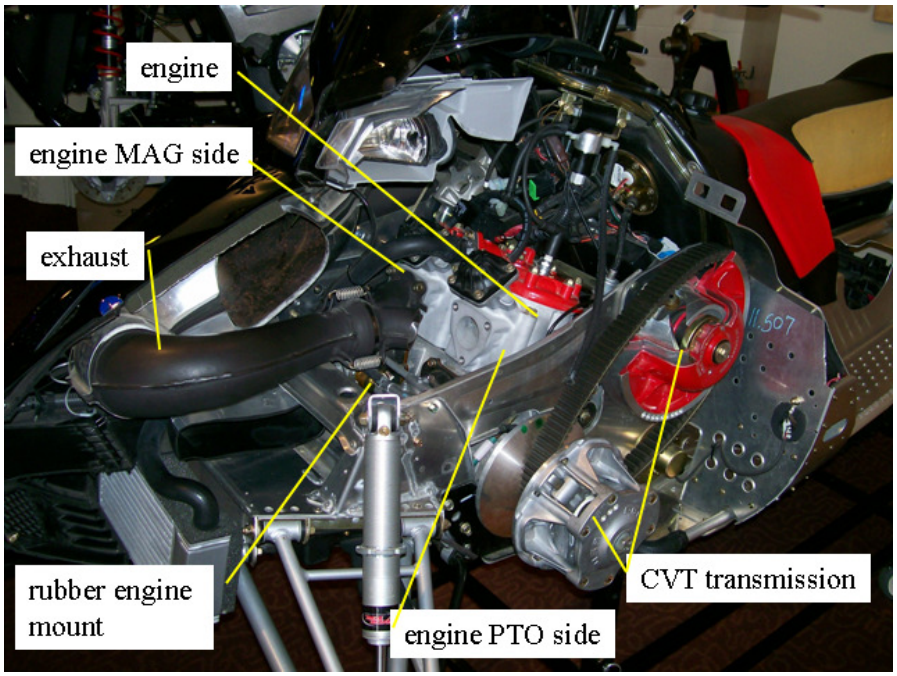

Figure 2.1.1 A typical snowmobile with a sectioned through the engine compartment.

The engine power is output to a Continuously Variable Transmission (CVT) mounted on the Power Take-Off (PTO) end of the crankshaft. Typical for snowmobile twin cylinder 2-Stroke engines, the magneto or MAG end would then describe the opposite end of the crankshaft, which contains the magnetic based electrical charge system on a flywheel on the end of a crankshaft. The use of the terms PTO and MAG are commonly extended to other nearby parts of the engine, and are referenced here for the purpose of naming convention.

Of particular interest for the structural evaluation of the crankshaft is the integration of the engine with the chassis and the integration of the engine with the rest of the driveline. The engine mounting scheme typically uses rubber 'puck' isolators, and is designed to provide good drivetrain performance, durability, and generate low vibration to the rider interfaces. CVT operational loads and the interaction of the engine's output torque and engine mounting are covered in detail later in this chapter.

2.2 Crankshaft Design Layout

Some details of the engine configuration is provide to help put the design of a crankshaft into perspective. Figure 2.1.2 shows a typical 2-stroke engine with a section cut-away on the PTO end cylinder and upper engine case. A few items are of particular interest for this research topic; first is the overall case structure, which constrains the crankshaft with bearings, and harnesses the combustion pressure developed to produce high loading on the crankshaft, which in turn produces torque output by the crankshaft. Second is the piston and connecting rod assembly which is packaged very tightly in the schematic. These components transmit the combustion forces to the crankshaft, but also impart high loading on the crankpin because of their own masses and the high velocities these components experience in the engine running condition.

The details of the components that make-up a typical multi-piece crankshaft are given Figs. 2.1.2. thru 2.1.4. A typical crankshaft is shown in the assembled state in Fig. 2.1.2, with the rod and main bearings present. Next a section view of the bare crankshaft is given so that the locations of the press-fit joints are clear (see Fig.2.1.3). The PTO outer web has a cylindrical hole in it, which the PTO inner web integral pin is fit into. The same approach is used on the MAG end of the crankshaft, as shown in Fig. 2.1.4, a reverse view of Fig.2.1.3. Four major press-fit joints are shown in Fig.2.1.4, including the press-fit joints used to fix the PTO and MAG inner webs to the main shaft. The press-fit joint of primary interest for this research is the PTO end crankpin joint between the inner and outer webs.

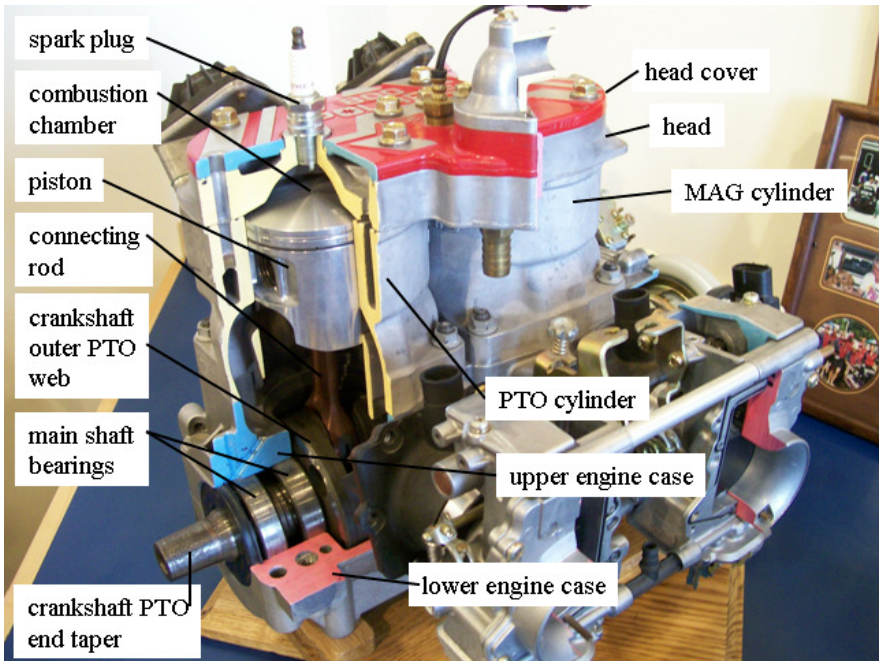

Figure 2.2.1 An engine sectioned through the PTO end case and cylinder.

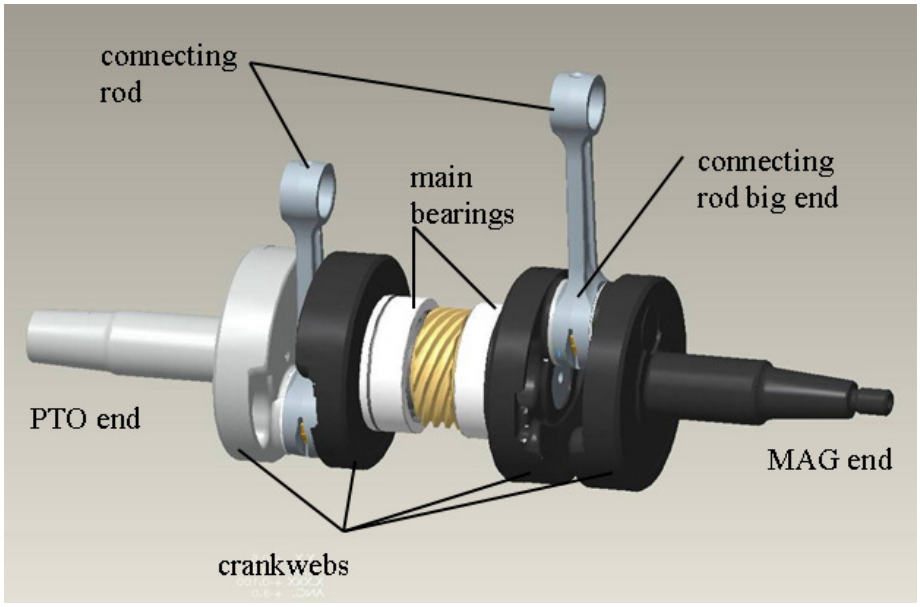

Figure 2.2.2 A typical 2-stroke twin cylinder crankshaft.

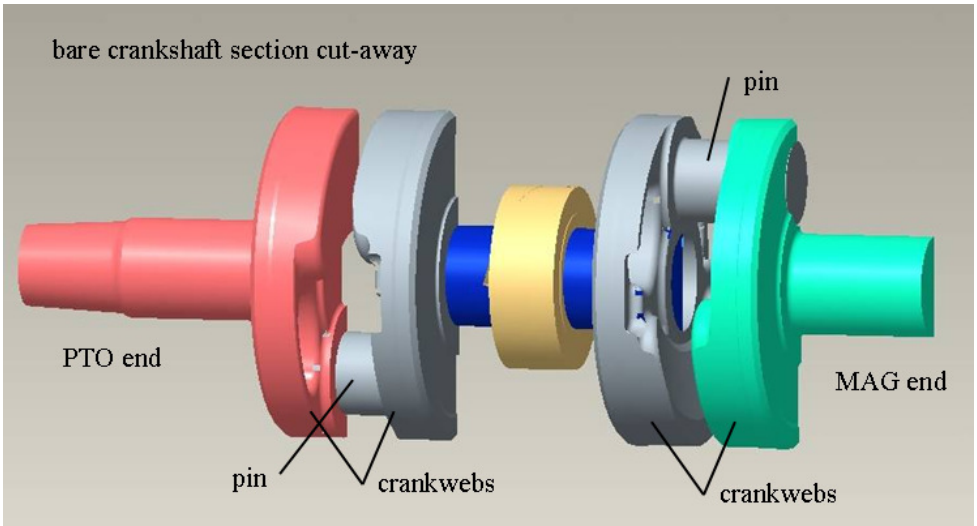

Figure 2.2.3 A bare two cylinder crankshaft with sections cut-away.

A multi-piece crankshaft construction offers the lowest mass solution both from a component perspective and a systems perspective. Prior to inserting the pin in the web cylindrical hole, the connecting rod and its bearing are set around the pin. This assembly is shown in detail in the next section. A one piece rod has a lower mass and requires less design space since it does not have a bolted joint on its big end (crankpin end). Since the connecting rod big end is smaller in size, a smaller overall engine package is also required. A close view of the section cut-away is provided in Fig.2.1.5 to demonstrate the perspective of the tight packaging present on all these components, a result of overall system mass minimization.

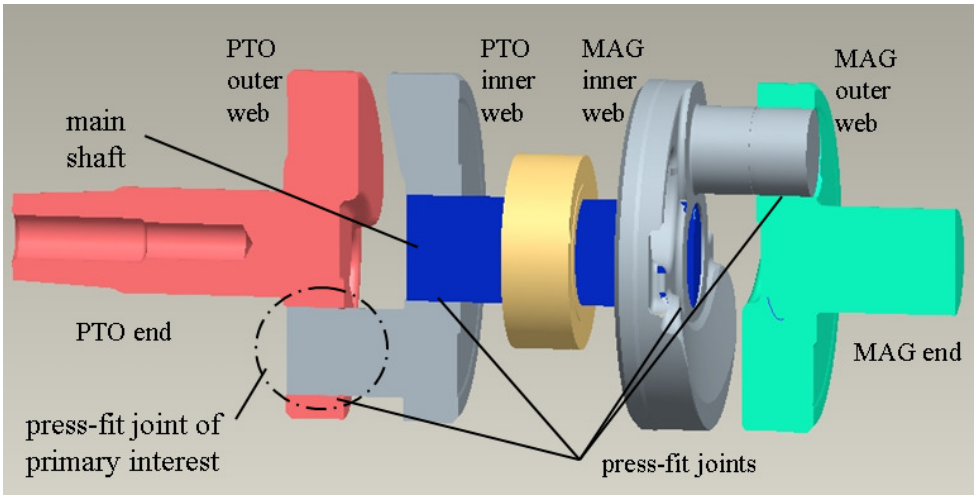

Figure 2.2.4 A reversed view of the sectioned crankshaft.

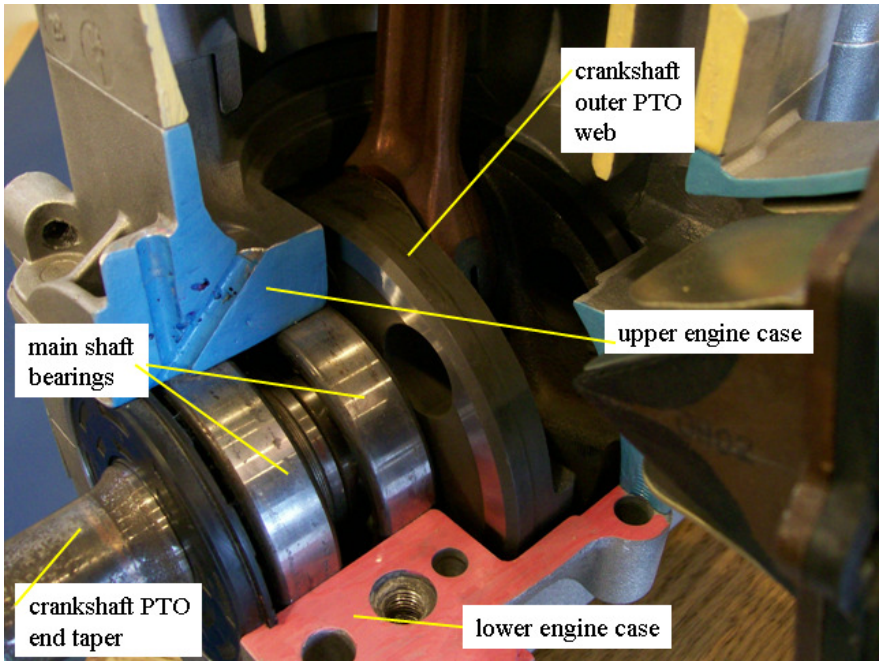

Figure 2.2.5 A close view of the section cut-away provided in Fig.2.1.1.

2.3 Crankshaft Design Approach

The crankshaft design is part of an overall design challenge, and is actually only a very small part of that effort. Figure 2.3.1 is a crankshaft design process diagram taken from [1]. The crankshaft sub-system interfaces with many other systems (engine case, cylinder, head, CVT, lubrication, electrical, etc.) and must meet design criteria for manufacturability, cost, durability, vibration, and packaging. Trading off all the design requirements of the overall engine system is a complex task. Cost and manufacturability often dictate the design solutions, include the re-use of existing expensive engine case tooling. Often this presents design challenges because of design space restrictions.

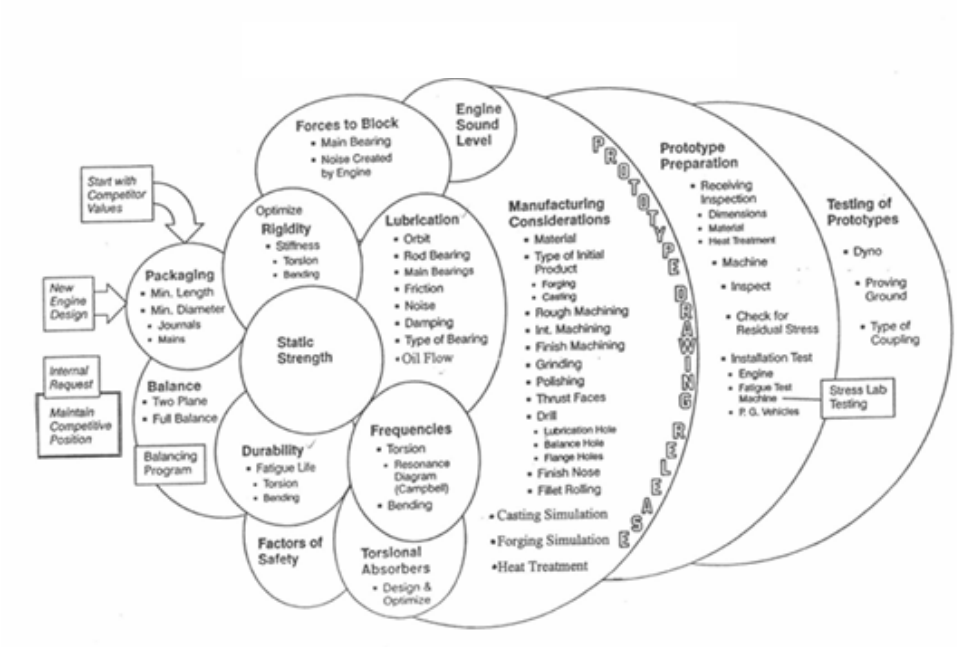

Figure 2.3.1 A crankshaft design process (from [1]).

To demonstrate the complexity of the design task, three component level design variables at the press-fit joint are examined. Figure 2.3.2 shows the pin radius r, the web outer diameter D, and web width w.

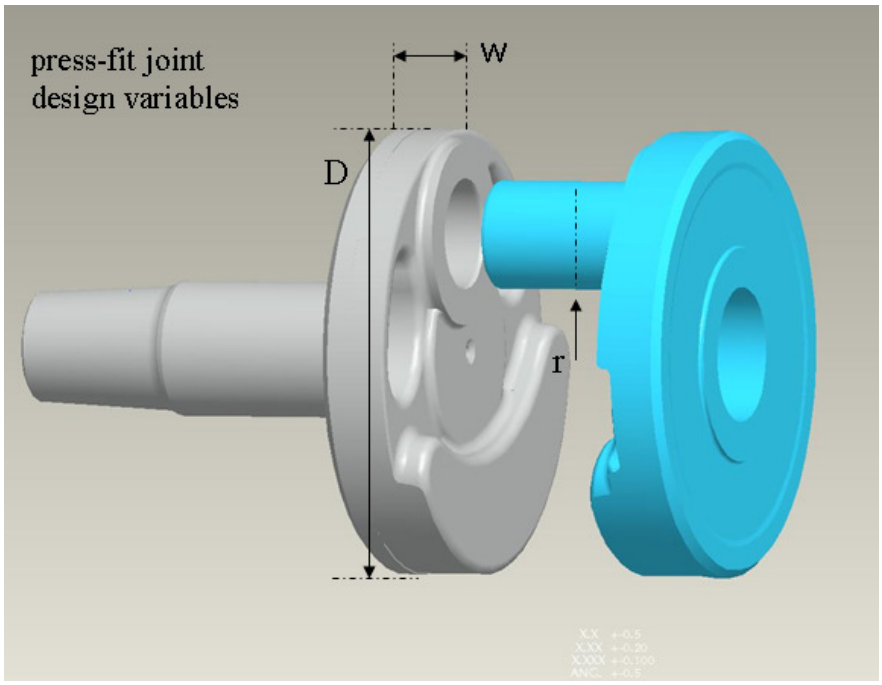

Figure 2.3.2 Design variables for the press-fit joint.

The design sensitivity of pin dimension r is shown to affect many items: torque retention of the press-fit; general pin bending (from the operating loads) and durability concerns; the modal response of the crankshaft in bending and torsion; the magnitude of the rotating imbalance; and the lower rod bearing size, durability, and packaging. The web width w needs to be sensitive to overall engine packaging width, the web bending stiffness requirement for controlling crank bending modes, imbalance, and press-fit joint torque retention. Finally the web diameter D requires design sensitivity to stresses on the top of the web from the press-fit joint; engine imbalance; overall engine packaging; connecting rod thrust washer area, etc. Therefore, to change one of these variables to improve aspects of the press-fit joint will affect many other design variables.

A design process flow chart is presented next in Fig.2.3.3, detailing the structural design approach for the crankshaft and how design tools are applied to the problem.

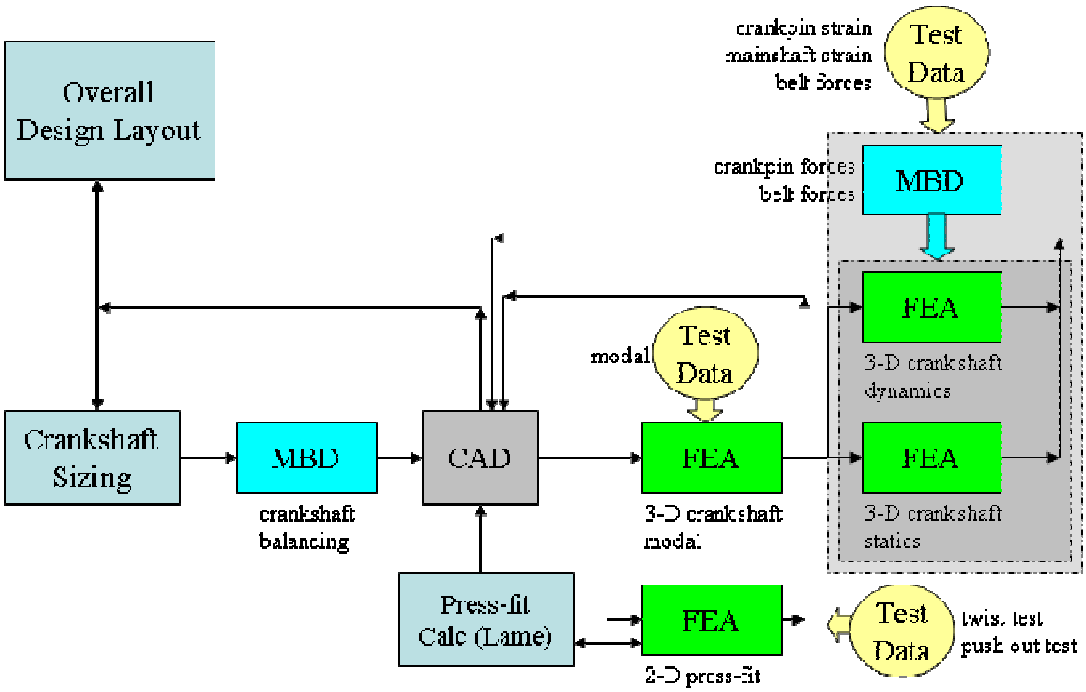

Figure 2.3.3 A process flow diagram for the structural design of a crankshaft.

The classical crankpin bending calculations are done early in the design process along with other sizing exercises (bearing capacity, packaging, connecting rod design) to compare to existing benchmarked engine parameters. The crankpin bending calculations use design load values such

as maximum combustion pressure, maximum rotational inertial loads for the reciprocating components, and the rotational inertia loads of the counter weights [2]. Pin size sensitivity is examined by calculation of general pin bending stress for the gross design loads (see Fig 2.1.9); shear moment diagrams are constructed using the design loads to calculate the pin bending moment input.

In Fig.2.3.4, the rotational inertia loads are calculated using a form of

$$F_{INERTIA} = mr\varpi^2 \qquad (2.3.1)$$

where m is equal to mass, r is equal to the radius of the throw of the crankshaft, and ω is the rotational velocity of the crankshaft about the spin axis [3].

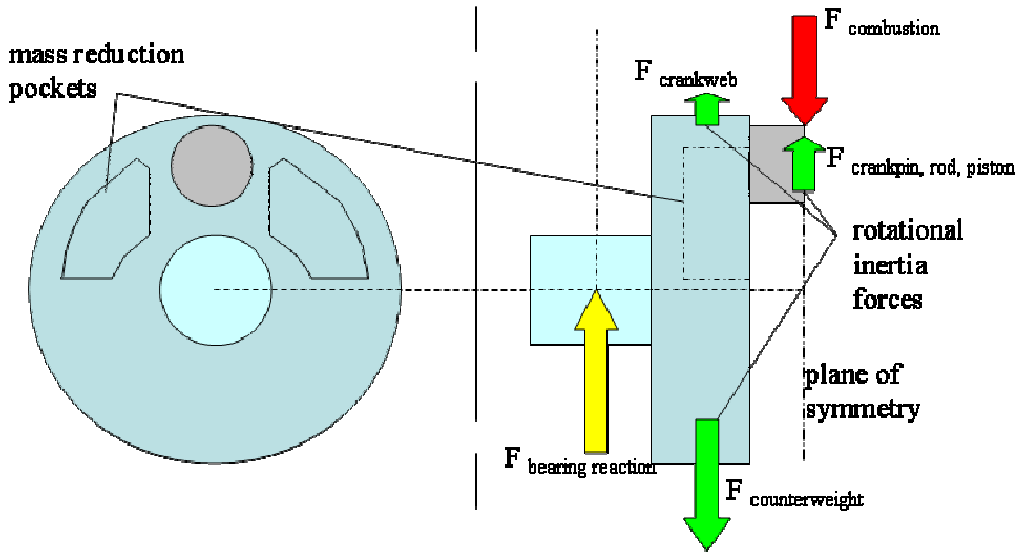

Figure 2.3.4 Crankpin bending calculation for approximate pin sizing.

The press-fit joint is initially sized using a torque retention design requirement. The value of torque the joint must carry is based on a safety factor applied to the peak torque pulse produced by the engine under the maximum power condition. As discussed in the introduction, the torque capacity of the joint is usually constrained by either 1) the assembly stress created in the pin at the SCA location, or 2) the assembly hoop stress in the thin section of material on the web directly above the crankpin. A joint without adequate torque retention capacity will result in relative motion between the pin and the web (the web 'walks' on the pin), which will lead to crankshaft failure.

The approximate average press-fit radial pressure is calculated with the Lame solution [4]. Average interface radial and hoop stresses are typically in agreement with the 2-D axisymmetric FEM model, which is a fact well covered in the literature. The details of the stress condition at the SCA are determined with the axisymmetric FEA model. Design values for the overall joint torque capacity are tested experimental with a 'joint push-out' or a 'joint twist' test, both of which are discussed in chapter 6.

Next, the overall CAD layout of the engine along with the sizing of the crankshaft by design equations, competitive benchmarking, and simplistic numerical tools would result in a somewhat detailed 3-D geometrical representation of the crankshaft in CAD.

At this stage it is very critical that the full crankshaft assembly modal analysis is performed. If any calculated natural frequencies coincide with the operating range or are spaced at a harmonic order of a critical engine speed, the design process may not go forward until an acceptable crankshaft geometry is determined for the modal criterion. Next the press-fit joint should be examined early for assembly stresses using a 2-D axisymmetric FEM model. Both of these tasks supported by experimental data that ensures quality numerical methods are in place.

After several design iterations to hit modal and press-fit design targets, fully detailed numerical models are used to evaluate the crankshaft behavior under operating loads. This numerical work may be done in the static or dynamic domain, depending on crankshaft modal targets, experience with other similar engines, numerical model size, and other technical risks. The iterative loop is completed until the stress target or fatigue life targets are met, prior to building a prototype. Again some experimental data should be available to compare to the detailed analysis work of the FEA methods. Also the FEA work should be validated later again with tests on the first prototype.

At any step in this process, the design effort may be reset back to the start because of changes required for other systems. Chapter 6 contains examples of experimental data that is used as correlation for the FEA models.

Please note that the FEA methods referred to in the structural design process in Fig. 2.1.8 are well documented in the literature review (section 3.1) and the numerical results chapters (4, 5, 7, and 8).

2.4 Crankshaft Operating Loads

The topic of crankshaft design would not be complete without some discussion on the operating loads. The basic load components present on the crankshaft are the crankpin loads, the rotational inertial load, and the CVT belt force which act on the PTO end of the crankshaft. The crankpin loads are comprised of combustion pressure force and reciprocating mass (connecting rod and piston) forces which vary with engine rotational position. The CVT belt force on the PTO end of the crankshaft is directly related to the power or torque output of the engine through the CVT. Figure 2.4.1 shows the relative position of the CVT and the resulting belt forces on the engine, in part determined by the direction of spin of the engine while running. The operating load time history information is covered in detail in chapter 5.

The engine and the engine loading environment is very complex, and difficult to represent with numerical methods. In particular, crankshaft torsional vibration coupled with the excitation of any crankshaft modes that fall with in the operating speeds are difficult to manage; the goal is always to design crankshafts with modes that do not fall within the operating range. This is not a major topic of this research effort, but is a considerable technical concern on any engine program.

The CVT loading is very complex due to both its own performance and also its interaction with the dynamic motion of the engine. The CVT consists of a primary and secondary clutch, for which belt position changes with speed and torque output. The primary clutch mounted on the PTO end of the crankshaft changes belt position with increasing engine speed. The secondary clutch, which is (see Fig.2.4.1) the next mating transmission element in the drivetrain, has a radial belt position that is sensitive to torque.

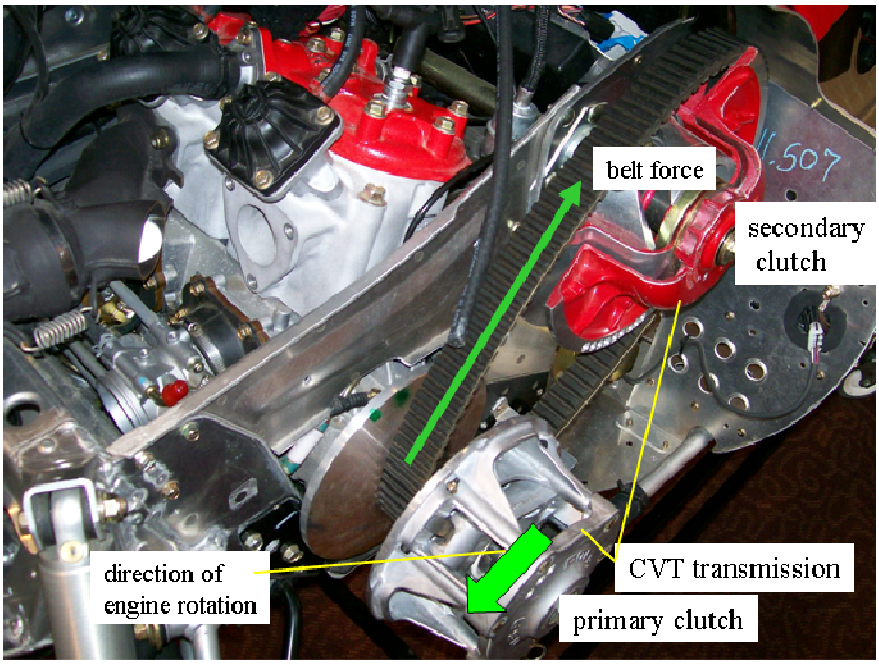

Figure 2.4.1 Belt forces the CVT places on the engine are described.

The transmission system works on the principle that belt position changes on each clutch to create the desired output ratio. For low engine speed / high torque conditions, the belt is 'low (small diameter)' on the primary clutch and 'high (large diameter)' on the secondary clutch, producing a low transmission ratio. And in the case of the high engine speed / high torque condition, the belt is 'high' on the primary clutch and 'low' on the secondary clutch, producing a relatively high transmission ratio.

Belt forces calculated for the crankshaft analysis assume a steady state position of the CVT, and are correlated to some degree with experimental data. When the CVT is not in a steady state, the loads are changed very quickly and it is a very dynamic environment to examine numerically. For this research, a reasonable simplification of the duty cycle for the engine would place the CVT at steady state.

To add to this complexity, the engine is typically mounted on rubber isolators for reduction of vehicle rider vibration as discussed earlier. The engine moves rigidly on these soft rubber mounts because of engine shaking and engine torque and imbalance loads. Since the distance between the primary and secondary CVT is not fixed there is relative motion between them as

the primary clutch moves with the engine (shaking), while the secondary clutch is attached to the chassis. Obviously the belt force from the CVT will then interact with the dynamic motion of the engine. High fidelity Multi-Body Dynamics (MBD) models are required to calculate accurate belt loads.

Finally, the customer usage of the performance engine was noted in the introduction section as aggressive and abusive. A typical endurance test duty cycle for a performance engine is described in Fig. 2.4.2 by engine speed (versus time) and in Fig.2.4.3 by normalized power output (versus time) [5]. This single cycle is repeated until the engine surpasses the validation time target. During the cycle the engine remains at speeds or conditions which create the highest damage in the engine systems to accelerate the testing.

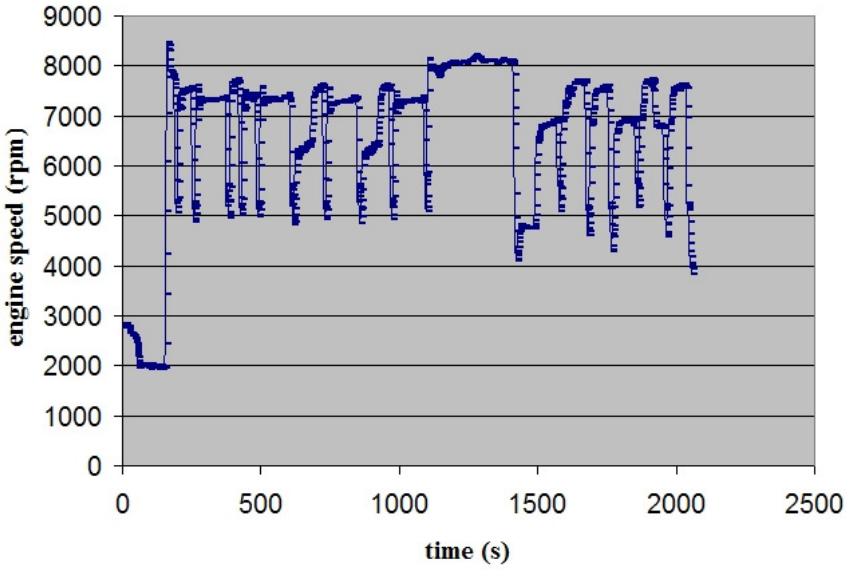

Figure 2.4.2 A typical engine duty cycle; engine speed versus time.

The duty cycle is usually specific for each engine, and is determined by actual customer usage profiles. Note that in the example provided, a significant portion of the test occurs between 7,000 and 8,000 rpm. This duty cycle suggest aggressive use of the engine, and would represent the extra abuse a performance oriented engine would see for a typical customer. Insight into the customer use of the engine, or the validation duty cycle is ideal when the engineer must select a fatigue approach or stress target for design.

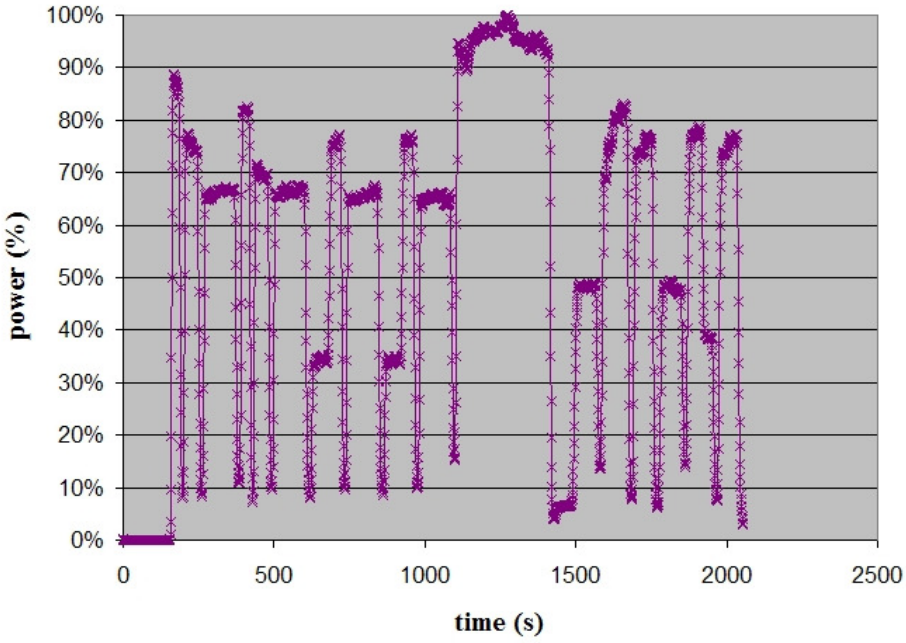

Figure 2.4.3 Normalized power versus time for a performance engine duty cycle.

2.5 Crankshaft Assembly Methods

Finally, a brief overview of the assembly process used for multi-piece crankshafts is provided. Prior to the assembly, each forged component is machined to high tolerances for best system level tolerance stack-up and crankshaft straightness. In particular the machining operation for the bearing surfaces, and the pin and the hole in the web for the press-fit joint are critical to the design.

After machining the crankshaft pieces are ready for assembly. Figure 2.5.1 shows a partially assembled crankshaft set in a fixture, ready for the PTO inner web to be pressed on the main shaft. A hydraulic press is used to force the web onto the main shaft, by overcoming the friction in the press-fit joint. Center main bearings and a gear are already shown assembled at this stage. The crankshaft is secured in a fixture, which provides support in the axial direction of the crankshaft (the direction the press exerts force in), and holds the crankshaft from rotation about its center axis. The PTO inner web is shown assembled onto the main shaft in Fig.2.5.2.

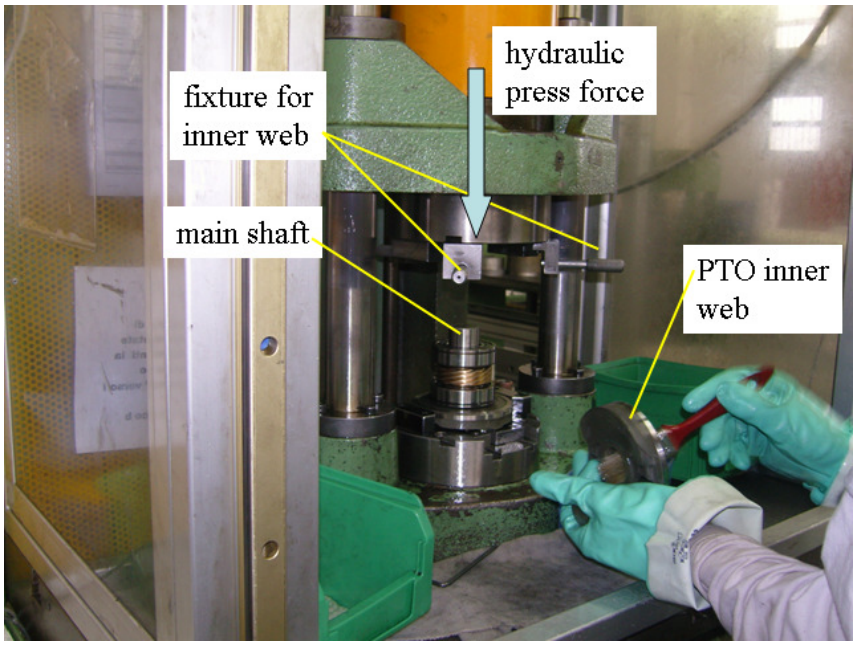

Fig. 2.5.1 PTO inner web prior to assembly onto the main shaft [6].

After all components of the crankshaft have been pressed together, the crankshaft is measured for proper alignment. For crankshaft that fall outside of the tolerance range, effort is taken to straighten these to within acceptable limits. The crankshaft may be 'hit' in the appropriate location and direction with a rubber mallet, causing the crankshaft to move or re-align at the nearest press-fit joints. The crankshaft may also be 'pinched' at the counterweights, on the opposite side to the crankpin, using large tongs, which also causes the crankshaft to move or re-align itself at the nearest press-fit joint. The straightening process requires some operator skill and experience when employing either the hit or the pinch tactic.

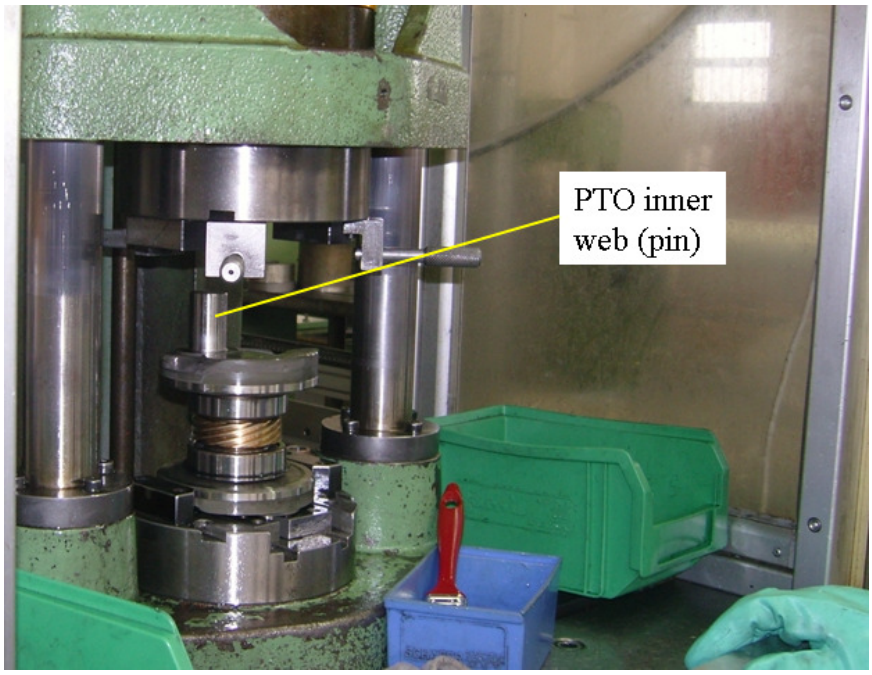

Fig. 2.5.2 The PTO inner web assembled to the main shaft [6].

Some comments should be provided about the assembly stresses created by any mis-alignment. A numerical evaluation of this problem most practically always considers perfect geometry and ideal insertion direction. What sort of stress conditions are created when the pin is inserted into the hole with the pin at a very small angle with respect to the hole axis? Deviations from the perfect case almost certainly occur in a manufacturing environment, with slight assembly differences. However, because of the violent nature of the operating condition and the vibrations it induces in the crankshaft, and because of the symmetrical nature of the press-fit joints present on a typical crankshaft, it is thought that the crankshafts press-fit joints naturally try to relieve any axis mis-alignment to maintain a symmetrical shape. FEA 'perfect assembly geometry' assumptions are thus noted and considered more practical than first thought.

3 Literature Review and Theoretical Background

3.1 Literature Survey

Current crankshaft numerical methods are challenging the boundary of software engineering tools and computer hardware limitations. As engineering tools and computational technologies grow, the techniques applied need to push the boundaries, but also still need to supply rapid feedback to affect the design cycle.

3.1.1 General Numerical Methods For The Design Of Crankshafts

Prior to an examination of any previous research in the area of multi-piece crankshafts, a review of the current state of numerical tools applied to crankshaft design is supplied for the context of this research.

Common numerical practices exist in the design of crankshaft systems, which are in constant evolution because of advances in engineering tools, engine design, and customer expectations. Improvements in commercially available engineering software (typically based on FEM methods) and the advancement of the computational ability of the desktop computer hardware have alone made great strides in the last 20 years of development. Commercial FEA software may be easily parameterized, so that tasks may be automated and analysis methods may be easily captured. Economic desktop computer hardware will readily handle large FEA problems over short time periods that previously required expensive super-computing facilities. Certainly the numerical methods presented in this research will be viewed differently after the next 20 years of computational development.

Initially, desktop computers were most suitable to run Computer Aided Design (CAD) geometry drawing packages that were available commercially for engineering and research. Classical design calculations were used to size the crankshaft structure, based on the geometric layout created in CAD [7]. The crankshaft pin and web sections (width, height, diameters, center of gravity value) taken from CAD measurements were finalized by free body diagrams, static bending moment calculations, as well as other design requirements [8]. Crankpin and main shaft fillet radii were sized using stress concentration factor tables. Geometry CAD iterations closely followed the structural calculations by hand to create a crankshaft of adequate design.

Obviously these classical design methods at some point were captured in computer software based mathematical spreadsheets. At this point the design formulas are calculated in a computerized format, and become easy to share with other design engineers or researchers. (A survey of crankshaft numerical design methods over time shows that this idea will repeat itself.)

In a similar fashion, the early implementation of FEM was applied in a simplistic manner to crankshaft design. Beam element formulations were used to calculate general pin bending stress for complex multi-cylinder and multi-input static load cases. Dynamic evaluation using FEM based beam elements soon followed, which examined crankshaft bending and crankshaft torsional loading [9]. Early commercially available FEM crankshaft design tools [10] employed these methods, and provided reasonable quick evaluation early in the design process, as the design input was readily parameterized and automated [11]. These software tools typically evaluated the dynamic response of the crankshaft in the time or frequency domain using modal super-position [10]. Note though that a detailed understanding of the crankshaft displacement and stress field is lacking in this approach. General pin bending and general structural deformations would be available, but detailed stress field information on the crankshaft would not have been understood. So, fillet radii values most likely would still have to use stress concentration tables to set the design value.

The early application of FEM solid element formulations to crankshaft design would have been limited in scope because of model creation time and computer hardware capability (solution time would be long [9]). FEM geometry creation or FEM mesh creation pre-processors would have been (manual) cumbersome and time consuming to create anything but a crude simplified crankshaft geometry [12].

Improvements in commercial FEM software allowed the import of crankshaft geometry from an external CAD package. Solid element automatic meshing algorithms progressed to a point to empower engineers to reasonably examine complex crankshaft geometry, allowing true 3-D design and optimization. FEA model and solution size was an obstacle though that required constantly improving computational resources. Improved computing finally allowed the

calculation of the previously un-available detailed stress fields for the multi-phase load environment of the engine, using static load assumptions.

At this stage in development of the crankshaft analysis tools, engineers were able to employ a form of the classical crankshaft design approach. Complex load calculation by classical techniques or by computer simulation along with engineering intuition was used in conjunction with high quality (geometry) 'CAD driven' FEA models. This analysis would have followed the architectural layout of the crankshaft using the more simplistic beam element tools, and would use knowledge of the detailed stress field to confirm the selection of the proper crankshaft architecture. Crankshaft design and optimization likely has progressed at a faster rate since the engineering tools reached this level of maturity.

Crankshaft FEA solutions in both the static and dynamic domain may be calculated; each with advantages and dis-advantages. Static solutions require less computational effort, and so may examine the crankshaft geometry with greater mesh refinement. The post-processing of data for a static model is also less demanding than for the dynamic evaluation. Research by [12] shows that the design margin of a crankshaft using a static approach is calculated at a lower value than when dynamic methods are used.

Static solutions are not adequate though when the crankshaft dynamic response is altered by interaction with natural frequencies of the crankshaft or other components of the drive-train system[13,14]. A good practice for any crankshaft design effort includes the FEM based modal calculation of the crankshaft natural frequencies, to check for modes that fall within the engine operating range. Dynamic analysis methods must be used for a crankshaft with natural frequencies that fall within the operating range. Figure 3.1.1 shows the dynamic displacement response of an in-line 4-cylinder crankshaft across a band of operating speed with a marked increase in response near 4200 to 4400 rpm [15]. Crankshaft modes are excited at this engine speed, and create much larger displacement responses.

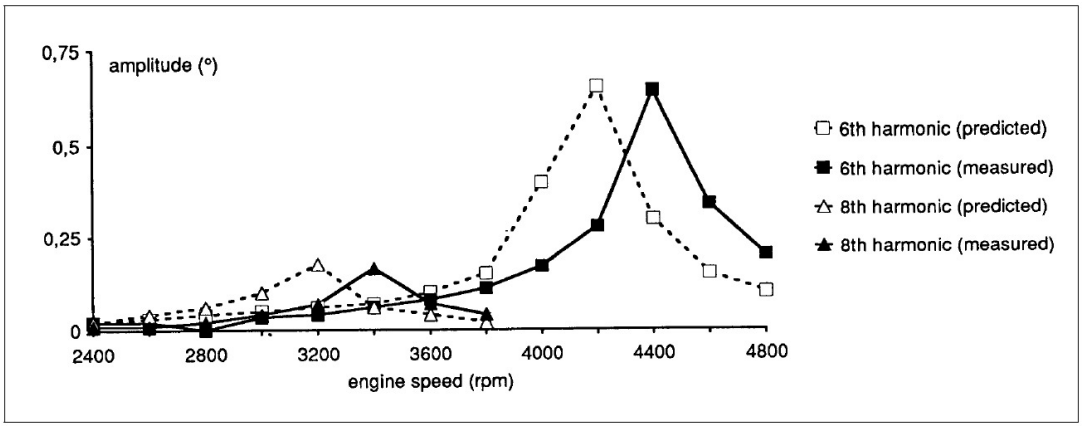

Figure 3.1.1 The displacement response of a crankshaft excited by natural frequencies [15].

When dynamic solutions are required, typically a crude FEA mesh is used to predict the overall behavior [12]. Solution time for a moderately meshed model (which has a linear material) using modal super-position can extend from 24 to 48 hours on a workstation class desktop computer to solve for 8 to 10 complete cycles of the engine.

If detailed results are required that are not captured with this crude model, sub-modeling methods may be employed. Sub-modeling works on the principle of capturing the boundary conditions of a segment of the FEM model behavior with a global crude mesh, and using these boundary conditions for a detailed model of the area of interest (see Fig.3.1.2). Several examples of sub-models exist in the literature; sub-models have been used for detailed stress evaluation [15] as well as locally employing non-linear material behavior or assembly stresses. Dynamic solutions that use modal super-position are linear in form, and therefore a sub-model could be used to model a local non-linear behavior.

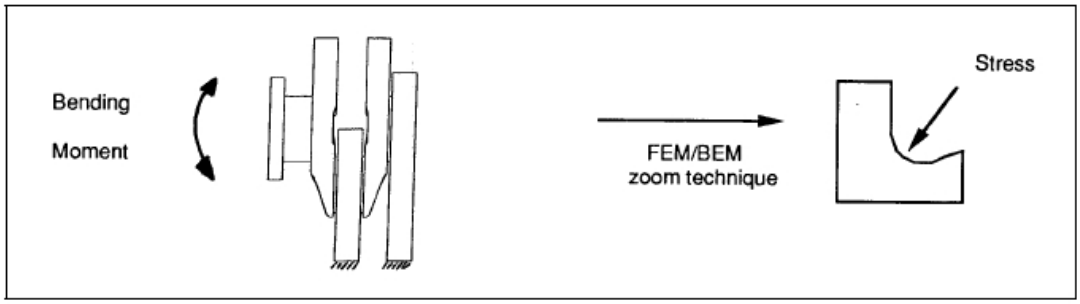

Figure 3.1.2 Sub-modeling technique for the detailed local examination of a global crankshaft FEM model [15].

For example, Henry et al [15] used 3-D geometry of the crankshaft and an elastic material assumption to calculate the response of the crankshaft (an in-line 4 cylinder diesel-Renault) considering inertial, combustion, and vibratory loading. The crankshaft response was calculated using a crude but efficient FEM mesh, and then the details of the stress field at the fillet radius between the pin and web were examined with a BEM / FEM approach. The boundary of the local FEM model was determined by the crude FEM system model.

In summary, numerical tools have been used in abundance for crankshaft design evaluation. Both static and dynamic analysis methods are routinely employed. Dynamic evaluations for the full 3-D geometry of a crankshaft system mostly use linear dynamic methods. Obviously non-linear methods would be required to model the interaction of the press-fit joint for a multi-piece crankshaft; highly refined meshes at the press-fit interface are required that use contact algorithms and a large number of equilibrium iterations. For a large model these iterations would be lengthy, and would not produce data in a time efficient manner, and therefore would not be a realistic design tool. Static crankshaft analysis has been shown to be a successful but conservative design tool, only if the crankshaft natural frequencies are out of the operating range of the engine [9]. Since data post-processing and evaluation will be very important in the examination of multi-piece crankshafts, static methods seem ideal as a first step. The conservative nature of a static analysis can be reduced by setting aggressive (low) safety factors through the evaluation of similar designs that have shown adequate durability.

An alternative approach to evaluating the press-fit joints in a multi-piece crankshaft may be to use linear dynamic models to capture the overall behavior of the crankshaft, and employ sub-modeling techniques to examine the press-fit joint. This approach assumes a continuous volume at the press-fit joint, and that any change in the press-fit joint stiffness with respect to load is minimal. This approach is the most costly from a solution standpoint (versus a non-linear static evaluation), as there are two significant numerical problems to solve. This approach is also more complex; there are more steps to execute and it would be viewed as a more cumbersome design tool.

In final then, the non-linear static approach is the first choice because of advantages in solution time, data post-processing, and ease of use. A sub-modeling approach would be warranted if a dynamic solution was required to accurately predict the crankshaft operating behavior.

3.1.2 Numerical Methods For Multi-Piece Crankshaft Analysis

Research has taken place studying the general behavior of the press-fit joint specifically for a multi-piece crankshaft [16]. The goal of this work was to create analytical formulas that could be used early in the design phase to predict the radial contact pressure for the joint and the circumferential (hoop) direction stress in the web. The radial contact pressure was required to size the joint for adequate torque carrying capabilities, and the hoop stress calculation for the web was required to design within a safe limit with respect to the yield point of the material.

The analytical equations were compared to a plane axisymmetric finite element solution; among the three included analytical solutions was the classical Lame' solution, which was indicated as inadequate because it does not capture any variation in the stress field in the hoop direction [17]. The typical crank-web geometry is assumed to a circular disk with an eccentric hole. Radial contact pressure uniformity is shown to be less sensitive to the eccentricity of the hole in the web, while the hoop stress variation in the web is very sensitive. The circumferential stress is shown to be not uniform, and depends on eccentricity of the hole in the web; as the hole gets closer to the edge of the web, higher stress values are obtained at the thinnest section of the web.

A brief synopsis on a 3-D numerical model of the press-fit problem is also given. The authors noted that at the extremity of the contact, where the pin protrudes from the web, theoretically infinite pressure peaks occur which are reduced by local material yielding. There is no indication of any geometric shape on the interior edge of the cylindrical hole in the web, and so it is assumed a 90 degree corner. Also, there is no data provided for distribution of the stress field calculated. The 3-D and 2-D models had good correlation in average stress values calculated.

Finally, [16] noted that the 3-D FEM assembly solution of a press-fit joint produced a rotation of the crankpin axis with respect to the main shaft axis, as shown in Fig.3.1.2.1. Differences in the web hoop stretch across the joint occur, as the side at which the pin protrudes out is stretched

more by the additional pin stiffness there. It is noted that a 3-D finite element model is required to calculate this pin mis-alignment produced by the press-fit. In is the experience of the author that any changes in the web stiffness by the introduction of pockets (which also affect rotational imbalance) near the press-fit joint may affect and compensate for pin mis-alignment due to the press-fit.

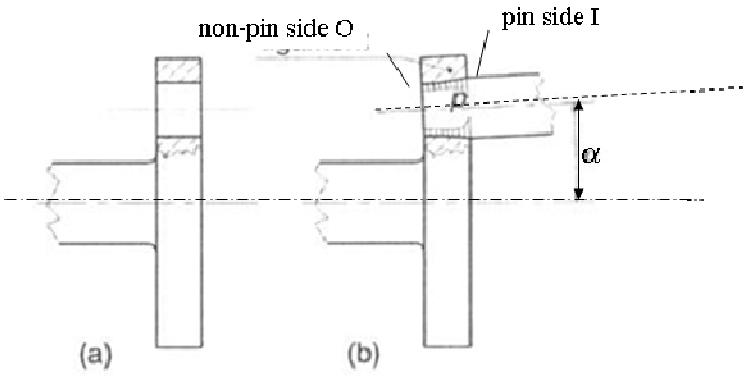

Figure 3.1.2.1: Pin mis-alignment (α) caused by the unequal stiffness; the web on the pin side I stretches more than the non-pin side O [16].

3.1.3 Numerical Studies Of Press-fit Joints Used In Other Applications

Little research work can be found on the numerical modeling of the multi-piece crankshaft press-fit joint. Press-fit or shrink-fit joints are used commonly in the construction of a locomotive axle, to fix the wheel / hub to a shaft. Research in this application of press-fit joints is more common; but the geometry solutions examined tend to be slightly different, and not as numerically challenging as the crankshaft situation. The design space available for the hub of the locomotive wheel tends to not have the premium on space that a high-performance engine has. Therefore, stress relieving features on the hub may be used that may not package easily in an engine, and also may create a weight penalty throughout the entire engine, by making the press-fit joint larger and subsequently stretching the engine case.

Research of particular interest by White et al [18] focused on the examination of several joints that would remove or reduce large axial strains created on the shaft, just beyond the interface between the plain hub and shaft. As is the case for a crankshaft, bending stresses in the shaft (the

locomotive axle) combined with any tensile axial stress concentration due to the press-fit joint are un-desirable and lead to early fretting fatigue failures. In [18], fatigue cracks are indicated to initiate just inside the hub seat surface, and are thought to originate from a combination of the high (mean) axial tensile assembly and (alternating) bending stresses combined with fretting wear.

White et al [18] identify that the high radial stress at the start of the hub seat or press-fit led to large tensile axial stresses on the free surface of the shaft, but do not discuss the mechanisms. An axisymmetric FEM model shows high stress components leading up to the plain hub joint (see Fig. 3.1.3.1), but does not solve for the large stress components across the end of the press-fit. It is not apparent whether a sharp corner is present on the end of the hub bore, or whether a fillet radius or triangular chamfer finish is used. A radial displacement plot (Fig. 3.1.3.2) across the area of interest shows a non-continuous change in the shaft outer diameter, which would indicate a stress singularity. The authors suggested that there is error in the solution exactly at the end of the 'seat' and did not quantify further the details of this geometry case.

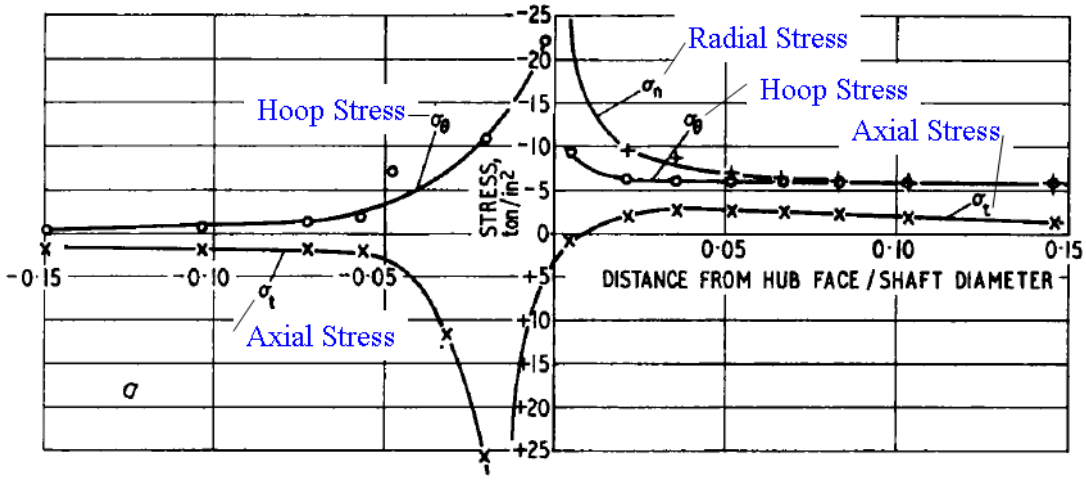

Figure 3.1.3.1: Shaft outer surface stress components at the press-fit joint for a plain hub and shaft on a locomotive axle [18].

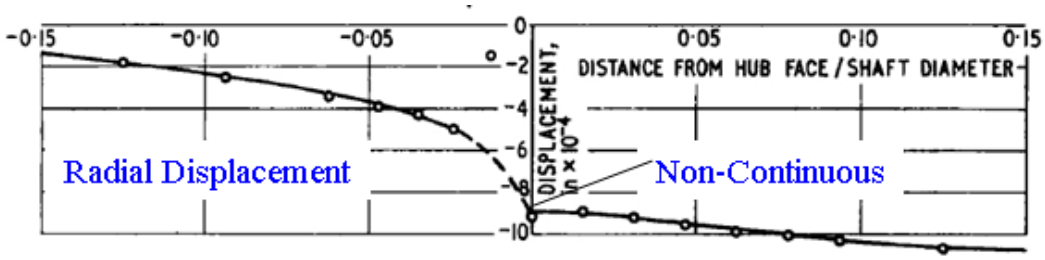

Figure 3.1.3.2: Shaft outer surface radial displacement at the press-fit joint for a plain hub and shaft on a locomotive axle [18].

The research paper [18] does not reference any comments on the shear stresses and their influence in the problem. A 'lubricated' surface friction was assumed as the surface of the press-fit, with a co-efficient of friction equal to 0, as it was deemed that any surface friction was not high enough to resist the axial growth in the problem created by the high radial pressures and Poisson's ratio.

Fillet radius and groove features were added to the shaft and studied with the same axisymmetric FEM modeling approach (see Fig.3.1.3.3), and it was shown that desirable compressive tensile stresses may be added to the shaft surface just outside of the press-fit. A fillet radius proved to be more effective at this, while the groove approach still created a maximum tensile stress from assembly at the base of the groove, which also happens to be the location of maximum bending stress. An over hang geometry for the hub may move this local maximum slightly further along in the groove away from the hub. These details will be compared directly in Chapter 8, Optimization.

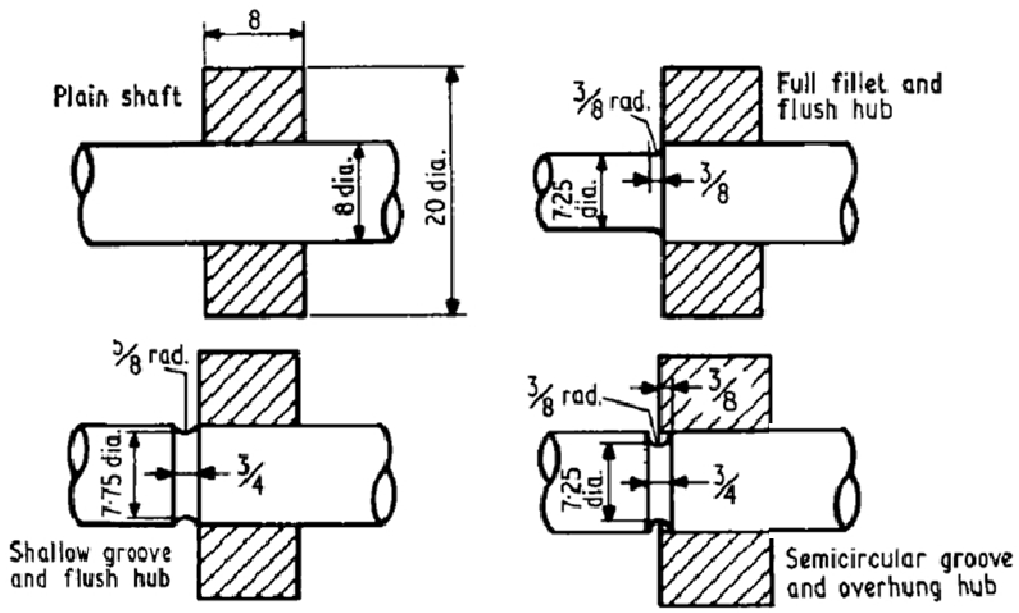

Figure 3.1.3.3: Hub and shaft assemblies considered in [18] for FEM evaluation.

Finally, White et al [18] comment on the addition of bending loads, from the wheel, into the press-fit joint. It is speculated that the addition of bending loads will be super-imposed on the assembly stresses, and that this will cause an equal un-loading and loading of each opposite diametrical corner pair of the hub internal surfaces. This point will also be demonstrated in this research body.

Note there are distinct differences in the load path between the crankshaft and locomotive axle. For a crankshaft application the pin subjects the web to bending loads induced by the combustion forces and the reciprocating (piston) inertial loads. The web also contains a counterweight that is opposite in position to the crankpin, which inputs bending loads back into the pin as the engine rotational velocity increases. Crankshaft torsional loading also needs to be carried by the press-fit joint. For the case of the locomotive axle, the wheel hub puts all the loading (bending and torsion) into the axle.

Kanber [19] uses Boundary Element and Finite Element Method solutions to examine a shaft on hub set of interference fit problems. Four types of interference problems are examined including a ring on a solid disk, a hub on a shaft, a hub on shaft with a shoulder, and a hub with a groove

on a shaft (see Fig.3.1.3.4). Axisymmetric models are used to study the variation in radial interface pressure along the shaft axis. The BEM and FEM solutions are in agreement, while the BEM solution has greater computational efficiency.

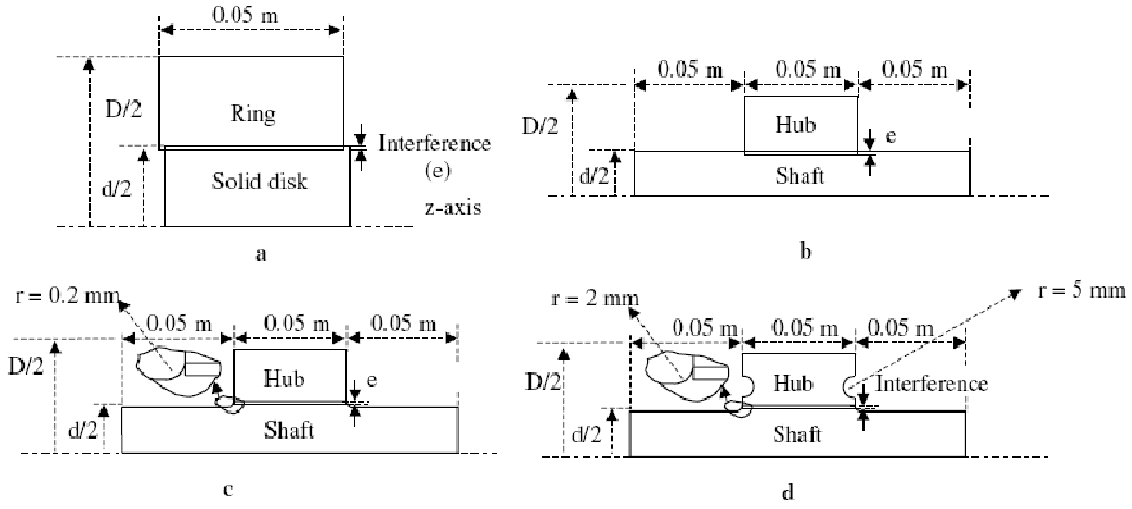

Figure 3.1.3.4 The four sets of hub on shaft geometry problems evaluated by [19].

Interesting comments are given regarding the 'hub on a shaft' design. The hub geometry considered had a 'sharp' corner on the edge of the hollow inner cylinder, causing what is described as stress deviations on the shaft. A stress concentration is acknowledged, and this location is cited to initiate fatigue failures for the loading cycles studied. Figure 3.1.3.5 plots radial interface pressure along the hub inner surface, showing a sharp rise in stress at the corner of the hub. No geometry definition for the 'sharp' corner or the mesh details there are provided in the research paper.

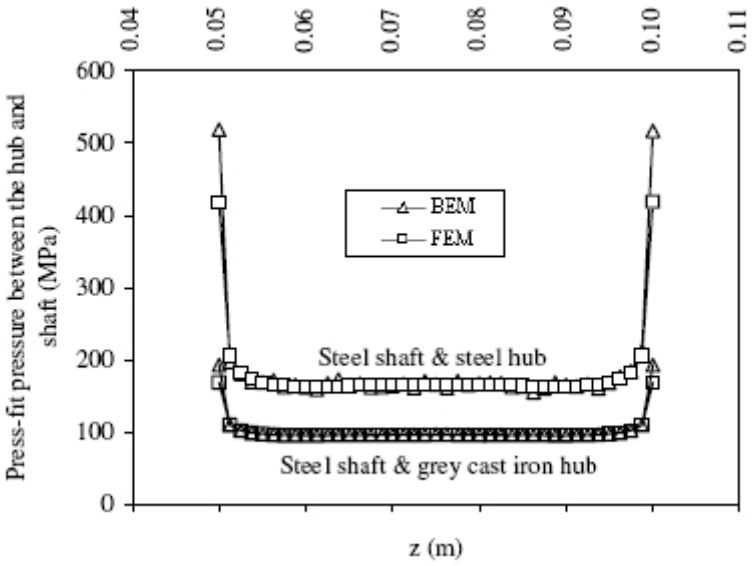

Figure 3.1.3.5: Radial interference pressure along hub inner surface from [19] for a hub with a 'sharp' corner.

The last two solutions explored, which use a shoulder and groove respectively, are relevant solutions to reduce the stress concentration present in crankshaft press-fit assembly, as shown in Fig.3.1.3.6. These groove and shoulder designs are shown to reduce the stress concentration of the sharp shoulder are similar to those explored by [18].

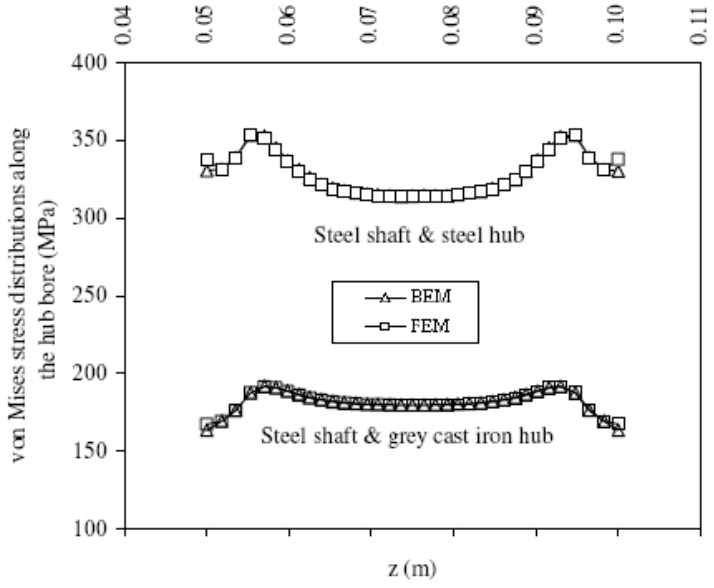

Figure 3.1.3.6: Radial interference pressure along hub inner surface from [13] with a groove.

Makino et al [20] also published research in the examination of a rail wheel hub pressed onto an axle. The goal of the research was to evaluate different round profiles on the edge of the hub using FEM and rotating bending fatigue tests. Figure 3.1.4.7 shows the axle assembly, while Fig. 3.1.4.8 shows the FEA modeling approach, which uses a one-quarter symmetry assumption. The mesh size at the SCA area appears to be relatively coarse.

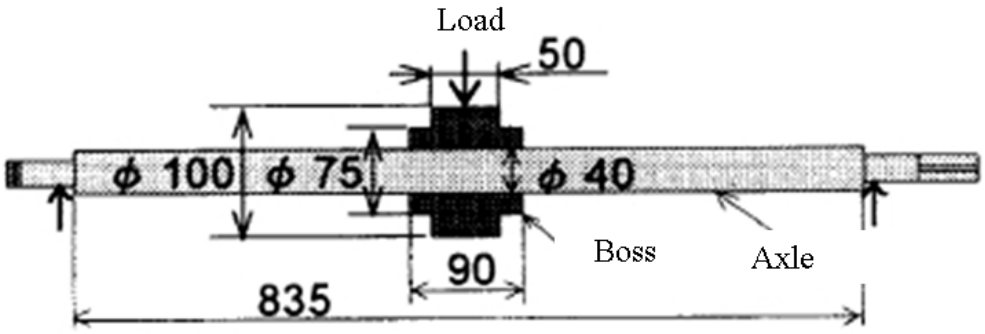

Figure 3.1.3.7 The rail axle press-fit assembly from [20].

(a) Whole view

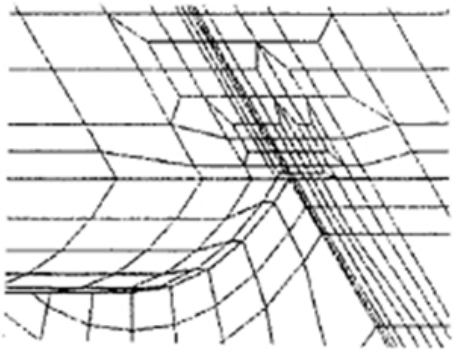

(b) Near contact edge

Figure 3.1.3.8 A one-quarter symmetry 3-D model from [20].

Three geometry cases were considered at the ID of the hub edge, a small radius, a large radius, and no round. Figure 3.1.4.7 plots radial stress on the axle surface across the 'equivalent SCA' area for the three geometry conditions. As the radius increases, the location of maximum stress is shown to increase and move inboard. This phenomena will be demonstrated in several instances in this research. The radial stress at the edge (x equals 0 in Fig. 3.1.4.7) is shown to increase at a higher rate for the 'no round' geometry.

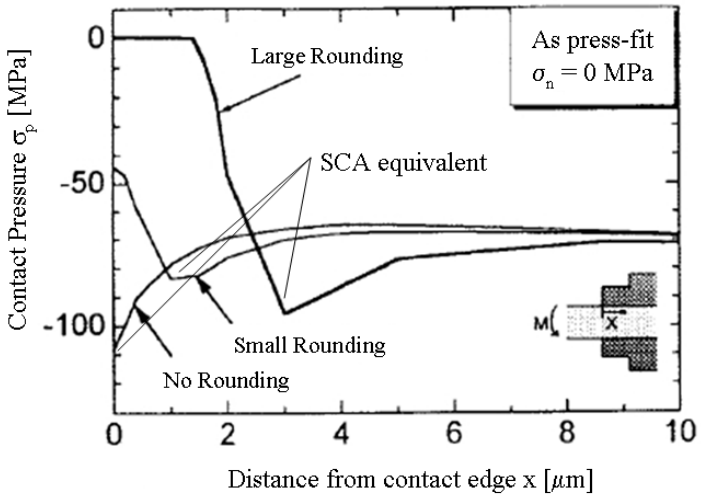

Figure 3.1.3.7 Radial stress at the 'SCA equivalent' location for three different geometry press-fit options [20].

Figure 3.1.3.8 shows the same radial stress distributions but includes the assembly plus wheel bending load; the model results are given for the 'tensile' side of the bending load input. The radial stress curves are shifted positive, indicated that the high radial stress from assembly is 'unloaded' as the bending load is input, another facet that will demonstrated in this research body. Note that the 'no rounding' edge finish curve has changed drastically in shape with the addition of the bending load, and the sharp concentration present at x equals 0 has been eliminated. It is interesting that the bending load curve remains approximately flat or linear. It would be fair to observe that the coarse mesh discretization present in the model has some effect on the stress curve continuity and likely the local maximum values calculated.

Axial stress plots across the axle OD at the area of interest are repeated for the assembly condition in Fig.3.1.3.9 for the three geometry cases. Note that the assembly maximum tensile

axial stress values are shown to increase slightly with the larger radius profile, while also demonstrating a compressive to tensile stress reversal.

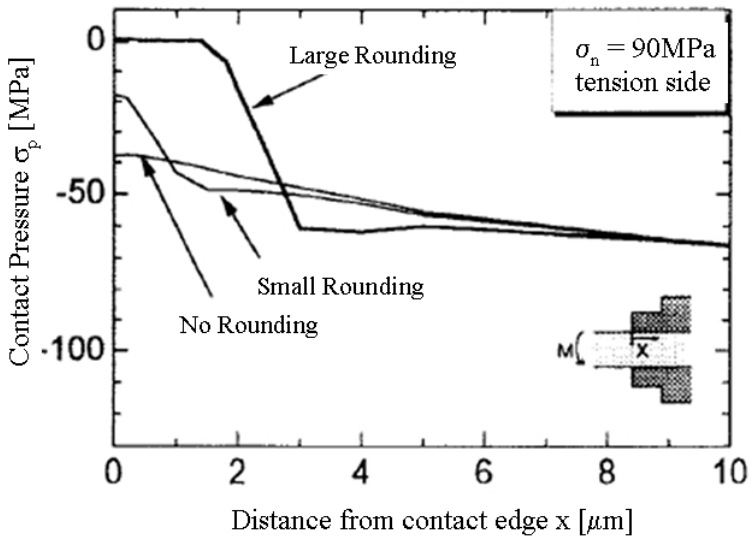

Figure 3.1.3.8 Radial stress at the 'SCA equivalent' location for press-fit plus bending [20].

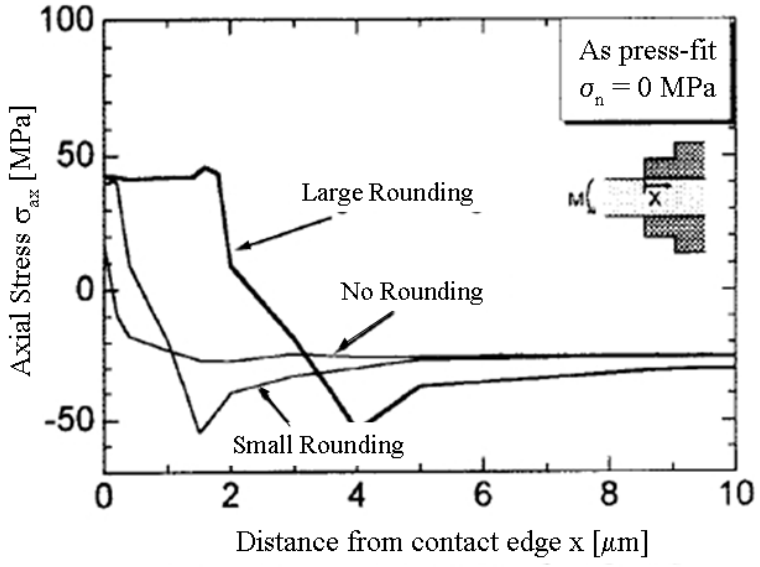

Figure 3.1.3.9 Axial stress at the 'SCA equivalent' location for three different geometry press-fit options [20].

Finally, in [20] the rotating bending bench fatigue test failures were shown to match the locations of high stress calculated in the FEA model. Another technical paper published based on the same research activity [21] focused on furthering this FEM and experimental based fatigue work.

Failures in service of the axle are identified as fretting fatigue, and the location of the cracks relative to the round profile on the hub is shown in Fig.3.1.3.10 from [21]. The focus of this research was to predict fatigue crack growth or fatigue strength using fracture mechanics; a broad assumption is used regarding the accuracy of the FEA model developed earlier in [21]; since the failure location matched the FEA results, the accuracy is deemed acceptable.

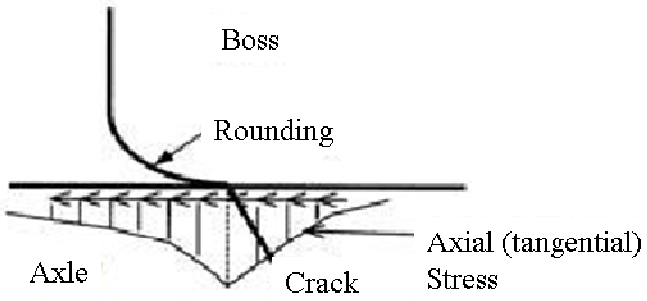

Figure 3.1.3.10 Rotating bending fatigue bench test crack location from [21].

In summary, there is sizeable work done in the area of press-fit joints used in other applications. For most of the research it is difficult to determine the profile of the edge geometry at the SCA, as the details of the stress field were not the focus of the effort. Missing in the literature are the calculation of sharp stress concentrations at the edge of the press-fit and the high sub-surface stresses that become obvious when adequate mesh density is used to describe the stress gradient at the SCA. Previous studies containing stress sensitivity comparisons to mesh density are also not present in the literature.

Note also that for these other applications, where design space is not as much of a premium as it is on a crankshaft, geometry features are added on the joint to relieve stress or create a compressive stress to extend the joint life. Therefore if these features can be easily added to the design, then there is not a great incentive to understand the true structural behavior of the press-fit joint which does not have the stress relief feature. This is likely one of the main reasons that little research has been published to date on the problem presented in this thesis.

3.1.4 Contact Stress And Sub-Surface Stress Studies From Other Applications

The numerical analysis of the press-fit joint on a multi-piece crankshaft assembly reveals some interesting sub-surface stress. Some relevant research in the area of contact stress is presented below.

Gawronski et al [22] discuss some favorable compressive residual stresses that are generated on gear teeth by both a surface hardening technique (vacuum carburizing) and by final grinding. These favorable stresses are super-imposed on top of the bending and contact induced stresses on the gear teeth by means of a FEA model using a sub-modeling approach. Details of the FEM model mesh are shown below in Fig.3.1.4.1.

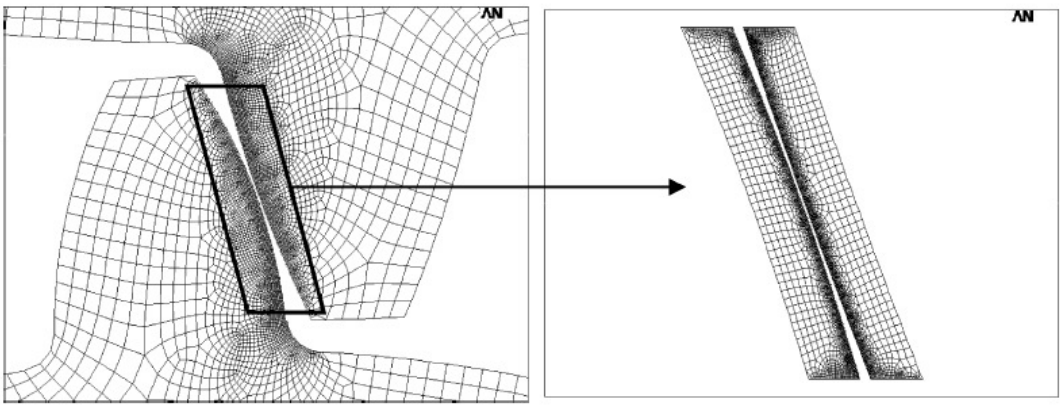

Fig. 8. FEM model of gear teeth mating.

Figure 3.1.4.1 The FEM model showing the gear teeth and sub-model area from [22].

Next in Fig. 3.1.4.2 (from [22]) a fringe pattern (detailed stress plot) is shown with peak equivalent stresses directly below the contact patch surface for the gear teeth loading, at some distance which is indicated as the Bielajew Point. This maximum equivalent stress location is given as 0.27 mm below the surface. The location of the maximum stress was of interest because of concern regarding the depth of the strengthening treatment, and whether this point fell within the case depth range. This is a similar concern in the case of accurately determining the location of the high sub-surface stress values due to contact (of curved surfaces) at the multi-piece crankshaft press-fit joint. Note that the maximum equivalent stress location appears to be directly below the center contact location. There is not any description of the shear stress field present, and whether it is a prominent component of the equivalent stress field. There also is not

any description about the mesh density requirement to accurately determine the stress field gradients and local maximums present.

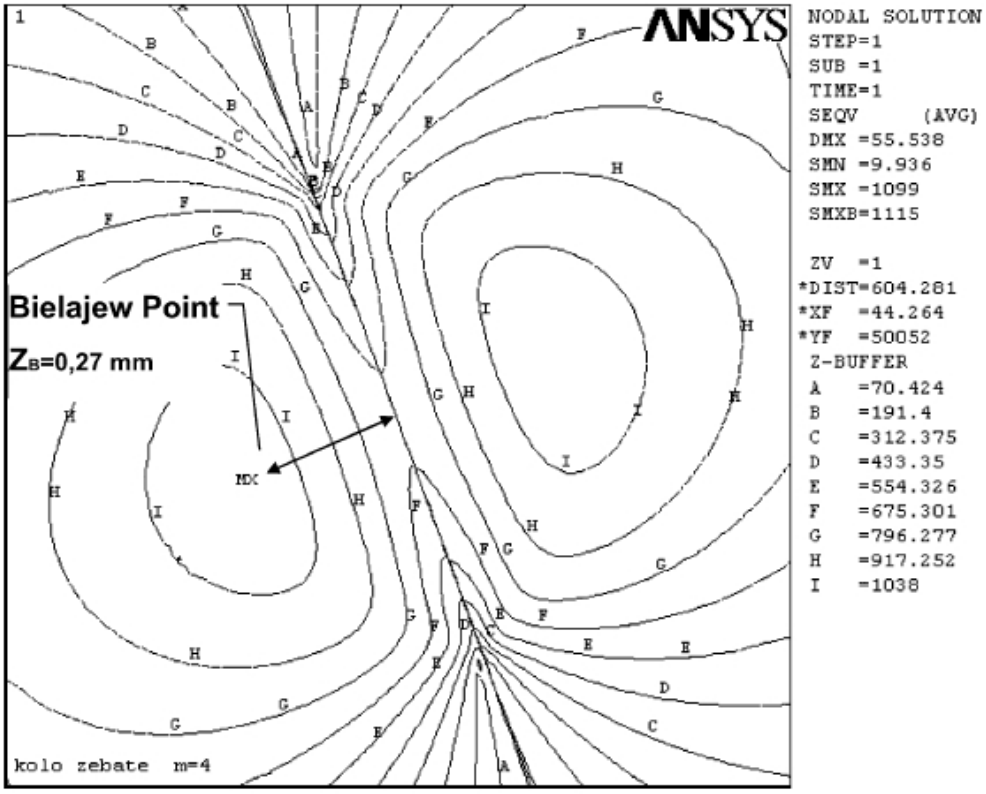

Fig. 9. Determination of the Bielajew point.

Fig. 3.1.4.2 FEM plot from [22] describing the location of a maximum sub-surface (equivalent) stress, the Bielajew point.

3.2 Theoretical Background

Developing accurate and practical FEA models of the press-fit joint that captured the details at the SCA proved to be very challenging. This section reviews the methodology created and some background theoretical information used to examine such press-fit joint problem. The problem is non-linear due to the necessity of using the contact elements. Note that all research presented uses a linear elastic material model. Also, the interfacial contact forces depend on the friction coefficient, which differentiate this problem from the Lame case that is friction independent.

3.2.1 Introduction to the Mathematical Solution for Cylindrical Contact

This research body presents the numerical evaluation of the high stress conditions typical of a multi-piece crankshaft press-fit joint for both the assembly and operating conditions. The novelty in this research is the determination of the Hertzian like stress field at the press-fit edge, designated the SCA. The high gradient stress fields present pose major challenges in the application of numerical tools for evaluation of the assembly and operating loads. The research work does not include any new numerical formulations, but does employ good numerical practices and high quality modeling techniques which will be discussed in this chapter.

The application of finite element method to solve an engineering problem is successful only if a practical description of the physical problem can be defined using a mathematical model. FEA may then be employed to solve this mathematical problem, approximately, as indicated in Fig. 3.2.1.1 [23]. The initial assumptions in both the mathematical model and the application of the numerical model usually require several iterations to obtain a set of useful tools that produce meaningful data in an efficient manner.

Generally, the structural evaluation of the multi-piece crankshaft needs to consider the assembly and operating conditions. The assembly condition requires the determination of the radial interference between the pin and the web to obtain the desired displacement and stress fields (after assembly). Subsequently, it is required that the operating loads the crankshaft experiences

(in addition to the assembly loads) be added, so that the mean and alternating displacement and stress fields in the crankshaft under combined load can be determined.

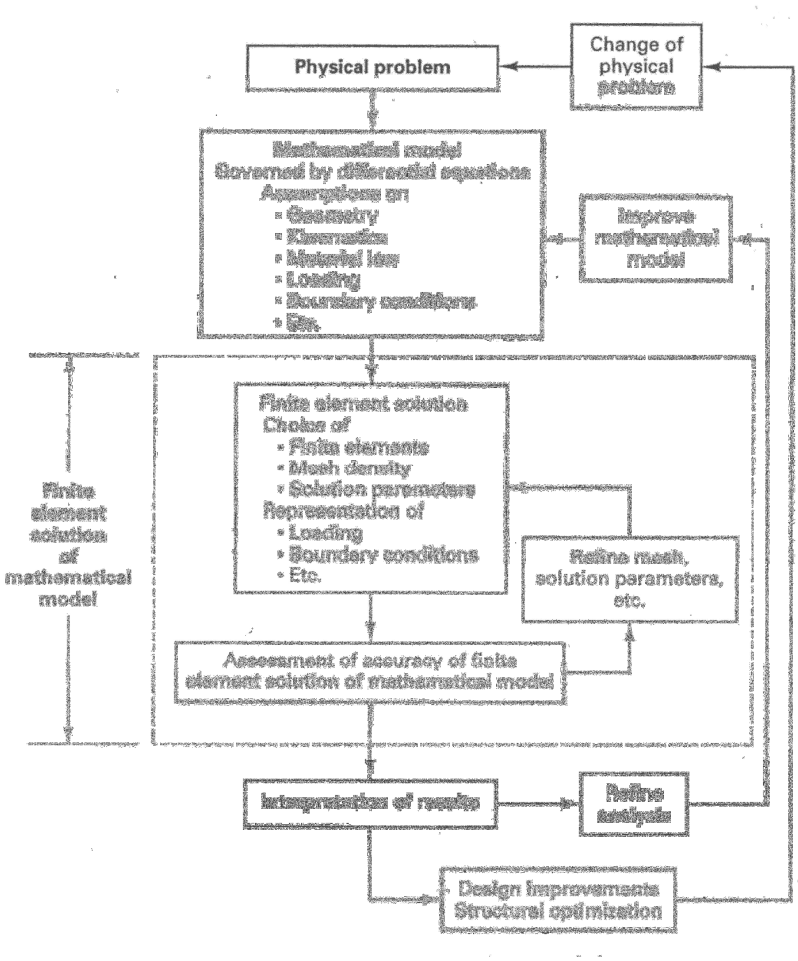

Figure 3.2.1.1 The finite element process [23].

In the preliminary analysis of the assembly state the Lame solutions are most commonly used [24]. Such a solution predicts the behavior of two elastic cylinders which have a radial interference δ. To employ the Lame formulas for the crankshaft press-fit problem, the web must be idealized as a concentric cylinder. A differential slice and a section view of such a hollow cylinder are shown in Fig. 3.2.1.2, which defines the parameters used. The Lame solution originates from the equilibrium equation in the radial direction:

$$-\sigma_r hrd\theta + (p\varpi^2)rhdrd\theta + (\sigma_r + d\sigma_r)(r+dr)hd\theta - \sigma_\theta hdrd\theta = 0 \qquad (3.2.1).$$

Note that the Lame solution assumes that the stress field is constant in the axial direction of the cylinder. The developed Lame solution takes the form

$$\sigma_\theta = \frac{p_i b^2}{a^2 - b^2}(1 + \frac{a^2}{r^2}) - \frac{p_o a^2}{a^2 - b^2}(1 + \frac{b^2}{r^2}) \tag{3.2.2}$$

for hoop stress σ_θ and

$$\sigma_r = \frac{p_i b^2}{a^2 - b^2}(1 - \frac{a^2}{r^2}) - \frac{p_o a^2}{a^2 - b^2}(1 - \frac{b^2}{r^2}) \tag{3.2.3}$$

for radial stress σ_r at radial position r, where p_i and p_o are the internal and external pressures while also *a* and *b* are the internal and external radius values respectively.

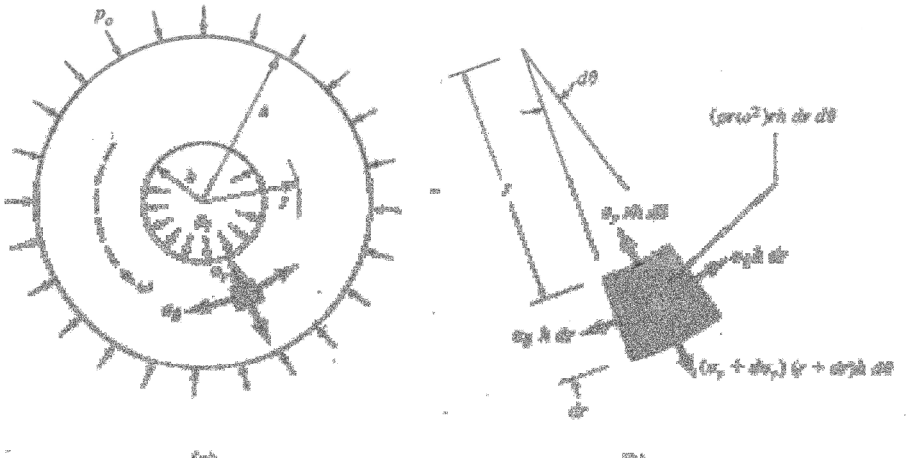

Figure 3.2.1.2 Equilibrium forces on a differential slice of a thick cylinder [24].

These formulas can be used for the problem of a press-fit between two cylinders with the knowledge that 1) radial stress σ_r at the interface must be equal and 2) the radial stress σ_r at the external and internal surface must be equal to zero or any applied pressure. Note the radial interference δ is required as input also. Figure 3.2.1.3 shows a typical radial and hoop stress distribution for two cylinders press-fit together (p_c is given for the plain strain state or for infinitely long cylinders). If there is internal pressure, one may super-impose the interference solution of two cylinder jackets with an internal pressure solution assuming the two cylinders are one continuous part.

The Lame's 'average' radial and hoop stresses values are useful in the design of a crankshaft, and are typically used to size the press-fit joint for adequate torque retention, while balancing / minimizing hoop stress on the outer cylinder (the web). There is significant research published in this area, which has been shown to correlate reasonably well to both test data (see chapter 6

for details) and the average values present on the more exact FEA solutions. However, this solution ignores the fact that the web is of a finite length.

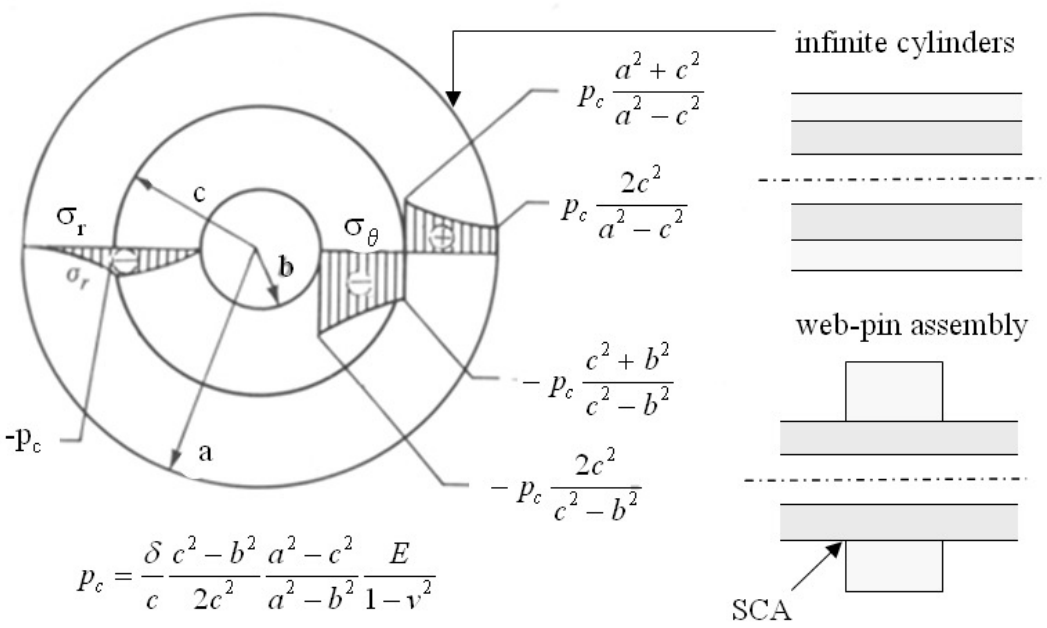

Figure 3.2.1.3 The stress distribution between two cylinders with radial interference [24].

The Lame solution will not be able to calculate the high stress condition at the SCA because the stress variation in axial direction is neglected. Also since the web is idealized as a concentric cylinder, the FEA solution for the 3-D geometry results in somewhat higher average radial and hoop stress values. The actual web geometry has a greater stiffness than the concentric assumption which produces 1) higher radial stress overall, and 2) more stretch of the web material just above the pin at Top Dead Center (TDC) to compensate for the sections which have a higher stiffness.

As outlined above, the Lame equations do not capture the details of the high stresses present at the SCA. Reference books typically suggest examining such stresses as a contact problem. The study of contact stress between two spherical bodies is generically called Hertzian contact stress, named after the originator. The body of work by Hertz has evolved into commonly available formulas that have been derived for several shapes of contacting elastic bodies.

Common formulations available include the following body shapes in contact:

1) sphere on sphere,
2) sphere on a flat plate,
3) cylinder on cylinder with both cylinder axis parallel to each other,
4) cylinder on cylinder with one cylinder axis perpendicular to the other,

where, for each instance the line of action of the force between the two bodies intersects the geometrical center of the radius of curvature for each body.

Logic may suggest the closest representation to the press-fit geometry at the SCA is the cylinder on a flat plate, which requires a few assumptions. Consider Fig.3.2.1.4, which shows the web mounted on the pin, with the 'true radius' web end finish equal to $0.5D_2$ highlighted as the geometry of interest for this calculation.

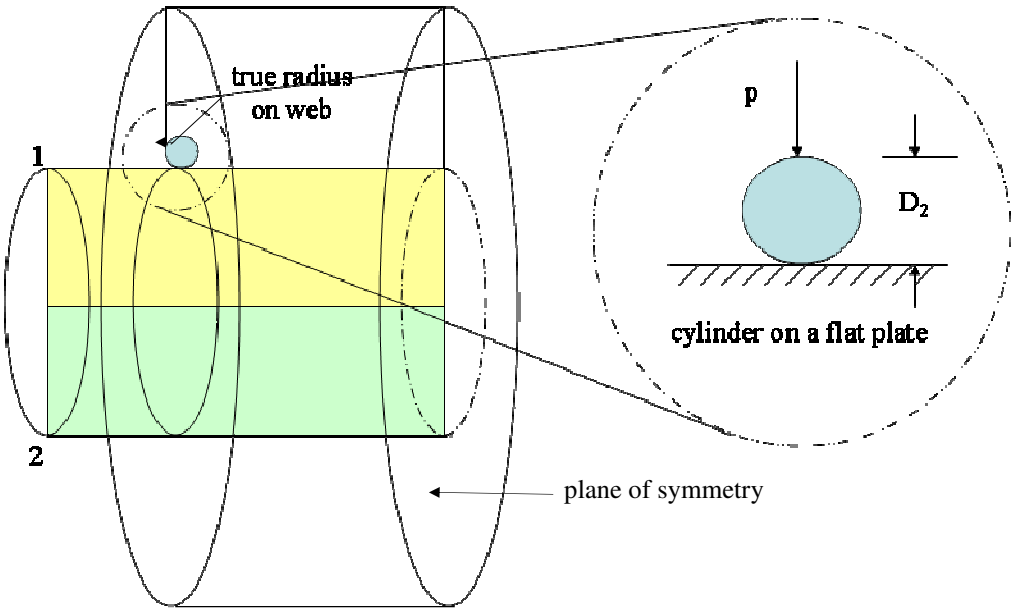

Figure 3.2.1.4 The 'cylinder on a flat plate' Hertzian contact assumption [25].

Next, the second cylinder (the pin) is considered flat ($R_2 >> R_1$), which is the equivalent of taking the pin and 'unrolling' it so that it is flat (see Fig.3.2.1.5). In addition, the same is done then to the web, it too is 'unrolled' to a flat profile. Radius R_1 is set then to the value of the true radius feature at the SCA. So in this manner the contact problem is simplified to be a thin narrow cylinder of radius R_1 that is loaded against a flat plat. Obviously, this is quite a stretch in assumptions, and is difficult to see any benefit to this approach.

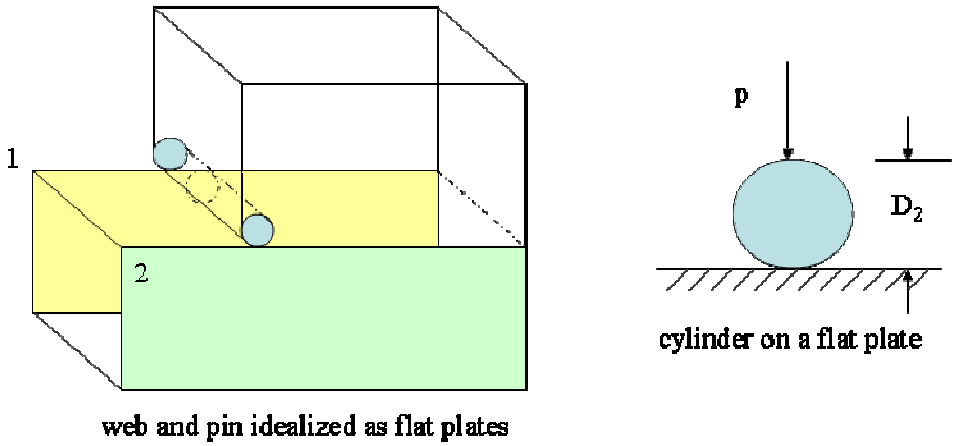

Figure 3.2.1.5 The axisymmetric geometry assumed as flat [25].

The Hertzian equations for the cylinder on flat plate assumption are

$$p_o = 0.591\sqrt{\frac{pE}{K_D}} \tag{3.2.4}$$

and

$$b = 2.15\sqrt{\frac{pK_D}{E}} \tag{3.2.5}$$

where $K_D = D_2$ [25]. The contact patch width b and maximum contact pressure at the surface p_o are shown in Fig.3.2.1.6 [26] which details the contact pressure distribution for the case of cylinder on parallel cylinder. The unit loading of the cylinder, p, is unknown, which in terms of the original problem geometry is logically a multiple of the press-fit interface radial stress.

Experimentation with the formula does suggest that the stress field present is Hertzian in nature, as will be discussed in Chapter 3. If the load input value p is varied until the maximum pressure p_o matches the FEA solution, the corresponding size b also matches the FEA solution. The application of these Hertzian formulas to the SCA press-fit problem is not viewed as a precise design tool. There has been no progress made in developing an theoretical formula relating average radial stress and the local maximum radial stress at the SCA. This difficulty is exactly the reason why a good numerical approach is needed.

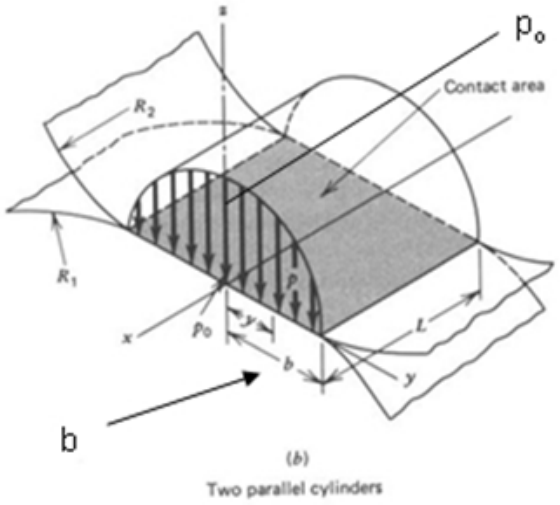

Figure 3.2.1.6 Hertizian contact pressure for two parallel cylinders [26].

3.2.2 Press-Fit Joint Numerical Model Challenges

So far important structural details required to design a proper multi-piece crankshaft are not obtainable with sufficient accuracy from simplified formulas. Finite element methods are very common in modern engineering to solve structural problems, which are applied here in phases to study the press-fit problem. Both simplified 2-D models and accurate full geometry 3-D models are used together with contact elements to examine the behavior of the press-fit joint. The axisymmetric 2-D models are used to study the press-fit problem around the SCA in great detail, while the 3-D full geometry models are used to study both the assembly and operating load behaviors.

3.2.2.1 Mesh Refinement Requirement For High Gradient Stress Fields

Significant portions of the research focus on controlling mesh density. The stress results presented are provided in terms of the element size at the SCA. Early in the research, prior to the 2-D assembly studies with element size h below 0.02 mm, it was thought that a stress singularity was present at the SCA. Further mesh refinement determined that the surface and sub-surface stresses converged to a finite value, which allowed determining the stress concentration at this location. It is therefore appropriate to discuss the mesh refinement required to model such high gradient stress fields.

A stress singularity may be defined as the stress magnitude going to infinity for an elastic solution, or also may be described as a material immediately yielding in the real world load situation. In the case of the stress concentration at the SCA, it is shown that the peak stress have a final limited value that is mesh independent (note that the material models used in the research are all linear elastic). Also note this converged value will be shown to fall within the elastic range of the surface hardened case depth of the high strength material.

Mesh refinement studies show how the maximum stress calculated at the SCA is sensitive to element size. Very small elements are required for convergence. This is due to the relatively small size of the curvature or 'kink' in the pin at the point of contact / no contact and the resulting small size of the local sub-surface maximum stress.

The level of discretization of the geometry needs to match size of the physical phenomena that is being numerically modeled , such as the pin kink (the curvature), or the sub-surface stress field, or the true radius edge finish. Figure 3.2.3.1 demonstrates this from a finite element perspective, displaying the actual and the finite element calculation of the maximum stress at the presence of a high stress gradient [27]. The actual stress is shown to increase at a higher rate as the x-axis goes to zero. For element size *h* equals 1 unit, the nodal stress at x equals 0 is calculated as 28 stress units by the extrapolation from the element 'a' Gauss point stress values (the stress values calculated very accurately at the Gauss points of element 'a' and then are linearly extrapolated to the nodal location for most 2D and 3-D elements). Next, for *h* equals 0.5 units, Fig. 3.2.6 indicates a stress value which is re-calculated at 39 units for x equals 0.

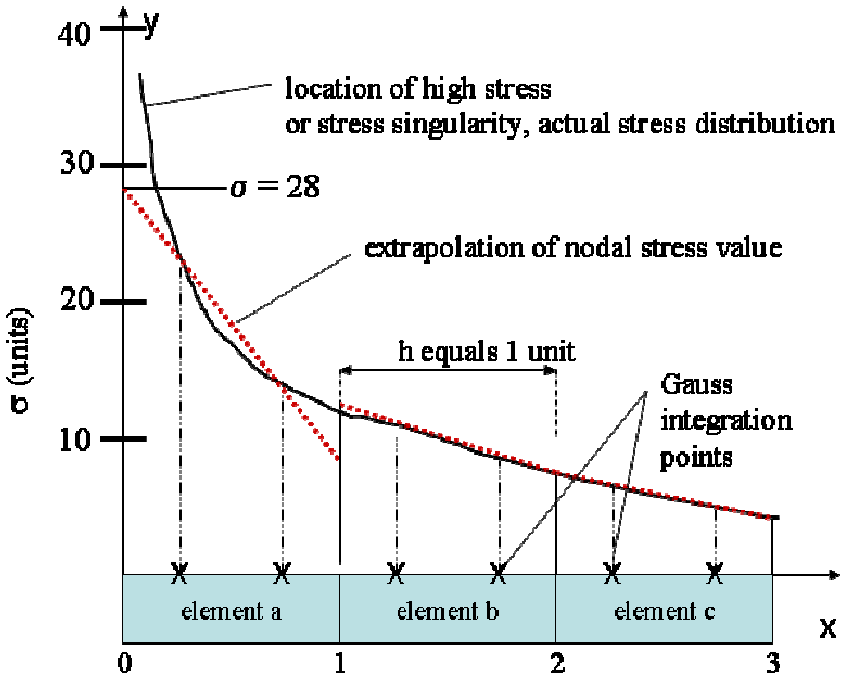

Figure 3.2.2.1 Variation in stress magnitude calculated with element size *h*.

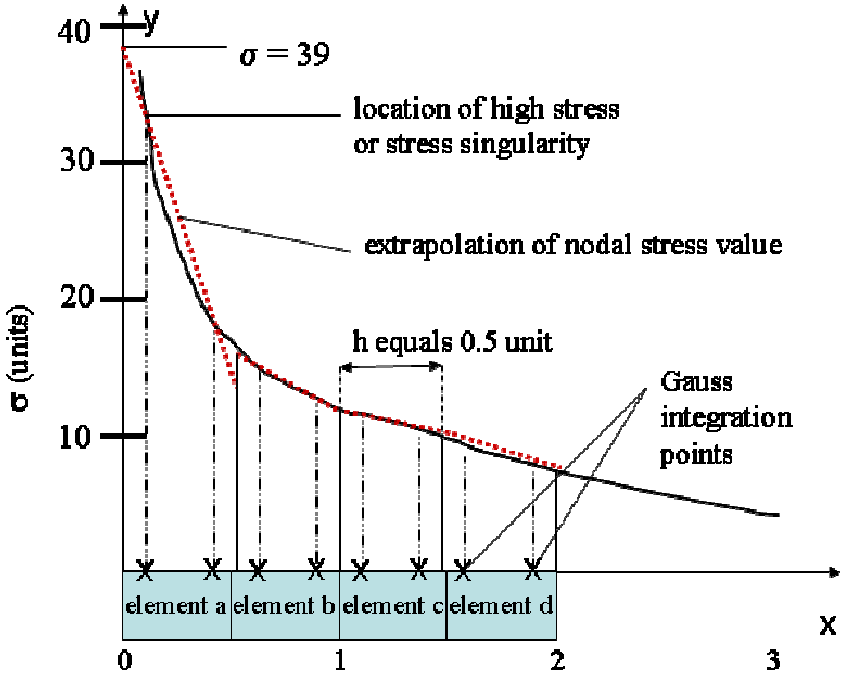

Figure 3.2.2.2 Variation in stress magnitude calculated with element size 0.5h.

As the element size decreases to match the stress field gradient, a more accurate result is determined. So, if in fact the stress field at x equals 0 goes to infinity, a decreasing element size

h will calculate an increasing maximum stress value without reaching a limit. In the other instance, when the maximum stress at x equals 0 has a definite value, as element size *h* is decreased the FEA solution will converge to that limit.

So, in this light, the element size at the SCA needs to be well controlled for accurate stress calculations for both the assembly and operating load conditions. The 2-D axisymmetric model is more numerically efficient, and was used in conjunction with mesh convergence studies to set the minimum mesh size for the 3-D work. Large model size and solution time are not a concern for the 2-D model, but are for the 3-D work, as stated previously.

3.2.2.2 Meshing Challenges For The 2-D Solution

The research used ANSYS, a well established finite element method commercial software. The 2-D axisymmetric models were created with parametric geometry based on the ANSYS command language. Details of this automated tool for press-fit design that is to be used by the design engineer is presented in section 8.5.

The axisymmetric model uses element PLANE82 [28], which is a 2-D 8 node structural element that approximates displacements by quadratic function and may be used for axisymmetric problems with the appropriate option set (KEYOPT(3) = 1). A mixed mesh was generated by the automatic meshing tool that ANSYS employs, which favored rectangular elements over triangular shapes. PLANE82 may also form a 6 node triangular element for the case of a mixed triangular and rectangular element mesh.

The 2-D meshing controls used were line and area based; the layout of the typical axisymmetric model used throughout the 2-D studies is provided in Fig.3.2.2.1. Areas around the SCA are used to control mesh size exactly but reduce element count and minimize solution time.

Major difficulties were encountered meshing the 2-D geometry, relating to the mesh quality in the transition zones. The ANSYS auto-mesher needed help to gradually change the element size as the mesh moved away from the high density mesh in the SCA area. Improvements in mesh quality in the transition zone was obtained by using several areas over which the element size

could be controlled to change gradually. Keep in mind that it is important that the 2-D axisymmetric model be very robust from a modeling pre and post processing standpoint. The intent of the evaluation tool created is that it be placed into the hands of less experienced design engineers which have low experience level in FEA. The tool needs to fit in a design environment and have a robust meshing approach.

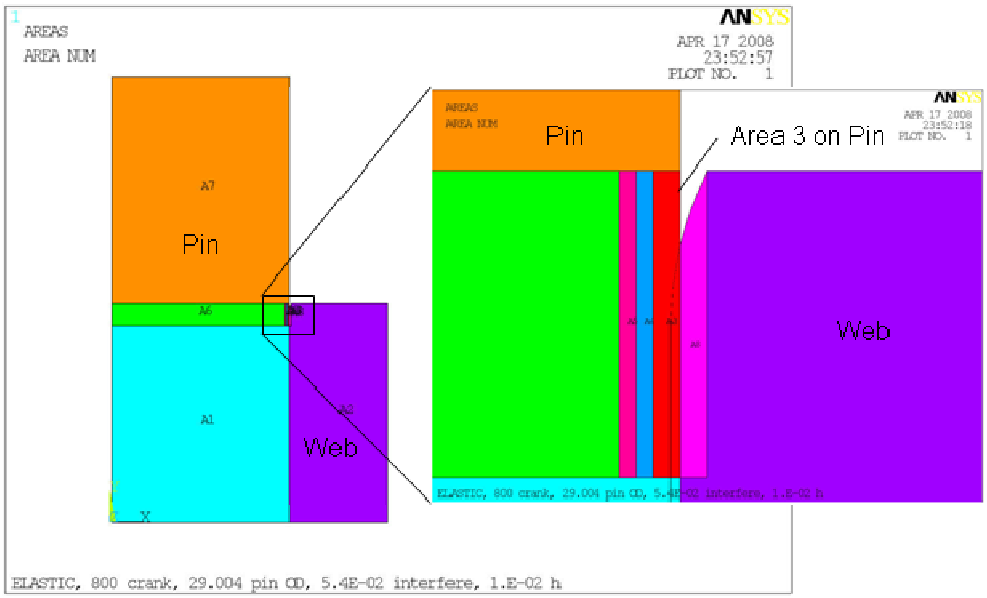

Figure 3.2.2.1 Area plots of the 2-D FEA model; mesh control with area 3 at the SCA.

3.2.2.3 2-D Contact Modeling At The Press-Fit Interface

The axis symmetric model uses a contact algorithm to examine the interference between the pin and web. TARGET169 and CONTACT 172 [28] are the contact pair which are surface to surface elements placed on the matching interface surfaces of the pin and web respectively. The contact algorithm uses a Lagrangian penalty function method, which increases the contact stiffness for any measured penetration. The discretization of the set of contact elements is determined by the solid elements below it. Both element sets share the same real constants, including the surface co-efficient of friction.

A single typical interference fit value was used as a baseline throughout the 2-D and 3-D solutions, which is a value that has passed endurance testing in a similar crankshaft design. The interference was added through contact algorithms to the FEA model by two methods, the first

by creating geometry with the desired interference fit, and the second by thermal expansion. Both solutions have advantages and disadvantages.

The desired interference fit method worked well for larger elements sizes, but as the size at the SCA became much smaller than the interference, the contact solution would not converge easily. The convergence issue stemmed from the reduction in size of the contact algorithms 'pinball region' search criterion for the matching contact and target nodes on the pin and web respectively. As the 2-D element size is reduced at the SCA, so is (the contact element size and therefore) the region of search, to a point that it is much smaller than the radial interference value. The pinball region could be set to a larger distance, but another shortcoming of the geometry based interference approach was non-uniform or 'spotty' contact pressure results. The geometry based method did not reliably create the desired smooth and continuous contact pressure.

The thermal expansion method created radial interference by applying a temperature change to the entire model while setting the web coefficient of thermal expansion to an artificially low value. An appropriate temperature change is applied to the model which expands the pin only and creates the desired radial interference. The temperature change was applied in a ramped fashion during the solution phase, and the number of sub-steps used to solve for the interference was set by the minimum element size at the SCA. This approach works well for all element sizes at the interface, and provided a more consistent or smooth contact pressure distribution. Negative aspects include an increased solution time required when a small sub-step size (resulting in many equilibrium iterations) is chosen for a highly refined mesh. Also, the thermally induced distortion often dominates the solution displacement plot and therefore is less meaningful to the analyst.

3.2.2.4 Meshing Challenges For The 3-D Solution

The approaches and challenges of the 3-D modeling followed closely those listed for the 2-D work. The 3-D mesh used both brick and tetrahedral elements, with a focus on controlling element size exactly at the SCA by using small cylindrical volumes on the pin OD and the web ID. An example of the manipulation of the crankpin geometry typical of the 3-D model is shown

in Fig.3.2.2.2. A thin cylindrical slice was segregated into a separate volume at the SCA to use for brick mesh control. The pin volume was also separated into wedges also so that different loading planes could be easily post-processed (see Fig. 3.2.2.2). There are more details shared on the geometry manipulation created for the 3-D models in chapter 5.

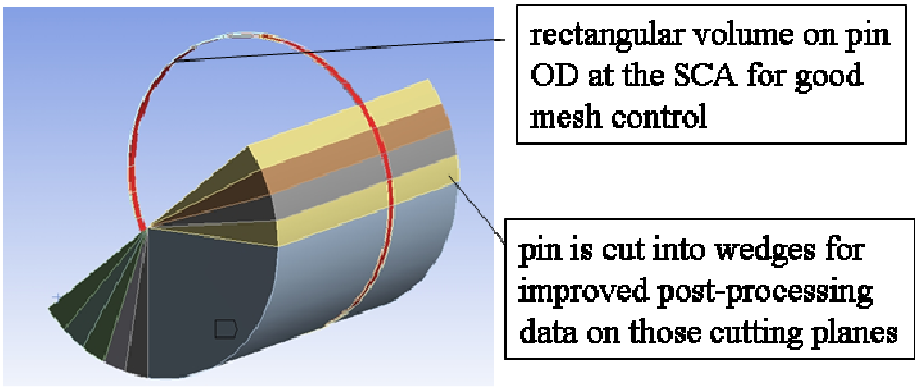

Figure 3.2.2.2 Pin geometry manipulation for mesh control and post-processing.

Without some manipulation of the pin and web geometry, it is not possible to create an efficient FE mesh with the desired brick elements present at the SCA. Different geometry manipulation schemes that did not work as well are also covered in chapter 5; a large effort was required to determine the best approach and without this effort the research would not have been possible. The final solution using a thin cylindrical volume at the SCA was the simplest and most robust for good mesh quality.

The size of the cylindrical volume at the SCA was 1.0 mm wide by 0.1 mm deep, which was based on the size of the stress discontinuity present at the SCA. Even the simple task of placing the relatively small SCA cylindrical volume at the correct axial position on the pin and web was laborious since the best location was found through trial and error.

The ANSYS brick element used is SOLID186 [28], a higher order 20 node brick element with quadratic displacement approximations. The brick element allows variation in shape and may be formatted by node numbering as a tetrahedral, pyramid, or prism (wedge) as needed by the local mesh and geometry requirement (see Fig.3.2.2.1). Brick elements are required at the SCA, and dominate the local volumes created there, while tetrahedral elements dominate the rest of the crankshaft volumes. Pyramid and prism elements are used in the transition from purely brick

elements at the SCA to tetrahedral elements elsewhere. The meshing details, including the geometry manipulation used to create the mesh are provided in detail for each 3-D model type used in chapter 5.

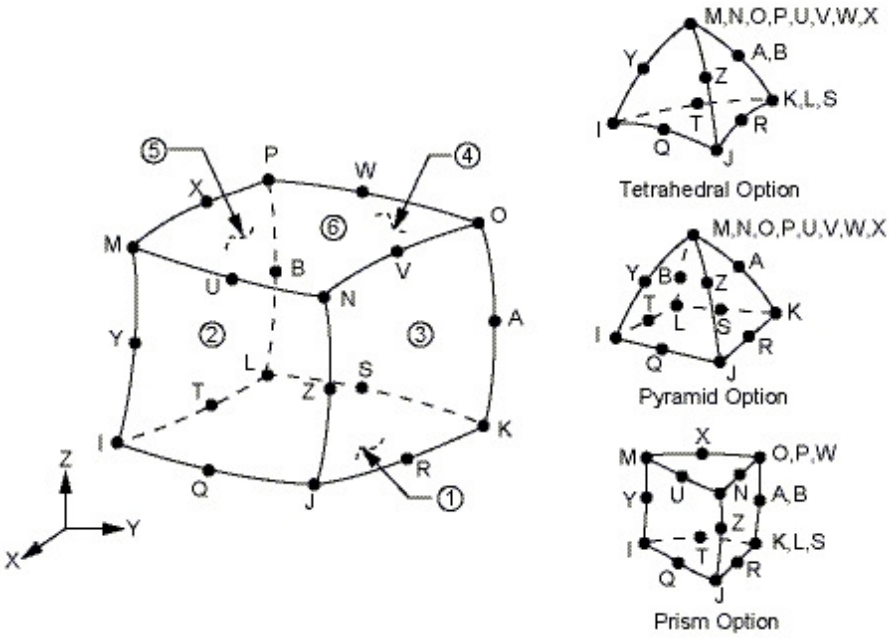

Figure 3.2.2.3 ANSYS SOLID186, 20 node brick element and its variations [28].

3.2.2.5 3-D Contact Modeling At The Press-Fit Interface

The 3-D press-fit joint interference was modeled using contact algorithms in a similar manner to the 2-D problems. ANSYS recommends CONTACT174 [28] and TARGET170 8 node surface element for deformable 3-D surfaces in structural contact. The number of nodes present is consistent with the number of nodes on the solid element face at the surface. The contact element is also capable of a 6 node format to match a wedge or tetrahedral element shape. The contact element is capable including surface friction, and again both the contact and target element use the same real constant set.

The 3-D FEA models introduced radial interference between the pin and web in the same manner as used for the 2-D studies; both thermal expansion and geometrical interference were used. The advantages of each approach listed above apply for the 3-D case. The thermal approach was

favored for the 3-D effort though because of the good consistency in contact results at the SCA, even with long solution times present.

Interference by thermal expansion also created two bi-products that were sometime difficult to deal with, especially the larger models. The thermal expansion on the full model is applied to the outer PTO web, which also creates axial growth and position change in the outer web relative to the pin. The result is a small mismatch between the mating brick element mesh volumes at the SCA on the pin and web; the desire here is to match the mesh exactly. The thermal expansion also requires that the spring boundary conditions for the PTO end bearings are reset so that reactions equal zero for the assembly load step.

3.2.2.6 Computational Challenges

Model size and solution time was not as critical for the 2-D models, although for such models the number of equilibrium iterations was around 8 times greater than for the 3-D models. A typical refined 2-D model with adequate refinement at the SCA (such as h=0.0075 mm) had 34,000 elements approximately which required 45 minutes to solve on a desktop class workstation (2 CPU at 2.13 GHz clock speed with 16 Gb RAM). The long solution time was a result of the large number of equilibrium iterations (32 to 38 total) required for each sub-step of the ramped temperature loading. Approximately 250 hours in computational time was spent directly on 2-D solutions for this research effort, not including the time required to create the automated 2-D axisymmetric model input deck.

Overall, three different 3-D models were used in this research. First a 30 degree symmetrical slice that is consistent geometry-wise to the 2-D model was created to examine the assembly solution differences between the exact same 2-D and 3-D geometry. Next a 'bench test' model using symmetry assumptions on the 3-D crankshaft geometry was created to minimize solution size. This model was created for ease of use to accelerate the numerical studies, which is also a practical requirement for any of the numerical design tools that are produced by this research effort. Finally the full 3-D geometry of crankshaft was examined with a 3-D FEA model for assembly and operating loads.

Solve time for the 3-D models are very significant because of the large model size plus the significant number of equilibrium iterations typical to evaluate the non-linear joint behavior. The minimum element size at the SCA was limited for all 3-D models to obtain reasonable solution times. Typically a one-quarter symmetry model using *h* equals 0.02 mm at the SCA had solution times in the order of 18 to 24 hours using a desktop class workstation. The average model consisted of 860,000 elements and required 15 to 19 equilibrium iterations.

The full model was restricted further in minimum element size since it could not take advantage of any symmetry in the geometry. The smallest element size that was practical to run and post-process was h=0.05 mm, which still involved a 120 hour (5 day) solution time. Approximately 1900 hours in computational time was spent on the 3-D solutions. Model sizes beyond this with extended solution times are not thought to add practical value in a design environment.

3.2.3 Development of Numerical Model Reliability

The introductory section in this chapter touched briefly on reliability of the computer simulation in Life Evaluation of the crankshaft design. All reliable FEA procedures require the integration of experimental tools and experimental data to develop sufficiently accurate FEA tools. Also, the efficient and practical application of FEA to the overall process may require several types of numerical models with varying degrees of fidelity used at different stages of the design challenge.

Figure 3.2.4.1 shows intent of this research process, which is to develop good reliability in the overall application of tools to the design of multi-piece crankshafts. All FEA processes, shown in yellow, have matching test components (shown in grey), so that good confidence will be present for the FEA tasks. The assembly (phase 1) and operating load (phase 2) FEA and experimental tasks are examined in chapter 6, and show good correlation.

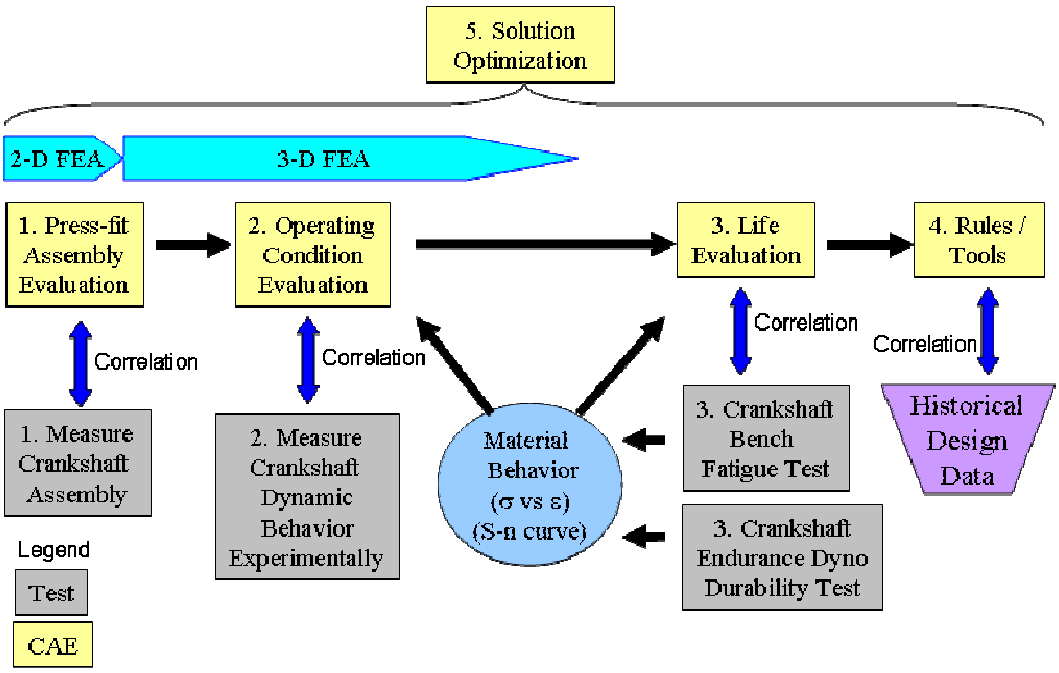

Figure 3.2.3.1 The multi-piece crankshaft process for development of good reliability.

Structural durability can not be discussed without reference to the material behavior, including the constitutive laws as well as the material fatigue (S-n) curve. As a start, fatigue data may be produced for the core material using test coupons. Usually though a strengthening treatment is applied to the crankshaft surface for improved durability; which means the core material fatigue curves are not applicable for the case depth of higher strength material. Fatigue data for the strengthened material must come from either 1) fatigue tests done on the actual or similar geometry, or 2) it must be calculated approximately using 'rules of thumb'.

It is difficult and expensive to develop a reliable fatigue process for high cycle fatigue applications such as a crankshaft. Collecting fatigue data from bench tests or from running engines usually requires long test time. Also, any failure of the crankshaft likely destroys the full engine. The biggest roadblock though is that the goal of any engineer working towards getting an engine into production is for the crankshaft to complete the full durability duty cycle without any failures. Without any fatigue failure, the ultimate performance of the crankshaft design in questions is still unresolved.

The idea of slight undersized crankpin testing [15] to induce early failure was promoted in section 3.1, but often this is not feasible in a program short of time and accurate production representative components. Therefore, fatigue approaches need to be developed with a durability specific bench test. For the multi-piece crankshaft, this is more important than a one piece design, because both pin bending fatigue and fretting fatigue may occur on the bottom of the pin at the SCA. At the time of writing of this thesis, such bench tests have not been developed, but the FEA 'bench test tools' have been used in chapter 8 to examine a proper loading approach. The lack of fatigue data remains the biggest challenge for further development of the FEA tools.

A mature FEA process will have experienced several iterations of the design – analyze – build – test loop, and will continue to develop more efficient tools. Phase 4 outlined in Fig.3.2.4.1 indicates that the FEA process and data will be studied in depth to develop design rules that may be used early in design. Historical (FEA and test) data will enhance the development of rules, and also facilitate a faster adoption if the historical data includes both successful and not so successful designs. The focus of this phase of the research is to examine the high stress condition present at the SCA, and determine a relationship between the high local stress maximums and the average radial contact pressure in the press-fit.

FEA tools that speed up the overall process are key for high computational effort problem sets in particular, which is the case for the multi-piece crankshaft. Tools have been created to examine both the assembly and operating load conditions with reduced effort. A user friendly 2-D axisymmetric model was created that automatically solves and post-processes the assembly problem. A practical 3-D full crankshaft model solution time limits the element size employed at the SCA, and so the accuracy of the stress field there is in question. Results from the higher quality 2-D press-fit analysis and the 3-D one-quarter bench test need to be used in conjunction with the full model. Also, the one-quarter bench test model may be leveraged early in the design process to reduce the number of iterations that need to be examined with the full crankshaft FEA model.

The final phase (5) optimization is highly desired in a robust FEA based design process. So, as more confidence is gained with the FEA tools, solutions with improved operating life may

examined. The primary focus of the optimization in this research effort is reduction in the assembly stress at the SCA.

4 FEM Modeling Of The Press-fit Assembly

This chapter presents the numerical results for the press-fit assembly problem.

4.1 Material Properties

For this research document the properties of the core material are assumed to be that of an average high strength steel, as provided in Table.4.1.1 [29]. For core material the ultimate tensile strength (UTS) is 1180 MPa (mean value) and yield strength (S_{YS}) is 785 MPa. The fatigue strength is calculated approximately using the 0.5UTS rule of thumb [30], and ranges from 515 MPa to 663 MPa if surface finish and gradient fatigue factors are ignored.

Table 4.1.1: Mechanical Properties of Crankshaft Components [29]

Sample ø (mm)	Description	UTS Low (MPa)	UTS High (MPa)	YS Low (MPa)	YS High (MPa)	Sn Low (MPa)	Sn High (MPa)	YS/UTS (Low)	YS/UTS (High)
Material A									
25 - 40	Core Material	1030	1325	785		515	663	0.762	0.592
25 - 40	Case Hardened	1900	2275	**1448**	**1348**	950	1138		
Notes:									
1)	Sn fatigue strength calculated using 0.5UTS 'rule of thumb'								
2)	Case Hardened material YS calculated using the ratio of YS / UTS for the core material								
	Calculated with YS/ UTS(Low) value								
	Calculated with YS/UTS(High) value								

The material is hardened on the surface to improve its strength properties. It is assumed that the case depth is 1.0 mm thick and that a significant increase in hardness strength is gained from the case hardening operation. The UTS of the case hardened material increases to 1900 MPa (low value of range) and the calculated YS increases to 1348 MPa (low value of range). Since it is very difficult to measure the YS improvement of the case hardened material, a value is calculated based on the core material ratio of YS to UTS plus the strengthened material UTS. Fatigue strength ranges from 950 MPa to 1130 MPa, and is calculated based on the UTS lower and upper bounds. The mechanical properties listed are considered typical for crankshaft applications, and are also given in Table 4.1.1 below. It is assumed that all pin and web components of the crankshaft are made with this material for simplicity.

Figure 4.1.1 provides a plot of HRC hardness vs case depth measured across the case depth for a sample piece [31]. The hardness measurement is converted to an ultimate tensile strength (UTS) value using a conversion table [32].

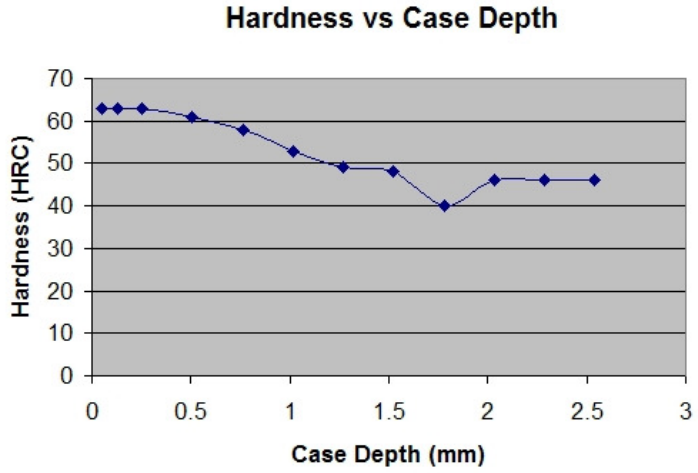

Figure 4.1.1 An example of the HRC hardness measurement across the section of case hardened crankshaft material.

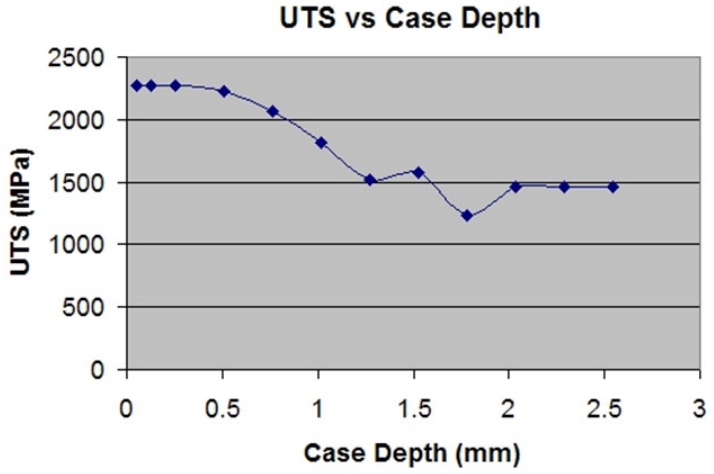

Figure 4.1.2 The ultimate tensile strength across the section of case hardened crankshaft material corresponding to the hardness measurement in Fig. 4.1.1.

4.2 2-D Elastic Axisymmetric FEM Solution For the Press-fit Assembly Problem

Several different finite element method (FEM) models are used to model the assembly and operational behavior of the crankshaft. The press-fit assembly problem is studied by adopting an assumption for the web of axisymmetric behavior in a close vicinity of the pin during the assembly process. It allows a representation of the 3-D geometry with a 2-D mesh.

4.2.1 2-D Axisymmetric Model Description

The press-fit joint receives strength from the stiffness of the web as it interferes and encloses the pin. The corresponding press-fit stresses should be maximum at pin/web interface and also quickly reduce when moving away from this interface. Therefore, the web may be idealized as an annular ring (see Fig. 4.2.1.1), concentric about the pin, of thickness equal to the web size directly above the pin. The modeling and analysis of the interference between the two then becomes much more numerically efficient, as an axisymmetric 2-D meshing may then be used.

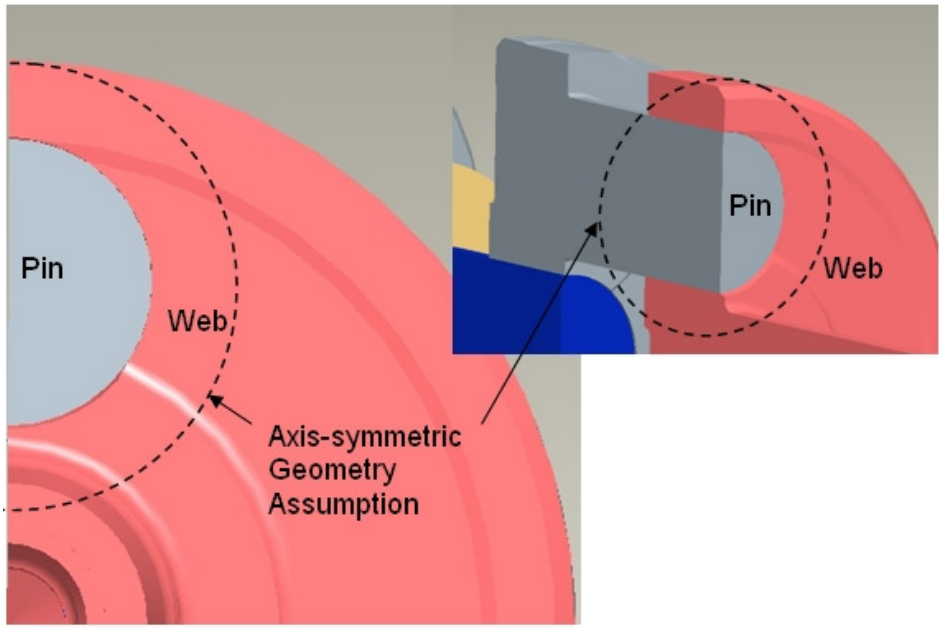

Figure 4.2.1.1 Idealization of the 3-D web-pin geometry into a axisymmetric model.

Figure 4.2.1.2 shows a typical 2-D meshing of the FEA model for simulating a press-fit. Note the radial interference and the geometry of the web at the end of the press-fit at location *A* as shown in the exploded view Fig. 4.2.1.3. The web geometry at A is also presented in Fig.4.2.1.3.

Internally at Polaris it is recognized as a “true radius” edge finish of the web. This geometry was chosen over other shapes based on optimization work aimed at reducing stresses in this critical area, and also considering manufacturability and cost as well. The details of the true radius geometry and optimization are covered further in Chapter 8.

The FEM results presented in this research used the values of geometrical parameters *a*, *r* as given in Fig.4.2.1.3 to define the connection's geometry, unless otherwise indicated.

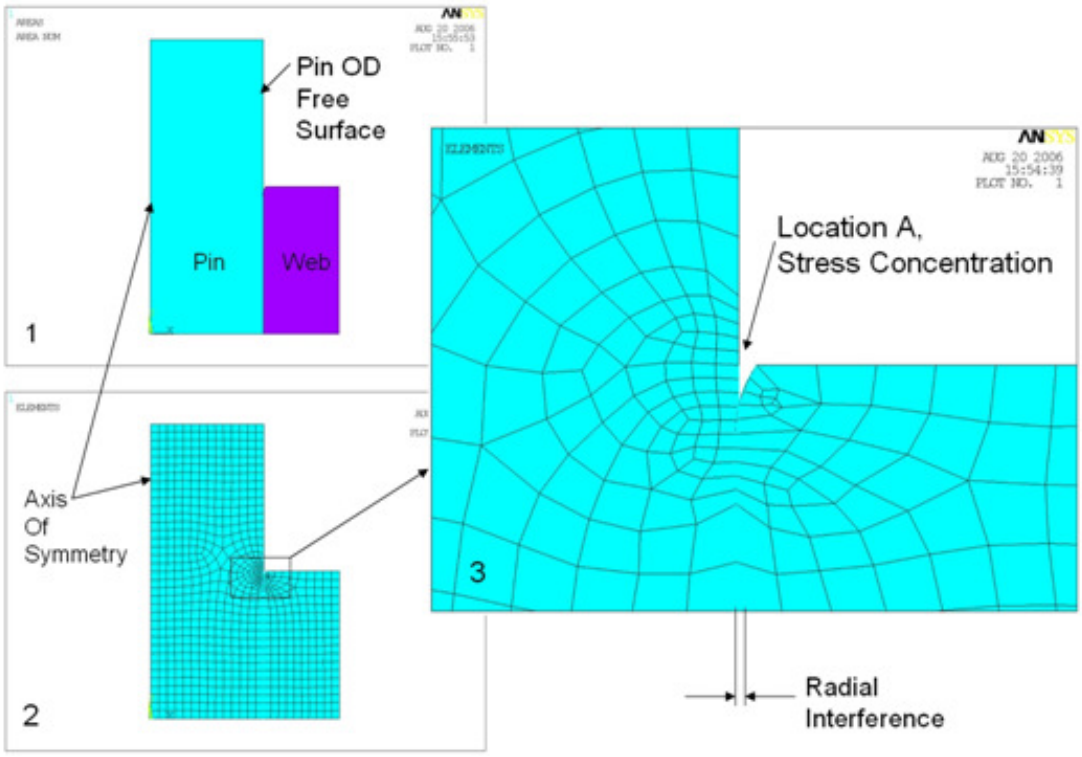

Figure 4.2.1.2 Details of the 2-D press-fit FEM model.

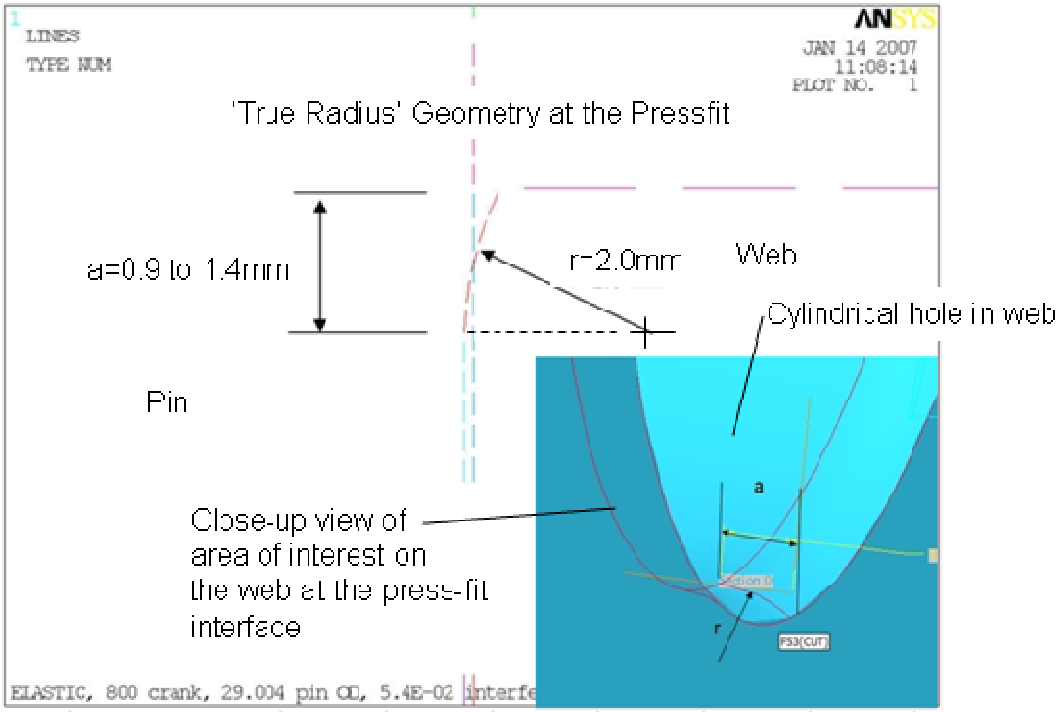

Figure 4.2.1.3 The geometry of the edge finish on the web hole at A.

4.2.2 General Characteristics of Displacement And Stress States

The numerical solution of press-fit reflects the fact that the radial displacement of the pin and web must be such that the interference indicated in Fig.4.2.1.2 vanishes. These displacements are plotted in Fig.4.2.2.1. Although the pin and web displacements are negative and positive respectively, both parts are compressed in the radial (r) direction. However, in the hoop (θ) direction the pin is compressed, while the web is stretched. This in turn causes (due to Poisson's effect) the pin to grow and the web to shrink in the axial y-direction (see Fig.4.2.2.2).

Figure 4.2.2.3 shows radial (x) stress for a typical elastic interference fit, which are compressive stresses in the pin and web, which became equal at the interface. Note a high stress concentration occurring at location *A* of the interface's end. Figure 4.2.2.4 provides a close-up view of the radial stress at this location *A*. Also note the location of maximum stress, which is just before (but not at) the end of the contact zone.

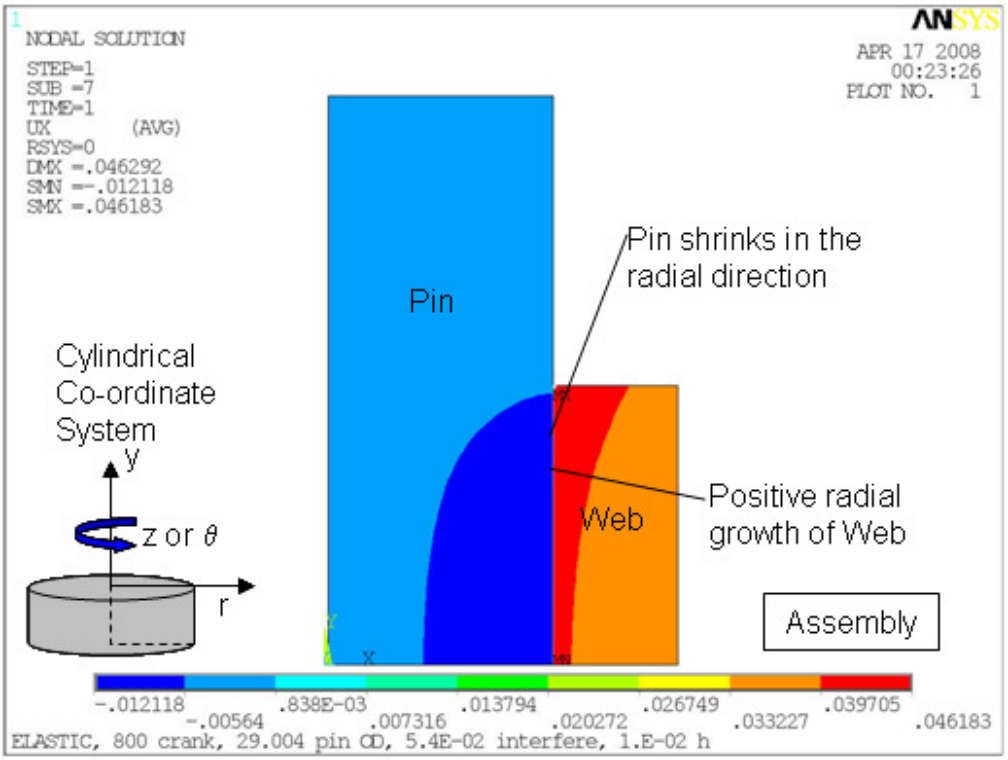

Figure 4.2.2.1 Plot of radial (r) displacement for a typical interference fit.

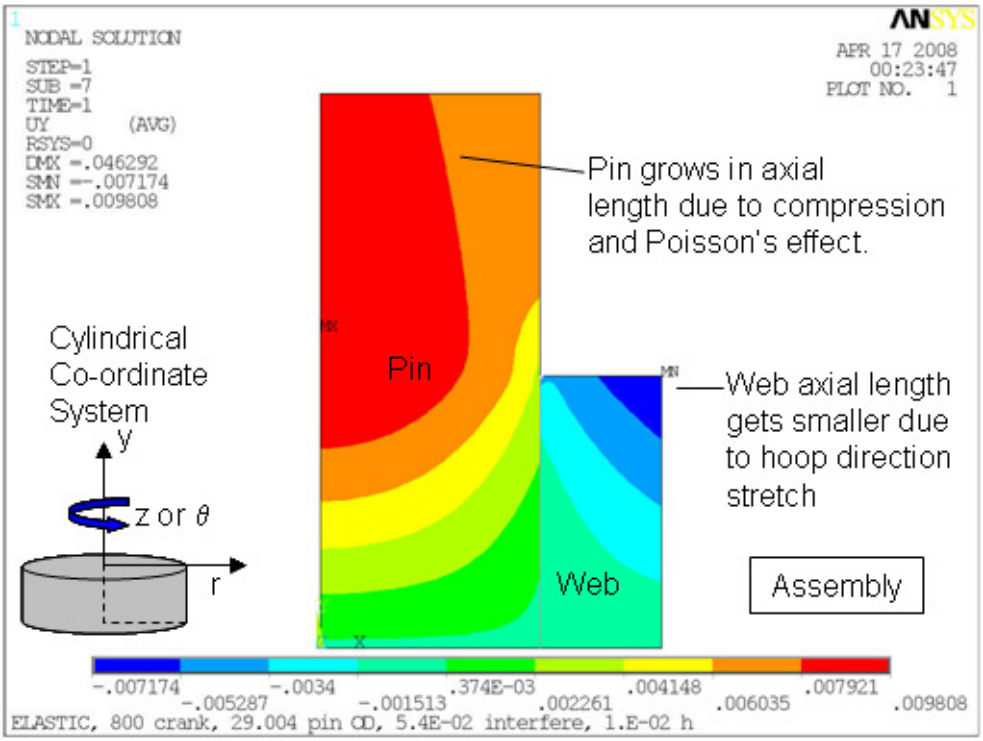

Figure 4.2.2.2 Plot of axial (y) displacement for a typical interference fit.

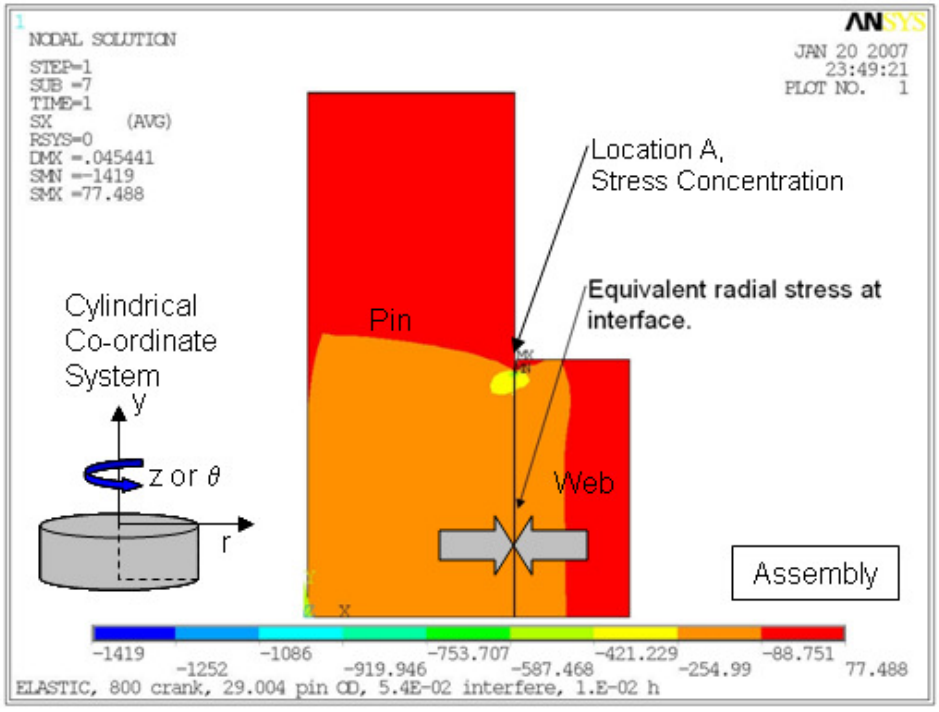

Figure 4.2.2.3 Radial stress distribution for a typical interference fit.

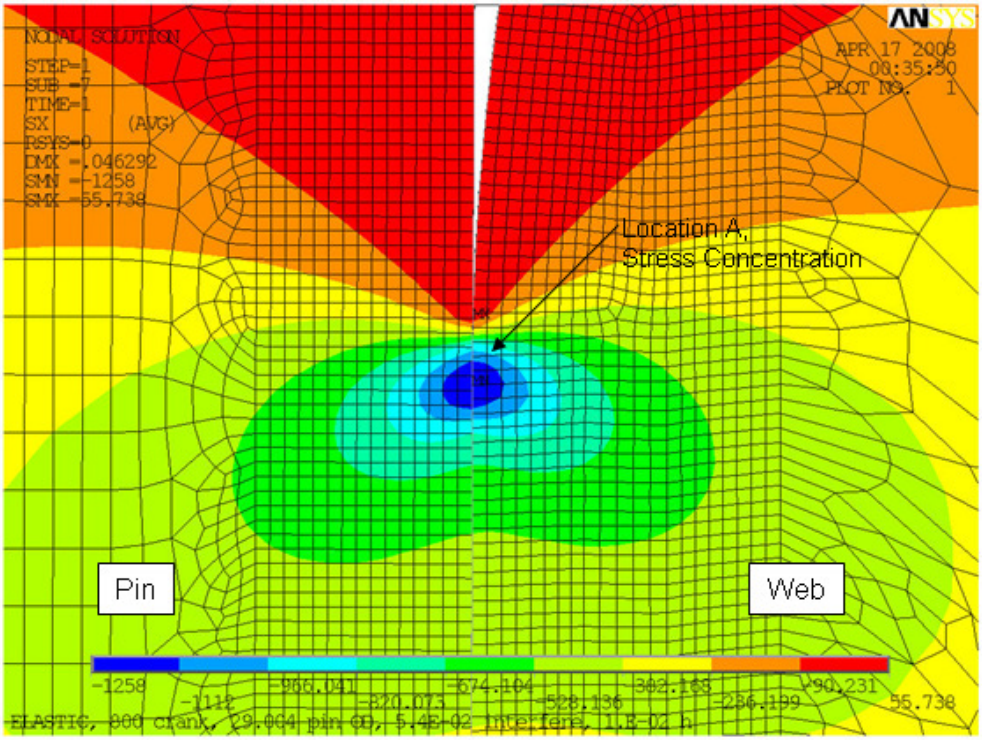

Figure 4.2.2.4 Radial stress distribution at Stress Concentration A (SCA).

As mentioned already, in the hoop direction the web is stretches and the pin is compressed, which is shown in Fig.4.2.2.5 A close up of the area at A (Fig. 4.2.2.6) indicates a stress concentration (SCA) that is higher for compressive σ_θ in the pin than for tensile σ_θ in the web.

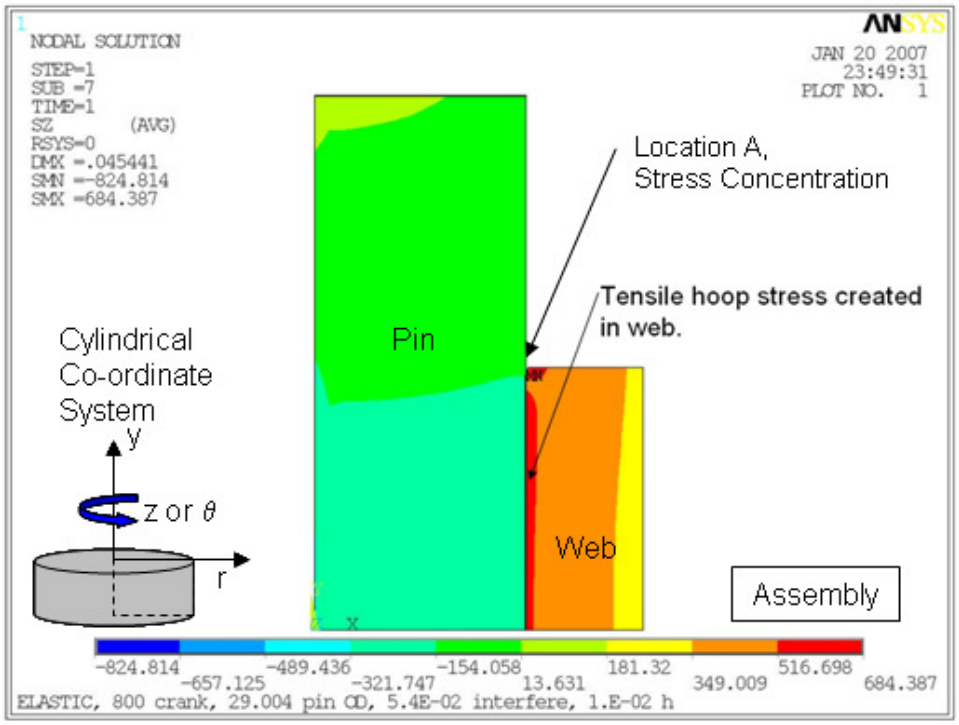

Figure 4.2.2.5 Hoop stress distribution for a typical interference fit.

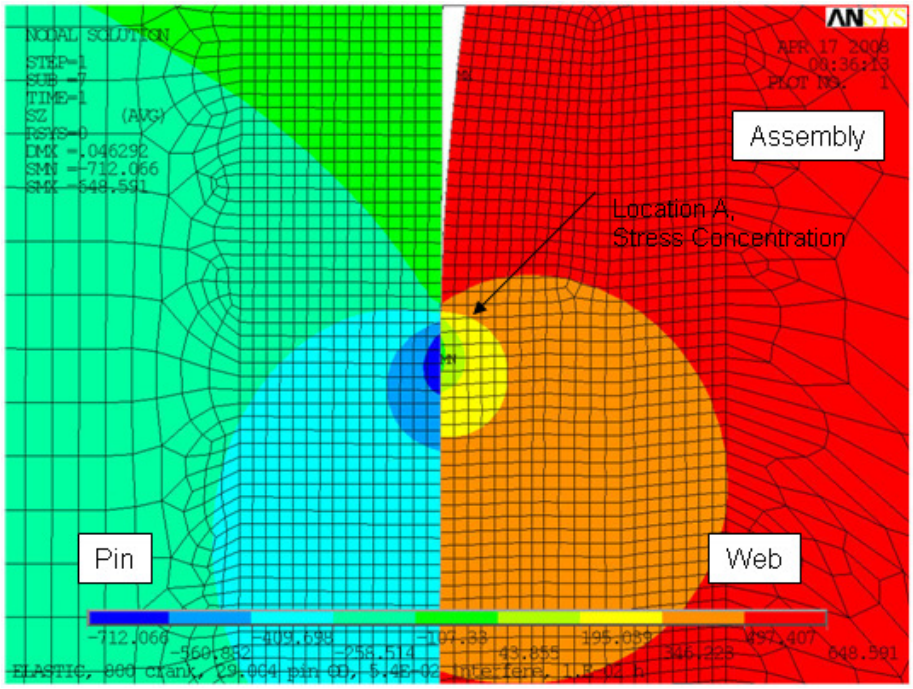

Figure 4.2.2.6 Hoop stress distribution at the SCA location for a typical interference fit.

The axial (y) stress plot in Fig.4.2.2.7 is generally consistent with the axial displacement plot (Fig. 4.2.2.2); that is because of Poisson's effect the pin is too long and must be axially compressed, while the web shrinks and must be axially stretched.

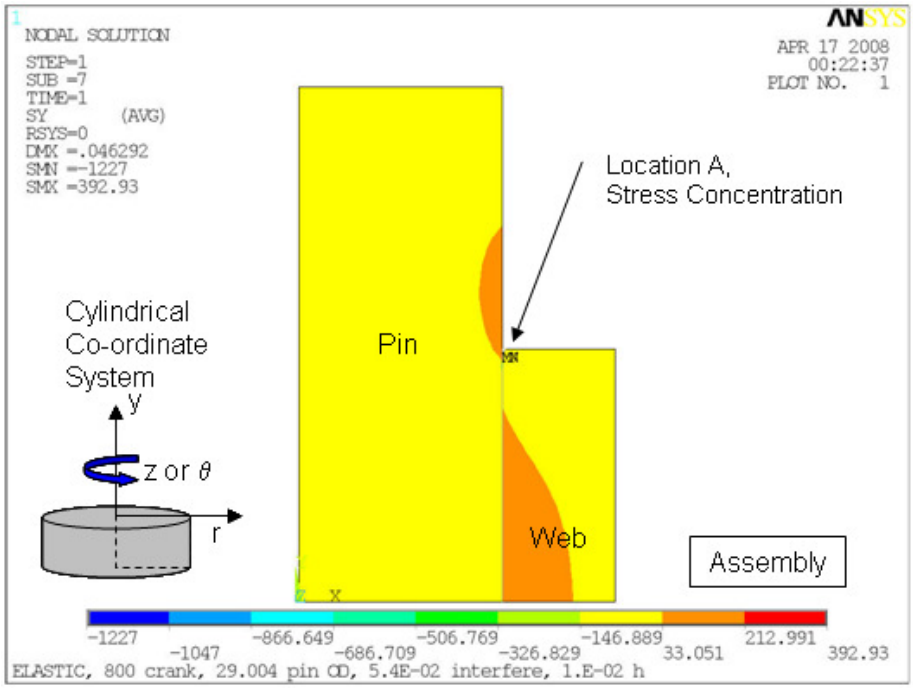

Figure 4.2.2.7 Axial stress distribution for a typical interference fit.

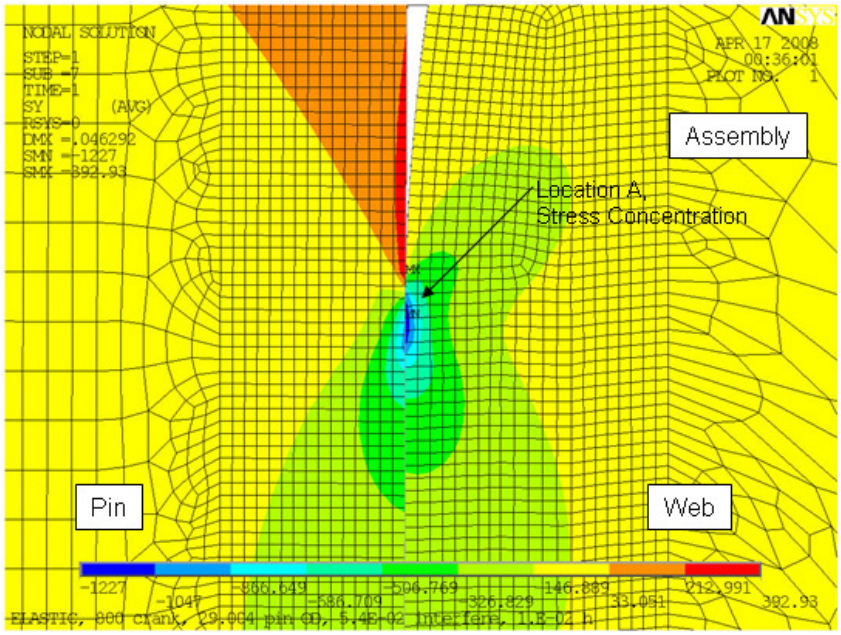

Figure 4.2.2.8 Axial stress distribution at the SCA for a typical interference fit.

However the situation is complicated somewhat at A where high compressive stresses appear in the web. Also, over a short distance the pin surface axial stress goes from compressive (at *A*) to tensile (on the pin free surface just past *A*).

Finally, the nature of the shear stress (τ_{xy}) is indicated in Figs.4.2.2.9 and 10. As can be seen this stress also rises significantly at location *A*.

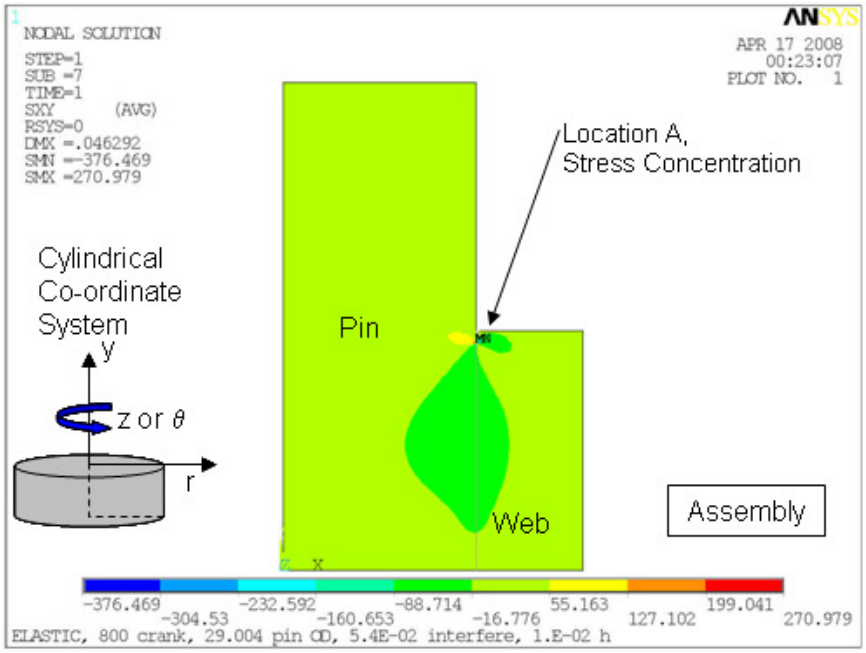

Figure 4.2.2.9 Shear stress distribution in pin and web for a typical interference fit.

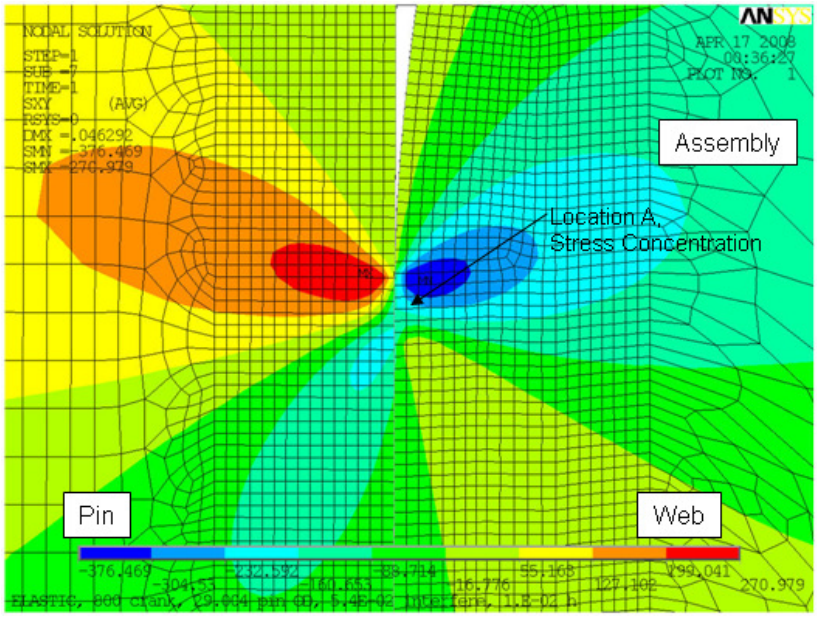

Figure 4.2.2.10 Shear stress distribution at the SCA for a typical interference fit.

Typically, the point of fatigue crack initiation is located on the pin, and therefore the stresses are of greater interest there. Each stress components, i.e. radial, axial, hoop, and equivalent are plotted along the OD of the pin in Figs. 4.2.2.14. Note the large stress gradients and high stress concentrations in the vicinity of *A*.

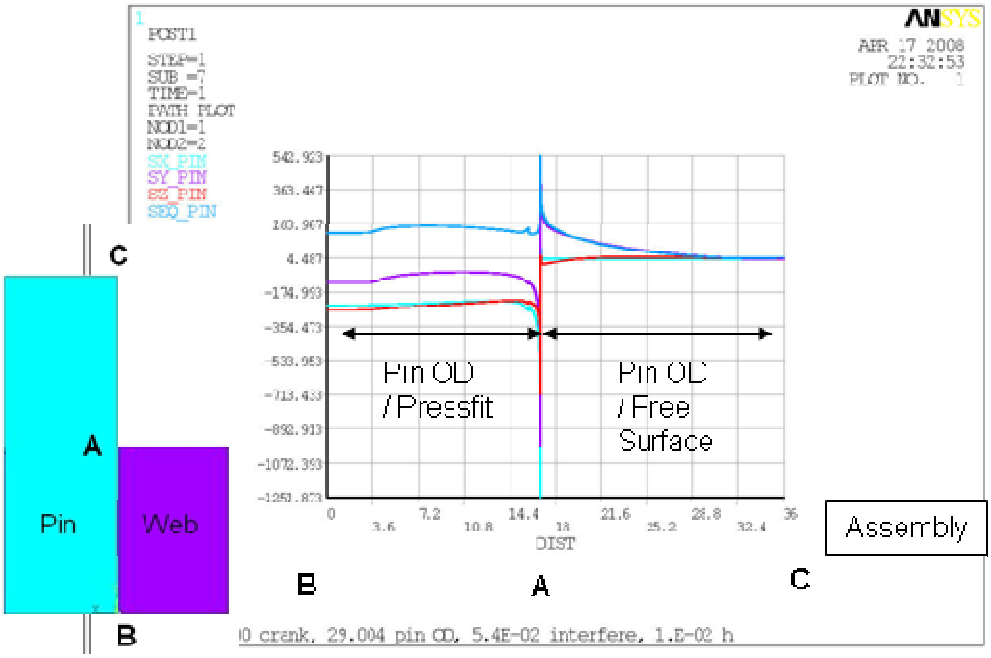

Figure 4.2.2.14 Plot of stress components along pin outer diameter path.

4.2.3 Factors Contributing to the Stress Concentration At A (SCA)

The previous section (4.2.2) describes the overall stress field for the press-fit problem, and reveals a high stress concentration at location *A* of the web-pin interface. In this section some factors are presented which contribute to the stress concentration.

The first is the effect of the geometrical transition from the no-contact to contact condition along the interface. Figure 4.2.3.1 is a close view of axial stress in the area of interest plotted on the deformed shape with the radial and axial displacements distorted 40x. The transition from contact to no contact occurs over a very short distance, and contains some segment with a high curvature denoted as a 'kink' on the profile of the OD of the deformed pin at location *A*. Such a kink is accompanied by a high stress gradient.

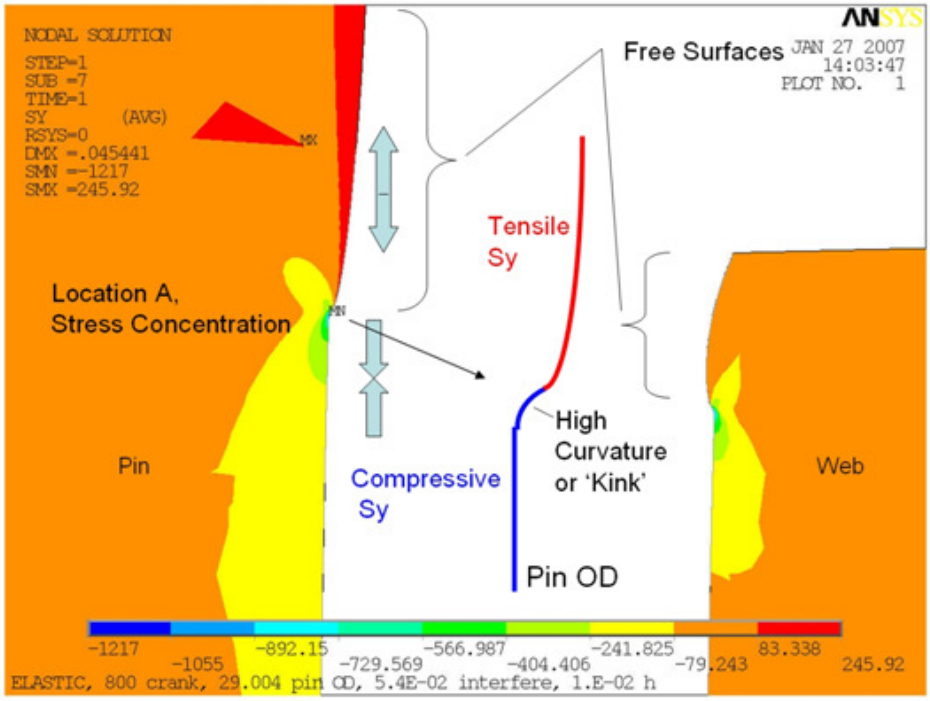

Figure 4.2.3.1 Details of the pin deformation, axial stress field is shown also.

A second factor is that the pin stress at A is magnified further because of Poisson's effect elongating the pin axially, due to the radial compressive stresses. The axial growth mismatch between the pin and web is counter acted by the interface shear stresses. In support of this, Fig. 4.2.3.2 shows that the axial displacement of the pin center is greater than the outer diameter. Axial stress on the free pin surface just outside of the contact region is counter-acted by the shear stress at the interface.

The third factor contributing to the stress concentration is variation in distance v of unsupported web beyond the point of first contact, as shown in Fig. 4.2.3.3. As v increases, a larger portion of the web cylinder is unsupported, and must then be supported by higher radial forces at location *A*. This is equivalent to using a very small or finite segment of the pin surface to force the total unsupported section of the web outward in the radial direction. This factor can be tested by varying the geometry of the 'true radius' so that the contact start location is moved further in or out.

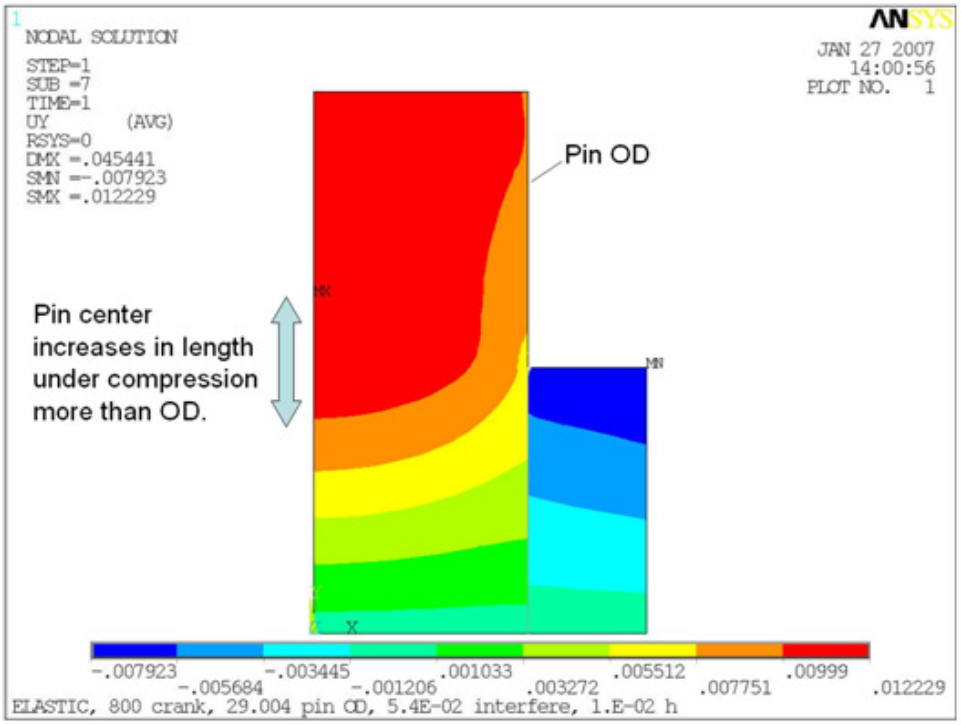

Figure 4.2.3.2 Displacement in the axial (y) direction for the pin and web.

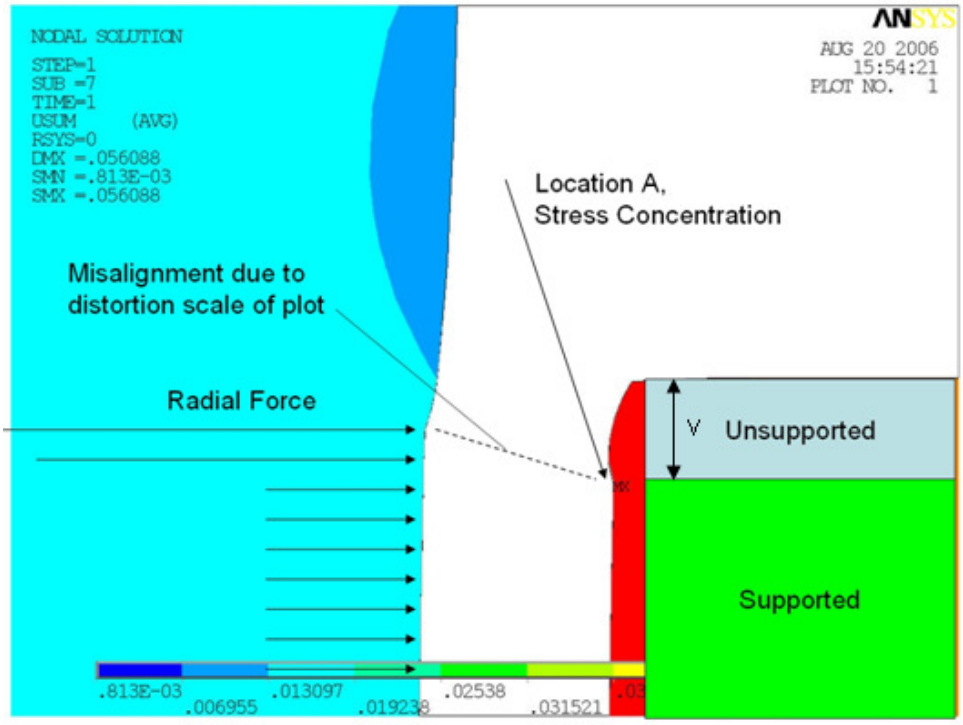

Figure 4.2.3.3 Effects of the unsupported web past location *A* on high radial stress at A.

4.2.4 Stress Details At The SCA

The behavior of the pin and web at the SCA under assembly is now examined in detail. Figure 4.2.4.1 shows the vicinity of the SCA and several areas that are selected for further mesh refinements in the FEM model. The area 3 with the deformation magnified 40x is shown in Fig. 4.2.4.2, with a 'kink' visible in the pin material at the SCA. Initially, prior to 'assembly', all elements in this area, from the free pin surface (top of rectangle) to the compressed pin surface (bottom of rectangle), were square in shape. When assembled, the elements at the top end of the area are longer than the bottom end, because of the compressive forces exerted on the pin by the web.

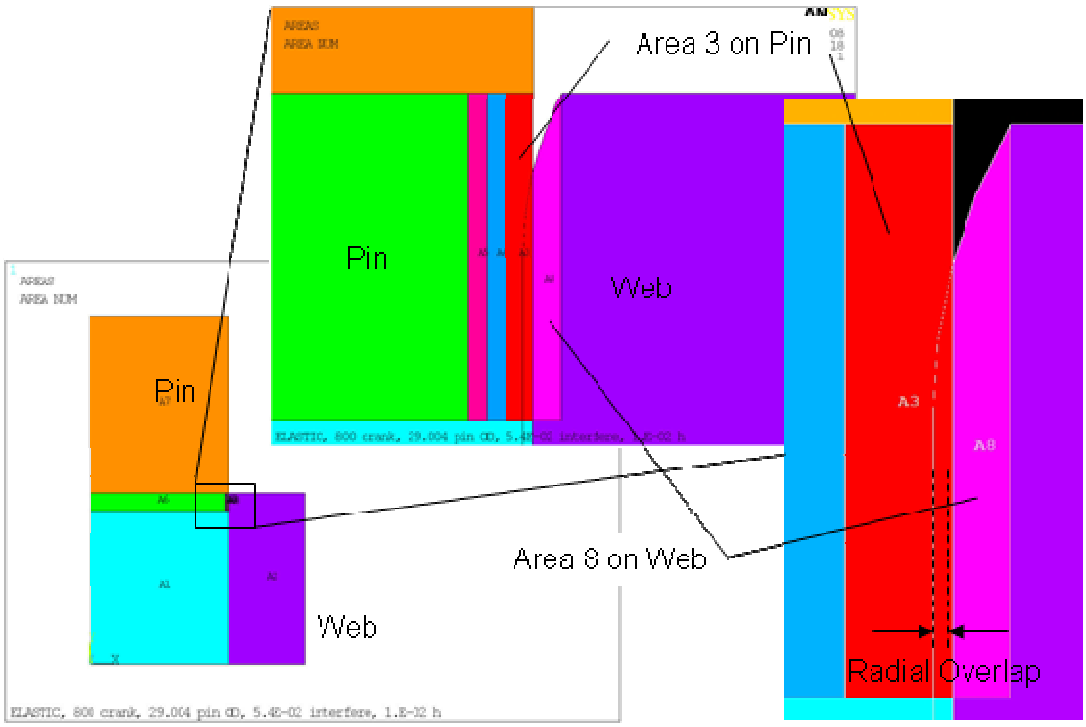

Figure 4.2.4.1 Identifying Areas 3 and 8 used in meshing refinement at the SCA.

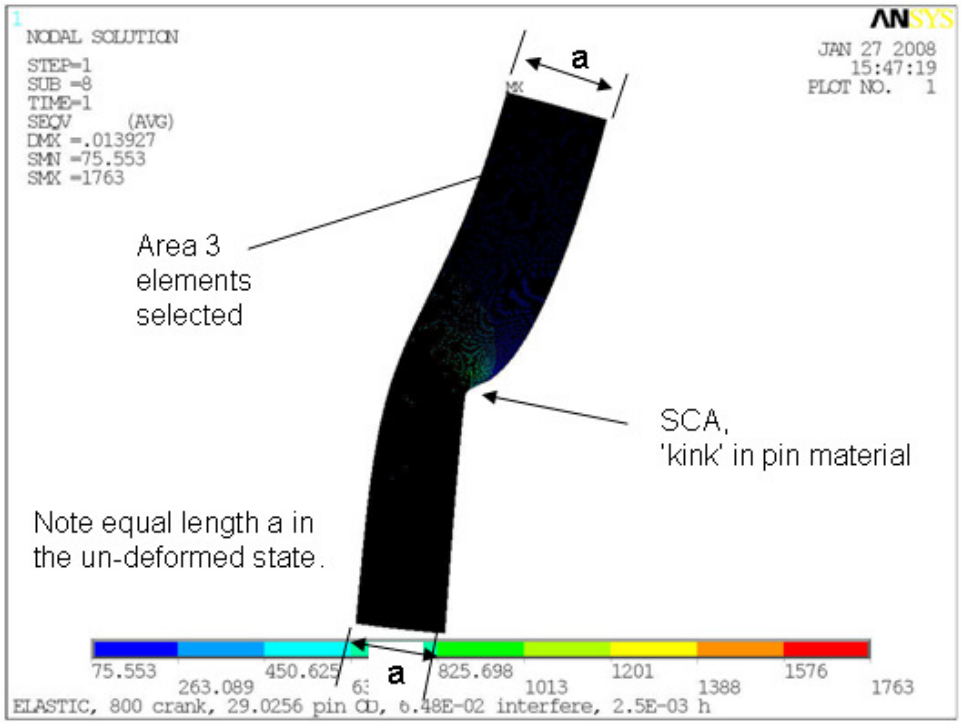

Figure 4.2.4.2 A deformed equivalent stress plot of area 3.

Two refined FEM models are studied in this section, one with a relatively coarse meshing defined by element size h=0.05mm, and one with a dense meshing defined by h=0.0025mm. Differences and similarities of the solutions rendered by these two models are discussed next to help in subsequent analysis of the problem. Note all stress plots are shown on the deformed shapes with a 40x magnification of displacements, similar to Fig. 4.2.4.2.

The radial stresses are shown in Fig. 4.2.4.3 and Fig. 4.2.4.4 for the coarse and fine mesh solutions respectively. High compressive radial stresses occur on the pin surface at similar locations for both solutions, but the refined mesh solution in Fig. 4.2.4.4 represents the continuous shape of the 'kink' at the SCA location more accurately.

The axial stresses are plotted in Fig. 4.2.4.5 and Fig. 4.2.4.6 for the coarse and refined mesh respectively. Note a transition from a high compressive stress at the SCA into a tensile stress on the free surface. The tensile stress is due to the high curvature of the pin surface, this stress is of particular interest because of its additive nature to any pin bending stresses from operating loads.

It should be noted that all three normal stress components in the radial, axial, and hoop directions have compressive stresses at the SCA.

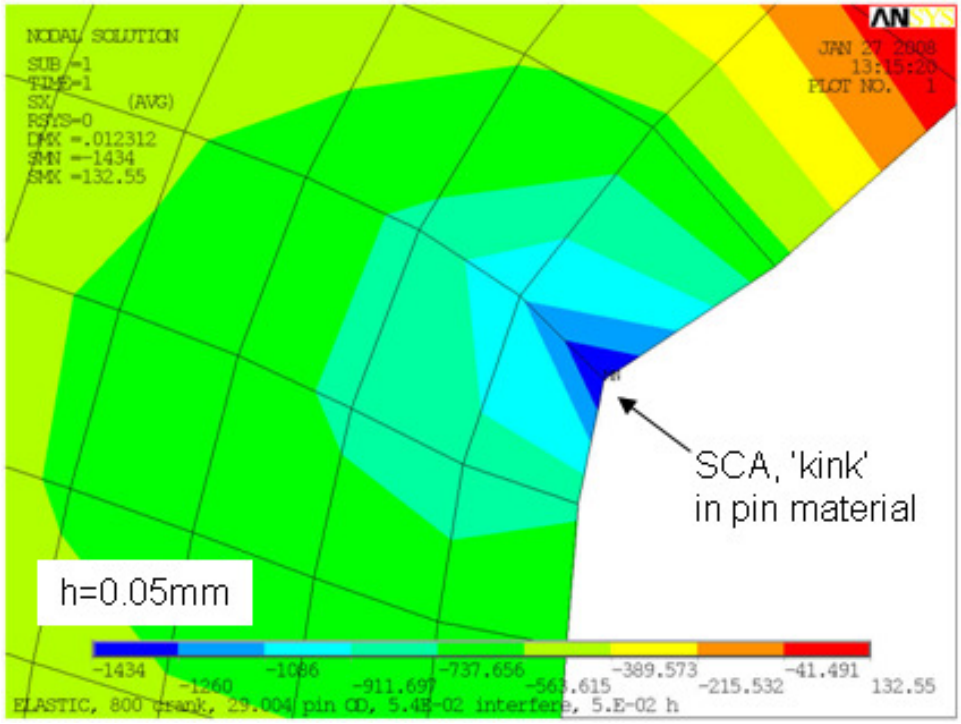

Figure 4.2.4.3 A plot of radial stress in area 3 for meshing h=0.05 mm.

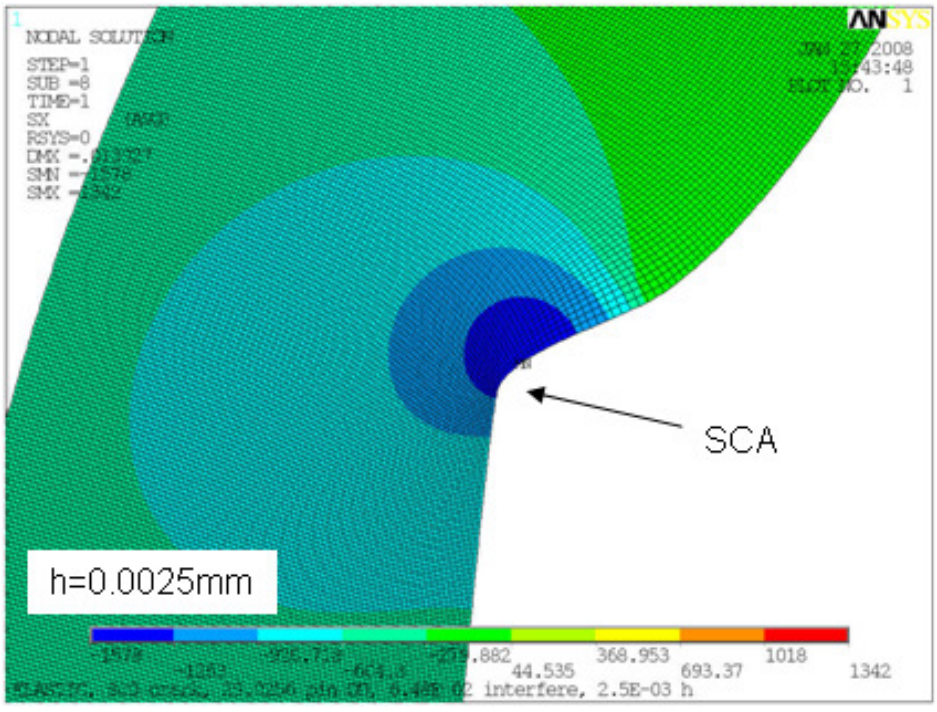

Figure 4.2.4.4 A plot of radial stress in area 3 for meshing h=0.0025 mm.

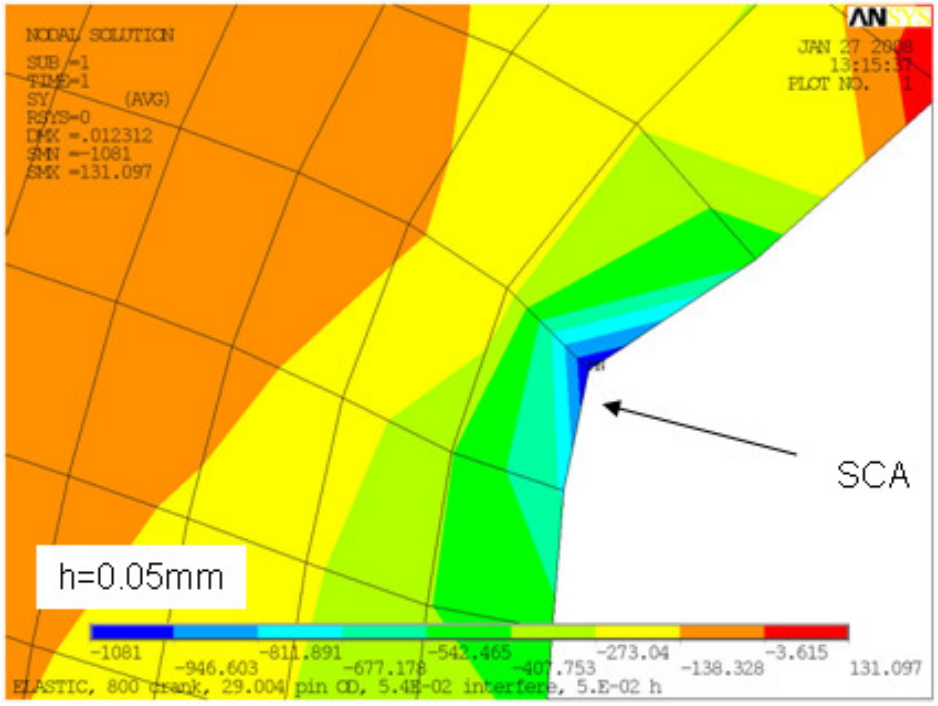

Figure 4.2.4.5 A plot of axial stress for meshing h=0.05 mm.

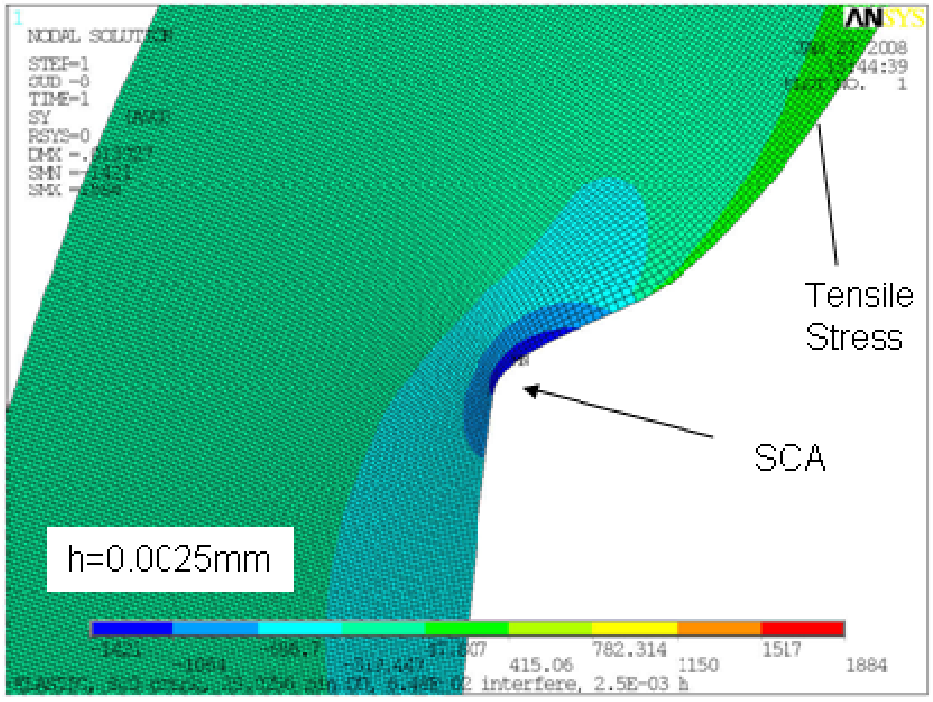

Figure 4.2.4.6 A plot of axial stress for meshing h=0.0025 mm.

The shear stresses are examined at the SCA in Fig. 4.2.4.7 (fine mesh). The maximum stress resides below the surface of the pin in the no-contact zone.

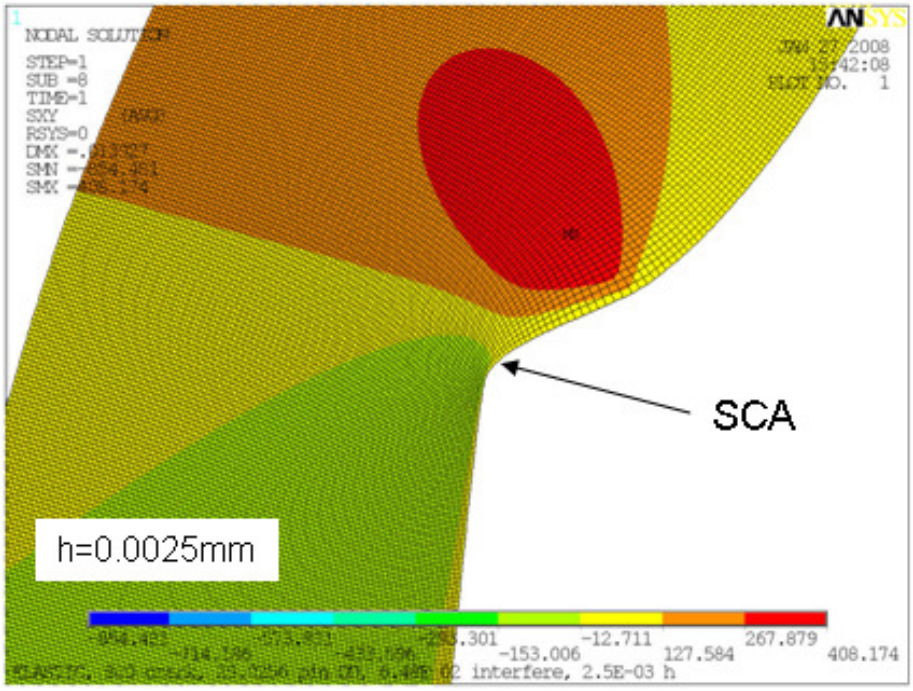

Figure 4.2.4.7 A plot of shear stress τ_{xy} at meshing *h* equals 0.0025 mm.

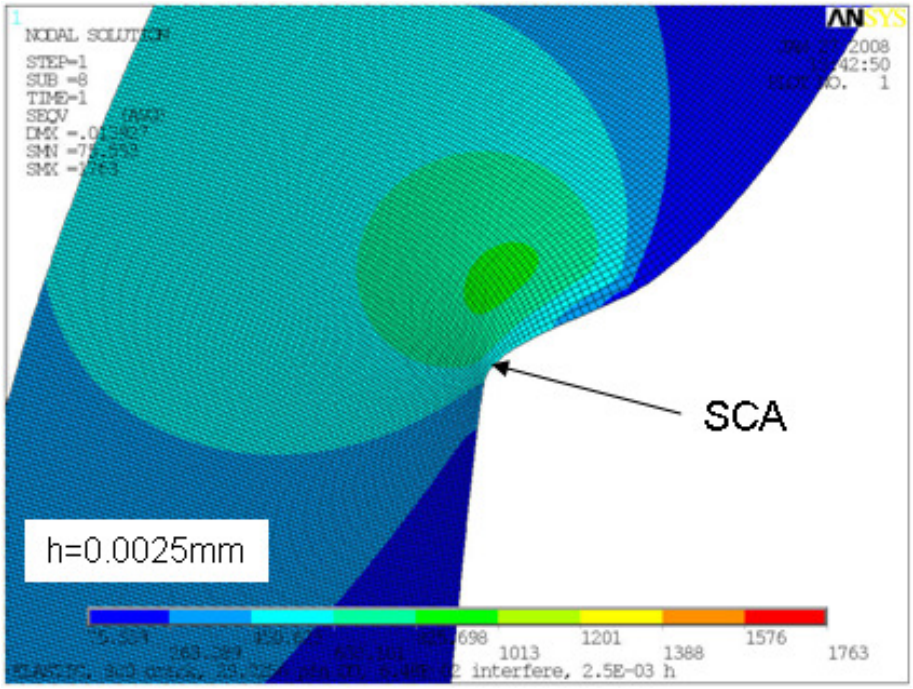

Figure 4.2.4.8 A plot of equivalent stress σ_{VM} at meshing *h* equals 0.0025 mm.

Finally, the Von Mises equivalent stresses are shown in Fig. 4.2.4.8. Similar to the shear stress, the maximum equivalent stress is located under the surface. The maximum τ_{xy} and σ_{VM} are in different but close elements for the dense mesh solutions.

A vector plot of the principal stress values are also given for this same close up view in Fig. 4.2.4.9. Note high compressive stresses, S3 (the values and directions of these stresses are indicated by arrows) dominating this nodal plot. Such stresses are created by the high radial compression and Poisson's effect.

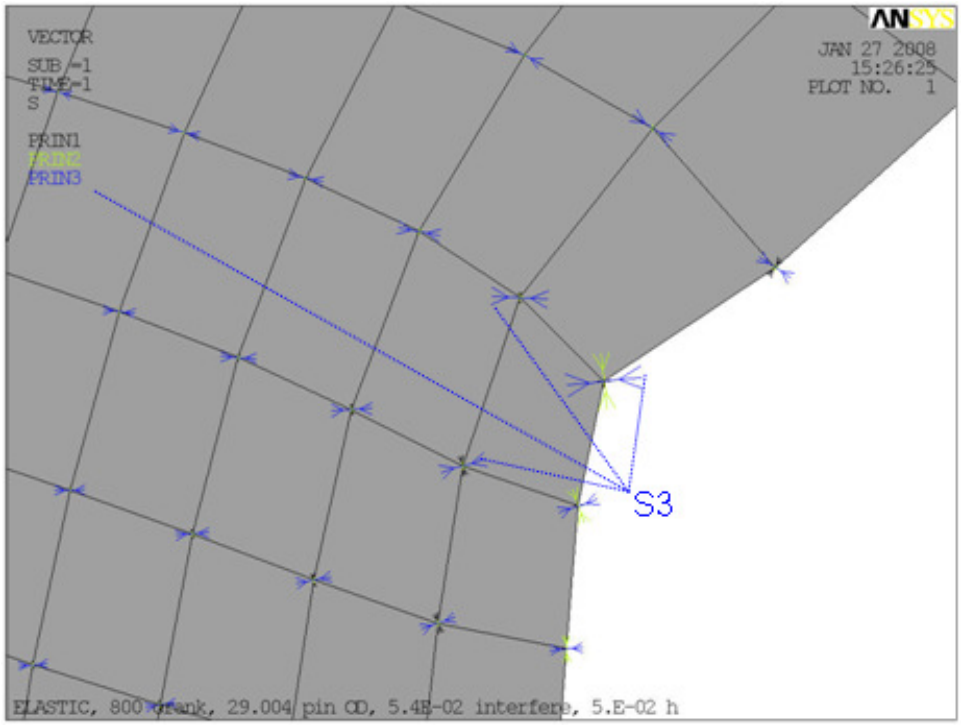

Figure 4.2.4.9 A local plot of principal stress vectors at the SCA for a coarse mesh.

The un-averaged (element) equivalent and shear stress distributions are shown in Figs. 4.2.4.10 and 11 respectively. Note the differences in stresses calculated for neighboring elements (along side KN in Fig.4.2.4.10, for example). These differences (stress errors) indicate high stress gradients in these locations. The stress errors are significantly smaller for the mesh with h=0.0025 mm. Further mesh refinement studies are presented in section 4.2.5.

Figure 4.2.4.12 shows the shapes of distorted elements in the vicinity of the maximum shear stress for the refined solution (it can be viewed as a close up of Fig. 4.2.4.2). At the transition from contact to no contact between the pin and web, the pin material at surface 'explodes' out in a radial direction past the SCA location to reach a 'free state' location at the distance of the pin radius. It forces the elements to severely distort from a perfect square shape to parallelograms.

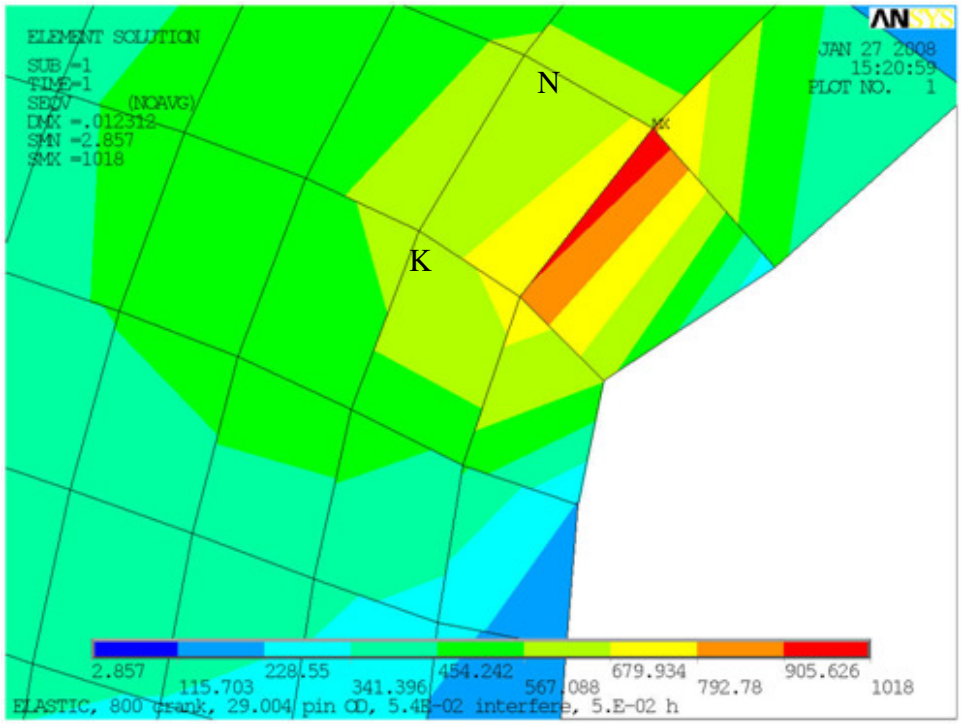

Figure 4.2.4.10 A coarse mesh σ_{VM} plot at the SCA showing the un-averaged stress.

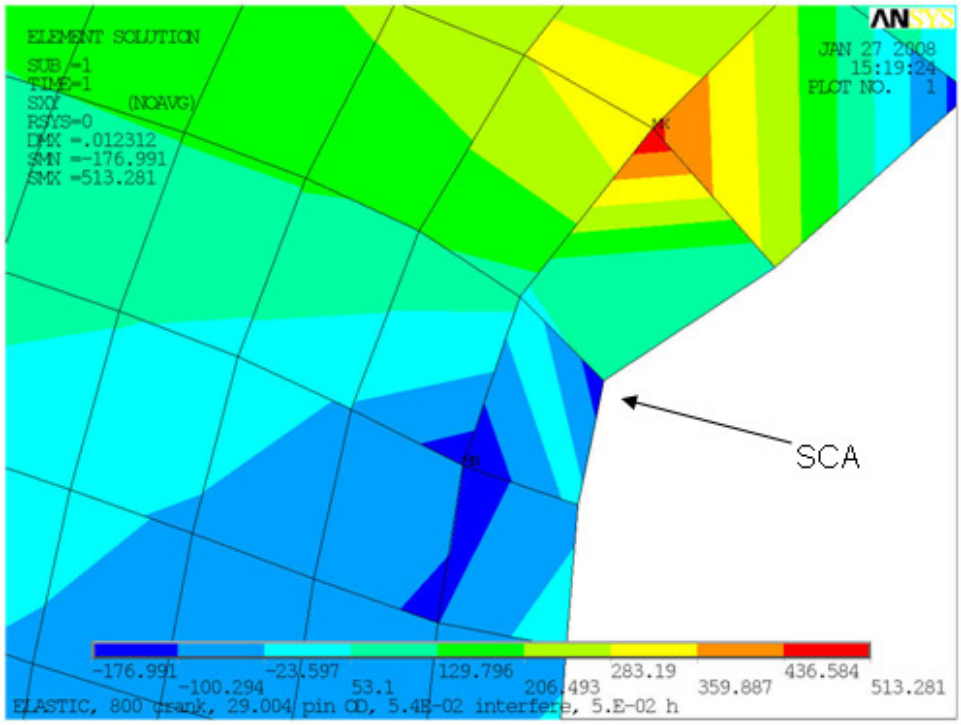

Figure 4.2.4.11 A coarse mesh τ_{xy} plot at the SCA showing un-averaged stress pattern.

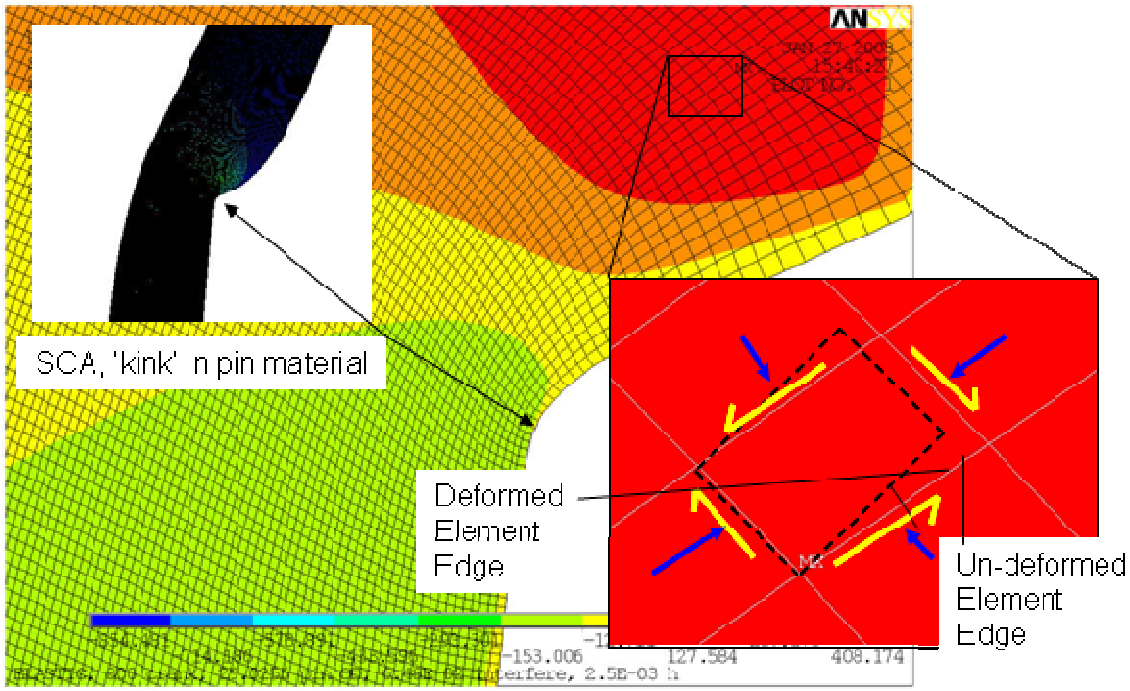

Figure 4.2.4.12 Distortion of elements for the refined mesh.

As described above, the stress distribution in the pin is similar to that for a Hertzian contact problem; a normal loading (radial contact stress in this case) which produces high compressive normal stresses directly below the contact. Then, because of Poisson's ratio, the material being compressed must expand or push out in directions normal to this direct pressure. However, material normal to this direct loading axis will try to resist this expansion, creating compressive stresses in these 'perpendicular to normal' directions as well. As the location moves away from directly beneath the contact, to a 'no contact' area, the shear stress becomes a maximum at some distance below the surface. The same situation can be observed on the top half of Figure 4.2.4.13 from [26], which provides a elemental breakdown of the stress state for a Hertzian contact problem. Note that the maximum shear stress location for both the press-fit FEM solution and the textbook Hertz contact problem both have maximum shear stress that is 'off to the side' from the location of maximum direct loading.

The press-fit stress field and that of a Hertzian contact stress field will be examined and compared next. Using terminology from [26], distance b in Figure 4.2.4.13 is defined as the radius of the contact patch surface area. For the press-fit problem, b can be interpreted as the

distance from maximum pressure (at A) to pressure equals zero. This assumes cylinders as the contact objects, one flat object (pin) and one cylindrical object (web), both of which are not planar in shape (see Fig.3.2.1.5 for the description of the axisymmetric geometry assumed as flat). Parameter p_o is defined as the maximum contact pressure, which for the press-fit is the maximum radial stress (σ_r) at the SCA. Both b and p_o are defined in Fig. 3.2.1.6 in section 3.2.

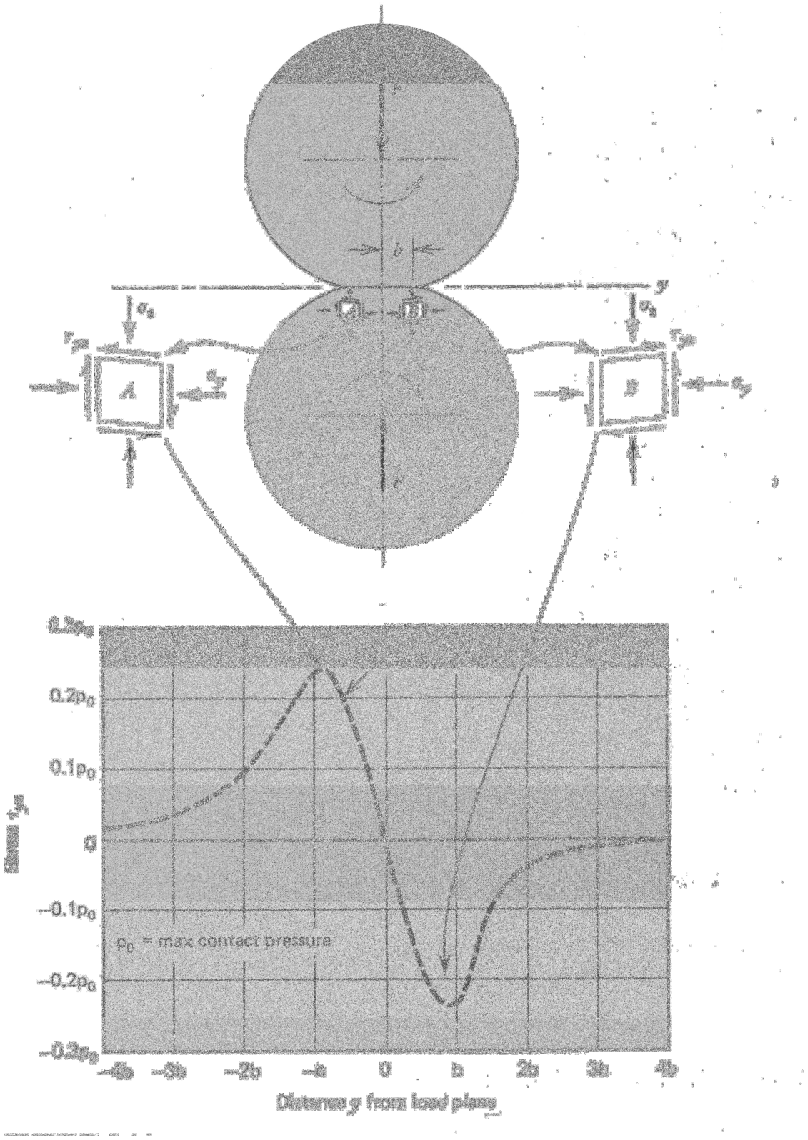

Figure 4.2.4.13 The stress state for two spheres/cylinders in Hertzian contact [26].

The radial stresses at the SCA for a refined mesh are depicted in Figure 4.2.4.14, the geometry parameter b identified from the plot path information is also shown. Note that the selection set has been expanded to include elements from both the pin and web. Figure 4.2.4.15 is a plot of

shear stress τ_{xy} at the SCA, and shows the same path information overlaid, a path for τ_{xy} below the surface at a distance 0.66b is also included.

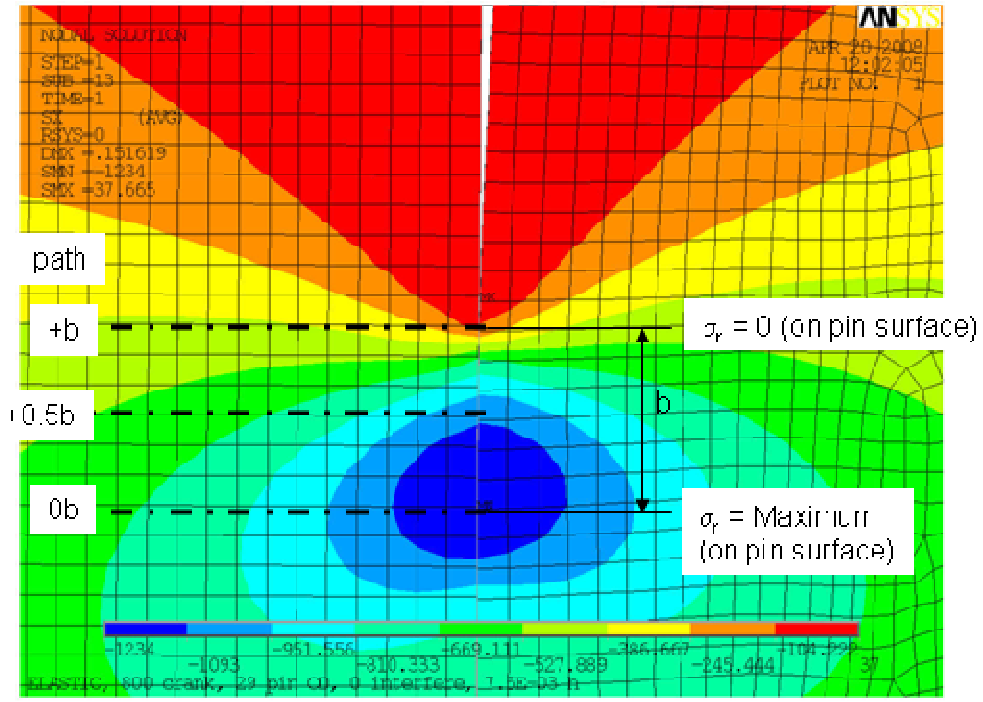

Figure 4.2.4.14 A plot of radial stress at the SCA showing plot path information.

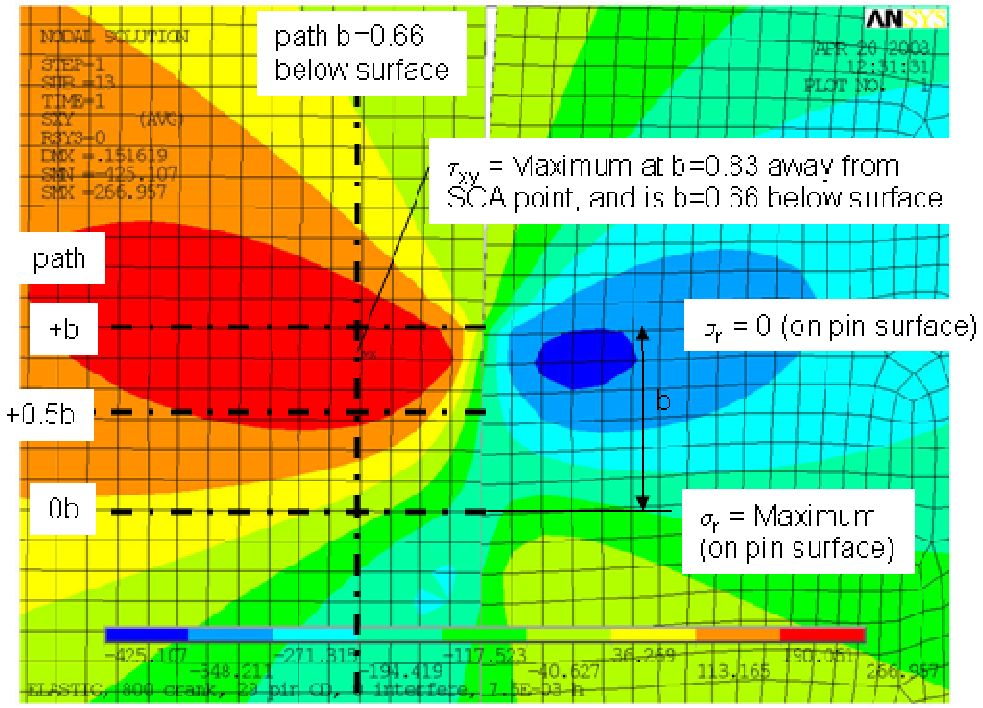

Figure 4.2.4.15 A plot of τ_{xy} stress at the SCA showing plot path information.

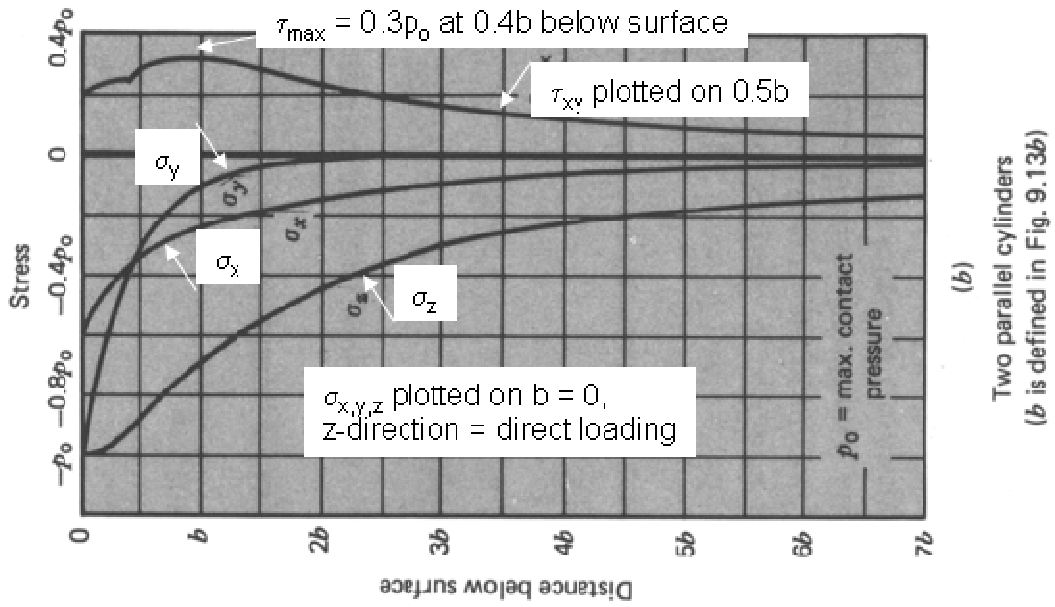

Figure 4.2.4.16 Normalized σ_r and τ_{xy} stress for a Hertzian contact from [26].

Figure 4.2.4.16 is taken from Juvinall [26] and shows stress component values plotted along paths that lead from the surface of the contacting bodies at *b* equals 0 for $\sigma_{x,y,z}$ and at *b* equals 0.4 where τ_{xy} is maximum.

The radial σ_r and shear τ_{xy} stresses for the press-fit problem are plotted in Figs. 4.2.4.17. The same stresses but normalized are plotted again in Fig. 4.2.4.18. All stresses are normalized in terms of maximum contact pressure σ_r at the SCA and the distance is normalized in terms of parameter b. The shapes of the 'Hertzian' plots in Fig. 4.2.4.16 and for the press-fit problem plots are very similar.

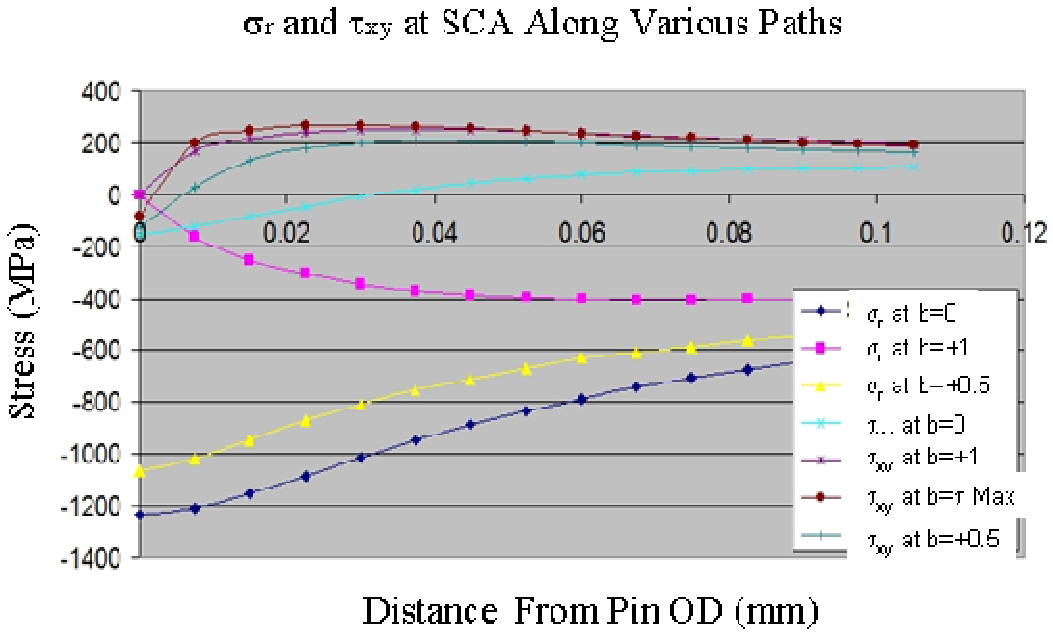

Figure 4.2.4.17 A plot of σ_r and τ_{xy} using various path locations for geometry unit b.

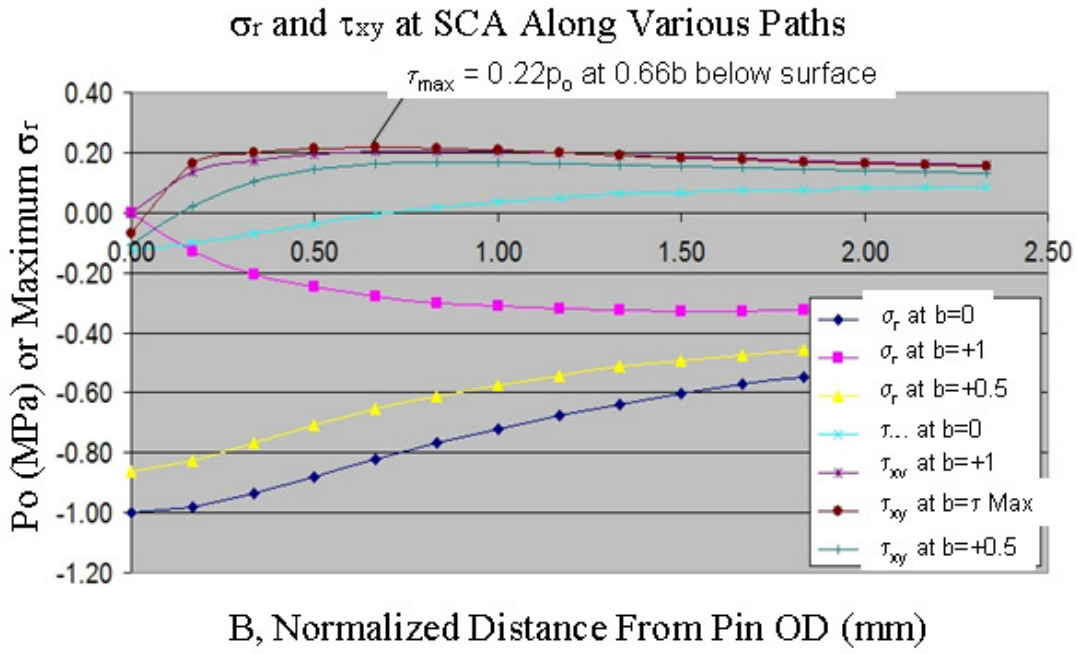

Figure 4.2.4.18 Normalized σ_r and τ_{xy} plots using geometry unit b path locations.

Note that for the Hertzian contact stress problem, the location of the maximum shear stress occurs at a distance 0.5b to the side of the maximum direct stress and at a distance 0.4b below

the surface. For the press-fit problem considered the FEA solution renders the maximum shear stress at location 0.83b to the side and 0.66b below the surface. The difference is most probably due to the fact that the press-fit problem is not symmetric about b equals 0 as is the Hertzian problem. Other parameters such as interference, pin and web axial length, and the true radius geometry of the web may also affect the maximum value and location.

Plots of τ_{xy} stress (in MPa and normalized) for the press-fit problem along a path of 0.66b below the surface (through the maximum τ_{xy} location) are shown in Figures 4.2.4.19 and 4.2.4.20. The shape of the shear stress curve again is very close in shape to that displayed in Fig. 4.2.4.13 taken from [26] for the Hertz problem. Because the press-fit problem is not symmetrical about the axis b equals 0, the maximum and minimum shear stress values are not equal as is the case for the Hertzian example.

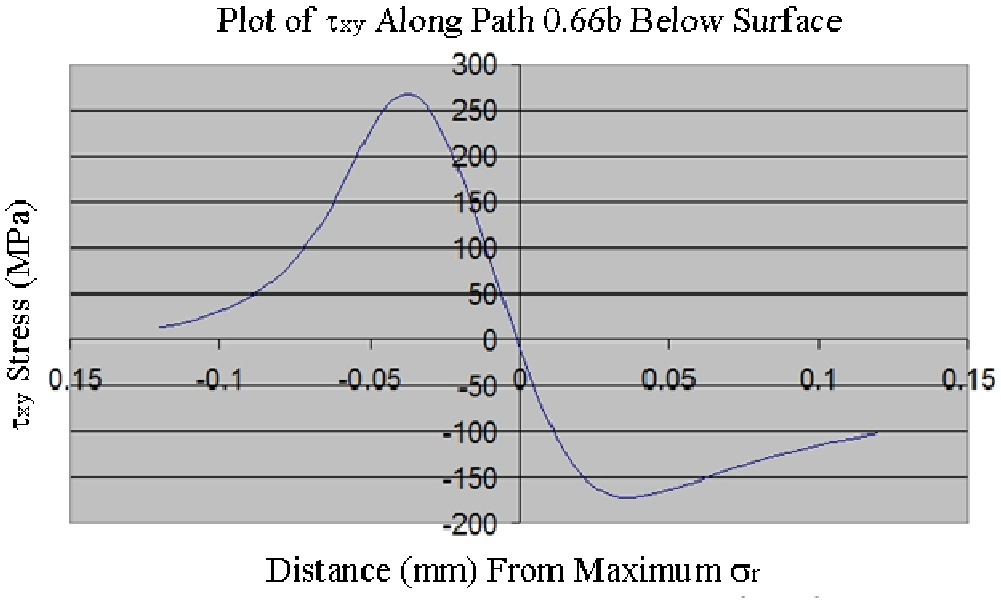

Figure 4.2.4.19 A plot of subsurface τ_{xy} stress along path 0.66b (τ_{xy} maximum).

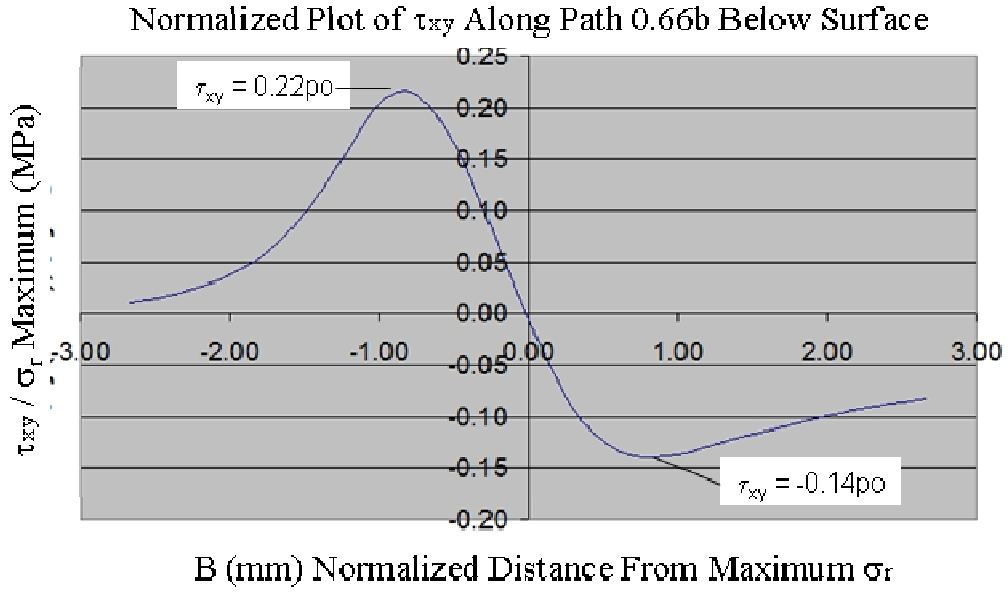

Figure 4.2.4.20 Normalized subsurface τ_{xy} stress along path 0.66b (τ_{xy} maximum).

4.2.5 Mesh Refinement Studies of Assembly Model At The SCA

As shown previously, high stress gradients are present in the vicinity of the SCA requiring a fine meshing at this location. A detailed sensitivity analysis of the maximum stress values versus element size is presented in this section. The 2-D geometry of the axisymmetric model was constructed in such a way (see Figure 4 2.4.1) so as to control the mesh density at the SCA. The pin and web geometry at the SCA is split into smaller rectangular areas to be used for mesh refinement. Other areas of the model will retain a coarse mesh for best numerical efficiency.

Figure 4.2.5.1 provides an example of meshing areas 3 and 8 with this approach by elements of size *h* equals 0.1 and *h* equals 0.0075 mm. It should be noted that one of the challenges in this task is to reasonably transition the mesh from fine to coarse size without creating unfavorable element shapes and aspect ratios. It worthwhile to add that the solve times increases from less than 1 minute for *h* equals 0.1mm to over 30 minutes for *h* equals 0.005 mm.

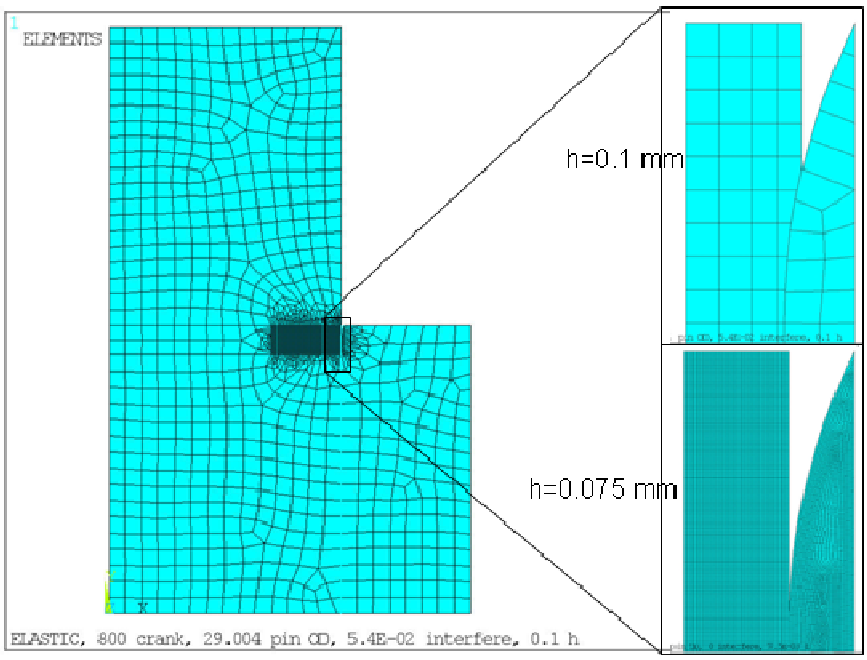

Figure 4.2.5.1 Areas 3 and 8 at the SCA with *h* equals 0.1mm and 0.0075mm.

Locations of maximum or minimum of particular stress components are different (see points A B C, and D in Fig. 4.2.5.2) and will be tracked independently.

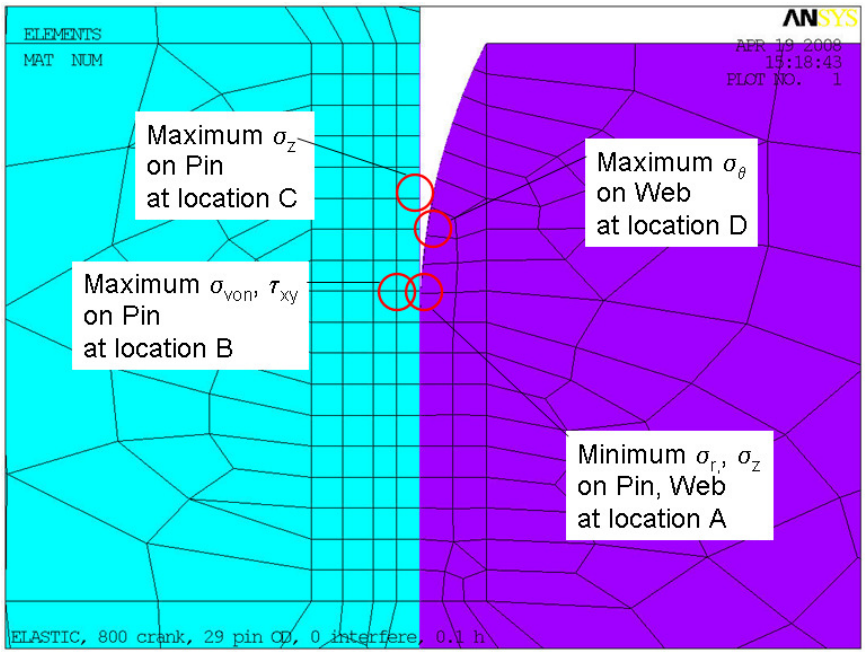

Figure 4.2.5.2 Stress component locations tracked for variation in element size *h*.

Figure 4.2.5.3 shows a typical relationship between the element size *h* and the pin minimum σ_r at location A. The value of *h* varied from *h*=0.005 mm to *h*=0.375 mm. The results were obtained assuming the surface friction coefficient u=0.13 and then u=0 (no friction). As can be observed the convergence in both cases is achieved at about *h*=0.05mm. The minimum σ_r values are approximately 11% lower when a surface friction is considered.

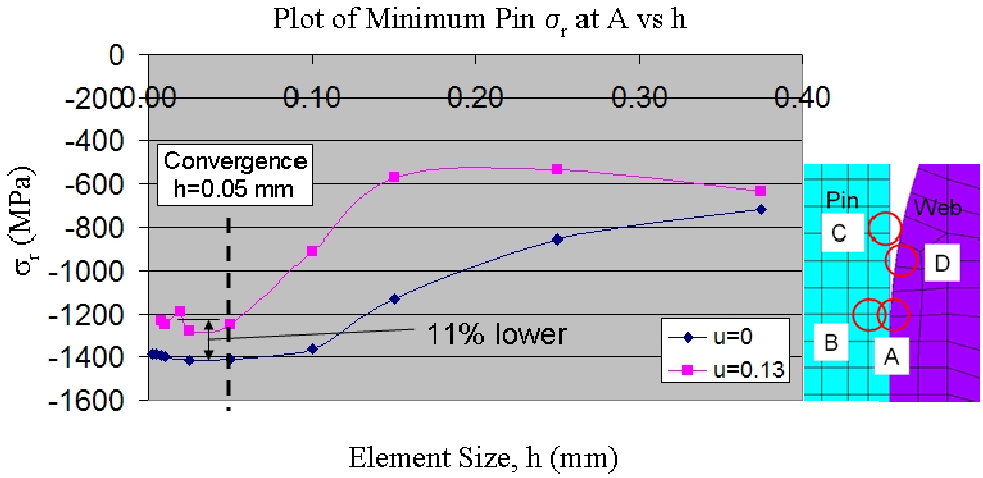

Figure 4.2.5.3 Plot of minimum pin σ_r at A versus *h* for different friction values.

Figure 4.2.5.4 plots the same results (i.e. minimum radial stress at A versus h) using a logarithmic scale (also called a log-log plot). The slope of the curve from *h* equals 0.05 mm and below is very flat indicating convergence.

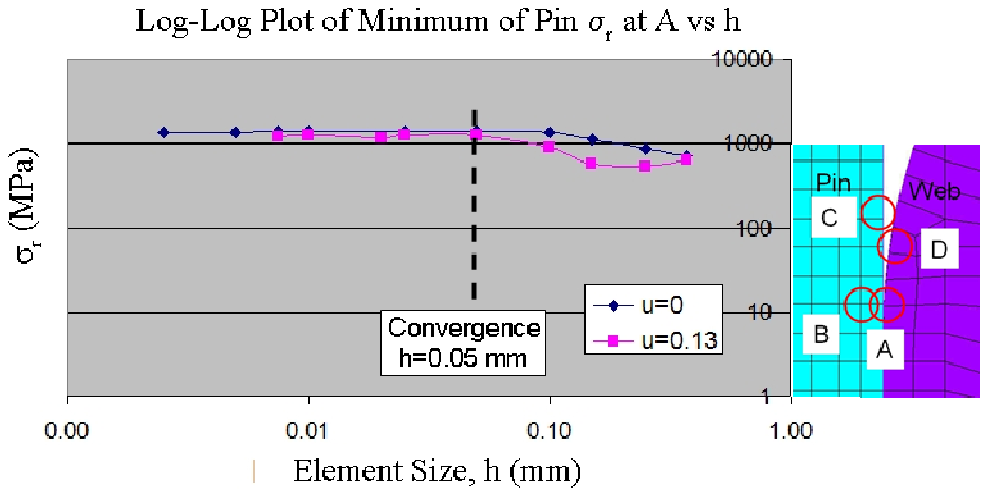

Figure 4.2.5.4 Log-Log plot of minimum pin σ_r at A versus element size *h*.

Note that the minimum axial and hoop stress values at A have nearly identical sensitivity and convergence curves in comparison to the radial stress values at A. Since the relative magnitudes of these stress components may be related because they occur at the same location, only the linear plots are shown to maintain brevity.

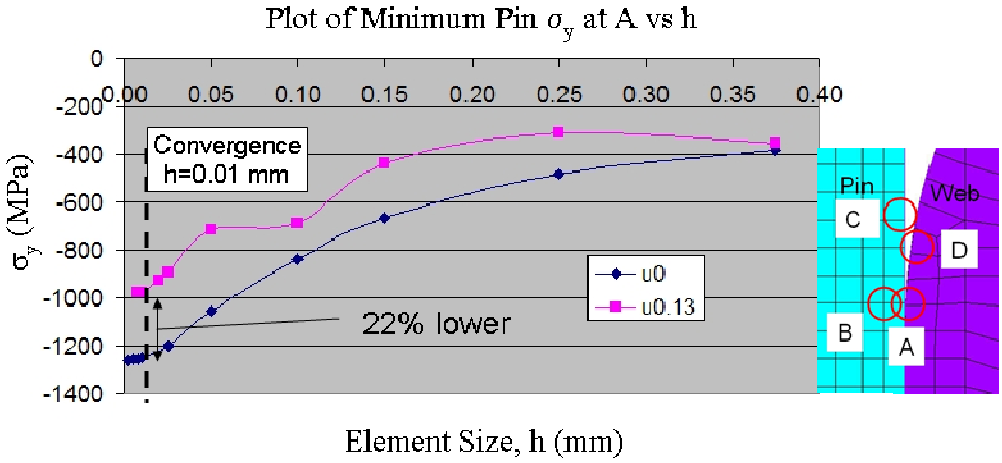

Figure 4.2.5.5 Plot of minimum pin σ_y at A versus element size *h*.

Pin minimum (compressive) axial stress occurring at location *A* does continue to grow with decreasing size h, as shown in Fig. 4. 3.5.5, until it levels of at *h* equals 0.01 mm. The log-log plot supports this convergence value of 0.01 mm.

The effect of *h* on the pin minimum σ_θ at location *A* is shown in Figs. 4.2.5.6 for the linear plot. The convergence has been reached again at *h*=0.01 mm (similar as for the axial stress). A surface friction solution (u=0.13) lowers values calculated by about 16 percent over the no friction solution.

As has been demonstrated in earlier sections, the axial stress on the surface of the pin changes from highly compressive at location *A* to moderately tensile on the free surface at C. Linear and log-log plots for axial stress at location *C* is contained in Figs.4.2.5.7 and 8. The tensile axial stress at C are much smaller than the (absolute) axial stress at A. For the no friction case (u=0) they converge for *h* smaller than 0.4.

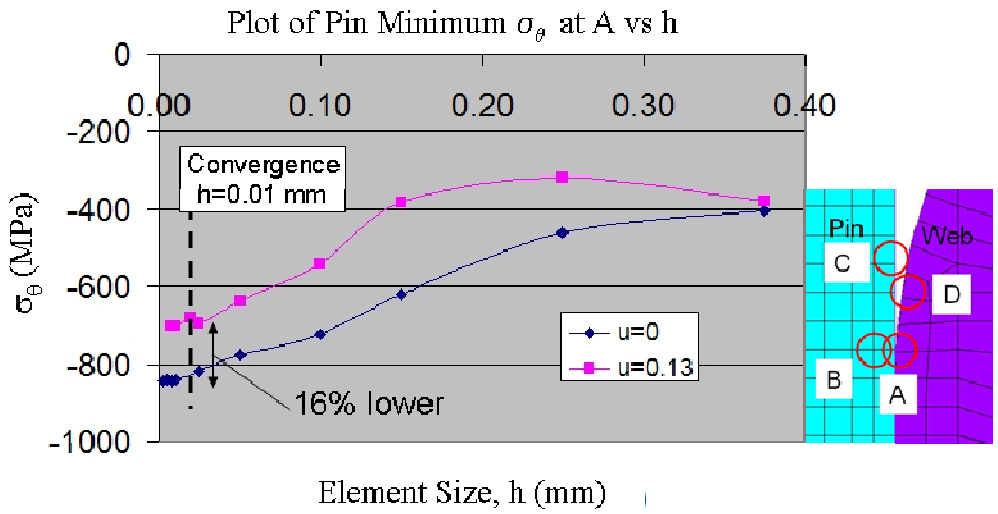

Figure 4.2.5.6 Plot of minimum pin σ_θ at A versus element size *h*.

However, for u=0.13 the plots show much slower convergence (which also might be consequences of how the friction effects are calculated). Note that the axial stress values for solutions considering friction are considerably higher, up to 220% for the smallest *h* used. Since the axial assembly stress is considered as mean tensile pin stresses for any life predictions, this difference is considered important. The fatigue life of the pin is always a design concern.

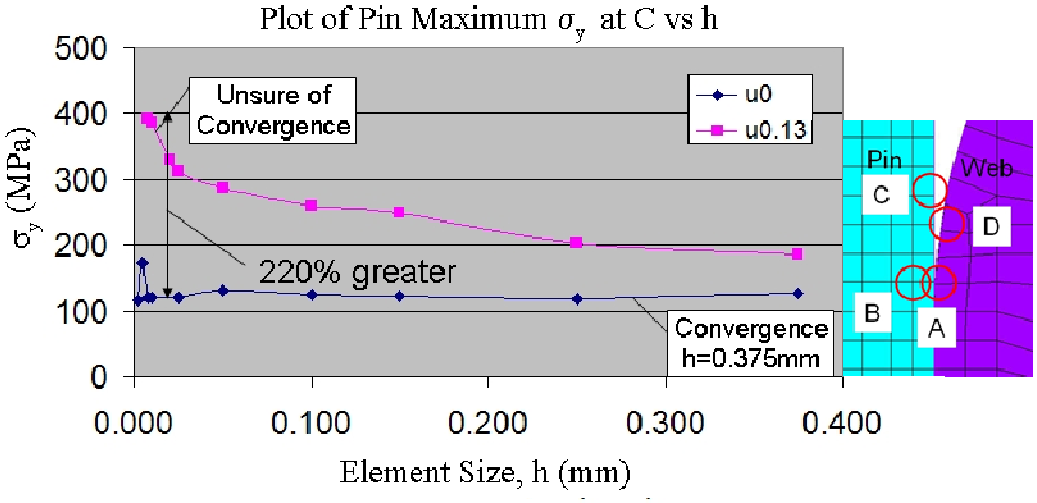

Figure 4.2.5.7 Plot of maximum pin σ_y at *C* versus element size *h*.

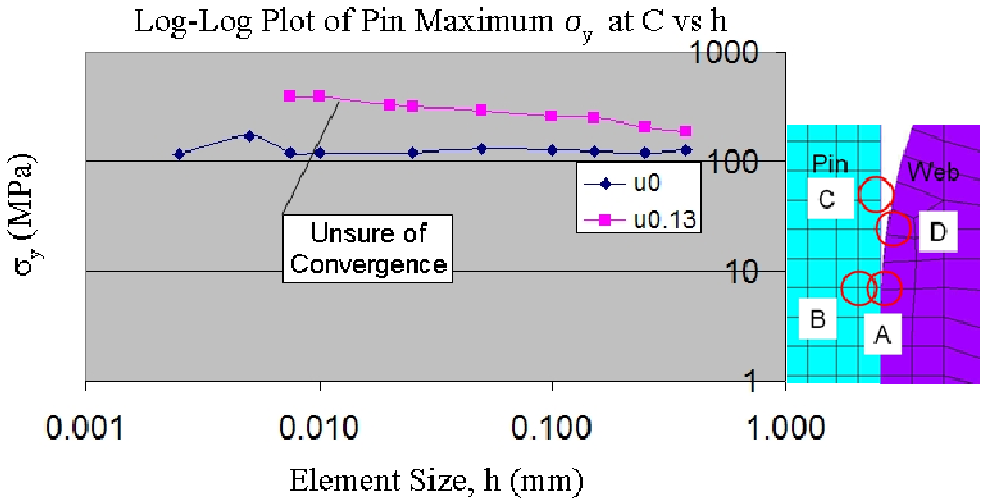

Figure 4.2.5.8 Log-Log plot of maximum pin σ_y at *C* versus element size *h*.

As discussed in the introduction section, it is unclear whether operating loads and vibrations will help relieve the effects of surface friction on the assembly, including the axial tensile stress at the SCA. One can logically assume that there could be slight relative motion near the start of the joint (at the SCA) between the mating parts in the press-fit joint, when the crankshaft is loaded during engine operation.

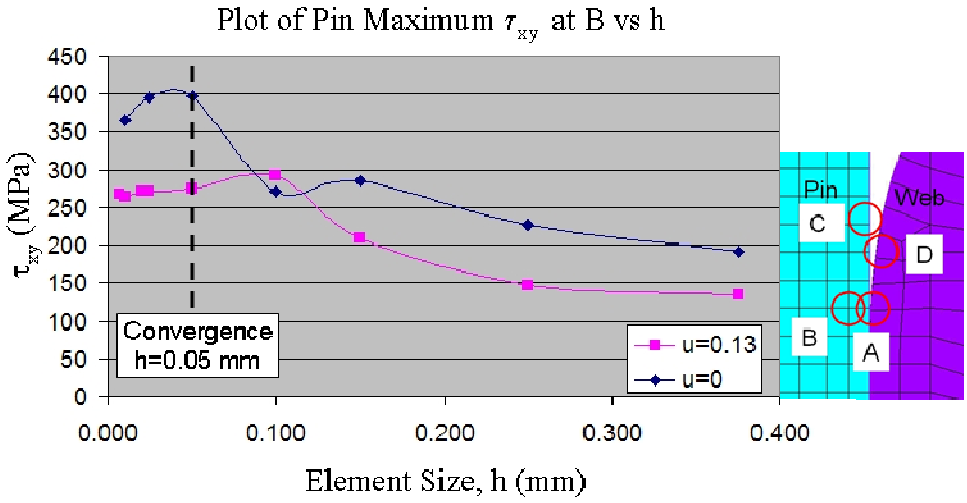

Figure 4.2.5.9 Plot of maximum pin τ_{xy} at *B* versus element size *h*.

Sensitivity of the pin maximum shear stress at *B* to mesh size *h* is depicted in Figs. 4.2.5.9 and 10. As can be observed the convergence is achieved at *h*=0.05 mm for both friction conditions. As is shown, higher shear stress is obtained for the no friction condition.

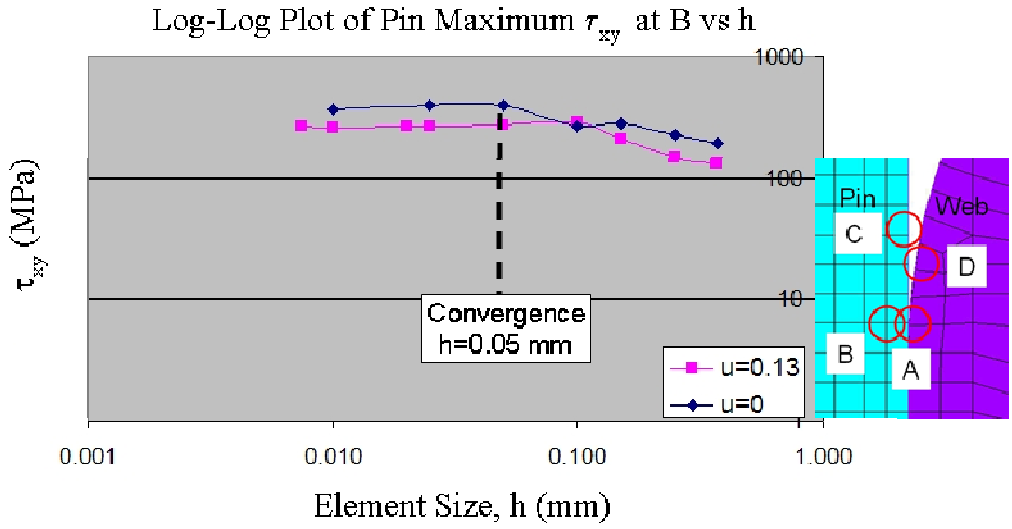

Figure 4.2.5.10 Log-Log plot of maximum pin τ_{xy} at *B* versus element size *h*.

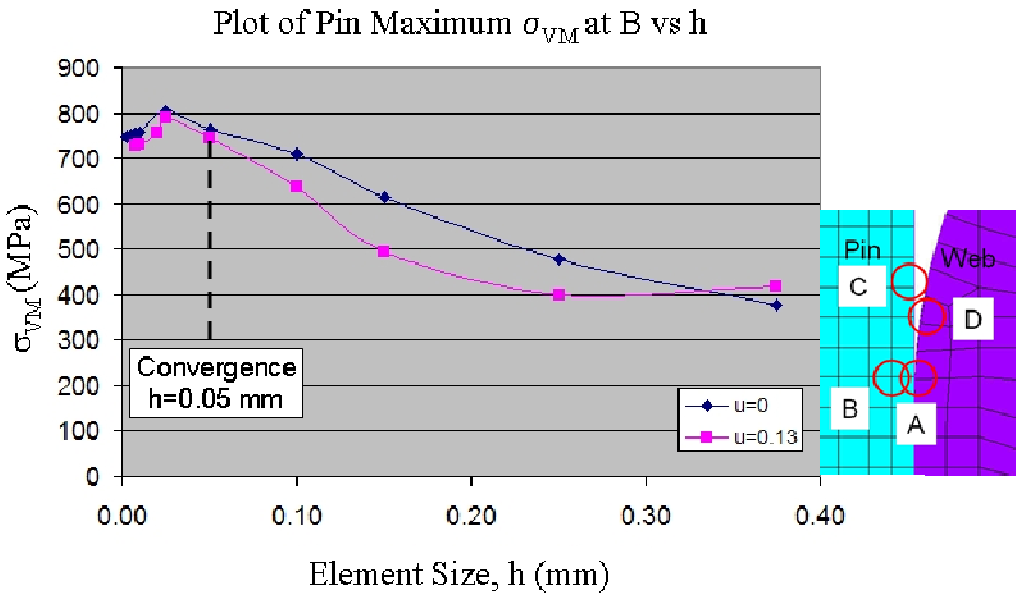

Figure 4.2.5.11 Plot of maximum pin σ_{VM} at *B* versus element size *h*.

The location of the maximum Von Mises stress in the pin is very sensitive to the mesh size. It moves from the pin surface for a course mesh to below the surface with decreasing *h* and

stabilizes there. Figures 4.2.5.11 and 12 show that at *h* equals 0.05 mm the value of this stress at location *B* converges, and that similar values for u=0 and u=0.13 were obtained.

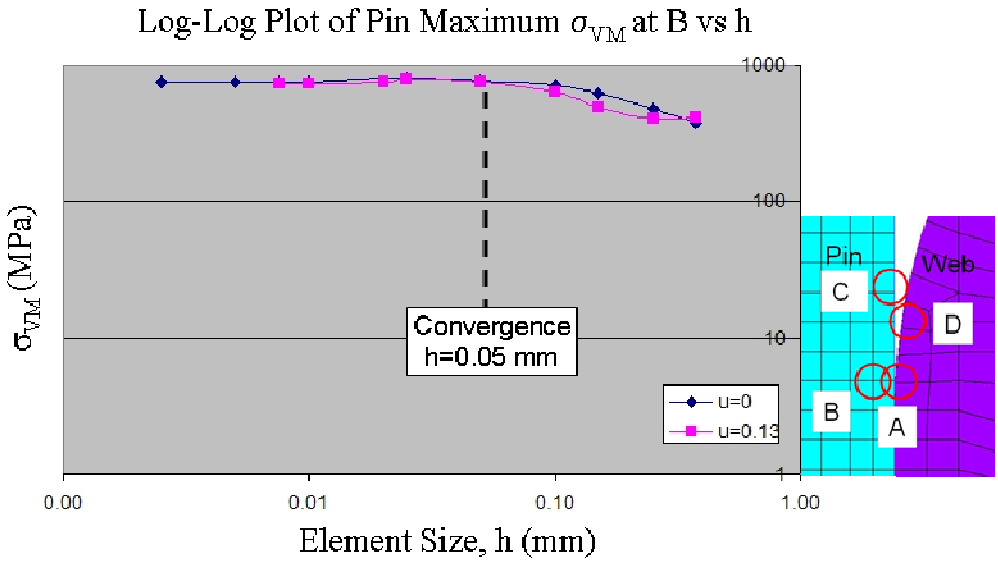

Figure 4.2.5.12 Log-Log plot of maximum pin σ_{VM} at *B* versus element size *h*.

The web maximum Von Mises stress (which are about 30% higher then in the pin) remains at the surface of the cylindrical hole (at location *A* in the web) for all values of *h*. The convergence is achieved at *h* equals 0.025 mm, as shown in Figs. 4.2.5.13 and 14. The values of these stresses are very little affected by friction.

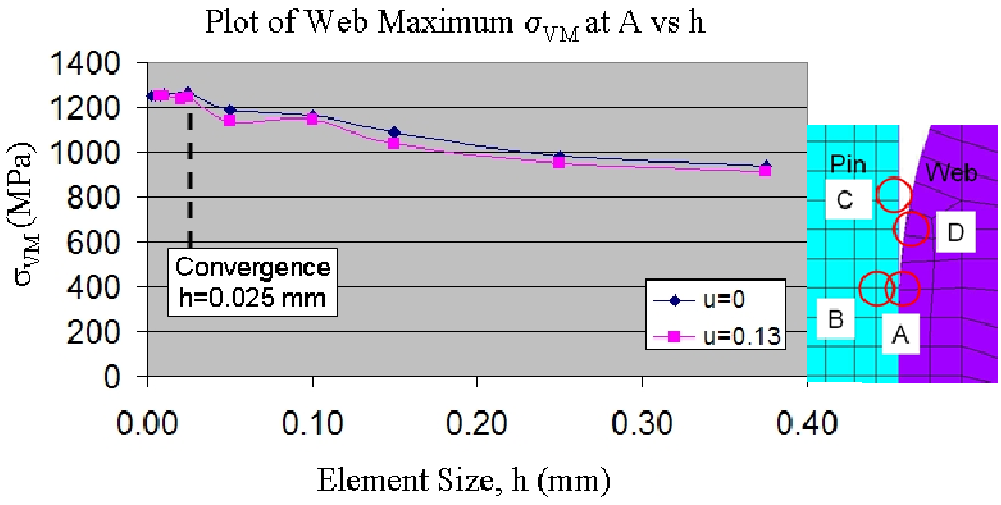

Figure 4.2.5.13 Plot of maximum web σ_{VM} at A versus element size *h*.

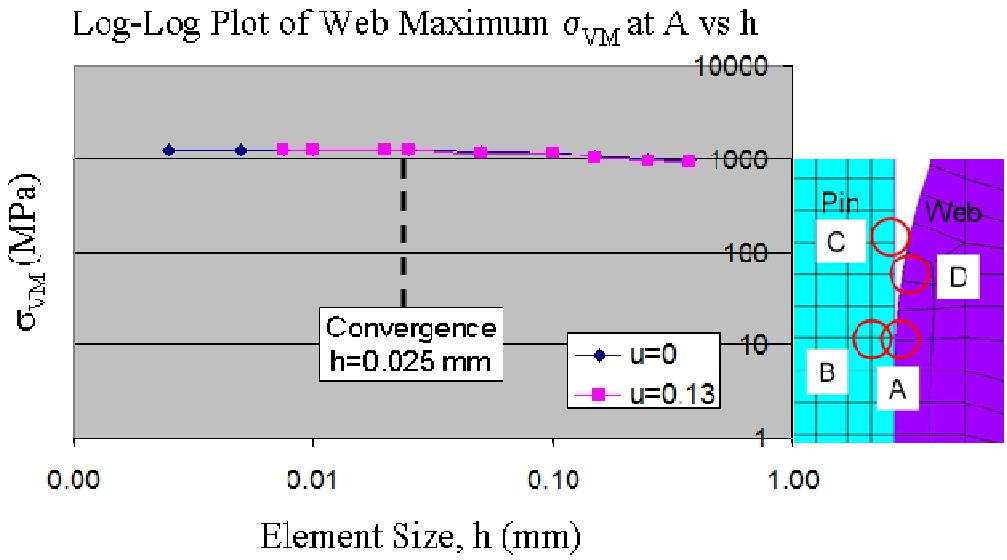

Figure 4.2.5.14 Log-Log plot of maximum web σ_{VM} at A versus element size *h*.

Hoop stresses in the web at or near the inner diameter of the cylindrical diameter are of great importance because their maximum value is typically used as a limit in design. The maximum hoop stress at location *D* (see Fig. 4.2.5.15) remains consistent throughout the element refinement studies, as it should, since its location is away from the high stress gradient at the SCA.

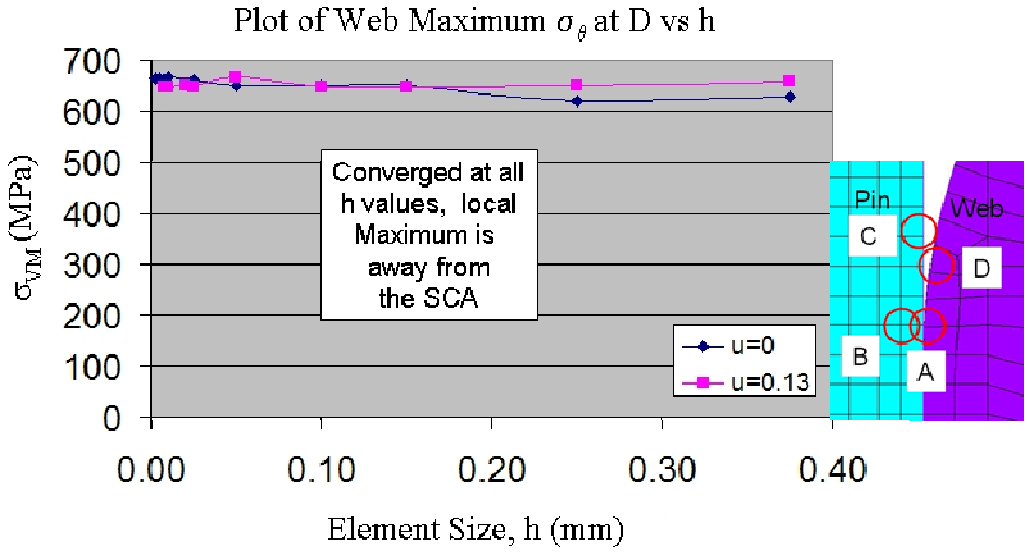

Figure 4.2.5.15 Plot of maximum web σ_θ at D versus element size *h*.

The results of this section permit to set element size targets to be used in the 3-D studies, so that details of the structural behavior are not lost by inadequate mesh refinement. Stress values generally converge by or near *h* equals 0.01 to 0.025 mm range, and so using *h* equals 0.01mm may be considered a good target. When surface friction is considered, stress values at the SCA are generally lower, but the tensile axial stress component on the free surface of the pin, at location *C*, is considerably higher.

Also, in should be emphasized that combining information from linear and log-log scale plots is a reasonably efficient way to check for convergence. Some scatter of the results in the plots is mostly because of error in the FEM solution due to contact element shape mismatch.

4.2.6 The Stress Field at the SCA And The Elastic Assumption

The results presented thus far were obtained assuming the elastic behavior of the material. This assumption is examined in detail in this section. Recall that the yield strength for the core material is 785 MPa, and for the case material hardened to about 1.0 mm depth is 1348 MPa.

Figure 4.2.6.1 shows Von Mises stress plot at the SCA for pin material. The maximum stress is 729 MPa, and is located approximately 0.035 mm below the surface, which is well within the harden core material.

Figures 4.2.6.2 and 4.2.6.3 show maximum (P1) and minimum (P3) principal stress plots respectively. Both plots indicate that the high equivalent stress at the SCA is dominated by compressive stresses. This has already been shown in previous sections. Some of the components stresses at the SCA, for example radial compressive stress 1231 MPa in Fig.4.2.2.4 are still below the case hardened yield strength (1348 MPa). The maximum tensile stress is only 61 MPa as indicated in Figure 4.2.6.2.

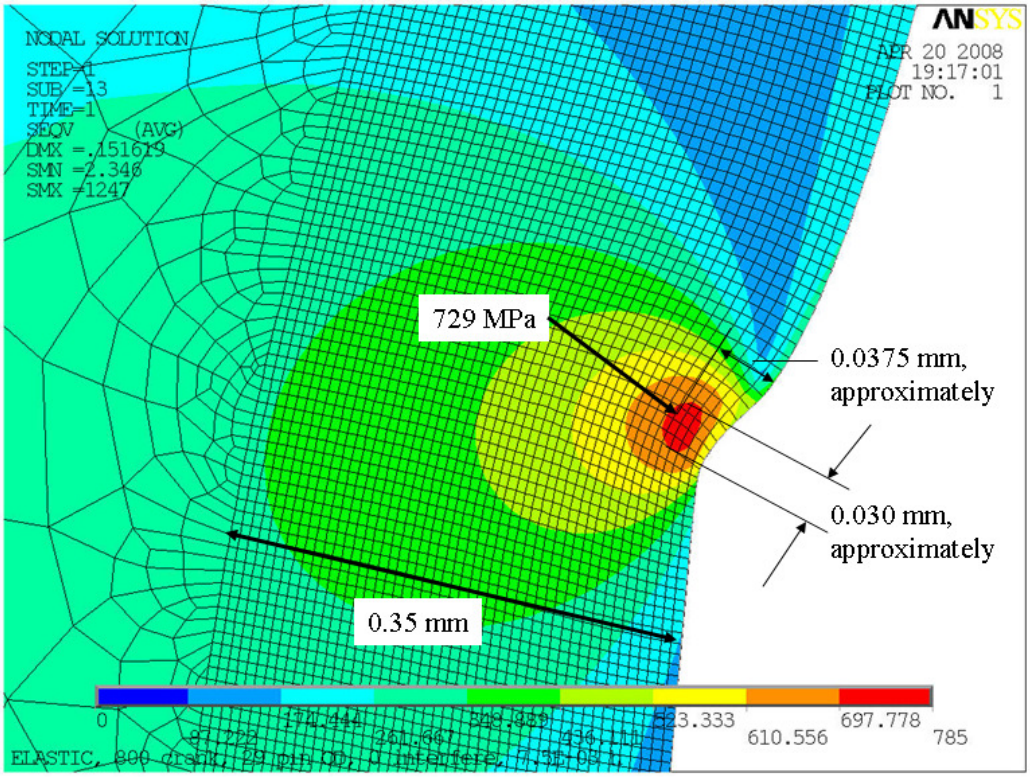

Figure 4.2.6.1 Von Mises stress plot at the SCA for the pin material.

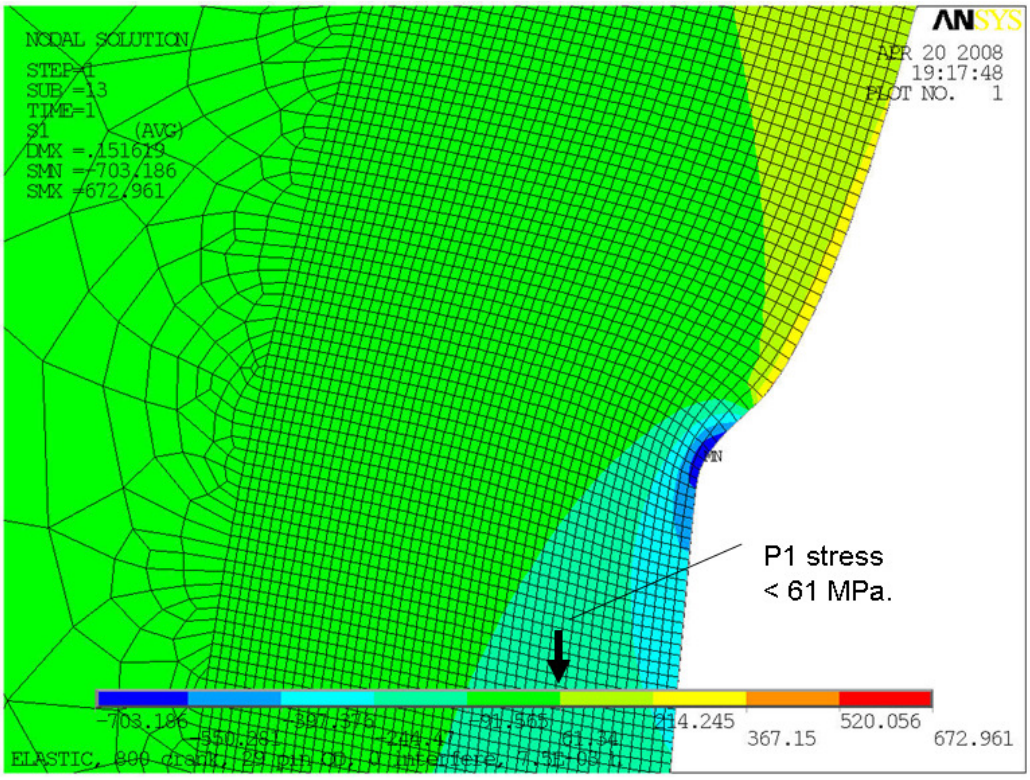

Figure 4.2.6.2 A plot of pin maximum principal stress (P1) at the SCA.

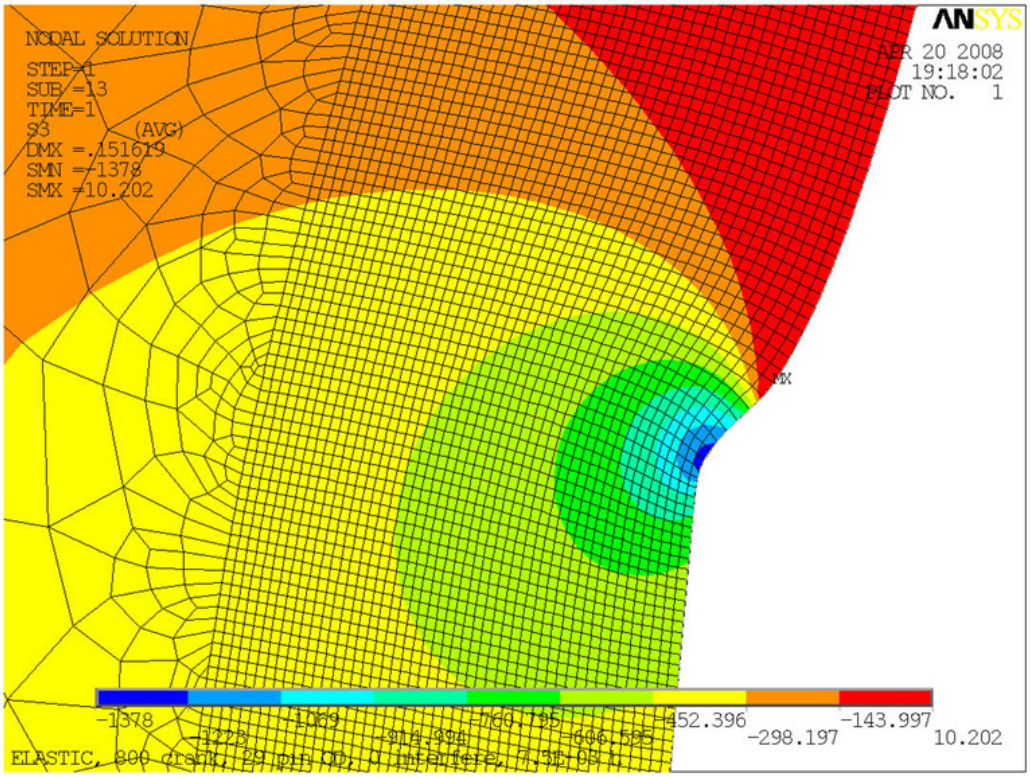

Figure 4.2.6.3 A plot of pin minimum principal stress (P3) at the SCA.

The web is examined next; Von Mises stress is plotted in Figs. 4.2.6.4. Maximum equivalent stress (1247 MPa) on the web occurs on the surface at the SCA, and is less than the case hardened yield strength (1348 MPa). As shown in subsequent plots this equivalent stress is also dominated by compressive stresses.

Next, Fig. 4.2.6.5 plots equivalent stress zoomed out from the web area shown in Fig. 4.2.6.4. The approximately grey circular area of 0.34 to 0.37 mm in diameter shows size of any web material that is greater than 785 MPa, the core material yield strength (S_{YS}). Contour bands that are red (see figure) and below have σ_{VM} stress values below S_{YS}. This area still falls within the 1 mm case hardened depth, although it is much larger than on the pin.

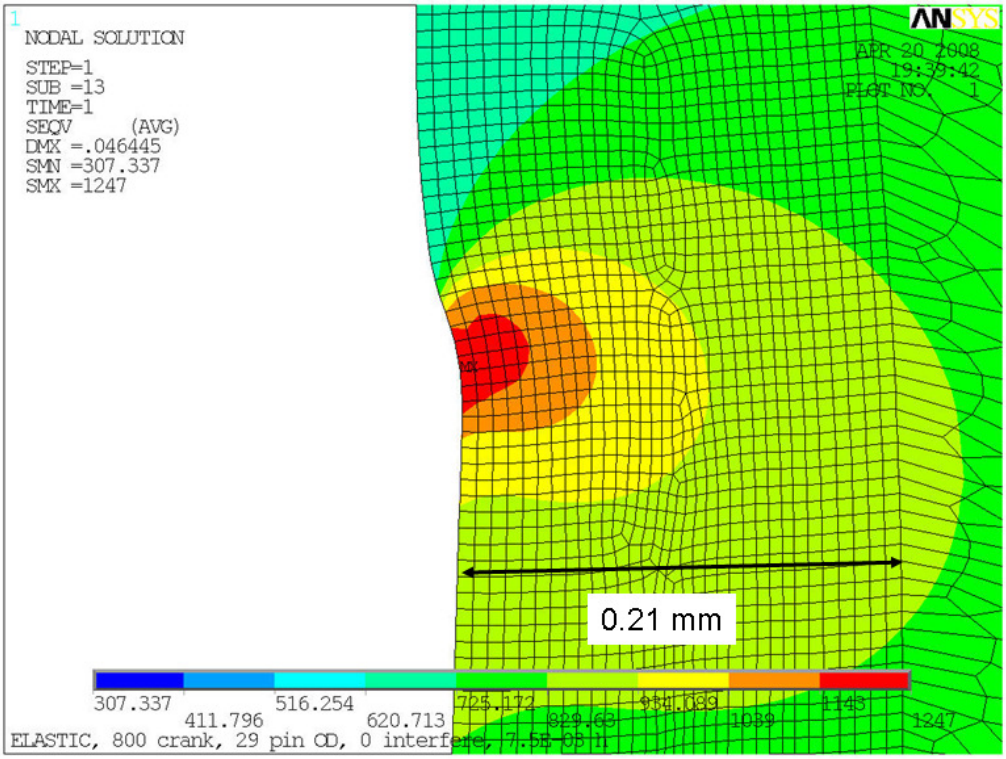

Figure 4.2.6.4 A plot of web Von Mises stress at the SCA.

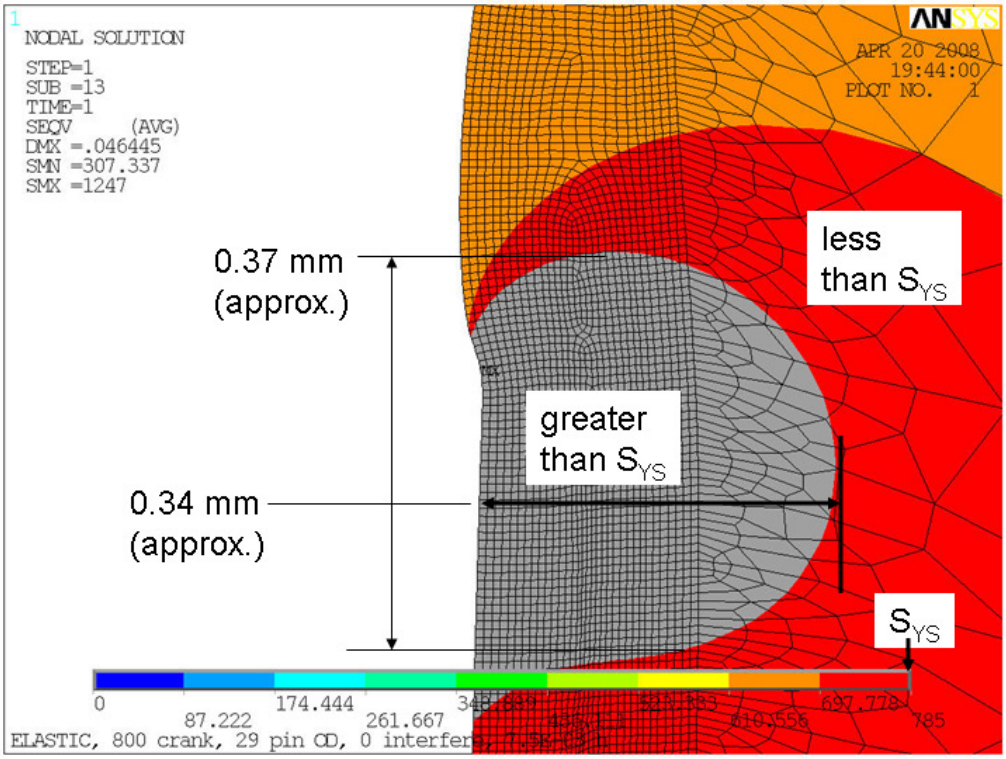

Figure 4.2.6.5 A plot of σ_{VM} showing the area of web material with stress greater than the core material S_{YS}.

The minimum principal stress (P3) is shown in Fig. 4.2.6.6. This stress component dominates the Von Mises stress plots in Figs.4.2.6.5 and 7.

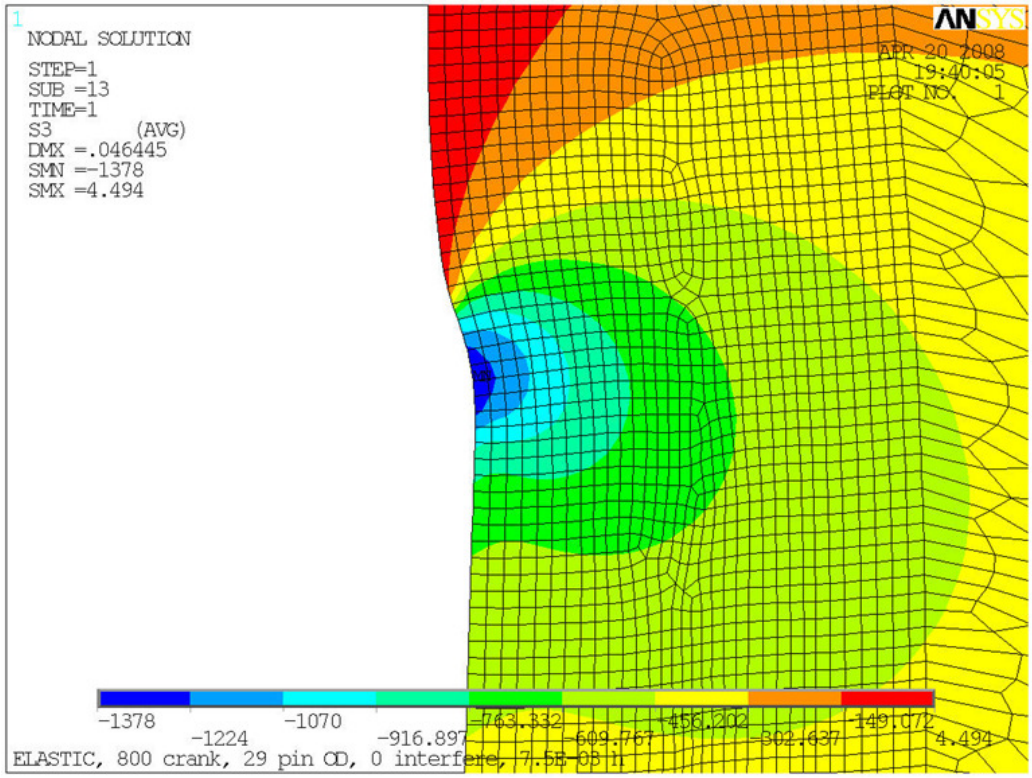

Figure 4.2.6.6 A plot of minimum principal stress (P3) in the web at the SCA.

Lastly, to illustrate a point about the compressive nature of the stresses at the SCA in the web, hoop stress is examined in Fig. 4.2.6.7. Along the length of the interface, generally there are tensile hoop stresses on the web side of the interface, except at the SCA. The hoop stress here is slightly compressive (-3 MPa), which is not intuitive, and can be linked to the phenomena of Poisson's effect and axial growth of the web and pin under interference. Note the hoop stress and P1 maximum principal stress plots are virtually identical.

Although high equivalent stress values exist at the SCA, the size of the high stress areas fall within the depth of the case hardened zone. Since the values of maximum equivalent stress are lower than the estimated case hardened yield strength, the elastic assumption appears to be a good choice for examination of these particular press-fit problems.

The elastic assumption will be examined further in Chapter 5 where detailed stress behavior at the SCA also for operating loads is analyzed.

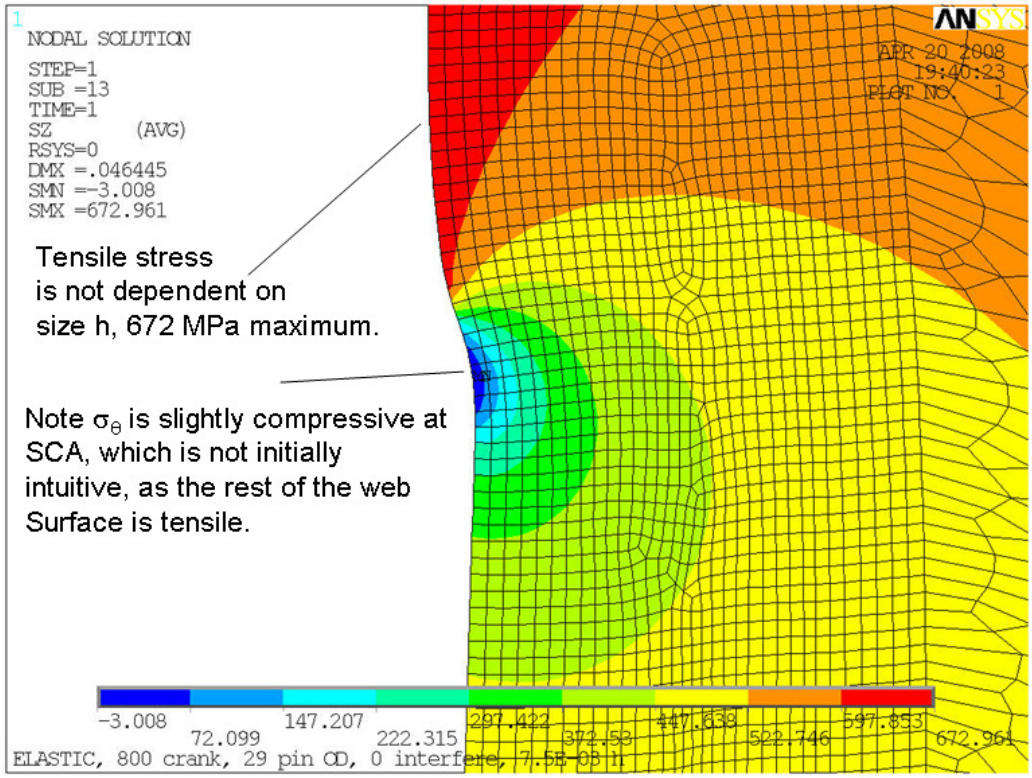

Figure 4.2.6.7 A web σ_θ plot at the SCA showing the contribution of compressive stress.

4.3 3-D Elastic Solution For The Assembly Problem: 30 Degree Symmetry Model

It becomes obvious that exploration of the pin and web assembly problem with 3-D modeling would require a very large numerical effort. To minimize the numerical challenge, efficient meshing techniques are required which minimize size and solution time, but also need to accurately calculate stress results at the area of interest (the SCA), similar to the 2-D axisymmetric models. A relatively small 30 degrees slice of the pin and web was chosen for the 3-D meshing investigations. The boundary conditions are set up in such a way that the model should behave axisymmetrically.

Also this 30 degree slice model was created to examine any differences with the solutions for the 3-D full crankshaft model. The 3-D full model has a web which is non-symmetrical about the pin

center axis. Since the 30 degree slice model is nearly the 3-D approximate of the 2-D axisymmetric model, comparison between the 30 degree slice and the 2-D axisymmetric model results may be made as well.

4.3.1 30 Degree Slice Models

In building the model several geometry modification approaches were considered while attempting a sufficiently accurate mesh at the SCA. From a meshing quality and meshing efficiency standpoint, a single rectangular area swept to form a ring or cylinder at the area of interest proved to work best. Other swept geometry combinations produced higher quality meshes, at a cost of producing too many elements.

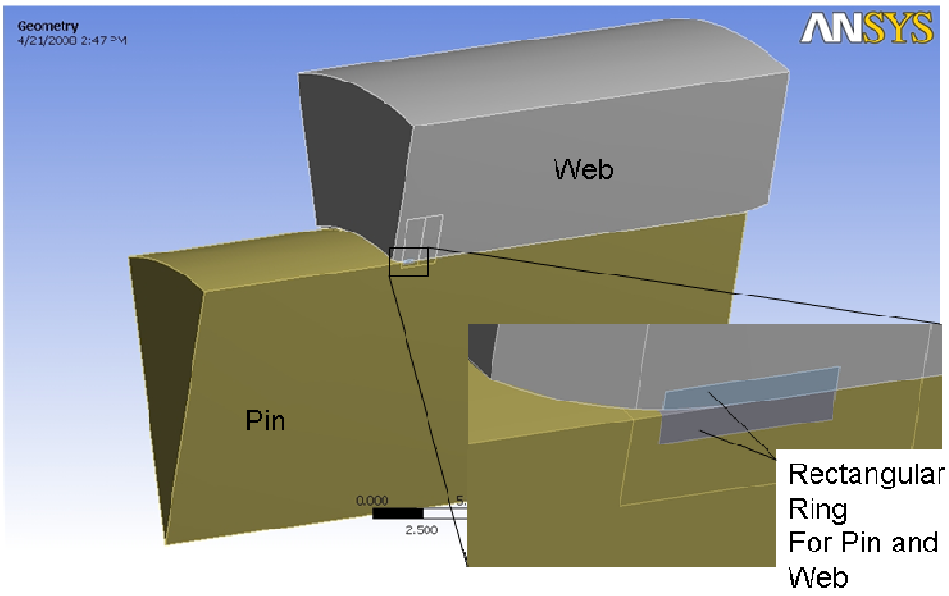

Figure 4.3.1.1 A 3-D slice model showing the rectangular ring volume at the SCA.

Figure 4.3.1.1 shows the rectangular ring volume at the SCA for both the pin and web, and Fig. 4.3.1.2 show the pin geometry detail separately. The size and location of the rectangular ring was set with knowledge of the size and location of the stress discontinuity at *A* calculated in the 2-D model. Trial and error was also used though with the variation in the size and location of the rectangle to obtain acceptable contact stress and a minimize model size.

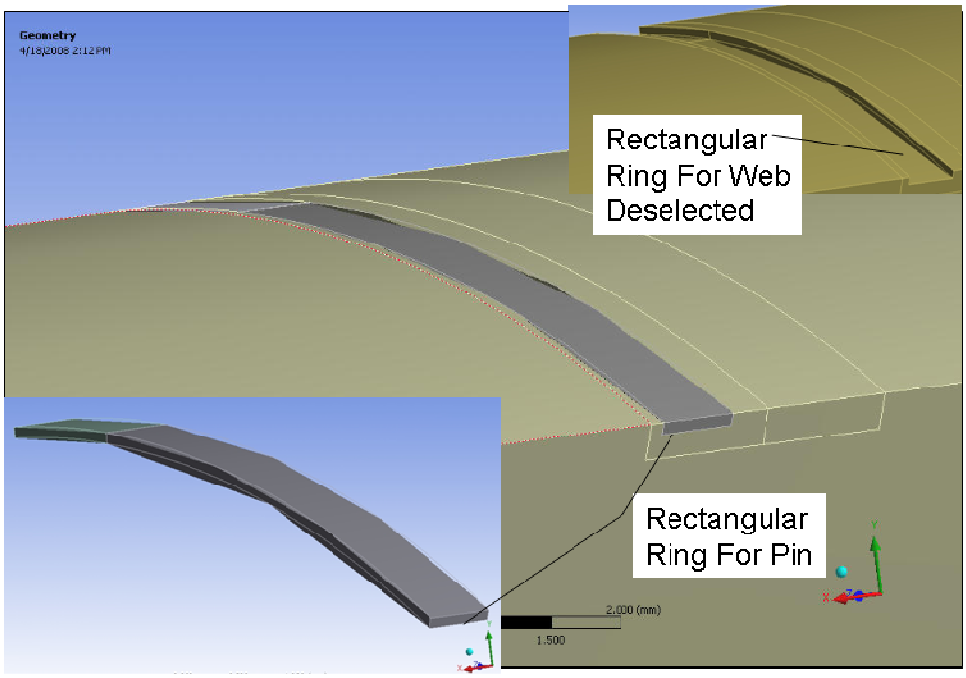

Figure 4.3.1.2 A 3-D slice model showing the ring volume at the SCA for the pin.

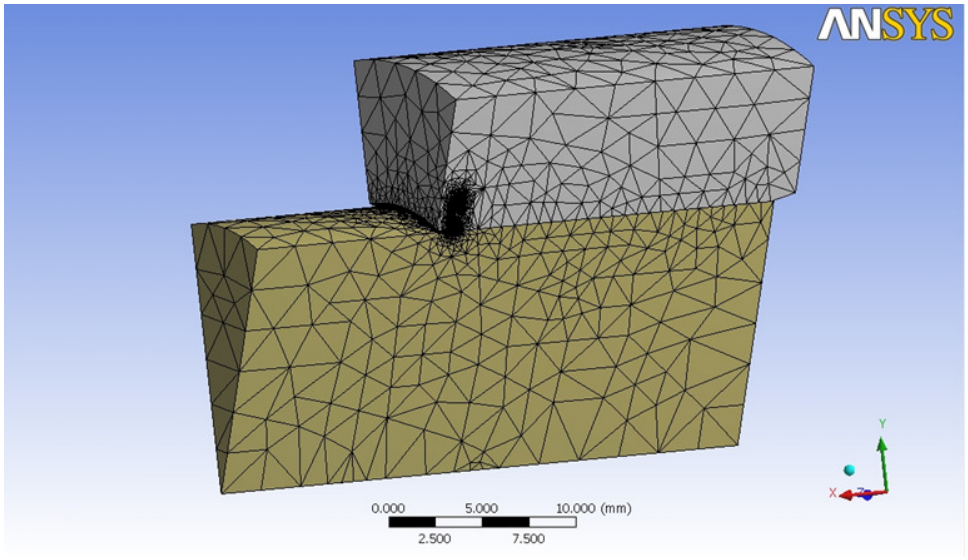

Figure 4.3.1.3 A typical mesh for the 30 degree 3-D slice model.

Mesh details at the area of interest are provided in Figs. 4.3.1.3 and Fig. 4.3.1.4. In particular note that the ring always used brick elements for best contact solutions results at the SCA. Also note that because the ring is split into two separate volumes, meshing refinement may be focused

on one area if desired. This mesh detail is provided because it will be shown that mesh quality and methodology will significantly impact accuracy.

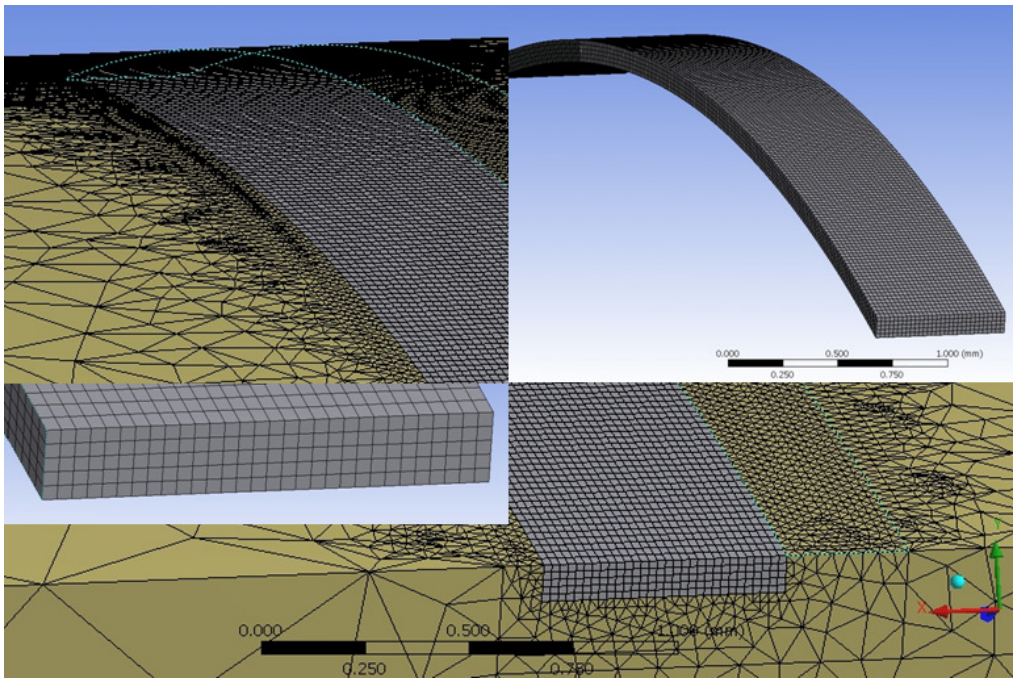

Figure 4.3.1.4 A typical mesh refinement on the pin by sweeping brick elements.

4.3.2 30 Degree Slice Model: General Stress State

The 3-D slice model's boundary conditions are given in Fig. 4.3.2.1. These conditions with an 'almost uniform' meshing in the circumferential direction should force the model to behave axisymmetrically. The interference between the pin and web is generated with a temperature change, where the coefficient of thermal expansion of the web is kept low (close to zero), allowing the pin to grow into the web when the appropriate temperature change is applied. This approach provided the most consistent results at the SCA, including good contact pressure distribution.

Equivalent stress is plotted in Fig.4.3.2.2 for a typical interference assembly problem, including a close up of the stress distribution at the SCA. (The results posted use an element size of *h* equals 0.002 mm). Generally, these 3-D patterns look very much like the 2-D results, but are lower in magnitude. For this combination of geometry, a variation in element size *h* was studied. A relative comparison between 2-D and 3-D results magnitudes is provided is section 4.6. Further

data for the slice model can be found in Appendix A, including investigations of alternative model constructions and meshing approaches.

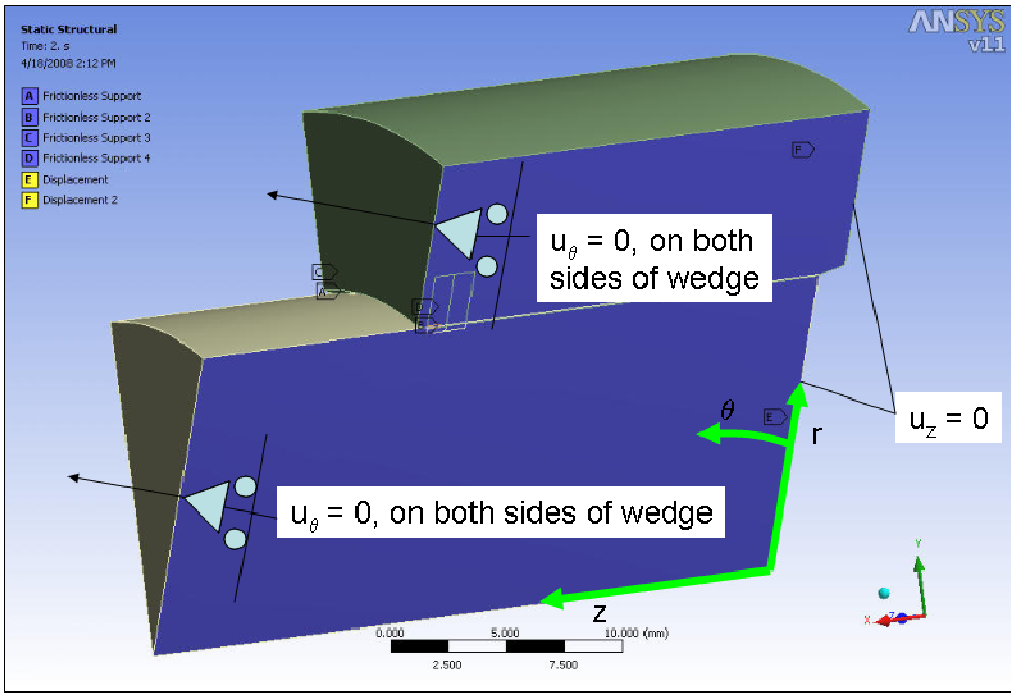

Figure 4.3.2.1 Boundary conditions for the 30 degree 3-D slice model.

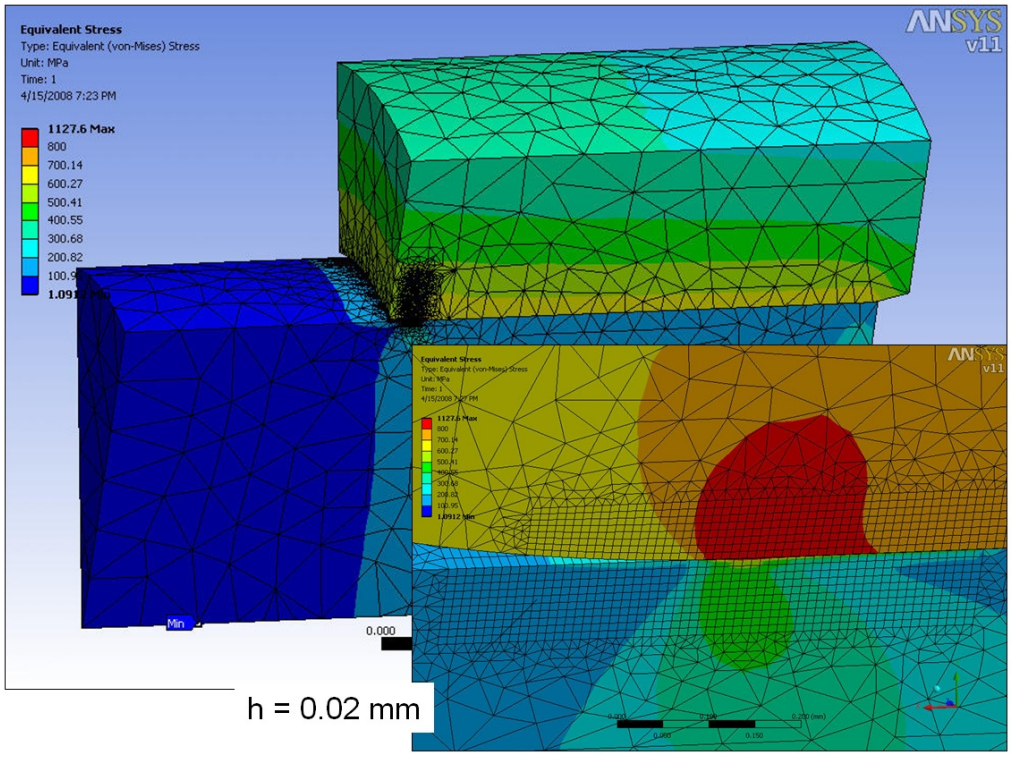

Figure 4.3.2.2 Assembly (press-fit) Von Mises stress plot, 3-D slice model.

4.4 3-D Elastic Assembly Solution: One-Quarter Bench Test Model

The FEM model construction approach that was determined to work most efficient with the 3-D 30 degree slice geometry is now tested on representative crankshaft geometry. Since model size is a concern, it is desired to use symmetry in these tests. Mesh density at the stress concentration will be refined as much as possible, the feasibility of which is determined by computer solution times (see section 3.2.2.6 regarding model size and solution time information).

The physical bench test to determine crankshaft durability in the laboratory usually consists of a cyclic load applied to one single crankpin of the crankshaft assembly.
The symmetry used in the following FEM modeling approach reflects the symmetrical nature of a pure bending bench test. Thus, this model has been given the name 'one-quarter bench test'. The test's results will be useful in the crankshaft quasi-static durability bench test usually consist of a cyclic load applied to one single throw or crankpin of the assembly.

The one-quarter bench test model is the most numerically efficient 3-D crankshaft geometry for study of the assembly problem. The numerical approach and general results for the assembly problem are presented next.

4.4.1 One-quarter Bench Test Model: Types of Models Explored

As is the case for the 30 degree 3-D symmetry model, several geometric volume shapes were examined to create a best approach for mesh refinement control at the SCA location. Mesh efficiency, interface contact pressure smoothness, and logical trend variation in stress magnitudes with mesh refinement were all considered as metrics for selection. Figure 4.4.1.1 provides some mesh details at the SCA area for three different FEA models that were created to examine the crankshaft assembly problem.

The same geometry approach as used for the 30 degree model was found to be robust for the one-quarter bench test model, a single rectangular area is revolved around the pin axis to create a cylindrical volume. Figure 4.4.1.2 shows the pin and web geometry details. The cylindrical ring volume that is 'cut away' from the pin is shown in detail for the pin geometry in Fig. 4.4.1.3. A mating cylindrical volume that is embedded in the web at the SCA is shown in Fig. 4.4.1.4.

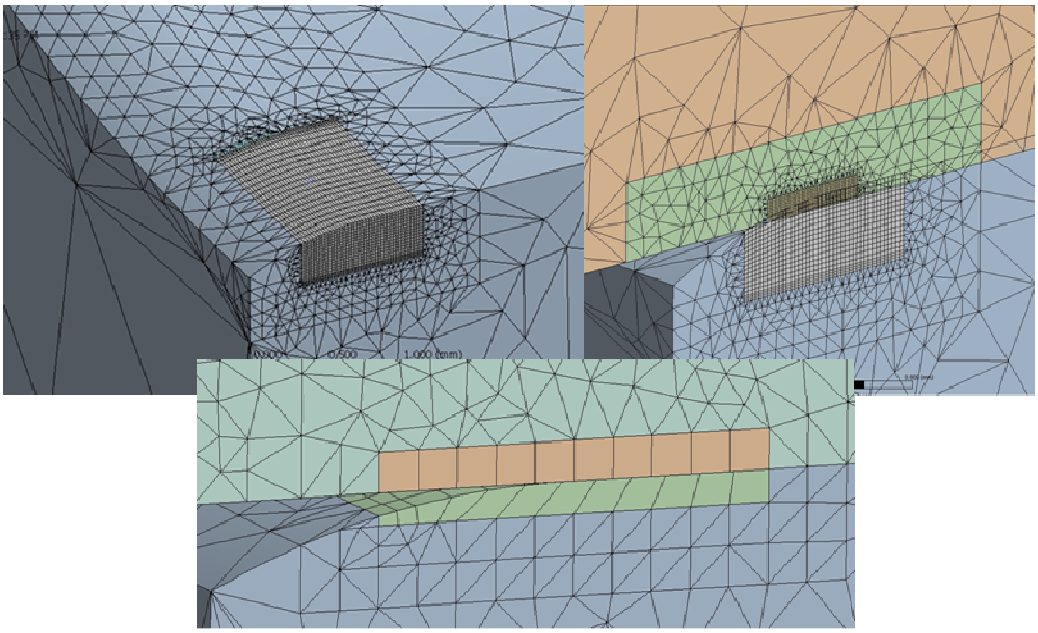

Figure 4.4.1.1 Meshing variations at the SCA which are guided by rectangular volumes.

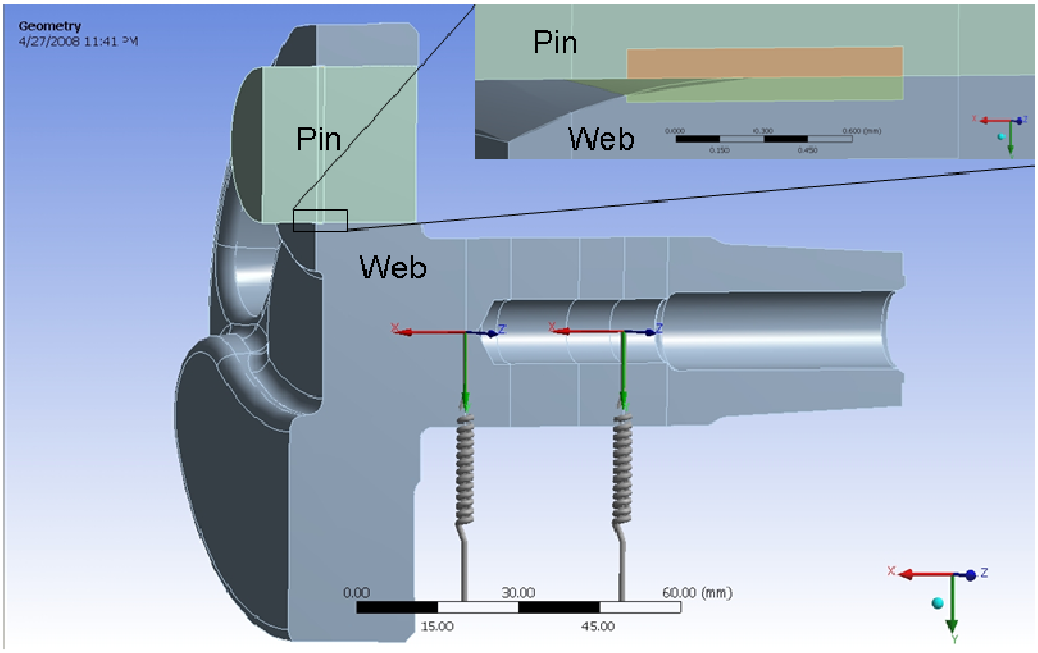

Figure 4.4.1.2 One-quarter bench model showing the geometry details at the SCA.

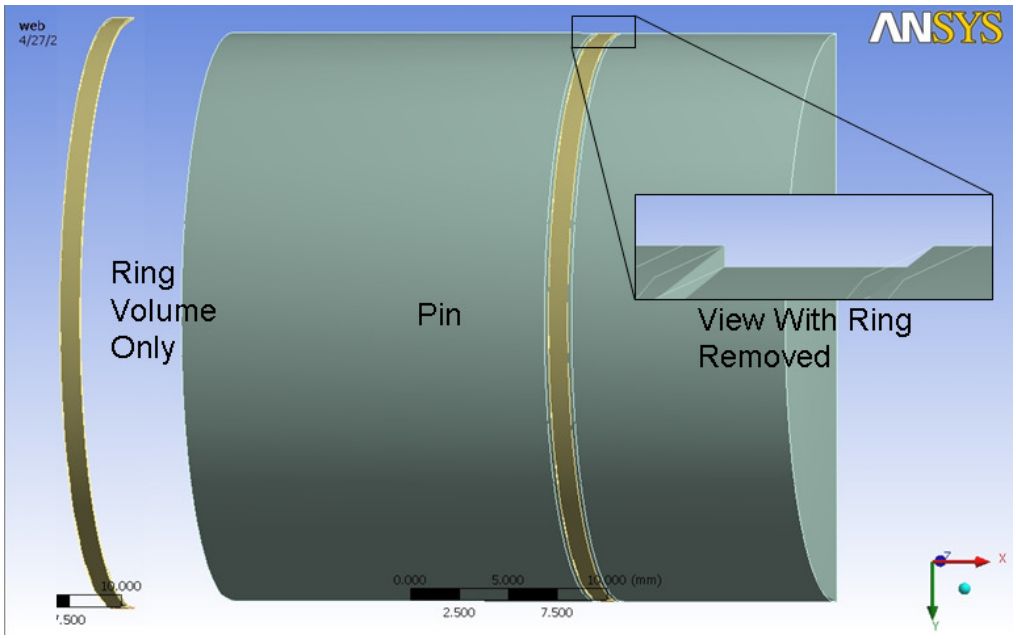

Figure 4.4.1.3 One-quarter bench model showing the pin geometry details at the SCA.

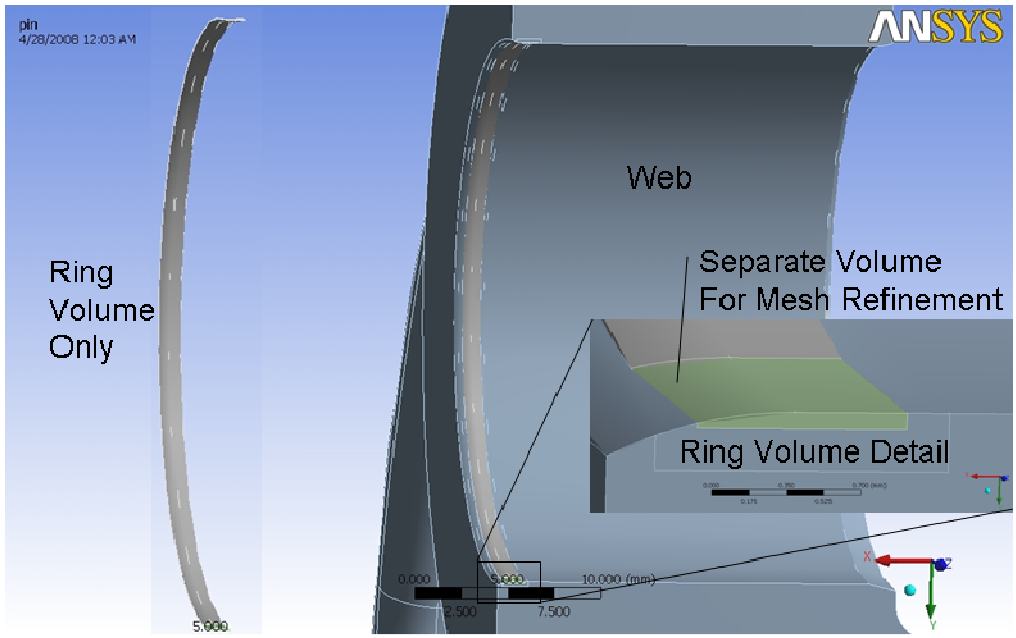

Figure 4.4.1.4 One-quarter bench model showing the web geometry details at the SCA.

The size and location of the rectangular ring was set using the size and location of the stress discontinuity at *A* calculated in the 30 degree slice model. Note the volume created here is wider in the pin axis direction. This same mesh will be used to examine operating loads as well, and the additional width is needed to calculate detailed stress values as the pin bends under load and the joint experiences any relative motion between parts.

Mesh details at the area of interest are provided in Figs. 4.4.1.5 to Fig. 4.4.1.7 for a mesh density of h equals 0.02 mm. In particular note that the rectangular ring predominantly uses brick elements for best contact solutions results at the SCA.

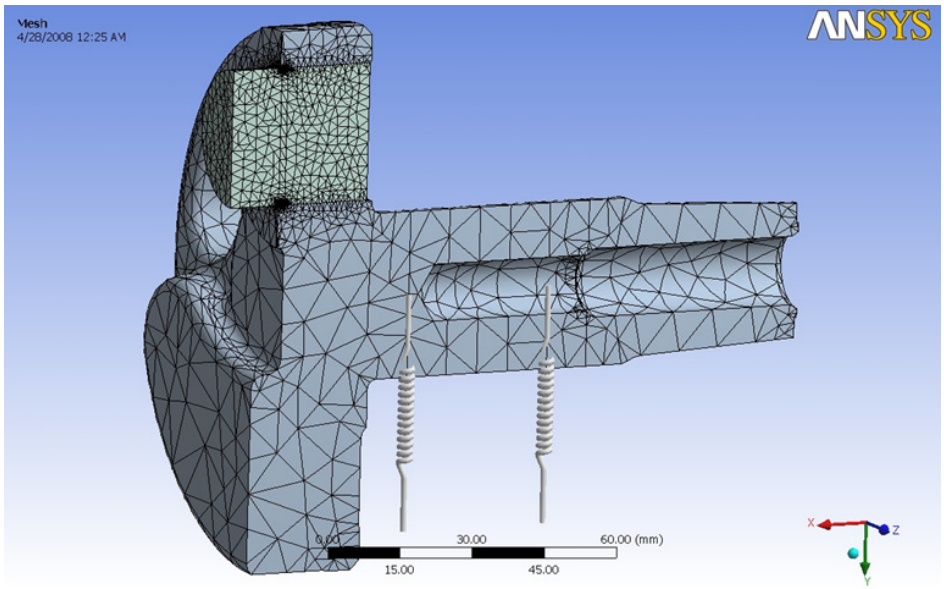

Figure 4.4.1.5 A typical mesh for the one-quarter bench model press-fit problem.

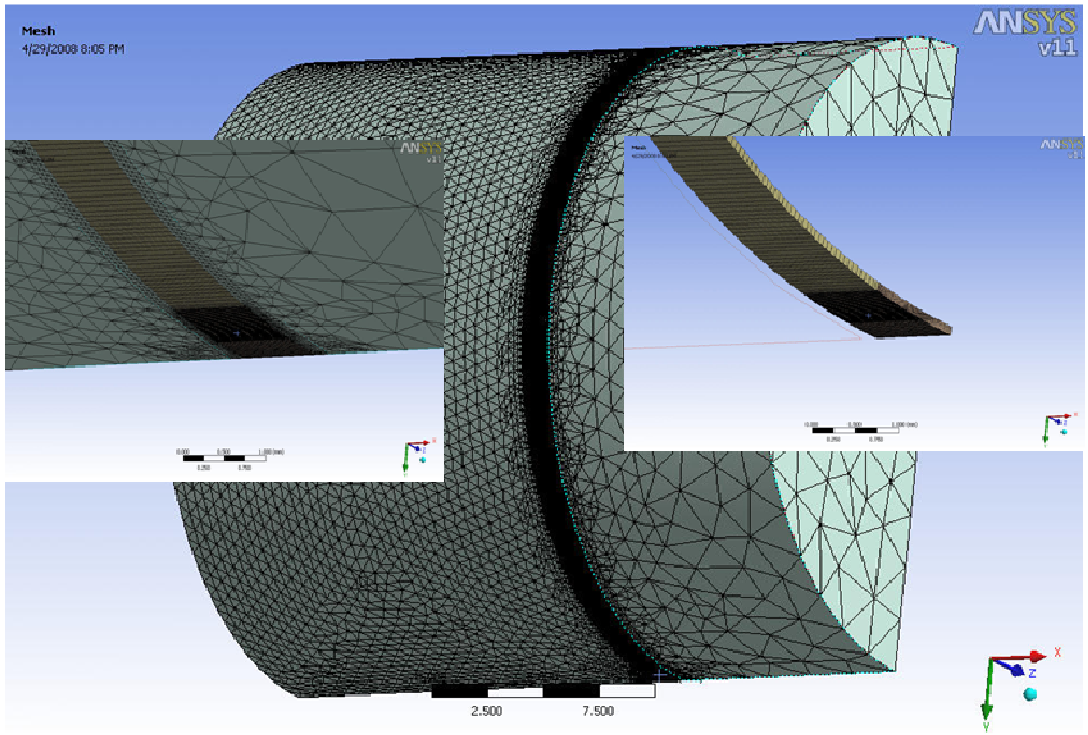

Figure 4.4.1.6 A typical pin mesh refinement, note swept brick elements on the ring.

Also note that because the ring is split into two separate volumes, meshing refinement may be focused on one area if desired. This mesh detail is provided since mesh quality and model methodology may significantly impact accuracy.

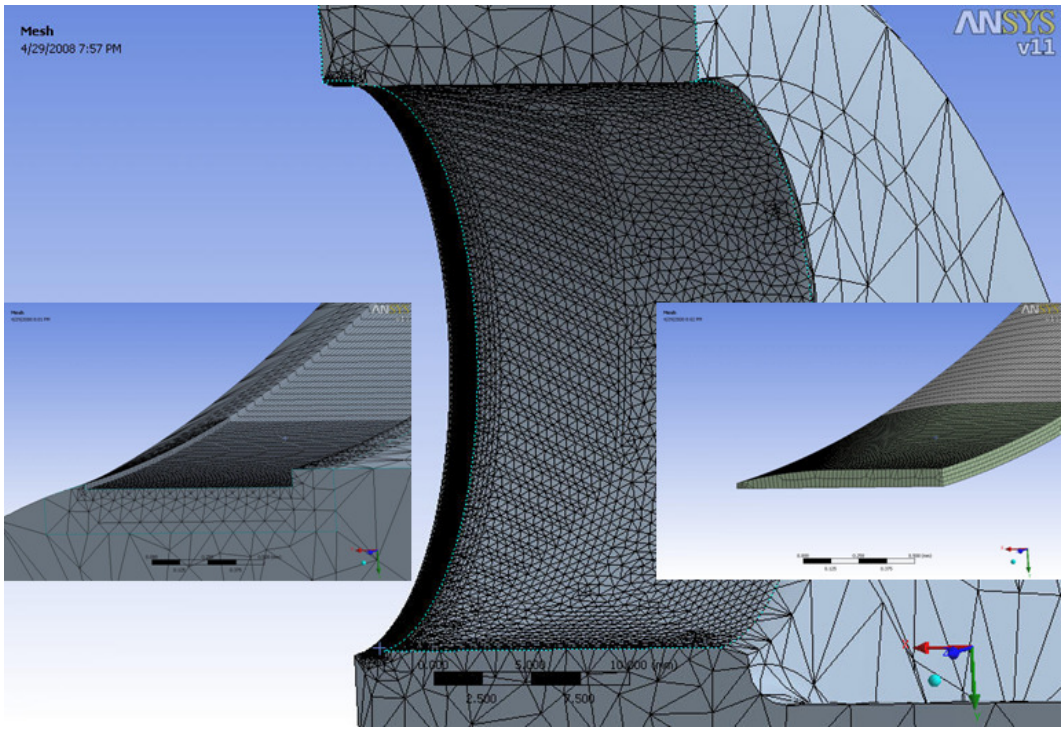

Figure 4.4.1.7 A typical web mesh refinement, note again the swept brick elements.

4.4.2 One-Quarter Bench Test Model: Assembly Results

Figure 4.4.2.1 shows the one-quarter bench FEA model details, including the two planes of symmetry used to minimize model size. The crankshaft is supported on the main shaft by roller bearings, which are in turn encapsulated by the crankcase upper and lower castings. The combined bearing and case stiffness that support the crankshaft are idealized as linear springs which act along the center of the bearings. Stiffness values used are based on historical experimental data.

Note that a temperature change based method is used to create the proper radial interference between the pin and web cylindrical hole. This method has provided consistent results. The thermal expansion of the web is kept low (close to zero) for the prescribed temperature change by setting the coefficient of thermal expansion sufficiently low. This allows the pin to expand

into the web to create the interference fit. Also note that all results presented in this section use a mesh refinement of *h* equals 0.02 mm.

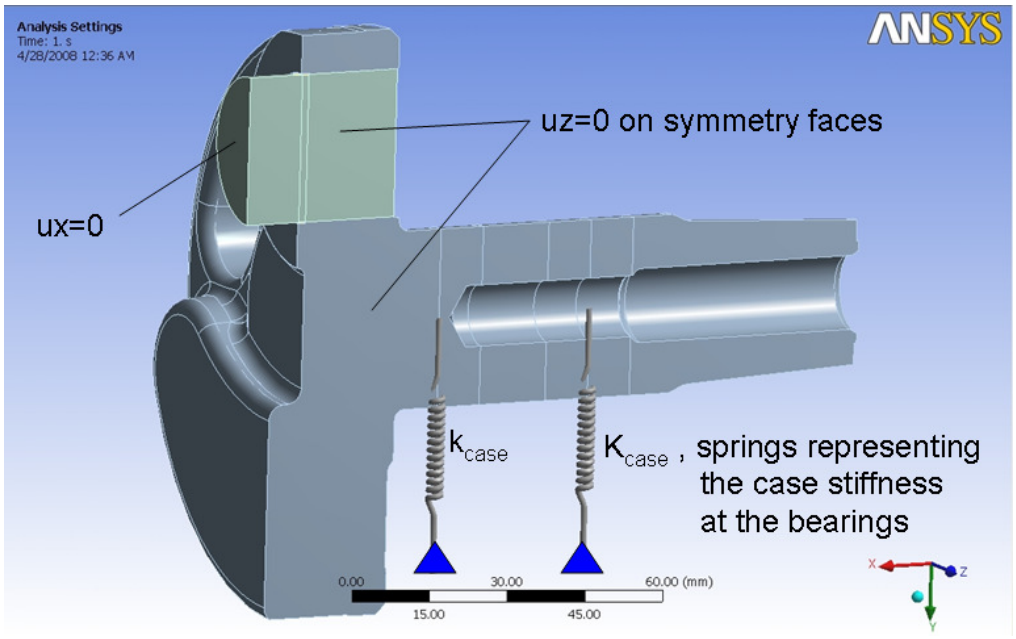

Figure 4.4.2.1 Boundary conditions for the one-quarter bench test model.

First the radial displacement plot (Fig.4.4.2.2) shows that most of the web radial displacement occurs in the section above the pin, which accommodates the larger pin.

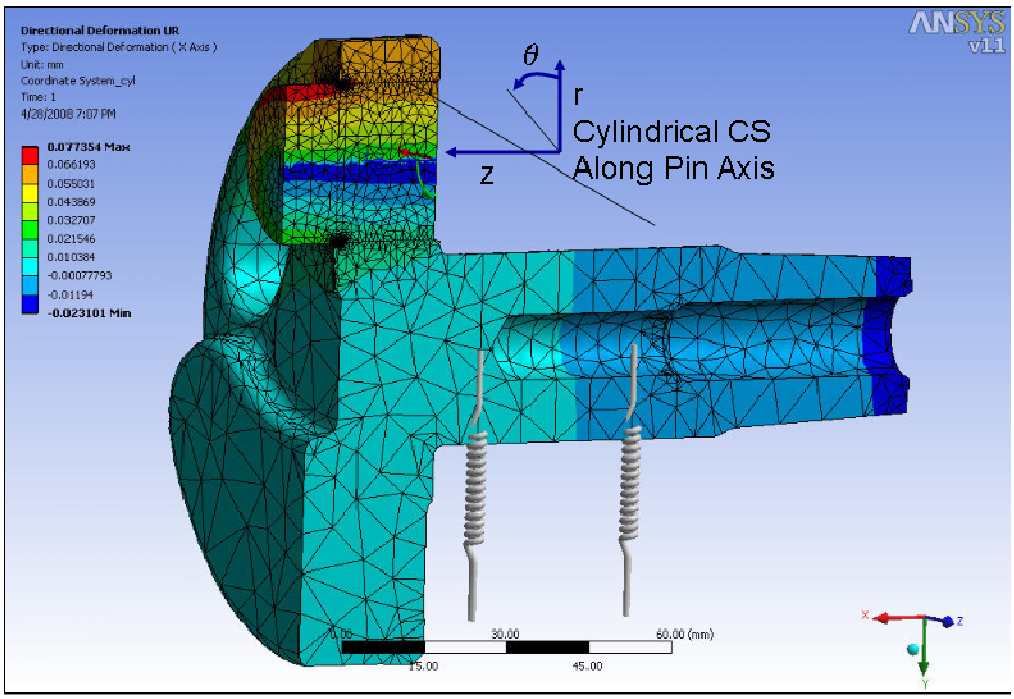

Figure 4.4.2.2 Assembly radial (u_r) deflection plot, one-quarter bench model.

The axial displacement plot (Fig. 4.4.2.3) shows that the pin only grows with the temperature change in this direction.

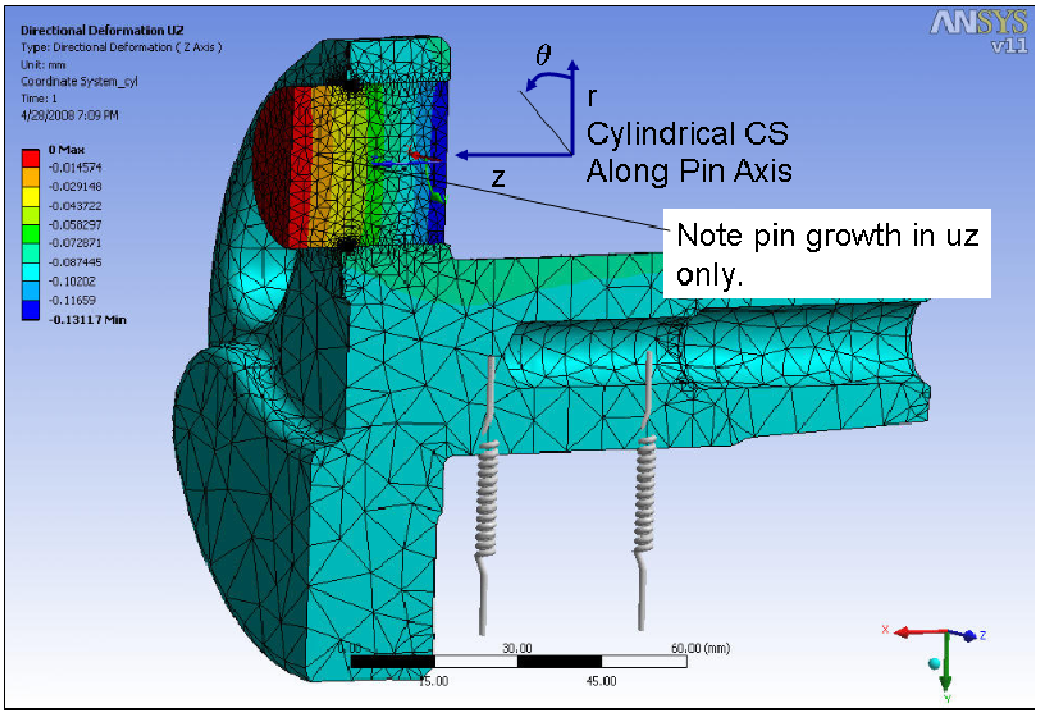

Figure 4.4.2.3 Assembly axial (uz) deflection plot, one-quarter bench model.

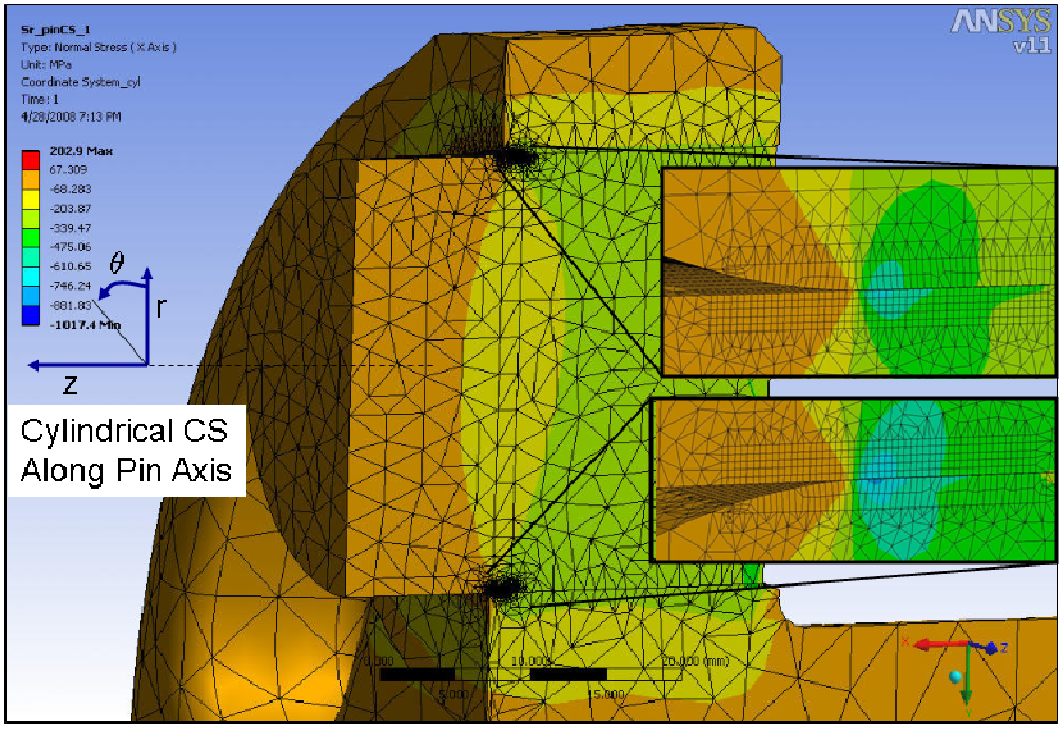

Figure 4.4.2.4 Assembly radial stress (σ_r) plot, one-quarter bench test model.

Radial stress (σ_r) based on the pin CS for the assembly problem is plotted in Figs. 4.4.2.4. The detailed close-up views show similar stress distributions at the SCA as shown for the 30 degree slice model. An isometric view of radial stress at the pin SCA area is provided in Fig.4.4.2.5, showing a reasonably symmetric response in the theta-direction.

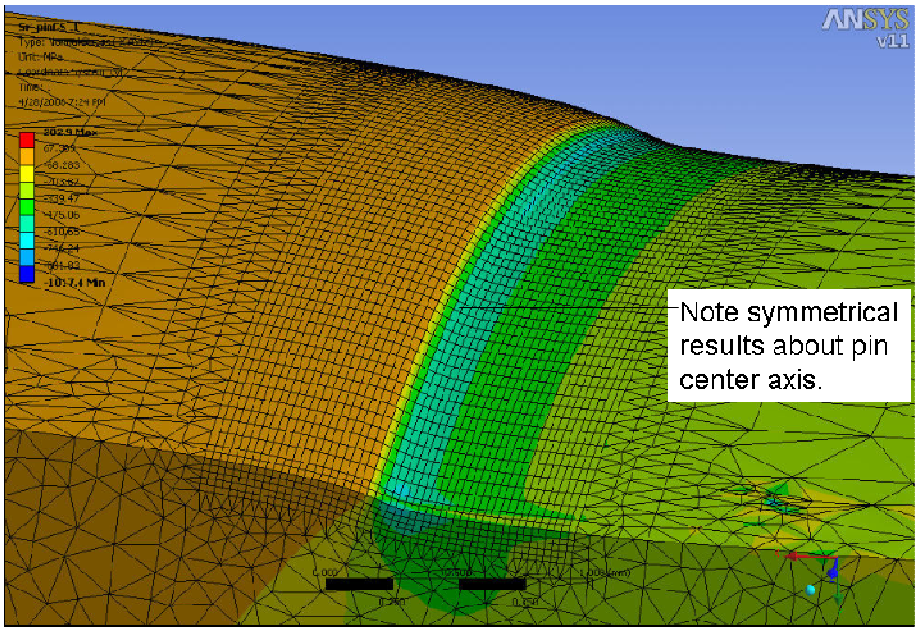

Figure 4.4.2.5 Assembly radial stress plot of the pin at the SCA.

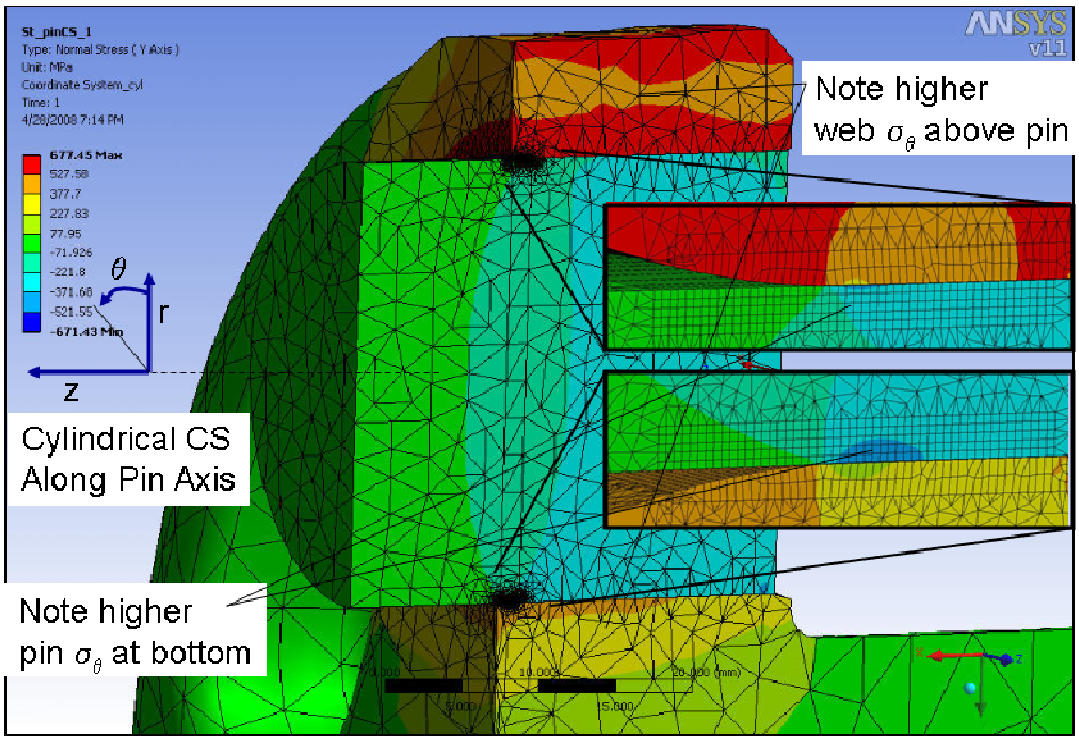

Figure 4.4.2.6 Assembly (press-fit) hoop stress (σ_θ) plot, one-quarter bench test model.

Hoop stress (σ_θ) is shown in Fig. 4.4.2.6 and indicates higher tensile stress in the web material above the pin in comparison to that below the pin. The magnitude of the web stress away from the SCA, above the pin, is close to the values calculated with an axisymmetric model. The local hoop stress distributions at the SCA are similar to those found in the 30 degree symmetry model. The values on the bottom of the pin are somewhat higher (11.8%) than those calculated on the top side of the pin, which is a good indicator of how reasonable the axisymmetrical assumption is.

A plot of axial stress (σ_z) is provided in Fig.4.4.2.7 for the one-quarter bench test model, which contains the local stress distributions at the SCA. Axial stress magnitude is calculated to be higher (16%) on the pin at the bottom.

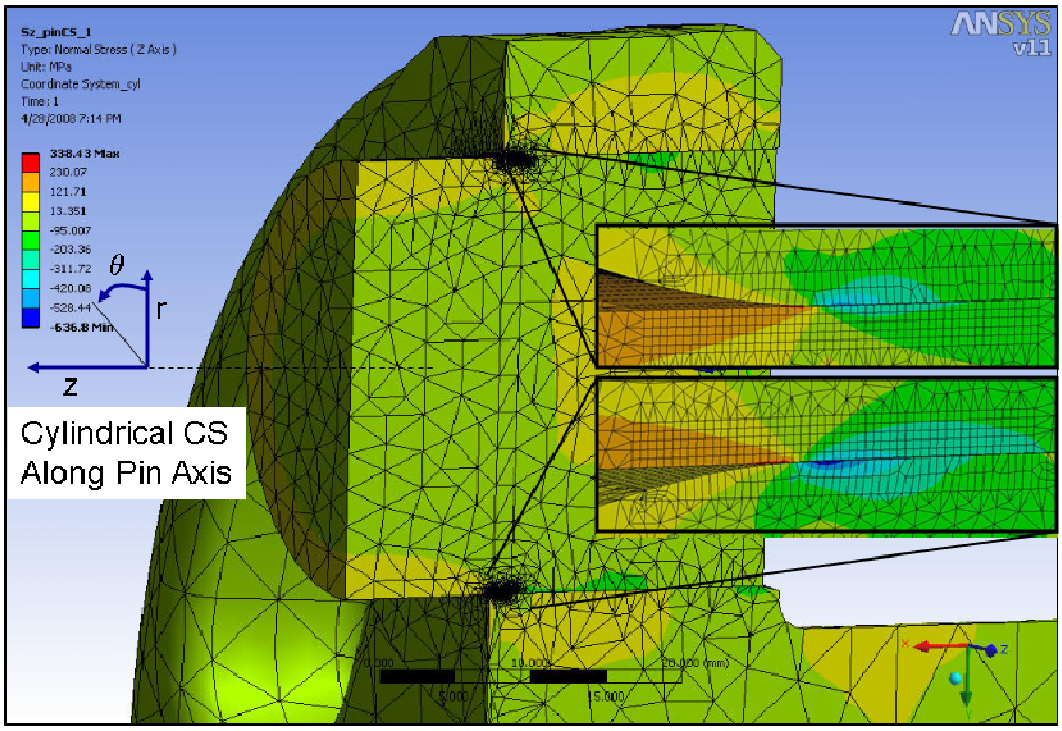

Figure 4.4.2.7 Assembly axial stress (σ_z) plot, one-quarter bench test model.

Figure 4.4.2.8 plots axial stress at the SCA with an isometric view displaying the symmetry section and the pin outer diameter. A favorable smooth stress distribution is shown with the axial stress changing from positive tensile on the free non-contact pin surface to negative compressive at the SCA. The tensile stress is of particular interest because of the potential of the operating pin bending stress to add to this assembly stress.

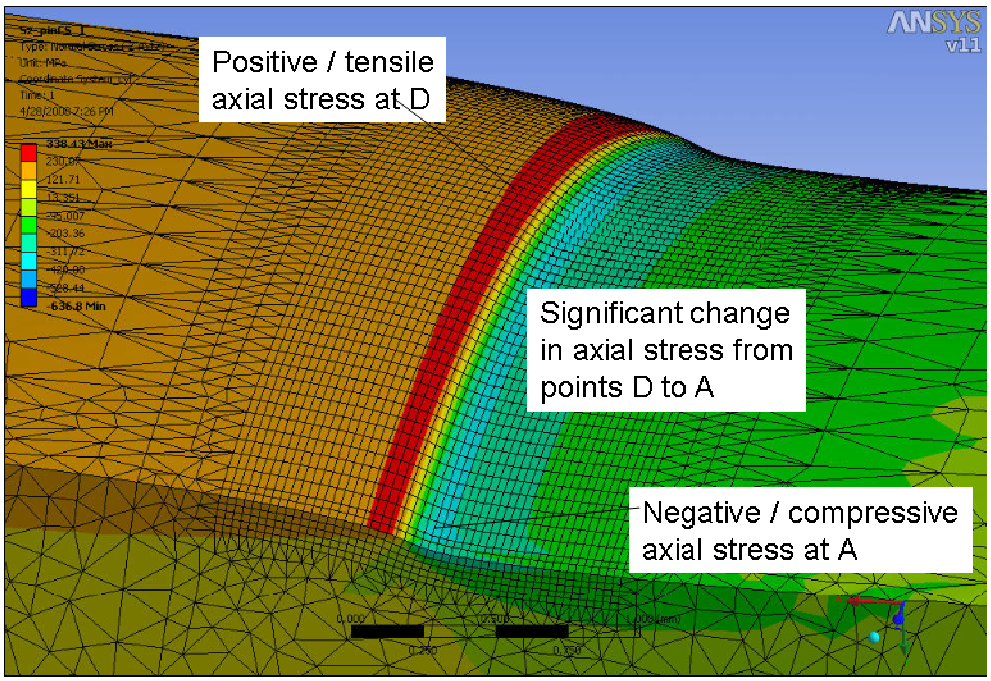

Figure 4.4.2.8 Assembly (press-fit) axial stress (σ_z) plot of the pin at the SCA.

Next the shear stress (τ_{rz}) component is displayed in Fig.4.4.2.9. Note that the shear stress local maximum at the SCA occurs below the surface, as was exhibited for the axisymmetric problems.

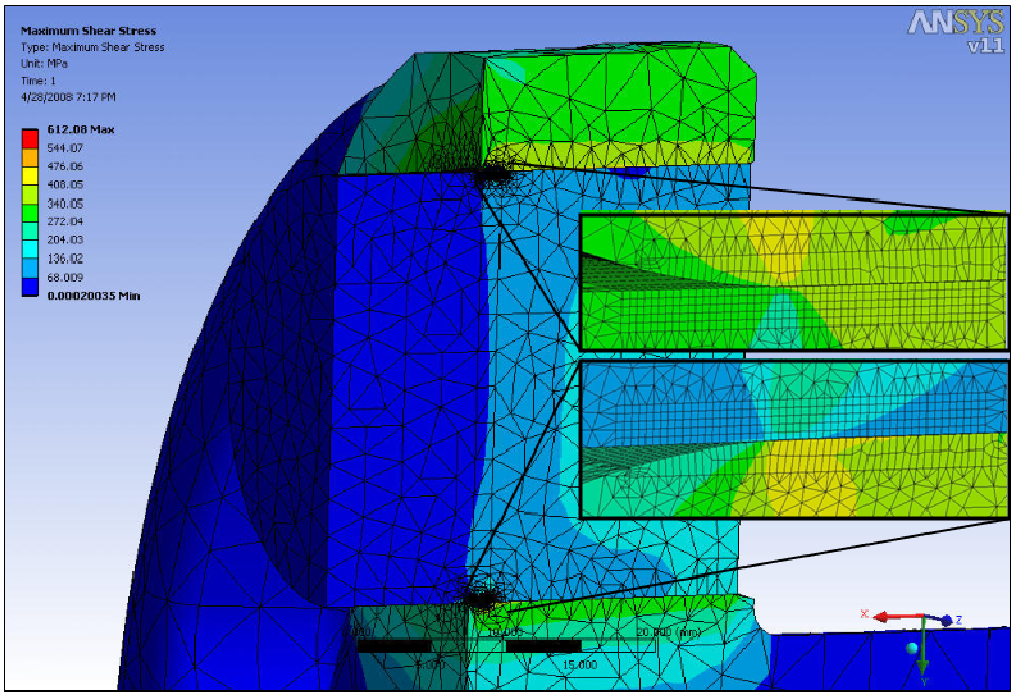

Figure 4.4.2.9 Assembly shear stress (τ_{xy}) plot, one-quarter bench model.

Figure 4.4.2.10 provides a comparison of the local maximum radial and shear stress locations at the SCA, in terms of the size of the 'Hertzian' contact patch introduced in Section 4.2.4. The maximum shear stress value is located at a distance 0.8b towards the pin free surface, from the '0b' (maximum radial stress) location. (The distance b is defined as the distance from maximum radial stress to zero radial stress, the point of no contact between the web and pin.) The maximum shear stress location occurs at a distance 0.6 *b* below the surface. Note that because of the element size *h* present, the distance measurement unit is + or – 0.2 *b*. In comparison the one-quarter bench model maximum shear stress location occurs at (0.8*b*,-0.6*b*; with a +/- 0.2*b* element size), while the 2-D axisymmetric model maximum shear stress location occurs at (0.83*b*, -0.66*b*; with a +/- 0.16*b* element size).

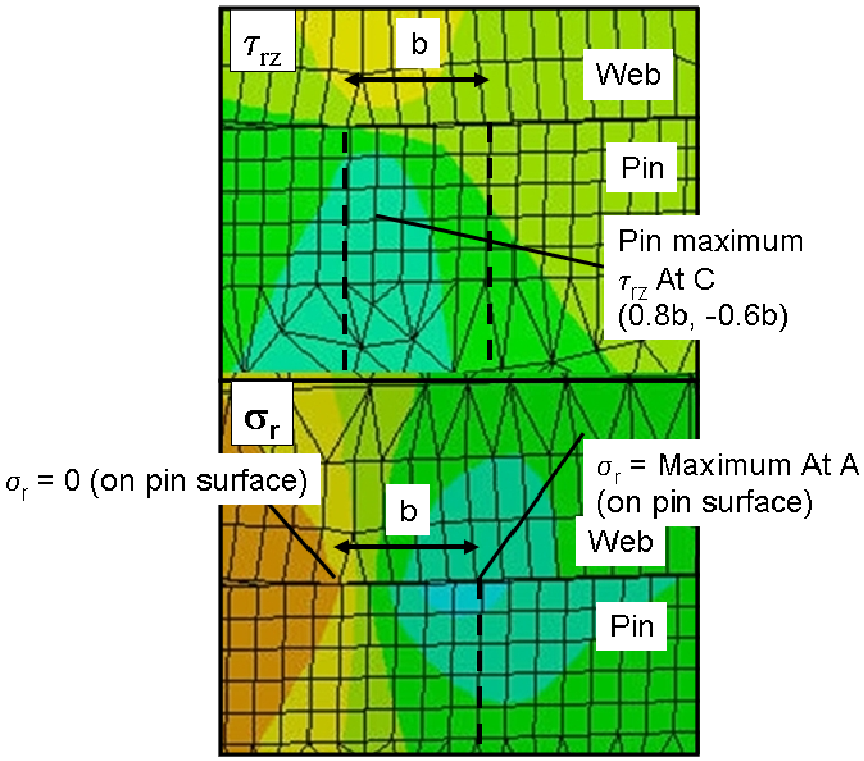

Figure 4.4.2.10 A comparison of assembly τ_{xy} and σ_r stress maximum locations.

Figure 4.4.2.11 plots assembly equivalent stress for the one-quarter bench test model. Note that as discussed previously, the web exhibits higher σ_{VM} stress on the top side of the joint, while the pin exhibits higher σ_{VM} stress on the bottom side of the joint.

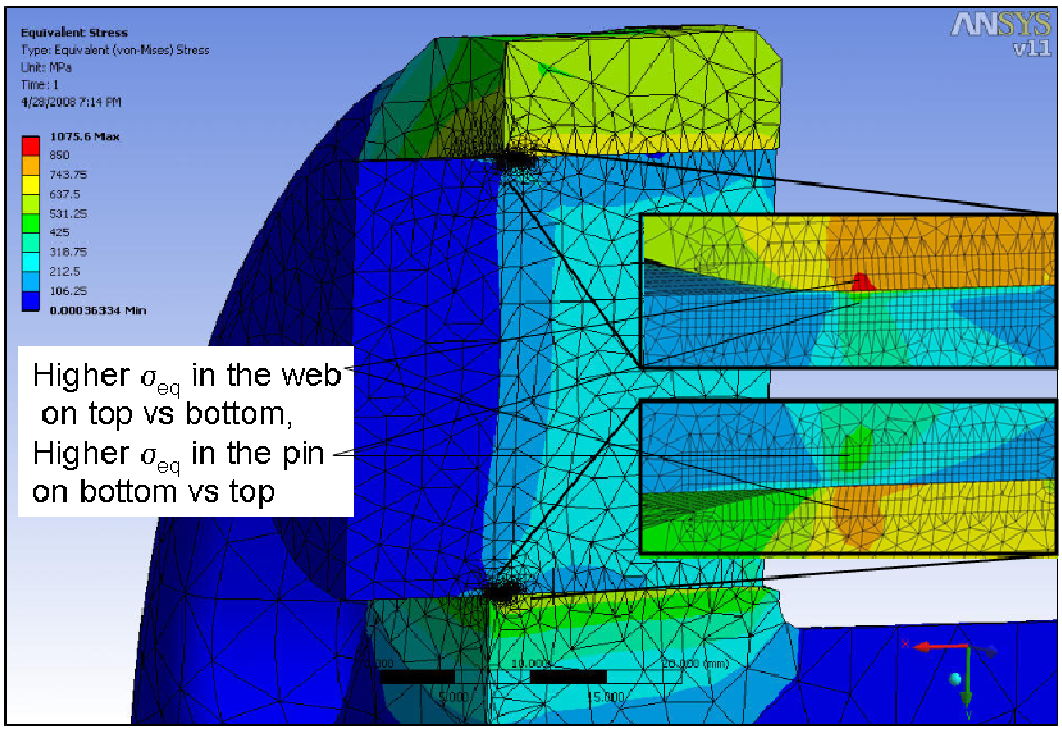

Figure 4.4.2.11 Assembly Von Mises stress (σ_{VM}) plot, one-quarter bench test model.

4.5 Comparison of Elastic Assembly Solutions Obtained from FEM Models

In the previous sections the crankshaft assembly was analyzed using axisymmetric and 3-D models. In this section the results of these models are compared and interpreted.

Figures 4.5.1 through Fig.4.5.6 provide plots of various stress components versus the element size calculated by the particular model at the given locations A thru D. In these figures the results of the axisymmetric models are indicated by u=0 and u=0.13 (u represents the value of the friction coefficient), the 30 degree slice models by 3D(30d), and the one-quarter bench test model by 3D(1/4). These results are discussed in the next subsection in detail.

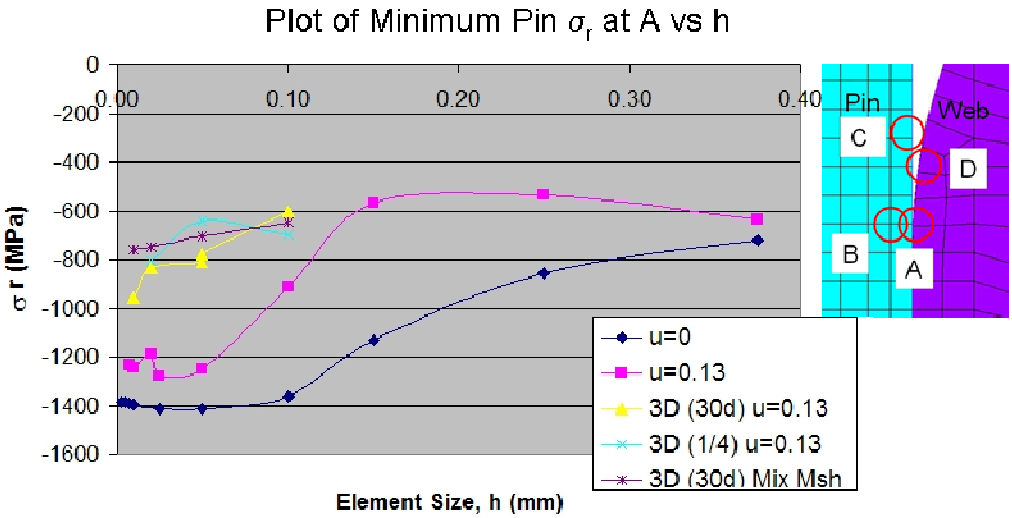

Figure 4.5.1 Plot of minimum pin radial stress σ_r at *A*.

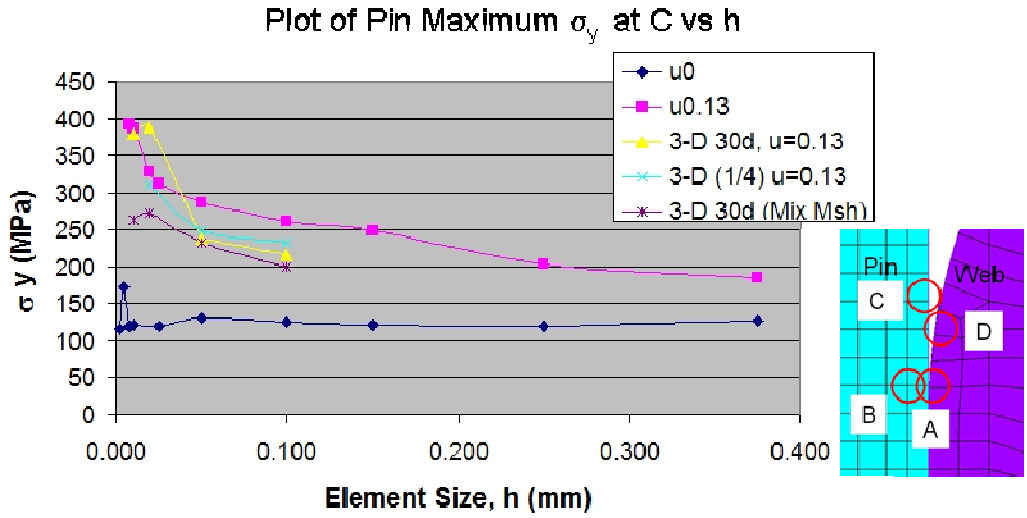

Figure 4.5.2 Plot of maximum pin axial stress σ_y at *C*.

4.5.1 Axisymmetric versus 3-D 30 Degree Slice Model

First, the axisymmetric model with 2-D meshing and the 3-D 30 degree slice model results are compared. The following points are made with respect to the comparison of these two models' results:

1. In Fig.4.5.1, the 3-D model under-predicts pin radial stress at *A* by 23%, but is still climbing, and does not converge (at *h* equals 0.01 mm, the minimum element size ran). Further refinement is expected to result in higher stress values. Axial and hoop stress values at *A* have similar trends in comparison.

2. The 3-D maximum shear stress value a location *B* on the pin has scattered data in Fig. 4.5.3. Overall maximum shear stress did not track well for the 3-D models in comparison to the axisymmetric model. In this comparison, the 3-D model under-predicts by 37%.
3. Pin 3-D equivalent stress greatly under-predicts (33%), and seems to converge, but this statement is given with caution, as there may not be enough data points to suggest this. Also, component stresses that make up the equivalent stress calculation are not converging.
4. The web 3-D equivalent stress at *A* in Fig.4.5.5 under-predicts the axisymmetric solution by 24%, and is trending upward.
5. The 3-D hoop stress on the web at location *D* tracks with the axisymmetric solution (2.9 % difference, see Fig.4.5.6), as it should, since *D* is located away from the stress gradient at the SCA.

The axisymmetric solution clearly calculates higher stress values for the same mesh refinement *h.* Several points can be made on this; first the axisymmetric solution due to the 2-D meshing and built in symmetry in the hoop direction is more numerically efficient. Less regular mesh patterns for the 3-D solution, and specifically any mesh deviation from uniformity in the hoop direction, will affect the results. For the 3-D model it is more difficult achieve convergence and keep a balance between local refinement, global element size, and overall model size.

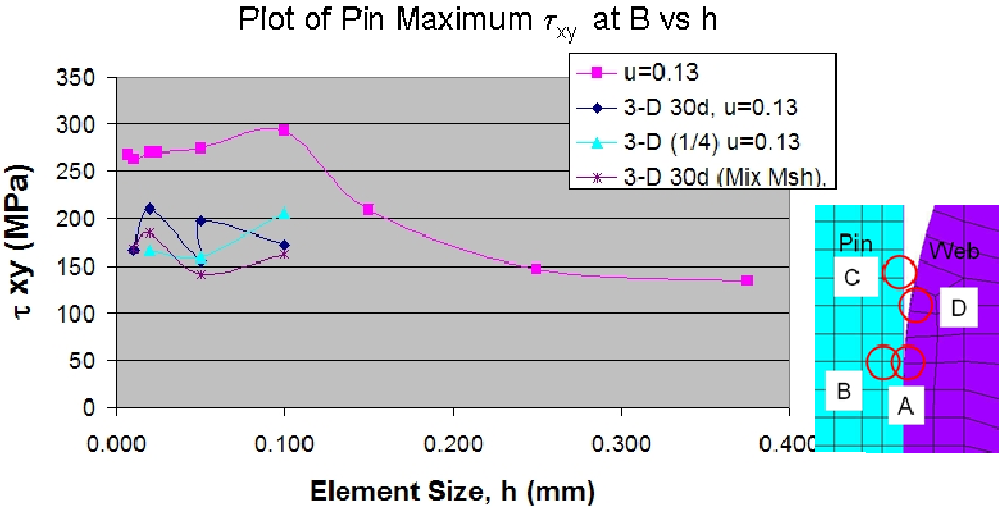

Figure 4.5.3 Plot of maximum pin shear stress τ_{xy} at *B*.

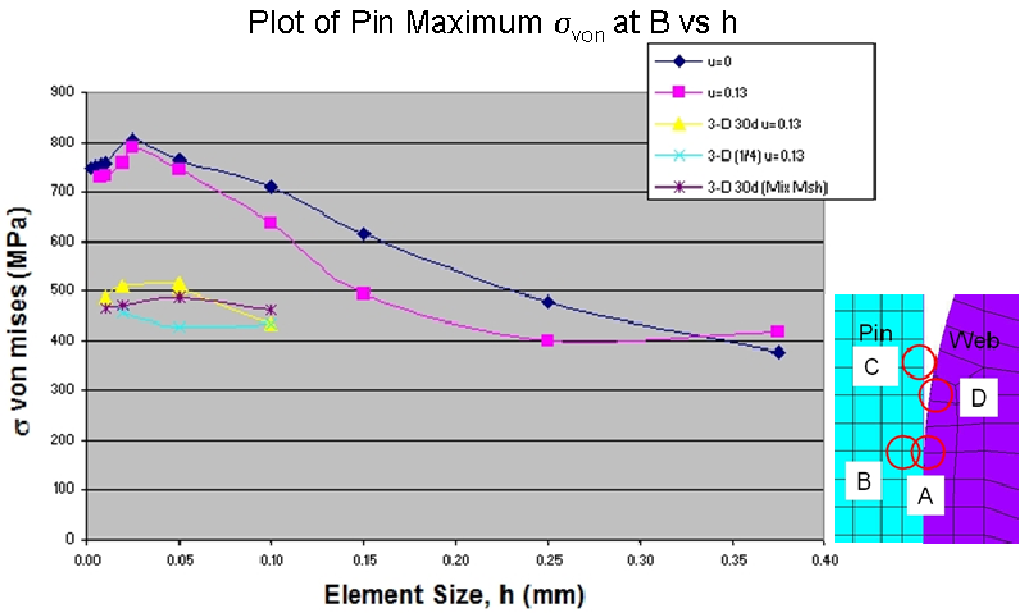

Figure 4.5.4 Plot of maximum pin equivalent stress σ_{VM} at *B*.

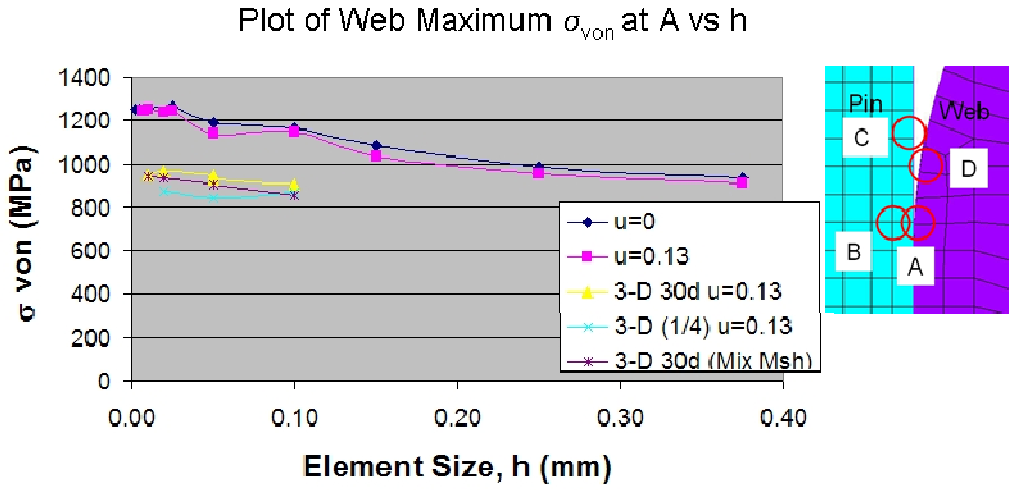

Figure 4.5.5 Plot of maximum web equivalent stress σ_{VM} at *A*.

Mesh quality in terms of element type is also of importance considering differences in the axisymmetric and 3-D solutions. The elements with linear shape functions are more numerically efficient but are less accurate. Linear triangular shaped elements suffer from an over-stiff behavior because of the direct interaction of any nodal displacement with the other two corner nodes on that face. Quadratic triangular elements reduce this error, but the triangular shape still requires that the displacement of any one corner node will interact with the other two corner

nodes, which by definition would be considered as 'all sides' of the unit element. Any 'over-stiff' behavior of the elements used, in particular at the SCA area with a high stress gradient, will result in lower deflections and therefore lower stress values calculated.

Therefore, in both solutions the quadratic elements are used (with complete quadratic shape functions). The axisymmetric solution uses the rings with the cross-section defined by 8-node (quadratic) 2-D rectangular elements. For the 3-D solution, generally 20 node quadratic brick elements were used.

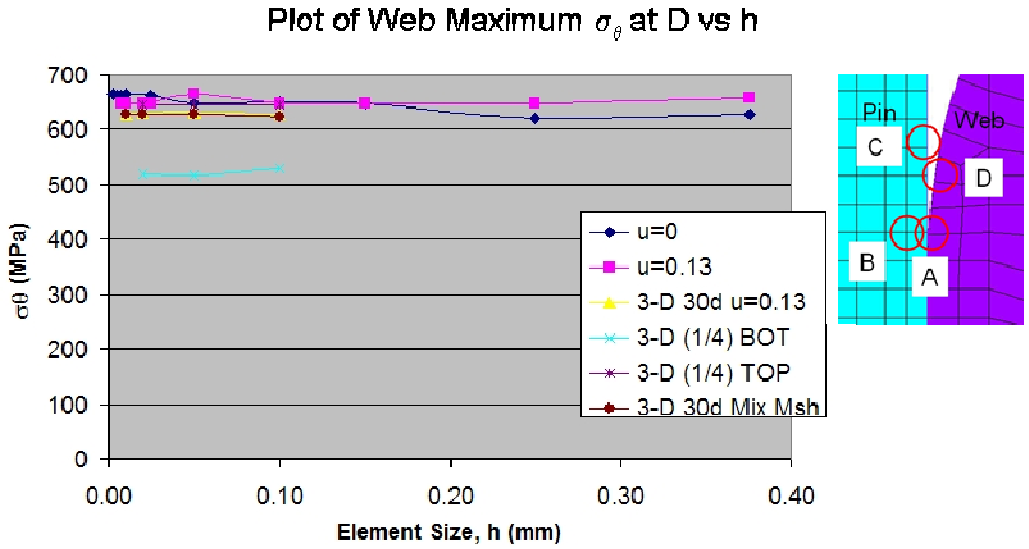

Figure 4.5.6 Plot of maximum web σ_θ at D versus size *h* comparing 2-D and 3-D results.

The general conclusion is that for this particular problem the convergence of the 3-D model was very difficult to achieve. The run times for the h=0.01mm were up over 24 hours. It is believe that higher stress values would be calculated with further mesh refinement of these models, however, such an approach does not seem to be practical and cannot be considered a useful design tool.

Finally, it should be noted that contact element uniformity on the matching pin and web surfaces has some effect on solution accuracy for both models. In particular, it is more challenging to match pin and web interface nodal locations at the SCA area with high mesh refinement when

radial interference is input by a material temperature change. This error is felt to be secondary, relative to any meshing or refinement effect.

4.5.2 3-D 30 Degree Slice Model, Uniform vs Mixed Mesh

The following summary points can be made in comparing the uniform and mixed mesh solutions for the 3-D 30 degree slice model (see Appendix A for mixed mesh 30 degree slice model details):

1. The coarse mesh solutions track compare well between the mixed and uniform mesh solutions.
2. The mixed mesh direct component stress value (σ_r, σ_θ, σ_z) at the SCA do not track with the consistent mesh values at the refined *h* values, and are much lower. The values calculated seem to be limited by the coarse element size for the coarse and refined element size pair.
3. Maximum shear stress (τ_{rz}) trends at location *B* are very erratic on the mixed mesh approach; note that this matches the consistent mesh approach.
4. Maximum pin and web equivalent stress values at *A* are very similar, but still the components do not track. (A calculated equivalent stress can not be used as the only data point for comparing two different solutions!)
5. The maximum web hoop stress value σ_θ tracks as it should at location *D* away from the SCA.

The differences in the mixed and consistent mesh are thought to stem from the poor mesh quality of the mixed mesh in the hoop direction. Based on the points above, a mixed mesh approach is not considered worth pursuing further for larger crankshaft geometry assemblies. Slight gains in numerical efficiency are seen for the 30 degree model but at the cost of a poor match in maximum stress values calculated at the higher mesh refinement. The efficiency of the mixed mesh approach would be greater for a full crankshaft 3-D model; but still may suffer an even greater error in the hoop direction calculations because of the larger circumferential distances considered when using full CAD geometry for the crankshaft components.

4.5.3 3-D 30 Degree Slice Model vs 3-D One-Quarter Bench Test Model

So far, the comparisons in sections 4.6 examined the differences in modeling approaches, for the same purely symmetric pin and web geometry. Comparisons are made now between the ideal 3-D symmetric '30 degree' model and the 3-D non-symmetric '1/4 bench test' model; all comments are directed at the one-quarter bench test model and how it matches to the 30 degree model:

1. The maximum pin radial stress at *A* is close in magnitude (-3.3%) and matches in trend at the *h* equals 0.01mm point, when comparing the one-quarter model results to the 30 degree symmetry model. (Note further refinement was not studied in the one-quarter bench test model as the solution time is greater than 24 hours for the *h* equals 0.01mm data point). The pin axial stress (-20%) and pin hoop stress (-10%) at *A* under-predict but otherwise follow the trends of the radial stress curve.

2. Pin maximum shear stress at *B* data does not match well for the one-quarter bench test model, the magnitudes are decreasing with smaller *h* which is opposite in trend, and it under-predicts by 20.7%. The one-quarter bench test model results will be affected to a greater degree by non-uniformity in mesh in the hoop direction, since the geometries considered are much larger in this direction than considered previously.

5. Both the pin and web maximum Von Mises stress trends match for the one-quarter bench test model, under-predicting by 10.4% and 11.4% respectively (see Figs.4.5.4 and 4.5.5).

7. Maximum web hoop stress at D matches well for the one-quarter bench model, as it should. Both the top and bottom values are plotted, which show the differences due to the variation in the web stiffness at top dead and bottom dead center locations on the pin.

Great effort was made with the 30 degree slice 3-D model to create an accurate stress field, in particular at the SCA. The one-quarter bench test 3-D model shows acceptable accuracy and tracking when compared to the 30 degree results, with the exception of the shear stress state. Note that both 3-D models (the one-quarter bench and the 30 degree slice) under-predict the maximum stress values at the SCA when compared to the 2-D axisymmetric model. A minimum element size of 0.01mm was used on the 30 degree slice model in comparison to 0.02 mm for the

one-quarter bench model. Therefore it is thought that even with a much greater model size and solution effort, a much larger 3-D one-quarter bench test model will not attain the level of stresses calculated with the 2-D model. It is for this reason that a much large model size with a much longer solution time has not been pursued with the one-quarter bench and the yet to be discussed full crankshaft geometry 3-D model.

5 FEM Modeling Of The Operating Loads

This chapter presents the numerical results for the operation loads applied to 3-D crankshaft FEA models.

5.1 Description Of The Operating Loads

The research presented to this point has focused on the structural details of the assembly problem. All of the following evaluations which consider operating loads use the assembly process as the first step in the numerical solution. In this chapter an analysis of the crankshaft press-fit joint under operating loads is presented using FEM modeling and computer simulation.

The running engine is a violent environment. The engine crankshaft rotates at very high angular velocity, while at the same instant high pressures developed during the combustion event drive the piston into the connecting rod, producing crankshaft torque output to the vehicle's transmission. These operating conditions are challenging to model numerically.

An engine section cut-away was presented in Fig.2.1.1, which showed the connectivity between the piston, connecting rod, and crankshaft. The crankshaft is supported by the engine case at six locations by bearing elements. The two-stroke engine displayed in Fig.2.1.1 is a twin cylinder configuration for use in a snowmobile (a recreational vehicle). Power is delivered from the engine to the vehicle's tracks (propulsion method) by a Continuously Variable Transmission (CVT). The CVT uses a rubber belt to carry the engine's torque; the belt force creates a torque reaction and bending moment on the crankshaft Power Take-Off (PTO) end (see Fig.2.4.1), as was discussed in chapter 2.

As a refresher, also recall Fig. 2.2.3 which shows a typical crankshaft assembly for a twin cylinder snowmobile engine. Each crankpin 'throw' is 180 degrees opposite to the other (an opposed twin crankshaft). The solid geometry of the crankshaft design is used to create the finite element mesh.

The operating loads that are required as input to the finite element model are calculated with a multi-body dynamics (MBD) software package, as shown in Fig.5.1.1 [33]. The software dynamics formulation considers the mass, inertia, and geometry of all components in the system. Besides predicting internal operating loads, the CVT belt loads plus the interaction of the engine with its mounting system to the vehicle are calculated. Belt loads may be influenced by the engine's mounting system.

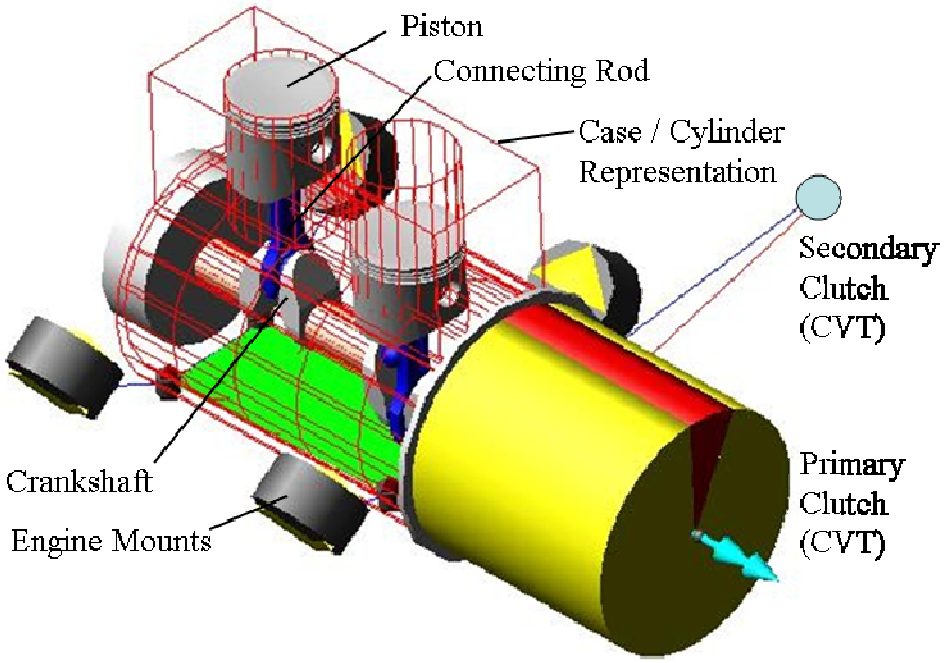

Figure 5.1.1 The MBD model to calculate operating load inputs for FEM [33].

A measured or scaled combustion pressure curve is used to drive the MBD solution, and the dynamic forces at all joints in the system are solved for over many cycles of the engine at several prescribed speeds. A typical combustion curve is provided in Fig.5.1.2. The combustion pressure peaks at approximately 17 degrees after top dead center (ATDC), and repeats on each cylinder for every cycle of the two-stroke engine.

The loads generated on the crankpins and on the PTO end of the crankshaft (by the CVT belt) are of particular interest in the MBD model. Figure 5.1.3 provides the local co-ordinate systems (LCS) of the belt force and the PTO and MAG crankpin forces. Note that while the local co-

ordinate systems for the crankpin forces rotate with the crankshaft position, the belt load co-ordinate system is stationary.

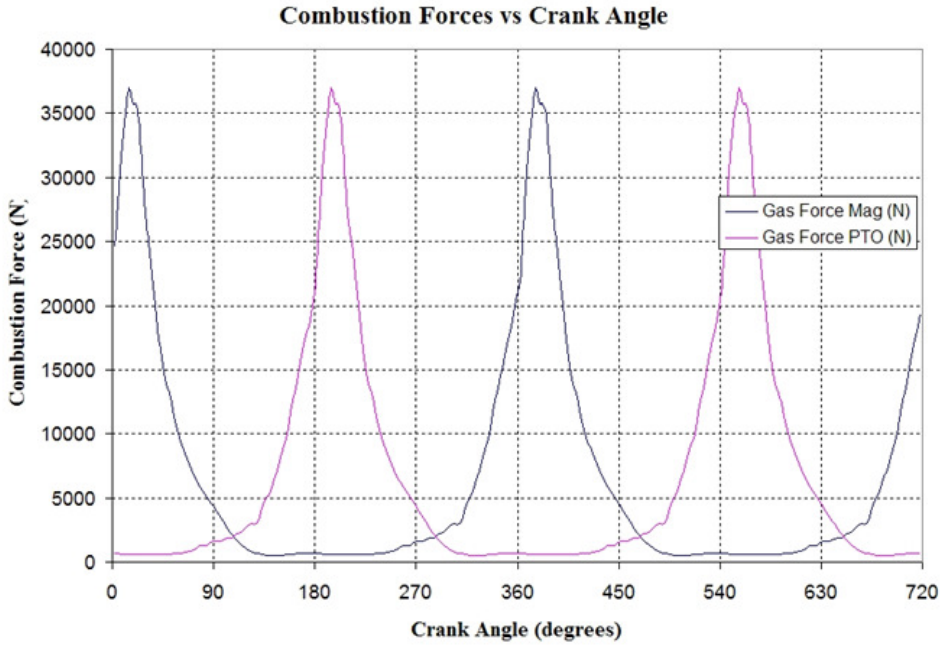

Figure 5.1.2 A typical combustion pressure curve for input to the MBD model [33].

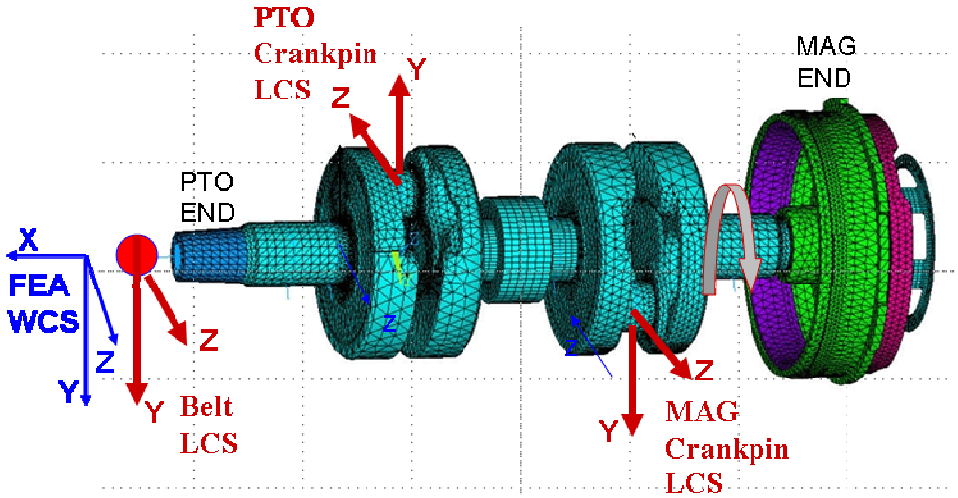

Figure 5.1.3 Local MBD model co-ordinate systems used for belt and crankpin loads.

Next the typical crankpin and belt forces are plotted in Fig.5.1.4 over 2 cycles of the engine with the combustion force activated. Note the timing of the peak combustion after TDC, just as the

reciprocating mass loads start to fall. The minimum loads generated on the crankpin at BDC are logically not sensitive to the combustion event.

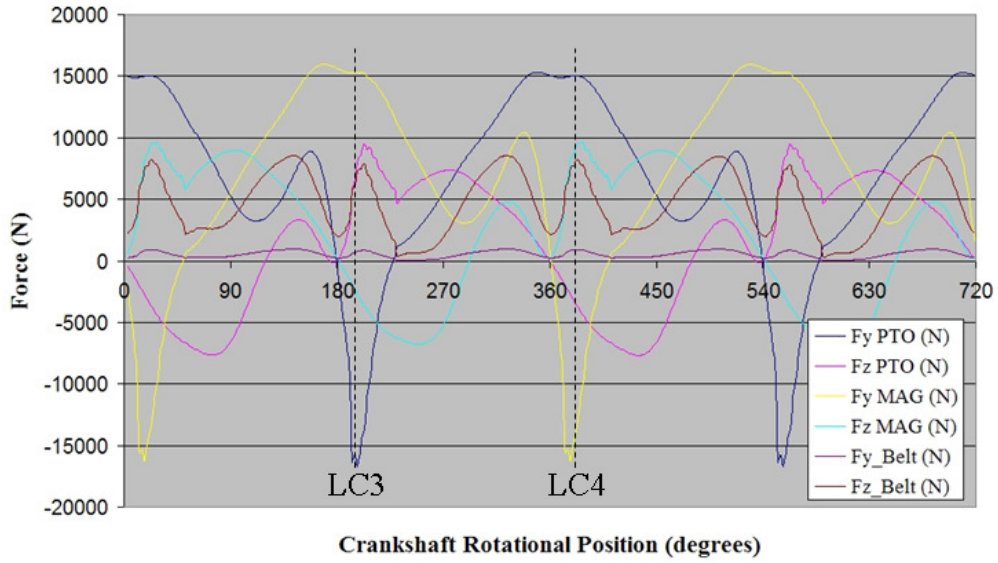

Figure 5.1.4 Operating loads calculated for the PTO and MAG crankpins [33].

For understanding the press-fit joint this research work uses static load cases and the large element size FEM models which are required to model the details of the SCA. Generally, such models cannot be reused for running dynamic cases in the time domain because the solution times would be prohibitively long, as was outlined in section 3.2. Also, the complexity of the joint behavior requires detailed post-processing of the numerical results. A static solution has been reported to calculate an overly safe design [15]; but also is deemed a very powerful design tool when coupled with experimental tests.

For brevity, and based on experience, the structural analysis of the crankshaft will focus initially on two load cases of primary interest. The first is a combustion event on the PTO crankpin (LC3 in Fig.5.1.4) which creates a high tensile stress condition on the bottom of the pin. The second is a high rotational inertia load on the PTO crankpin (LC4 in Fig.5.1.4) which bends the pin in the opposite direction creating a compressive stress on the bottom of the pin. These two load conditions typically create the highest stress reversal on the pin, and combined may be used early in design to examine crankshaft durability. Note also that the PTO end crankpin is the focus of

the numerical work as the belt forces present on there also influence the stress state of the crankpin.

Typically the crankshaft stress and deflections are highest in a maximum horsepower (maximum speed) or maximum torque (moderate speed) condition. For this study, the crankshaft structure is evaluated at maximum horsepower at 8,000 rpm. For a less computationally challenging linear static evaluation of a one-piece crankshaft, many engine speeds and load instances could be evaluated.

For the second load case of interest, when the PTO crankpin is near BDC, the opposite MAG crankpin is nearing the maximum combustion pressure. So, the PTO crankpin experiences high bending load (from the PTO piston reciprocating mass) and also must transmit the torque from the MAG cylinder combustion event. By definition, the static assumption generates belt forces at the same moment, which also further loads the PTO crankpin.

5.2 Operating Load Results For The One-Quarter Bench Model

Results from the one-quarter bench model are reviewed next as there are many aspects of the loaded press-fit joint to understand before progressing to a structural model of the full crankshaft assembly.

5.2.1 One-quarter Bench Model Description

The one-quarter bench test model uses symmetry to reduce model size, and also may replicate the sort of physical durability test that would be exercised in the lab to prove out crankshaft life. Initially the one-quarter bench test is studied with inertial loads applied due to rotations of the crankshaft. A lab environment would not likely use a rotating crankshaft, and so the results presented in the section are not exactly the behavior of the structure in the lab tests. Such tests are discussed in section 8.4 showing how 'equivalent' static loads are determined to match closely the behavior of the press-fit joint in rotating crankshafts.

The details of the one-quarter bench test FEA model are provided in Fig.5.2.1.1. Model construction and mesh quality are the same as outlined in section 4.5.1. The one-quarter bench

test model assumes symmetrical geometry about two planes, which is true only for one of the planes, plane x-y in Fig.5.2.1.1. The crankshaft geometry is not symmetrical about the y-z plane at the mid-span of the crankpin, as is assumed. Inner and outer web stiffness values would be very similar, but the crankcase stiffness and the support that it provides to the main bearings of the crankshaft will be higher towards the center of the engine. General deflection and stress values may be examined with a full crankshaft model check to validity of this symmetry assumption.

The linear elastic model is used to study four static load or time steps, which are provided in Table 5.2.1. The first load step is assembly, results for which have already been presented in section 4.4. Next the rotational velocity is applied (time step 2), followed by a pin force Fy equal to the magnitude at maximum combustion (time step 3). Lastly, time step 4 evaluates the case of a maximum reciprocating inertia load, which applies a pin load Fy in the opposite direction to time step 3.

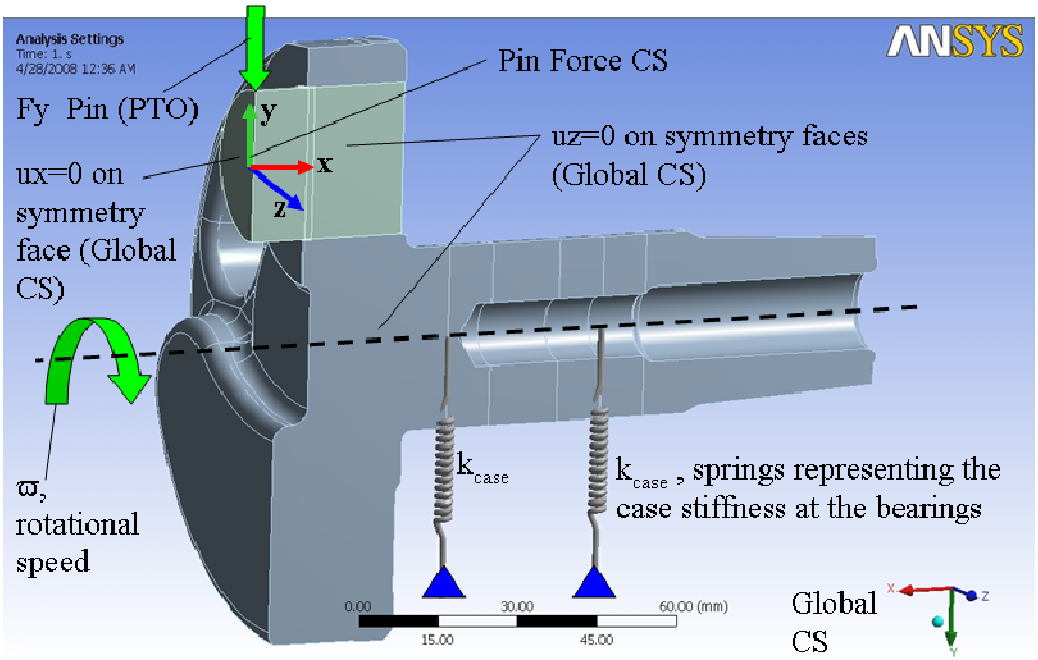

Figure 5.2.1.1 One-quarter bench model boundary conditions and load inputs.

The structural state of the crankshaft at time step 2 (assembly plus rotating speed) may be idealized of as the mean stress state, while time steps 3 (combustion) and 4 (reciprocating inertia) will produce the alternating maximum pin bending stress in opposite directions. Time step 3

occurs while the crankshaft is close to top dead center or TDC (the piston's highest point of travel), while time step 4 occurs while the crankshaft is at bottom dead center or BDC.

Table 5.2.1 One-quarter bench test load steps using the pin local CS (see Fig.5.2.1.2).

Time Step	Assembly	Rotational Speed, ϖ (rad/s)	Fy Pin (PTO) (N)
1	Yes	-	-
2	Yes	837.75	-
3	Yes	837.75	-4185.0
4	Yes	837.75	3751.3

Note that because of the symmetry assumption, loads in the z-direction of the pin local CS that produce a torque output for the crankshaft are not considered. This short-coming will be evaluated in section 8.4 with the full crankshaft assembly.

5.2.2 Operating Load Results

General behavior under load for the one-quarter bench test model is indicated in Figures 5.2.2.1-3 with the total displacement vector sum plotted on the deformed shapes. The total displacement for assembly time step 1 indicates stretch of the web around the pin, as discussed in Chapter 4.

As the crankshaft spins to the operating speed (8,000 rpm), the counterbalance lobes on the web introduce a bending moment to the pin, as described by the deformed shape in Fig.5.2.2.1. Since this loading is constant at a single engine speed, it may be considered as the mean state of the crankshaft under operating loads.

The pin combustion load (time step 3) Fy further increases the bending load on the pin, as shown in Fig. 5.2.2.2. Lastly the reciprocating load on the pin in load step 4 bends the crankpin and web assembly back in the reverse direction, as shown in Fig.5.2.2.3. The order of these displacement plots provides a reasonable description of the type of durability duty cycle that the crankshaft must withstand.

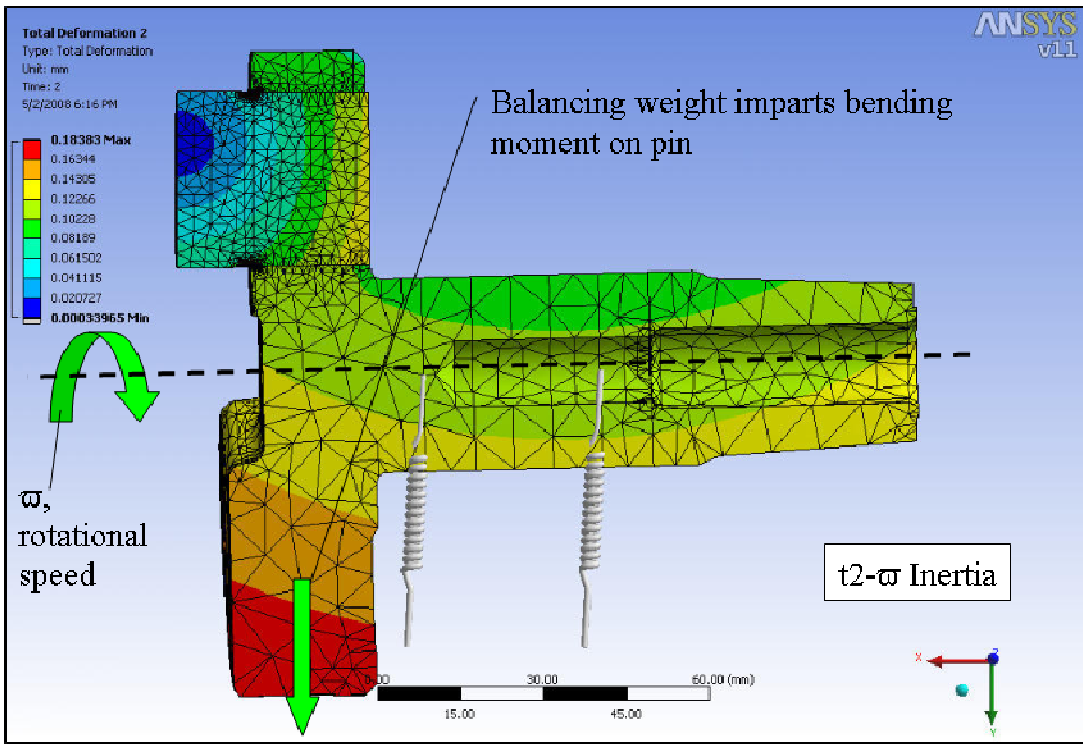

Figure 5.2.2.1 Total displacement plot, rotational inertial loads (time step 2).

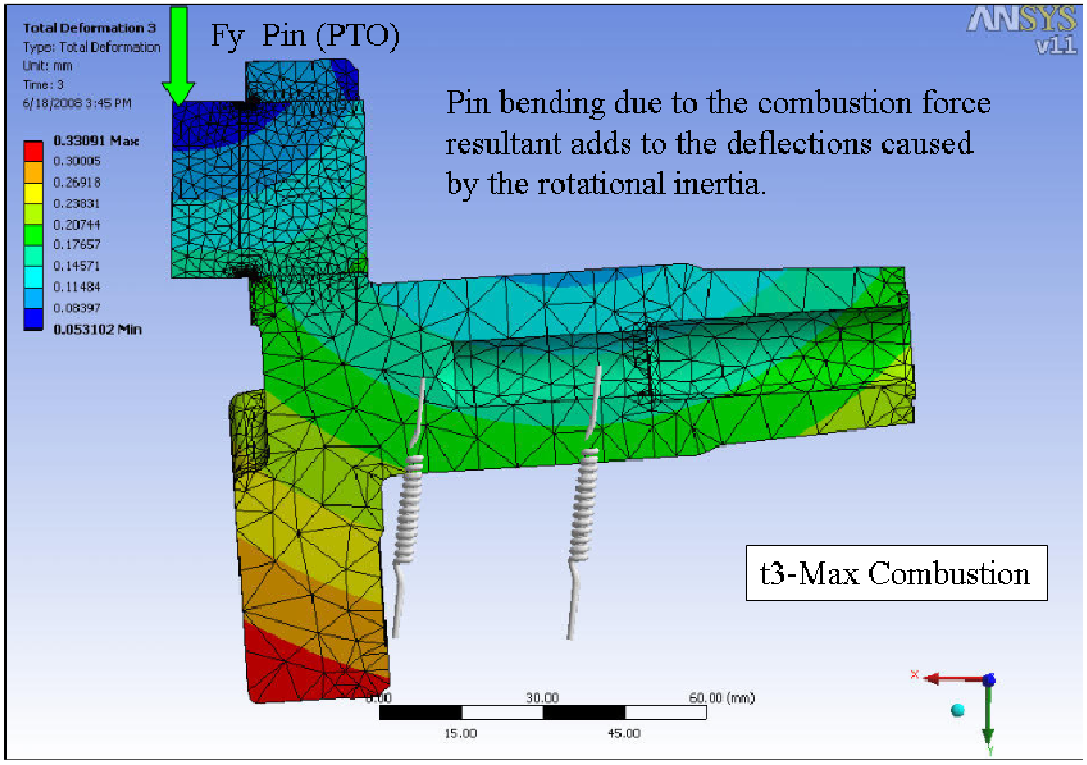

Figure 5.2.2.2 Total displacement plot, maximum combustion load.

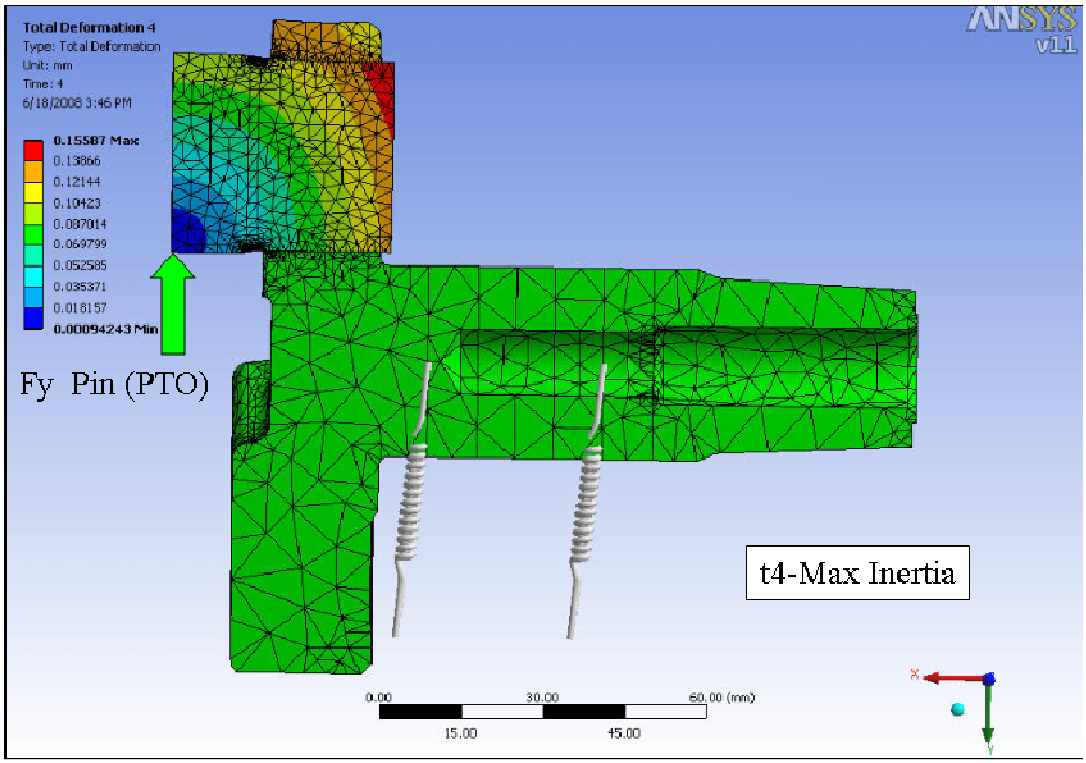

Figure 5.2.2.3 Total displacement plot, maximum reciprocating inertial load.

The next set of images show equivalent (σ_{von}), maximum (P_1) and minimum (P_3) principal stress plots for each load step. These plots introduce the subject of press-fit joint loading. The joint loading is not intuitive, and so the details need to be explained first.

Figure 5.2.2.4 shows the three stress plots (σ_{von}, P_1, P_3) for the assembly time step 1. As examined in Chapter 4, there is a great amount of detail needed to understand this state.

Second, in Fig.5.2.2.5 the rotational speed load is applied, which begins to bend the bottom of the pin in a tensile manner. The counterweight mass opposite to the pin 'pulls' the pin towards the crankshaft centerline; the pin attempts to stay straight but the counterweight applies a bending moment to the pin through the press-fit joint. Even with these general stress plots, the bottom of the pin at the end away from the SCA is shown to begin to load in the P3 plot. This larger negative P3 compressive stress at the pin web interface indicates higher compressive radial stress.

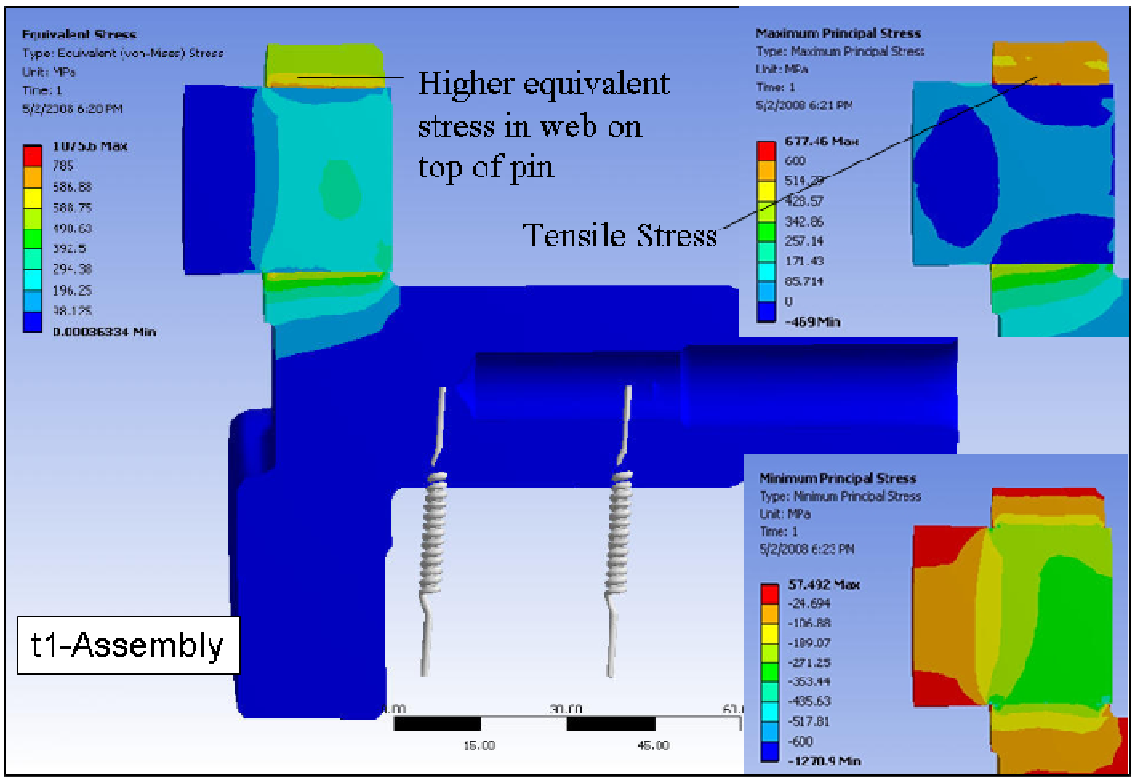

Figure 5.2.2.4 Equivalent, maximum and minimum principal stress plots (assembly).

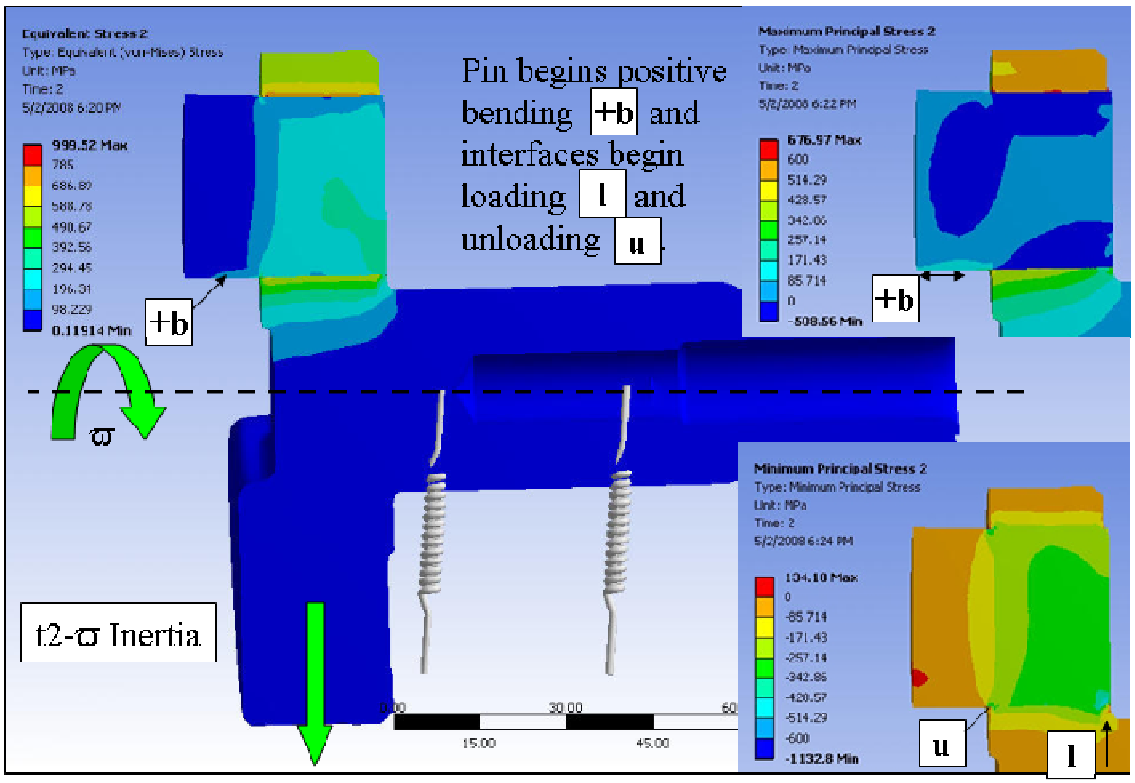

Figure 5.2.2.5 Equivalent, P1 and P3 principal stress plots (rotational inertia).

Next the pin is loaded further by the combustion event in time step 3 (shown in Fig.5.2.2.6) which increases the tensile bending stress on its bottom side.

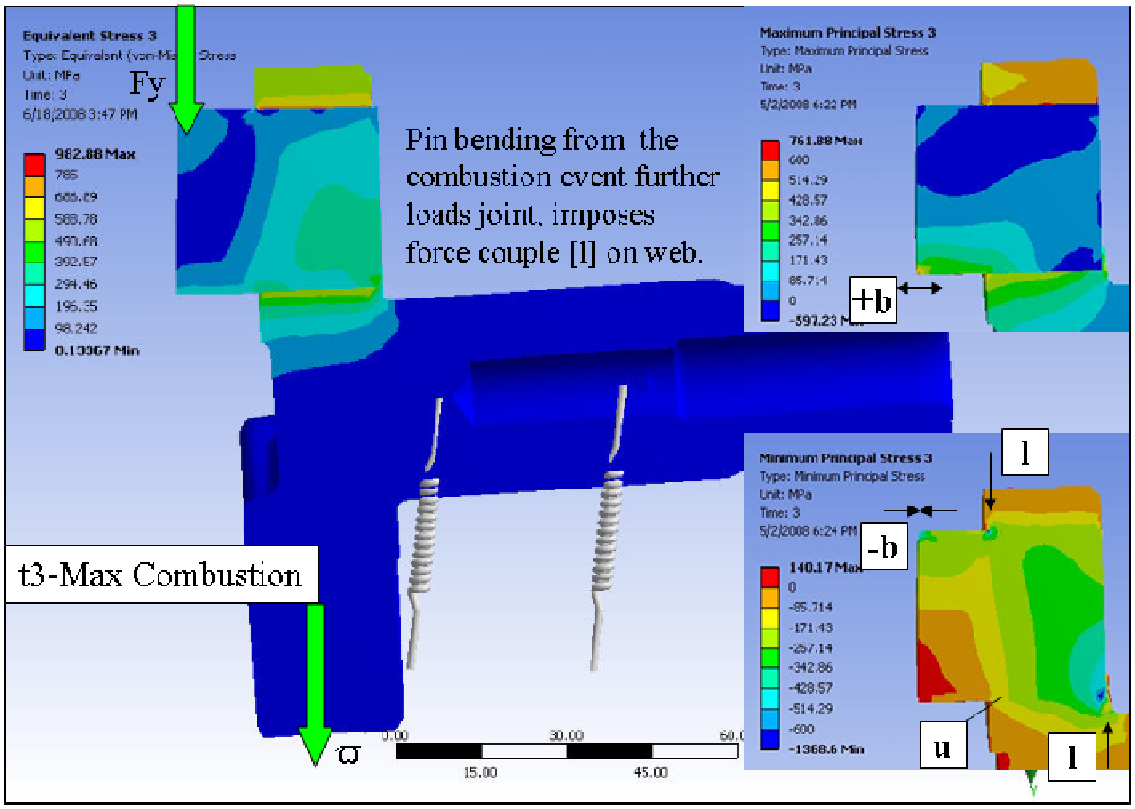

Figure 5.2.2.6 Equivalent, P1 and P3 principal stress plots (maximum combustion).

At the joint interface, the combustion load appears to further increase stress on the bottom of the pin end (away from the SCA). This also unloads the bottom of the pin at the SCA, which is not intuitive. Note that the rotational inertia loads (LC2) are present in this time step also.

During load step 4, the reciprocating loads applied to the pin are opposite in direction to those in load step 3. These reciprocating mass loads act in an opposite direction to the counterweight inertia load (see Fig.5.2.2.7), which clearly creates tensile axial stress on top of the pin, and compressive stress on the bottom. A detailed explanation of joint loading is to be provided after a further description of the general stress is provided next.

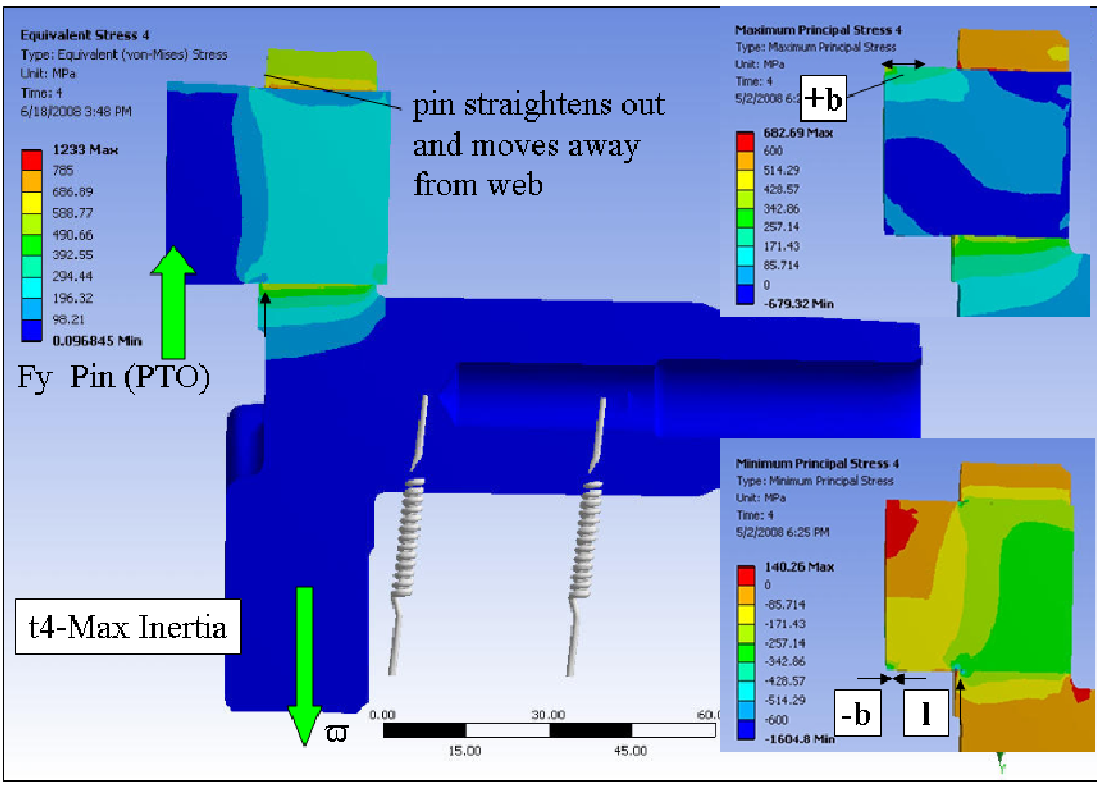

Figure 5.2.2.7 Equivalent, P1 and P3 principal stress plots for load step 4.

Equivalent and maximum principal stress are plotted together in an isometric view for load case 3 in Fig. 5.2.2.8. For all the load cases considered, the web stress state is dominated by the assembly interference; some minor stress sensitivity is shown in the thin web material above the pin though. The pin bending stress does show some sensitivity to loading, as shown in Fig.5.2.2.8.

Next joint loading is examined for the operating loads using a set of highly distorted radial stress plots. Figure 5.2.2.9 shows the web only, with a close up view of the radial stress on the press-fit bore. The radial stress is reasonably uniform (both in the axial and hoop directions), and has local stress concentrations at each end.

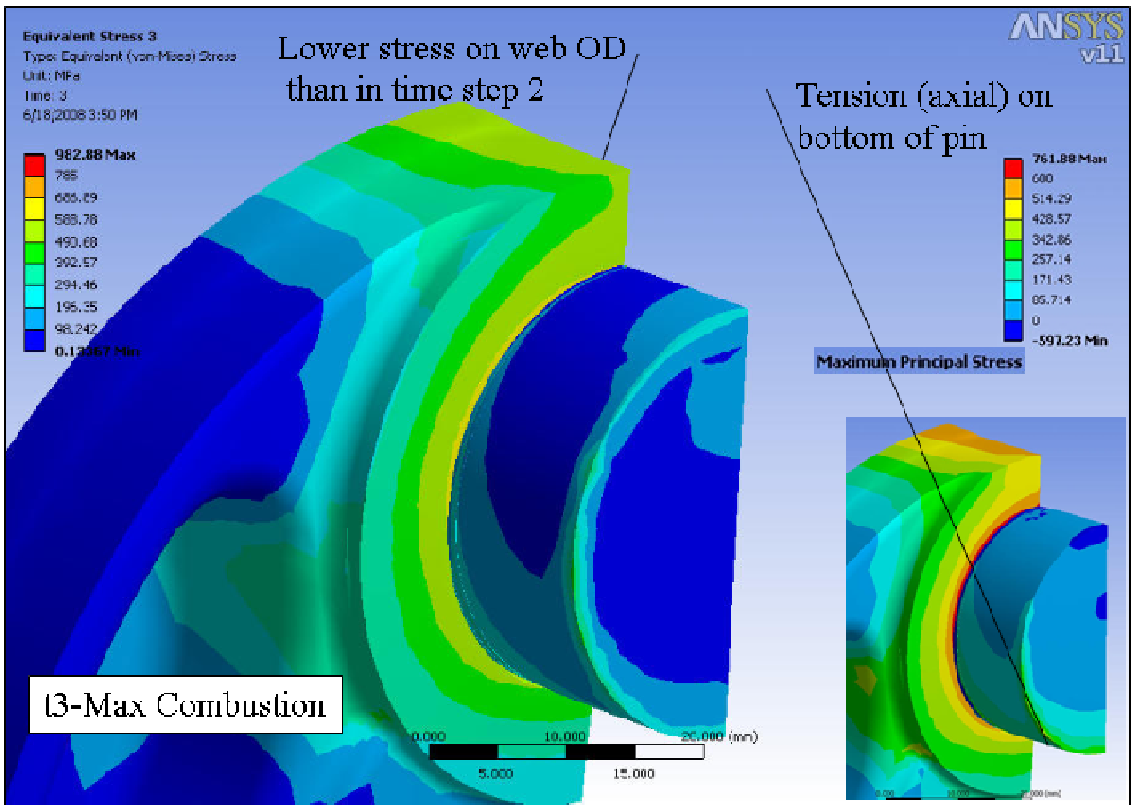

Figure 5.2.2.8 Equivalent and P1 principal stress plot (maximum combustion load).

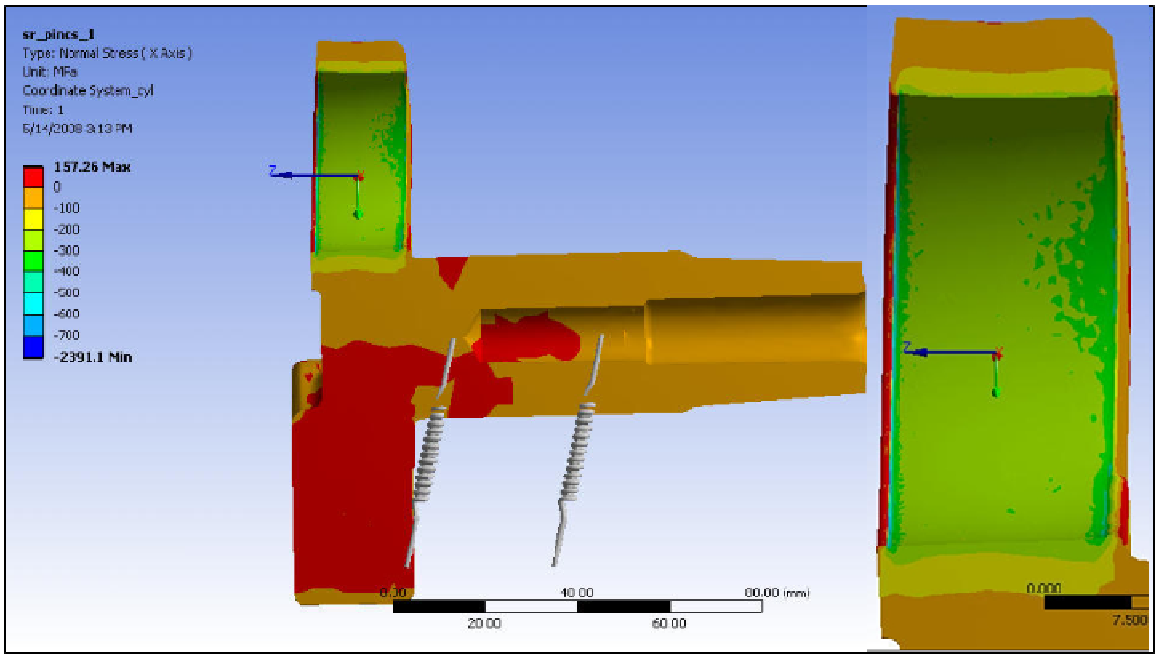

Figure 5.2.2.9 A highly distorted radial stress plot of the web (assembly).

As the crankshaft spins to operating speed for LC2, the counter-mass creates a bending moment on the pin. The counter-mass is supported by bearings offset along the crank axis; the moment on the pin is a bi-product of the offset axial bearing support. The counter mass moves laterally as the structure deforms under rotational load, and the radial contact stress increases at opposite 'corners' of the pin, (as shown in Fig.5.2.2.10) as the pin opposes this moment.

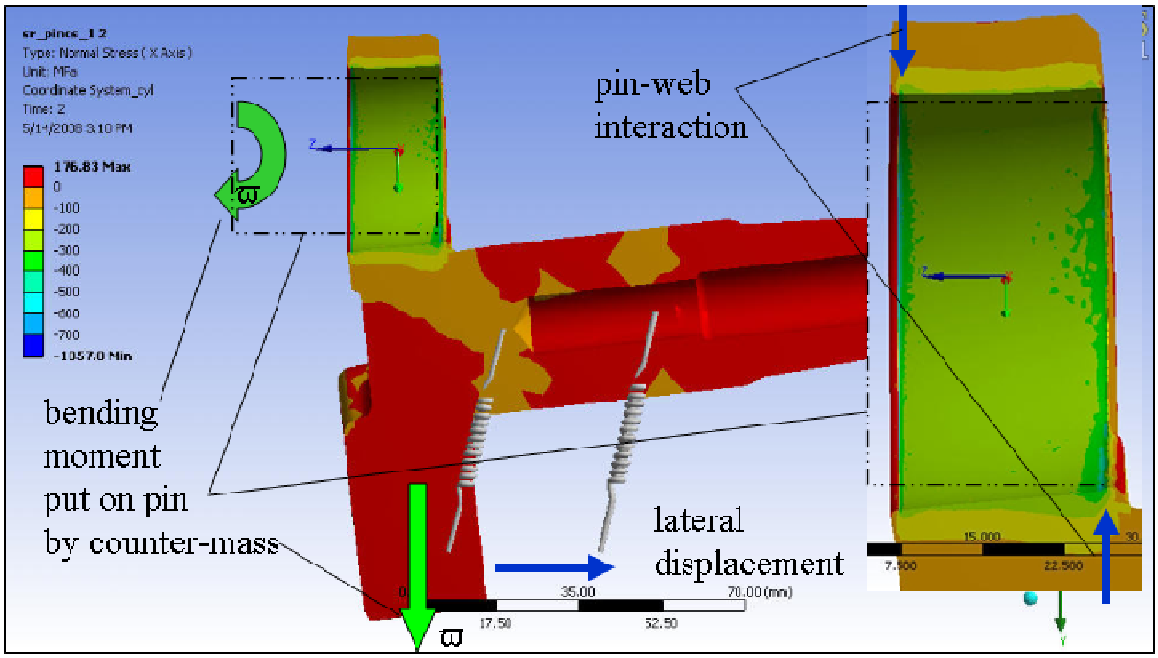

Figure 5.2.2.10 A highly distorted radial stress plot of the web (rotational inertia).

As the combustion force is added to the structure in load step 3, (see Fig.5.2.2.11) both the pin and web continue to deform, so much so that the pin radial interface pressure partially unloads at the SCA, and the bottom end corner of the pin is loaded further. The blue set of vertical force vectors (Fig.5.2.2.11) on opposite diagonals of the bore are indicative of the bending moment carried by the pin or joint.

In time step 4 the pin force and the counter balance inertia forces cancel somewhat, and the joint becomes more evenly loaded again. The radial stress distribution is shown to be very uniform across the bore in, similar to the assembly state of Fig.5.3.2.9.

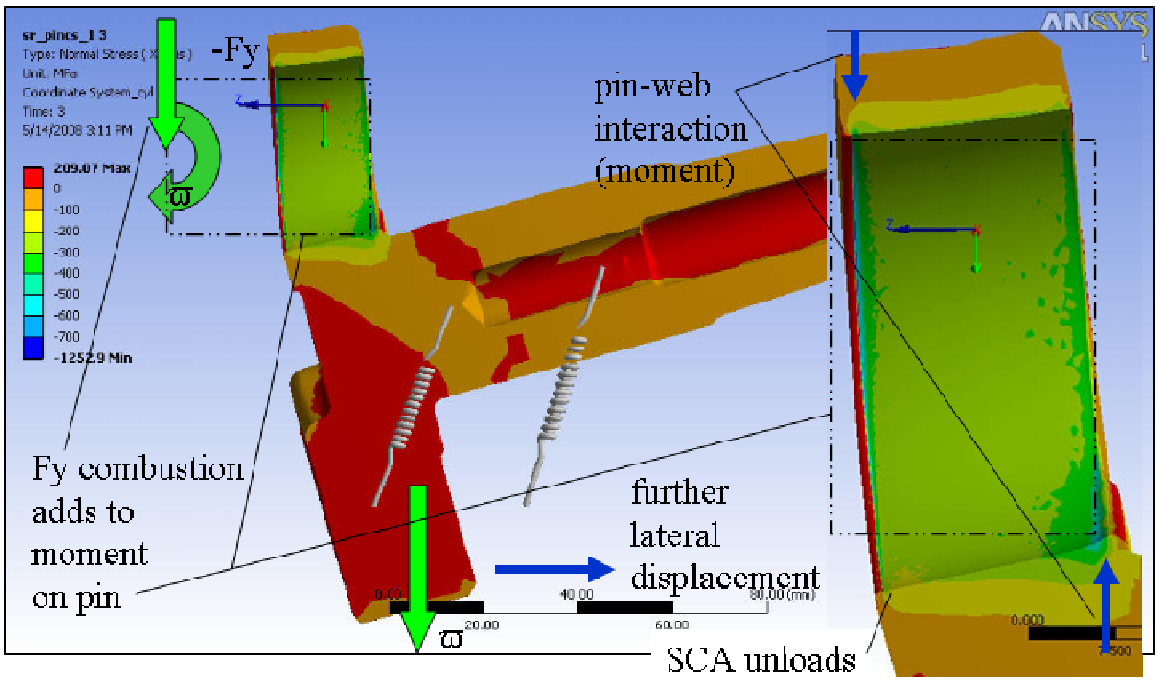

Figure 5.2.2.11 A highly distorted radial stress plot of the web (load step 3).

Next Fig. 5.2.2.12 details the changes in pin radial stress for time steps 1 thru 4, which also support the discussion on the joint loading. Radial stress at the bottom end corner of the pin is sensitive to the bending loads carried through the joint.

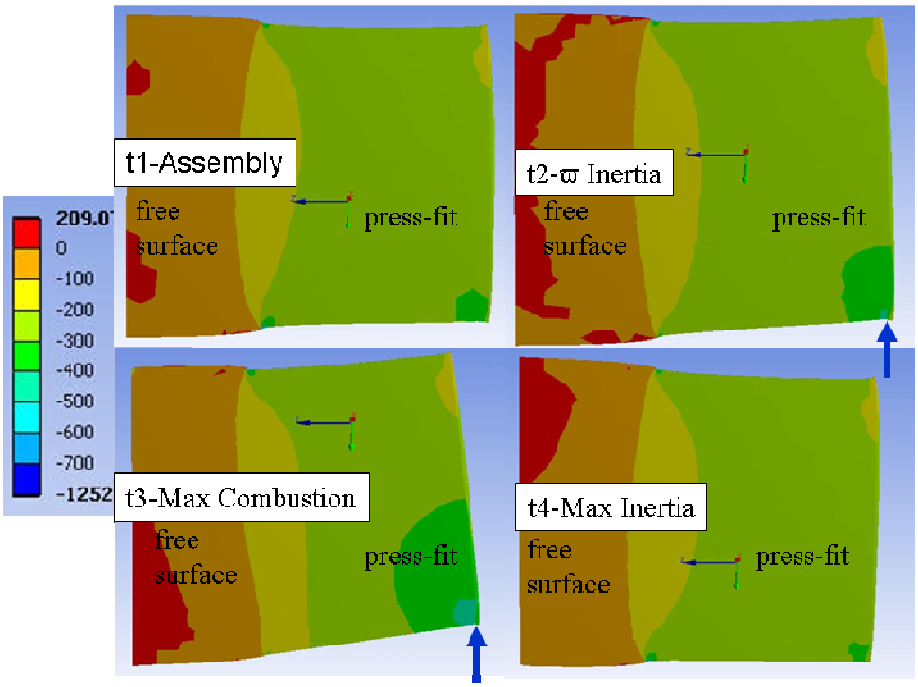

Figure 5.2.2.12 A highly distorted pin radial stress plot, time steps 1 thru 4.

Pin axial stress plots are now shown for all 4 time steps. In Fig.5.2.2.13 a high stress gradient is shown across the SCA, which was detailed in Chapter 4. As the rotational velocity is applied, tensile axial stresses are created on the bottom of the pin (see Fig. 5.2.2.14) just outside of the contact with the web. Also, pin compressive axial stress is still present on the other side of the SCA.

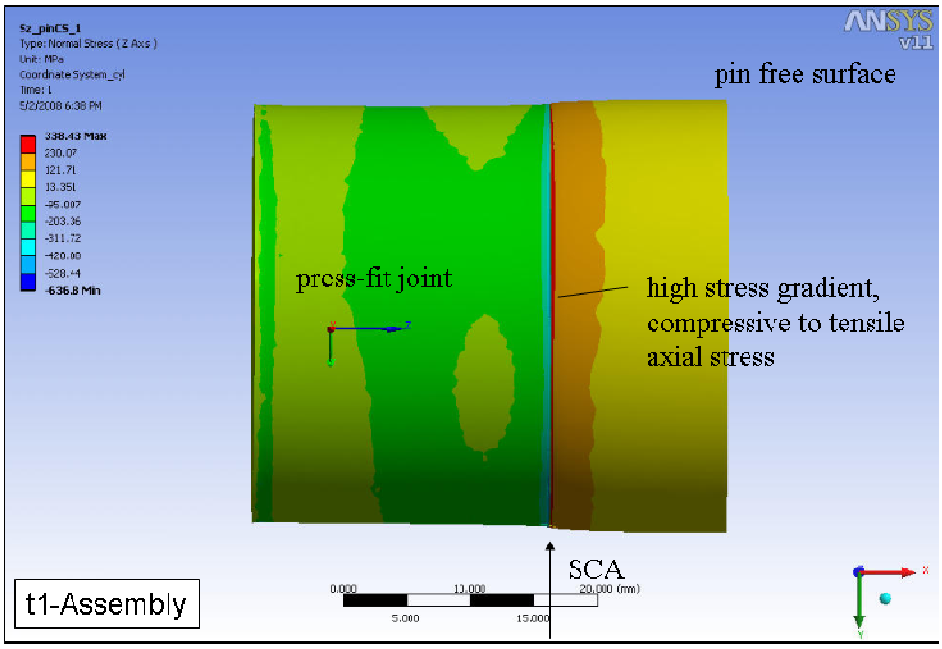

Figure 5.2.2.13 Pin axial stress (σ_z) plot (assembly).

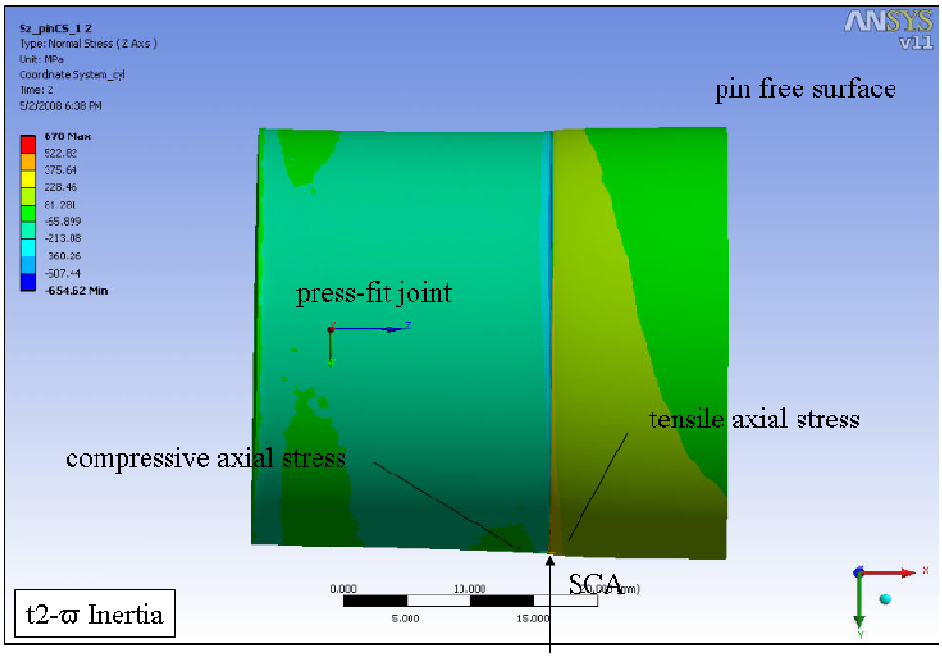

Figure 5.2.2.14 Pin axial stress (σ_z) plot (rotational inertia).

In Fig. 5.2.2.15 the time step 3 combustion forces create tensile axial stress across the SCA entirely, as the radial compressive stress at the SCA have now completely unloaded (see Fig. 5.2.2.15). Compressive axial stress on the top side of the pin at the SCA is prevalent also for time step 3.

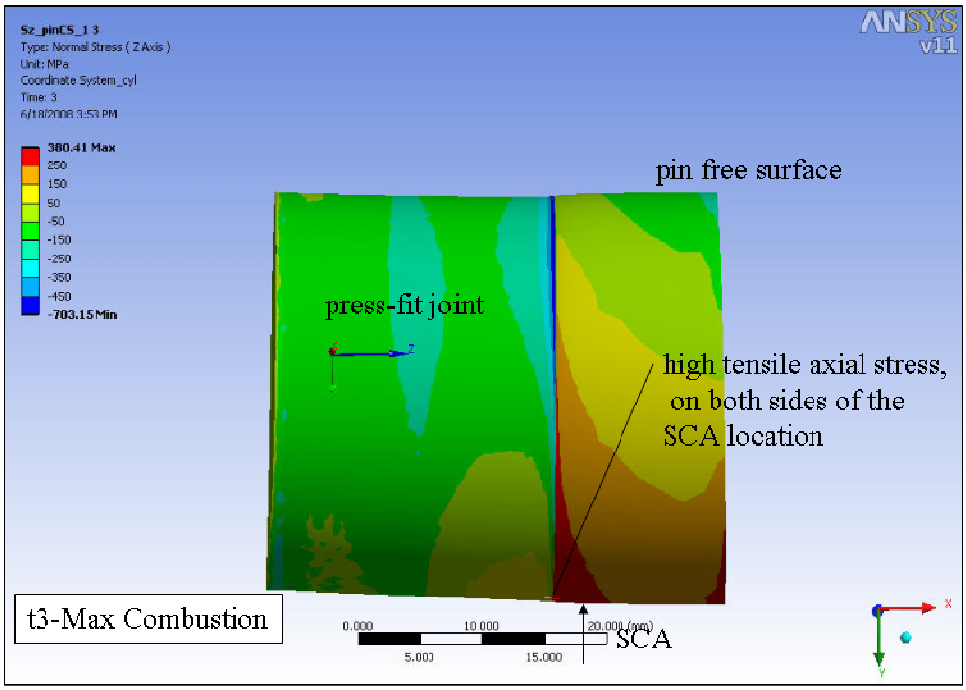

Figure 5.2.2.15 Pin axial stress (σ_z) plot (maximum combustion).

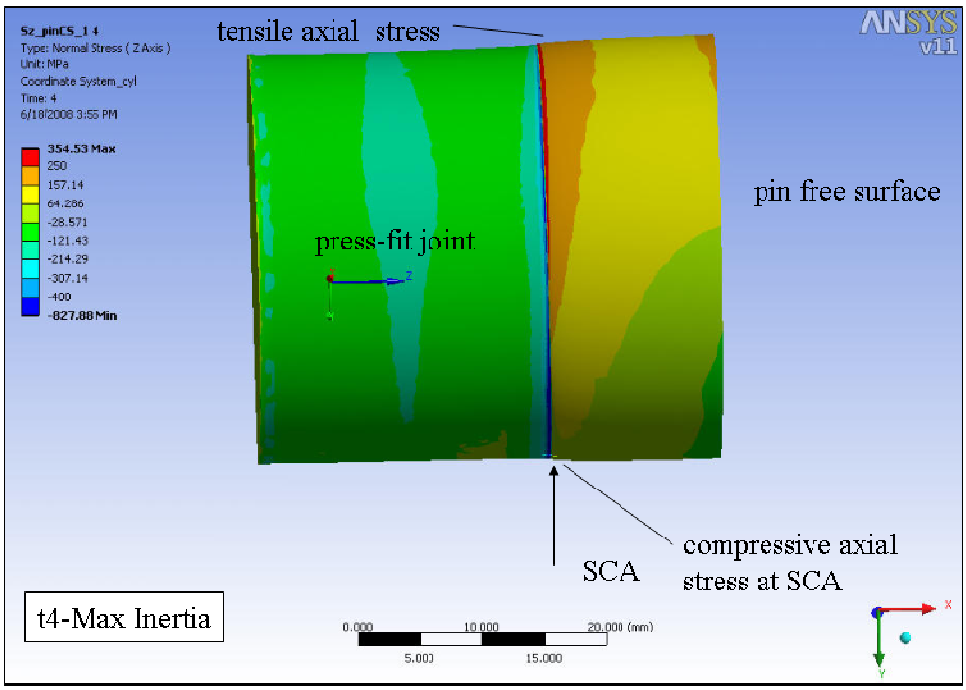

Figure 5.2.2.16 Pin axial stress (σ_z) plot (maximum reciprocating inertia).

Finally Fig. 5.2.2.16 shows that axial stress at the bottom of the pin now becomes compressive again, including at the SCA, because of the opposite direction loading in time step 4. Exact details of the axial stress field at the SCA are provided in section 5.2.4.

Next, Fig. 5.2.2.17 plots hoop stress at the web bore for load cases 1 thru 4, which only shows minor sensitivity to the bending loads imparted on the joint in load cases 2 and 3. Stress distributions and magnitudes do not change a great deal.

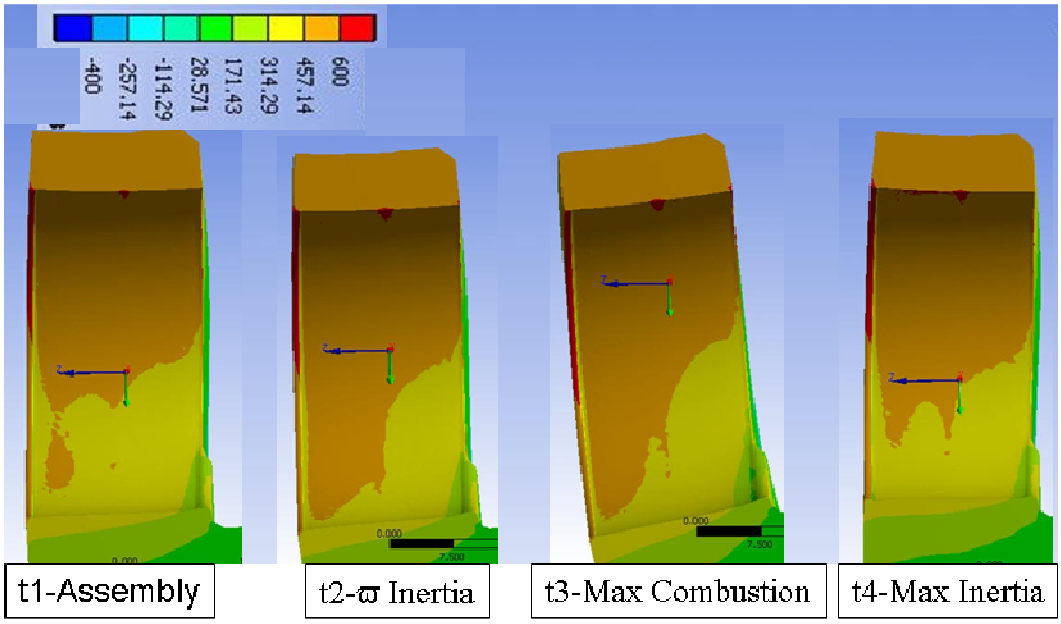

Figure 5.2.2.17 Hoop stress (σ_θ) plots for the web, time step 1 thru 4.

The final set of plots in this section examines the details of the stress field at the SCA over all time steps. A close view of the radial stress field at the SCA, on the bottom of the pin is provided in Fig.5.2.2.18 or all four load cases. Radial stress is shown to unload the assembly pressures in load steps 2 and 3. For load step 4 the interface radial stresses begin to load again, but do not return to the same level as for assembly. This indicates that the mean radial stress state at the bottom of the pin is unloaded (as the engine spins faster), and does not again become as highly loaded as during assembly, even upon application of the operating loads.

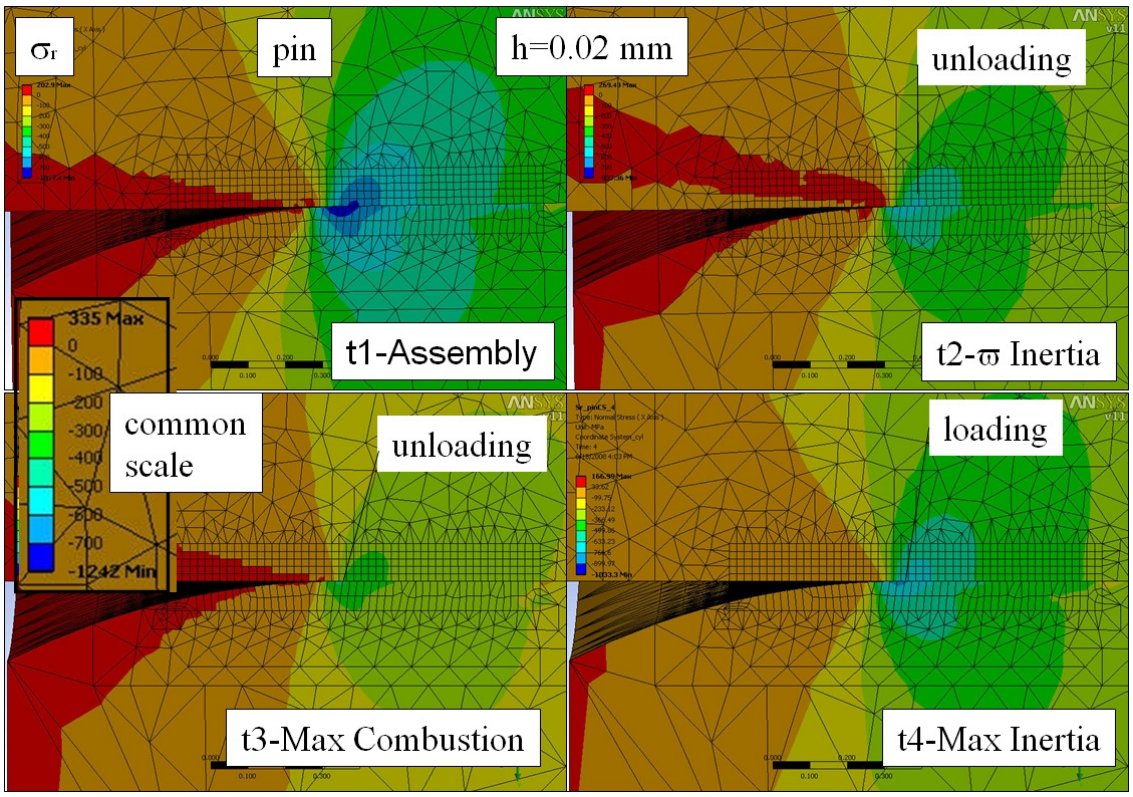

Figure 5.2.2.18 Radial stress (σ_r) plot near the SCA at BDC, time steps 1 thru 4.

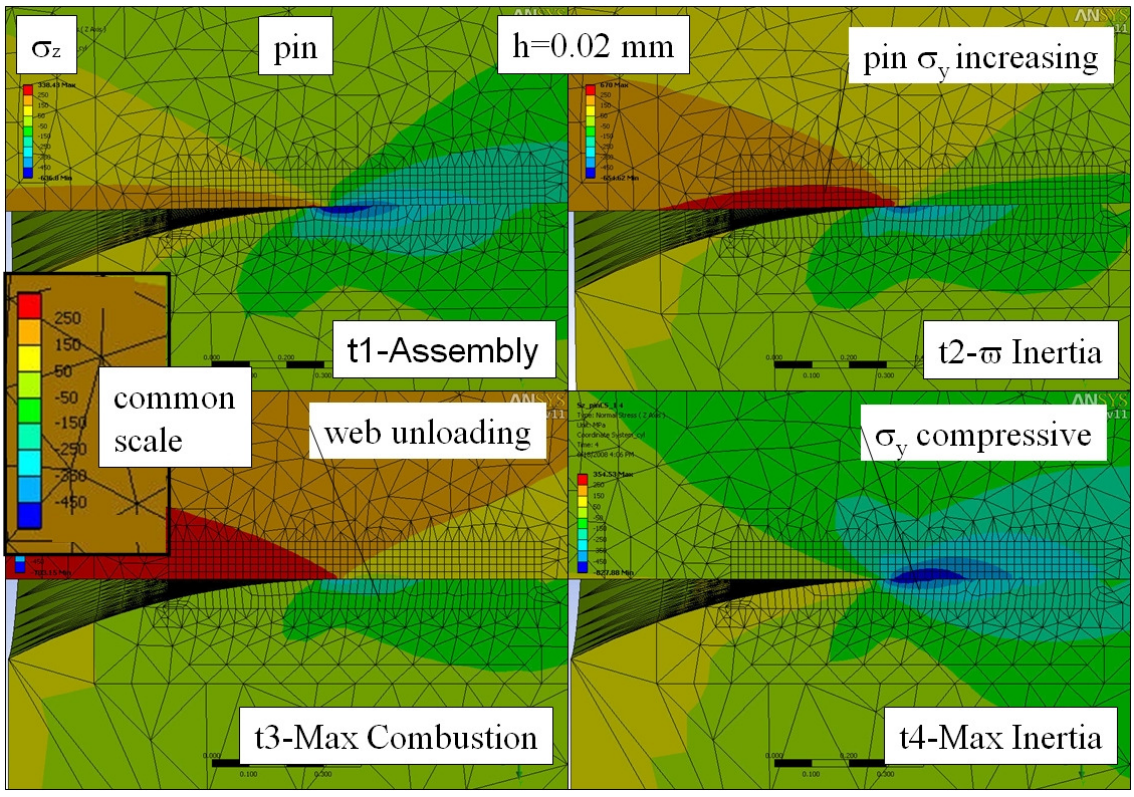

Figure 5.2.2.19 Axial stress (σ_z) plot near the SCA at BDC, time steps 1 thru 4.

Figure 5.2.2.19 shows a near view again at the SCA (bottom of pin location) for axial stress for load steps 1 thru 4. As the pin bends, axial stress increases in time steps 2 and 3. Note though that the web stress is very low at the SCA, indicative of the radial stress unloading there shown in the previous plot. Because the web has a very low radial stress at the SCA at time equals 3, it may not carry axial stress through the radial contact and friction of the two mating surfaces. High compressive axial stresses dominate the SCA area for load step 4. Compressive radial stresses shown in the previous figure allow the joint to carry the pin bending loads in the axial direction at the outer diameter of the pin.

Shear stress at the SCA is shown for load cases 1 thru 4 in Fig.5.2.2.20 on the bottom of the pin. Shear stress increases during time step 2 as the rotational spin creates higher axial tensile stress while there is still the compressive radial stresses present at the SCA. Note that radial stresses were shown in chapter 4 to be primarily responsible for the shear stress. As the pin radial stress unloads, the pin surface nearly loses the kink from assembly, and the shear stresses are lowered (LC3). Shear stresses become significantly higher for time step 4 when the reciprocating mass loads are applied, and the highly compressive radial stresses are introduced again at the SCA.

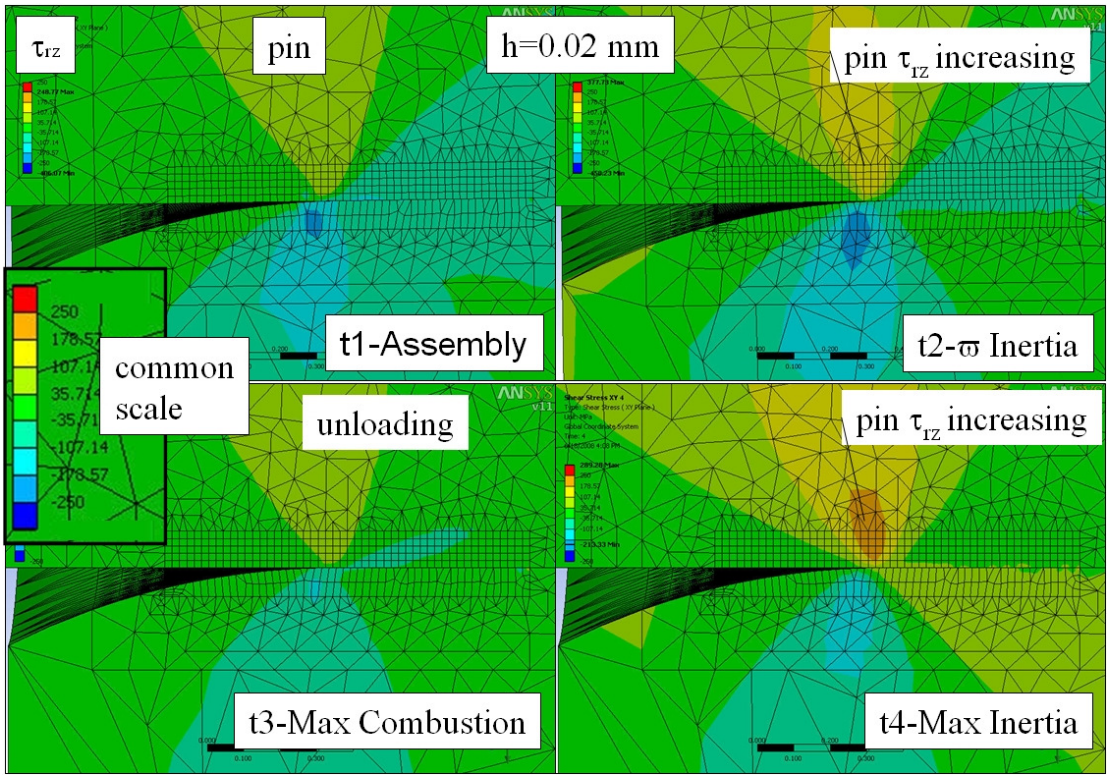

Figure 5.2.2.20 Shear stress (τ_{rz}) plot near the SCA at BDC, time steps 1 thru 4.

Figure 5.2.2.21 plots equivalent stress at the SCA (bottom of pin) for time steps 1 through 4. The equivalent stress plots do not lend themselves to as much description as do the component stresses, but generally show the joint loading and unloading outlined previously.

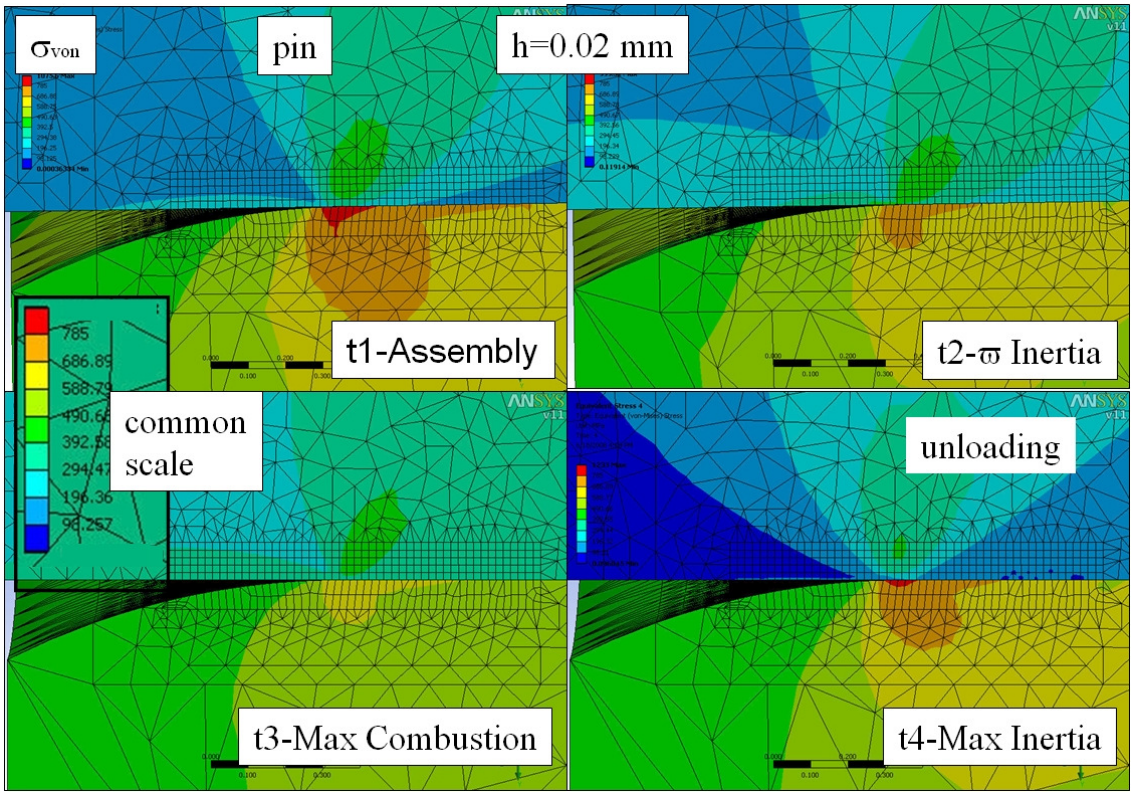

Figure 5.2.2.21 Equivalent stress (σ_{VM}) plot near the SCA at BDC, time steps 1 thru 4.

Finally Fig. 5.2.2.22 shows equivalent stress at the SCA on the top of the pin for all 4 time steps. Generally component stresses are higher on the top side of the pin, but do not have as significant changes in the alternating magnitudes. Because the focus is on the bottom of the pin area and durability concerns there, details at the top side of the pin are not included to maintain brevity.

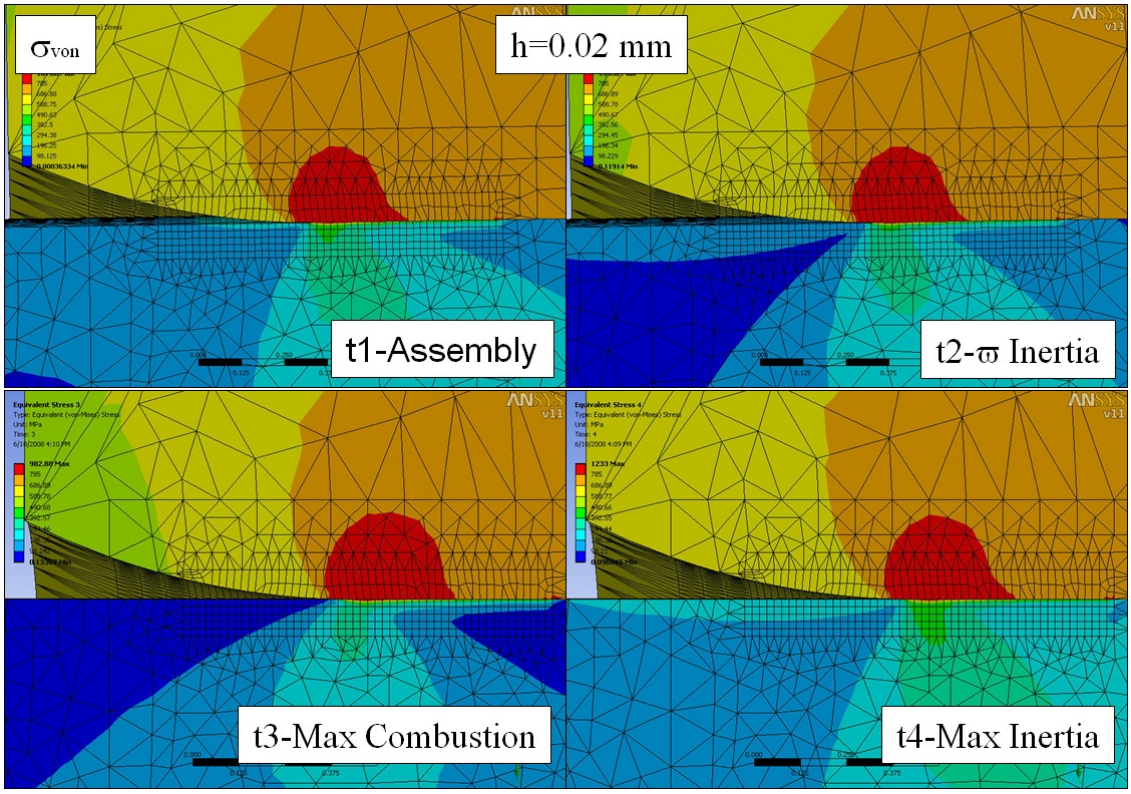

Figure 5.2.2.22 Equivalent stress (σ_{VM}) plot near the SCA at TDC, time steps 1 thru 4.

5.2.3 Variation of Local Stress Maximums At The SCA By Load Step

In sections 4.3.5 and 4.6, the effects of element size h on the assembly local stress maximum values at the SCA were determined. The values of these stress components are again presented for variation in element size across load steps 1 to 4. Figure 5.2.3.1 describes the stress components at the SCA and their locations A, B, and C.

Pin minimum σ_r at the surface (location A) is shown for load cases 1 thru 4 in Fig.5.2.3.2 for *h* equals 0.1 mm, 0.05 mm, and 0.02 mm. (Results presented in this section all contain models with these three element sizes.) The bottom side of the pin unloads assembly σ_r through load cases 2 and 3, while the top side of the pin increases in compressive σ_r. And, as expected the reciprocating mass loads that are opposite in direction for time step 4 (vs 3) in turn creates higher compressive σ_r at *A* on the bottom side of the pin. The top side of the pin unloads to near the original level (t1) for time step 4 also. Note the difference in σ_r from time 1 to 3 is much greater

on the bottom side. A good overall match in stress values exist for the changes in elements size *h.*

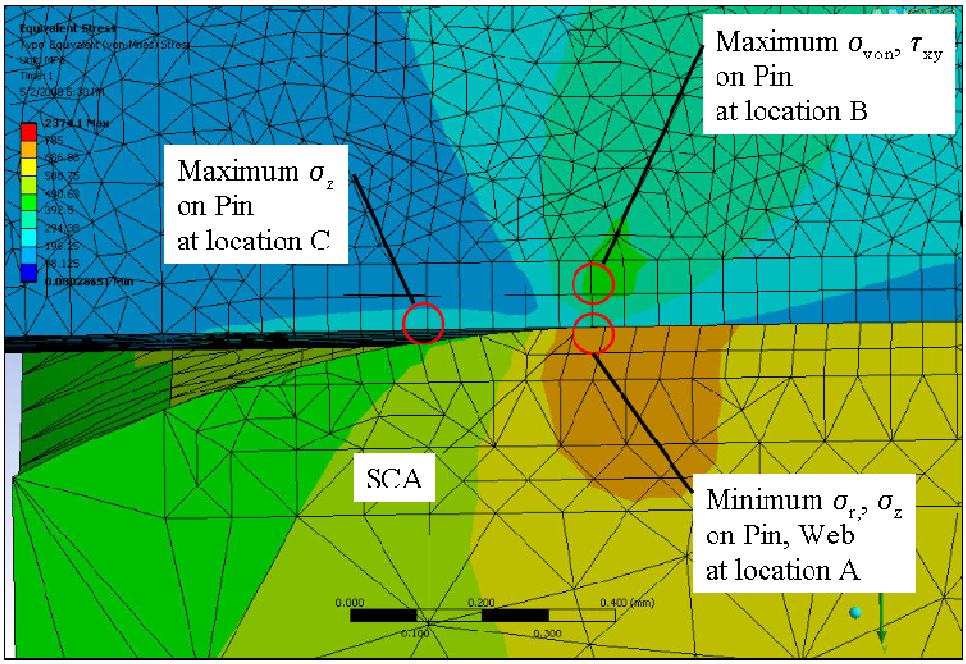

Figure 5.2.3.1 Locations of stress component of interest at the SCA.

Next minimum pin σ_θ at *A* is shown for load cases 1 thru 4 in Fig.5.2.3.3. The data here closely follows that shown for the previous radial stress plot. This is logical, since the σ_θ is driven by the radial compressive stresses and Poisson's ratio.

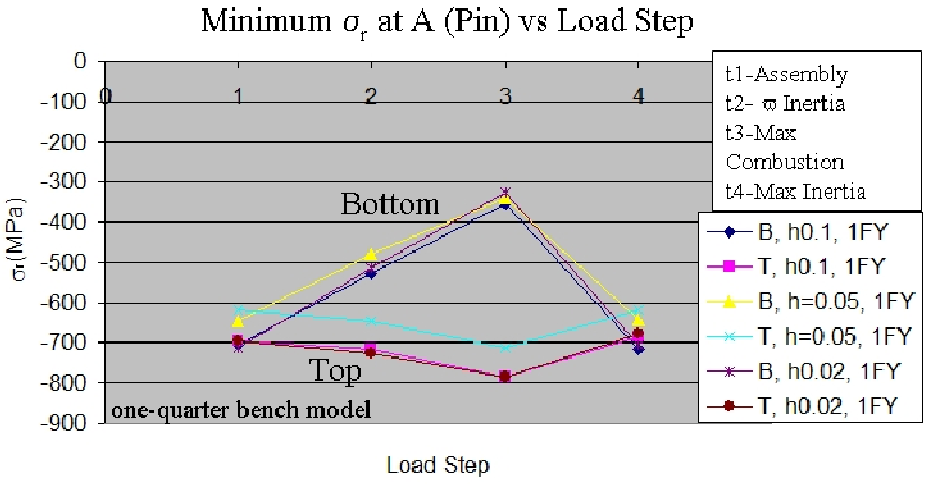

Figure 5.2.3.2 Local minimum σ_r at *A* (pin) versus load step and element size *h.*

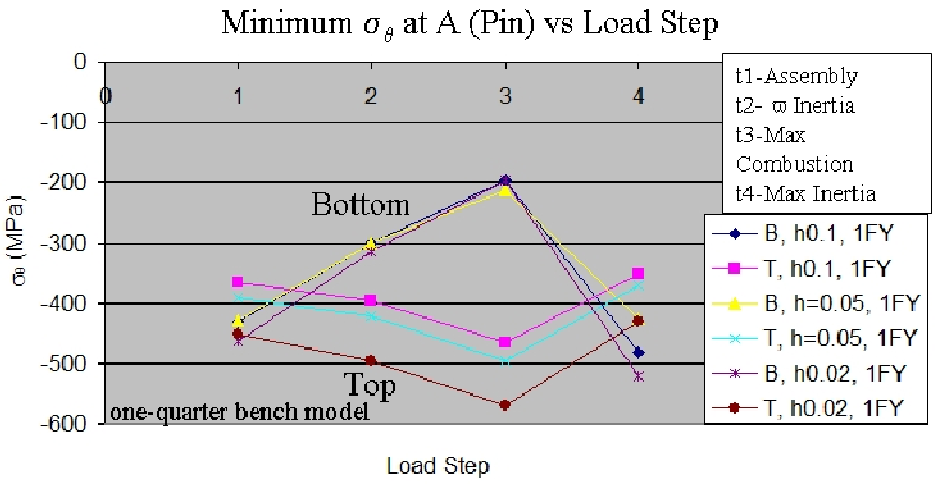

Figure 5.2.3.3 Local minimum pin σ_θ at *A* versus load step and element size *h*.

The maximum tensile σ_z at location *C* is plotted next for the top and bottom of the pin in Fig.5.2.3.4. Load step 2, assembly plus rotating inertia, actually creates the highest stress condition on the bottom of the pin. As the pin bends further and further, and the radial stress 'unloads' at *A*, the stress concentration (the kink) is removed and σ_z is lowered. The reversal of pin loading Fy for load case 4 creates a highly compressive σ_z. The top side of the pin develops increasingly compressive axial stress for load cases 2 and 3, and then reverses trend as well for load case 4. The *h* equals 0.02 mm solution calculates significantly higher axial stress for both the top and bottom, supporting the previously presented findings that suggest *h* equals 0.02 mm is required for accurate results.

Shear stress maximum values located on the pin at *B* just below the surface are shown in Fig.5.2.3.5. As described earlier, when the bottom side of the pin σ_r unloads at *A*, the τ_{rz} follows. High compressive σ_r at *A* for load case 4 drives the high τ_{rz} on the bottom of the pin. The top side stress values are less prone to change, in part this may be due to the thin flexible nature of the web material just above the pin. If the pin bends and moves a certain distances, a flexible section is less prone to unloading because it is stretched a greater amount than a relatively stiff section.

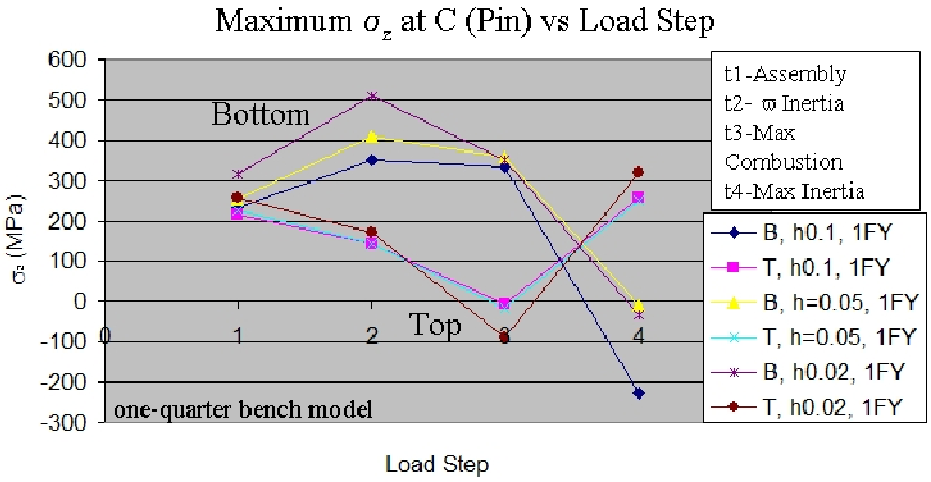

Figure 5.2.3.4 Local maximum pin σ_z at *C* versus load step and element size *h*.

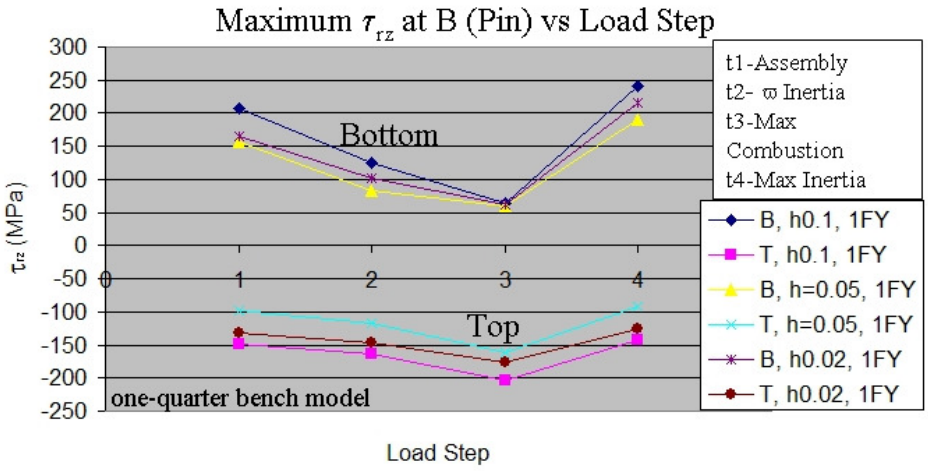

Figure 5.2.3.5 Local maximum pin τ_{rz} at *B* versus load step and element size *h*.

Figure 5.2.3.6 shows the trend in maximum σ_{VM} on the pin at *B* for load cases 1 thru 4. The σ_{VM} value is not changing significantly, only by 10 percent of the total magnitude for the bottom location.

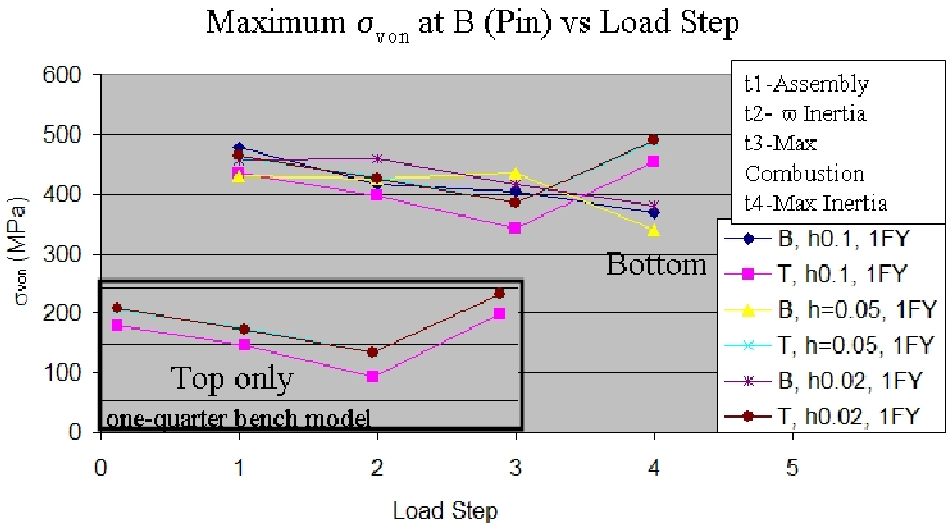

Figure 5.2.3.6 Local maximum pin σ_{VM} at *B* versus load step and element size *h*.

The web maximum σ_{VM} at *A* is shown in Fig.5.2.3.7. Since the web σ_r component significantly unloads from assembly to time step 3 (combustion), the σ_{VM} values must follow this same trend. Equivalent stresses on the top side of the pin are very constant across the load steps, and show only slight sensitivity to element size.

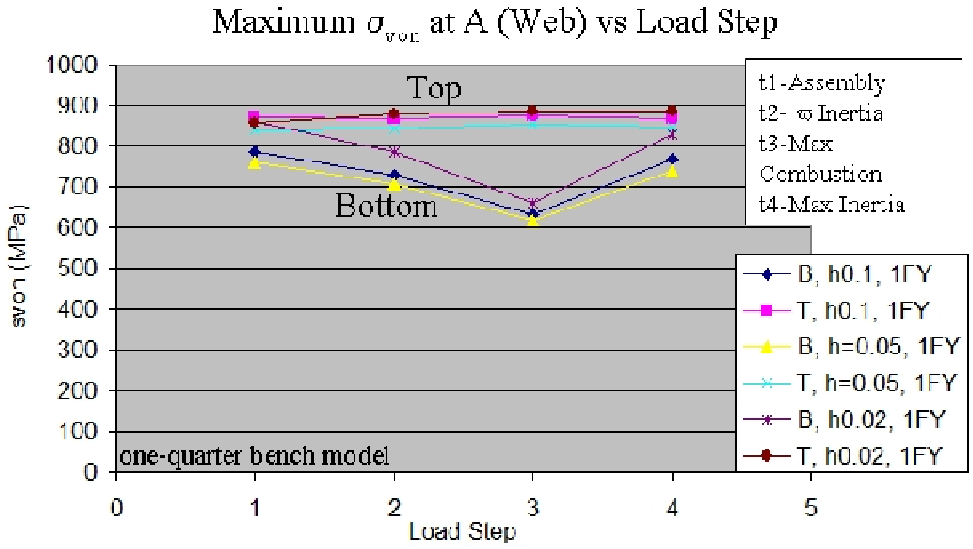

Figure 5.2.3.7 Local maximum web σ_{VM} at *A* versus load step and element size *h*.

5.2.4 Variation of Pin Axial Stress By Load Step And Element Size

Axial stress is of particular interest because of the potential negative consequences to crankshaft life. Figure 5.2.4.1 provides a close up view of the axial stress on the bottom side of the pin for the assembly load step, using *h* equals 0.02 mm. The high axial stress gradient along a line from point f to point g in Fig.5.2.4.1 is now plotted for all load steps and mesh refinement.

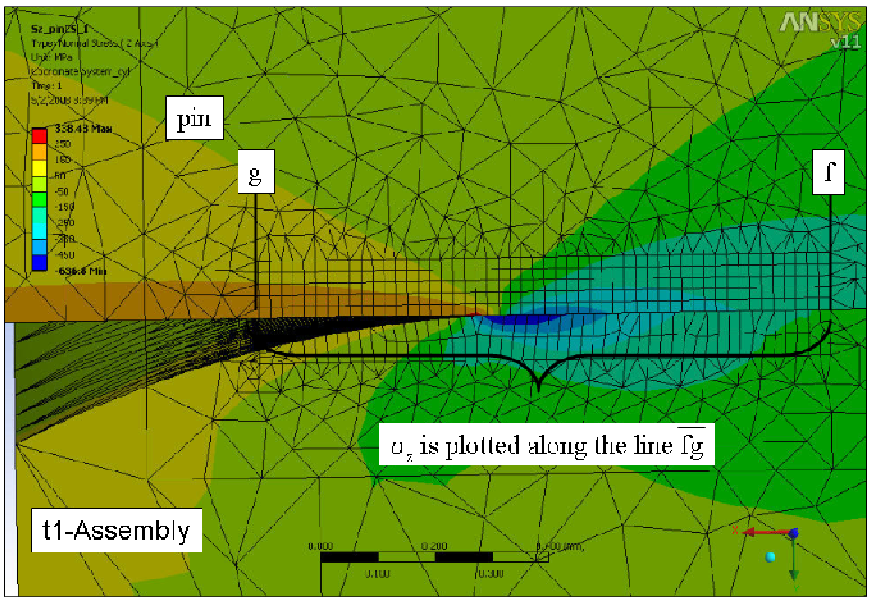

Figure 5.2.4.1 Axial stress at the SCA indicating the location of line fg of interest.

Figure 5.2.4.2 shows axial stress along line fg for load cases 1 thru 4 for the bottom side of the pin. The axial stress curve present on the bottom of the pin for LC1 (assembly) is offset in a positive direction by the pin bending (positive axial) stress of LC2. Note also that the LC3 maximum tensile stress at location *C* is lower than for LC2, even though the combustion loads are added to the spin loading. This decrease is caused by the 'radial unloading' present at the bottom side of the pin for LC3, while for LC2 the 'kink' is still present when the spin load is added to the assembly state. The tensile axial stress added during LC2 with the 'kink' in the pin present maintains the stress concentration effect of the kink, while for LC3 this multiplier is not present.

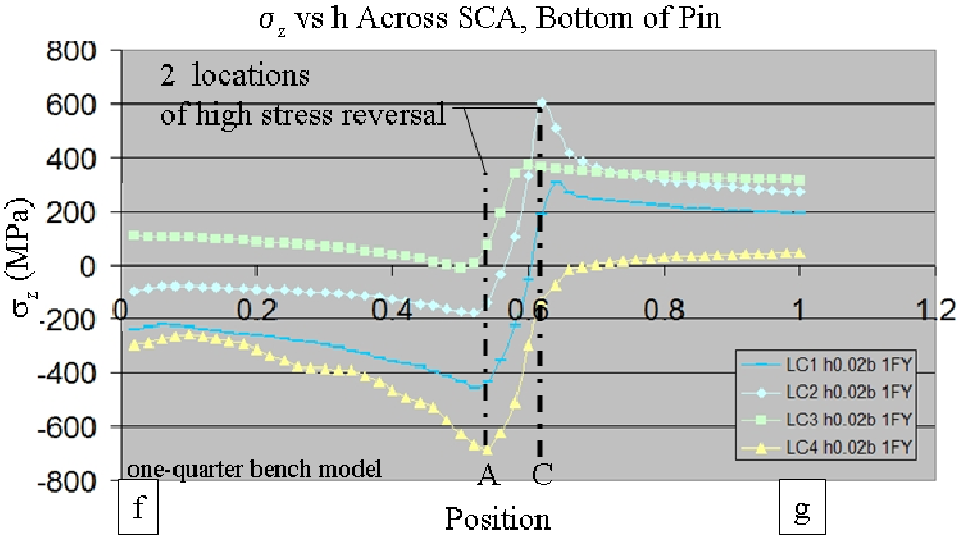

Figure 5.2.4.2 Axial stress along line fg for load cases 1 thru 4, bottom of pin.

Load step 4, which has pin loading in the opposite direction (vs load case 3), offsets the axial stress curve in the negative direction. Note that the location (*A*) of the minimum compressive axial stress and the location (*C*) of maximum tensile axial stress occur in two locations approximately 0.1 mm apart. These two locations of high stress reversal will potentially have a negative impact on crankshaft life.

An incremental pin combustion loading was evaluated to check if a larger tensile axial stress could be determined. Figure 5.2.4.2 showed that the maximum value for load case 3 was lower than that calculated for load case 2. Next Fig. 5.2.4.3 plots axial stress for 50, 100, 150, and 200 percent increments of the pin combustion load of time step 3. The axial stress values along line fg is shown to be very sensitive to this loading; the initial 50% combustion load decreases maximum σ_z, but then increasing the combustion load through to 150% increases maximum σ_z again. For the application of 200% combustion load, a further reversal occurs again in maximum σ_z, and this value begins to decrease once more. Potentially a further study is required here with smaller increments in combustion force to confirm for which load increment the maximum value is found.

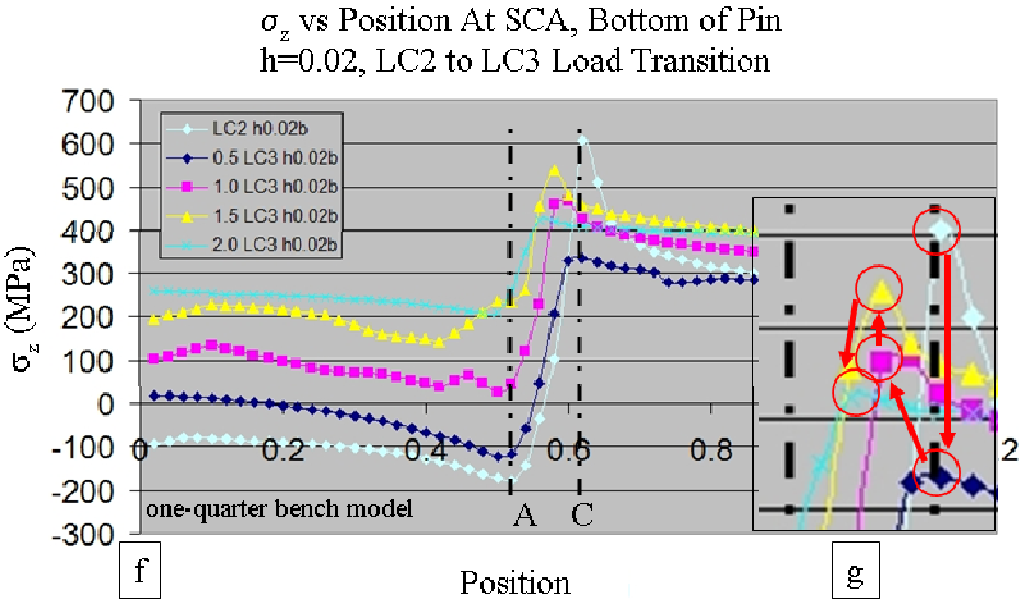

Figure 5.2.4.3 Axial stress along line fg for increments of load case 3.

Figures 5.2.4.4 thru 5.2.4.6 show the effect of mesh refinement on axial stress along line fg for time steps 2 thru 4. Mesh refinement in particular is required to accurately evaluate load case 2 and 4 (see Fig.5.2.4.4), which are shown to still have the most 'kink' present in the pin. For example, load case 3, the combustion event, is not sensitive to the mesh refinement because the pin has 'unloaded' at this point. For all load cases, increased mesh refinement is shown to produce a higher axial stress gradient; the axial stress turns from positive to negative over a shorter distance.

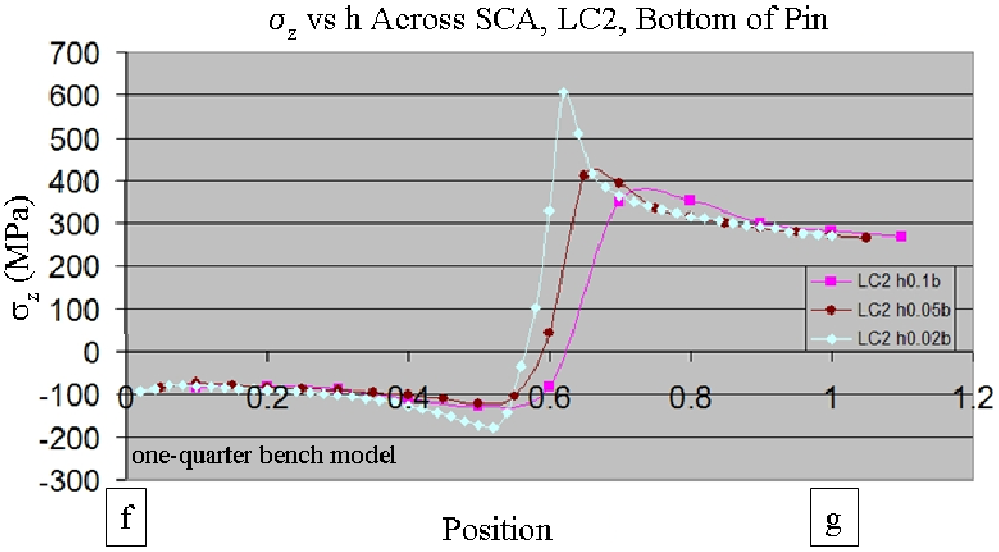

Figure 5.2.4.4 Axial stress versus *h* along line fg for load case 2, bottom of pin.

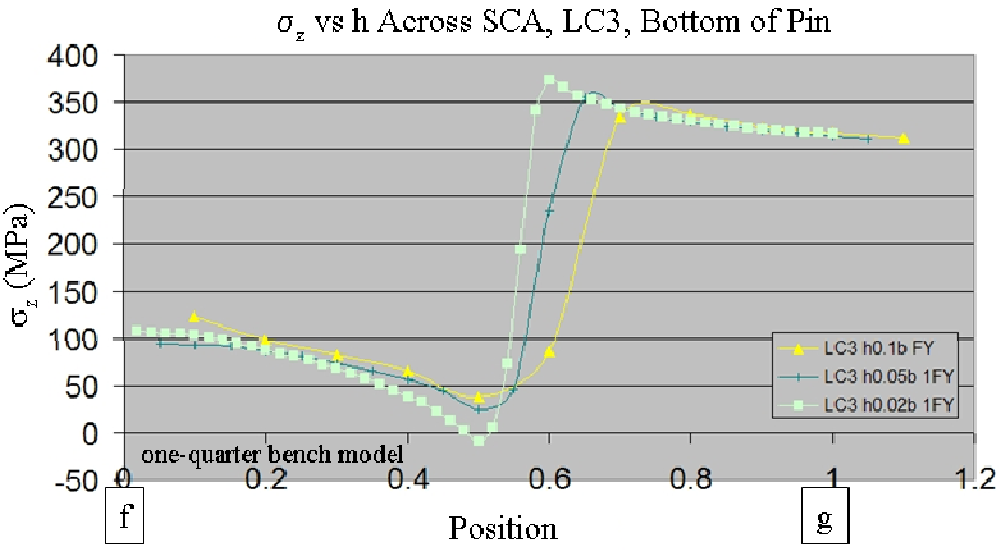

Figure 5.2.4.5 Axial stress versus *h* along line fg for load case 3, bottom of pin.

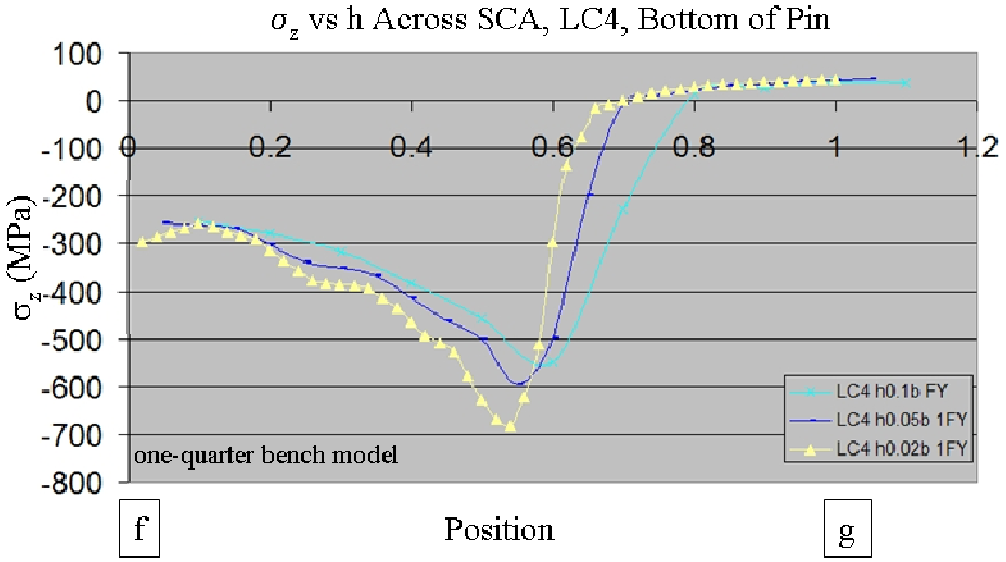

Figure 5.2.4.6 Axial stress versus *h* along line fg for load case 4, bottom of pin.

5.2.5 Cyclic Pin Axial Stress Across the SCA

Figure 5.2.4.2 indicated that locations *A* and *C* on the surface of the pin have significant axial stress reversals. Axial stress is plotted again in Fig.5.2.5.1 for the load cases 1 thru 4, with the crankshaft rotational position noted at position *A*. Position *C* is more complex to show because of the significant change in stress at top dead center (0^o, TDC) near the combustion event. At location A, the maximum tensile stress occurs during the combustion event at 17 degrees after top dead center (ATDC). At location *C*, the maximum tensile stress occurs just prior to this, during LC2, or approximately when the pin force F_y crosses towards the zero mark. During combustion, the stress is reduced slightly at *C* as the radial stress component is unloaded and the kink removed from the pin outer surface.

Finally, the axial stress σ_z is plotted against crank angle using the data in Fig. 5.2.5.2. Some interpretation of the data is required to do so; for instance pin force F_y is close to zero at the TDC position, and so the LC2 value (free spinning) is assigned. The values at *A* and *C* for the 90 ATDC and 270 ATDC are assumed to lie somewhere along the line from LC3 to LC4, which is a logical assumption given the load inputs described in Figure 5.1.7. Solutions for more crank angle positions with the full 3-D crankshaft assembly could help confirm these assumptions.

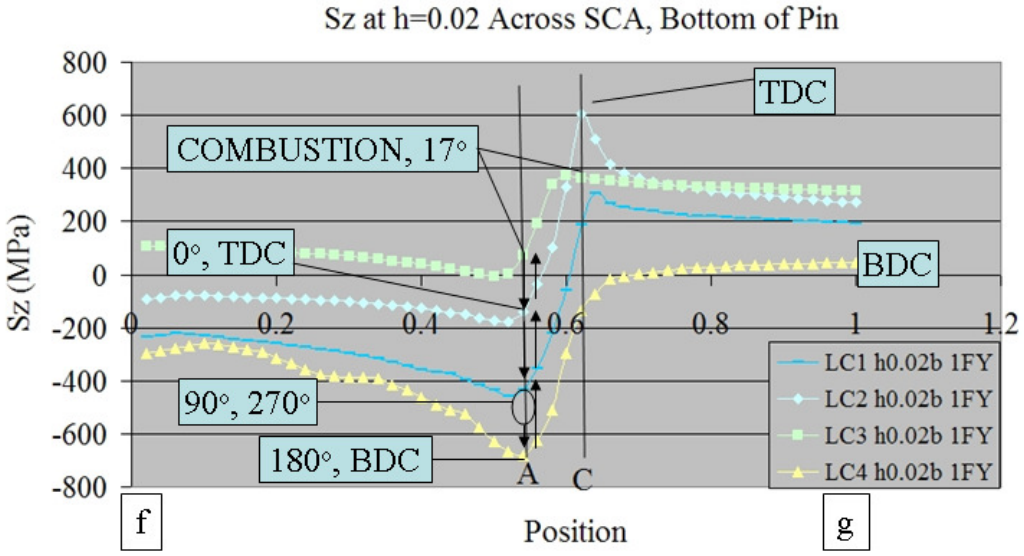

Figure 5.2.5.1 Axial stress versus engine cycle position for locations *A* and *C*.

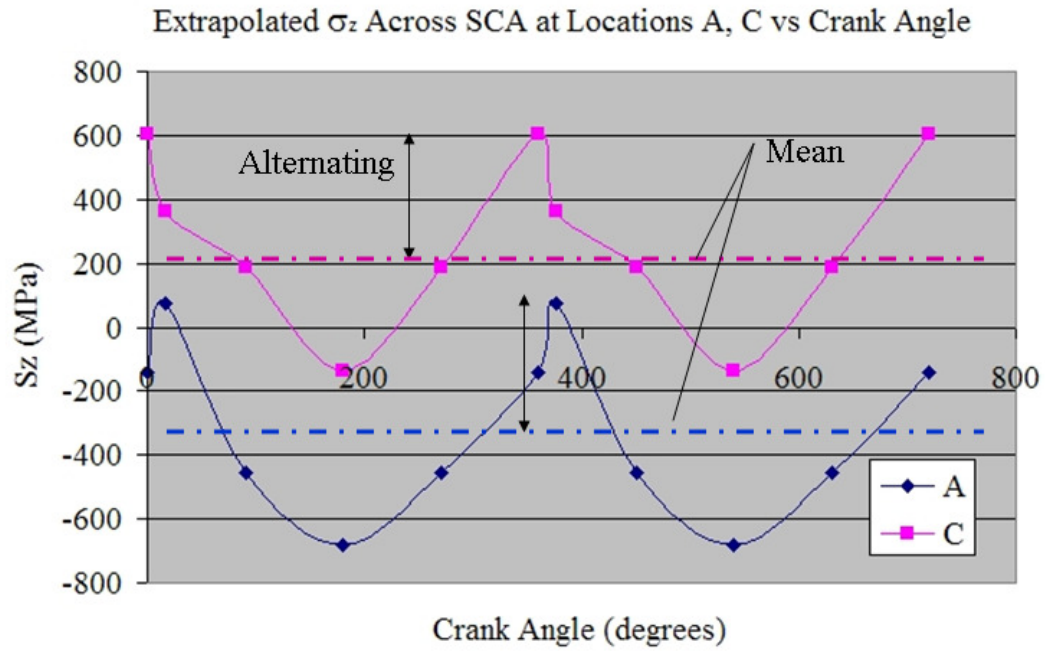

Figure 5.2.5.2 Stress σ_z at locations *A* and *C* extrapolated over 2 complete engine cycles.

5.2.6 One-quarter Model Results Summary Comments

In summary the press-fit joint under load was shown to carry the general pin bending by interface σ_r based force couples on opposite diagonal corners of the joint. So as pin bending varies under operating loads, so too does the σ_r at the interface; which in particular loads and unloads the highly compressive σ_r at the SCA. Some maximum stress components at the SCA follow the trend of the maximum σ_r as these are dependent on the compressive σ_r and Poisson's ratio.

For the range of element sizes studied, the local maximum values stress did not change significantly, but did show some sensitivity. The maximum tensile σ_z at the bottom of the pin for LC3 though is not sensitive to mesh size because the 'kink' has been reduced by the unloading as the pin bends which significantly reduces the stress gradient. The maximum tensile σ_z in particular showed sensitivity to mesh size, due to the large stress gradient at the SCA, where the σ_z changes from tensile to compressive over a 0.1mm span.

5.3 Numerical Results For the Full Geometry 3-D Crankshaft Model

5.3.1 Full Geometry 3-D Crankshaft FEA Model Details

The modeling approach used to study the full 3-D geometry is now presented. In Fig.5.3.1.1 a side view of the crankshaft is presented, and includes the naming convention given to each piece in the crankshaft construction. As has been discussed earlier, the PTO crankpin and neighboring PTO inner and outer web are of particular design interest because of the relatively higher loading in comparison to the MAG end. The PTO belt loads combine with the PTO crankpin combustion and inertial loads to create a typically higher stress field. Therefore, in this study the press-fit joint on the PTO crankpin is studied in detail, while the MAG side press-fit joint is ignored and assumed continuous for the sake of numerical efficiency.

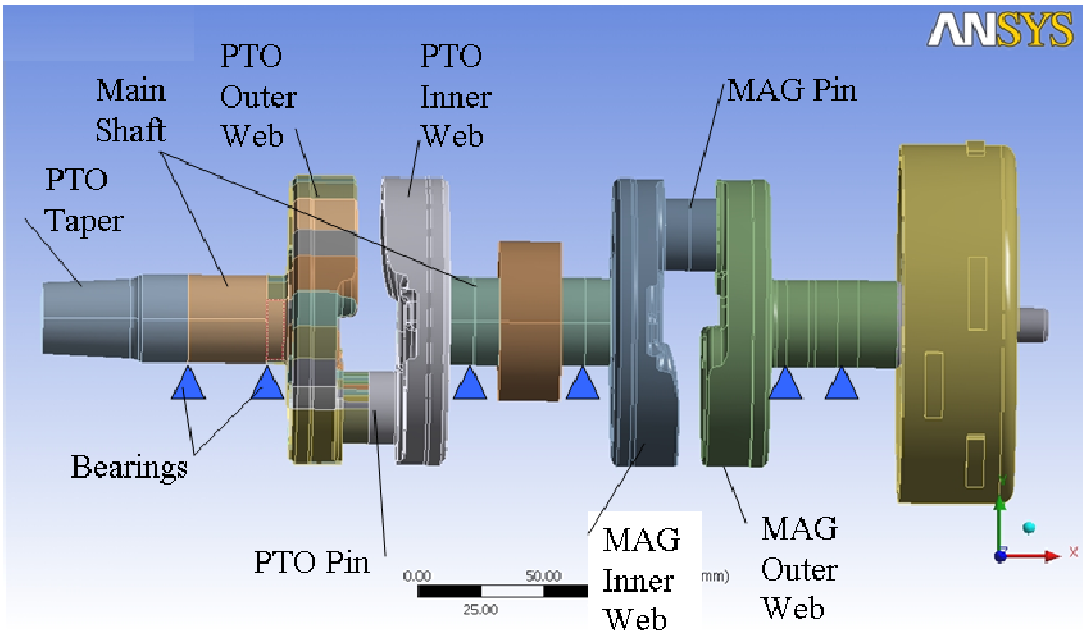

Figure 5.3.1.1 A side view of the crankshaft geometry including the naming convention.

To enhance the post-processing of the results at the PTO crankpin press-fit joint, the pin and web are split in to volume segments. Figure 5.3.1.2 shows an end view of the crankshaft, which has volume split in pie shaped wedges that center on the crankpin longitudinal axis.

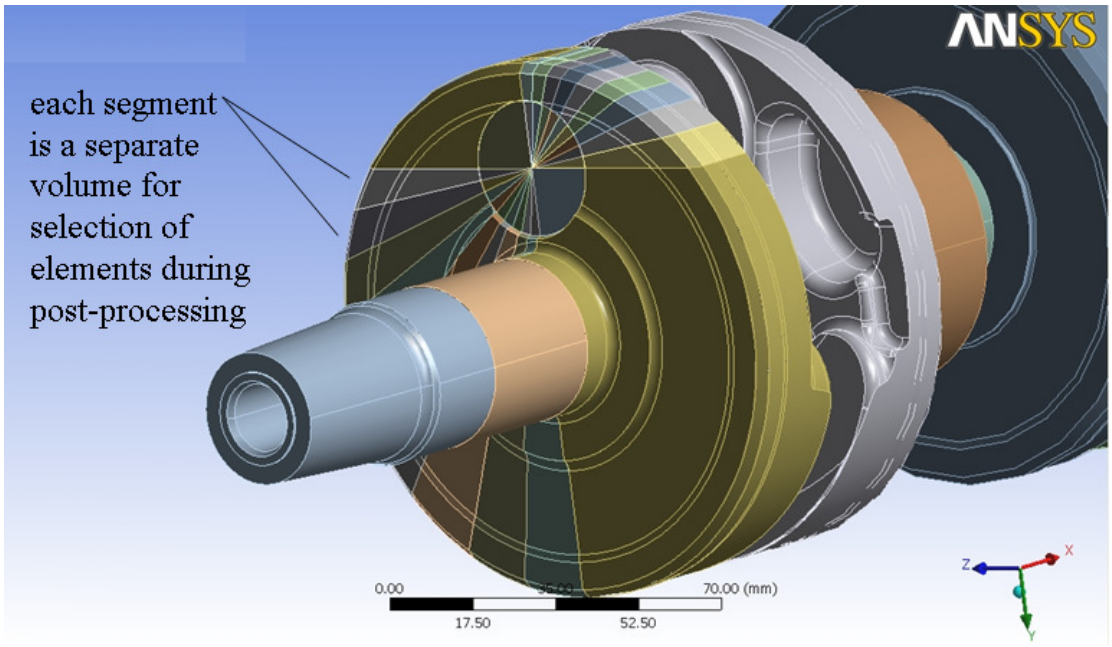

Figure 5.3.1.2 The volumetric make-up of the PTO outer web.

Figure 5.3.1.3 shows the crankpin only, which has a partial selection set of the wedge volumes for each of the two views. Note that the 10^{o} pie shaped segments include the thin profile rectangular cylinder at the SCA, on both the pin and web. This thin cylindrical volume is used for good control of the mesh at the SCA, an approached that is demonstrated in the other 3-D models.

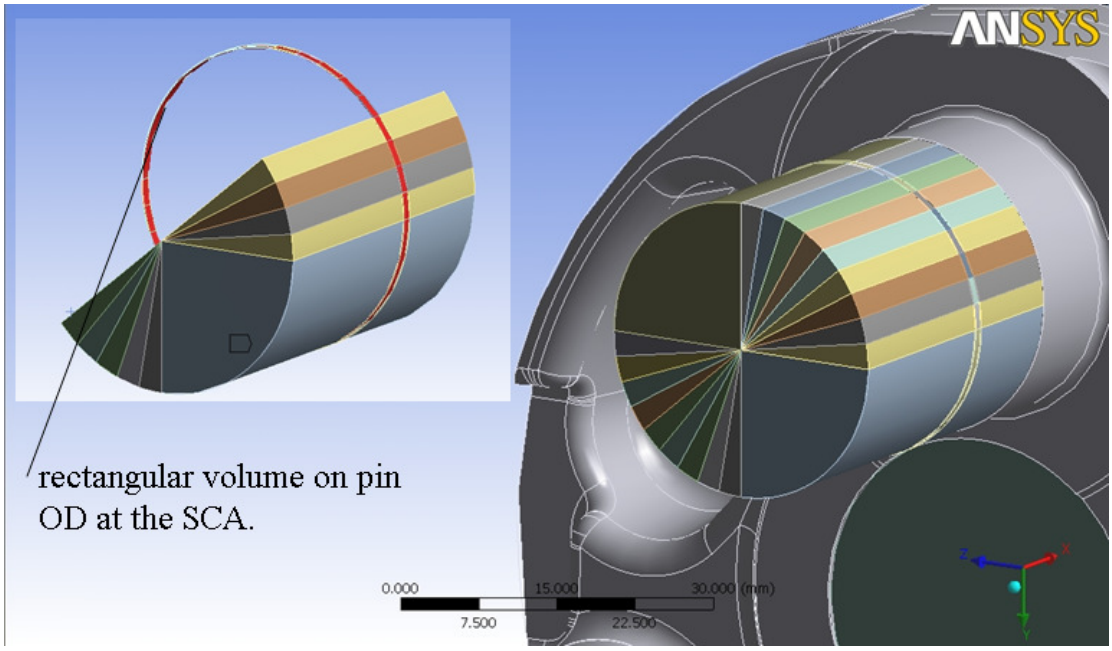

Figure 5.3.1.3 The pin is cut into pie shaped segments for element selection during post-processing.

Note that Appendix B contains further details of the modifications of the full 3-D crankshaft Geometry.

The geometry approach presented above was key to creating an efficient mesh. Figure 5.3.1.4 shows the solid element FEM mesh for the full crankshaft assembly. Overall the mesh used is described as coarse except for at the SCA cylindrical volume, as the focus of the model is good accuracy in the stress field in the vicinity of the SCA.

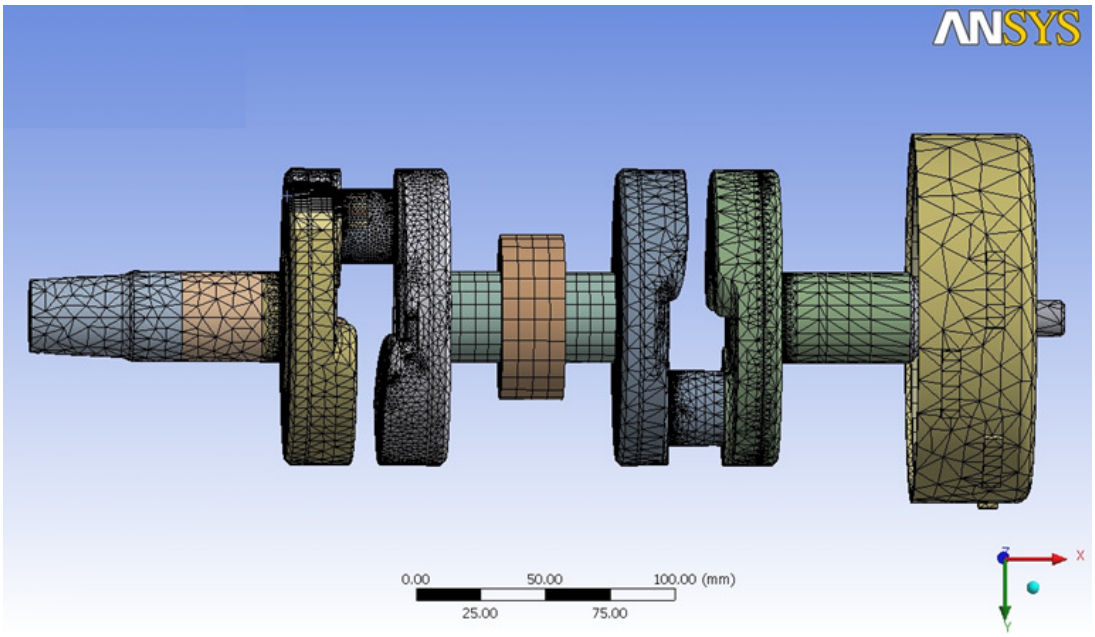

Figure 5.3.1.4 The FEM solid element mesh of the crankshaft assembly.

The pin mesh refinement at the SCA is shown in Fig. 5.1.4.5; the high refinement in the cylindrical volume at the SCA transitions to a relatively coarse mesh in the neighboring segments of the pin. Notice the different colored pie shaped sets of elements present for post-processing. Also note that the thin cylindrical volume at the SCA contains only a brick element based mesh. The element size is controlled in both thin cylinder volumes on the pin OD and the web ID so that stress sensitivity studies may be mapped relative to element size.

The solid mesh is a mixture of 20 node brick and 10 node tetrahedral quadratic elements, which require prism and wedge elements in the transition from a brick shape to tetrahedral shape (see bottom right corner of Fig.5.1.4.5).

The PTO outer web meshing approach is shown in Fig.5.4.1.6; again showing a color coded element selection set comprised of pie shaped wedges centering on the crankpin axis. Further mesh details are also contained in Appendix A.5.3.1.

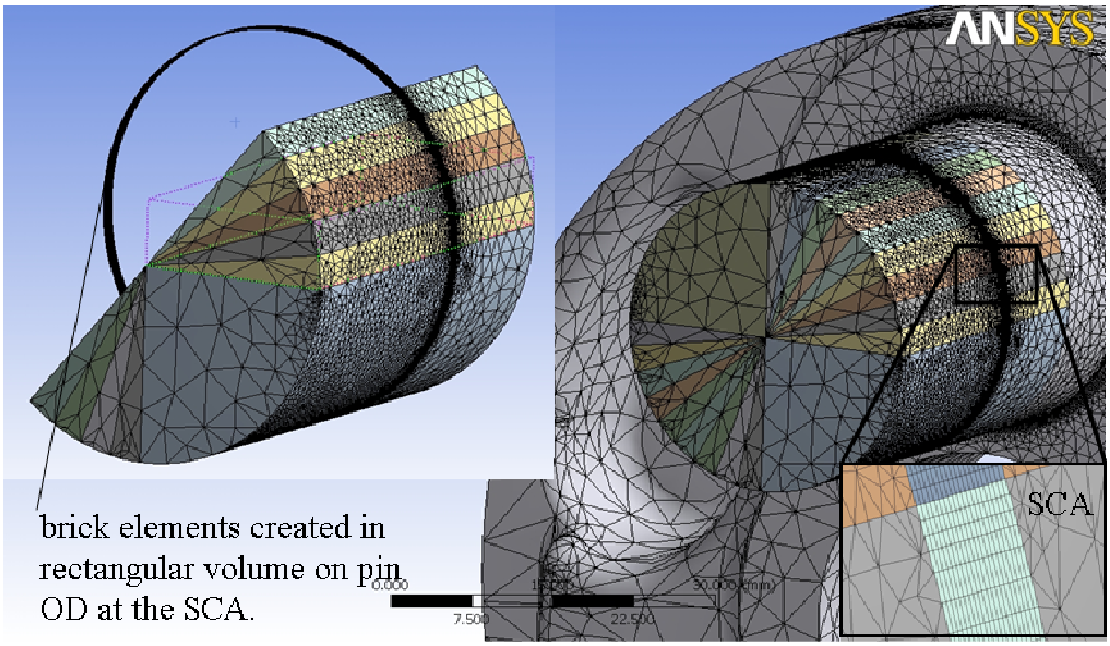

Figure 5.3.1.5 The PTO outer pin mesh showing the details of the mesh at the SCA.

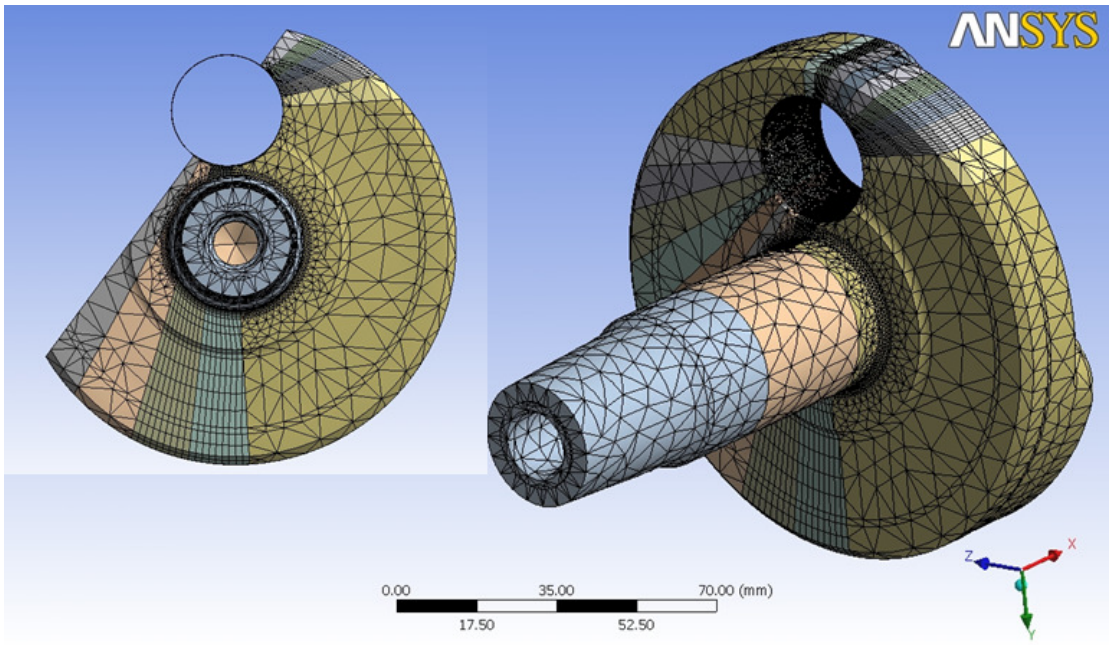

Figure 5.3.1.6 The Wedge segmented mesh for the PTO outer web.

The load inputs and boundary conditions for the full 3-D crankshaft FEA model are explained well in Fig.5.3.1.7. At each bearing location, the crankshaft FE model is supported by the case using a linear spring with a directional stiffness that is equal to the case stiffness. These stiffness values are based on historical values which have provide good strain and modal correlation with

experimental data. The load inputs described in section 5.1 apply to this model, and are captured in Fig. 5.3.1.7. The torque produced by the crankshaft during the combustion events is transferred out the PTO end of the crankshaft; and a rot x equals 0 boundary condition is used on a torsional spring there to constrain the crankshaft rotation.

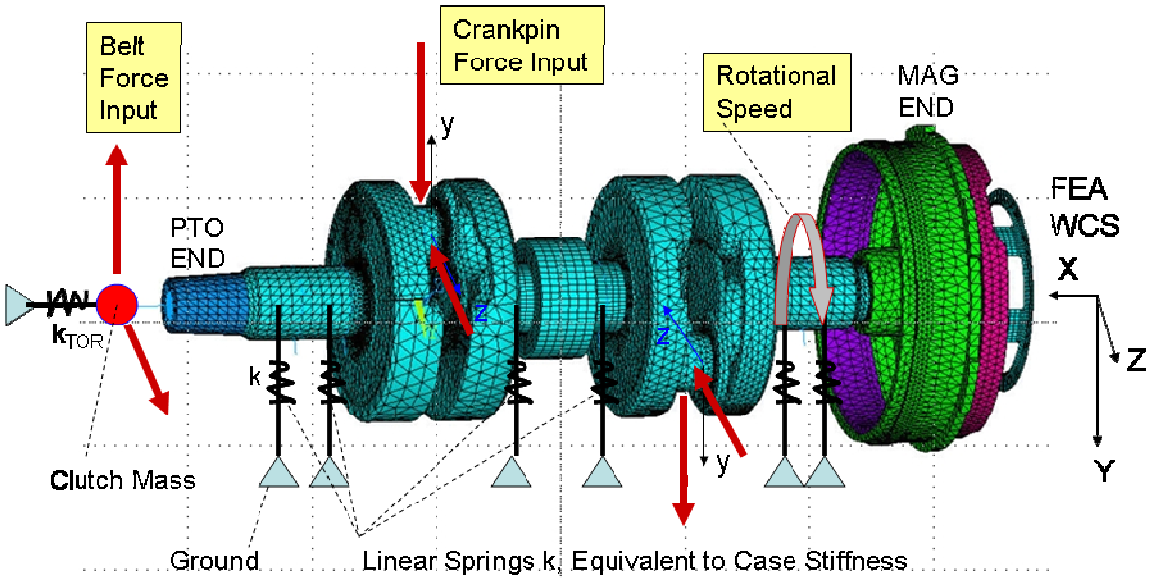

Figure 5.3.1.7 The FEM model, including load inputs and boundary conditions.

The load cases studied with the full 3-D FEA model are given in Table 5.3.1, which are created with a MBD model as described in section 5.1. Load step 1 is the solution for the press-fit assembly, and the same 'typical' radial interference is used in this model as has been used throughout the research. Load step 2 studies the effect of applying a rotational inertia (8,000 rpm) on the crankshaft. Load step 3 examines the crankshaft structure for the application of maximum combustion loads on the PTO crankpin, and finally load step 4 examines the crankshaft for a maximum reciprocating loads on the PTO crankpin. The rationalization for the selection of load case 3 and 4 are provided in section 5.1, which are based on engineering logic and experience.

Table.5.3.1 Full 3-D Crankshaft Model Operating Load Cases

Time Step	Assembly	Rotational Speed, v (rad/s)	Fy Pin (PTO) (N)	Fz Pin (PTO) (N)	Fy Pin (MAG) (N)	Fz Pin (MAG) (N)	Fy Belt (N)	Fz Belt (N)
1	Yes	-	-	-	-	-	-	-
2	Yes	837.75	-	-	-	-	-	-
3	Yes	837.75	-16740.0	8053.0	15314.0	2735.0	1389.0	-7168.0
4	Yes	837.75	15008.0	-2857.0	-16217.0	-8333.0	-1449.0	7156.0

5.3.2 Full Geometry 3-D Crankshaft FEA Assembly Results

First the assembly behavior is examined for the full 3-D model using a typical radial interference, which is time step 1. The resultant displacement plot in Fig.5.3.2.1 shows that virtually all the deflection is on the PTO outer web, as all other press-fit joints are ignored in this study. The interference is created between the web and pin by applying a uniform temperature change to the model, and setting all components to have a very low coefficient of thermal expansion except the PTO outer web. The temperature change creates the desired radial interference between the pin and web through thermal contraction of the PTO outer web. The displacements shown in Fig.5.3.2.1 are dominated by the thermal distortion.

Figure 5.3.2.2 plots displacement in the y-direction, for which the magnitudes are reduced significantly in comparison to Fig.5.3.2. 1. The press-fit assembly creates a non-parallel tilt on the PTO outer web main shaft, as the web stiffness is not constant along the axial length of the pin. As a start, the web has mass reduction pockets near the pin bore for the purpose of crankshaft balance. Also the pin stiffness is higher on the inner side of the joint, which stretches the web more, creating additional the misalignment. Since the pin terminates at the end of the joint, it is more easily compressed than on the other end of the joint where the pin continues through the web.

Since the press-fit joint behavior and assembly stresses have been covered in great detail in chapter 4, further study of the full 3-D model will not be presented for this time step. Additional FEM data is presented in Appendix C, where it is shown that the 3-D model and one-quarter model provide very similar results for the assembly problem.

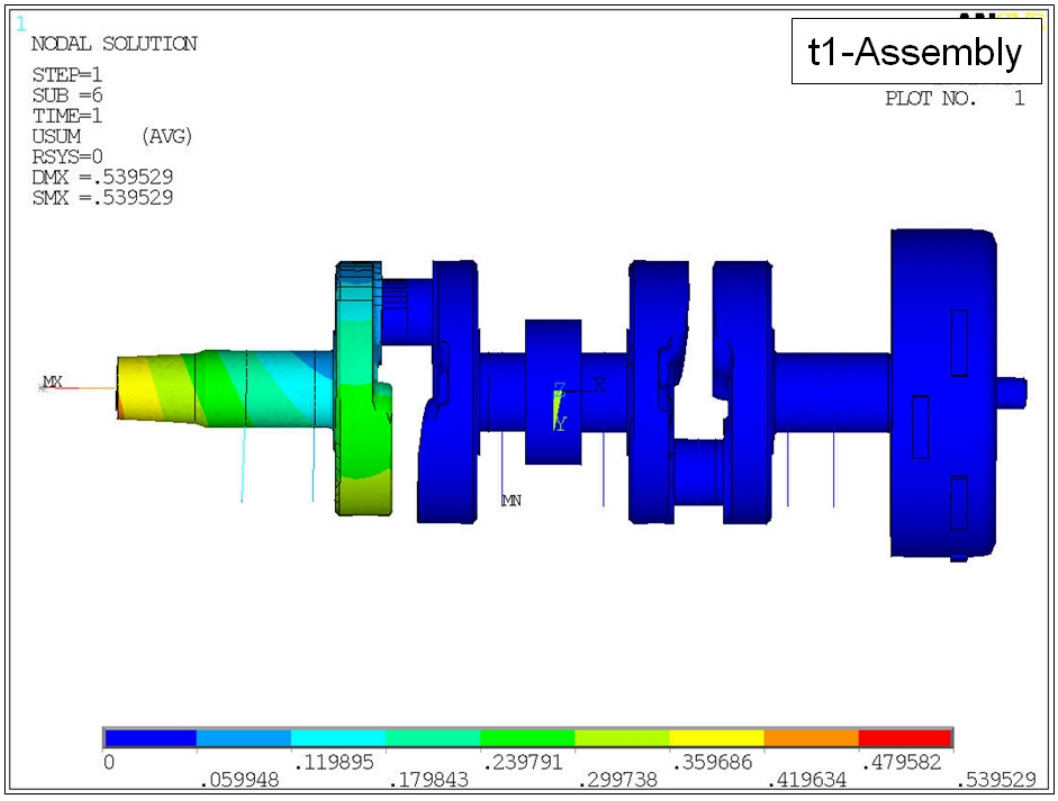

Figure 5.3.2.1 Resultant displacement plot for LC1 assembly.

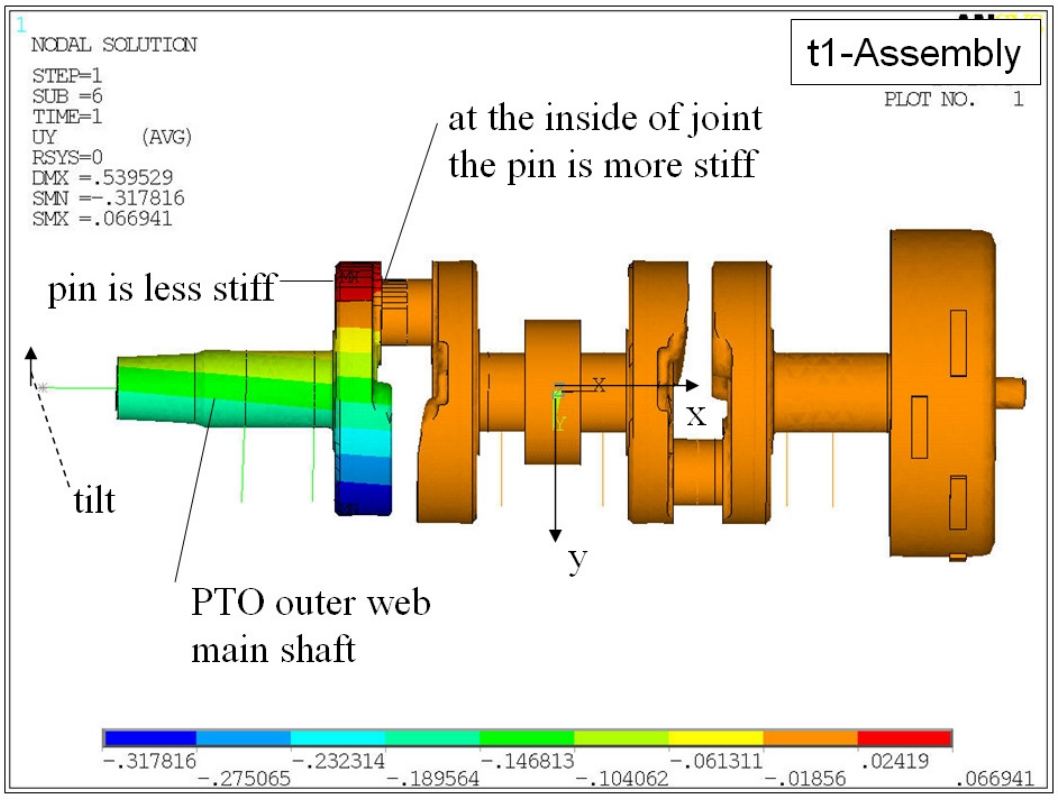

Figure 5.3.2.2 Y-direction displacement plot for LC1 assembly.

5.3.3 Full Geometry 3-D Crankshaft FEA Rotational Inertial Results

Next, results for time step 2, which is the rotational inertia load case, are examined for the full 3-D model. The solution for time step 2 also includes the press-fit assembly interaction, which is solved for in the previous time step.

The resultant displacement plot in Fig.5.3.3.1 shows that the most significant deflection is still on the PTO outer web. The induced temperature change used in time step 1 to create the desired radial interference created high x-direction displacement of the PTO outer web. This displacement dominates the plot, which is a negative aspect of using the thermally based interference, since the results are less useful to the analyst.

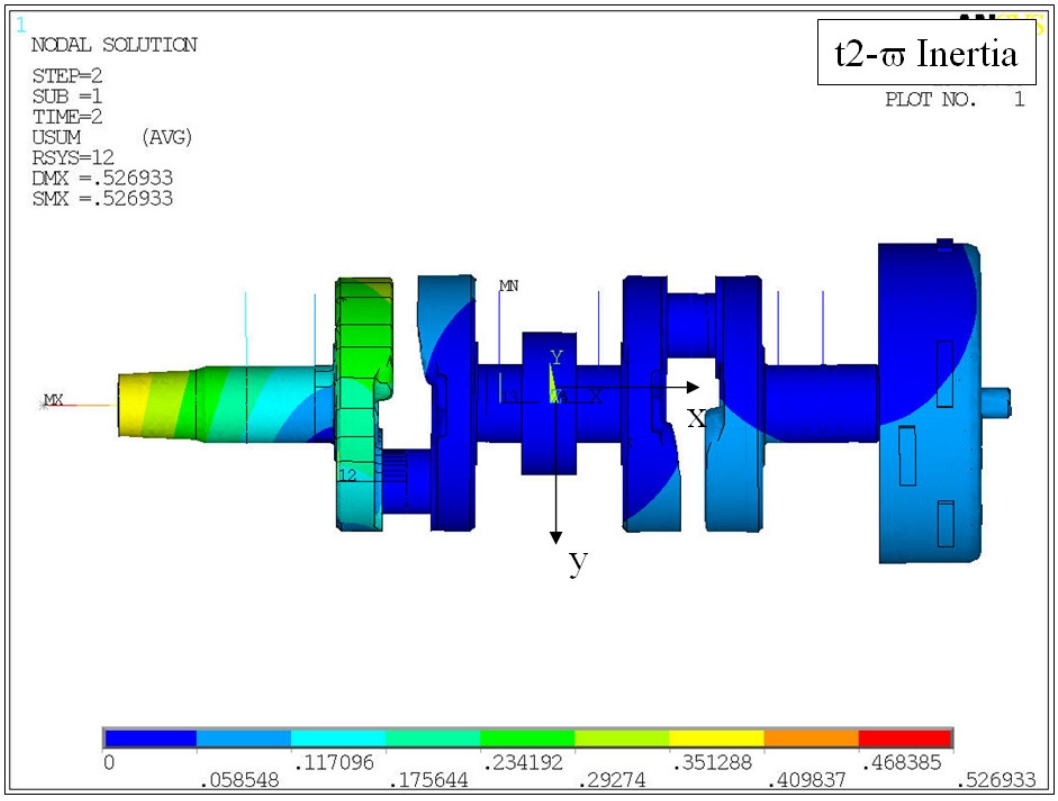

Figure 5.3.3.1 Resultant displacement plot for time step 2.

Equivalent stress is provided for time step 2 for the full crankshaft model in Fig.5.3.3.2. The crankshaft stresses are shown with a lower stress scale (0 to 300 MPa) detailing the local maximum equivalent stress values at the critical fillet radii on the design. These local maximum stress values are much lower than maximum values at the SCA. It is useful to track the local

stress maximums at various locations on the crankshaft, away from the press-fit, for comparison to other models and modeling methods to ensure consistency.

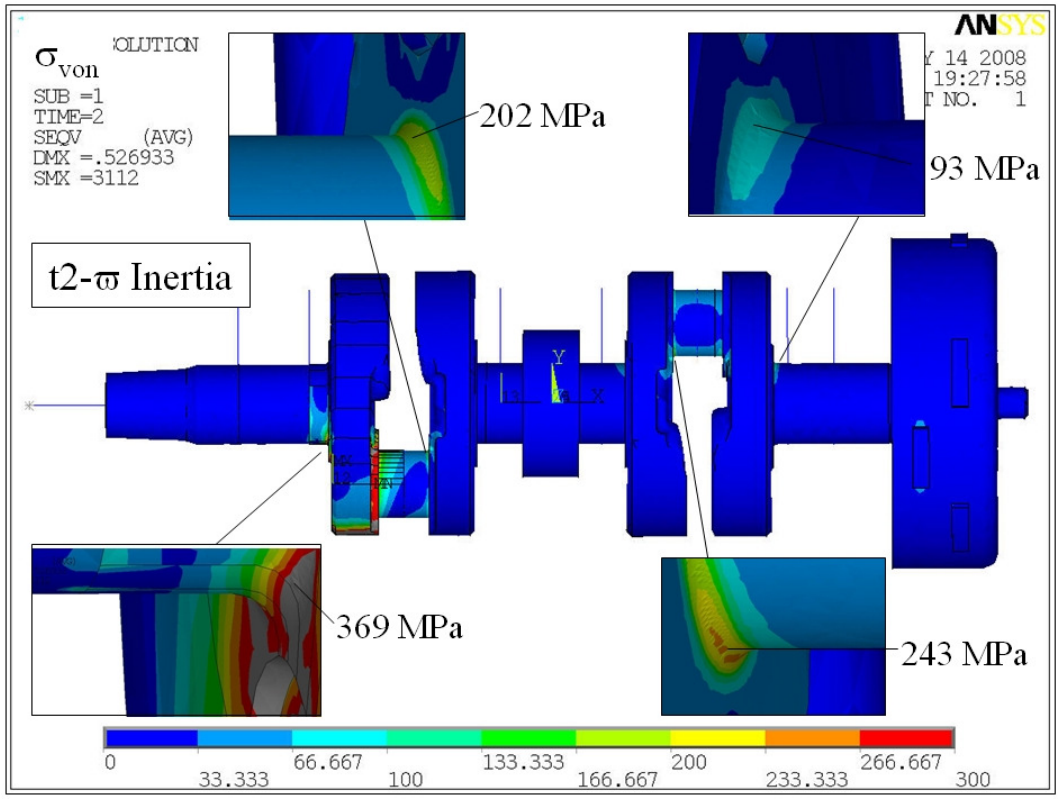

Figure 5.3.3.2 Local equivalent stress maximums on the crankshaft, time step 2.

The behavior of the one-quarter model and the full crankshaft model are very similar for load step 2 because of the symmetrical nature of the geometry and loading combined. Stress magnitudes are very similar also when comparing the two models. Therefore, supporting displacement and stress plots for the rotational inertia loading on the full crankshaft model is contained in Appendix D.

5.3.4 Full Geometry 3-D Crankshaft Time Step 3 FEM Results

Numerical data for the full 3-D crankshaft model is now presented for time step 3, which is a maximum combustion load on the PTO crankpin. The solution for LC3 includes both the press-fit assembly (LC1) and the rotational inertia loads (LC2) which are solved for in the previous time steps.

A front view of the resultant displacement plot for the crankshaft assembly is given in Fig.5.3.4.1, while a top view is shown in Fig.5.3.4.2. The displacement plots indicate that the belt force on the PTO end has a significant influence on the overall structural distortion. The main shaft on the PTO end of the crankshaft (beyond the PTO outer web) is shown to deform under the belt and combustion loads. Note that a significant portion of the displacement calculated is still due to the thermal contraction of the PTO outer web in time step 1.

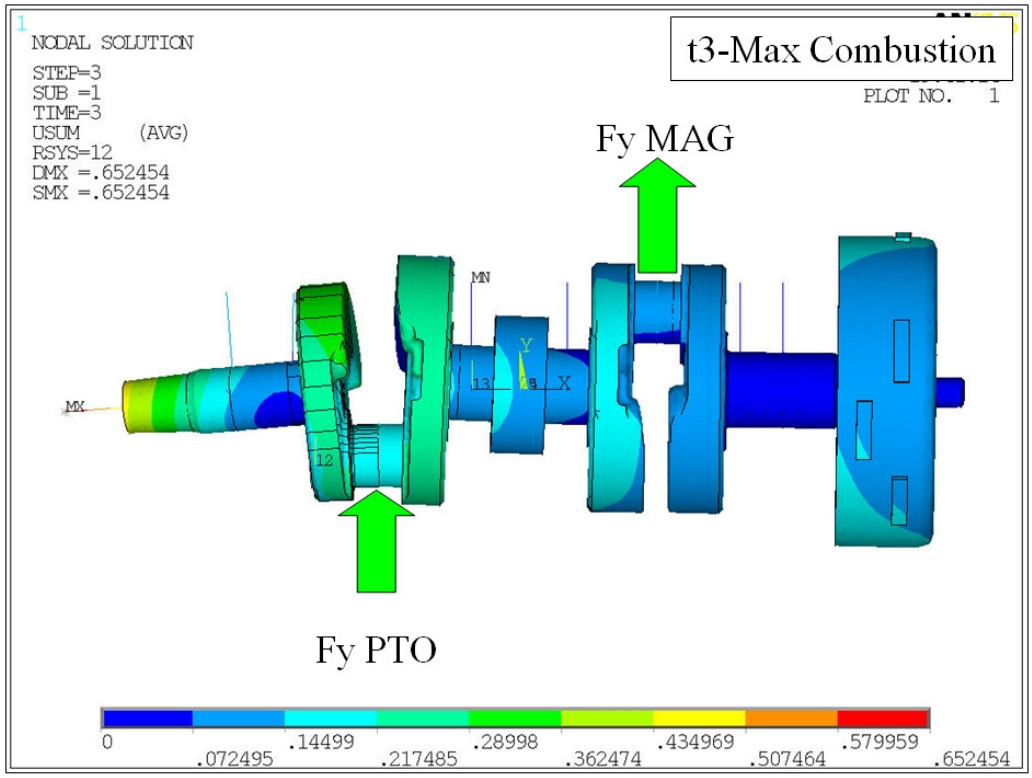

Figure 5.3.4.1 Resultant displacement plot for time step 3.

A Von Mises equivalent stress plot is shown next in Fig. 5.3.4.3 for time step 3, providing local maximum equivalent stress values at critical fillet radii on the crankshaft. The local maximums are tracked to ensure consistency among the different meshing and modeling approaches. There is a significant rise in stresses at the PTO crankpin fillet for time step 3 vs 2, due to presence of the combustion loading.

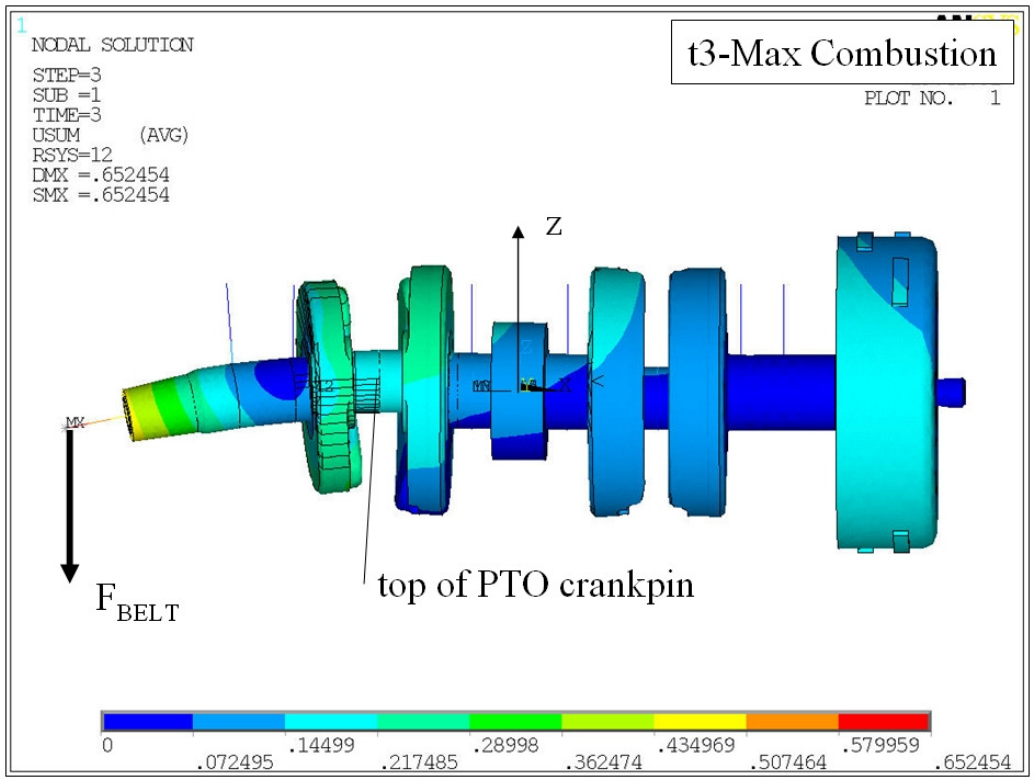

Figure 5.3.4.2 Top view of resultant displacement plot for time step 3.

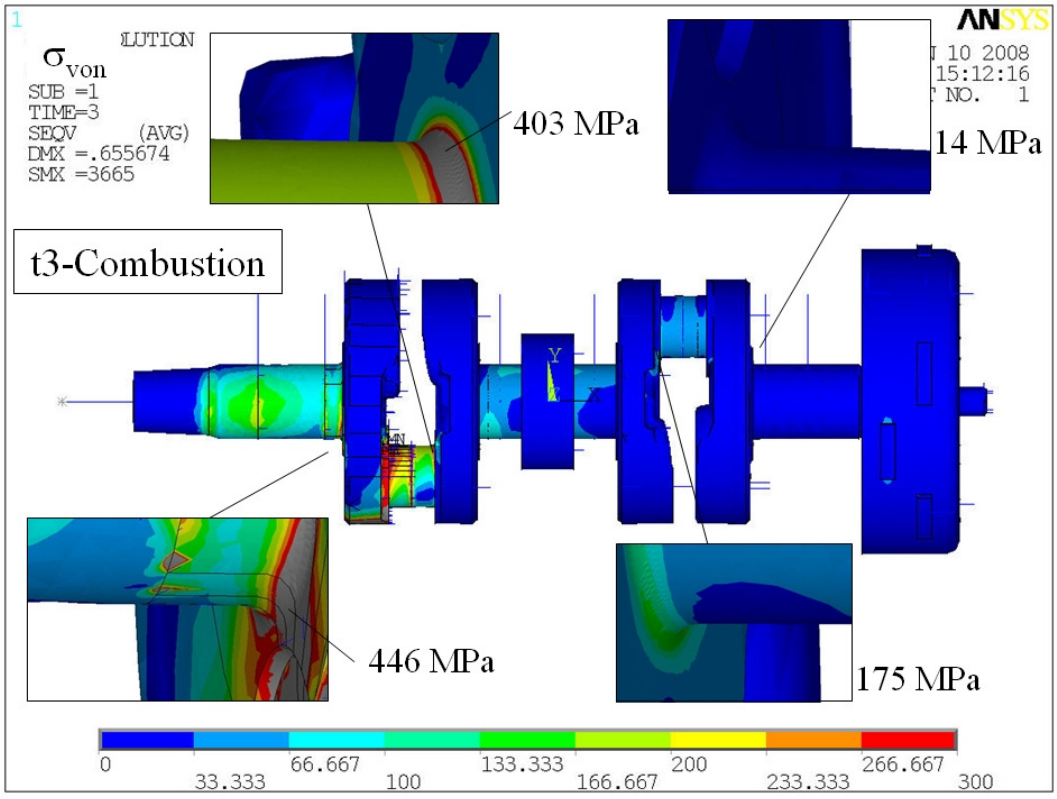

Figure 5.3.4.3 Local equivalent stress maximums on the crankshaft, time step 3.

For LC2 the equivalent stress on the PTO outer web was dominated by the press-fit assembly stress. However for LC3 the stress field starts to show sensitivity to the crankpin combustion and belt loads. The LC3 equivalent stress plot in Figure 5.3.4.4 and 5.3.4.5 shows that the belt force creates stress patterns typical of bending on the main shaft next to the PTO taper. The stress fringe patterns on the crankpin are shown to be affected by the combined crankpin and belt loads.

Engineering logic suggests the location of maximum stress on the PTO crankpin, shown in Fig.5.3.4.5 is potentially a location of high fatigue damage. Therefore, stress fields on the pin and the web are studied in detail on cutting plane A which passes through this maximum location (see Fig. 5.3.4.6). Cutting plane A also passes through the crankpin center axis. The cutting plane is used simply to describe the elemental selection set present for post-processing the data. In section 5.3.1 it was shown how the PTO crankpin and outer web were split into pie shaped volumes for improved post-processing. The viewing of results on cutting plane A uses the pie shaped volumes for selection.

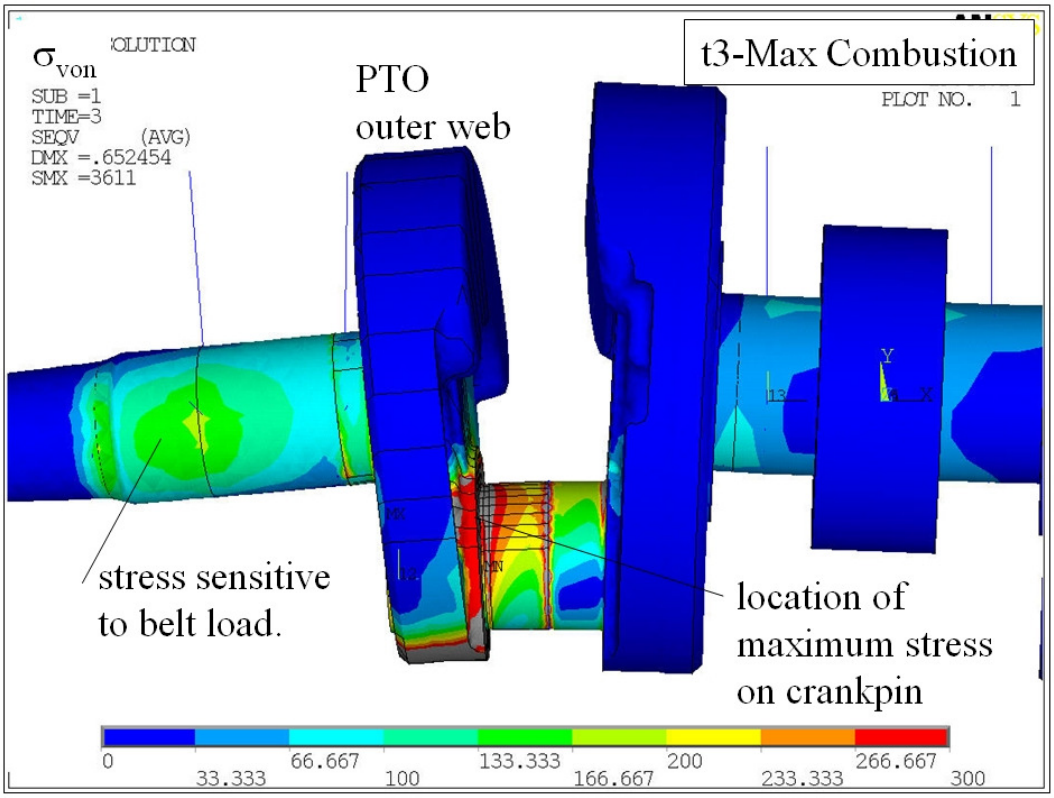

Figure 5.3.4.4 Front view of PTO end equivalent stress plot for time step 3.

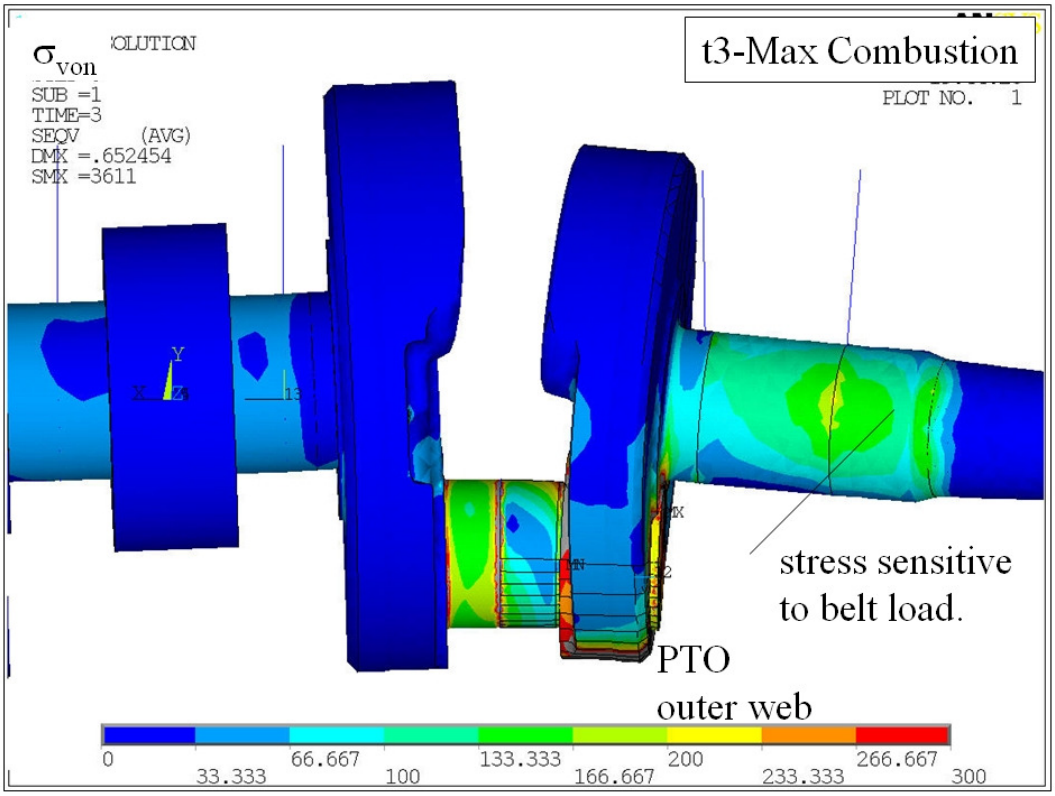

Figure 5.3.4.5 Rear view of PTO end equivalent stress plot for time step 3.

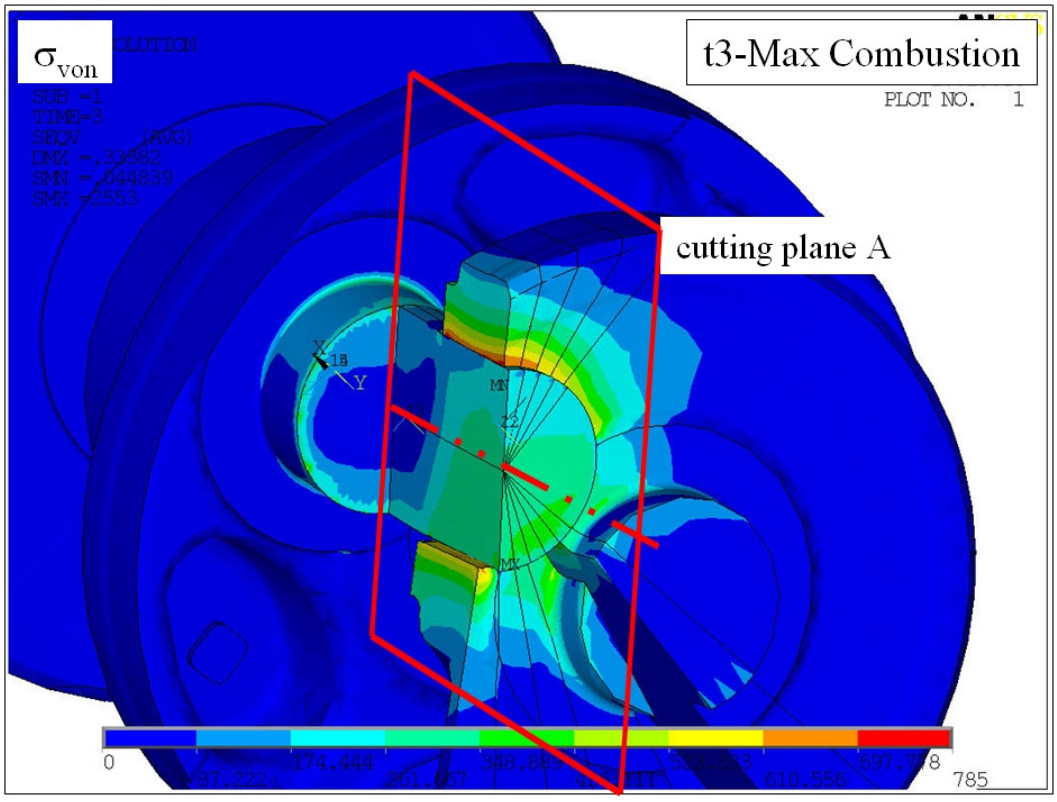

Figure 5.3.4.6 The plot of σ_{VM} across cutting plane A for time step 3.

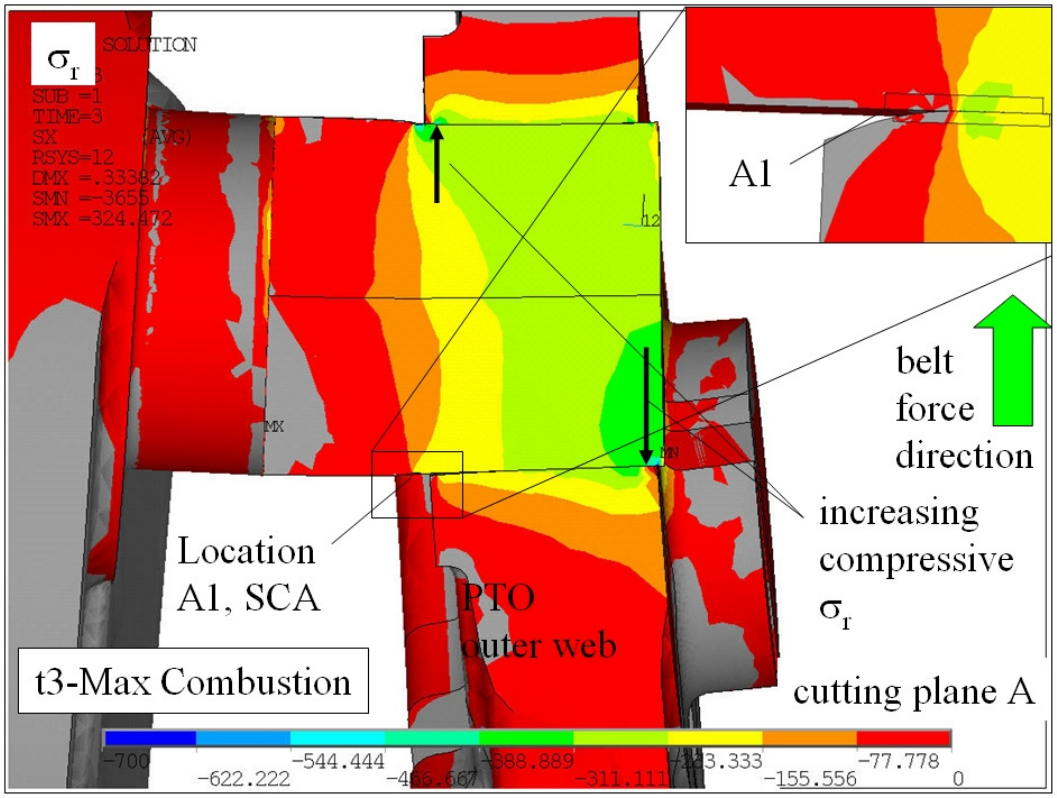

Figure 5.3.4.7 The plot of σ_r across cutting plane A for time step 3.

Now a set of plots viewing the stress field on cutting plane A will be examined. Figure 5.3.4.7 plots σ_r on cutting plane A, and shows the increasing σ_r on diagonal corners oriented in a manner to carry the pin bending loads due to the combustion and belt forces. Location A1 (see Fig. 5.3.4.7) is the location of maximum σ_{VM} on the pin as shown in 5.3.4.5, at which the σ_r appears to reduce in comparison to the values there for LC2. The joint carries the load through σ_r and a 'force couple' in a similar fashion to that demonstrated with the one-quarter bench model.

For LC2, the rotational inertia loading on the counterweights created tensile σ_z on the bottom of the pin. Figure 5.3.4.8 plots σ_z on cutting plane A, and the tensile σ_z in LC3 is shown in increase in magnitude on the bottom fibers of the pin for this section. Both the combustion load and the belt force combine to bend the crankpin and add to the tensile stresses present. Note that the stress plots use identical scaling throughout all load cases to permit easy comparison. The σ_r unloading shown for LC3 in Fig.5.3.4.7 coincides with the increased tensile axial stress on the

pin, as was demonstrated for the one-quarter bench test model. Location A1 is the maximum tensile axial stress on the pin for LC3.

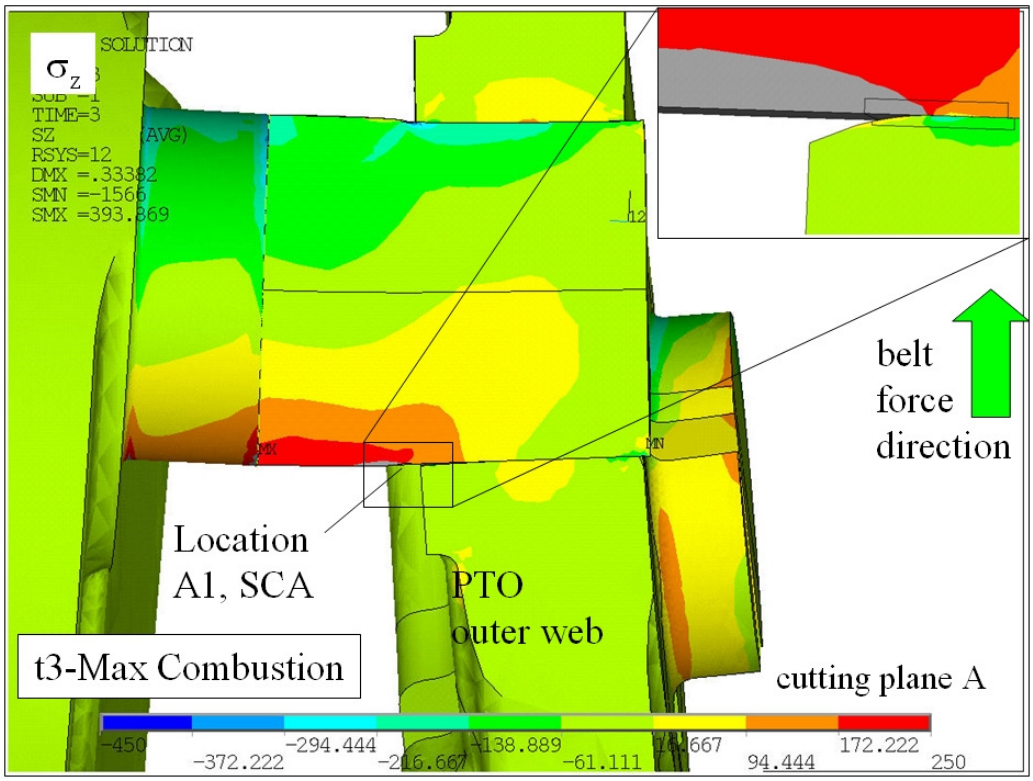

Figure 5.3.4.8 The plot of σ_z across cutting plane A for time step 3.

Note that the hoop stress plot for cutting plane A is not provided; although the web stress is dominated by the high assembly hoop stress, the hoop stress component is not that sensitive to the operating loads.

5.3.5 Full Geometry 3-D Crankshaft Time Step 4 FEM Results

The final time step (4) evaluated using the full crankshaft FEM model is the application of maximum reciprocating inertia loads on the PTO crankpin. The solution for LC4 also includes both the press-fit assembly (LC1) and the rotational inertia (LC2) which are solved for in time steps 1 and 2 respectively. As presented earlier (see Table 5.4.1), the PTO end crankpin local y-direction load is positive, in the direction of the crankpin throw, and is generated by the connecting rod and piston reciprocating inertia loads. The MAG crankpin local y-direction load is negative, and is generated by the combustion event on the MAG cylinder. The directionality of these loads relative to the crankshaft geometry is shown in Fig.5.3.5.1

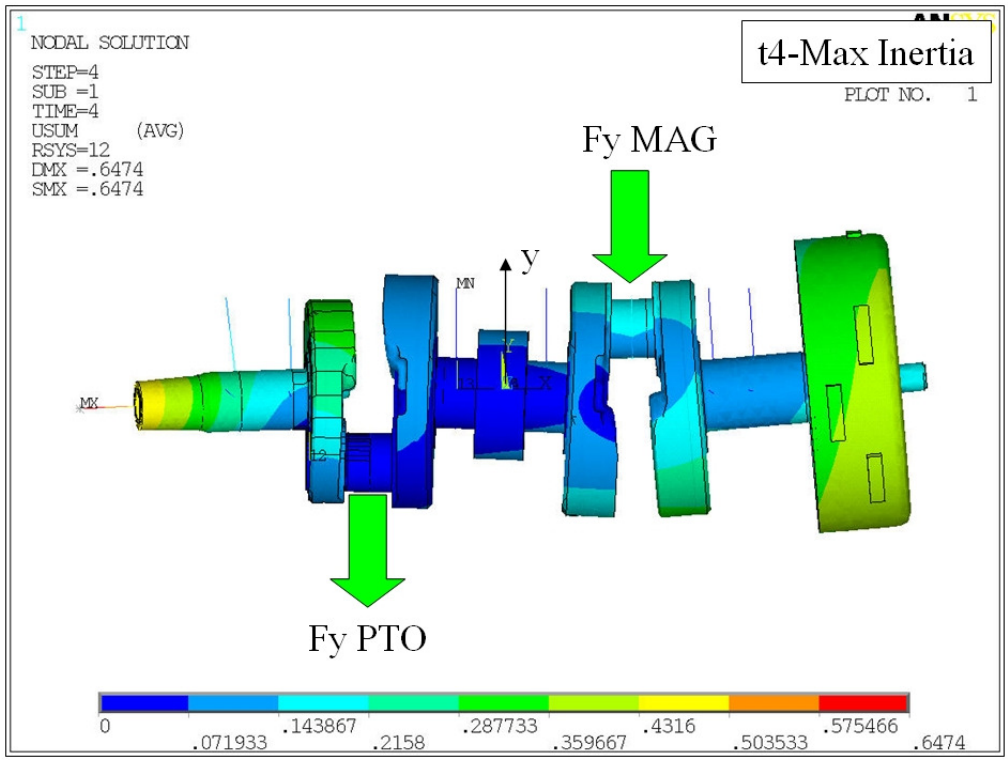

Figure 5.3.5.1 Resultant displacement plot for time step 4.

Figure 5.3.5.1 displays the LC4 resultant displacement plot for the crankshaft assembly. Note for the first time there is significant displacement on the MAG end of the crankshaft due to the combustion load input on that crankpin. A top view of the resultant displacement plot is shown in Fig.5.3.5.2, which also includes the direction of the belt force for this event. Note that the LC4 belt force is approximately opposite in direction to the LC3 belt force. Figure 5.3.5.2 indicates that LC4 belt force on the PTO end has a significant influence on the overall structural distortion, as is the case for LC3.

Local equivalent stress values at the crankshaft critical fillet radii are shown in Fig. 5.3.5.3, which uses a lower stress scale range (0 to 300 MPa) to emphasize the higher locations of stress. Note that the MAG crankpin fillet radius, on the bottom of the pin, has significant stress present in LC4.

In Fig.5.3.5.4, an equivalent stress plots of the rear view of the PTO end main shaft shows that the main shaft is sensitive to the belt load with bending like stress patterns present on each side,

as was demonstrated for LC3. The stress field on the crankpin is also shown to be sensitive to the belt force, which is indicated by the high pin stresses near the PTO outer web in Fig.5.3.5.4.

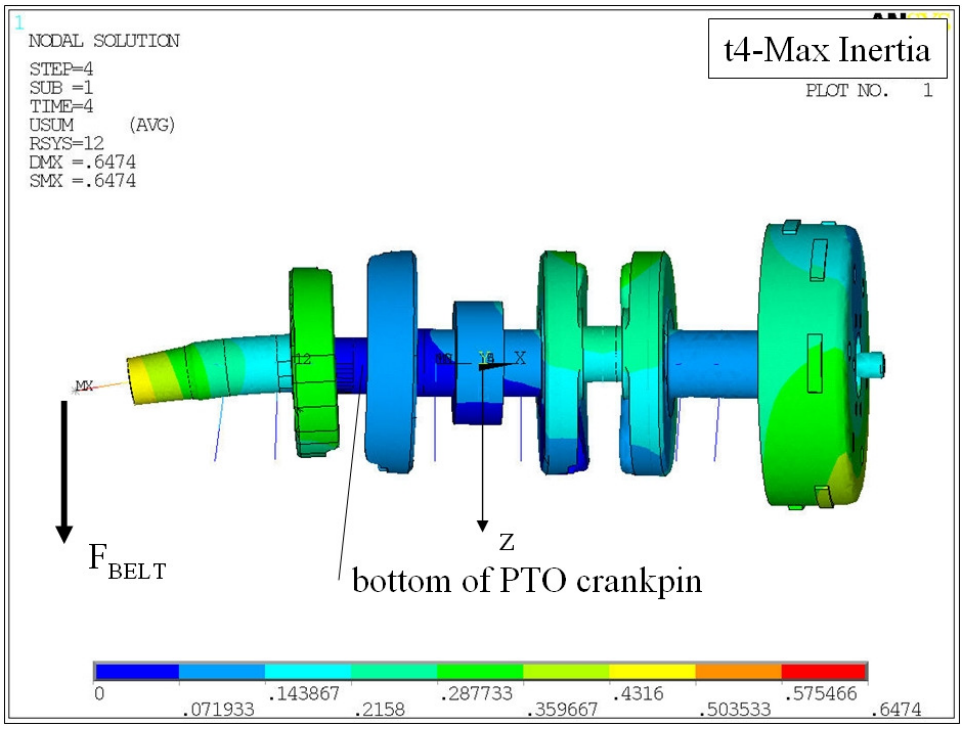

Figure 5.3.5.2 Top view of resultant displacement plot for time step 4.

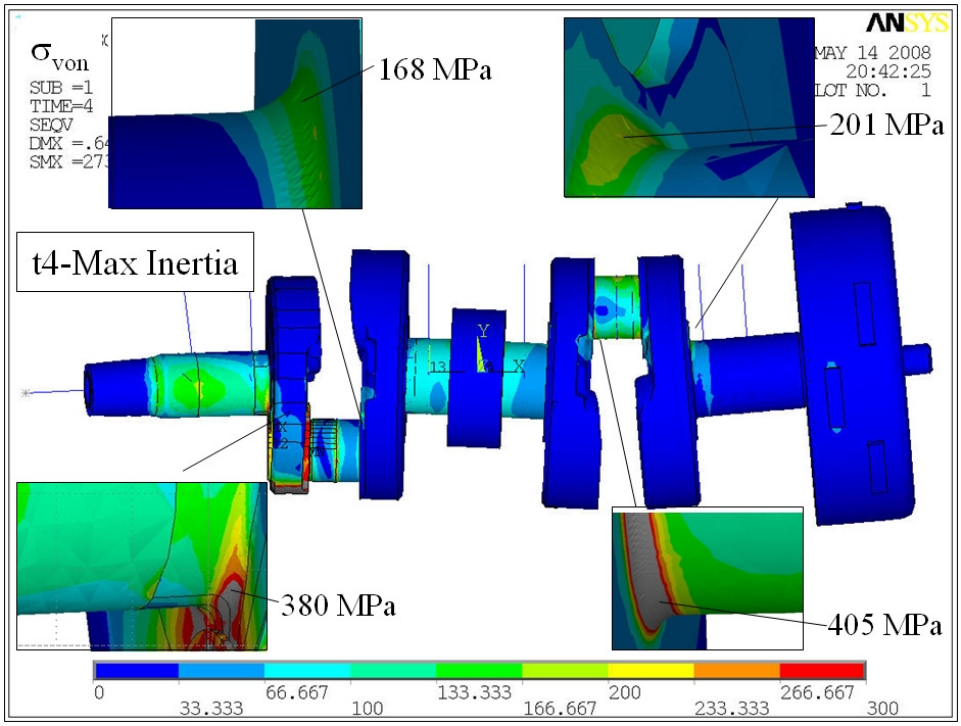

Figure 5.3.5.3 Fillet radius local equivalent stress maximums for time step 4.

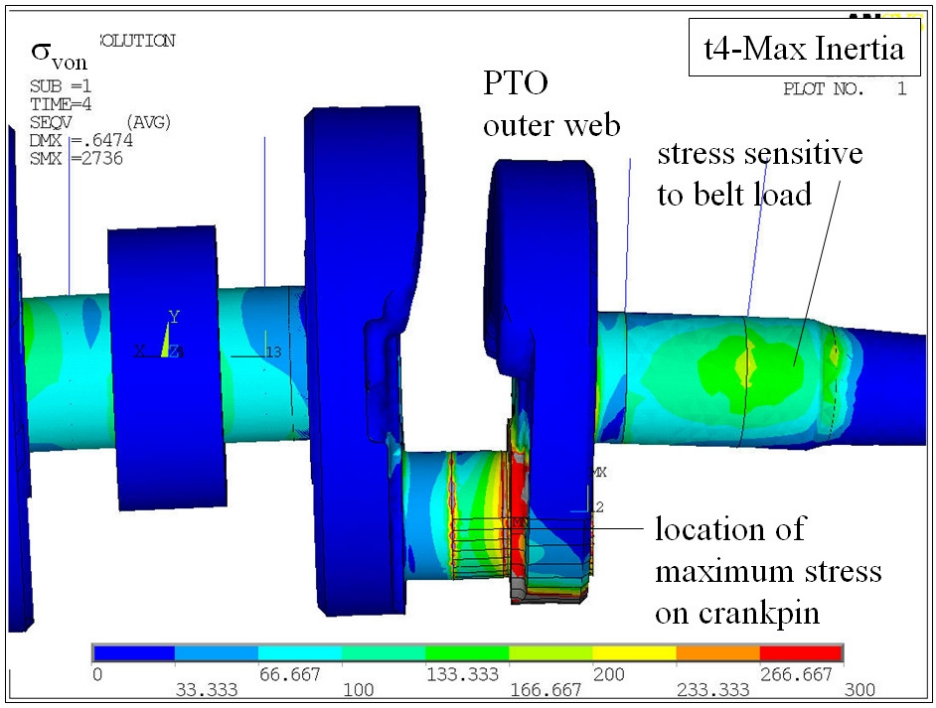

Figure 5.3.5.4 Rear view of PTO end equivalent stress plot for time step 4.

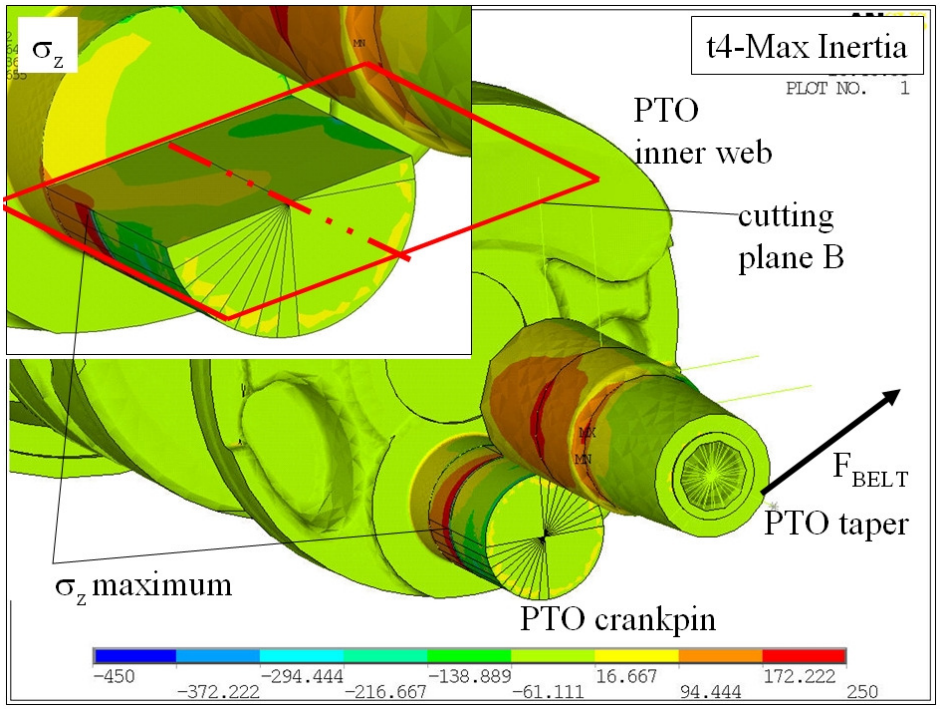

Figure 5.3.5.5 A plot of σ_z across cutting plane B for time step 4.

In LC3 the maximum pin σ_{VM} was used to identify a cutting plane (A) for sectioning of the pin so that sub-surface stresses could be studied. The crankpin σ_z generated in LC4 is plotted in

Fig.5.3.5.5, and denotes a cutting plane B which bisects the crankpin axis and the maximum crankpin axial stress (which is also identified). Cutting plane B is near to a horizontal orientation, and is considered to be sensitive to belt load more so than crankpin load. For load case 4, the PTO crankpin inertia load is opposed in part by the web counterweight loading, which overall generates less distortion than when the combustion load is applied for LC3. The viewing of results on cutting plane b uses the pie shaped selection sets presented in section 5.3.1.

Stress results across plane B are now used to describe how the joint behaves during LC4. First σ_r across cutting plane B is shown in Fig. 5.3.4.6, where the belt force is carried across the joint by increasing σ_r at opposite corners of the web/pin interface. The lower left hand side corner of the pin/web interface in Fig.5.3.5.6 designated as location B1, and is the location at which the maximum axial tensile stress is generated.

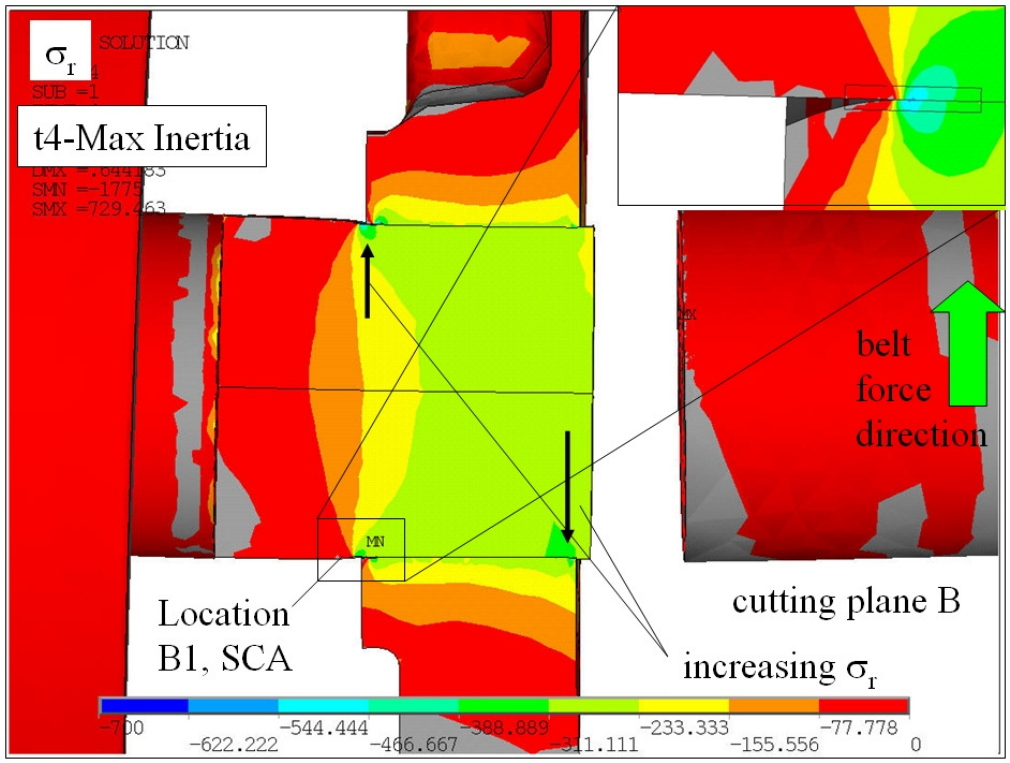

Figure 5.3.5.6 A plot of σr across cutting plane B for time step 4.

Next axial stress is plotted on Plane B in Fig.5.3.5.7 for LC4. The maximum σ_z on the pin at location B1 is shown to coincide with belt force direction and the σ_r unloading (see Fig.5.3.5.6), which the other 3-D models have demonstrated as well.

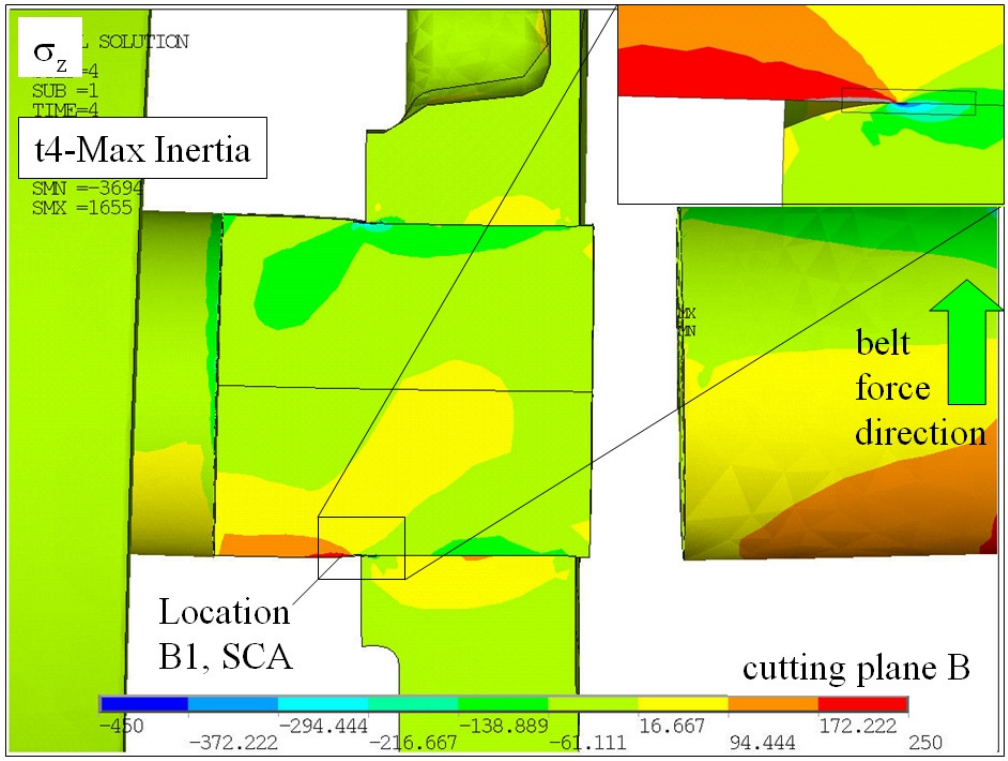

Figure 5.3.5.7 A plot of σz across cutting plane B for time step 4.

5.3.6 Full Geometry 3-D Crankshaft FEM Results Summary

Numerical results for all load 4 cases have been presented in previous sections for the full crankshaft 3-D FEM model. There is a significant amount of data to post-process and present to describe the detailed behavior at the SCA. Summary plots that examine the stress field across the time steps are now presented. Cutting planes A and B, which were introduced in sections 5.3.4 and 5.3.5 respectively, will be put to use again.

5.3.6.1 PTO Crankpin Results On Cutting Plane A

First, results on cutting plane A are examined at the PTO crankpin. Radial stress is plotted on plane A for the PTO crankpin in Fig.5.3.6.1 for load cases 3 and 4. Note the locations of the SCA designated A1 (bottom of plot) and A2 (top of plot). Location A1 is shown to unload σ_r for load step 3, and begin loading again in time step 4 when the crankpin input loads reverse direction.

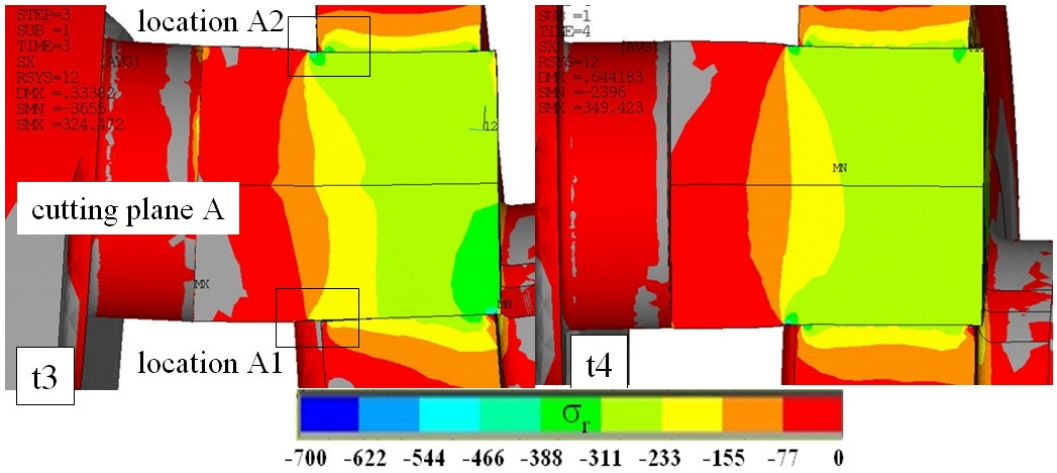

Figure 5.3.6.1 Plot of σ_r on plane A of the PTO crankpin for times 3 and 4.

Next Fig. 5.3.6.2 plots σ_z on plane A for the PTO crankpin for load cases 3 and 4. As a reminder, A1 is the location of maximum axial stress on the pin for time step 3, combustion on the PTO crankpin. Clearly the pin reverses the direction of bending for LC4, but the tensile σ_z are still much higher at location A1 in LC3 versus location A2 in LC4.

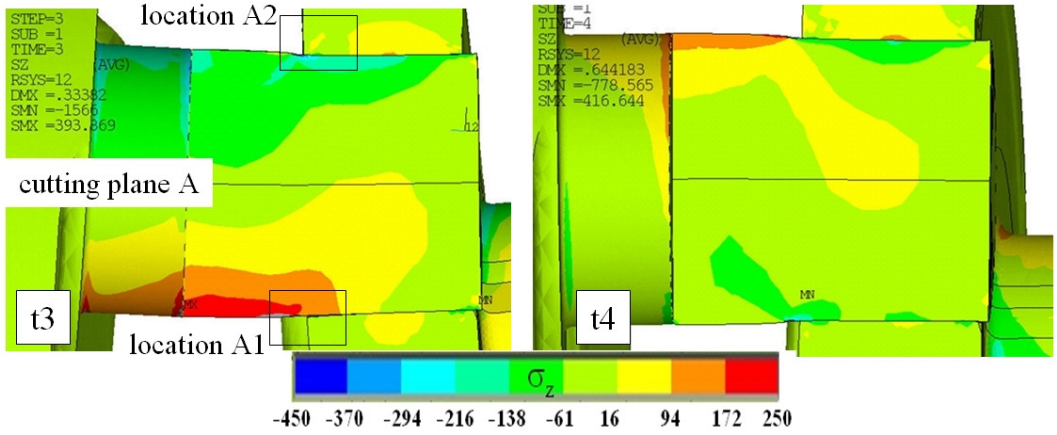

Figure 5.3.6.2 Plot of σ_z on plane A of the PTO crankpin for times 3 and 4.

Equivalent stress is also plotted on plane A for load cases 3 and 4 in Fig.5.3.6.3. The σ_{VM} plots are not as descriptive as the stress component plots. The web stress due to the press-fit stretch is significant throughout, and the pin shows some stress sensitivity to the joint loading for the LC3 combustion event.

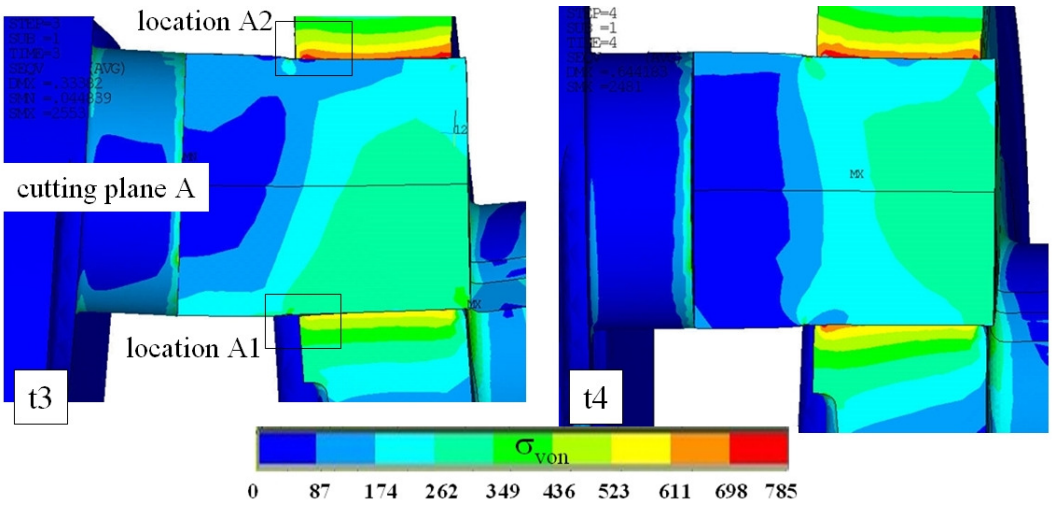

Figure 5.3.6.3 Plot of σ_{VM} on plane A of the PTO crankpin for times 3 and 4.

The details of the stress field at location A1 are now examined for load cases 1 thru 4. Figure 5.3.6.4 plots σ_r at location A1 using a common scale for all. The σ_r is shown to unload for LC2 and LC3, and then begins to increase again for LC4. This exact behavior was demonstrated in the one-quarter bench model also, at the bottom of pin position.

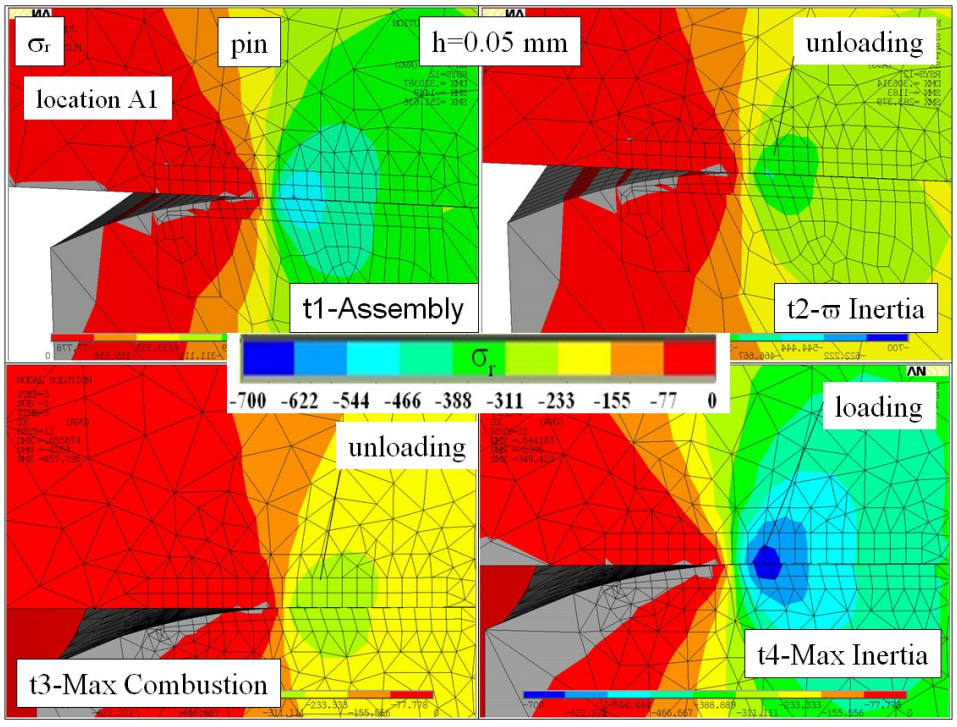

Figure 5.3.6.4 Radial stress (σ_r) plot at location A1 for load steps 1 to 4.

The axial stress at location A1 is plotted next in Fig.5.3.6.5 for load cases 1 thru 4. The location A1 at the bottom of the joint increases in σ_z for LC2 and LC3; σ_z then becomes highly compressive for LC4 (which again is similar to the one-quarter bench model).

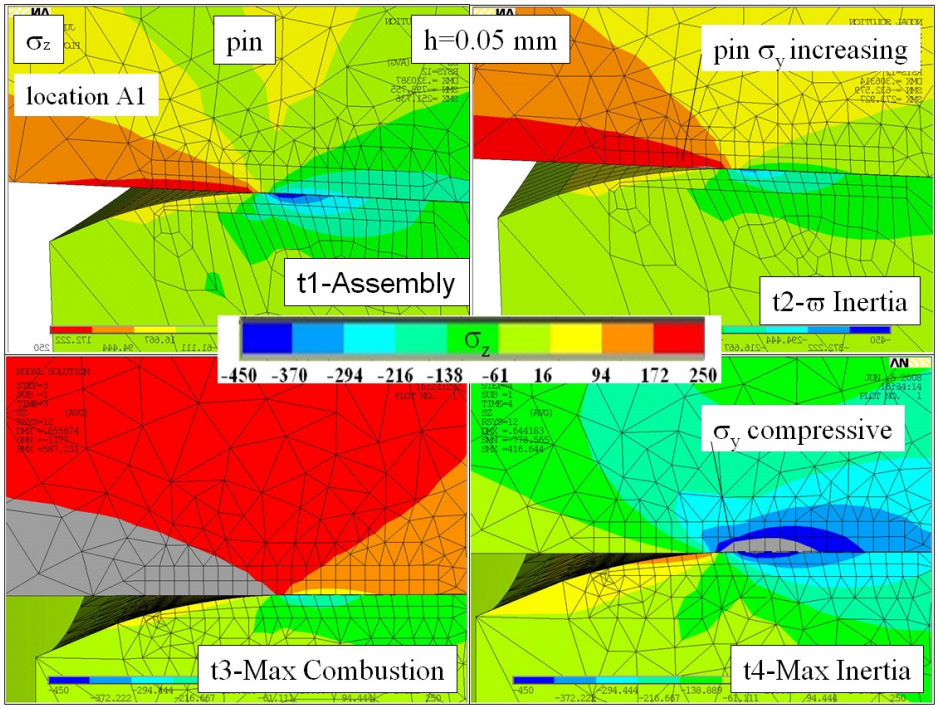

Figure 5.3.6.5 Axial stress (σ_z) plot at location A1 for load steps 1 to 4.

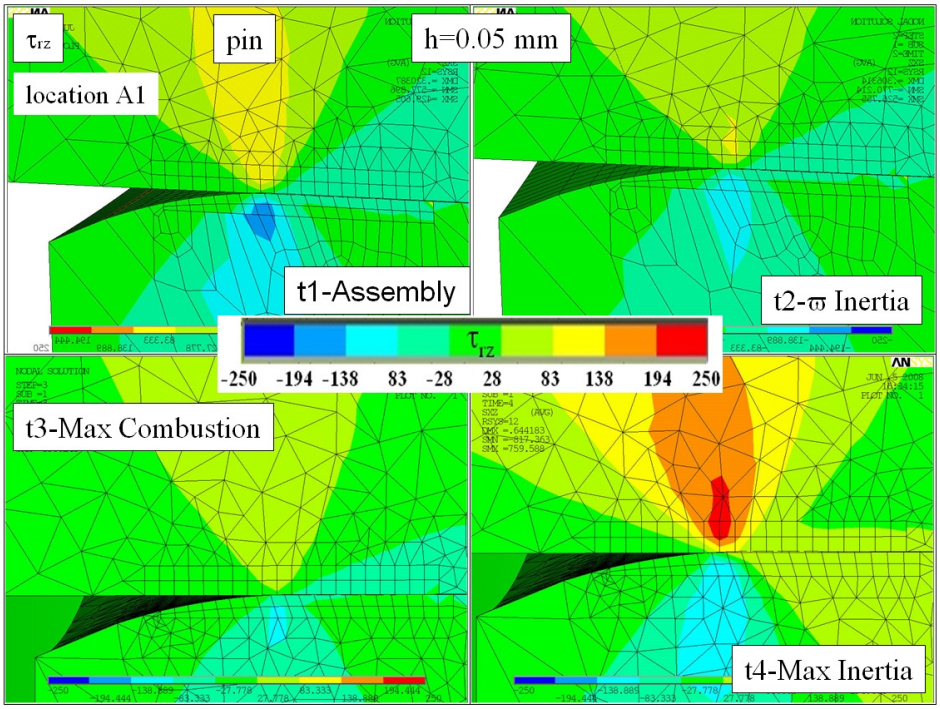

Figure 5.3.6.6 Shear stress (τ_{rz}) plot at location A1 for load steps 1 to 4.

So far in this thesis τ_{rz} and σ_r increases trend with each other. In Fig. 5.3.6.6 the highest τ_{rz} is present in LC4 for location A1, due to the high compressive σ_r caused as pin bending reverses direction with the application of the reciprocating inertial loads. Shear stress also follows the same trend that was introduced with the one-quarter bench model.

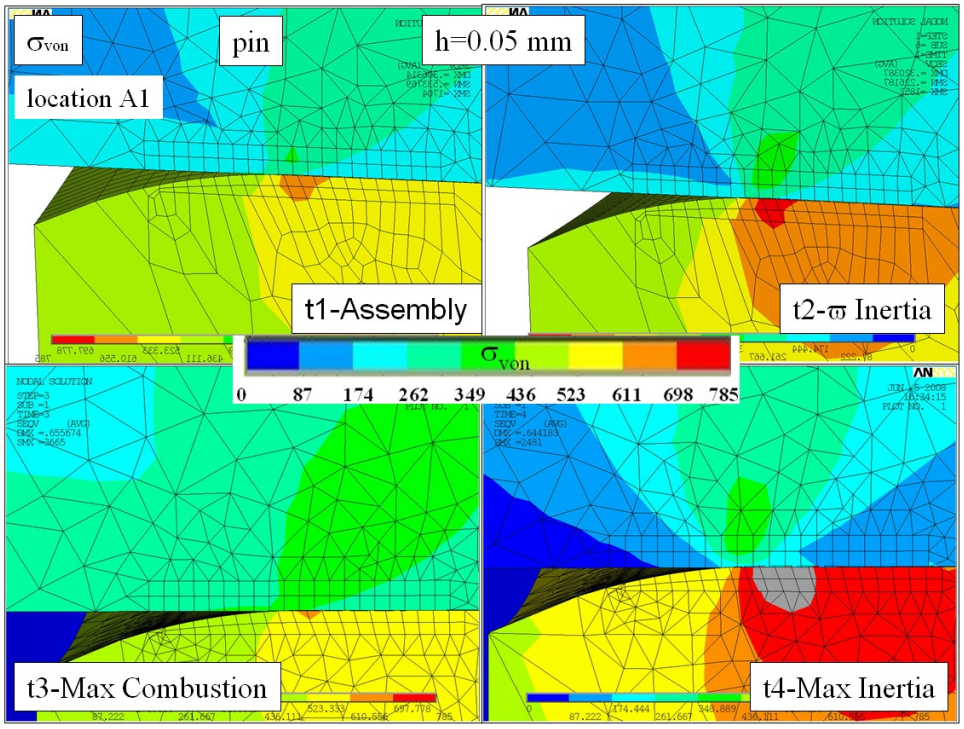

Figure 5.3.6.7 Equivalent stress (σ_{VM}) plot at location A1 for load steps 1 to 4.

Figure 5.3.6.7 plots σ_{VM} at location A1 for load cases 1 thru 4. The highest equivalent stress state is for load case 3, PTO crankpin combustion. The web σ_{VM} does show some sensitivity to the loading, and high stress is created at the web for LC4 due to the compressive radial loading.

Equivalent stress is also plotted at location A2 in Fig. 5.3.6.8; the stress field in the web also is significantly higher than in the pin, while the stress field displays the traits of loading and unloading.

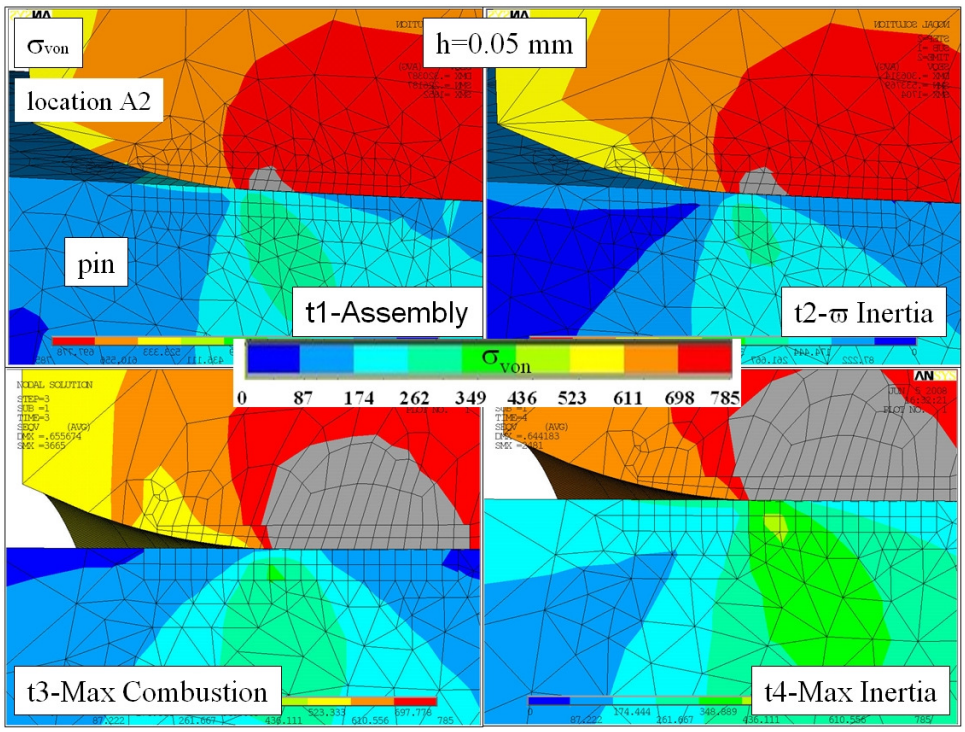

Figure 5.3.6.8 Equivalent stress (σ_{VM}) plot at location A2 for load steps 1 to 4.

5.3.6.2 PTO Crankpin Results On Cutting Plane B

To maintain brevity in this thesis, the full set of detailed results for the stress condition on the PTO crankpin for cutting plane B is contained in Appendix E. The press-fit joint is shown to carry load across plane B in a similar manner as demonstrated for cutting plane A. The data suggests that PTO crankpin bending on plane A is more significant for time step 3 than crankpin bending on plane B for time step 4. Thus, results on plane A were chosen for presentation in the summary section. Note that stress at the two locations A1 and B1 will load and unload in an opposite manner for time steps 3 and 4, because of their relative positions on the crankpin.

5.3.6.3 Variation of Local Stress Maximums At The SCA By Load Step

The next set of plots examines the load step variation in local stress maximums or minimums at the SCA location. Locations A1 and A2 from plane A and locations B1 and B2 from plane B are considered; as a reminder location A1 and B2 are near to each other separated by a 40 degree angle (see Appendix A.5.3.6).

First minimum σ_r at the SCA is plotted in Fig.5.4.3.9 for load cases 1 thru 4. Radial stress is shown to unload and load on each respective side of the pin as bending varies with load case. The response of locations A1 and B1 are opposite because of their near opposite locations on the pin. The σ_r at location A1 is shown to vary the greatest, because of the significant unloading at time step 3. The identical plots for hoop stress σ_θ and shear stress τ_{rz} follow the trend of radial stress (see Fig.5.3.6.10 and 5.3.6.11); this has been identified previously in this chapter also.

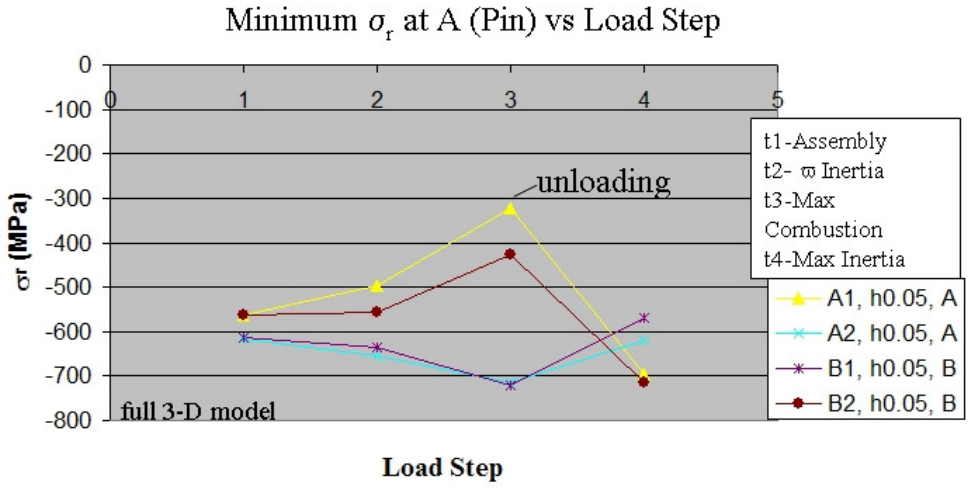

Figure 5.3.6.9 Local minimum σ_r at *A* (pin) vs load step and element size *h*.

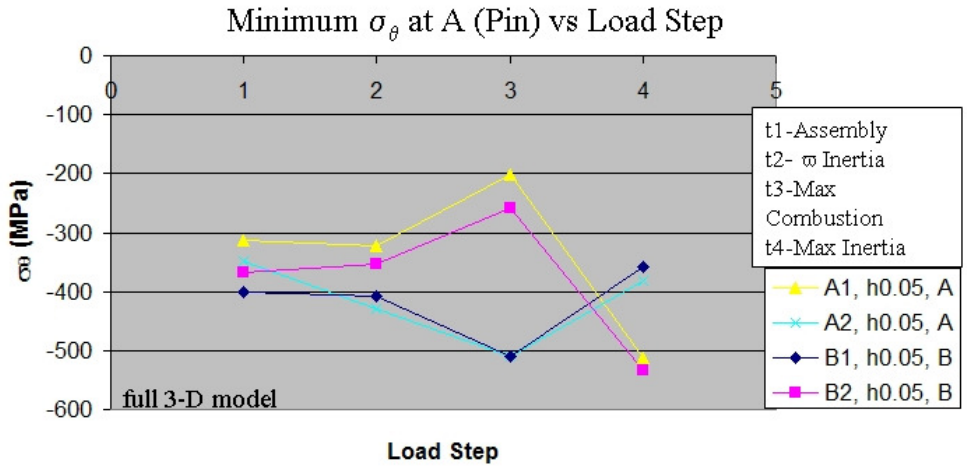

Figure 5.3.6.10 Local minimum pin σ_θ at *A* vs load step and element size *h*.

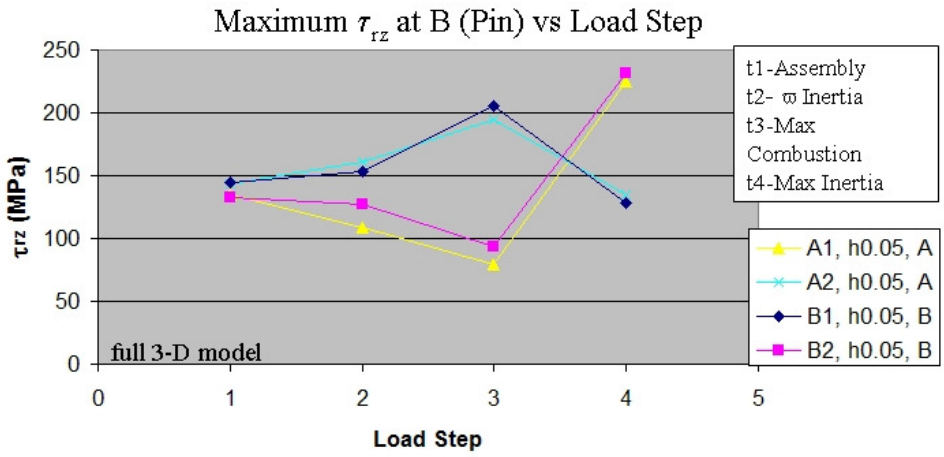

Figure.5.3.6.11 Local maximum pin τ_{rz} at *B* vs load step and element size *h*.

Maximum σ_z is plotted next in Fig.5.3.6.12, and the stress variation due to crankpin and belt loading matches the expected results. Note also here that stress variation at locations A1 and B1 are opposite as should be the case.

The last set of plots in this series is the Von Mises equivalent stress which is plotted for the pin and web locations at the SCA in Figs.5.3.6.13 and 5.3.6.14 respectively. Low variation in equivalent stress is shown for the pin in Fig. 5.3.6.13, which is also true for the higher magnitude web equivalent stress.

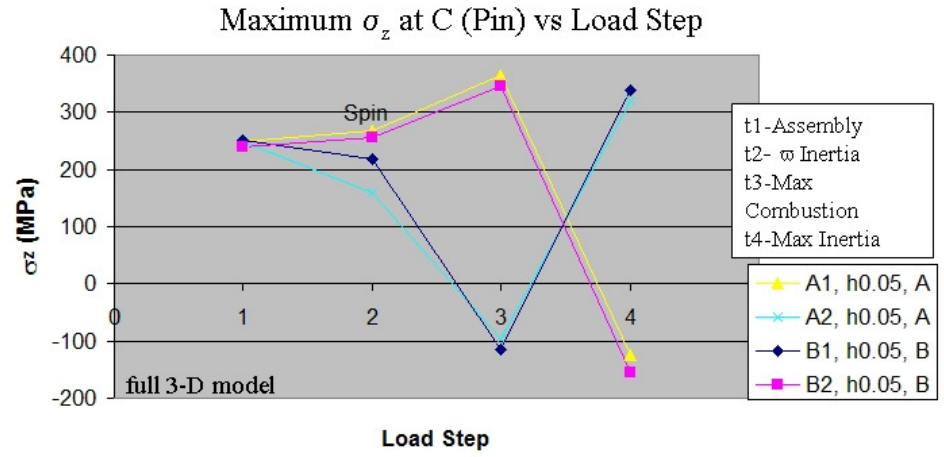

Figure.5.3.6.12 Local maximum pin σ_z at C vs load step and element size *h*.

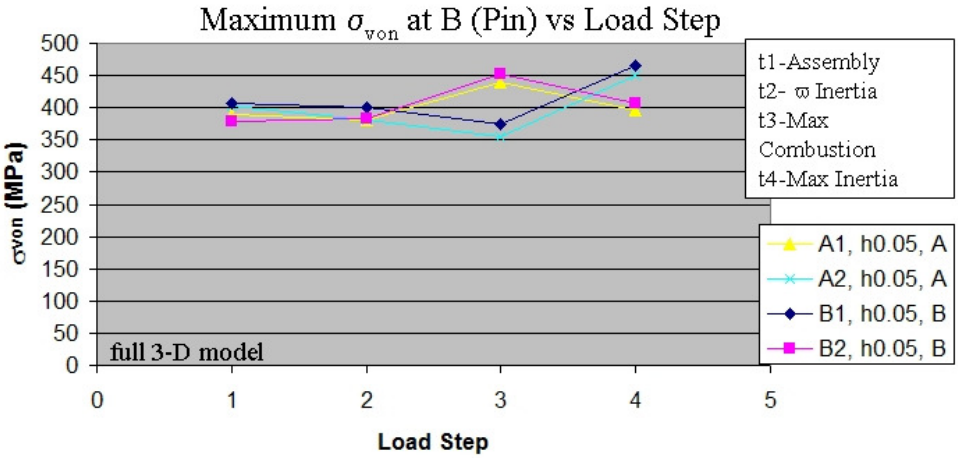

Figure 5.3.6.13 Local maximum pin σ_{VM} at *B* vs load step and element size *h*.

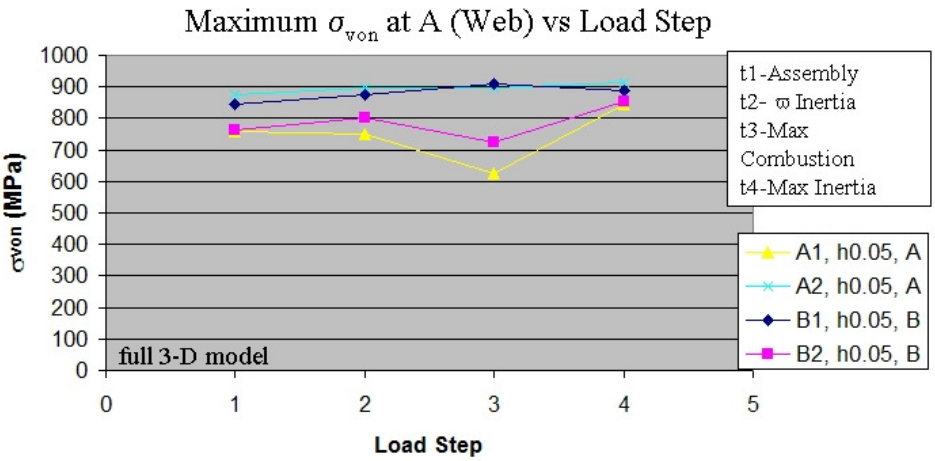

Figure 5.3.6.14 Local maximum web σ_{VM} at *A* versus load step and element size *h*.

5.3.6.4 Variation of Pin Axial Stress With Load Step And Element Size

The axial stress is now examined along a 1mm SCA zone (line fg in Fig.5.3.4.1) for cutting plane A across all 4 load cases. Figure 5.3.6.15 plots σ_z along line fg for location A1. The axial stress curve is shown to be displaced in a positive direction from LC1 by the (bottom of) pin bending created by LC2 and LC3. The curve for LC4 is displaced in a negative σ_z direction by LC4 because of the compressive axial stresses created by the reciprocating inertia loading. The axial stress along line fg for location A2 follows the reverse trend established for A1 (see

Fig.5.3.6.16) since the same load inputs produce compressive instead of tensile axial stress changes.

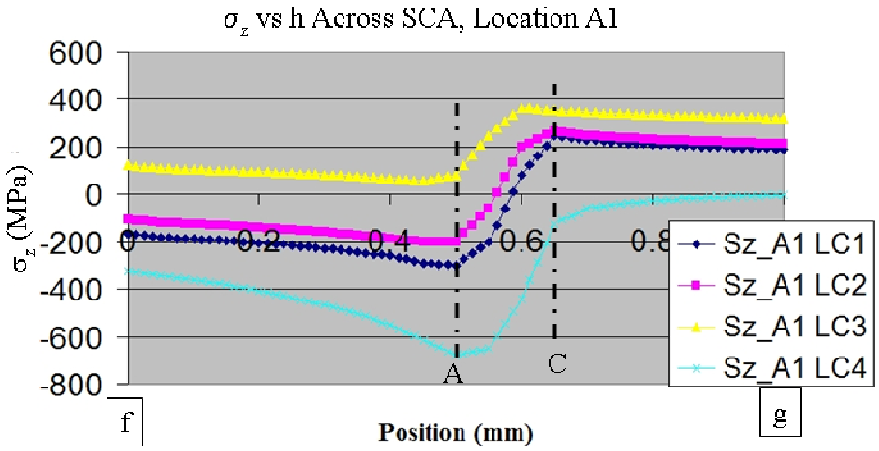

Figure 5.3.6.15 Plot of σ_z along line fg for load cases 1 thru 4, location A1.

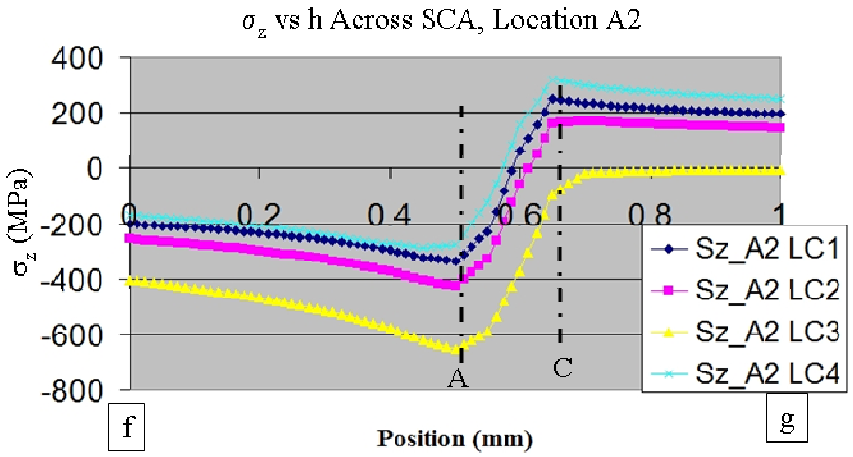

Figure 5.3.6.16 Plot of σ_z along line fg for load cases 1 thru 4, location A2.

5.3.6.5 Summary Comments On Full 3-D Model Results

The review of the full 3-D model press-fit joint behavior indicates that that the operating loads are transmitted across the joint in a similar fashion to the one-quarter bench model. A cutting plane which bisects the pin center axis and maximum axial stress location on the pin surface (at location *C* near the SCA) may be used to effectively observe the joint loading and the sub-surface stresses. Results from both the full 3-D and one-quarter models are compared next.

5.4 Comparing Numerical Results For The 3-D Models

Since the one-quarter bench test model uses an efficient mesh, solutions with a smaller mesh density (h equals 0.02 mm) could be analyzed. In comparison, solution time and mesh density was limited to *h* equals 0.05 mm for the full 3-D model. It is desired to compare results between the two models, first to check for the effect of a limited element size on maximum stress calculated. Note also the one-quarter bench test model does not contain crankpin tangential loads or the belt force. And so also it is desired to check if the one-quarter bench test is a reasonable approach for examination of the stress condition at the SCA.

5.4.1 Variation of Local Stress Maximums At The SCA By Load Step

General comparisons of the joint loading and the stress component behavior at the SCA in section 5.3 indicate both models produce generally the same response. The results presented next will examine how closely the stress magnitudes match. Note that for this section, comparisons are made between location A1 (full 3-D model) and the bottom of the pin (one-quarter model), as both are the locations of maximum axial stress, and are the location of primary durability concerns for each model. The terms bottom of pin and location A1 can be interchanged in the descriptions below.

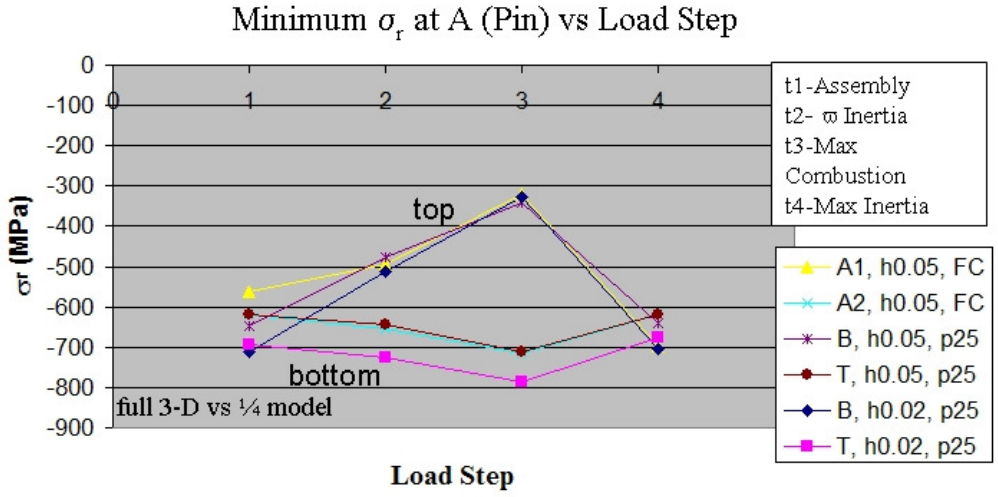

Figure 5.4.1.1 Local minimum σ_r at *A* (pin) versus load step comparing 3-D models.

The maximum radial stress at location *A* is plotted against load step for the two 3-D models in Fig.5.4.1.1. The one-quarter bench test model includes results for *h* equals both 0.05 mm and 0.02 mm on both the bottom and top position on the pin, while the full model displays results for *h* equals 0.05 mm at locations A1 and A2. The plots trend very similar, and in particular the *h* equals 0.05 mm solutions on the bottom of the pin are nearly identical. The *h* equals 0.02mm one-quarter model is offset approximately 71 MPa lower than either of the *h* equals 0.05 mm models, likely due to the increased mesh refinement.

A similar comparison of hoop stress σ_θ is given next in Fig.5.4.1.2 where it is shown that the bottom hoop stress curves trend in a similar fashion for the one-quarter and full 3-D models. The exception is the full 3-D assembly value which is lower by 27 % compared to the one-quarter bench test model. Since the radial stress values compared earlier between models are very similar, this data point is suspect and may be the result of a poor quality (splotchy) contact solution.

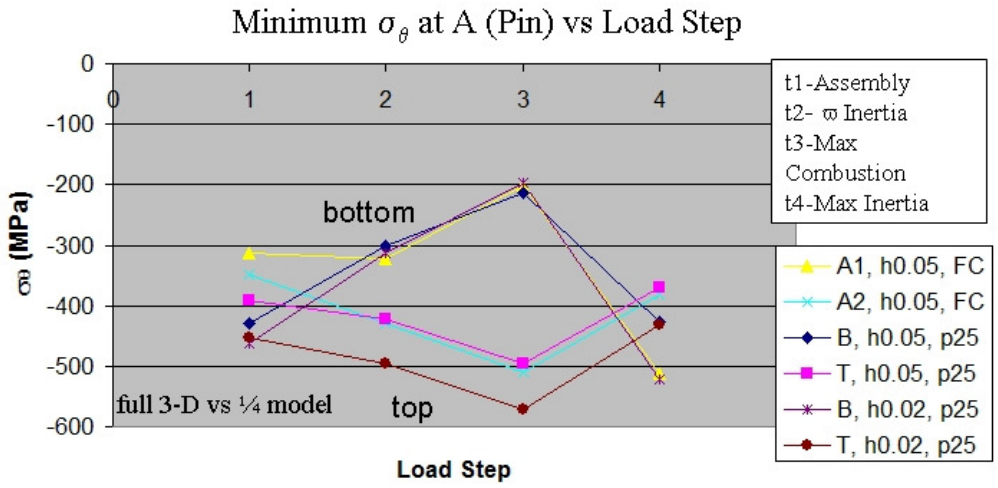

Figure 5.4.1.2 Local minimum pin σ_θ at *A* versus load step comparing 3-D models.

Next local maximum axial stress at location *C* (on the SCA) is compared in Fig.5.4.1.3 for the two models. On the bottom of the pin, the model results deviate at LC2 when the rotational inertia load is applied, but are very close for LC3 and LC4. In particular, it is interesting how close the axial stress values are for the PTO crankpin combustion event in LC3. Since the 'kink'

present at the SCA tends to be reduced during combustion, it is logical that mesh density present will have less affect on the accuracy. Thus, the *h* equals 0.05mm full 3-D model is thought to have adequate mesh refinement to accurately predict stress at the SCA for LC3.

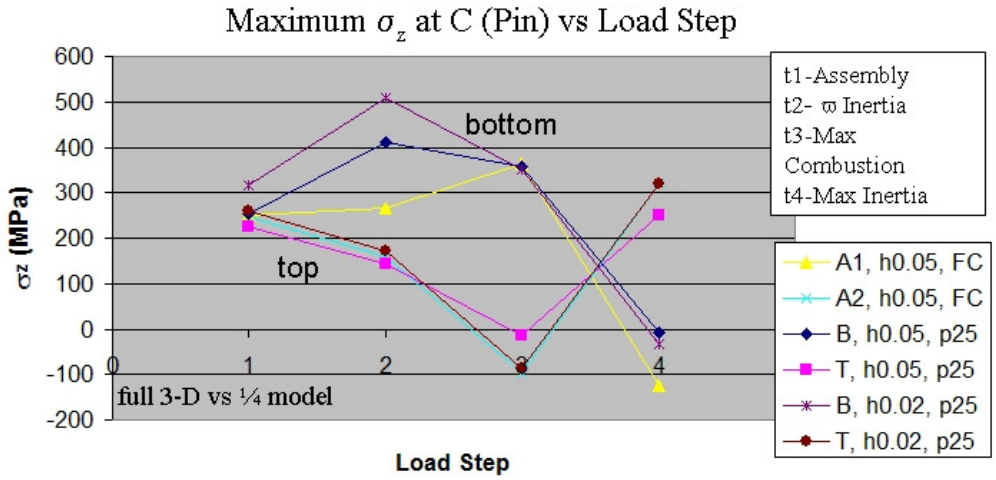

Figure 5.4.1.3 Local maximum pin σ_z at C versus load step comparing 3-D models.

The difference in the axial stress at the rotational inertia (LC2) load step requires some explanation. The one-quarter bench model work showed that the maximum axial stress is sensitive to mesh density for LC2 (see section 5.2), and also the LC2 (rotational inertia) value was calculated as being higher than for LC3 (combustion). This sensitivity to mesh size is explained by the kink, which is still present in LC2, When a bending moment is applied to the bottom of the pin, the kink acts as a stress multiplier, until that kink becomes less pronounced.

One final point may be made at the difference between the full 3-D and the one-quarter model here. The location A1 (cutting plane A) is offset 50 degrees from the bottom of pin position (BDC). The position of A1 for the full model is less sensitive to the spin loading (LC2) of the crankshaft because it is closer to the neutral axis for the crankshaft under this particular loading.

Next shear stress τ_{rz} is compared in Fig.5.4.1.4 for the two modeling approaches, and very good correlation is shown. This is expected as good radial stress correlation was shown in Fig.5.4.1.1 also.

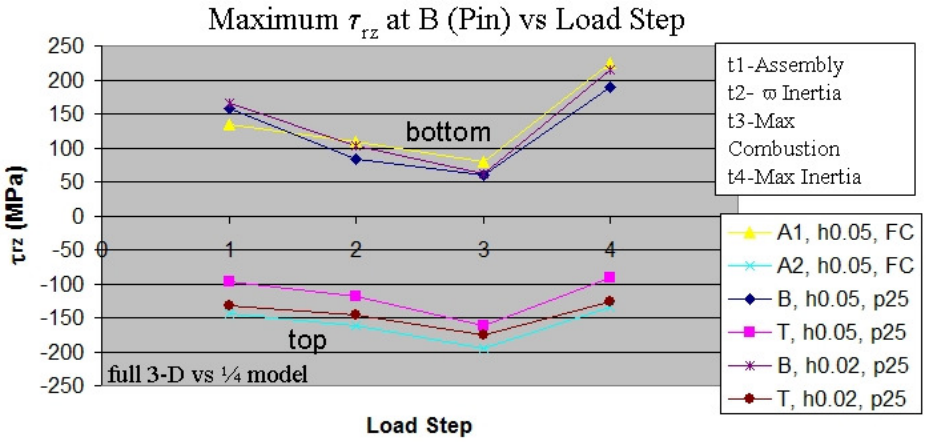

Figure 5.4.1.4 Local maximum pin τrz at *B* versus load step comparing 3-D models.

Figure 5.4.1.5 plots local maximum equivalent stress on the pin at location *B* (on the SCA) for the two models. Over both time steps 1 and 2, the full model (*h* equals 0.05 mm) is approximately 10% lower than the one-quarter 0.05 mm *h* model and approximately 15% lower than the one-quarter 0.02 mm *h* model. Closer correlation is shown over time steps 3 and 4.

The last in this series of figures is the maximum web equivalent stress plot which is provided in Fig.5.4.1.6. Reasonable correlation is shown for the web stress between the full and one-quarter model.

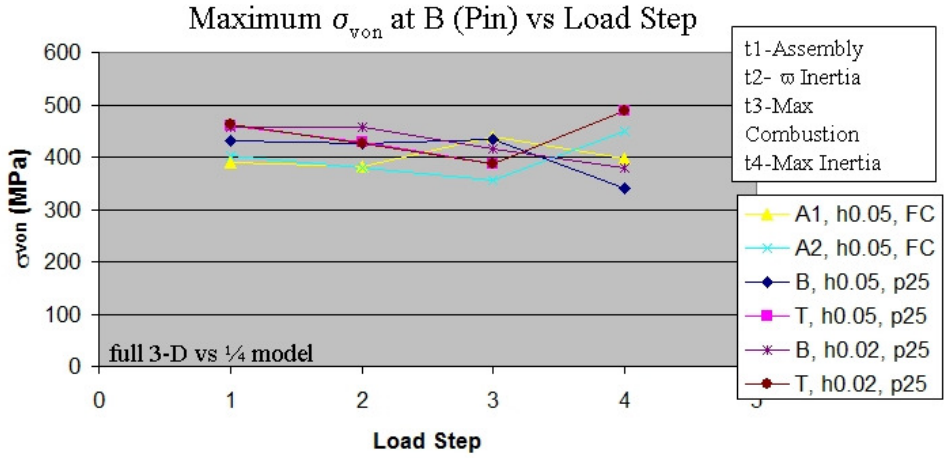

Figure 5.4.1.5 Local maximum pin σvon at *B* versus load step comparing 3-D models.

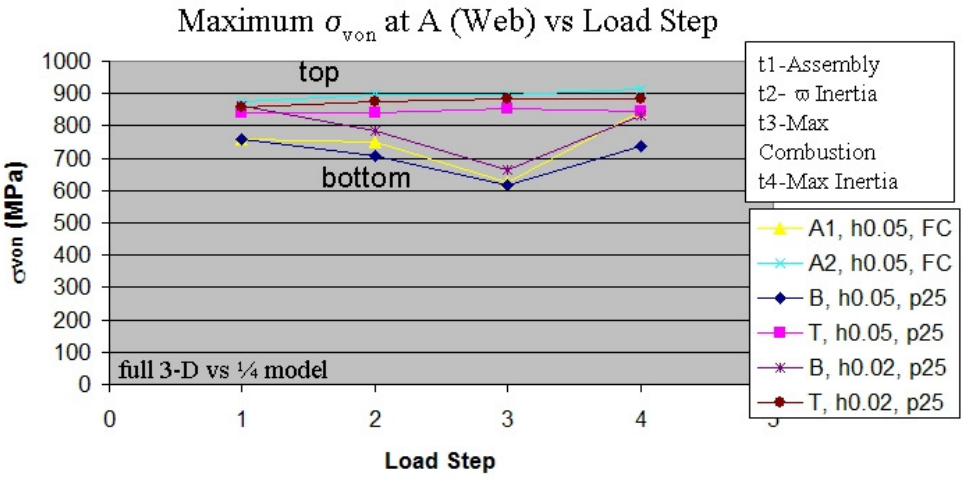

Figure 5.4.1.6 Local maximum web σ_{VM} at *A* vs load step comparing 3-D models.

5.4.2 Variation of Pin Axial Stress By Load Step And Element Size

The final series of plots examines axial stress σ_z plotted along line fg across the bottom of the pin (one-quarter model) and at position A1 (full 3-D model) as studied previously. Results posted for the one-quarter model uses a 0.02 mm mesh size, while the full 3-D model results use a 0.05 mm mesh size.

First the axial stress at the bottom of the pin (or location A1) is plotted for LC2 in Fig.5.4.2.1. The difference in maximum value at location *C* is significant between the two models, and is due to element size limitations in the full model, and also the proximity of the full model A1 location to the neutral axis for this loading. Further work will be outlined in chapter 10 which would examine further the differences in results here. The primary difference in results here is thought to be due to the mesh refinement limitations in the full model.

In contrast, a comparison of axial stress for load case 3 is given for the two models in Fig.5.4.2.2. Good correlation is shown for LC3, the combustion event, because the pin bending unloads the radial stress at the SCA, which reduces the presence of the kink in the pin material, and allows convergence on axial stress with a larger element size.

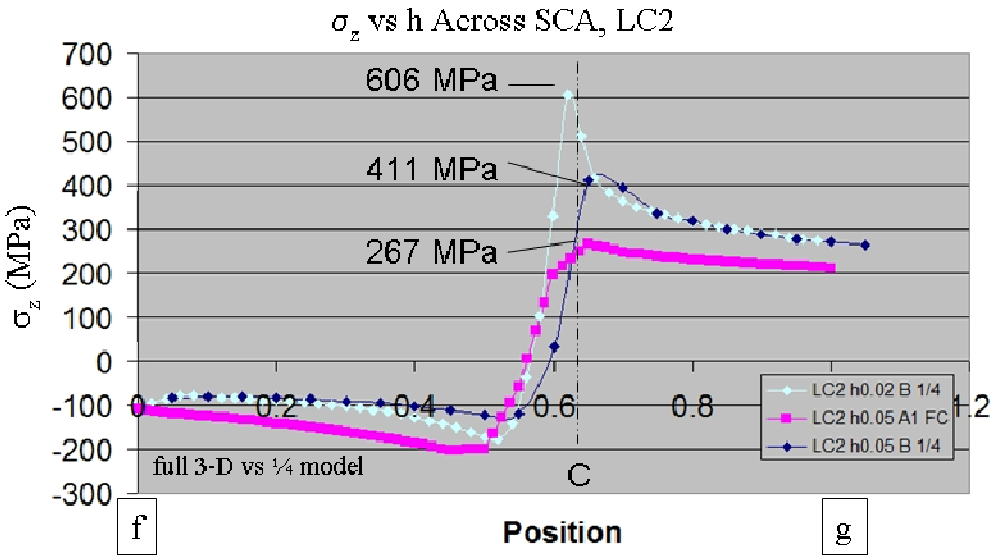

Figure 5.4.2.1 Plot of σ_z along line fg for load case 2 for both 3-D models.

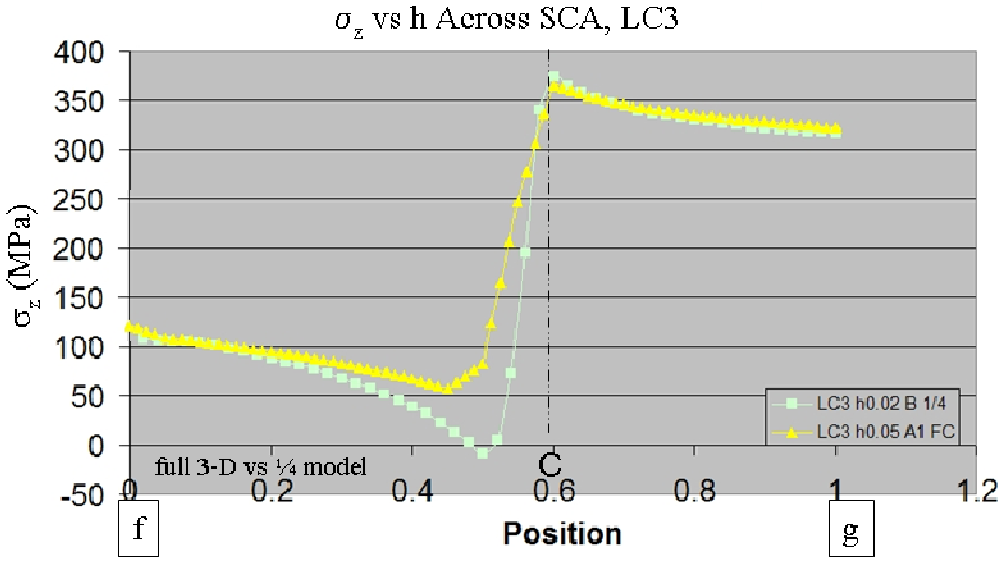

Figure 5.4.2.2 Plot of σ_z along line fg for load case 3 for both 3-D models.

Finally, LC4 σ_z results for the one-quarter and full 3-D model are compared in Fig.5.4.2.3. Both models are in compression at location *C* for this load case, due to the PTO crankpin reciprocating inertia loads, and do not differ significantly (-45 MPa for the one-quarter model and -125 MPa for the full 3-D model).

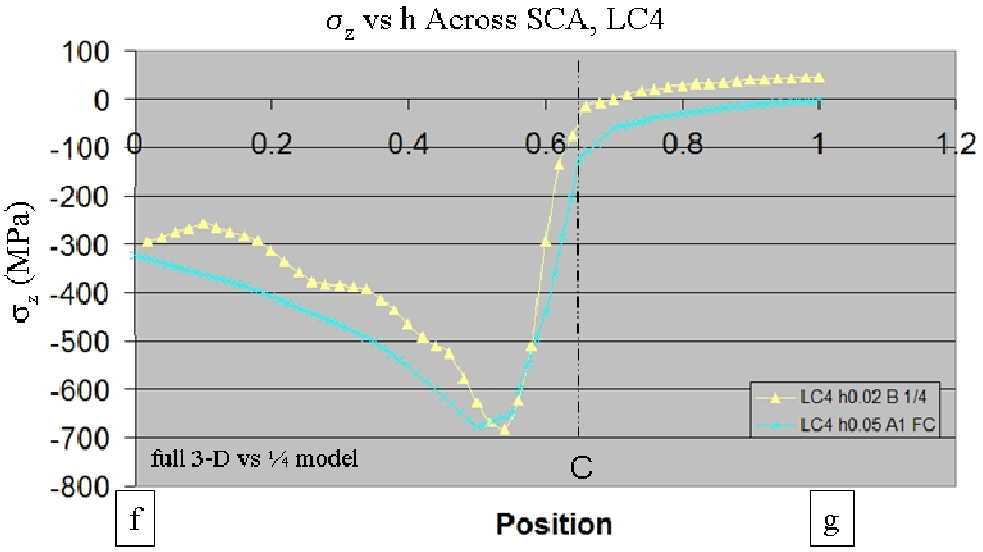

Figure 5.4.2.3 Plot of σz along line fg for load case 4 for both 3-D models.

5.4.3 Summary Comments

In summary, the detailed stress calculations at the SCA compare well between the 3-D full FEM model and the one-quarter bench test FEM model. Thus it is thought that the one-quarter bench test model could be used more efficiently in the early design stage, and that after a prospective design has met stress design targets, hopefully only a final evaluation would occur with the full 3-D FEM model.

This approach suggests that pin bending due to crankpin loading is the most significant durability concern, while PTO end belt force loads have a secondary impact. In chapter 10 some future work is proposed to study this idea. One needs to take care in using this assumption. Analysis with the full geometry should always take place as the final task to guard against departures from this relationship, and results from this model should take precedence over the one-quarter model. It is thought that with significant changes in crankshaft architecture, the idea of successfully leveraging a reduced one-quarter bench test model would need to be reconfirmed.

5.5 Combined 2-D And 3-D Predictions

A comparison of the press-fit assembly stress state for the 2-D and 3-D models is provided in section 4.5. The 2-D axisymmetric FEA model is shown to generate higher local stress maximums at the SCA because of the high mesh refinement and excellent 2-D mesh quality present, which is not feasible with the 3-D full crankshaft assembly due to the model size and solution time required. The 2-D studies of *h* versus maximum stress at the SCA determined that convergence was obtained in the range of *h* equals 0.05 to 0.01 mm. However since solution time limited the minimum element size studied to *h* equals 0.05 mm with the full 3-D model, it is uncertain whether assembly stress convergence has been reached.

Based on an acceptable small difference in results between the perfect axisymmetric 2-D model assumption and the full 3-D web geometry, it may be reasonable to assume that the 3-D model solution would converge to near the 2-D values. Therefore it may be appropriate to combine the converged 2-D assembly stresses with operating load 3-D stresses using super-position.

A few assumptions are required to take this step; the first is that the axisymmetric solution is an accurate representation of the 3-D stress field. Both the 2-D and 3-D solutions show very similar variation in stress along the pin axial direction. The 3-D solution variation in the hoop direction though is not nearly so symmetric. Considering the pin only, radial stress is reasonably consistent about the circumference in the hoop direction. This may be explained simply by the fact that a summation of the compressive forces at the pin-web interface both on top and on bottom of the pin must be equal. Since this is the case however, the thin section of material on the web above the pin is stretched significantly more than the thick web material below the pin. The 2-D model assumption does use a web outer diameter equal to the thin section of web on top of the pin, and so maximum hoop stress on both models are close in magnitude.

The second topic that must be discussed is the use of the principle of super-position of the 3-D alternating results with the 2-D assembly stress since the loaded press-fit joint behavior is non-linear. A non-linear response of the local stress values at the SCA to joint loading is created

since the severity of the 'kink' at the SCA is changed as local interface radial stress σ_r increases (LC4) or decreases (LC3).

For both 3-D models it has been demonstrated that as the location A1 on the bottom of the pin is loaded in tensile axial stress, while at the same time joint loading produces reduced local radial stress, the local stress maximum values converge for a lower element size *h*. So, for the 3-D solutions there is confidence in the stress state at A1 for LC3, even for a larger element size *h* (see section 5.3.3).

However, for the case when a 'kink' is still present during the application of the operating loads, (LC2 and L4), there is greater error in the FEM solution because element size *h* may not match well with the stress gradient present. The highly compressive stress state is of interest because of the potentially damaging sub-surface stresses created, and also because of the wear that may result with any relative motion or joint slippage present in conjunction with the high radial interface stress.

Since location A1 was identified as the most likely location to have a durability issue on the full 3-D model, the alternating stress state at this location is studied for the entire series of plots. Also, the one-quarter model results are provided for the bottom of pin location.

In Fig.5.5.1, alternating σ_r stress from the 3-D models are super-imposed on the 2-D assembly stress. Note that both the 3-D and the 2-D plus 3-D results are contained. Notice that the scatter is greater for the combined solution, as all solutions start at the same 2-D assembly radial stress value for LC1. The radial stress component that is super-imposed on this LC1 'starting position' is the 3-D determined change in radial stress. Therefore the 3-D plus 2-D solution will follow exactly the 3-D solution trends for each time step. Note that the hoop stress plot is not provided since it is very similar in form to the radial stress data shown in Fig.5.5.1; so far hoop and radial stress values have shown to track one another.

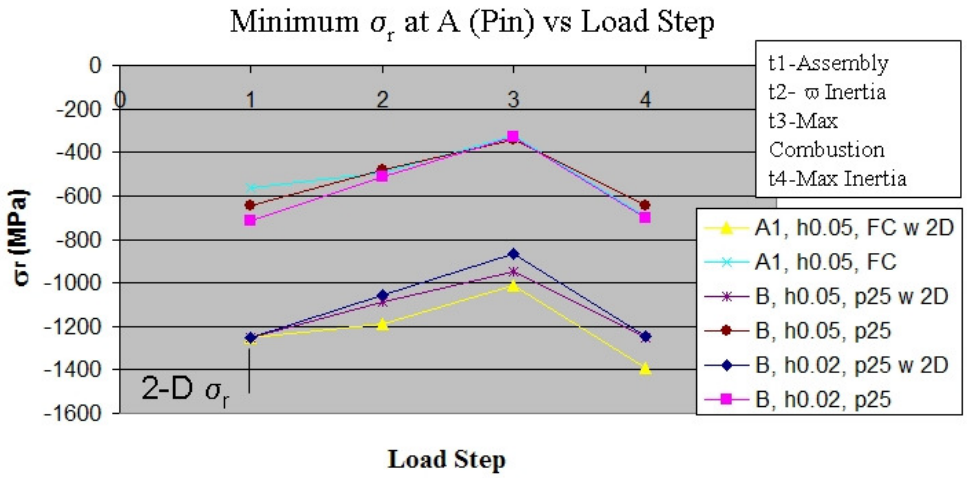

Figure 5.5.1 A plot of 3-D model σ_r at *A* versus load considering 2-D assembly stresses.

Figure 5.5.2 plots σ_z for the combined and 3-D model solutions across the four load steps; the combined model trends match the 3-D solutions. Note that there has been much discussion already in the previous sections about the difference in calculation of maximum σ_z at location *C* for the one-quarter and full 3-D geometry models. Mesh refinement and proximity to the neutral axis were listed as factors creating lower σ_z calculated for the full model.

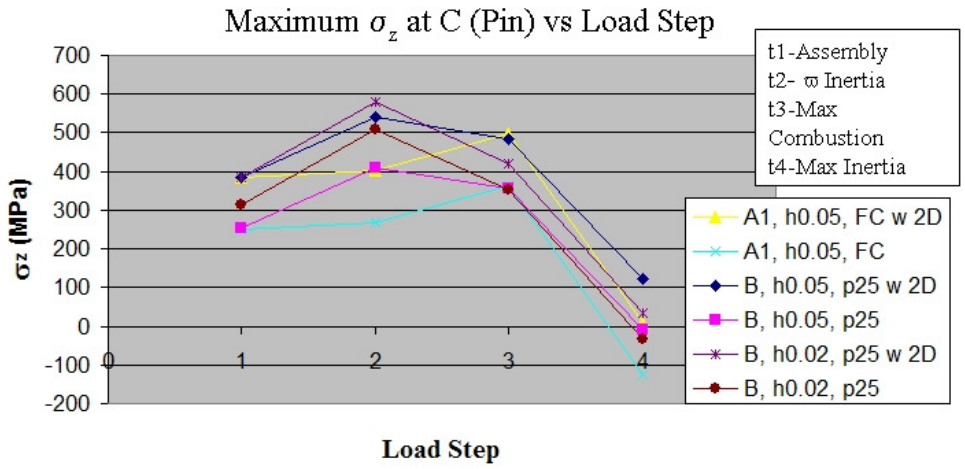

Figure 5.5.2 A plot of 3-D model σ_z at C versus load using the 2-D assembly state.

The shear stress at location *B* is examined next in Fig.5.5.3, and very good trend matching is shown with the combined 2-D plus 3-D solutions. Maximum sub-surface shear stress has been shown to be not as sensitive to mesh refinement as some of the other local maximum stress values.

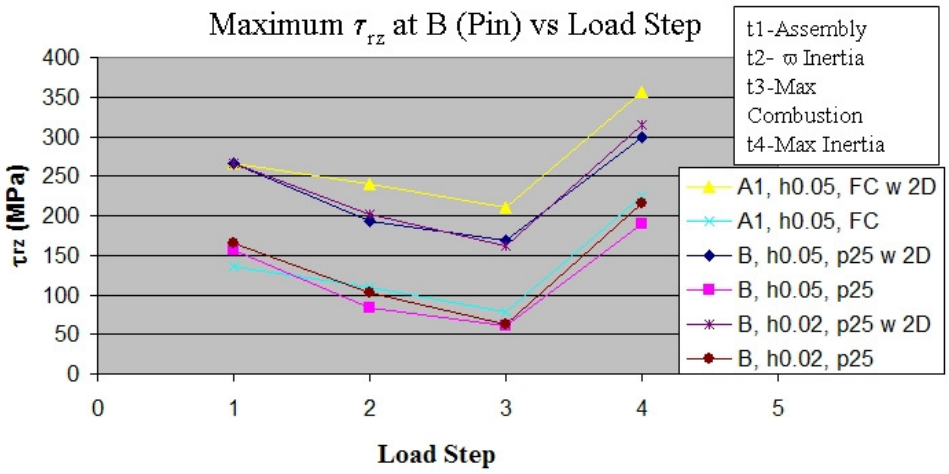

Figure 5.5.3 A plot of 3-D model τ_{rz} at *B* versus load using the 2-D assembly state.

Equivalent stress at location *B* just below the pin OD surface is examined next in Fig.5.5.4. Since the equivalent stress value is calculated from the direct and shear stress components, a calculation of the super-position σ_{von} at load steps 2 thru 4 is required using the super-position component stresses from the 3-D model. Note that only the full 3-D model uses this approach. The 2-D plus 3-D data points published in Fig.5.5.4 for the one-quarter model simply add the magnitudes of 2-D and 3-D σ_{von} stress. Lower equivalent stress is shown to be produced when calculated for the full model using the 2-D plus 3-D component stresses. This fact is logical since the equivalent stress calculation uses the 'the square root of a sum of squares' style of formula, which would decrease the effect of any stress variation added to any larger base stress values.

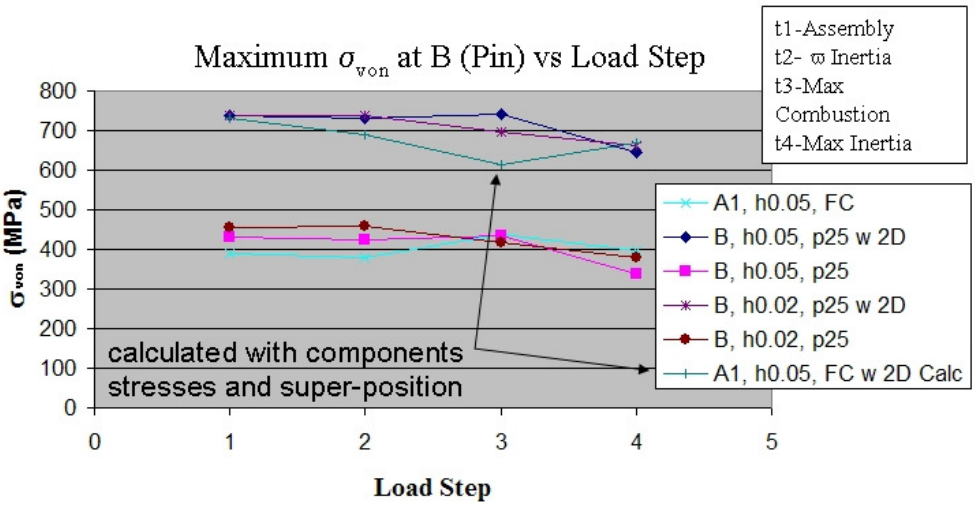

Figure 5.5.4 A plot of 3-D model σ_{von} at *B* versus load using the 2-D assembly state.

Finally equivalent stress in the web at location *A* is plotted in Fig.5.5.5 for the 3-D and the combined 2-D plus 3-D solutions. At time of this writing, data was not available to calculate the combined equivalent stress values at LC2 thru LC4 using component stress information. High web equivalent stress is shown to match the trend of the 3-D data.

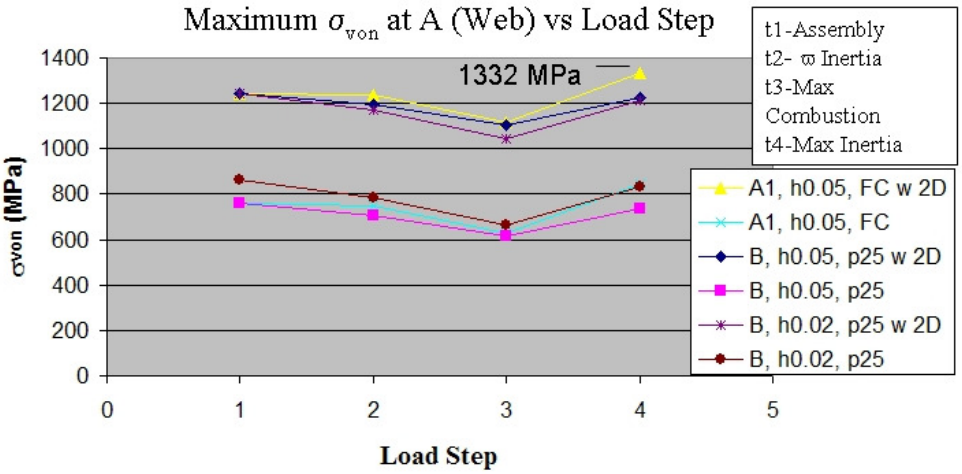

Figure 5.5.5 A plot of 3-D model σ_{VM} at *A* (web) versus load using a 2-D assembly.

5.6 Evaluation Of Material Yielding For the Operating Condition

In section 4.2.6 the stress state was examined for any material yielding at the SCA generated by the press-fit assembly. The stress magnitudes plus the size of the discontinuity were examined, and it was demonstrated that the area of high sub-surface stresses fall within the depth of strengthened material. Also it was demonstrated that the maximum values calculated were below the range of calculated yield strength (see section 4.1). Table 4.2.1 lists the mechanical properties of the crankshaft, and calculates a yield strength ranging from 1348 to 1448 MPa for the high strength, case hardened material.

The stress field at the SCA does not change a great deal in size or shape while under operating loads, as is shown throughout Chapter 5. The largest area of high stress identified in chapter 4 for the 2-D assembly model is web area on top of the pin. Figure 5.6.1 shows the web area on top of the pin at location A2 for load case 4; the size of the high stress area (0.4 mm) falls within the depth of hardened material (1.0 mm). Note a scaling of 0 to 785 MPa, which is the core material S_{YS}, is used to demonstrate this fact.

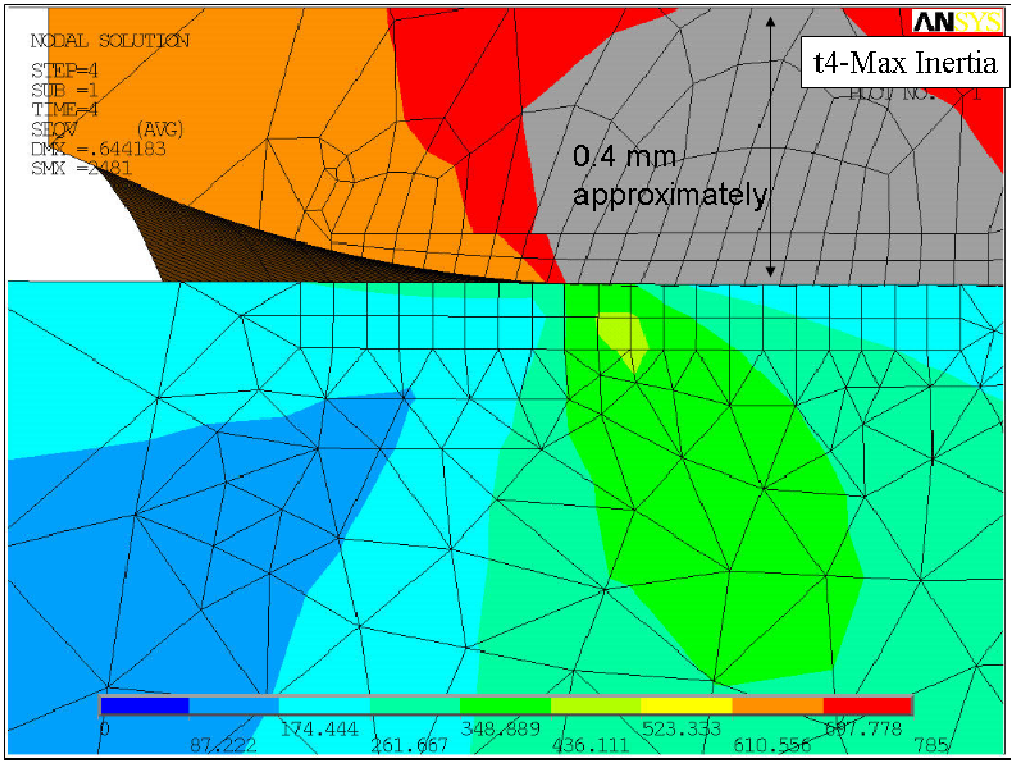

Figure 5.6.1 A plot of LC4 σ_{VM} on the web at location A2 for the full 3-D model.

Note that even with the combined 2-D plus 3-D calculated stress which is provided in the previous section 5.5, this area will still fall within the case depth. The super-position approach only affects the local maximum value; this shape and size of the stress field and the general stress values away from the maximum location will not change significantly.

The combined 2-D plus 3-D component stress values examined in section 5.6 all fall under the yield strength value of 1348 MPa, excluding the radial stress value at *A*. The highly compressive σ_r value on the pin of near 1400 MPa in Fig.5.5.1 which is calculated at A1 for the combined solution is less of a concern since it is compressive. Typically a significantly larger value of compressive stress is allowed in design if also the equivalent stress falls within the yield value. Note that for the case, the pin maximum equivalent stress at location *B* does not climb above 800 MPa for the combined 2-D plus 3-D solution.

Finally the web equivalent stress value at *A* calculated for the combined solution at location A1 as shown in Fig.5.5.6 as 1332 MPa for LC4. This value falls very close to yielding, and should examined closer with a more refined element size. If yielding occurs, a solution using elastic-plastic material models is required. Potentially any yielding of the web will relieve some of the pin local elastic stresses at the SC

6 Verification of the Numerical Models

Experimental verification is a necessary step in any mature FEA and design process. Well correlated FEA models lead to more realistic results of the computer simulation which may drive the process to save time in redesign, validation, and tooling costs. In this chapter some basic experimental data is presented to gain confidence in the finite element models created for the press-fit and operating load problem sets.

6.1 Experimental Verification Of The Press-Fit Operation

The average radial contact pressure in a press-fit joint may be used to calculate the torque retention capability of a joint, with knowledge of the surface coefficient of friction. The 3-D numerical models presented show that radial stress is fairly constant about the circumferential direction of the bore. Though, the radial stress distribution has sharp stress concentrations at each end of the web / pin interface.

Experimental tests may be conducted to measure the torque carrying capability of the press-fit joint in a multi-piece crankshaft. The crankshaft web with the cylindrical hole may be held rigidly, but not directly on the thin web section above the pressed in pin. A pure torque load is then input on the assembled crankshaft about the pin axis (on the integral pin web) using a hydraulic powered rotary actuator. The torque input is applied at a slow rate until the joint breaks free, with the pin twisting in the web cylindrical hole. Figure 6.1.1 shows typical test data [34] indicating that the joint broke free when a torque of 1092 Nm was applied.

The error in the average radial contact pressure (calculated using an average surface friction value) with this experimental method may be minimized by collecting many test samples. Pin outer diameter and web inner diameter need to be measured so that variation in radial interference values track with the variation in break free twist. This test also generates confidence in the surface friction coefficient values.

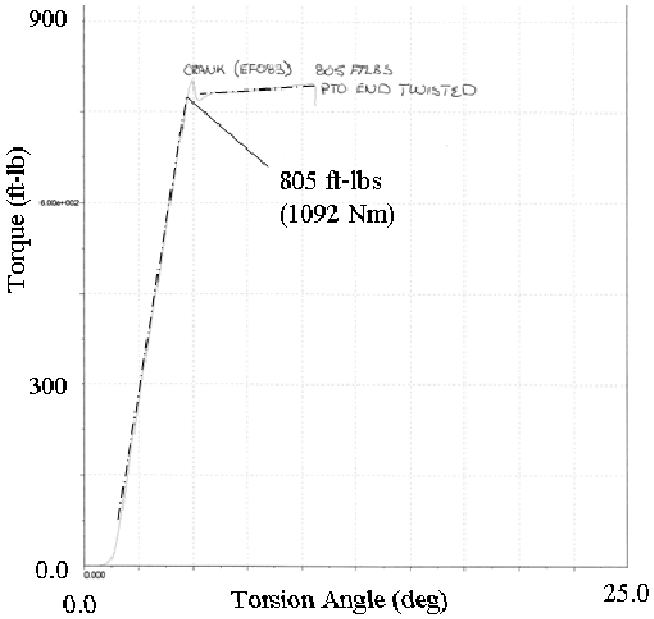

Figure 6.1.1 Experimental torque data for a crankshaft 'twist test' [34].

The average radial stress predicted by this test should be slightly greater than the FEM or Lame based average value calculated in the center of the press-fit area, away from the edges. The higher contact pressures at the edges present greater torque resistance than the average value used in the simple hand calculation, and so the opposition to twist free with the actual test will be slightly greater than the design calculation.

A static 'push out' test may also be used to check the joint integrity. This test approach and reasoning is very similar to the twist test, except the assembled crankshaft is pushed apart very slowly using a hydraulic ram, and the maximum push-out force in monitored. This push-out force may be used to with the joint geometry, average design radial contact pressure, and average coefficient of friction to check joint integrity.

6.2 Experimental Verification Of Operating Behavior

Dynamic operating strain on the crankshaft may be measured for design validation and numerical model correlation. In particular, the general numerical methods that are applied to crankshaft systems, as presented in this thesis, can be verified.

Note the test data presented here is not from the crankshaft design studied in this research paper, at the time of writing this test data was not available yet. The goal of the data presented in this section is to show general correlation of the numerical methods applied. The experimental work presented here is not the work of the author and is courtesy of Polaris testing department.

General measurements that ensure crankshaft overall behavior is understood are also required to calibrate the numerical methods. If the overall behavior of the crankshaft can be calculated with FEM and confirmed with experimental data, then the computer simulation tests may be used to calculate other design information which may not be measured. For example, it is up to the finite model to calculate the detailed stresses at the press-fit joint.

Note that the strain field is difficult to measure near the press-fit joint during engine operation because of design space restrictions. The ideal measurement would be axial strain measured on the free surface of the crankpin, very near to the SCA location. However, the connecting rod and thrust washer allow little room for strain gauges.

Some typical crankshaft strain measurements are shown in Fig.6.2.1. Dynamic strain is measured on the main shaft just inboard of the PTO taper on which the drive clutch mounts. Axial strain is measured in 4 equally spaced locations, at top dead center (TDC), 90 degrees after TDC, bottom dead center (BDC), and 90 degrees before TDC (see Fig.B.2). This set of gauges will measure general bending in the main shaft to capture the strain field induced by belt forces on the PTO end. Since these strain gauges are sensitive to any bending of the main shaft, their presence will also check for any modal response issues in the crankshaft.

Another torsion strain gauge may be set on that same main shaft on the PTO end of the crankshaft, as the PTO end bearing spacing allows. The gages measure shear strain, in the theta direction which is sensitive to torque output to the clutch on the end of the crankshaft.

The dynamic strain is measured at specific engine operating conditions that are key to understanding the design performance. Usually the operating conditions measured place the crankshaft in a ‘worst condition’ to create the highest strain response. These conditions include

maximum engine speed combined with full torque load; maximum engine torque with low engine speed; a high engine speed (over-wind) with low load, and also possibly a moderate engine load while the engine is ran across the full range of engine speed.

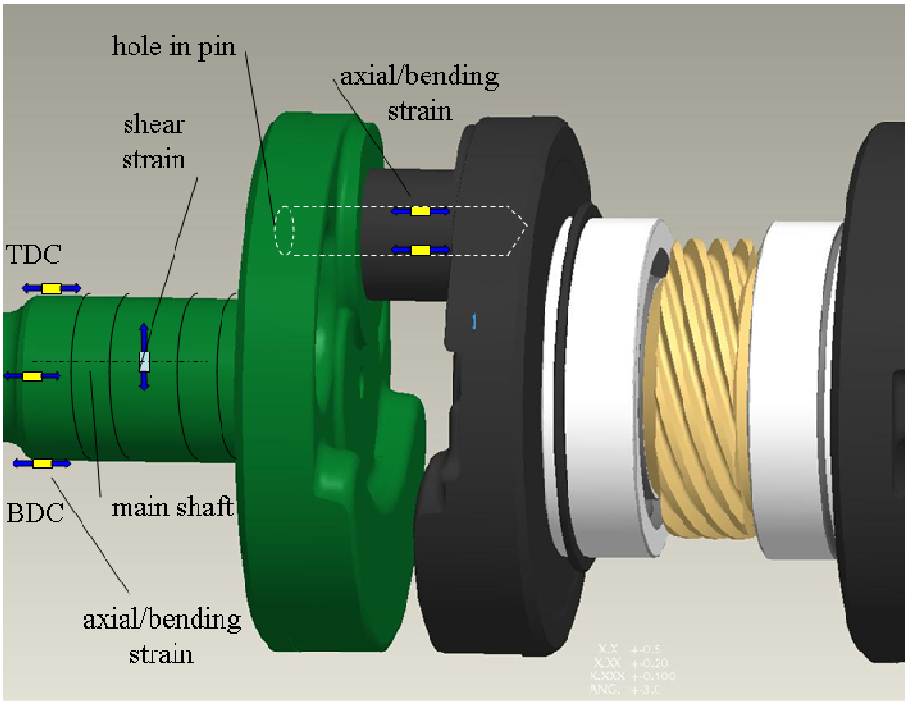

Figure 6.2.1 Typical locations for strain measurement on a multi-piece crankshaft.

Figure 6.2.2 displays two cycles of typical dynamic strain measured on the PTO end of a crankshaft for a maximum load / high engine speed situation [35]. A minimum compressive axial strain of -700 με is measured at the 90 degrees ATDC position gauge location (on the PTO end as shown in Fig.6.2.1). Figure 6.2.3 shows an axial stress plot from a full 3-D FEM model which correlates well to the measured strain. Strain in the FEM model is measured at -690 με for the application of a typical 'PTO crankpin maximum combustion' load case (which is LC3 in chapter 5). The strain measurement location is sensitive to belt force, and so this correlation may be thought of as a check on the belt load calculations, as well as crankshaft structural behavior. The strain measured on the PTO end of the crankshaft may also be calibrated to output as a (CVT) belt force. Belt force calculated by the MBD model, which is a FE model input as well, may be correlated to this experimental measurement.

Note that the crankshaft design from which these measurements were taken is very similar to that studied in this research. As well, the numerical approach used to model this crankshaft is identical to those implemented here. The method of using static load cases described in section 5.1 are used to check that the crankshaft meets the intended stress targets for adequate design life.

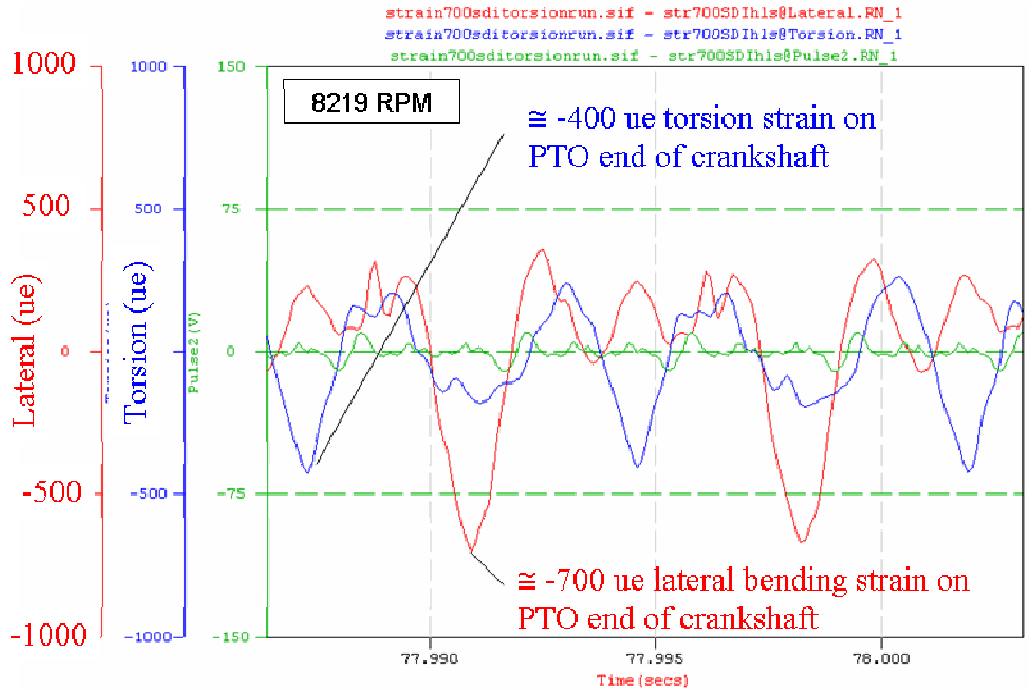

Figure 6.2.2 Typical dynamic strain measured on the PTO end of the crankshaft [35].

If reasonable, a third set of gages may be placed to measure distortion of the PTO crankpin as shown in Fig.6.2.1. However, wire routing and gauge application are a challenge to do so. These gauges are placed on an internal cylindrical hole in the crankpin, with the hole created by a drill machining operation specifically for the strain measurement. The gauges measure general pin bending, and are sensitive to the combustion load and the reciprocating mass load. This measurement may only occur if strain sensitivity is acceptable (the hole is large enough) while also not moving the bending natural frequencies of the crankshaft to an undesirable low value in the operating range. A finite element model containing the modified pin geometry may be required to check the feasibility prior to the test.

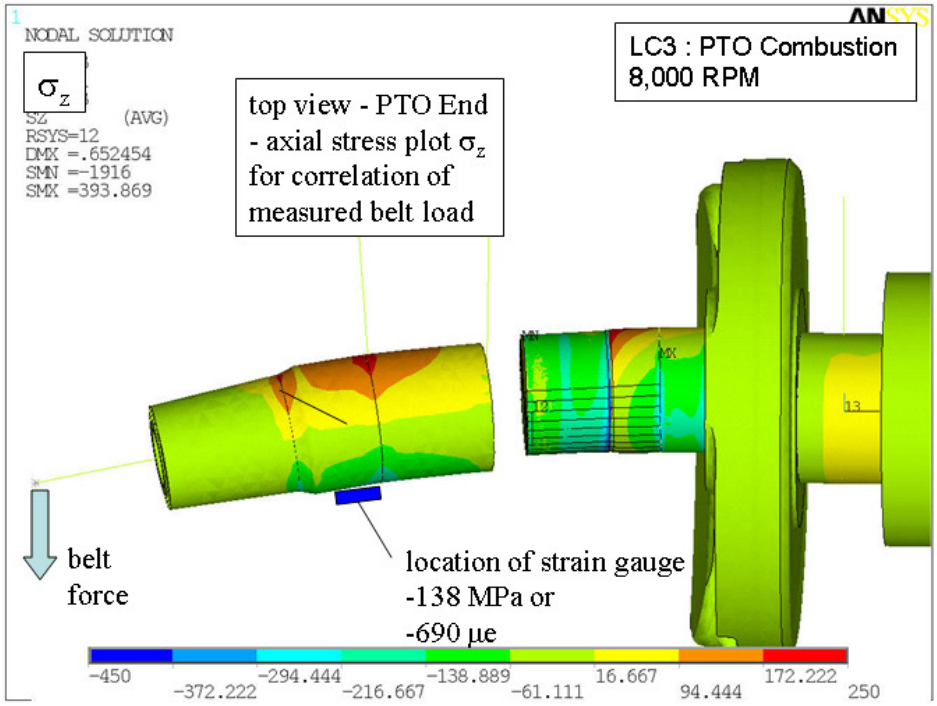

Figure 6.2.3 Axial stress results for a similar engine configuration showing correlation to the measured strain.

Figure 6.2.4 provides typical dynamic strain measured internally on a crankpin, as described above, which is calibrated as a force output [35]. The strain values may be correlated to the crankpin vertical bending predicted with the crankshaft FEM model. Strain or force data from several engine speeds and design configurations is contained in Fig. 6.2.4. Note that this strain measurement does not display the constant pin bending strains due to the rotation inertia of the crankshaft itself. This strain is considered steady state, with low variation from cycle to cycle, and is removed from the signal using a low-pass filter for this test only.

Correlation to the measured crankpin loads may be shown with the MBD model results; the calculated MBD loads at the crankpin are used as inputs to the FEM model. Figure 6.2.5 shows vertical direction crankpin loads generated for the same engine and operating conditions via the MBD model [35]. The signature of the time history loads calculated with the MBD model matches the measured data, and the maximum and minimum values fall within the range of engine configurations studied.

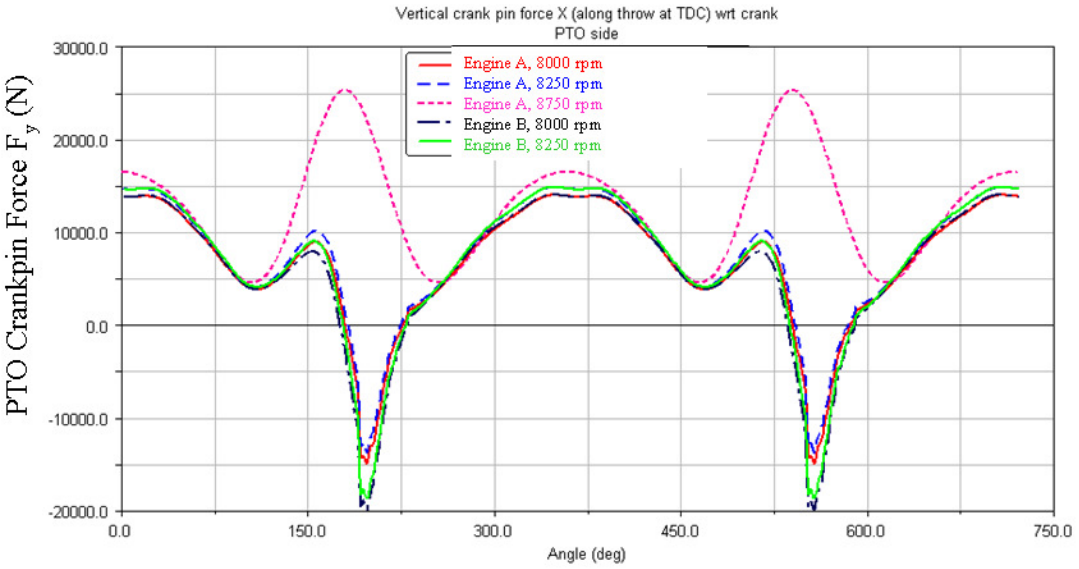

Figure 6.2.4 Dynamic experimental pin bending strain calibrated as a force output [35].

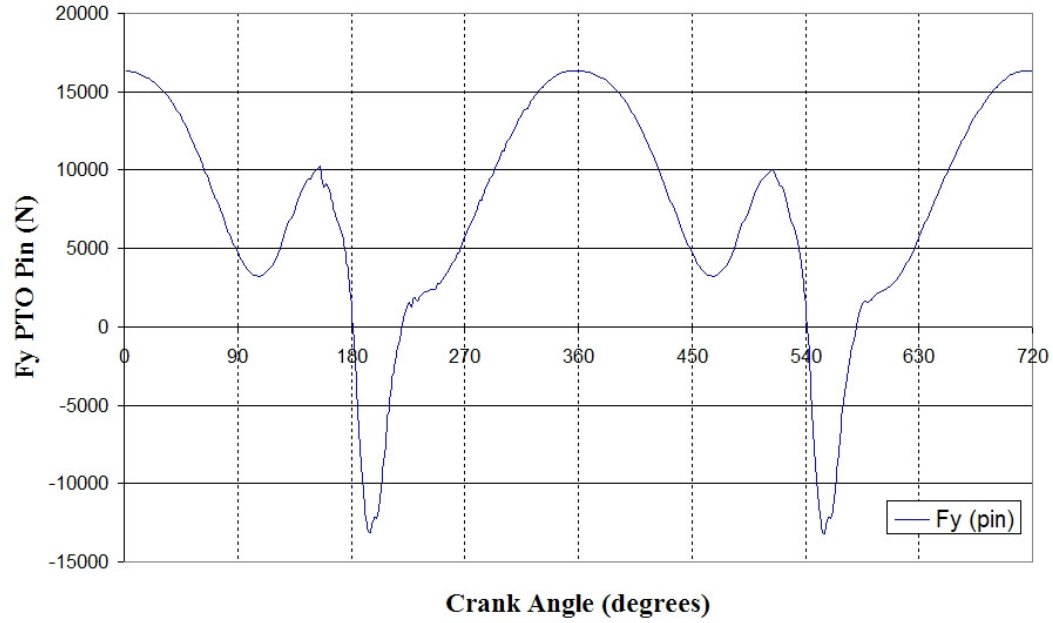

Figure 6.2.5 Dynamic crankpin Fy calculated with MBD for FEM model input [35].

An example of good correlation between dynamic measured strain and FEM for the static load case approach is given in Appendix F. The modeling approach is equal to that in this research effort for the full crankshaft model, and shows correlation in the range of 5 to 16 %, which is very acceptable.

6.3 Summary Comments Regarding Model Reliability

In this chapter some basic experimental data was presented to gain confidence in the FEM models created for the press-fit and operating load problem sets. Good correlation between measured strain on a crankshaft and calculated strain on the FEM model has been demonstrated using the methods outlined in this research work. The approach consists of static load cases which are chosen based on engineering logic and the successful implementation on other similar engine programs.

The crankshaft operates in a very dynamic environment, and so the validity of the static assumption has to be a point of concern in the FEM model reliability. Typically both dynamic and static FEM methods would be applied on a crankshaft design at appropriate junctures. However, since the behavior at the press-fit joint requires a very detailed mesh, model size and solution time only allow the evaluation of a static solution.

As mentioned in section 3.2, static FEM approaches applied to a crankshaft design evaluation typically yields a design with an extra safety margin [9]. This statement can be considered valid only if the crankshaft dynamics are not affected by natural frequencies of the crankshaft itself. In that case, dynamic FE methods must be used instead of a static approach as provided here.

As a pre-caution when employing static analysis methods only, the numerical calculation and experimental measurement of the crankshaft natural frequencies is a necessary first step to evaluate whether the static approach is sufficient. Considering all of the background information given above, it seems reasonable that an acceptable understanding of the press-fit joint is yielded by the static FEM approach used in this research body.

If dynamic methods are required to evaluate the crankshaft behavior, sub-modeling used in conjunction with a continuous material assumption at the press-fit joint could be used. The sub-modeling approach is described in section 3.2, and is an area to be discussed in chapter 11 as future work for this research effort.

The discussion above indicates that the overall structural behavior of the crankshaft is adequately described by the FEM approach used. Currently though there is a lack of fatigue data to:

1) characterize the types of fatigue failures at the press-fit joint according to the stress condition,
2) determine a good case hardened material fatigue curve, and
3) create high confidence in the design fatigue or stress targets which may be calculated with a FEM model.

Durability testing which may create actual fatigue failures in the crankshaft are required to elevate the FEM tools to the next level of reliability. The durability data points may be produced by either the engine operating or an 'equivalent damage to the operating condition' bench test. This task is to be outlined in chapter 11, Future Work.

7 Optimization Of the Press-fit Joint

7.1 General Comments Regarding Optimization

The interference fit pin joint is used in many applications in modern machine design. By reducing the magnitude of the stress concentration the life of this type of joint could be improved [18]. However, the FEM and computer simulations have to be used to design a better joint, simple formulas and engineer's intuition are usually not sufficient.

No detailed explanation of the problem of some basic press-fit design, which considers a pin inserted in to a hole with the edge finished as a round, has been available in the literature. These details have been explained in the research body presented so far. Having a better understanding of the joint's mechanics, it is worthwhile to revisit some classic solutions to the press-fit stress concentration, and how these might be applied to a multi-piece crankshaft design.

Also of note, the ‘optimized’ solutions found in the literature survey [18, 19] evaluate the assembly condition only, and do not examine operating loads. As was shown in Chapter 5, the manner in which the joint carries the load is not intuitively obvious. So, in this light it is also worthwhile to study the performance of alternative solutions under operating loads.

Lastly, since there will always be situations with high performance engines where the durability limit will be pushed, ‘back-up’ plans are important to have. These back-up plans are usually required when there is not a significant amount of design and development time left in an engine design program. So, these back-up plans need to be researched and ready for quick implementation.

7.2 Press-Fit Joint Optimization: Shoulder Solution

7.2.1 Introduction To The Shoulder Solution

The first optimization phase examines the shoulder solution to reduce the assembly stress at the press-fit SCA. The shoulder solution extends a revolved section out at the machined face of the web ID, which is flexible, and allows a more gradual change in stiffness for the press-fit joint. This style of feature can be found in machinery design for applications such as gears pressed onto shafts [36]. The details of the geometry are provided in Fig 7.2.1.1; r_{SH} is the radius of the shoulder, and t_{SH} the thickness of the shoulder in the radial direction. Note that distance 'a' is shown in Fig. 7.2.1.1 also, which is the distance from the vertical face of the shoulder to the tangent point of the 'true radius' curve on the ID surface of the web bore. The distance 'a' used in this study is equal to the value used throughout the research presented.

The shoulder feature is machined from the baseline geometry, therefore it may be added to the base design if durability issues arise through validation. If the shoulder is added external to the width of the baseline web, it extends the length of the entire engine by the radius of the shoulder, something that is not desirable from a mass and packaging standpoint. For example, a twin cylinder engine containing two shoulder features of 4.0 mm in length, the engine would grow in length by about 1.5%, resulting in an increase in mass.

Therefore, it may make the most sense to keep this shoulder feature incorporated within the width of a typical web, and deal with any decreases in crankshaft bending stiffness by other means. Introduction of the shoulder feature in this manner reduces the torque carrying capacity though; as around 10 percent of the axial length of the joint will have a somewhat reduced radial contact pressure, which is also an undesirable trade-off. Typically the interference of the joint has already been reduced to the low end of the allowable range when durability is a concern. Increasing interference to offset this loss in effective length may not be an option as the hoop stress in the web at the interface is typically already close to yield because of the low amount material in the web at the TDC (Top Dead Center) location.

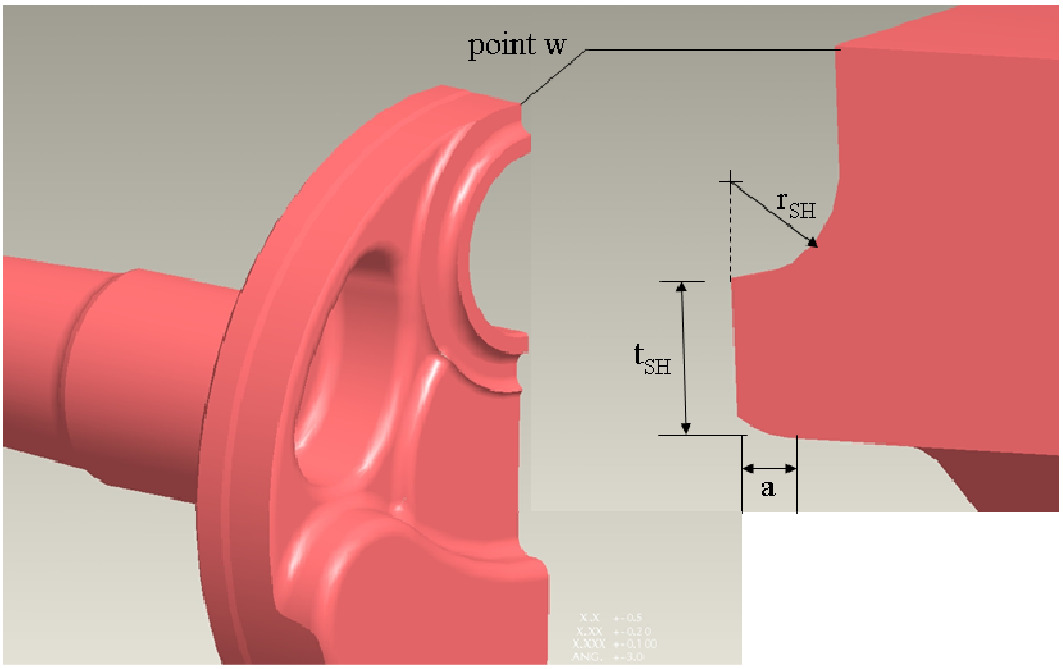

Figure 7.2.1.1 Geometry for the shoulder optimization solution.

Since the shoulder feature in this case removes web material and makes it weaker in bending, it may not be ideal as the overall crankshaft bending stiffness will be lowered and the associated bending modes of the crankshaft will also be lowered. Potentially a washer may be fastened to the web structure to add to the web bending stiffness as well as provide a low friction surface to locate and control the connecting rod axial motion.

From a practical standpoint, one concern with this design solution is a reduction in the thrust surface area available for the connecting rod washer. To overcome this issue, a washer with an ID greater than the OD of the shoulder must be used, and the washer thickness could be set equal to that of the shoulder. Care must also be taken to not reduce the shoulder thickness too much when attempting to relieve the stress concentration, creating a sharp edge that may crack easily with any machining imperfections (burrs).

7.2.2 Characteristics Of The Stress Field At The Shoulder

First the characteristics of the joint are explained for the shoulder feature. The introduction of a flexible shoulder feature reduces the local radial contact pressure at the SCA, allowing the web to expand more readily beyond the prescribed interference. Figures 7.2.2.1 and 7.2.2.2 plot radial stress for the baseline and shoulder solutions respectively using a typical interference. The minimum radial stress at the SCA is reduced to 50 percent for the chosen r_{SH} (2.0mm) and t_{SH} (1.5mm) values.

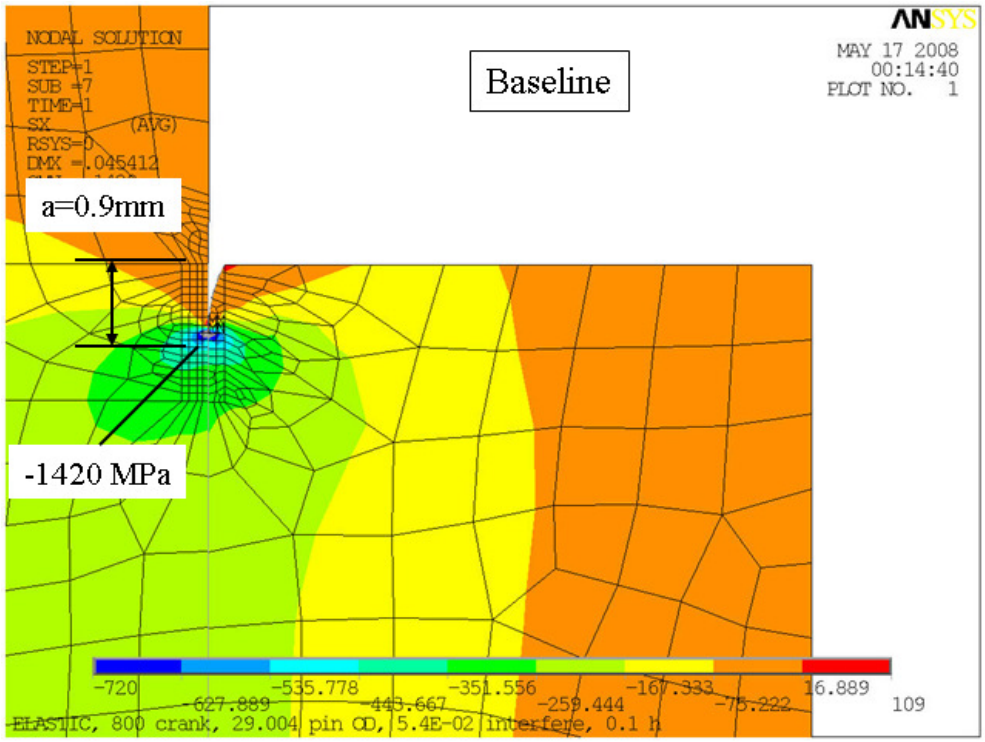

Figure 7.2.2.1 Radial stress plot, baseline (no shoulder) solution.

Next the hoop stress plot for the shoulder solution, given in Fig. 7.2.2.3, indicates a tensile stretch of the shoulder feature. High tensile stress in this area may be a concern if the value of t_{SH} becomes too thin. Higher hoop stress on the shoulder is required though to make this design approach work; the shoulder's flexibility allows for a more gradual loading of the pin.

Shear stress τ_{xy} is provided in Fig. 7.2.2.4, indicating the shear distortion band of web material (note the 50 to 84 MPa yellow-green stress scale color) that must maintain continuity between the shoulder and the main body of the web. The shoulder radial and hoop direction

displacements are higher than the main body displacements, and there is a transition zone of shear distortion, similar in nature to that described in section 4.3.4.

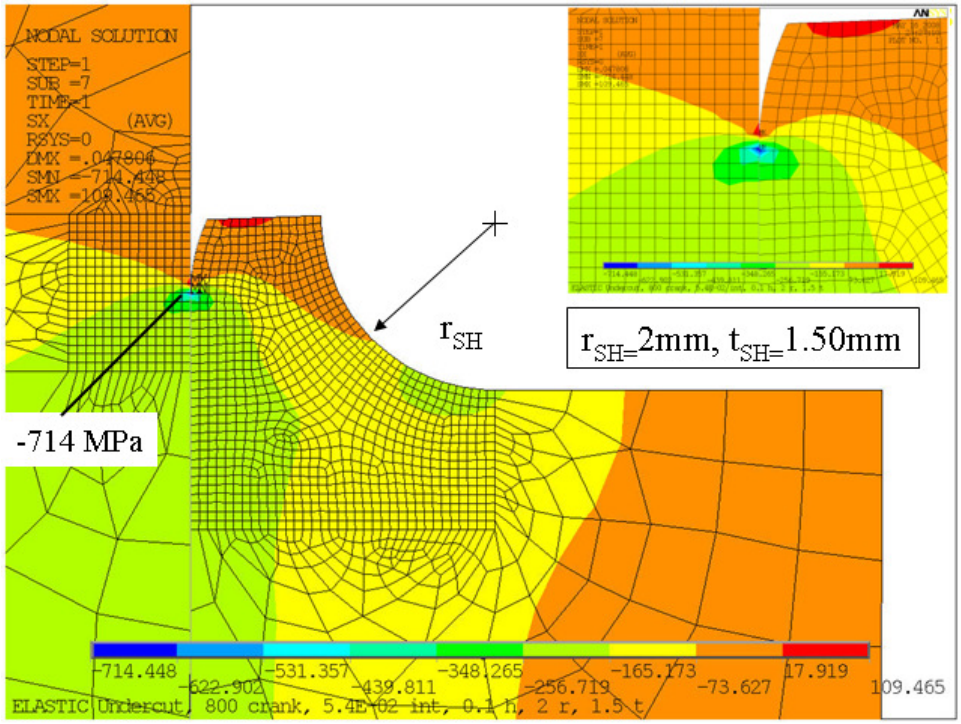

Figure 7.2.2.2 Radial stress plot with shoulder solution for a typical interference fit.

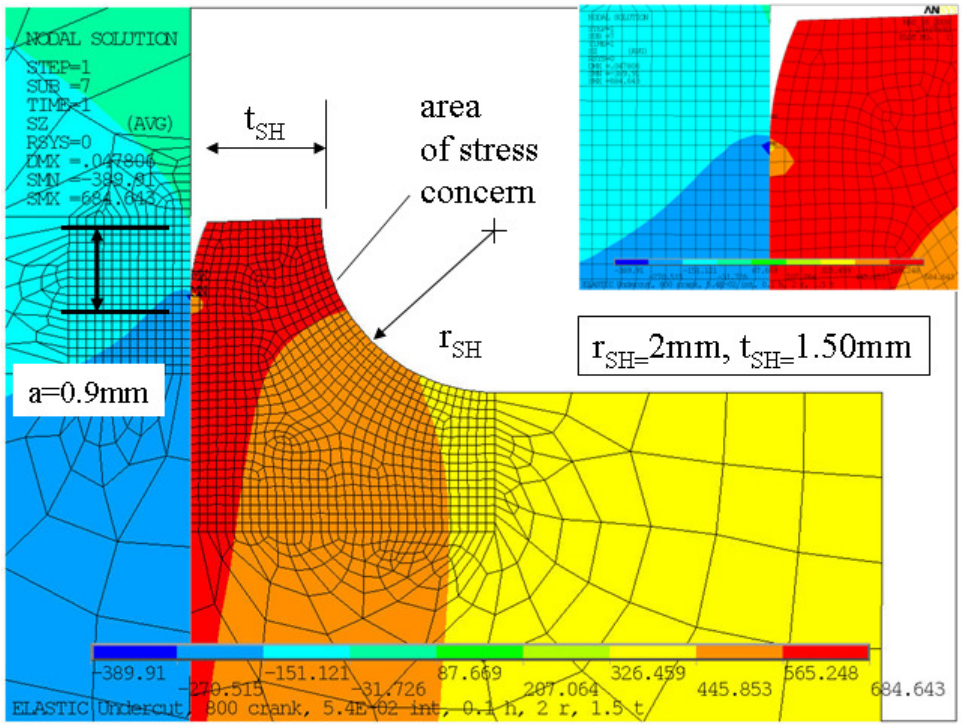

Figure 7.2.2.3 Hoop stress plotted at the SCA for the shoulder solution.

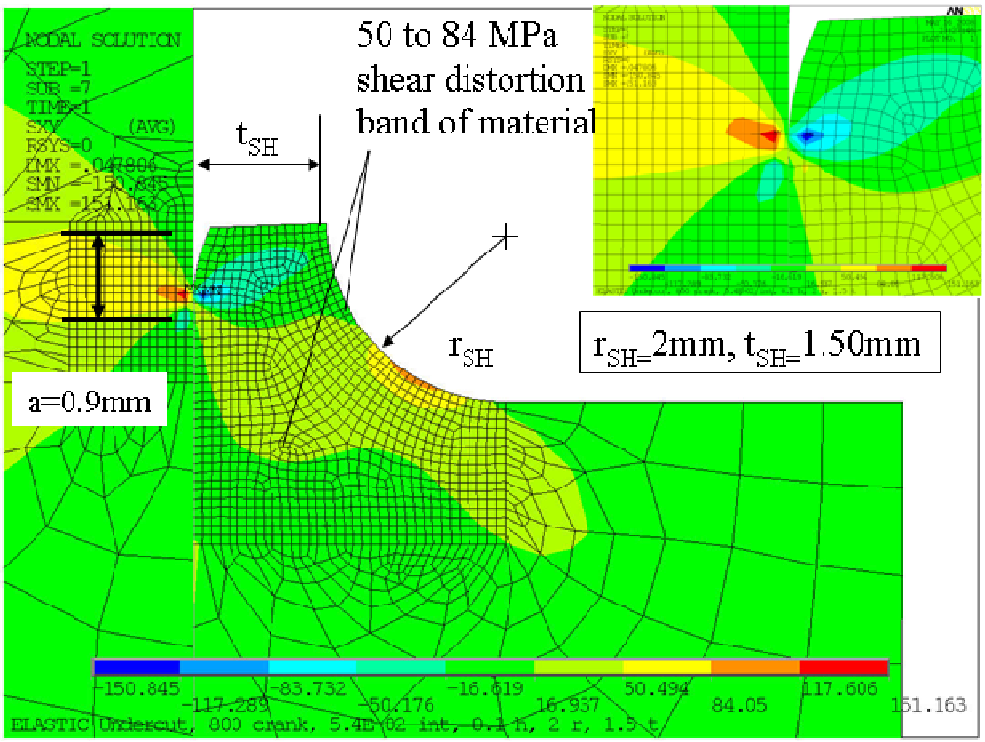

Figure 7.2.2.4 Shear stress plotted at the SCA for the shoulder solution.

7.2.3 Optimization Of The Shoulder Feature

The optimization results for a shoulder solution are now presented for the 2-D axisymmetric FEM model. The two parameters of the optimization study for the shoulder solution are as follows:

1) t_{SH}, the shoulder thickness.
2) r_{SH}, the radius of the circular fillet between the shoulder and the web.

Optimization trends for variation of t_{SH} and r_{SH} are shown in Fig.7.2.3.1 to Fig 7.2.3.4. The plots contain values of local maximum stress at the SCA for varying t_{SH} while r_{SH} is held constant.

The variation in pin minimum radial stress at the SCA shown in Fig.7.2.3.1 indicates that a lower r_{SH} values, the shoulder is not that effective. The effectiveness of the shoulder solution seems to be related to the relative size of r_{SH} and a. Between r_{SH} equals 1 and 2 mm, the shoulder becomes much more effective. The shoulder feature simply must reduce stiffness past the point

of radial contact at the interface, which is driven by the distance 'a'. Pin maximum equivalent stress shows similar trends in Fig. 7.2.3.2

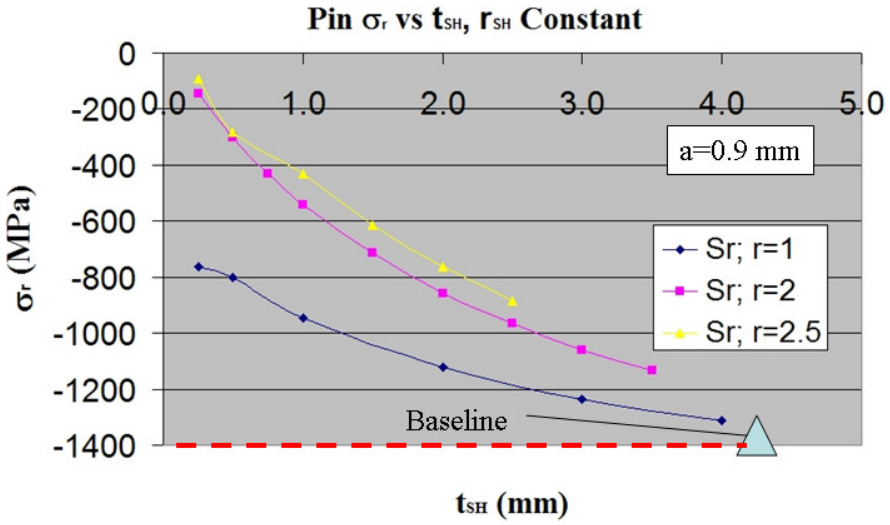

Figure 7.2.3.1 Variation in pin σ_r (at *A*) with t_{SH} for a constant shoulder radius.

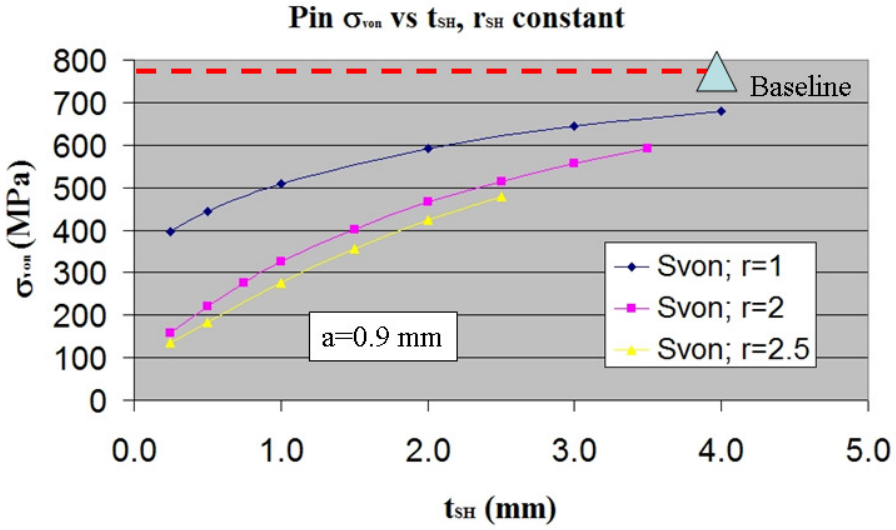

Figure 7.2.3.2 Variation in pin σ_{VM} (at B) with t_{SH} for a constant shoulder radius.

Figure 7.2.3.3 plots maximum web Von Mises stress at location *A* for varying t_{SH} and constant r_{SH}. This maximum stress at the surface is relieved by the shoulder feature which gradually changes stiffness, and eliminates the sudden change in stress. Again, it is demonstrated that in general the radius r_{SH} must be greater in size than the true radius distance 'a' to create the

preferential gradual change in stiffness. Since a = 0.9 mm for all studies, Fig.7.2.3.3 shows clearly that when r_{SH} and 'a' are approximately equal, the shoulder feature does not help to lower stress on the web. As r_{SH} increases past 'a', there is a sizeable impact on the stress magnitudes of the web.

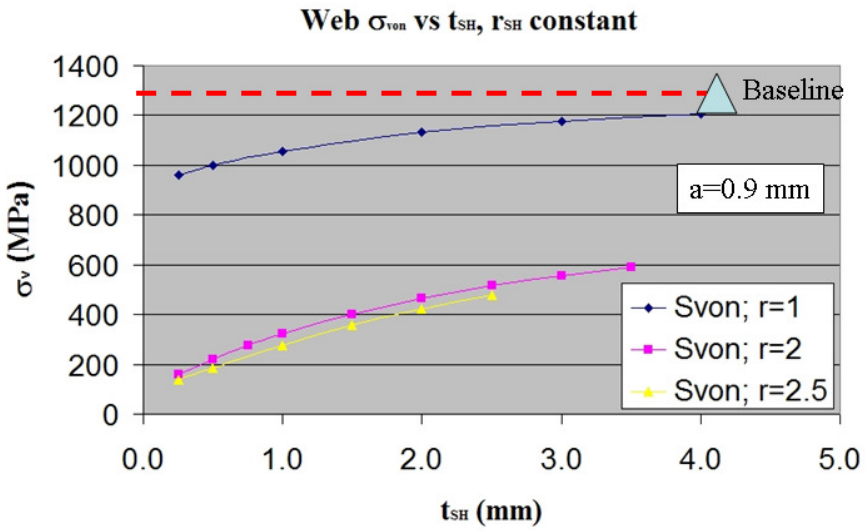

Figure 7.2.3.3 Variation in web σ_{VM} (at *A*) with t_{SH} for a constant shoulder radius.

The equivalent stress variation in the shoulder fillet is plotted in Fig.7.2.3.4. The stress there is much more sensitive to the thickness t_{SH} of the shoulder than to the radius size r_{SH}. As the shoulder thickness decreases, it flexes more and stress levels increase.

When choosing a design, care must be taken to balance relief of the stress concentration at *A* (on the pin) with increasing stress levels created on the shoulder. Note the radial stresses on the shoulder fillet radius are compressive in nature, while the hoop stress created are tensile.

To pick an optimum configuration, the stress state must be considered for assembly and operating conditions. It is relatively efficient to study the stress state for assembly with a 2-D model. In comparison the operating condition stresses must be studied with a 3-D model, research work which requires a substantially greater computational effort. Therefore, an improved solution will be chosen based on 1) the 2-D optimization of the assembly stress, plus 2) engineering judgment will be used with respect to the general stress distributions calculated

for operating loads. The area on the web where the shoulder feature would be created exhibits a low stress conditions on the baseline web geometry for evaluation under the operating load conditions.

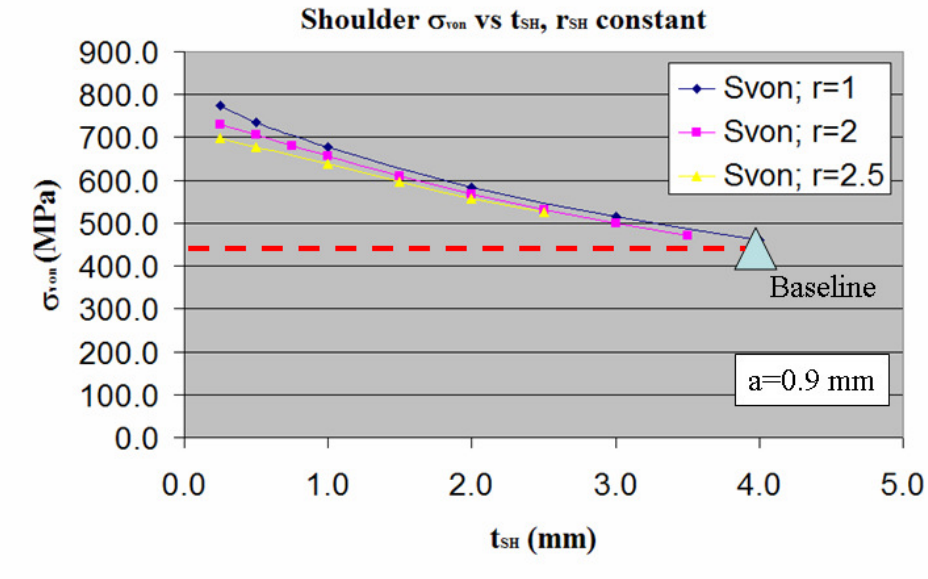

Fig. 7.2.3.4 Variation in shoulder radius σ_{VM} with t_{SH} for a constant shoulder radius.

In conclusion, the following configuration is chosen; r_{SH}=2.0mm, and t_{SH}=1.5mm. Using r_{SH} equals 2.0mm helps minimize the impact of the shoulder feature on the length of the press-fit joint, as the curves for r_{SH} equals 2.0 and 2.5 mm do not differ that greatly for any of the stress measures plotted. Shoulder thickness t_{SH} equals 1.5 mm is chosen so that the feature here retains a practical thickness, yet still offers a reduction in the (radial) stress concentration by 50%.

7.3 Press-Fit Joint Optimization: Undercut Solution

7.3.1 General Description

The next optimization phase examines the undercut feature, which removes a circular segment of material from the end surface of the web, directly above the area of the singularity. This solution, as shown in Fig.7.3.1.1, is ideal for a crankshaft, as it may be added at any point (ie. later) in the design process if need be. Prior to examining the numerical data, there are several concerns to acknowledge.

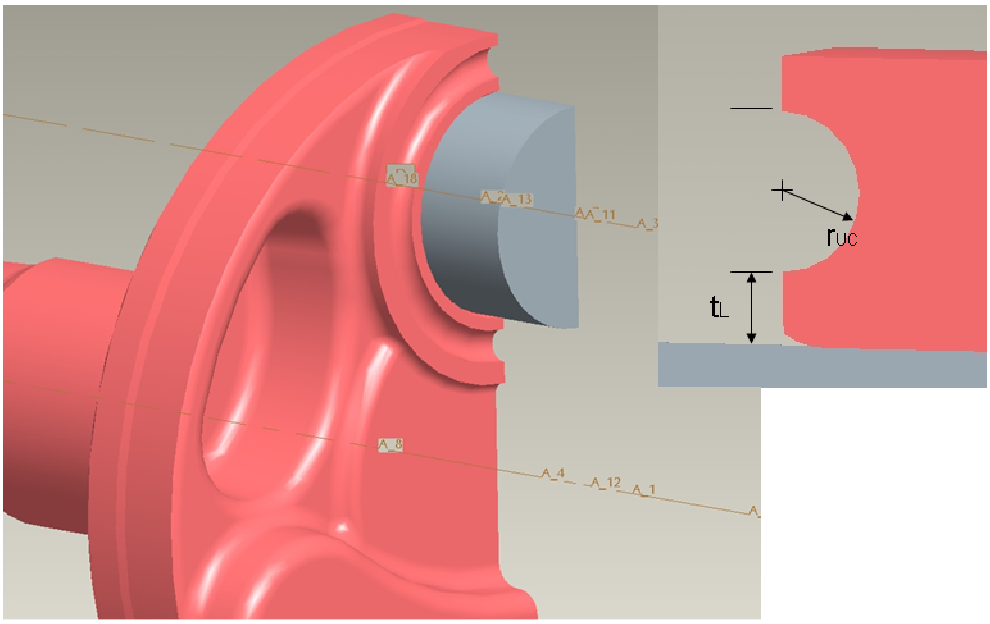

Figure 7.3.1.1 The geometry describing the undercut optimization solution.

From a practical standpoint, one concern with this design solution applied to crankshafts is a reduction in the thrust surface area available for the Connecting Rod washer. A 'half moon' bushing or washer may fill this void created by the under cut to increase the thrust face surface area. Care must also be taken to not reduce the 'lip' thickness t_L to a point that burrs from the machining operation will induce early cracking.

If the area of the cut removed is large, it will reduce the effective length of the press-fit joint, which is also an undesirable trade-off. Typically the interference of the joint has already been reduced to the low end of the allowable range when durability is a concern, as mentioned in section 7.2.

7.3.2 Assembly Optimization Of The Undercut Solution

The 2-D axisymmetric model was used again for examination of the press-fit problem, employing an undercut geometry shape at the SCA area. All configurations studied had the same true radius parameter values employed previously in this research. Figure 7.3.1.1 above includes locations of the parameters of the optimization study for the under cut solution; the undercut 'lip' thickness t_{UC} is the distance between the web ID and the lowest point on the cut, while r_{UC} is the radius of the half circle cut of material removed.

To show stress sensitivity to the undercut feature, three design iterations are examined in brief. Design 1 (Fig. 7.3.2.1) uses an undercut radius r_{UC} equals 2.0 mm and a lip thickness t_{UC} equals 1.5 mm. Designs 2 and 3 have lip thickness values t_{UC} of 1.0 and 0.50 mm respectively, all using a constant undercut size, r_{UC} equals 2.0 mm. For design 3, with t_{UC} equals 0.5 mm, the local maximum radial stress at the SCA has been reduced to a value of 36% of the original.

As the undercut moves closer to the SCA (see design 2 in Fig.7.3.2.2), the pin radial loading at the interface shifts inwards, away from the end. This occurs at the distance r_{UC} approximately, which is the length of relief the undercut provides. The axial stress plot provided for design 3 in Fig.7.3.2.4 supports this fact, as the axial direction stress on the interface requires the normal direction radial stress to carry load through friction at the interface.

Figure 7.3.2.5 plots hoop stress due to assembly for design 3, for which high tensile hoop stress at the flexible lip indicates that it stretches more readily, which relieves the stress concentration at the SCA. A shear distortion across a band of web material (see a design 3 plot of τ_{xy} Fig.7.3.2.5) just below the undercut is required to allow this lip to stretch in the hoop direction and displace in the radial direction.

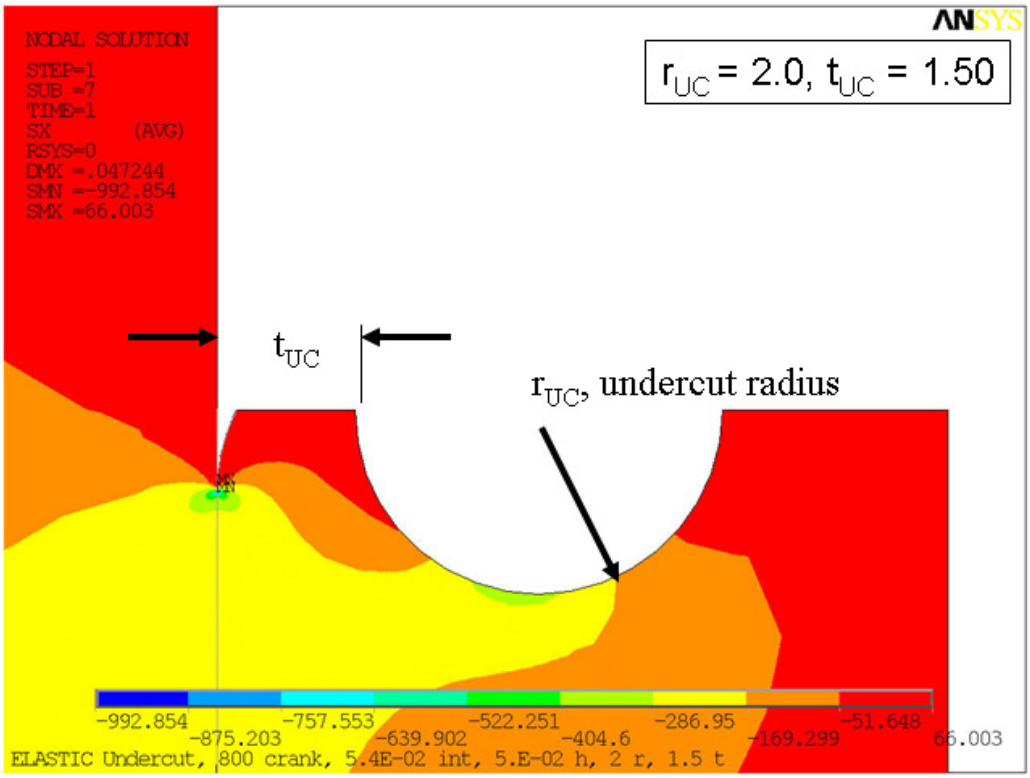

Figure 7.3.2.1 Radial stress plot, undercut geometry design 1.

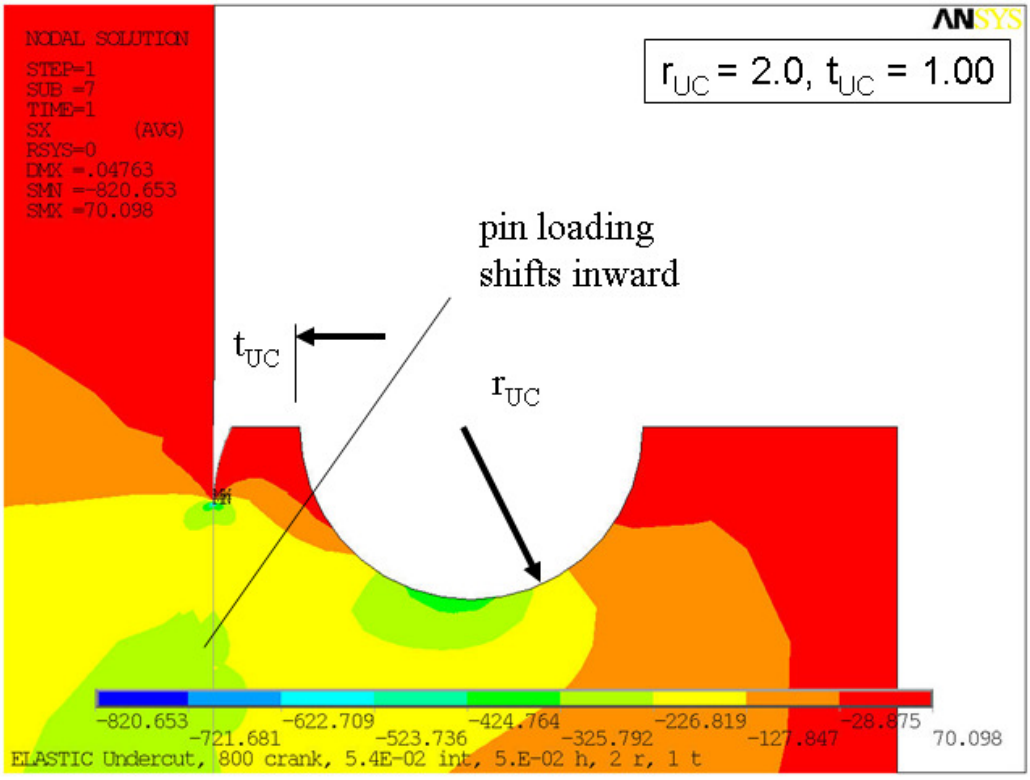

Figure 7.3.2.2 Radial stress plot, undercut geometry design 2.

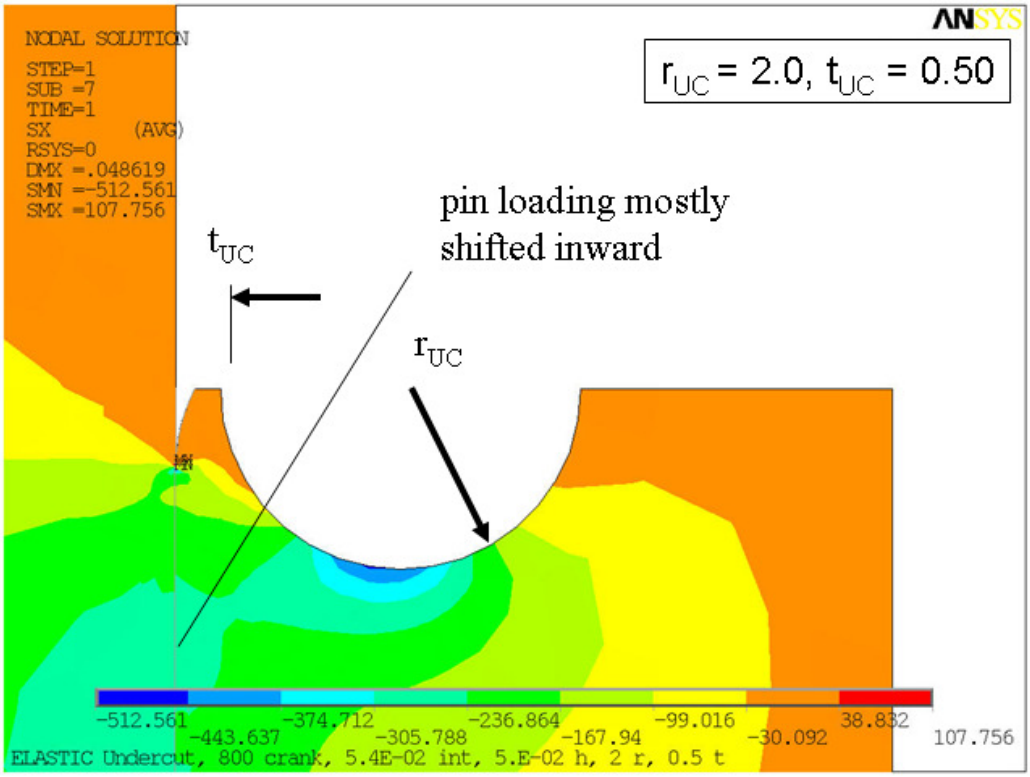

Figure 7.3.2.3 Radial stress plot, undercut geometry design 3.

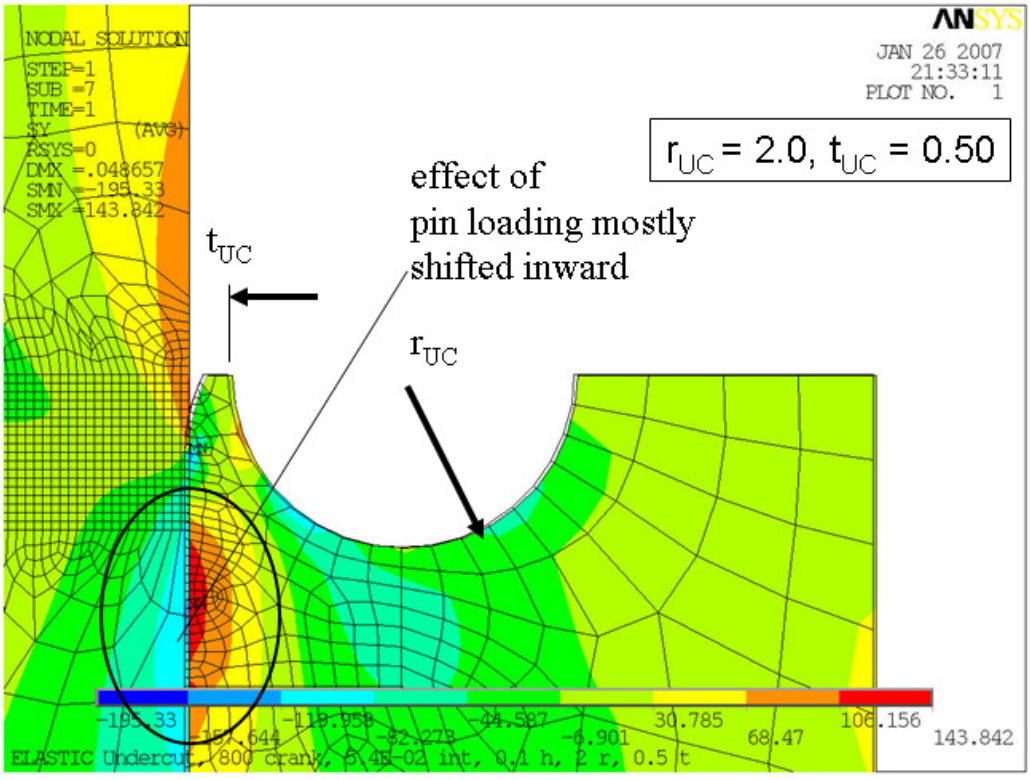

Figure 7.3.2.4 Axial stress plot, undercut geometry design 3.

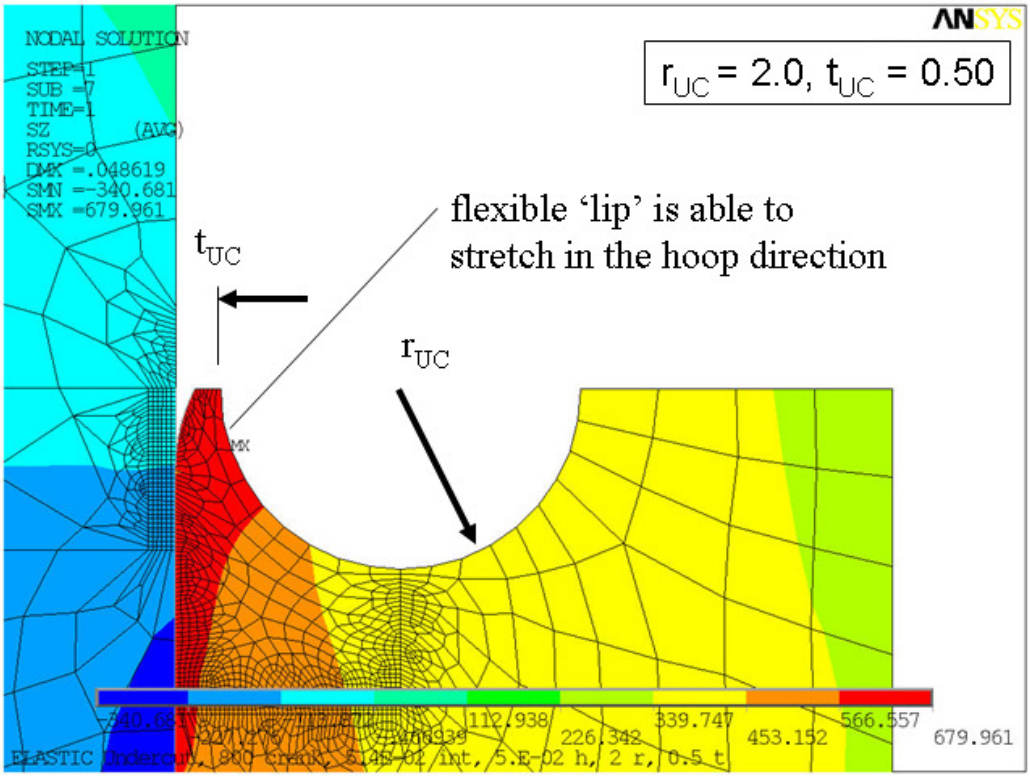

Figure 7.3.2.5 Hoop stress plot, undercut geometry design 3.

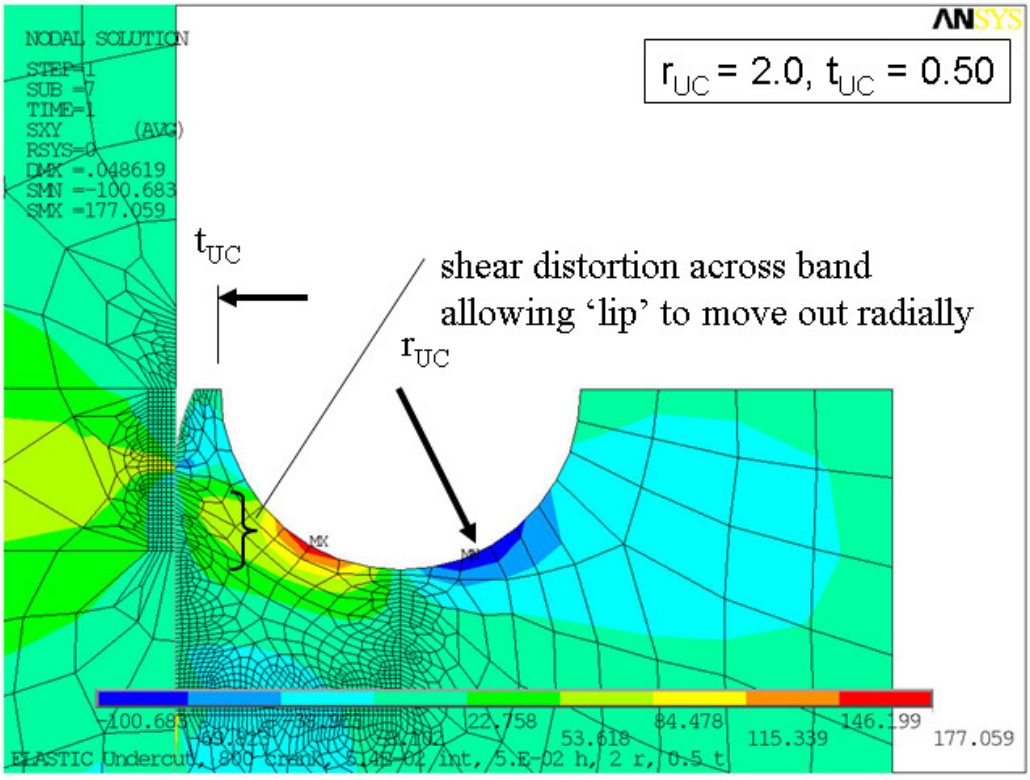

Figure 7.3.2.6 Shear stress plot, undercut geometry design 3.

There is a significant reduction in the in equivalent stress at the SCA location (Fig.7.3.2.7) when compared to the baseline solution in Chapter 4. Local maximum stresses are lower, and the undercut feature creates a wider axial distribution of stress.

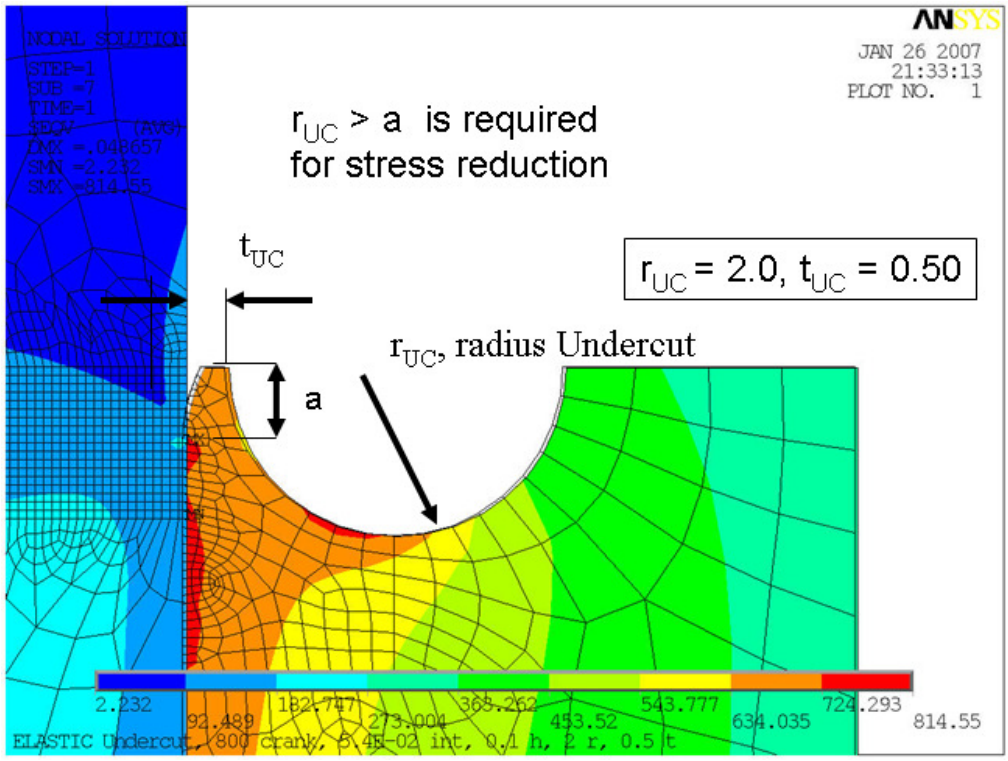

Figure 7.3.2.7 Von Mises stress plot, undercut geometry design 3.

Optimization trends for variation of t_{UC} and r_{UC} are shown in Figs. 7.3.2.8 thru 7.3.2.11.

Figure 7.3.2.8 plots minimum pin radial stress at location *A* for decreasing lip thickness over constant groove sizes. The undercut feature quickly begins reducing the minimum radial stress, even at larger lip thickness values. If the undercut radius r_{UC} is larger than the true radius distance 'a' the undercut is far more effective as shown in Fig.7.3.2.8.

Next pin maximum Von Mises stress at location *B* is plotted (Fig.7.3.2.9) for the ranges of r_{UC} and t_{UC} studied. Equivalent stress is reduced with decreasing lip thickness and is shown to be much more effective for r_{UC} values greater than 1.0 mm. Again, this is dependent on the size of parameter 'a' of the true radius geometry.

Next the web maximum equivalent stress is shown for the optimization study in Fig.7.3.2.10. The maximum stress at location *A* is affected less by the presence of the undercut in comparison with the reduction in stress in the pin. Good web stress reductions are still created though near location A.

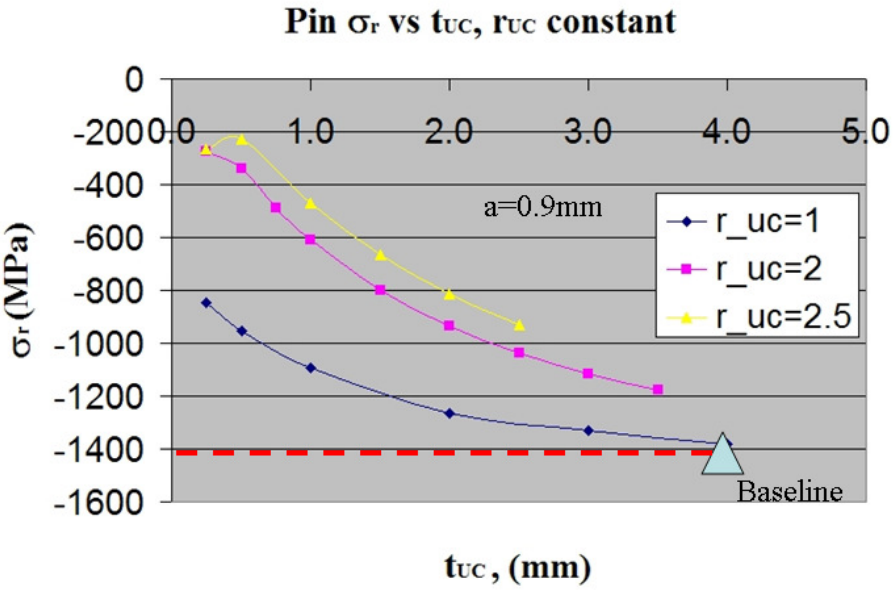

Figure 7.3.2.8 Variation of pin maximum σ_r (at *A*) with t_{UC} and constant undercut radius.

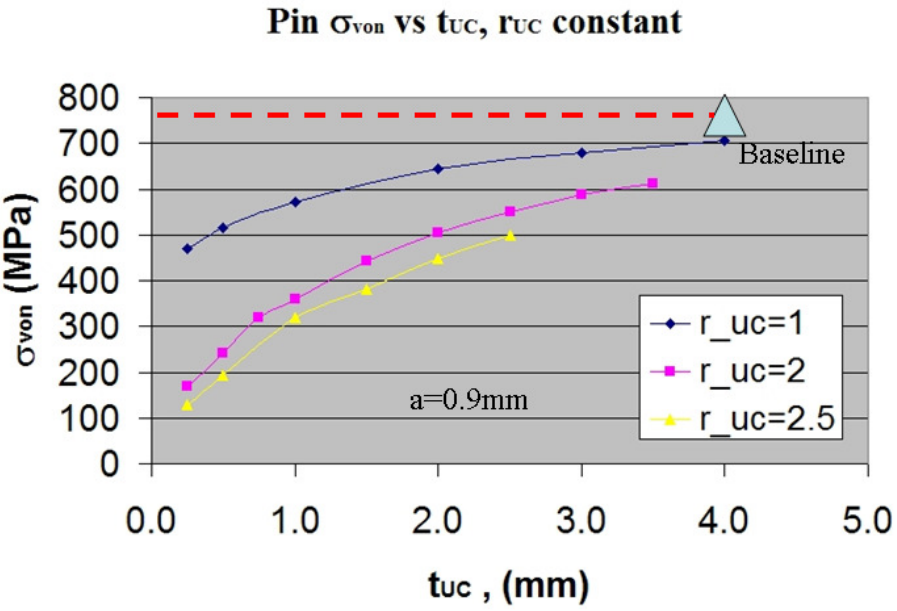

Figure 7.3.2.9 Variation of pin maximum σ_{VM} (at B) with t_{UC} and constant r_{UC}.

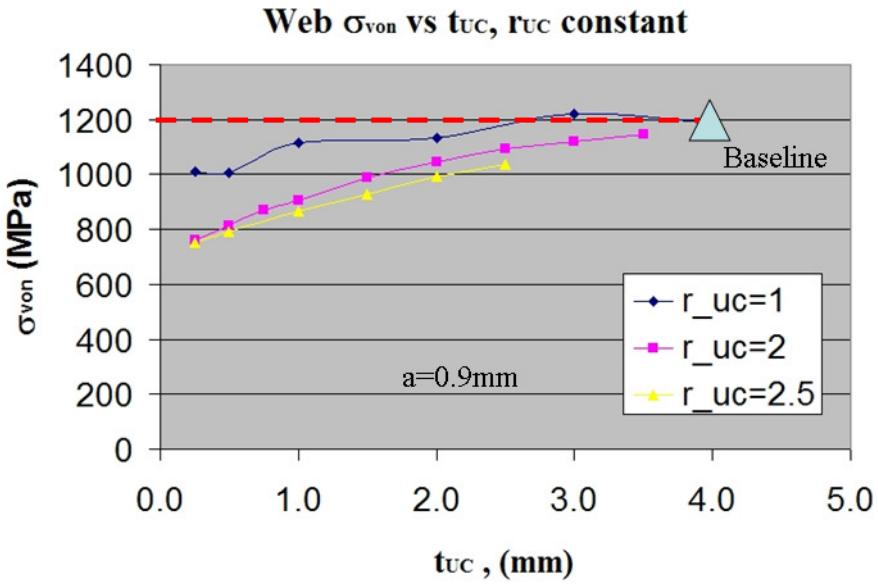

Figure 7.3.2.10 Variation of web maximum σ_{VM} (at *A*) with t_{UC} and constant r_{UC}.

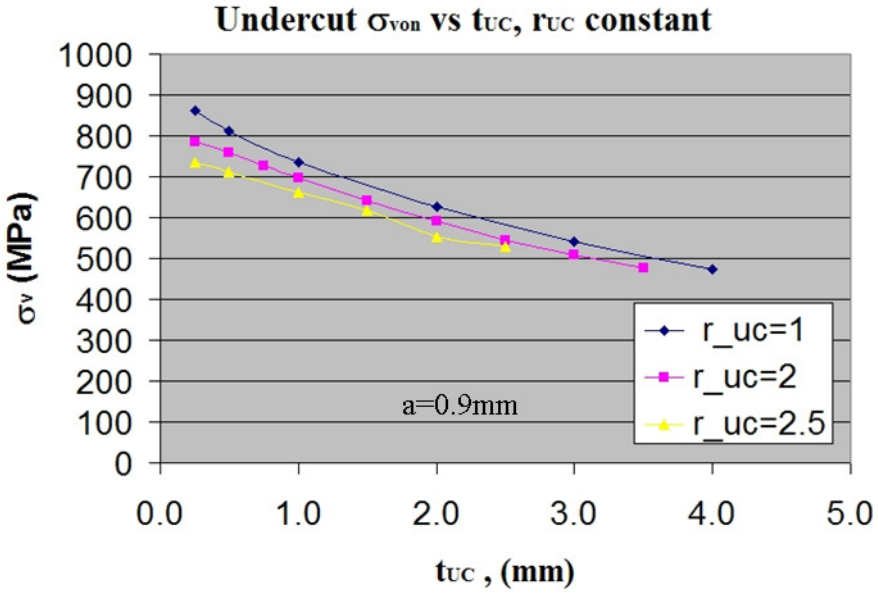

Figure 7.3.2.11 Variation in web undercut maximum σ_{VM} with t_{UC} and constant r_{UC}.

Finally, the maximum equivalent stress that occurs on the surface of the undercut was tracked for the various design combinations of r_{UC} and t_{UC} in Fig.7.3.2.11. When considering an undercut radius of 2.0 mm or greater (since the lower sizes are not as effective), at around t_{UC} equals 1mm the stresses climb to the 700 MPa region. The core material has a yield strength of 785 MPa, and

so if an untreated material condition is assumed here the lip thickness should not decrease past this point in any proposed design.

In summary, when choosing a design care must be taken to balance relief of the SCA area with the stress levels created in the web undercut. The radius r_L must be greater in size than the 'true radius' round feature of the web ID at the concentration.

If the size of the undercut removed is large, it was thought that it may reduce the effective length of the press-fit joint, which is an undesirable trade-off. However, the numerical results shown indicate that a higher average radial loading is created inboard of the undercut feature which offsets partially the reduction in joint length.

7.3.3 3-D Numerical Results For An Undercut One-quarter Bench Solution

Based on the 2-D optimization trend data, 3-D undercut geometry was studied using parameters r_{UC} equals 2.0mm and t_{UC} equals 1.0mm. This was thought to offer the best reduction in stresses at the SCA and also create aggressive but acceptable stress conditions in the undercut area. A one-quarter bench model was chosen as the FEM approach of greatest efficiency which could also describe the basic joint loading that is observed in Chapter 5. The same operating load cases presented in Chapter 5 are used here for the evaluation of the undercut geometry.

As expected, the manner in which the press-fit joint carries the operating loads does not change with the presence of the local undercut feature. The joint loading described in Chapter 5 remains, and is covered in detail in Appendix A.7.3.

Since the press-fit joint loading is well understood, the next step is to ascertain what level of mean and alternating stresses develop in the undercut region for the application of the operating loads. The general stress behavior of the undercut feature is described below in Fig. 7.3.2.7 for load step 3, the maximum combustion load case. The equivalent and maximum principal stress plots are given, as was provided for the baseline geometry in Chapter 5. Identical stress plots are provided for the other three time steps in Appendix A.7.3.

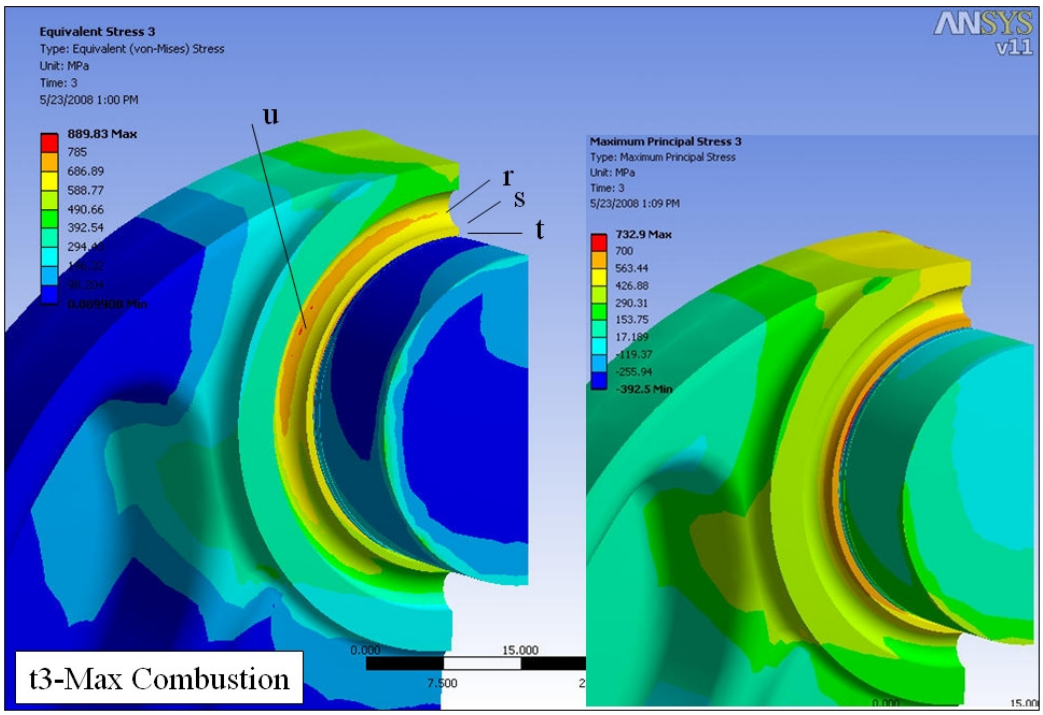

Figure 7.3.3.1 Equivalent and maximum principal stress plot isometric view, time step 3.

The stress distribution shown in Fig. 7.3.3.1 does not vary a great deal for the time steps considered, including stresses at the undercut feature. Local stress values on the undercut at locations r,s,t, and u, (see Fig. 7.3.2.7) were examined at each of the four load steps as provided in Table 7.3.3.1. The stress variation is very low, with a maximum mean (774 MPa) and alternating value (18.7 MPa) occurring at location u. Note the stress values predicted with this 3-D model match the 2-D results provided section 7.3.2.

Table 7.3.3.1 Von Mises Stress Values for the Undercut Design, Load Steps 1 Thru 4

Load Step	σ Von Mises at Location, (MPa)			
	r	s	t	u
1	460.5	647.7	684.9	755.6
2	456.3	639.4	673.8	772.5
3	443.5	623.2	656.1	792.9
4	466.6	654.7	690.9	766.8
Min	443.5	623.2	656.1	755.6
Max	466.6	654.7	690.9	792.9
Mean	455.1	639.0	673.5	774.3
Alternating	11.6	15.8	17.4	18.7

It is clear so far that the undercut feature allows more flexibility of the lip (web) to create a more gradual loading of the pin. Next the stresses on the ID of the lip (web) are examined with a maximum principal stress plot in Fig.7.3.3.2 for the combustion load case 3; two stress scales are used to clearly identify the variation in stress. Maximum P1 stress is tracked in Table 7.3.2.2 at locations l, m, and n for all load cases. A small stress variation is shown in this area also for the 4 load cases studied.

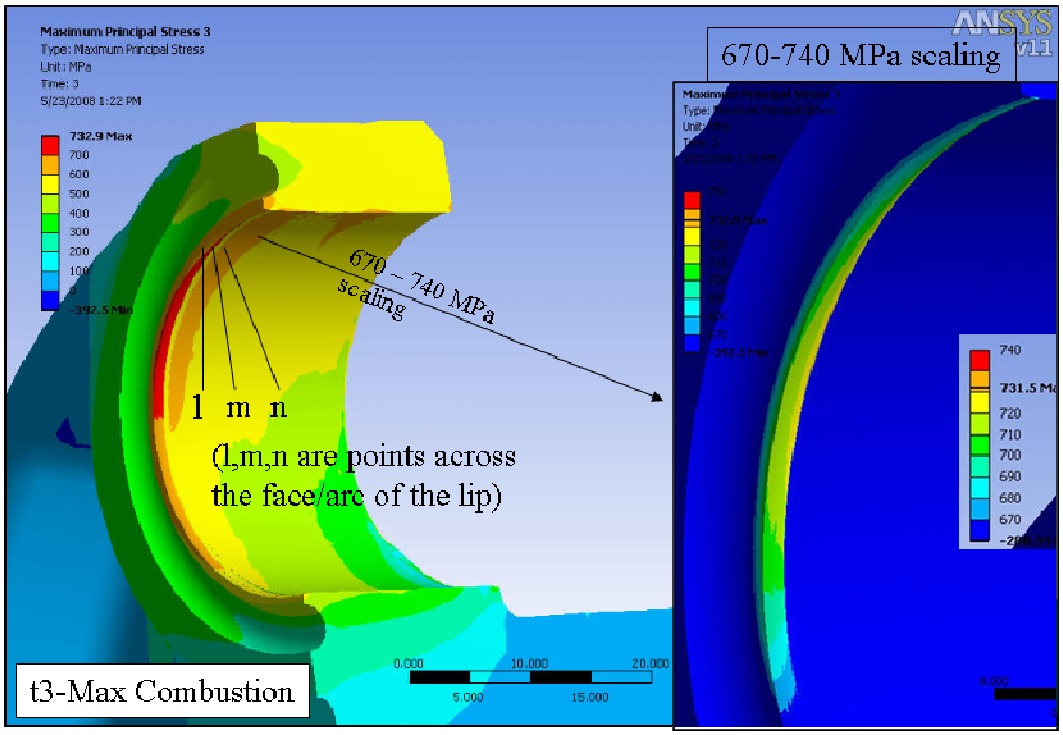

Figure 7.3.3.2 Maximum principal stress plot, time step 3.

Table 7.3.2.2 Maximum Principal Stress on the Undercut Design, Load Steps 1 to 4

Load Step	P1 at Location, (MPa)		
	l	m	n
1	702.8	706.0	722.0
2	706.2	711.8	717.8
3	710.0	716.1	732.1
4	711.6	714.3	766.8
Min	702.8	706.0	717.8
Max	711.6	716.1	766.8
Mean	707.2	711.1	742.3
Alternating	4.4	5.1	24.5

The behavior of the general stress field has now been described for the undercut, and so next the detailed evaluation of stress field at the SCA is presented. Pin radial stress at the SCA (bottom of the pin) is provided for the four load cases in Fig.7.3.3.3 (using an element size of *h* equals 0.05 mm). Figure 5.2.2.18 shows the radial stress plots for the baseline geometry, which has the same scaling. Stress magnitudes are lower for the undercut solution (by 50%), but still show the loading and unloading behavior present for the specific load cases in the baseline geometry.

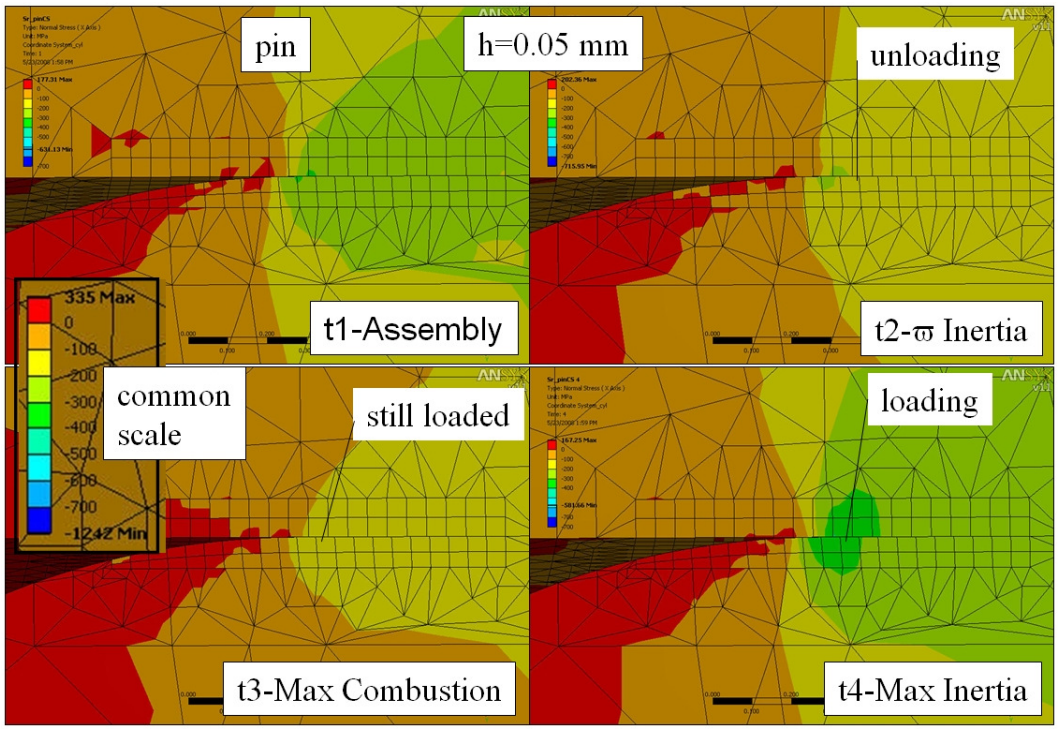

Figure 7.3.3.3 Radial stress (σ_r) plot at bottom of pin, time steps 1 thru 4.

Note the Chapter 5 results use *h* equals 0.02 mm, while the undercut results presented here use *h* equals 0.05 mm, which may produce slightly different numerical values. However, the larger element size solution used here for the undercut solution should produce acceptable accuracy since the stress gradient is considerably lower. Local maximum stress for the undercut solution with *h* equals 0.05 mm will be compared later in this section to the baseline geometry which uses several element sizes.

Figure 7.3.3.4 shows axial stress at the bottom of the pin in the vicinity of the SCA for load steps 1 thru 4. Again, stress magnitudes and local stress gradients at the SCA are reduced somewhat from the baseline geometry in chapter 5, especially for the highly compressive load step 4.

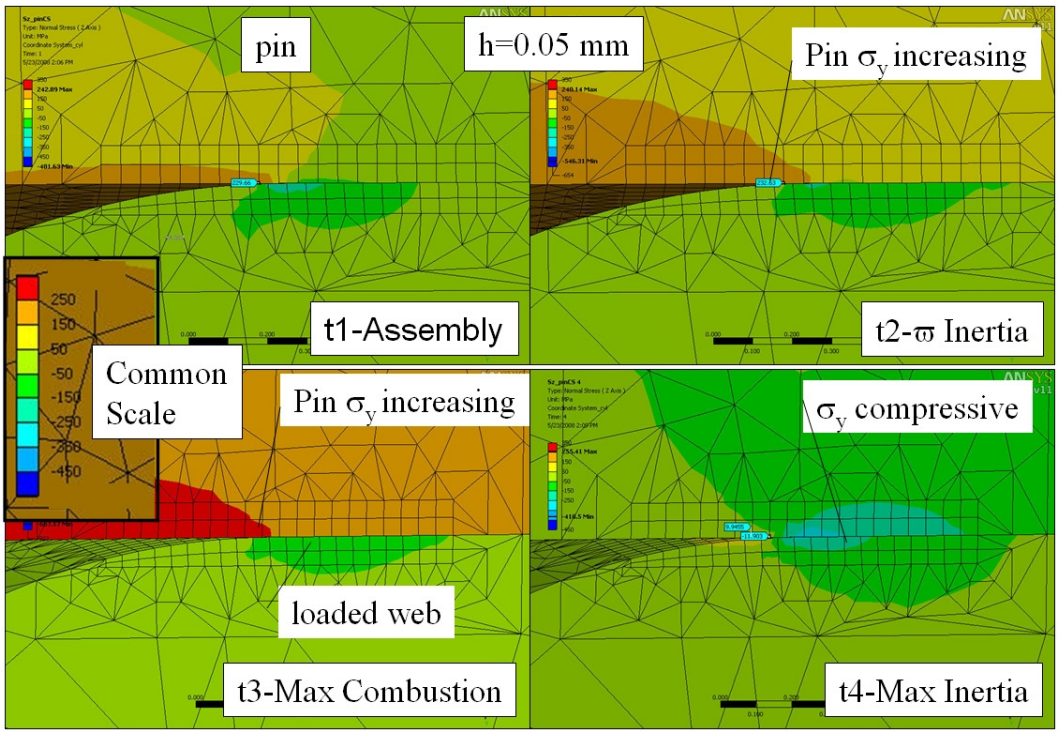

Figure 7.3.3.4 Axial stress (σ_z) plot at bottom of pin, time steps 1 thru 4.

The stress plots at the SCA above demonstrate the general decrease in stress at the SCA due to the undercut. The variation in local maximum stress values at the SCA are now compared to the baseline design. The maximum pin radial stress at *A* is plotted for the 4 time steps in Figure 7.3.3.5. The baseline shows results for *h* equals 0.1, 0.05, and 0.02 mm, while the undercut presents *h* equals 0.05 mm results. Radial stress is decreased by around 50% for load steps 1,2, and 4, but converges for the 3rd load step. The stress values converge because of the unloading present at the bottom of the pin for the combustion load step 3, at which the local stress field has a very low 'kink' which is not sensitive to the presence of the flexible undercut.

Next maximum axial stress at location *C* is shown for the baseline and undercut geometry in Fig.7.3.3.6. Axial stress is decreased with the undercut feature because of the reduction of the 'kink' in the pin during assembly (see section 4.3.4). The undercut feature also reduces maximum equivalent stress on the web at *A* by around 30%, as shown in Fig. 7.3.3.7.

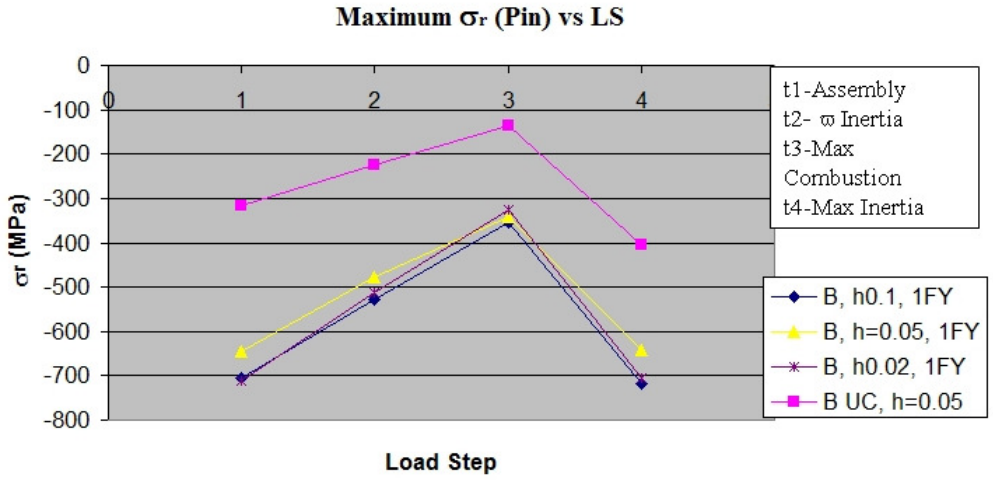

Figure 7.3.3.5 Minimum pin σ_r at *A* versus load step, baseline and undercut geometry.

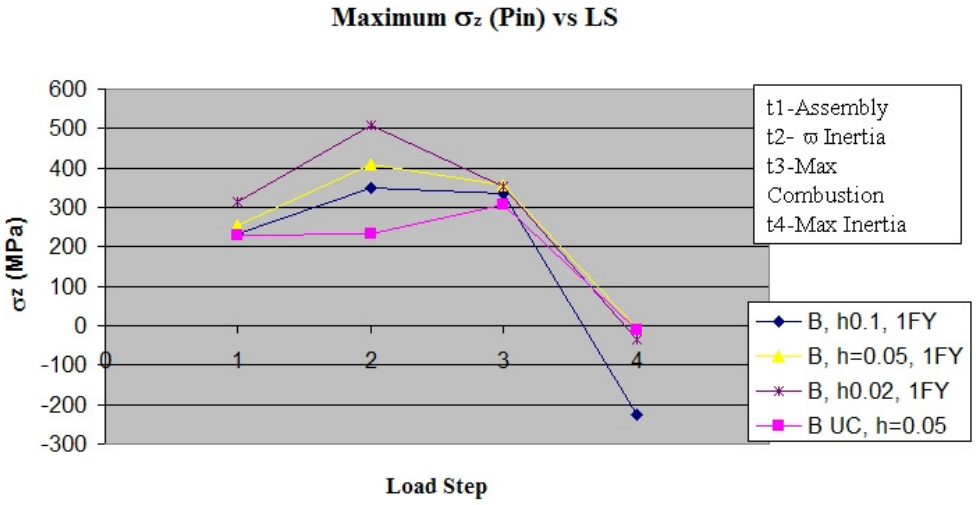

Figure 7.3.3.6 Maximum pin σ_z at *C* versus load step, baseline and undercut geometry.

Now the axial stress details at the SCA are examined on the bottom of the pin across line fg in a similar fashion to the plots in Chapter 5. Fig.7.3.3.8 plots pin surface axial stress at the SCA for load step 3 for both the undercut and baseline geometry. The axial stress distribution is similar to the baseline geometry, but the change in axial stress from location *A* to *C* is reduced in magnitude. The baseline geometry has a very large change (331 MPa), while the undercut feature (which is loaded less in the radial direction) has a more moderate change (133 MPa). A comparison of load steps 1,2, and 4 are provided in Appendix A.7.3.

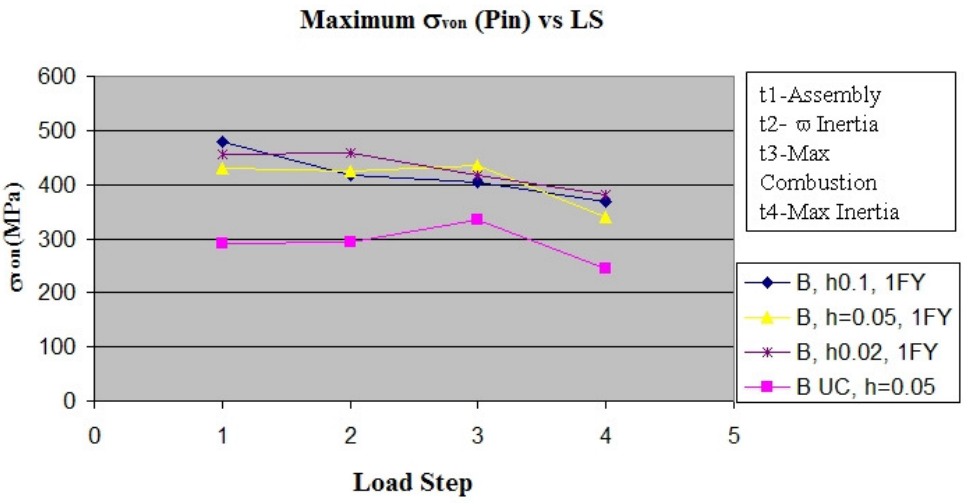

Figure 7.3.3.7 Maximum pin σ_{VM} at *A* versus load step, baseline and undercut geometry.

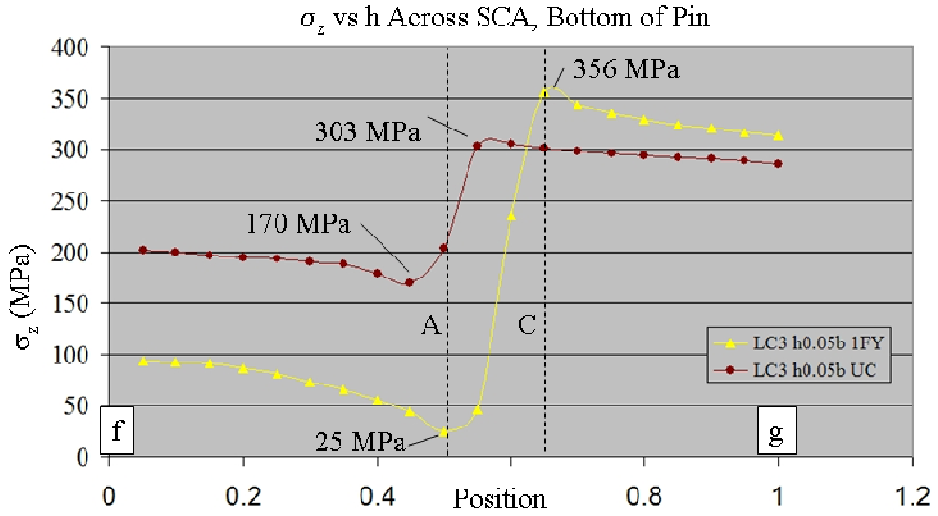

Figure 7.3.3.8 Stress σ_z along line fg for LC3, for the baseline and undercut (UC) data.

Finally, the axial stress values at locations A and C are extrapolated over two engine cycles for the baseline and undercut (UC) geometry as shown in Fig.7.3.3.9. Mean axial stress at *A* is reduced from -338 MPa to -22 MPa while alternating axial stress is reduced greatly from 643 MPa to 325 MPa with the presence of the undercut feature. Also, mean stress at *C* is increased from 29.5 MPa to 110.5 MPa, while alternating stress is decreased from 576 MPa to 121 MPa.

The gradual transition in stress allowed by the undercut features greatly decreases the alternating stress values.

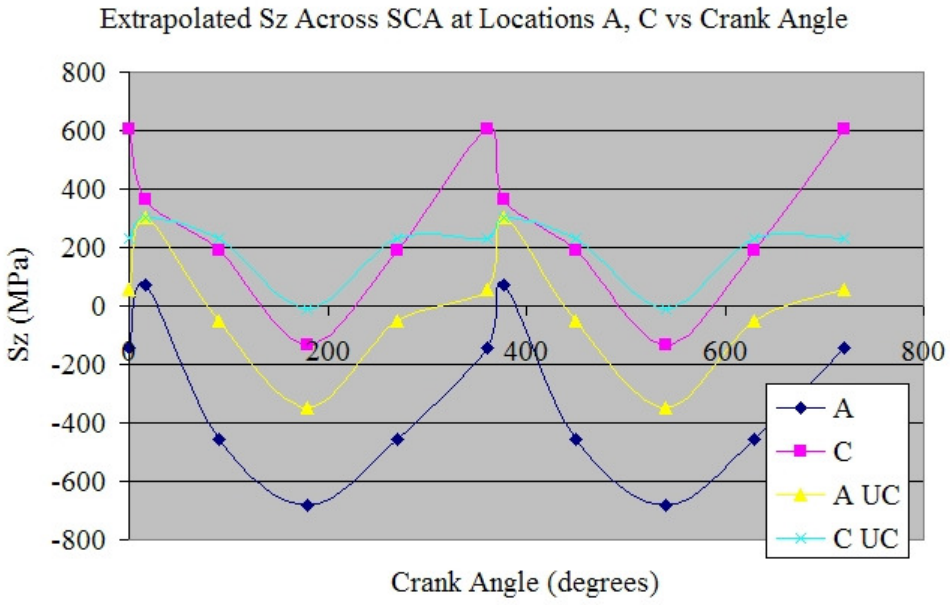

Figure 7.3.3.9 Extrapolated σ_z at locations *A* and *C* plotted over 2 complete engine cycles for the baseline and undercut (UC) designs.

7.3.4 Summary Comments

The undercut feature significantly reduces the local assembly stresses at the SCA, and also creates less stress sensitivity to the operating loads applied because of the gradual transition in web stiffness at the 'lip'. A surface strengthening treatment would be required at the undercut to counteract the high mean tensile stress present, which are required fundamentally to obtain the flexible lip. The optimized undercut geometry parameters chosen appear to be a good design choice worth investigating further through fabrication and durability testing.

Only one element size (0.05 mm) was evaluated with the 3-D model, but it is assumed that the undercut geometry will follow similar but lower element size sensitivity trends displayed for the baseline geometry. Since the stress gradient has been reduced significantly, the undercut results should be less sensitive to element size at the SCA.

8 Rules and Tools

A detailed analysis of a multi-piece crankshaft due to the assembly and operational loading has been presented thus far. After the complex characteristics of the problem is sufficiently understood, the last phase of this research is to simplify the numerical results to make them friendlier to engineering applications. In this chapter modified design rules for the assembly press-fit and design tools for multi-piece crankshafts, which were derived by adopting the results of the FE simulations, are presented.

8.1 Stress Relationships At The SCA For The Press-fit Problem

The numerical data presented in this thesis is now examined to create design 'rules of thumb' so that this knowledge may be leveraged earlier and more easily in the design process. Tools that do not produce data in a reasonable manner may not be deemed as effective for modern design practice.

Note that many 2-D axisymmetric FEM models of the assembly problem have been studied, but the component stress distributions calculated were very similar. The stress field was dominated by compressive stress at the SCA, with equivalent and shear stress peaking just below the surface.

To examine the effects of press-fit interference on the stress components at the SCA, a study was performed by applying the interference varied by + or -50%, in 10% increments, and tracking the local stress maximums at locations *A* thru *D*. Note that true radius geometry parameters 'a' and 'r' were left constant throughout this study, as well as element size *h* was set at 0.005 mm.

The pin maximum stress values are shown in Fig.8.1.1 for the range of interference considered. All stresses appear to grow in a linear fashion as the interference value increases (which is similar to Lame's problem). Note that for all plots in this section, the x-axis interference scale is given in terms of a percentage of the baseline interference value (which is x=0); for example an interference value of +20% higher uses the x equals 20 mark.

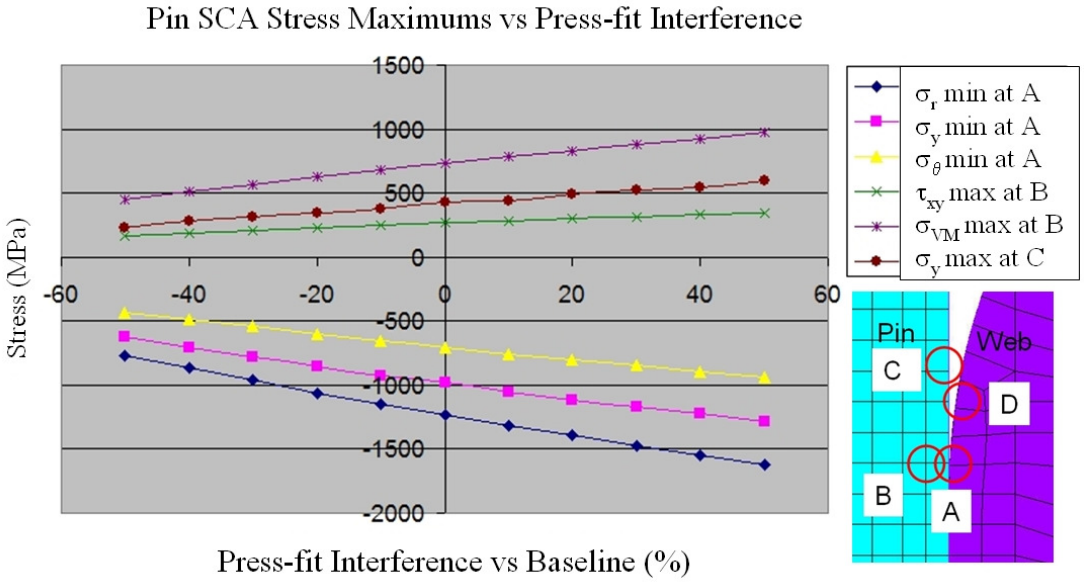

Figure 8.1.1 Local SCA pin stress maximums versus press-fit interference variation.

The minimum (or maximum compressive) local radial stress value at location *A* is a key component of the high stresses at the SCA. The stress field present at the SCA is predicated by the radial contact between the pin and web, including the peak compressive local radial stress. The other stress components are normalized with respect to the minimum (negative) σ_r value at *A*. Figure 8.1.2 plots the normalized pin stress components across the range of interference studied; For the range of interference studied, the stress components follow closely the local minimum σ_r, which is indicated by a horizontal line. Local minimum axial (σ_y for the 2-D models) and hoop (σ_θ) stress at location *A* are calculated at a ratio of 0.80 and 0.57 respectively, both with very low variation across the range of interference. Local maximum Von Mises and Shear Stress at location *B* occur at a ratio of -059 and -0.21 (negative signs indicate positive Von Mises and Shear stresses), again with variation small enough to consider this constant across the ranges of interference. The only stress component that did not track closely was the maximum axial stress at location *C* on the pin. An average value of -0.34 with a variation of 20% across the press-fit range was calculated, which may be due to the questionable convergence of this axial stress component at the *h* equals 0.005 mm value (see section 4.3). This indicates that only an approximate estimate of the maximum axial stress may be derived if the minimum σ_r at *A* is known.

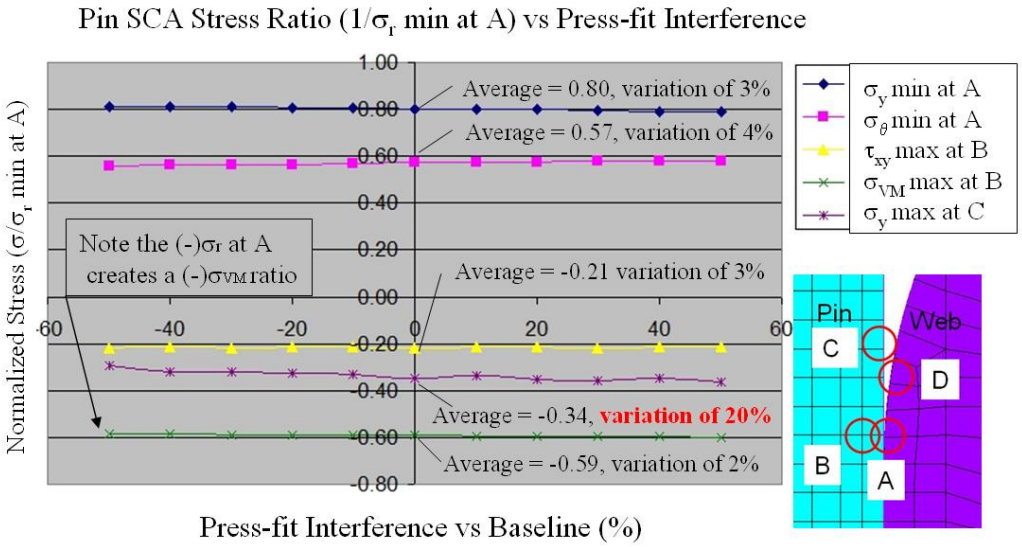

Figure 8.1.2 Normalized pin SCA stress maximums versus interference variation.

Next, the relationship between average σ_r at the interface (away from the SCA) and the local minimum σ_r at the SCA is evaluated. If one is to plot these radial stress components across the range of interference considered, both appear to change in a reasonably linear rate. If the minimum σ_r curve is normalized with respect to the average σ_r, as plotted in Fig.8.1.3, the minimum σ_r value does not track linearly (showing a 36.5% variation). As interference increases, the average σ_r increases, but minimum σ_r at location *A* does not increase at a multiple of this rate of change. An explanation could be that as the true radius feature becomes loaded higher and higher, the local stiffness increases, just like for a Hertzian contact problem between two spheres. The contact stress between two spheres increases at a reduced rate as more surface area comes into contact.

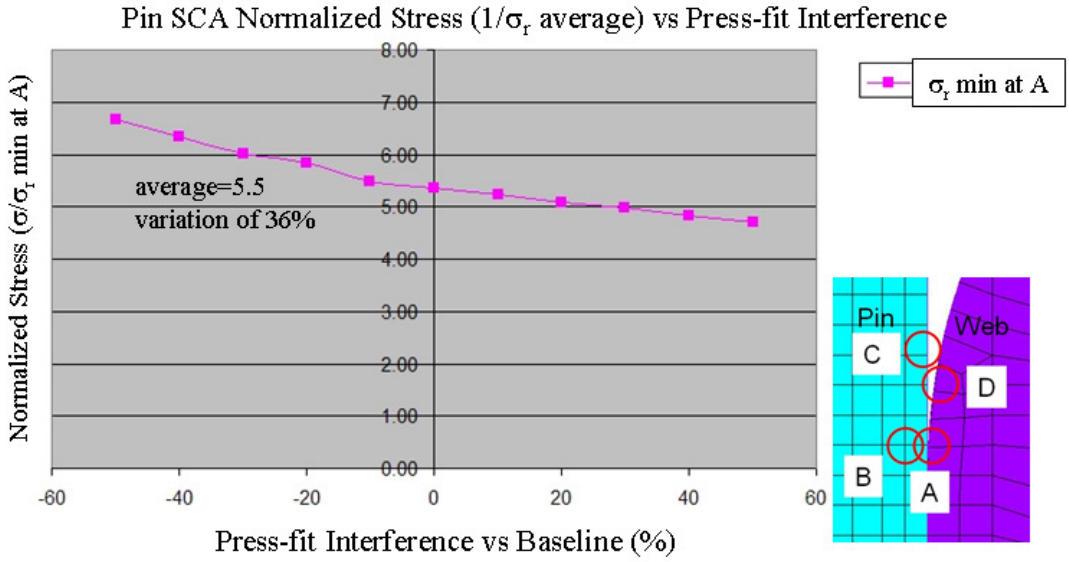

Figure 8.1.3 Normalized ($1/\sigma_r$ average) minimum pin σ_r (SCA) versus interference.

It is critical to understand the relationship between the average σ_r and the local minimum. A design formula may readily calculate the average σ_r at the interface using Lame [24] or other approaches. If an approximate relationship between average contact pressure and local minimum σ_r can be determined, the stress component ratios determined in this section can be used with confidence based only on a calculated average σ_r. Historical press-fit designs are further evaluated in section 8.3; the range of interference for this study is quite wide and may not be fully practical.

Finally web local stress maximums are examined in Fig. 8.1.4. Also included in the plot is the local minimum σ_r at *A*, since it has been demonstrated as a key measure of the stress field. Stress in the web varies linearly versus interference as expected. The web stress components are normalized across the interference range in terms of minimum σ_r in Fig. 8.1.5. The relationship shown is not a constant ratio, as both the web hoop stress ratio (at D) and the web equivalent stress ratio (at *A*) increase with higher interference. The web hoop stress ratio varies by 34 percent, while the web Von Mises stress ratio varies by 17 percent across the range of interference.

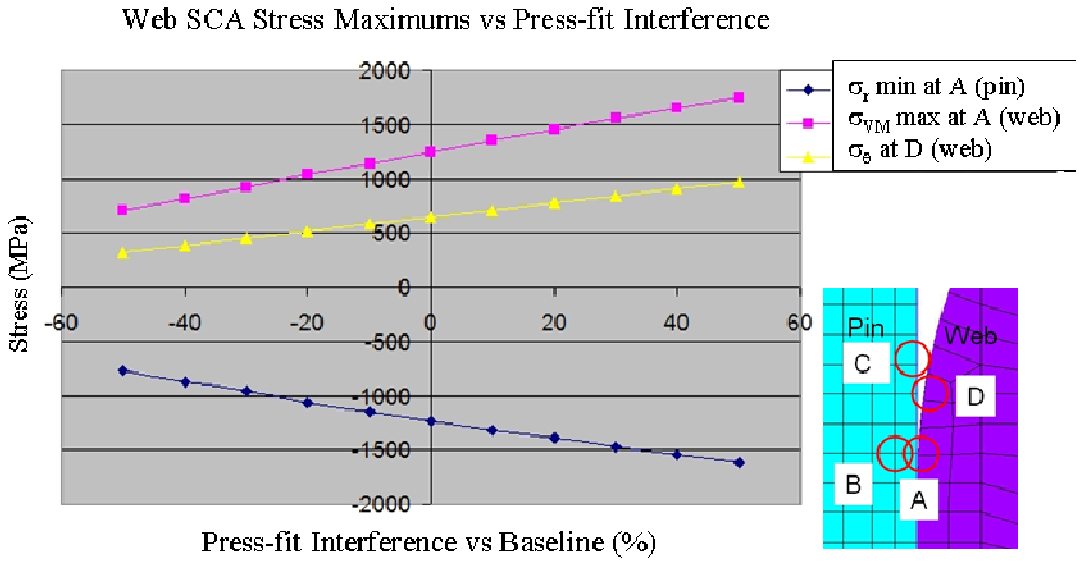

Figure 8.1.4 Web σ (SCA) versus press-fit interference, including pin σ_r minimum at *A*.

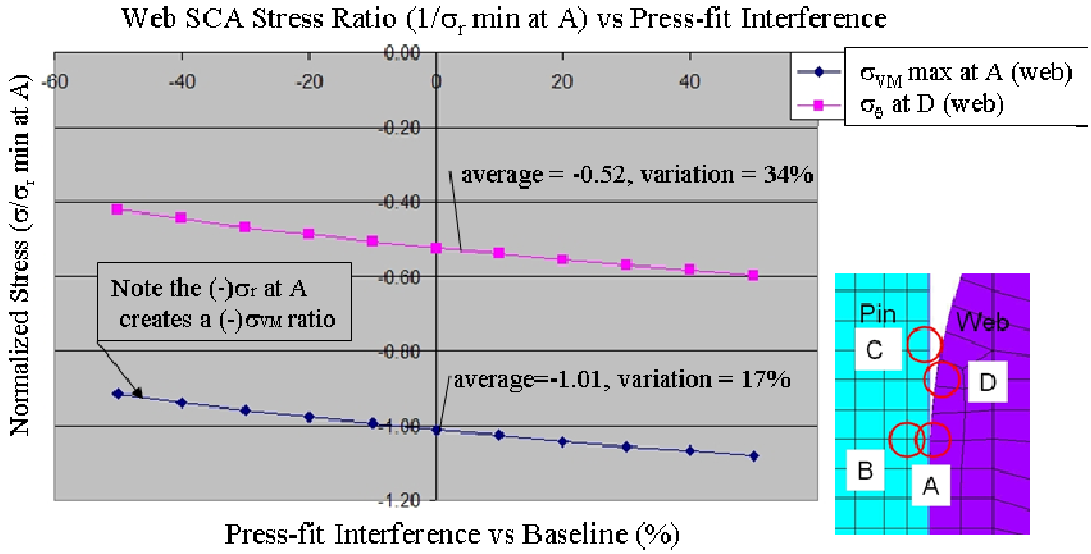

Figure 8.1.5 Normalized ($1/\sigma_r$ min at *A*) web σ (SCA) versus interference variation.

It may be expected that σ_θ at *D* does not track exactly with the σ_r component; location *D* is away from the SCA, and is more of an overall measure of the press-fit interference. In fact, Fig. 8.1.6 plots the web hoop stress normalized with respect to the average σ_r at the press-fit interface, and

exhibits a constant ratio. The σ_θ on the web at location *D* is -2.82 times the average radial contact pressure, a ratio which only by varies by 3% across the interference range.

Figure 8.1.6 also plots the web maximum σ_{VM} at *A* normalized using the average σ_r. The stress ratio shown is not constant across the range of interference for this case either.

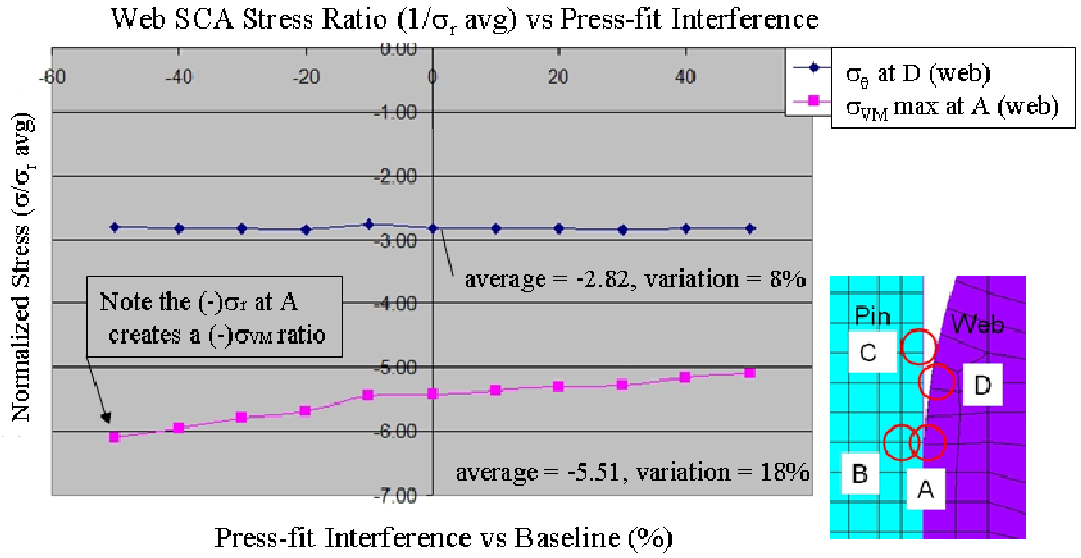

Figure 8.1.6 Normalized ($1/\sigma_r$ average) web σ (SCA) versus interference variation.

For the pin stress components calculated at *A*, it is straightforward why the ratio holds constant for differing interference. The stress state is compressive in the radial direction due to the end stress concentration, and the hoop and axial direction stresses are compressive as well, driven by Poisson's ratio. As interference increases, all the stress component values increase together at the same rate.

The web stress state is similar because of the high compressive σ_r state at *A*, but is also dissimilar because of the generally tensile σ_θ present in the web, as it stretches around the pin. At location A, this generally tensile σ_θ does become slightly compressive, but not to a significant amount (in the baseline 2-D problem, Fig. 4.3.2.6. indicates this value at *A* ranges from -107 to 43 MPa). As interference increases, the maximum σ_θ rises but at a different rate than the compressive σ_r. And so it appears that the combination of the direct stress components that make-up the σ_{VM} calculation on the web are changing at a different rate than the σ_r value at *A*.

8.2 Effects of True Radius Geometry on Stress Relationships at the SCA

The previous section 8.1 examined the relationships between local maximum stresses at the SCA with the variation in press-fit interference. This section will examine some variation in parameters which define the true radius geometry, but will maintain a constant press-fit interference. Some simple tests are required to check if the stress ratio rules established in section 8.1 hold true for true radius geometry changes also.

First, using a constant interference value with the 2-D FEM model, the sensitivity of pin's σ_r is examined at *A* for a wide range of true radius parameters *a* and *r*. As the value *a* is reduced in Fig.8.2.1, σ_r decreases as well. The decrease was thought in part due to the reduction in stiffness of the 'overhung' web material that extends out past the point of first contact between the pin and web. Minimum σ_r at *A* is calculated for several values of radius *r* in Fig.8.2.1 as well.

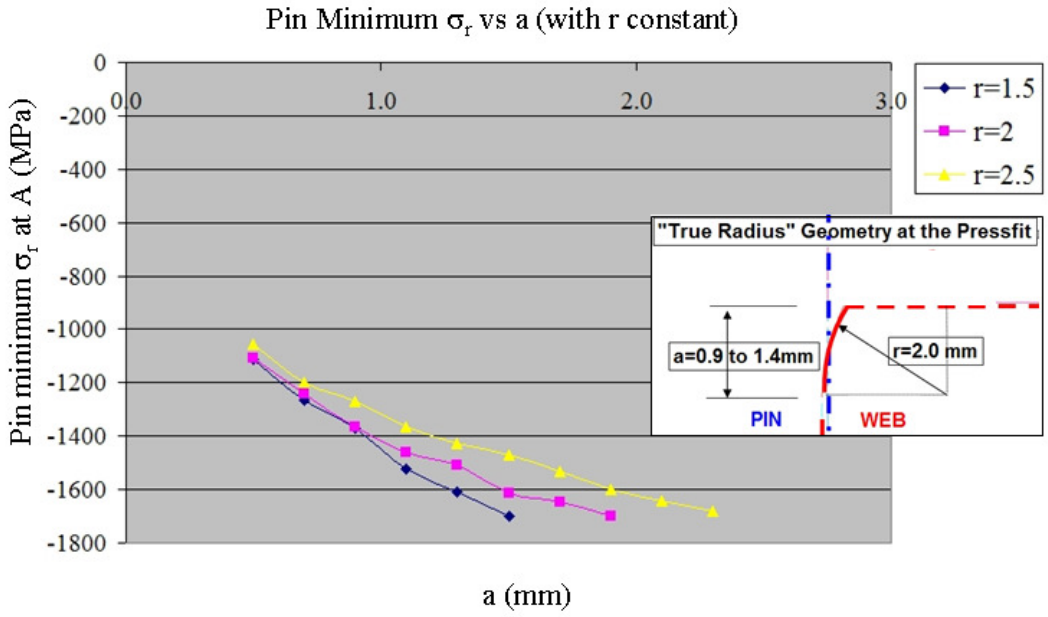

Figure 8.2.1 Minimum pin σ_r at location *A* versus parameter *a* for constant *r*.

Over the wide range of variation in parameters *a* and *r*, the response of minimum σ_r at *A* is not exactly linear, but could be approximated as such over a short range.

Next, the geometry parameter *a* for the true radius end finish was set at values of 0.9 mm, 1.15 mm, and 1.40 mm and the press-fit problem was re-evaluated using *r* equals 2.0 mm. (Note, the baseline press-fit geometry used throughout the research has a value of *a* equals 0.90 mm.) Figure 8.2.2 plots minimum σ_r at *A* and average σ_r for the three values of *a*.

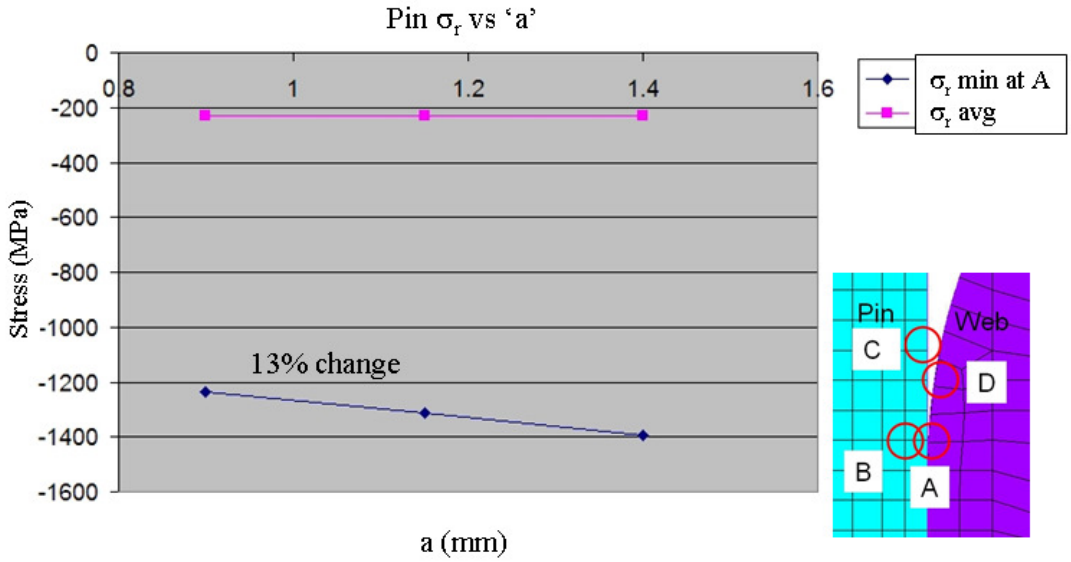

Figure 8.2.2 Average and minimum σ_r (at *A*) versus parameter *a*.

Figure 8.2.2 agrees with Fig.8.2.1, and indicates that minimum σ_r (at *A*) decreases with *a*, while average σ_r remains constant throughout which produces a horizontal curve. The minimum σ_r at *A* normalized with respect to average σ_r will not create a constant ratio across the range of '*a*' (see Fig. 8.2.3.). This data may seem redundant, but the σ_r magnitudes and ratios are important data to have for use of these rules early in design, since the average σ_r may be calculated by hand approximately.

The normalized ($1/\sigma_r$ minimum at *A*) pin stress values are plotted in Figs. 8.2.4 for the studied range. The stress ratios established in the previous section for interference variation also hold true for parameter '*a*' variation.

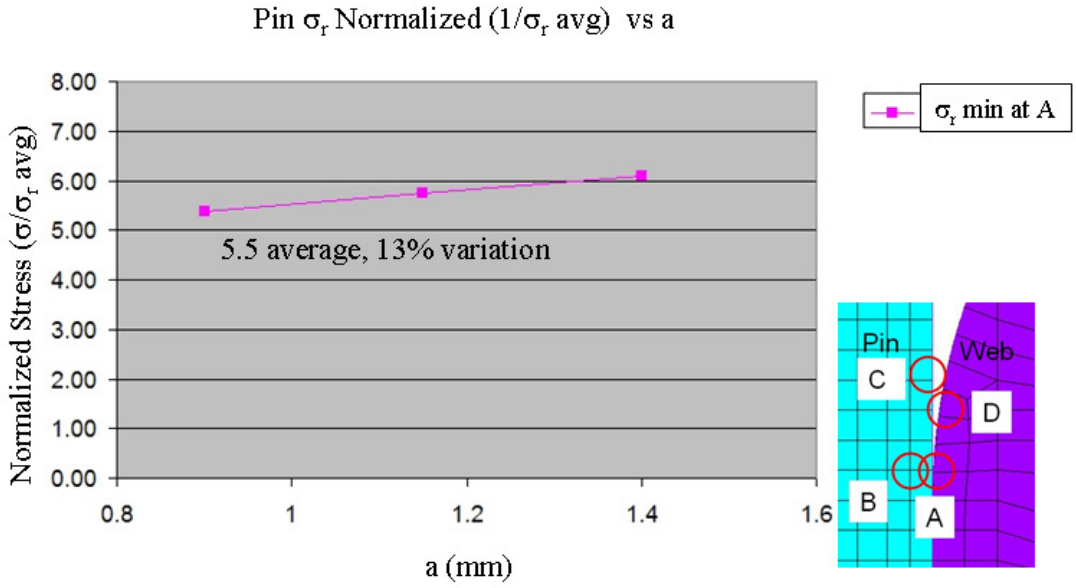

Figure 8.2.3 Normalized ($1/\sigma_r$ average) minimum pin σ_r versus parameter *a*.

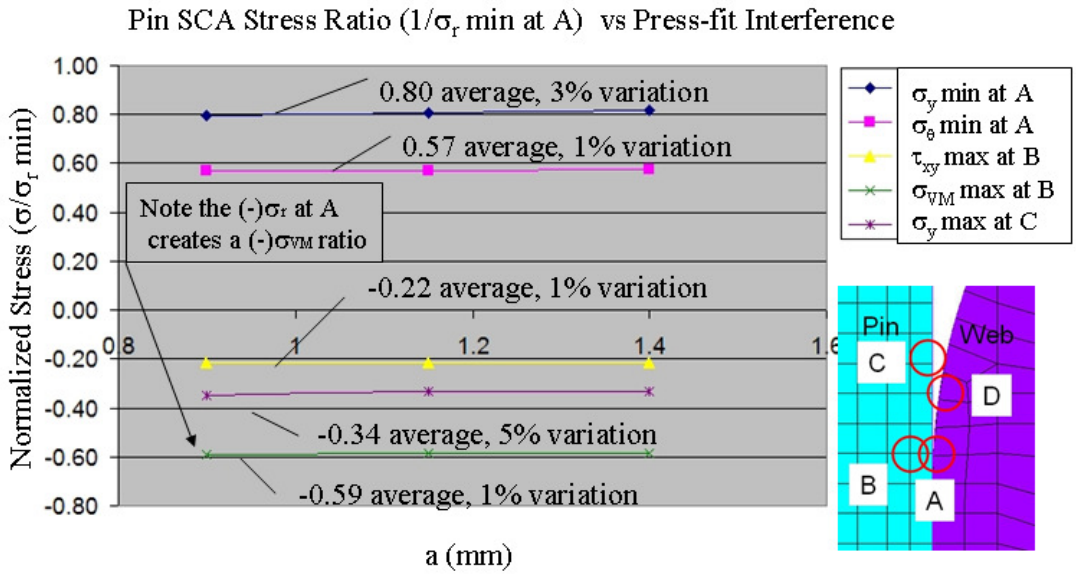

Figure 8.2.4 Normalized pin SCA stress maximums versus interference variation.

In a similar fashion, the web local maximum stresses calculated for the variation in a result in the same normalized stress ratios (see Fig. 8.2.5) as presented in section 8.1.

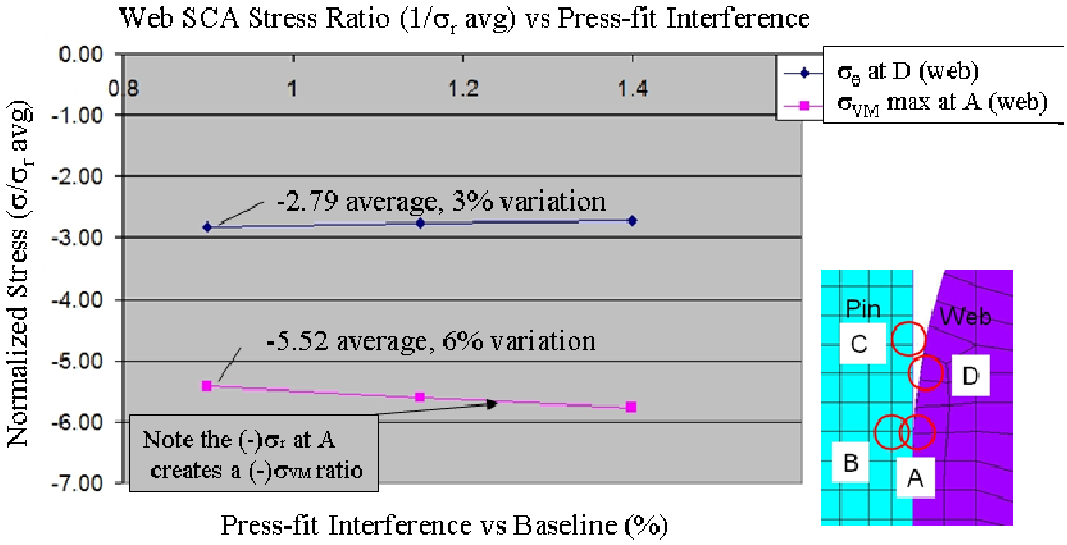

Figure 8.2.5 Normalized web stress ($1/\sigma_r$ average) versus parameter *a*.

In summary, both sections 8.1 and 8.2 show that with the knowledge of the maximum radial stress component, other local maximum stress components at the SCA may be determined with acceptable accuracy using multipliers based on stress ratios. Greater error is introduced into this approach if the local stress components at the SCA are to be derived from the average contact pressure. But this approach is acceptable and could be used very early in the design selection stage reducing the numerical effort. In order to evaluate how practical this assumption is, historical designs are examined with the same approach.

8.3 Stress Relationships At The SCA: Variation In True Radius Parameter *a*

Sections 8.1 and 8.2 demonstrate that with the knowledge of the maximum radial stress component, other local maximum stress components at the SCA may be determined with acceptable accuracy using stress ratio multipliers. If the local stress components at the SCA are to be derived from the average contact pressure, then a greater error is introduced into this approach. Practicality of these assumptions will be evaluated against some available historical designs. This approach might be used very early in the design selection stage to reduce the numerical effort.

Historical press-fit designs from various engines are presented that use the same basic web and pin geometry, including the true radius feature on the edge of the web hole. All the engines included are of 2-stroke twin cylinder configuration with crankpin sizes that vary from 27 to 30 mm diametrically. Web shapes differ throughout, as does the amount of material on the web at TDC above the pin. Local stress maximums are examined at the SCA for each engine in a similar manner to that in the two previous sections, 8.1 and 8.2.

Average radial stress was chosen for the x-axis of the plots in this section since it conveniently categorizes the engines according to the aggressiveness of the press-fit. Since stress component data will trend upwards with increasing average press-fit, the data from each engine will be most informative when categorized by the average interface σ_r. With this approach the stress component data points for each engine are also always grouped on a vertical line.

Figure 8.3.1 plots σ_r values versus average radial interface stress for the 7 engines considered. Minimum σ_r at *A* increases with increasing average press-fit, which agrees with engineering logic and the data from section 8.1 (see Fig. 8.1.4).

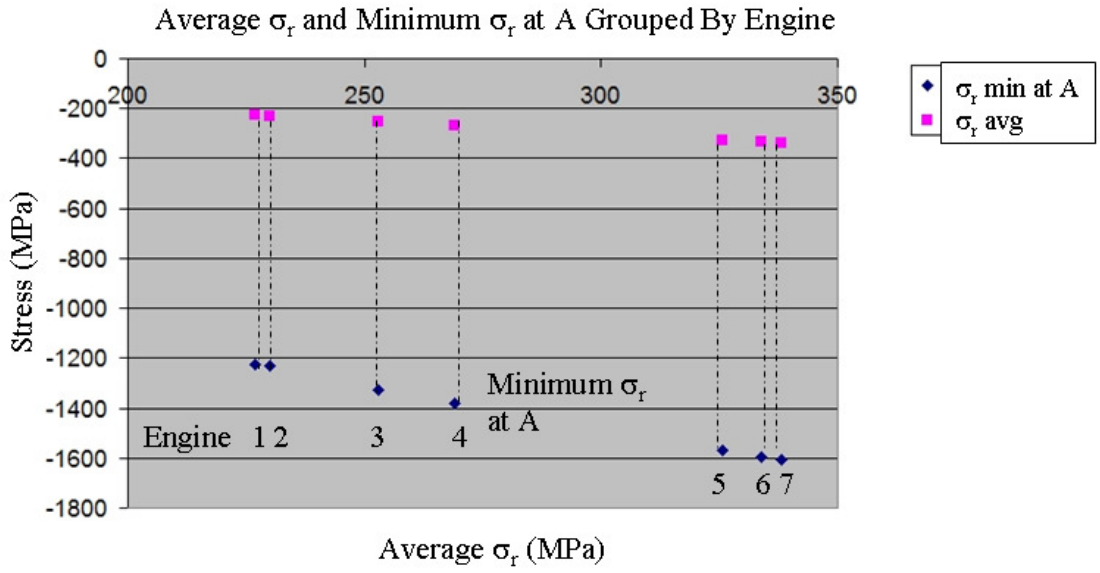

Figure 8.3.1 Historical pin σ_r magnitudes plotted against average σ_r.

Note that the average σ_r ranges from -227 MPa to -338 MPa, which equates to a mean value of -282MPa plus or minus 19.5%. To put this range into perspective, for section 8.1 a mean value of -229 MPa plus or minus 50% was examined (-115 Mpa to -344 MPa). The range press-fit interference for these historical engines is not as wide as the band of interference studied in section 8.1, but the upper limits are very close in magnitude.

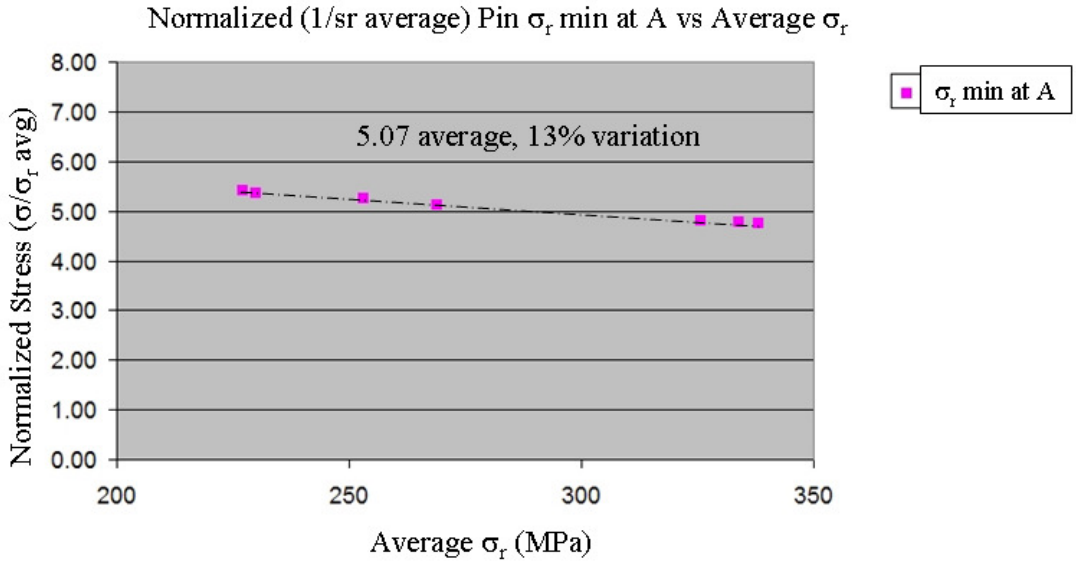

Figure 8.3.2 Normalized (1/ /σ_r avg) pin minimum σ_r at *A* plotted against average σ_r.

Normalized minimum σ_r (with respect to average radial stress) is plotted in Fig.8.3.2. The average ratio is 5.07, showing 13% variation, which is consistent with previous findings. The variation is lower (13% vs 36%) for the historical study because the range studied is more narrow.

The historical pin and normalized pin stress values are plotted against average radial stress in Figs.8.3.3 and 8.3.4 respectively. The stress ratios for axial σ_y (0.80), hoop σ_θ (0.58), shear τ_{xy} (-0.21), and equivalent σ_{VM} stress (-0.59, a ratio which is negative because of the negative radial stress divisor) are very consistent and match those calculated in 8.1 and 8.2. The ratio for maximum pin axial σ_y stress (-0.35) at *C* matches the previous trends also, which also has a somewhat larger but acceptable variation (9 %).

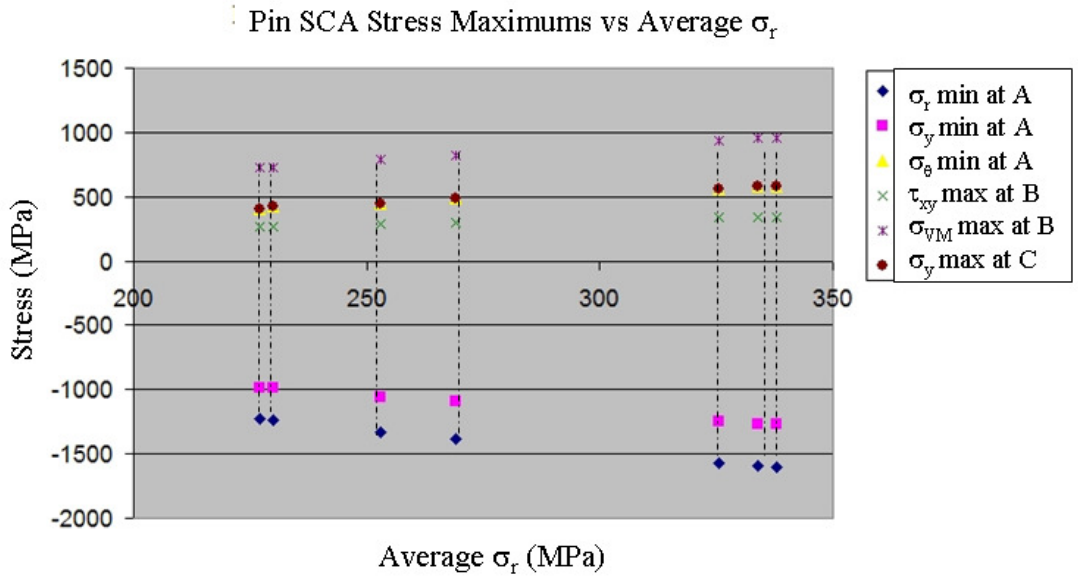

Figure 8.3.3 Historical pin stress magnitudes plotted against average σ_r.

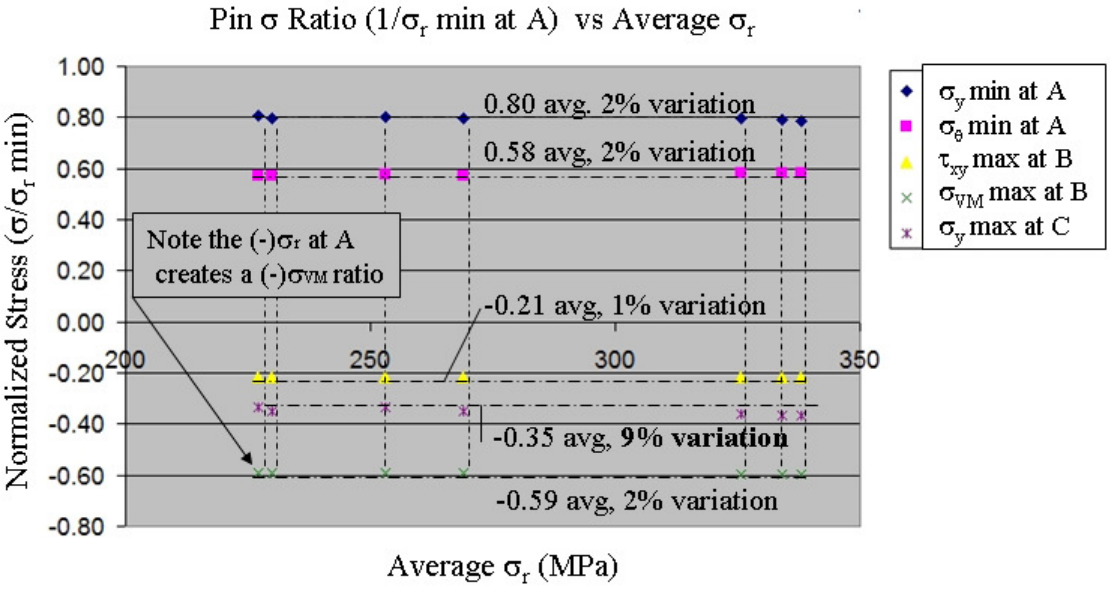

Figure 8.3.4 Normalized pin SCA stress maximums versus average σ_r.

Finally the web stress components are examined in Figs. 8.3.5 and 8.3.6. Some of the historical press-fit designs have very aggressive (high) interference values. Of note in Fig.8.3.5 is the

maximum web hoop stress at location *D* indicated as 839 MPa for engine 7. Significant equivalent stress values (1616 MPa) at point *A* on the web are also indicated. A detailed examination of the 2-D press-fit and 3-D operating loads would be appropriate before further comment on these stress levels. Greater variation in the stress values exist here because of the variation in the historical web geometries. The normalized web stresses match the trends shown in section 8.1 and 8.2 as expected. The hoop stress value at location *D* average ratio is -2.55 with respect to the average radial interface stress. The maximum equivalent stress ratio value averages at -5.02 (the ratio is negative, not the calculated Von Mises stress!) with a variation of 13%.

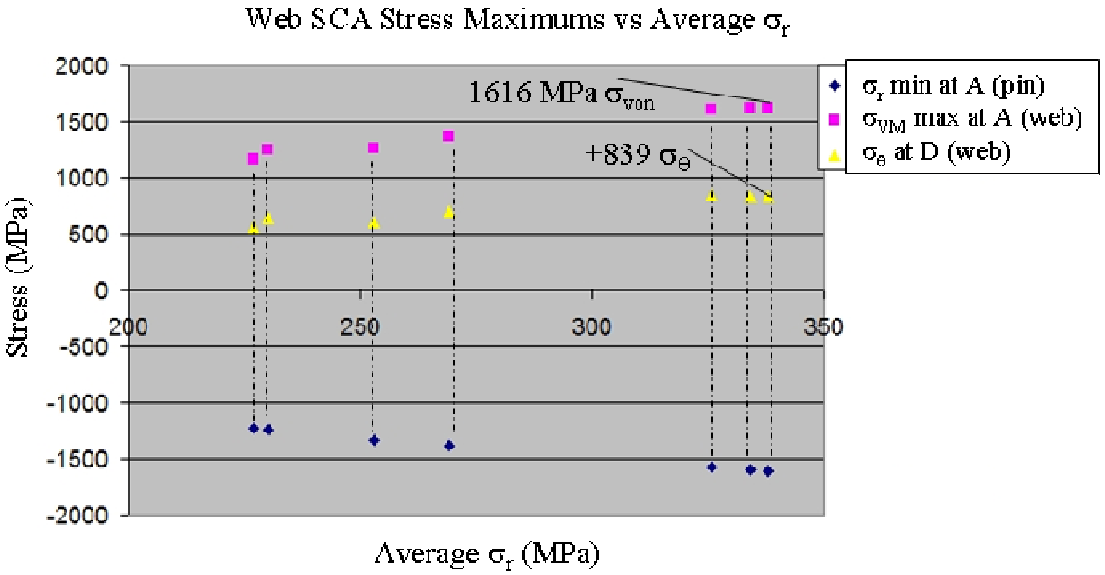

Figure 8.3.5 Web stress magnitudes at the SCA versus average σ_r.

The historical engine data supports the previous findings. Stress ratios can be used to predict local maximum stress components at the SCA, based on the average radial contact pressure. Accuracy will vary, but will fall in the 10 to 15 percent range. The accuracy may be improved by using the extrapolated lines on the plots presented for those stress component ratios that show a greater variability. For example, on Fig.8.3.2, instead of using the average value of 5.07 to calculate minimum radial stress at *A*, a ratio of 4.8 could be read of the graph if a press-fit average design value of -325 MPa was required for adequate torque retention in the joint. This

level of accuracy is felt to be adequate early in the design process, as the error in this assumption will be lower than the range of stresses due to the manufacturing geometry tolerance.

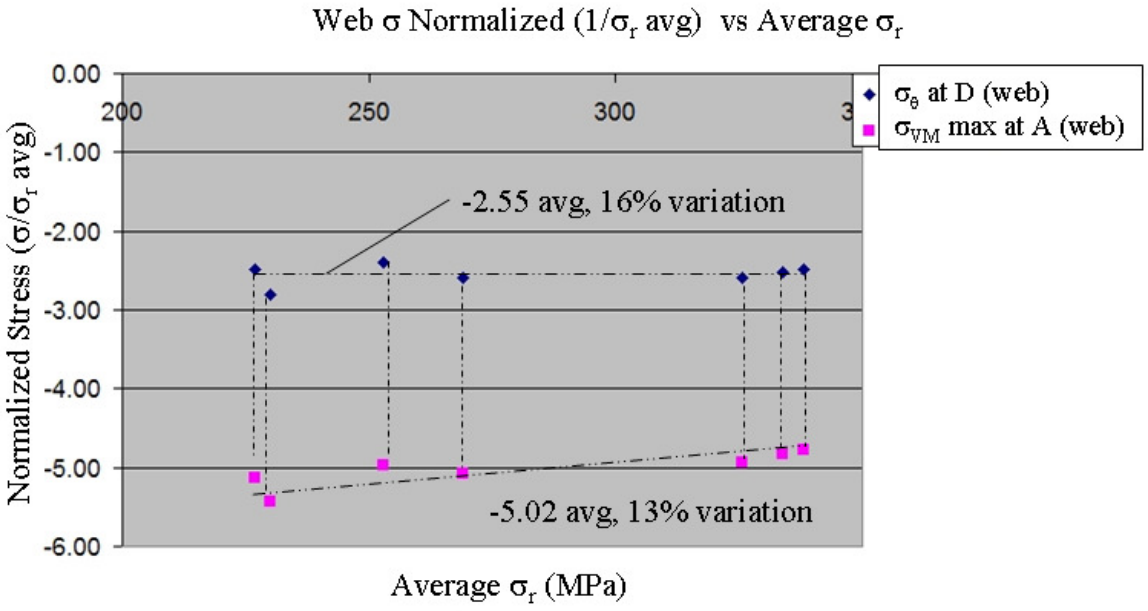

Figure 8.3.6 Normalized ($1/\sigma_r$ avg) web stress versus average σ_r at the interface.

8.4 Press-Fit Evaluation Tools

In the engineering environment complex numerical tasks should be automated as much as possible to shorten the time frame necessary for applying a particular numerical tool. It should produce data faster and may speed up the design process. Besides automation of these complex tasks, the numerical tool may also be more efficiently applied by applying reasonable assumptions which focus on the key design metrics only.

A user friendly input deck was created using ANSYS command language to examine the press-fit problem with a 2-D axisymmetric solution. This tool was created so that model creation would be automated based on a few geometric parameter inputs at the beginning of the text file. The user need only input the pin and web inner and outer diameters values, along with the respective pin and web axial lengths. Besides saving time by automating the model creation

process, high quality results are also ensured since the meshing approaches and other modeling details are captured in the macro.

Two versions of the input deck exist, one which creates a geometry based interference, the other which creates a temperature based interference. The temperature based approach assumes the pin and web interface start with a zero interference. The desired interference is then created by applying the uniform temperature change to the pin which expands based on the coefficient of thermal expansion of a steel material.

The input deck only takes a few minutes to modify to obtain the desired geometry. After a solution time of approximately 35 to 40 minutes, results are then available for a highly refined mesh at the SCA. An input deck also was created for post-processing the results. General displacement and stress plots of the entire model and of the SCA local area are created automatically. Stress data along the path of the pin outer diameter and the web inner diameter are also provided.

The input decks are placed in Appendix H.

8.5 An Equivalent One-Quarter Bench 3-D Model

In section 5.2, the one-quarter bench model was described as being similar to the physical durability test that would be exercised in the lab to prove out crankshaft life. Though, an oversight of this model is that rotational inertial loads would not be applied typically in a physical testing laboratory. Durability bench tests are now presented which show how crankpin loads may be applied without rotating inertia to match closely the operating condition behavior of the press-fit joint presented in section 5.2.

Radial and axial stress are now examined at the SCA region for the operating load and bench test conditions. These two stress components will be the focus of the study, as a good match is desired between the bench and operating load response. The other maximum stress components at the SCA are shown to be a ratio of the highly compressive σ_r in sections 8.1 – 8.3, and so σ_r is a good metric for comparison.

First, σ_r across the SCA region is shown in Fig.8.5.1 for the operating load time steps 1 thru 4, which includes the rotational inertial loading (denoted as LC2). The radial stress on the bottom of the pin is plotted using *h* equals 0.05 mm, and is shown to unload after assembly (LC1) through spin up (LC2), and further unload from the combustion event (LC3), and finally re-load compressively for the reciprocating inertia load (LC4). At location *A* in Fig. 8.5.1, the spin load case 2 effectively shifts the radial stress curve higher. For a recap of the joint loading please see section 5.3.

To recreate the operating load stress (with spin) response shown in Fig.8.5.1, the FE model from section 5.3 is studied using crankpin loading only (no spin). In this study the loads applied to the crankpins are described as multipliers of the crankpin loading at LC3 and LC4. For example Fig.8.5.2 plots minimum σ_r at *A* across the SCA for crankpin loading which varies from 2.25 times LC3 to 1.0 times LC4. Note that the legend in Fig.8.5.2 designates the 'No Spin' loading as NS. The variation in the crankpin loading is shown to shift the radial stress curve in a similar fashion, unloading and further loading the point A with compressive radial stress.

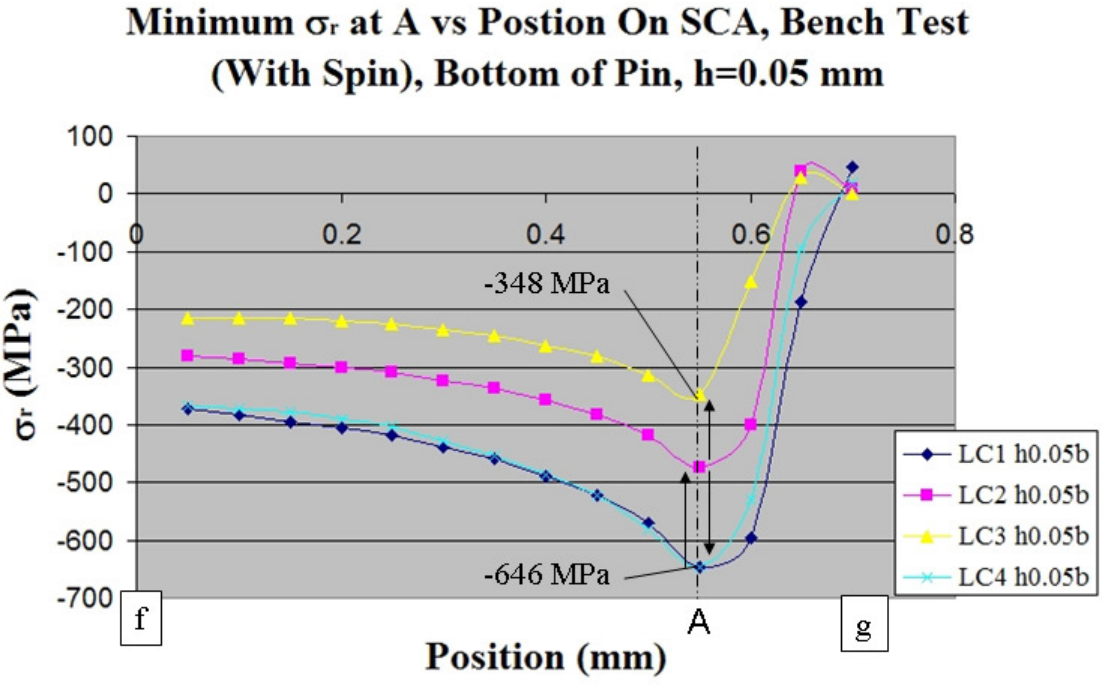

Figure 8.5.1 Plot of σ_r across the SCA on the bottom of the pin (operating loads).

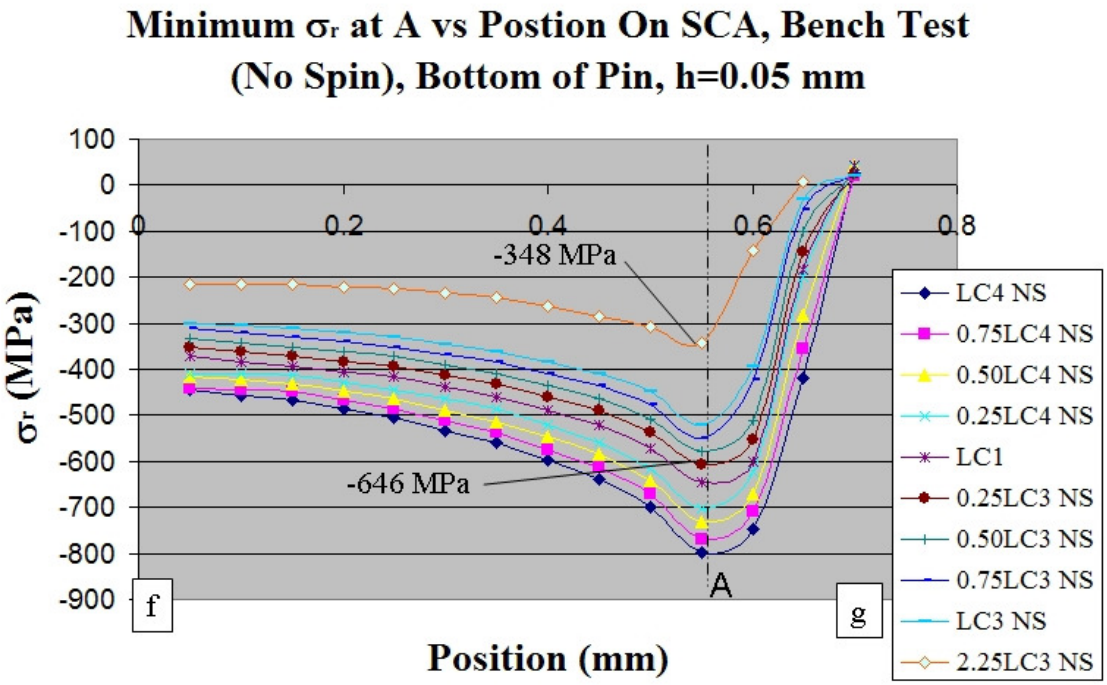

Figure 8.5.2 Plot of σ_r across the SCA for crankpin load variation (no rotational inertia).

Next, Fig. 8.5.3 plots σ_z on the bottom of the pin for the operating load cases (1 to 4), which is the other metric which needed to be matched for the physical bench test. Note that local minimum and maximum stress values are given at locations *A* and *C*. Location *C* is the location of maximum σ_z on the free surface of the pin just outside the press-fit contact area. The spin load (LC2) and combustion load (LC3) are shown to increase tensile σ_z, while LC4 creates compressive σ_z.

Note the peak stress that occurs at location *C* for both load cases 2 and 3. The spin load retains a sharp gradient in stress at the SCA with a peak at location *C*. The combustion load though tends to unload σ_r (see Fig.8.5.1), which reduces the stress concentration affect of the 'kink' in the pin, resulting in an overall reduction in maximum σ_r at location *C*. This subject is covered in section 5.3, and is not intuitive on a first examination; this behavior creates some difficulty in recreating the stress field without a spin load.

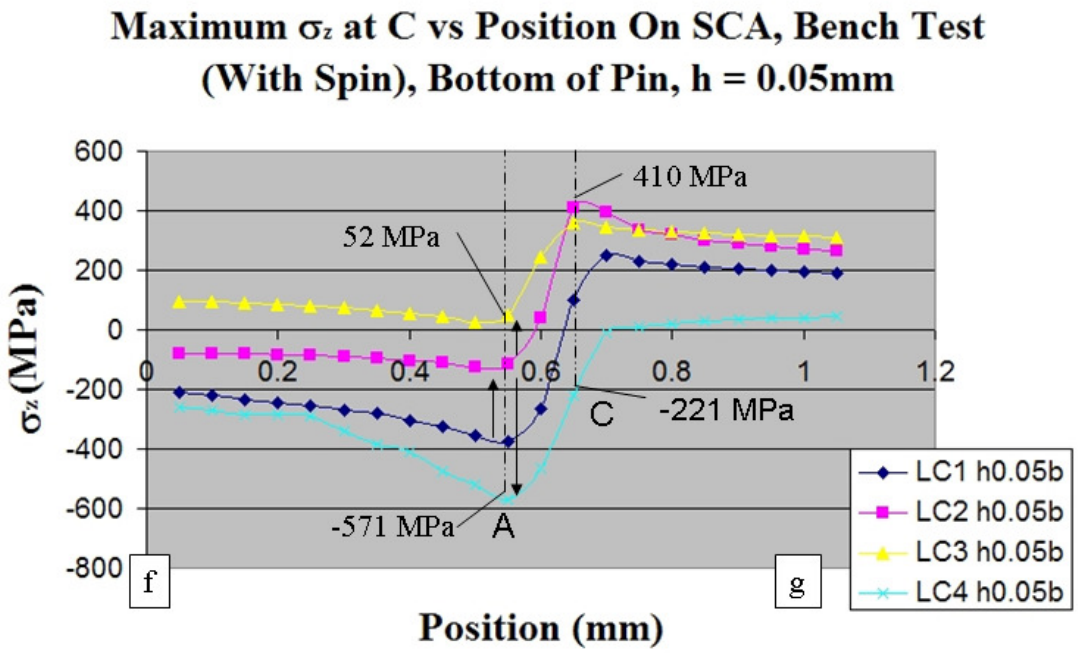

Figure 8.5.3 Plot of σz across the SCA on the bottom of the pin (operating loads).

Axial stress at the SCA is now examined for the application of crankpin loads without rotational inertial (spin) loading on the crankshaft. Figure 8.5.4 plots the σ_z distribution at the SCA for crankpin loading in fractions of the forces applied for LC3 and LC4. The operating load (with spin) minimum and maximum values of stress at locations *A* and *C* are noted also. The application of higher LC3 (combustion) loads produces increasing tensile pin stress on the bottom side while the opposite direction LC4 crankpin loading creates compressive stress.

Figures 8.5.2 and 8.5.4 demonstrate that crankpin load variation may shift the σ_r or σ_z curves in a positive or negative direction to match the operating load curves. First, a match of the operating load σ_r curve is provided with option 1. Figure 8.5.5 plots σ_r for the operating condition LC3 and LC4, which respectively create the maximum and minimum σ_r value at *A*. For the no spin case, LC1 (assembly) and 2.25 LC3 are shown to match approximately.

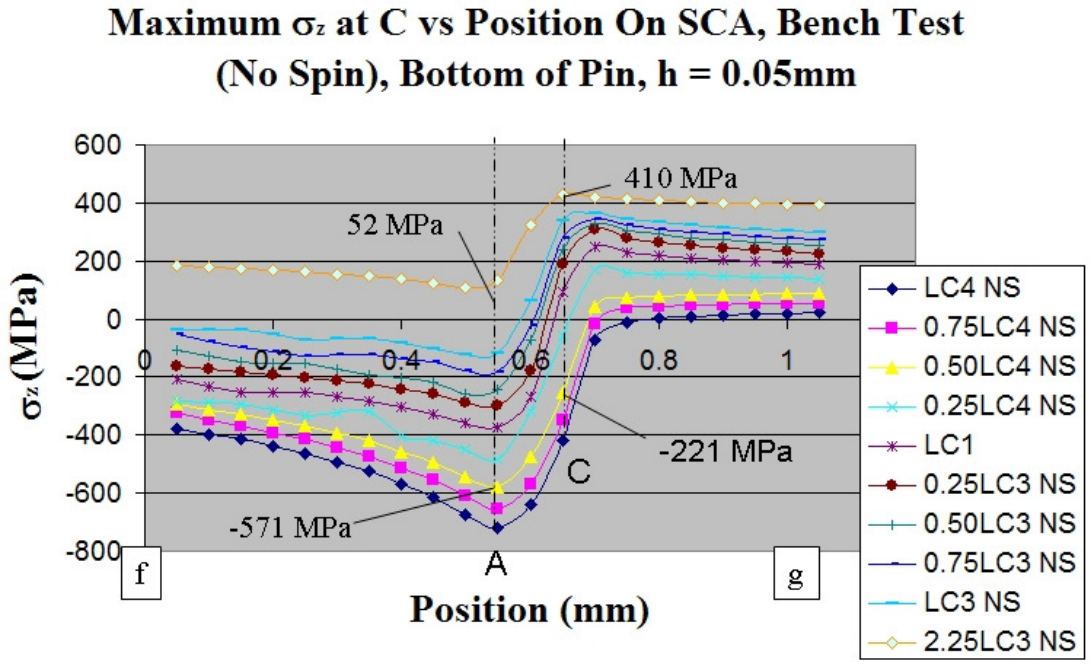

Figure 8.5.4 Plot of σ_z across the SCA for crankpin load variation (no rotational inertia).

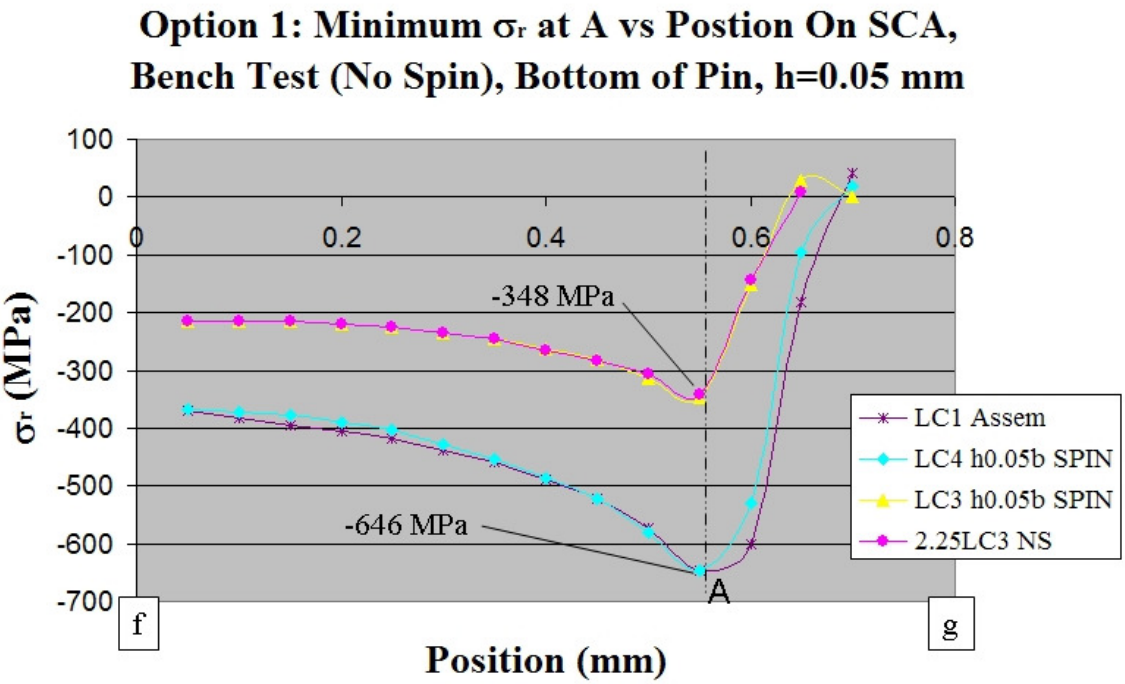

Figure 8.5.5 Plot of σ_r across the SCA for the baseline and bench test option 1.

However, if there is a match between the radial stress profiles for the baseline and no spin case, axial stress will not match, as shown in Fig.8.5.6. Figure 8.5.6 provides the difference in stress values between the goal and 'no spin' load cases. Option 1 creates generally higher (tensile) axial stress across the SCA region, because of the elevated combustion loads (a 2.25 multiplier on LC3). Maximum tensile stresses at *C* are 71 MPa higher (19%), and the alternating load is 338 MPa, which is 58% lower.

A second option is to match the axial stress components at locations *A* and *C*; a best match for this is shown in Fig.8.5.7. Because of the 'radial unloading' of location *A* for a combustion force, an exact match of σ_z can not be obtained. In choosing between a match of axial stress at *A* or *C*, location *C* was targeted since the maximum tensile value occurs there. Crankpin loads of (1.0 x) LC3 NS (no spin) and (0.5 x) LC4 NS provide an approximate good fit at the lower and upper bounds. The equivalent cyclic bench test loading is –LC3 NS to +0.5 LC4 NS. The only mismatch in σ_z occurs at the maximum stress Location *A* as the no spin load case 3 creates a 168 MPa shortfall in σ_z.

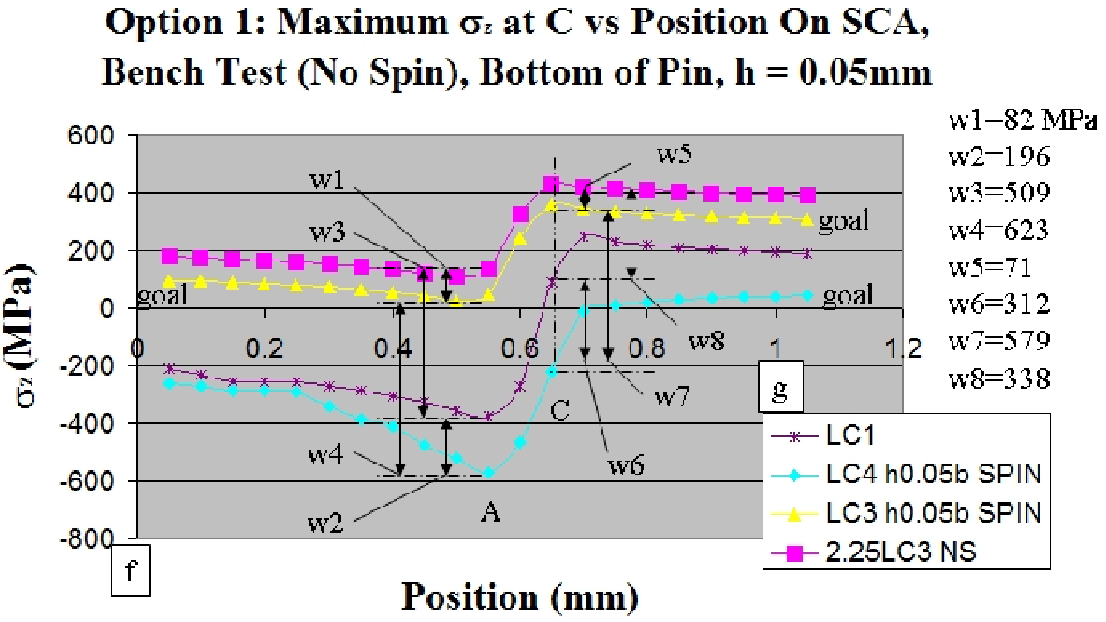

Figure 8.5.6 A plot of σ_z across the SCA comparing the baseline and bench test option 1.

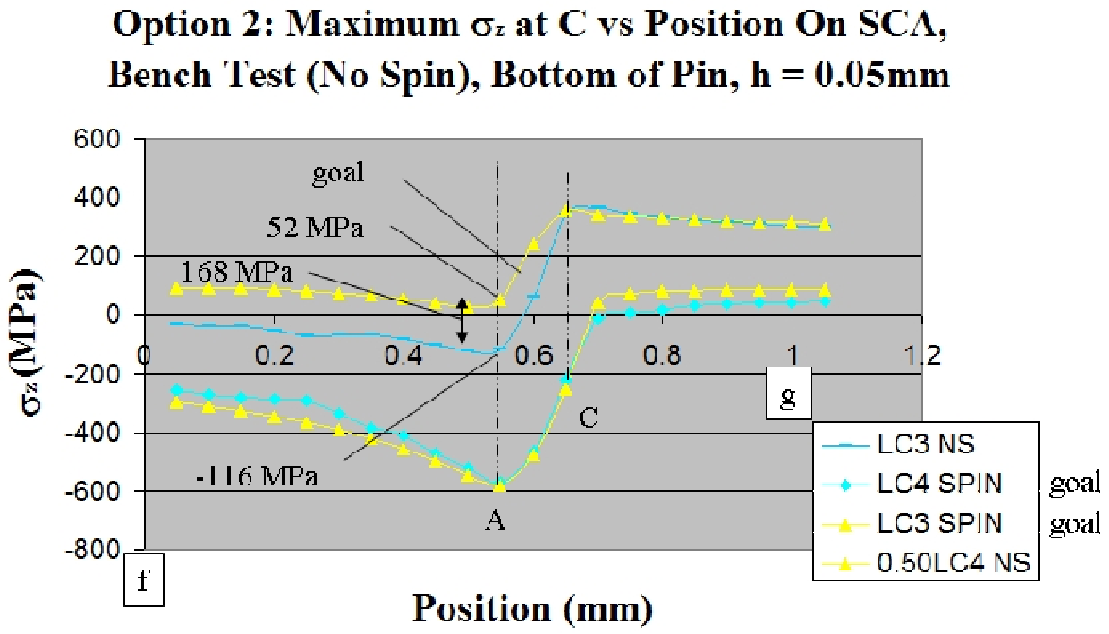

Figure 8.5.7 Plot of σ_z across the SCA for the baseline and bench test option 2.

Since in option 2 the σ_z is matched approximately, a mismatch is created in σ_r across the SCA between the spin and no spin cases. Figure 8.5.8 compares radial stress curves for option 2 showing generally higher compressive radial stress for the 'no spin' data. The baseline data in Fig.8.5.1 shows that rotating inertia (LC2) reduces or unloads the maximum radial stress at *A* while adding reciprocating inertial loads on the crankpin (LC3) reverses this trend. And so for the test options present which do not contain the spin loading, the unloading effect on the bottom of the pin is missing. Hence larger compressive radial stresses are created on the bottom of the pin while the alternating component is not as great (29% lower).

In summary, both options 1 and 2 re-create accurate stress fields at A and C for σ_r and σ_z conditions respectively. Option 1 though creates σ_z components that are 19% higher at location *C*. Option 2 creates compressive σ_r components that are 13% larger. Each stress component may create a different failure mechanism; the σ_r is indicative of the high subsurface stresses, which could trigger fretting fatigue when relative motion occurs between the two mating surface,

as the literature [18] indicates. Also, a high σ_z at *C* could initiate a fatigue crack if magnitudes are sufficient.

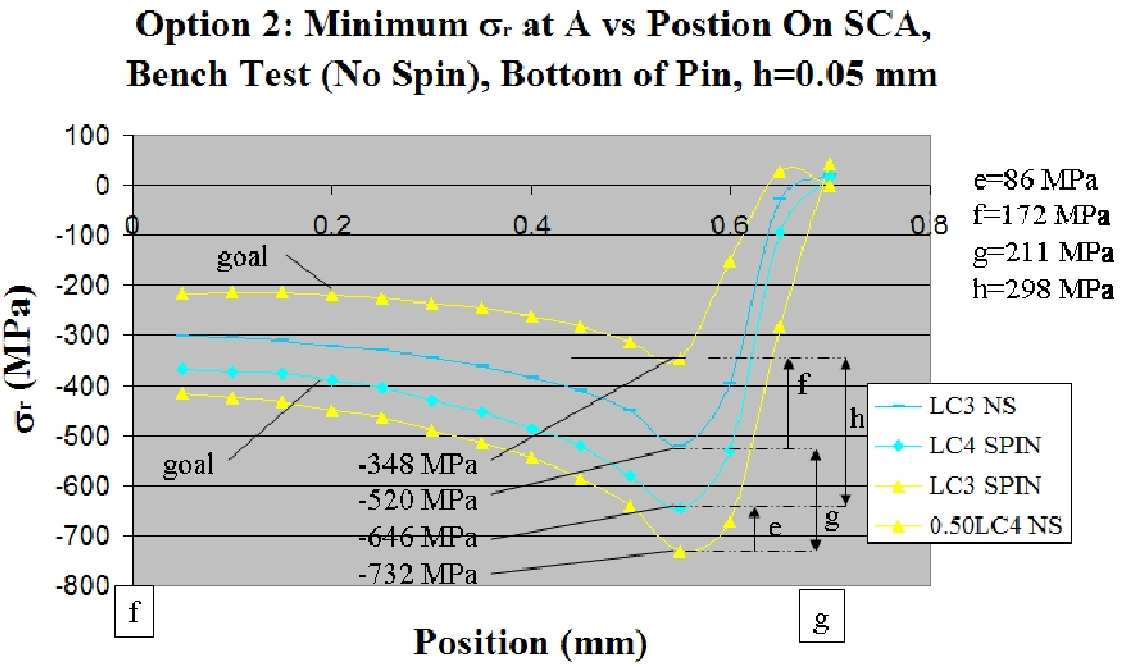

Figure 8.5.8 Plot of σ_r across the SCA for the baseline and bench test option 2.

The relative stress magnitudes seem to suggest that fretting fatigue damage is the more likely of the two for this combination of geometry and press-fit interference. Maximum σ_{VM} below the surface at *B* will be greater than the maximum σ_z at *C* if a ratio of 0.59 (from section 8.1) is used to calculate the σ_{VM} stress (based on the value of minimum σ_r at *A*). Therefore bench test option 1 which matches maximum radial stress at location *A* would be more appropriate for the exact replication of the sub-surface stress field.

Option 1 has another advantage with respect of matching σ_r variation at *A*; the amplitude variation is 29% lower for option 2. If the radial stress at the bottom of the pin at *A* is not given a chance to unload, it also may not allow (incorrectly) any relative motion between the pin and web, and therefore not re-create the fretting fatigue accurately. In the case of option 1 for which σ_z is higher, and creates a bending fatigue failure at *C*, then a bench test loading with option 2 can be pursued.

Of course the bench test durability work is more valuable if the damage accumulated may be accelerated. For option 1, it is simple to increase the minimum value o σ_r by increasing the combustion direction load on the crankpin, which further unloads the σ_r at the bottom of the pin. As this crankpin load is increased, the propensity for relative motion between the joints also increases, which could induce a fretting fatigue. Since little research effort has focused on this aspect, an initial concern would be that the power laws present for a steel fatigue curve are not representative of the fretting fatigue behavior. Careful testing is required to increase crankpin loads for the purpose of accelerating the test. At some point as this load becomes large enough, the tensile axial pin stresses at *C* may dominate the fatigue testing. The overly aggressive loading schemes could then result in an incorrect failure mechanism, and so it is recommended that load magnitudes are to be set higher in gradual increments.

9 Conclusions

The conclusions are grouped into sections related to the particular chapters of the thesis; starting with general via technicalities of the FEM models to optimizations and proposed engineering tools.

9.1 General Conclusions

The over-reaching objective of this research is to enhance the application of numerical tools used in industry to further the durability and application of engines with multi-piece crankshaft construction (Objective 1). It is early in the use of these tools to truly affect implementation in a large scale and more time is required. Because of the use of these tools, and perhaps the implementation of design optimization ideas to increase life, hopefully lighter, more durable, or more cost effective designs are created for the customer. Generally these engines will continue to push the performance envelop with very good specific horsepower and hopefully acceptable customer quality, with better overall performance than that of competitive performance snowmobiles that employ very good but somewhat heavier 4-stroke engines.

A second broad objective in this research is to assemble the engineering process and tools to calculate accurately the detailed stress field present on the press-fit joint for assembly and engine operating conditions (Objective 2). A related goal of the research focused strictly on the numerical aspects which is that the overall FEM analysis of the multi-piece crankshaft is organized in this research to examine both the press-fit assembly phase and the engine operating condition, which requires 2-D and 3-D geometry based FEM models (Objective 6). The discussion on these similar objectives can be handled together nicely. In chapter 2 a process diagram was presented for the design of a crankshaft. Based on the work in this research, the process diagram presented in chapter 2 was modified for a multi-piece crankshaft to include all the new tools and information developed, as described below and shown in Fig. 10.1.1:

1) The rules developed in chapter 8 that relate average radial stress at the interface to maximum local stress values at the SCA are applied early in the design process along with the general sizing of the press-fit (which uses the Lame [24] solution).

2) Efficient automated tools have been created based on a 2-D axisymmetric approach to examine the exact details of the stress concentration at the SCA, for the elastic assumption, and are inserted after the design calculations outlined in 1) above.

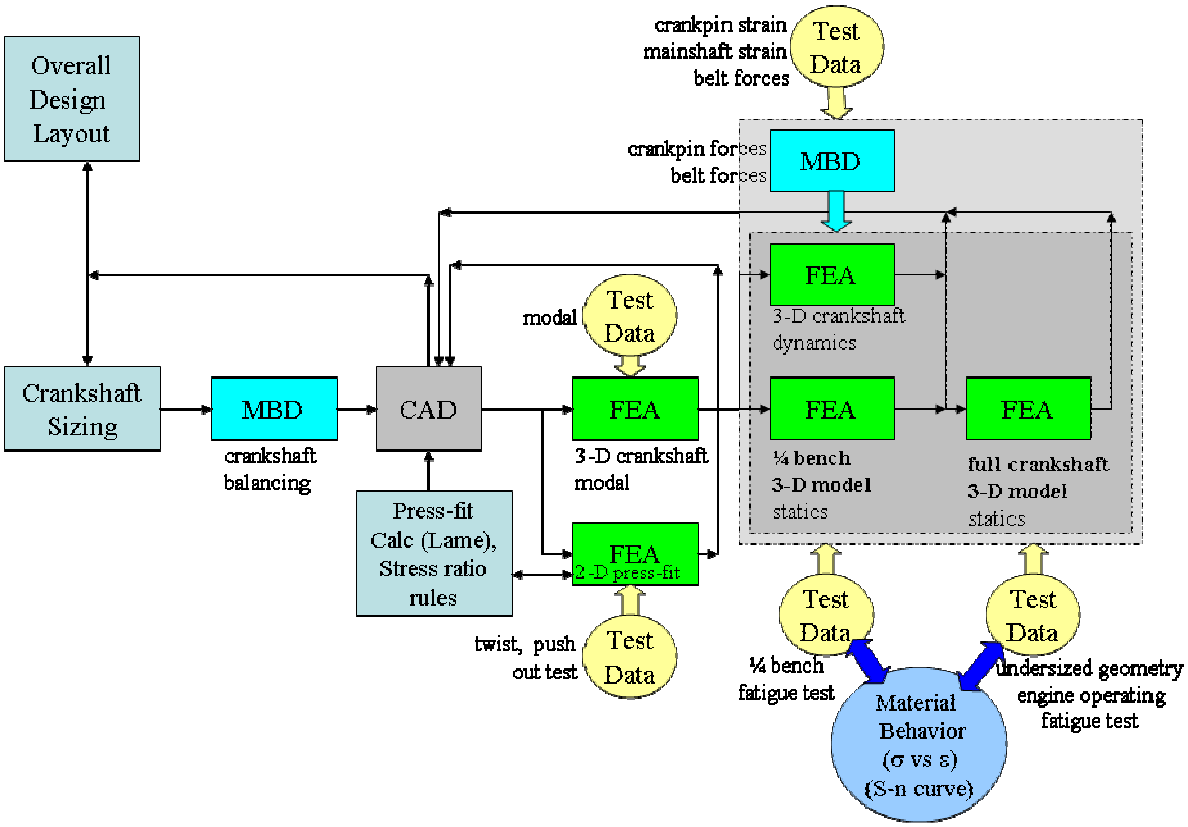

Figure 10.1.1 The modified process diagram for the structural design of a multi-piece crankshaft.

3) The one-quarter 3-D model should be used to carry out fast design iterations for operating loads before a larger effort is exerted to examine a higher quality design using the full 3-D model.

4) A physical bench test that uses a symmetry configuration similar to the one-quarter bench virtual model is to be added to the validation process. This durability test induces high cycle fatigue failures which help validate the design and improve the CAE virtual models, including providing valuable fatigue data points for the case strengthened material. Since fatigue failures may be induced by pin cracking at the pin BDC position or pin cracking induced by fretting, fatigue data points are very valuable to better leverage the results of the FEM models.

Note that the one-quarter bench FEM model is to be used to replicate the operating loads with and without the rotational inertia load.

5) Finally, crankshaft durability could be examined in the engine or running condition using slightly undersized geometry to induce early failure. Perhaps it is not typical to promote ideas in the conclusion which are not part of the research, but fatigue data from real parts is imperative to improve overall reliability in this and any CAE process.

9.2 Conclusions From Chapter 4, Assembly FEM Models

The research first focused on the assembly press-fit stress problem. Chapter 4 examines the assembly state with 3 different modeling approaches; the 2-D axisymmetric model, the 30 degree slice model, and the 3-D one-quarter bench test model. Details of the stress field at the SCA were examined and also the structural behavior was explained. *A critical objective identified was to define the characteristics of the assembly stress field at the SCA (Objective 3) which create the high stress gradient, and are defined as:*

1) The amount of unsupported web material that is beyond the SCA point of first contact between the pin and web, which must be stretched by the interference at the SCA. The differential slice of pin material at the SCA stretches a much wider slice of the web which creates a radial stress concentration.

2) A highly compressive 'kink' due to the rapid (but continuous) transition in shape of the 'free' pin to the smaller 'press-fit' diameter, which is also where the change to full contact or interference occurs over a short distance. There is a tensile axial stress also present near the kink on the free surface of the pin, which is due to the reverse in curvature of the pin outer surface to maintain continuity.

3) The axial stress created between the pin and web at the interface caused by the change in axial length of the pin and web. Poisson's ratio causes the pin to get longer under compression, while the web gets shorter while under stretch, resulting in shear stress at the interface acting in the axial direction.

As the details of the high stress gradient present at the SCA were examined and understood, high sub-surface stress components were shown to exist in the FEM assembly solution. *The high sub-surface stress values at the stress concentration are understood as follows (Objective 5):*

1) At the surface of the pin at the SCA, very large compressive stress components exist, as the high contact radial stress is constrained by the pin material with high compressive axial and hoop stress components.

2) At the same time, a kink in the pin material is present, where the compressed pin under interference fit wants to regain the free state as quickly as possible. High shear stresses are required below the surface for the pin to grow in this manner. The combination of high sub-surface shear stresses and (still near to the pin surface) high compressive direct stress components creates high a maximum equivalent stress below the pin surface as well.

3) The stress field described above in 1) is shown to have the size and shape of a Hertzian contact stress field, which was calculated with theoretical formulas [26] for the press-fit idealized as a flat plate and flat cylinder.

Once the press-fit joint assembly behavior was understood, including the characteristics of the stress field at the SCA, meshing studies were employed with 2-D and 3-D FEM models to determine the element size required to capture the high stress gradient there. *An objective of the research is to define the mesh sensitivity and refinement that is required for acceptable stress accuracy (Objective 4):*

1) The 2-D mesh studies showed convergence of the local maximum values to a limit at *h* equals 0.025 mm to 0.01 mm, and so using *h* equals 0.01 mm may be considered a good target.

2) When surface friction at the interface is considered in the 2-D axisymmetric model, the maximum stresses converges to a lower limit; except at the maximum tensile axial stress at location *C*, which was not shown to converge yet at *h* equals 0.005 mm. It is uncertain whether the convergence had not been reached yet, or whether this variation is due to the variability in the FEM model.

3) The assembly stresses for the 3-D models had reduced accuracy versus the 2-D values because of (solution time) limitations in minimum element size at the SCA that may be studied; the convergence of the 3-D models was very difficult to achieve. It is unclear whether the 2-D maximum stress values at the SCA may be calculated with a 3-D model which is not axisymmetric, even with larger refined 3-D models.

4) Combining information from both linear and log-log scale plots is a reasonable way to check for convergence. Variance in the FEM solution over the entire range of *h* studied results

in some variation in maximum stress data points which differ somewhat from the expected smooth shaped curve. Using a linear scale only to check for convergence is more sensitive to the variance in the FEM solution.

The meshing studies which tested stress sensitivity to element size at the SCA required that efficient FEM meshing strategies were employed. *The most successful meshing strategies were presented along with some that were not as successful, and are described as (Objective 7):*

1) The most successful and efficient meshing strategies employed were also the simplest tested. Since the high gradient stress condition at the SCA was limited to a very small segment of the pin and web, a thin cylindrical section was be used at the interface, which determined that the mesh there would be based preferentially on bricks. The optimum size and location of the rectangular volume was determined based on knowledge of the stress field at the SCA, and also based on trial and error. The size and location of the brick elements on both the pin and web were equal for best results. The bricks elements created a nice smooth contact pressure, and are the most efficient to fill the refinement volume at the SCA.

2) An acceptable meshing strategy was not possible without leveraging CAD to separate the pin and web SCA region into the cylindrical volumes.

3) Strategies that did not work as well included the construction of complex multi-tiered volumes near the SCA which resulted in better transition zones (refined to larger element sizes) but generated too many elements. A mixed mesh approach was examined which used a refined mesh (at pin bottom) and coarse mesh (at pin top) but resulted in lower maximum stress values in comparison because of the non-symmetrical nature of the mesh.

9.3 Conclusions From Chapter 5, Operating Condition FEM Models

After the assembly problem was well understood, two 3-D FEM models were used to examine the press-fit joint of the crankshaft for the engine operating load conditions. A full crankshaft 3-D geometry model was considered along with a more efficient one-quarter bench test model. *The behavior of the 3-D press-fit joint under operating loads was defined and discussed, including the details at the SCA, in a similar fashion to the 2-D assembly data, and is as follows (Objective 8):*

1) As the crankshaft and pin experienced bending from rotational inertia or crankpin forces, the joint carried or transmitted load from the pin by a force couple on the pin acting at opposite diagonal corners of the press-fit. The pin bending or force couple effectively 'loads' and 'unloads' the radial stress at the interface (SCA), which accordingly changes the Hertzian-like stress field present.

2) The pin loading / bending also creates compressive and tensile axial stress at the bottom of the pin, on the free surface near the SCA. For the instance when the crankpin is loaded by combustion forces (LC3), the high tensile axial stresses coincide with the radial stress unloading at the SCA (which reduces the severity of the kink). The maximum tensile axial stress (at location *C*) is shown to have a non-linear relationship with crankpin loading, due to two factors. One, it is suspected that the radial stress unloads in a non-linear fashion because that is the nature of a spherical contact (the web true radius feature is assumed as a cylinder). Two, the kink geometry acts as a stress concentration to the pin axial stress, and so both the axial stress value is increasing with increasing combustion forces, while at the same time the stress concentration of the kink reduces as the joint radial stress unloads there.

3) Both 3-D models predicted the same joint behavior under load. The only difference is the location of maximum pin bending changes because of loading differences.

The 3-D FEM studies were limited in mesh refinement at the SCA because of extended solution times. The element size of 0.01 mm which was recommended by the 2-D stress sensitivity studies was not feasible in the 3-D models, which had *h* equals 0.02 mm and 0.05 mm refinement for the one-quarter bench and full 3-D models respectively. *The implications of mesh refinement on stress local maximums were described, and also the* d*etailed 2-D axisymmetric solutions with a highly refined mesh at the SCA were extended to the 3-D domain for press-fit assembly (Objective 9):*

1) Mesh refinement is required at the SCA to accurately evaluate the rotational inertia load (LC2) and the reciprocating mass load (LC4), which are shown to still have the most 'kink' present in the pin. Since mesh refinement was limited, it is likely that these local maximum (compressive) values are under-predicted. Potentially damaging high sub-surface shear and equivalent stresses would be generated by this loading. Alternatively, the combustion event (LC3) is not sensitive to the mesh because the pin has 'unloaded' in the radial direction at this

point, which removes the kink / stress concentration. So, there is good confidence in the accuracy of the maximum stress values calculated for the damaging tensile axial stresses on the surface of the pin. For all load cases, increased mesh refinement is shown to produce a higher axial stress gradient; the axial stress turns from positive to negative over a shorter distance, approximately 0.1 mm.

2) It is suspected that local maximum values calculated with a highly refined 2-D axisymmetric model would be matched with the 3-D solution if a higher mesh refinement was practical. Therefore the higher value 2-D assembly stresses calculated were used as starting basis for the 3-D full crankshaft geometry solutions. The local stress values tracked over operating load cases were determined using the principle of super-position.

9.4 Conclusions From Chapter 6, Numerical Verification

After the behavior of the multi-piece crankshaft was understood for the assembly and operating loads, the verification of the numerical models was examined. *It is an objective of the research process to develop good reliability in the overall application of CAE tools to design multi-piece crankshafts. (Objective 10):*

1) For assembly, good overall correlation between the FEA and Lame solution radial pressure at the interface exists which is a well researched fact.

2) The detailed stress field at the SCA may only be examined by the FEM virtual test with which there is confidence.

3) For the operating conditions, the overall structural behavior of the crankshaft may be modeled to an acceptable level using static load cases which are determined as worst case based on experience and experimental data. This approach is the only practical route, as model size and the non-linear contact iterations at the joint do not allow a dynamic evaluation in the time domain that is feasible. This is only acceptable if the crankshaft passes a modal test, and experimental data should always be used to confirm this modeling approach.

4) Testing which is dedicated to fatigue failures through a) bench test or b) undersized crankshaft geometry (in a running engine) which induces high cycle fatigue failures earlier is required yet to fully prove the numerical methods.

9.5 Conclusions From Chapter 7, Press-fit Joint Optimization

After good reliability of the numerical models is demonstrated, the next step considered in the research was optimization. Since the high assembly stress state dominates the stress field for all the subsequent operating load cases, design solutions which minimize or reduce the local stresses at the SCA were studied for assembly with the 2-D model. *The improved understanding of the press-fit joint and the overall crankshaft behavior was leveraged to study design improvements as follows (Objective 14):*

1) The size of the feature was determined to need to extend past the SCA point in order to create the flexibility to relieve it in the radial direction. The flexibility or gradual change in web stiffness which was introduced by the relief feature allowed significant reduction (40 to 60%) in the maximum stress values at the SCA for assembly, while still maintaining acceptable stress levels on the features itself, which by default must stretch (ie. have significant stress).

3) The undercut and shoulder features are classic stress reduction methods which are implemented in reference books for other applications. However, a body of research could not be found that implements these ideas and solves exactly the assembly stress field at the SCA for multi-piece crankshaft design, or also solves for the operating load conditions.

4) An optimized undercut solution was examined for the operating loads, where the stress magnitudes and variations are shown to be acceptable from a design stress target perspective. Radial stress is decreased by around 50% for load steps 1,2, and 4, but converges for the 3rd load step (which has an unloaded radial stress) . Care had to be taken to balance the relief of the SCA area stresses with the higher stress levels created in the web at the undercut. A surface strengthening treatment would also be required at the undercut to counteract the high mean tensile stress present, which is required fundamentally to obtain the flexible lip.

5) The calculation of maximum stress values is thought to be more accurate with the undercut or shoulder feature since the stress gradient will be reduced.

9.6 Conclusions From Chapter 8, Rules And Tools

The last phase of this research is to simplify the numerical models and results to make them easier to implement as engineering tools. *In particular for the multi-piece crankshaft research effort, geometry symmetry assumptions are used to reduce model effort, size, solution time, and data post-processing. (Objective 11)*

1) The one-quarter 3-D model was based on symmetry assumptions to reduce model size by over one-half, and improve computational efficiencies. The detailed comparisons of the stress field and press-fit joint behavior in chapter 5 suggest that this virtual bench test creates a very similar response to the full 3-D crankshaft FEM model. The symmetry assumption allows a more accurate evaluation by using a smaller element size *h.* Also, the one-quarter bench test model offers greater accuracy with solutions times in 1/5 the time when compared to the full 3-D geometry model.

2) Since a physical bench test likely would be a stationary without any crankshaft rotation, a 'no-spin' one-quarter bench test was also calibrated in chapter 8 so that modified input loads creates similar stress behavior in the pin at the SCA as calculated with the operating conditions. Because of the non-linear behavior of the press-fit joint, load inputs for the physical testing may not simply use operating crankpin loads. The one-quarter bench test model will become extremely valuable when physical durability testing occurs in the lab, which will create fatigue data and help improve material information.

Another goal was to evaluate the behavior of a press-fit joint quickly using an analysis template, as described below (Objective 12):

1) A user friendly axisymmetric model template was created that generates, solves, and post-processes the axisymmetric model automatically. The manual task of creating each model would require many hours, which is reduced to several minutes with the template, and only needs the entry of a few geometry and mesh refinement parameters.

The 2-D axisymmetric model was used to study the effect different variables had on the local maximum stress values at the SCA. *The following design rules were created for assembly stresses at the SCA, as an aid in fast upfront design (Objective 13):*

1) It is desired to define the relationship between the average and the maximum σ_r since the design engineer may calculate by theoretical formula the approximate average value using Lame[24]. A study of the variation in interference (or average σ_r) for the baseline press-fit geometry revealed that the ratio of maximum σ_r at A does not vary linearly with the average σ_r at the interface, but a curve defining this relationship is available in Chapter 8 (for the particular true radius geometry used in this research). This is due to the non-linear variation in the contact patch size between two loaded cylinders.

2) The maximum local stress components at the SCA follow the magnitude of the local maximum radial stress. Therefore, the average radial stress may be used to calculate the maximum radial stress at A using the curve defined (see Fig.8.1.3), and the other local stress maximums may be determined using the ratios below:

- σ_{axial} minimum at *A* (pin) = 0.80 σ_r minimum at *A*
- σ_{hoop} minimum at *A* (pin) = 0.57 σ_r minimum at *A*
- τ_{xy} maximum at *B* (pin) = -0.22 σ_r minimum at *A*
- σ_{von} maximum at *B* (pin) = -0.34 σ_r minimum at *A*
- σ_{von} maximum at *A* (web) = -0.59 σ_r minimum at *A*

Note that the ratios of some stress components were more consistent with respect to σ_r minimum at A than others.

3) Press-fit studies on historical engine designs supports the previous findings. Simple ratios can be used to predict local maximum stress components at the SCA, based on the average radial contact pressure. Accuracy will vary, but will fall in the 10 to 15 percent range. The accuracy may be improved by using the extrapolated lines on the plots presented for those stress component ratios that showed variability.

10 Future Work

The numerical tools researched in the thesis should facilitate design process of multi-piece crankshafts for various types of engines. The main benefit of applying these tools should be a significant reduction in costly testing of usual design alternatives (the ultimate aim would be to test only the final computer refined and optimal design). Despite the progress made, the numerical tools presented should be continuously upgraded and modified to be better able to simulate the real behavior.

10.1 General Future Work

In the future, the following general areas require work:

1) The complete design, analysis, and experimental validation process for multi-piece crankshafts should be put to use through several engine programs to improve the level of historical data and process maturity.

10.2 Future Work with the 2-D Assembly FEM Models

Some aspects of the (2-D) assembly problem have not yet been thoroughly investigated, including:

1) Further examine whether convergence has been reached for maximum axial (pin) stress at C by studying models with increased mesh density below 0.005 mm.

2) Study the Hertzian stress distribution parameters b the for variation in press-fit geometry and interference, to determine the sensitivity of the position (depth) of the local maximum sub-surface stresses.

10.3 Future Work with the 3-D Models

Many aspects of the (3-D) assembly problem have not yet been thoroughly investigated, including to following:

1) When more powerful computer hardware is available, larger 3-D model sizes can evaluate further the convergence of the maximum stress value at the SCA beyond *h* equals 0.02 mm.

2) Further study the SCA area stress solution differences in the 30 degree slice and full crankshaft geometry models. In particular determine, at much higher mesh refinement, the

sensitivity of the maximum stress values calculated with the near axisymmetrical (30 degree slice model) and non-symmetry geometry (crankshaft web).

The following tasks require further research to better define the 3-D modeling effort of the operational loads:

1) Re-calculate the stress conditions at the SCA for the pin and web using a higher density mesh refinement. In particular, the details of the high compressive stress condition on the pin and web should be studied for LC4, on the bottom of the pin. There is high confidence in the calculation of the stress condition there for the LC3 tensile condition since the radial interface pressure has unloaded at that time. It is desired to determine any increase in the sub-surface stresses at the bottom of the pin (SCA) for an increased mesh density.

2) The web maximum equivalent stress value (1332 MPa) at A1 calculated for LC4 (full 3-D crankshaft FEM model) falls very close to yielding, and should examined closer with a more refined element size. If yielding occurs, a solution using elastic-plastic material models is required. Potentially any yielding of the web will relieve some of the pin local elastic stresses at the SCA.

3) Evaluate relative displacement or sliding between the pin and web surfaces at the SCA for the operational loads. This relative displacement value could become a design metric with the eventual increased knowledge in this area. The knowledge of joint relative motion will become relevant when crankshaft durability bench tests start producing fatigue data points, specifically when fretting is a contributing failure mechanism.

4) Map the non-linear joint behavior in full, as only 3 specific load cases have been evaluated. Other operating load conditions could be studied. For example, in chapter 5 the local maximum axial stress on the pin at C varied nonlinearly with the application of different crankpin combustion loads. (see Fig. 5.2.4.3) Potentially other non-intuitive maximum stress conditions exist. At minimum the one-quarter FEM model should be used to study more combustion and inertial load increments determine exactly when the maximum tensile axial stress at C occurs.

5) Examine the press-fit joint's sensitivity to PTO crankpin and belt forces, so that it can be determined how effective the bench test approach is when it does not include the belt forces. To do so, one would examine the changes in stress maximums with the full 3-D crankshaft FEM model for LC3, with and without the belt forces. Potentially one could also examine historical

designs (of the same architecture) with to determine whether good correlation in local stress results at the SCA is shown between the full model and the one-quarter bench test model.

6) Use sub-modeling methods to examine the press-fit joint behavior for a dynamic FEM crankshaft solution. A relatively coarsely meshed continuous (one piece) crankshaft is used to calculate the dynamic response, from which the boundary conditions are taken for certain time steps of interest. These boundary conditions are then imposed on the detailed non-linear sub-model of the joint, which includes refined meshing at the SCA and a contact algorithm to replaces the continuous joint. This solution approach is of interest when the crankshaft modes fall within the operating range and exhibit a heightened dynamic response.

10.4 Future Work: Experimental Verification

The following future work will be performed as part of the engine program's regular testing regime:

1) Collect crankshaft strain data to verify the dynamic behavior of the engine, and correlate to the FEM model predictions.

In the future, it is extremely important that the following experimental activities take place so that this research area can take the next step forward in progress:

1) Perform durability bench tests so that substantial fatigue data is generated. There are two challenges with the bench test. First, the fatigue damage accumulated in the bench test must be correlated to the engine running condition. This becomes difficult with the non-linear joint behavior present and the designs susceptibility to both fretting and fatigue cracking failure mechanisms. The second challenge is the lack of knowledge of the strengthened materials fatigue curve. A second fatigue test which examines the strengthened material only, with a simple geometry shape (perhaps a pin coupon in bending) could help generate a material specific fatigue curve. If one is to examine the numerical aspects of this problem, it is numerically challenging to calculate an accurate stress value, and it is also challenging to develop a representative material fatigue curve.

2) Consistently generate crankshaft fatigue failures in the running condition. This may be done either through undersized components or by testing the crankshaft component for extended lengths, past the typical validation confirmation mark.

10.5 Future Work: Tools And Rules

Any further implementation experience with these numerical tools for multi-piece crankshaft design will result in the opportunity to enhance them. Future work in this area includes:

1) Further develop the one-quarter bench test FEM model to support physical bench testing by a) supplying the equivalent static loads which create the equivalent response as to when rotational inertia loads are applied to the crankshaft and b) leveraging the FEM model stress results along with fatigue calculations to compare with and correlate to fatigue data from the durability bench tests.

2) Examine the structural response of the press-fit joint for a pure bending moment input to the crankpin using tje one-quarter bench test FEM model. This load input would be similar to that for a common high frequency – high cycle crankshaft durability bench test apparatus. It would be important to understand this type loading on the joint, including what stress field it produces at the SCA before any durability testing could be done with such an apparatus.

10.6 Future Work: Optimization

The optimization work thus far in the research focused on reducing the high mean assembly stress in the press-fit joint. Future work in this area could consist of:

1) Examine how the torque retention has been changed for the optimized solution, through both FEM and experimental methods. One concern with the undercut design is that it reduces the torque retention capacity of the joint since it decreases the interface radial pressure at the SCA.

2) Perform durability testing (bench or in running engine) with the optimized under cut design.

3) Further develop other stress relieving features at the press-fit SCA such as the classic groove solutions in the pin, which create compressive axial stress at the pin surface.

4) Re-examine the undercut 3-D one-quarter bench test model with a higher mesh refinement; h equals 0.05 mm was used, which could be decreased in size. This size however should be adequate since the stress gradient in the area of concern has been improved substantially by the presence of the undercut.

References

[1] R.G. Dubensky, “Crankshaft Concept Design Flowchart for Product Optimization”, SAE 2002 World Congress, SAE Technical Paper Series 2002-01-0770, 2002.

[2] Private conversation and hand calculation work examples with Martin Heinrich, Engine Design Manager, Roseau, MN, 1999.

[3] Meriam J.L. and Kraige L.G., “Engineering Mechanics Volume 2 Dynamics, Second Edition”, John Wiley & Sons Inc., 1986, pg 295.

[4] Cooke D.C. and Young W.C, “Advanced Mechanics Of Materials”, MacMillan Publishing Company, 1985, pg 90.

[5] Private email communication with Brian Galbraith, Polaris Powertrain test engineer, May 2008.

[6] Private email communication with Ron Danielson, Polaris Powertrain design engineer, May 2008.

[7] Heath A.R., McNamara P.M, "Crankshaft stress analysis - combination of finite element and classical analysis techniques", Trans of the ASME Journal of Engineering for Gas Turbines and Power, v 112, n. 3, July 1990, 268-75.

[8] Mr. Martin Heinrich, Warroad, MN, retired engine design engineer, Polaris Industries. Private conversation. 1999.

[9] Hyunkwon K., and Kyuhoon C., "Crankshaft stress analysis procedures in engine design", Proceedings of the 6th International Pacific Conference on Automotive Engineering, 1991, p 313-319.

[10] Parikyan T., Reach T., Priebsch H., "Structured model of crankshaft in the simulation of engine dynamics with AVL/EXCITE", ASME Internal Combustion Engine Division (Publication) ICE, v37, n3, Engine Systems: Lubrication, Components, Exhaust and Boosting, System Design and Simulaiton, 2001, p 105-114.

[11] Parikyan T., "Unified approach to generate crankshaft dynamic models for 3D and torsion vibration analyses", ASME Internal Combustion Engine Division (Publication) ICE, v40, Design, Application, Performance and Emissions of Modern Internal Combustion Engine Systems and Components, 2003, p 305-310.

[12] V. Prakash et al; "A FEM Based Approach to Crankshaft Dynamics and Life Estimation", SAE 980565, 1998.

[13] Wikstrom A., and Andersson T, "Simulation of engine vibrations and comparison with experiments", Proceedings of the Tenth International Congress on Sound and Vibration, 2003, p 2973-2980.

[14] Kimura J. et al; "Experiments and Analysis of Crankshaft Three-Dimensional Vibrations and Bending Stresses in a V-Type Ten-Cylinder Engine: Influence of Crankshaft Gyroscopic Motions, SAE 971995, 1997

[15] Henry J.P., Toplosky J., and Abramczuk M.; "Crankshaft Durability Prediction – A New 3-D Approach", SAE 920087, 1992.

[16] A. Strozzi and P. Vaccari, "On the press fit of a crankpin into a circular web in pressed-up crankshaft", *Journal of Strain Analysis*, Vol.38 No.3, 189-199, 2003.

[17] Zhang Y., McClain B. and Fang X.D., "Design of Interference Fits via Finite Element Method", International Journal of Mechanical Sciences, 42,1835-1850, 2000.

[18] D.J. White and J. Humpherson, “Finite-Element Analysis Of Stresses In Shafts Due To Interference-Fit Hubs”, *Journal of Strain Analysis*, 4:2, 105-114, 1969.

[19] B. Kanber, “Boundary Element Analysis of Interference Fits”, Turkish J. Eng. Env. Sci., 30, 323-330, 2006.

[20] T. Makino, M. Yamamoto, and K. Hirankawa, “Effect of Contact Edge Profile on Fretting Fatigue Crack Initiation Site in Press-Fitted Axle”, Japan Society of Mechanical Engineers, Part A v63, n615, Nov. 1997, p 2312-2317.

[21] T. Makino, M. Yamamoto, and K. Hirankawa, “Fracture Mechanics Approach to the Fretting Fatigue Strength of Axle Assemblies”, ASME Second Int. Symposium on Fretting Fatigue, 2000, pg 509-522.

[22] Z. Gawronski, B. Krushzynski, P. Kula; “Synergistic effects of thermo-chemical treatment and super abrasive grinding in gears’ manufacturing”, Journal of Materials Processing Technology, 159 (2005) pgs 249-256.

[23] Bathe K.J., ”Finite Element Procedures”, Prentice-Hall, Inc., 1996, pg3.

[24] Cooke D.C. and Young W.C, “Advanced Mechanics Of Materials”, MacMillan Publishing Company, 1985, pg 90.

[25] Young W.C., “Roark’s Formulas for Stress & Strain 6th Edition”, McGraw-Hill Inc., 1989, pg 650.

[26] Juvinall R.C., “Fundamentals of Machine Component Design”, John Wiley & Sons Inc., 1983, pg 260.

[27] Szyszkowski W. and King J. “Stress Concentrations Due to Thermal Loads In Composite Materials”, Computers and Structures, v56, n 2-3, Jul 17, 1995, p 345-355.

[28] ANSYS Theory Volume IV User's Manual, Revision 5.2, ANSYS Inc, 275 Technology Drive, Canonsburg, PA, 15317, USA, 1997.

[29] Private email communication with Larry Hosaluk, Polaris Powertrain design engineer, April 2008.

[30] Juvinall R.C., "Fundamentals of Machine Component Design", John Wiley & Sons Inc., 1983, pg 202.

[31] Private email communication with Larry Hosaluk, Polaris Powertrain design engineer, April 2008.

[32] http://emat.eng.hmc.edu/database/rockwell_conversion.htm, 2008.

[33] Private email communication with Tim Giese, Polaris CAE engineer, May 2008.

[34] Private email communication with Larry Hosaluk, Polaris Powertrain design engineer, May 2008.

[35] Private email communication with Dan Krings, Polaris NVH engineer, April 2008.

[36] Cooke D.C. and Young W.C, "Advanced Mechanics Of Materials", MacMillan Publishing Company, 1985, pg 102.

[37] Jeff King Internal FEA Report, Polaris CAE engineer, May 2005.

[38] Private email communication with Dan Krings, Polaris NVH engineer, April 2005.

Appendix A: 30 Degree Symmetry Model Supporting Data

This appendix provides supporting information to section 4.4, a review of the 30 degree slice model construction and results. The 30 degree slice model was created to examine efficient meshing practices, and also to compare its results for assembly to the 2-D axisymmetric and 3-D model.

A.1 30 Degree Slice Models

As discussed in section 4.4, a single rectangular area swept to form a ring or cylinder at the area of interest proved to work best for good meshing control. Figure A.1.1 shows the rectangular ring volume at the SCA for the web.

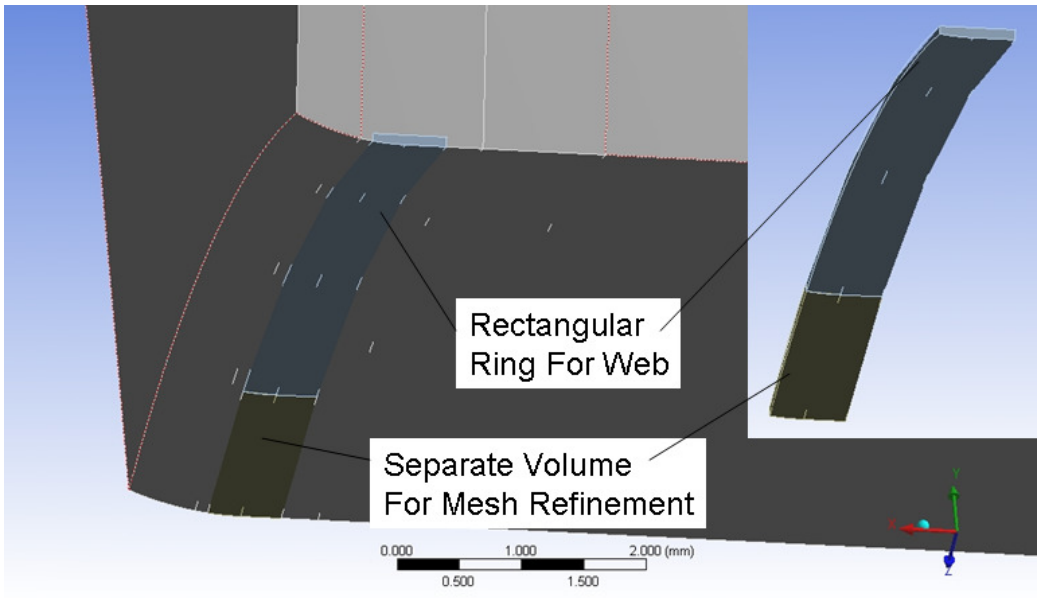

Figure A.1.1 A 3-D slice model showing the ring volume at the SCA for the web.

Trial and error was also used with the variation in the size and location of the rectangle (see Fig. A.1.2) and matching mesh (see Fig.A.1.3) to obtain acceptable contact stress, but still minimize model size.

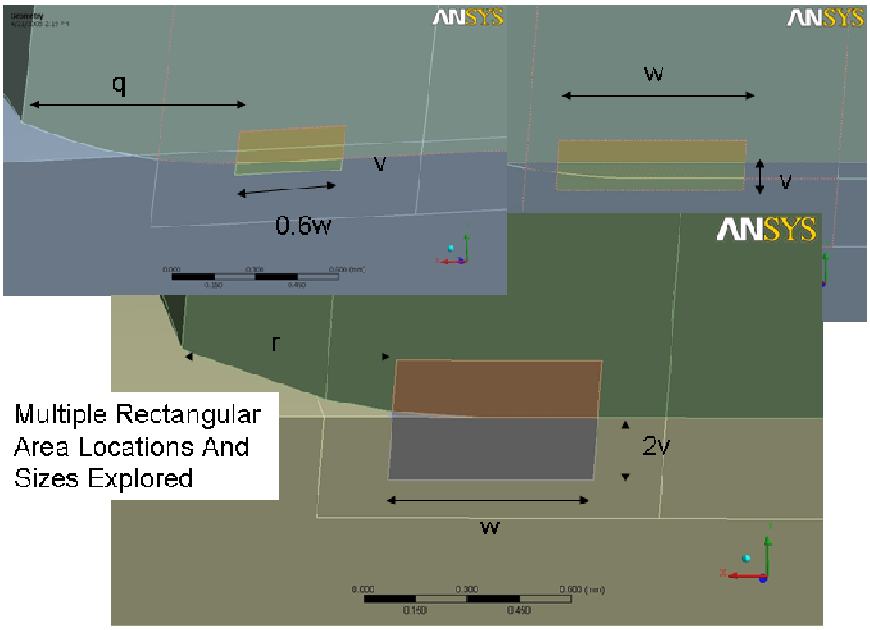

Figure A.1.2 Multiple rectangular areas were studied at the SCA.

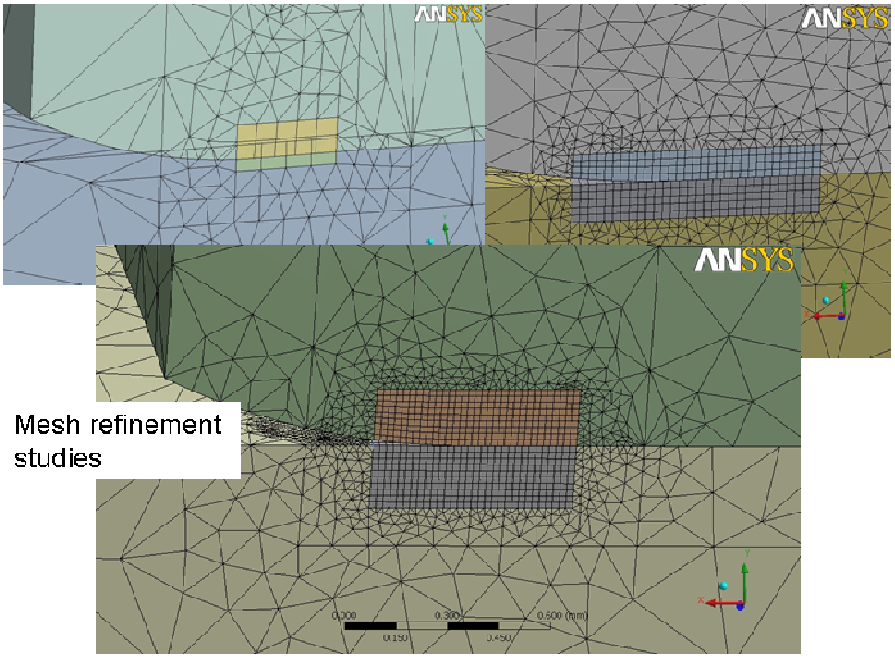

Figure A.1.3 Mesh variation for the rectangular areas at the SCA.

Mesh details for the thin rectangular volume on the web (at the SCA) are provided in Fig. A.1.4, note ring always used brick elements for best contact solutions results.

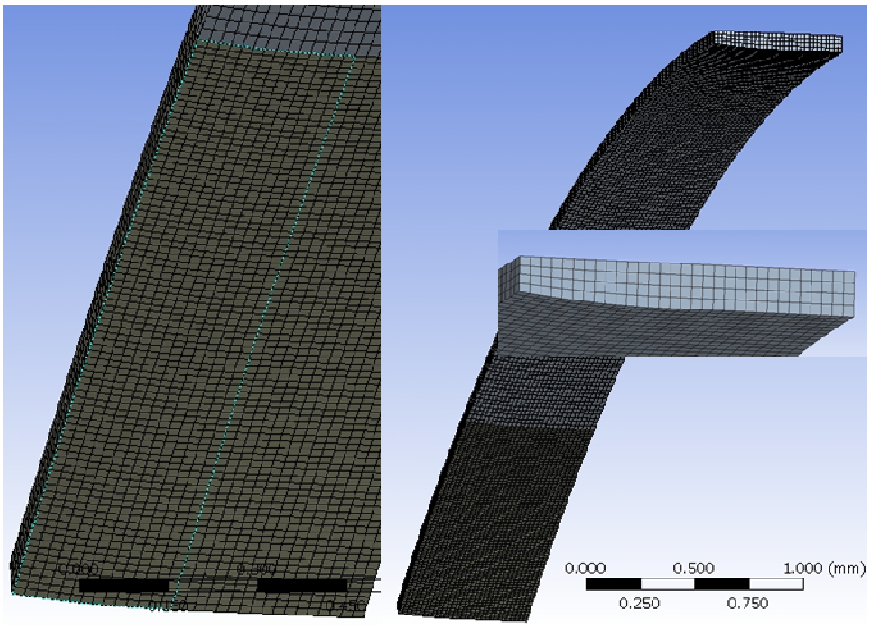

Figure A.1.4 A typical ring (brick) mesh using a 2 volume approach.

A.2 30 Degree Slice Model: General Displacement And Stress State

Figure A.2.1 shows the radial displacement plot for the 3-D slice model. The interference between the pin and web is generated with a temperature change.

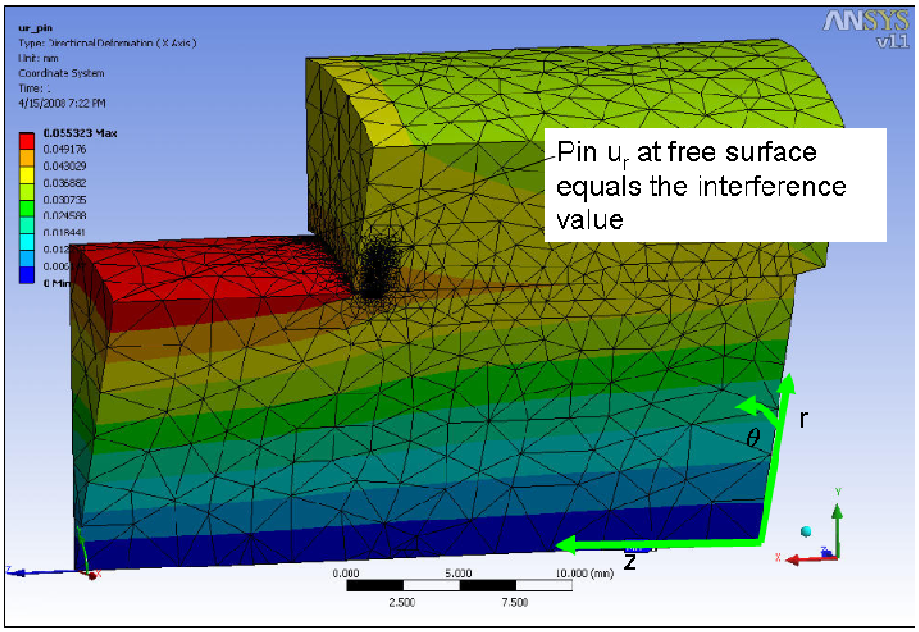

Figure A.2.1 Assembly (press-fit) radial deflection plot, 30 degree slice model.

Component stress (σ_r, σ_z, τ_{rz}) for the assembly problem are plotted in Figs. A.2.2 thru A.2.4. In each plot, a close up of the stress distribution at the SCA is provided. The results posted use an

element size of h equals 0.002 mm. Generally, these 3-D patterns look very much like the 2-D results, but are lower in magnitude.

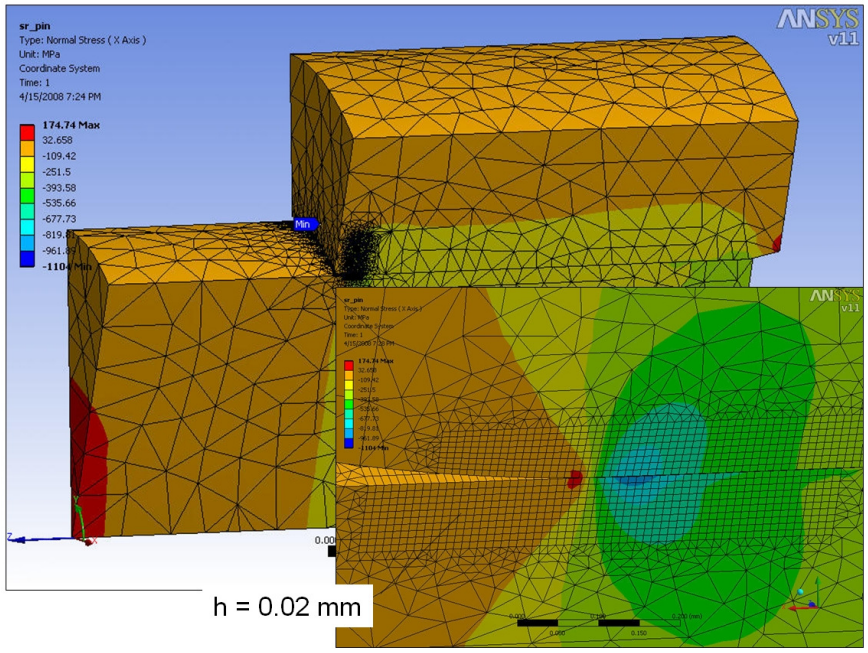

Figure A.2.2 Assembly (press-fit) radial stress plot, 3-D slice model.

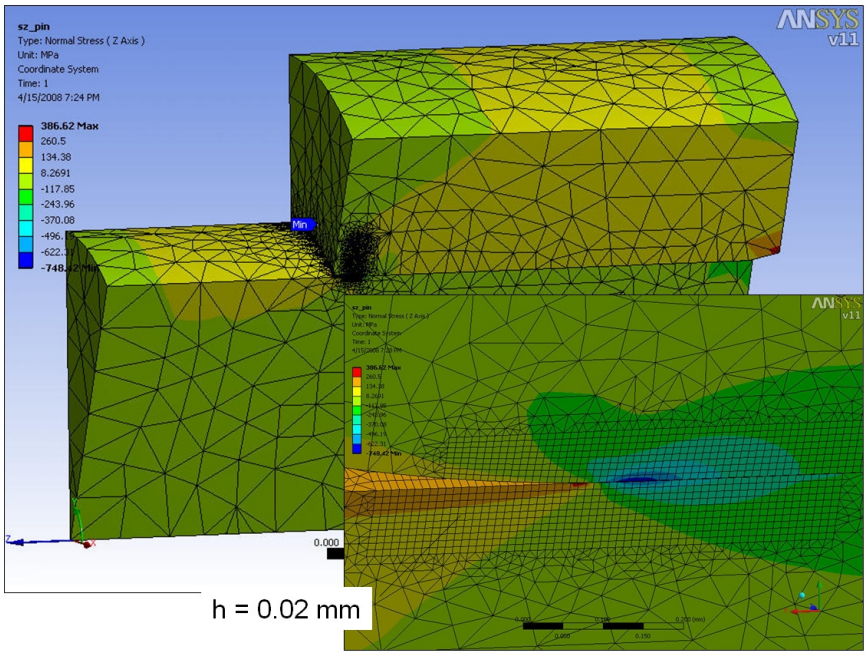

Figure A.2.3 Assembly (press-fit) axial stress plot, 3-D slice model.

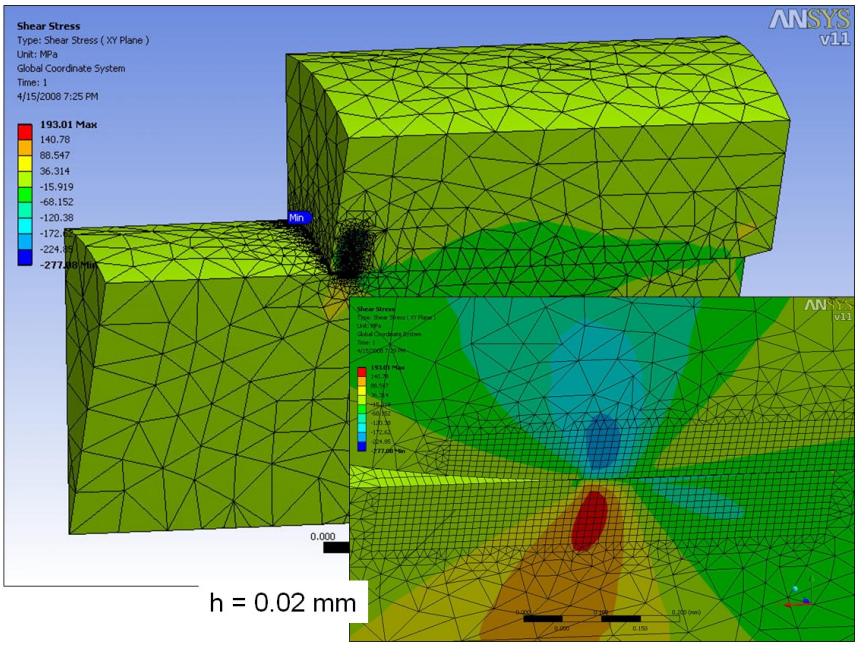

Figure A.2.4 Assembly (press-fit) shear stress plot, 3-D slice model.

Figure A.2.5 shows a highly distorted equivalent stress plot of the pin at the SCA. The 3-D plot demonstrates the 'kink' of the pin free surface that the 2-D model exhibited.

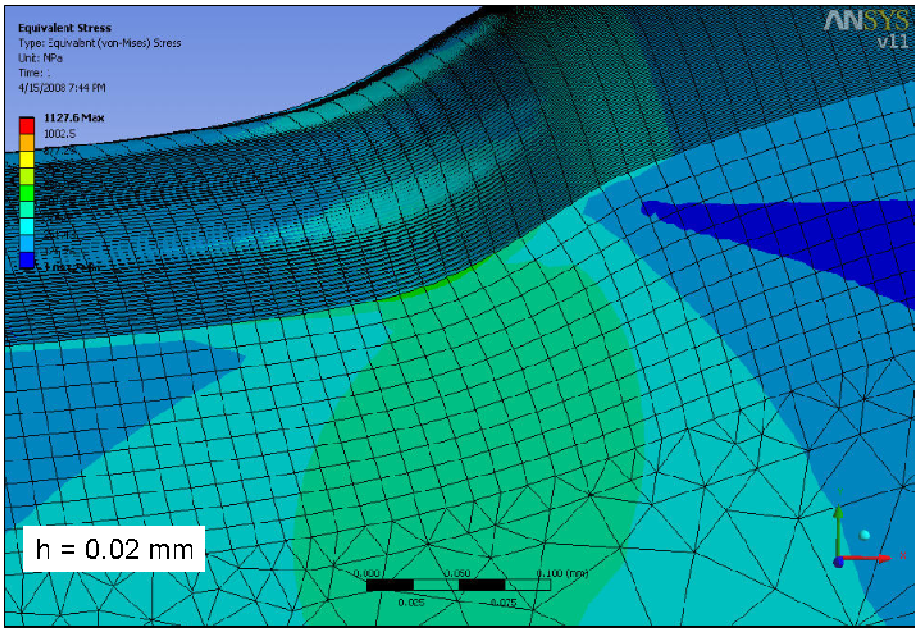

Figure A.2.5 A distorted plot of assembly σ_{VM} stress of the slice model pin.

Finally, in Fig.A.2.6 the (radial) contact pressure distribution at the SCA is shown on the pin surface. Peak surface normal pressure matches peak radial stress on the pin surface, as is required. Note how consistent the pressure distribution is in the hoop direction.

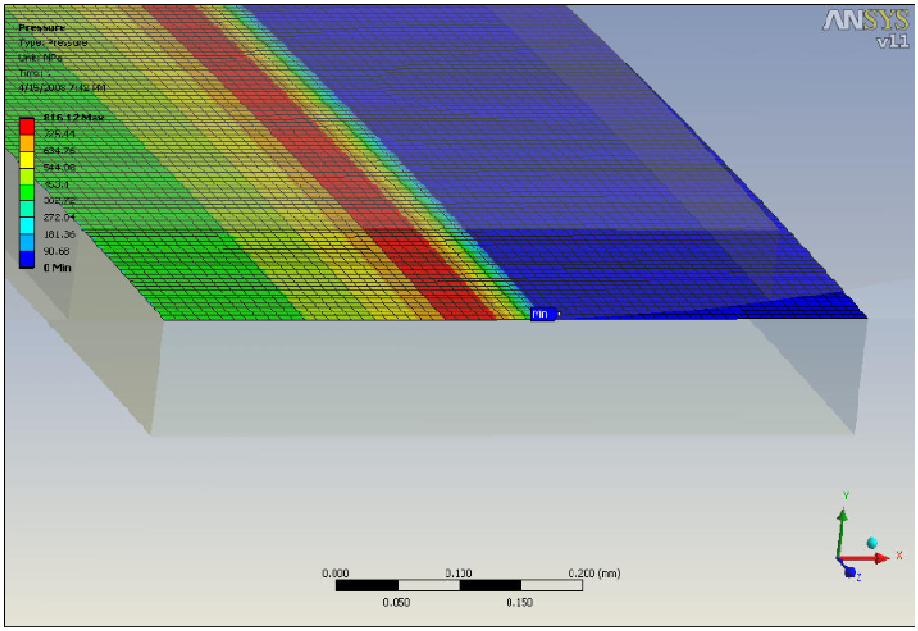

Figure A.2.6 Assembly contact pressure plot at the SCA, 3-D slice model.

A.3 30 Degree Slice Model: Results For A Mixed Mesh

In order to reduce the model's size, alternative meshing approaches were examined. Mesh size was varied across the theta (θ) direction, using a fine mesh at one end and a coarse end at the other in order to minimize the number of elements used.

The mesh sizing was controlled with the ring volume on both the pin and web, and is shown in Fig.A.3.1. For example, the mesh size may change from *h* equals 0.02 mm to *h* equals 0.1 mm across the θ distance of the ring. For these studies, this approached was termed 'mixed mesh'.

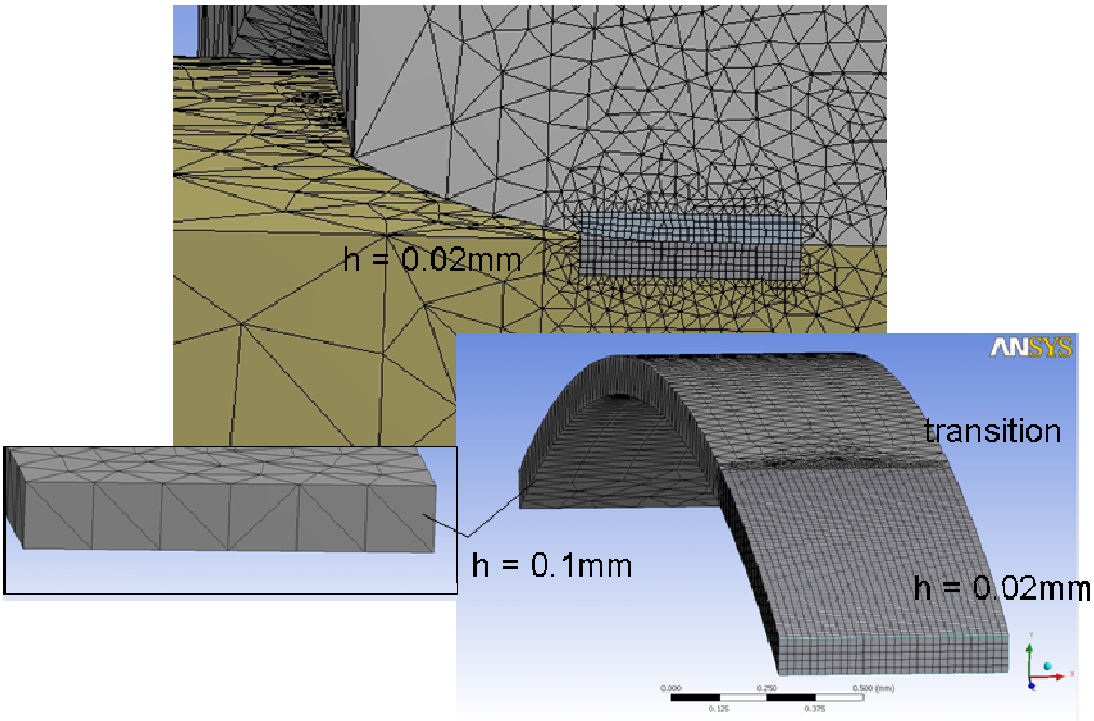

Figure A.3.1 Details of the Mixed Mesh model showing mesh variation across the geometry volume of interest at the SCA.

Figure A.3.2 shows an isometric view of the pin detailing σ_z stress at the SCA. This view provides the variation in the stress field across the pin outer diameter. For an axisymmetric solution, there should be no variation in the hoop (θ) direction. But to the mixed mesh models all stress components exhibit some variation in stress in the circumferential direction, and in particular shear stress variation is very noticeable in Fig.A.3.2. Section 4.6 provides a more detailed examination of the effect of mesh density for the mixed modeling approach.

Surface contact pressure is provided for a mixed mesh in Fig.A.3.3. Poor mesh quality at the SCA, on the surface, is shown to greatly effect the maximum pressures calculated. In particular the tetrahedral elements at the transition point from refined to coarse mesh appear to have a large affect on the stress field.

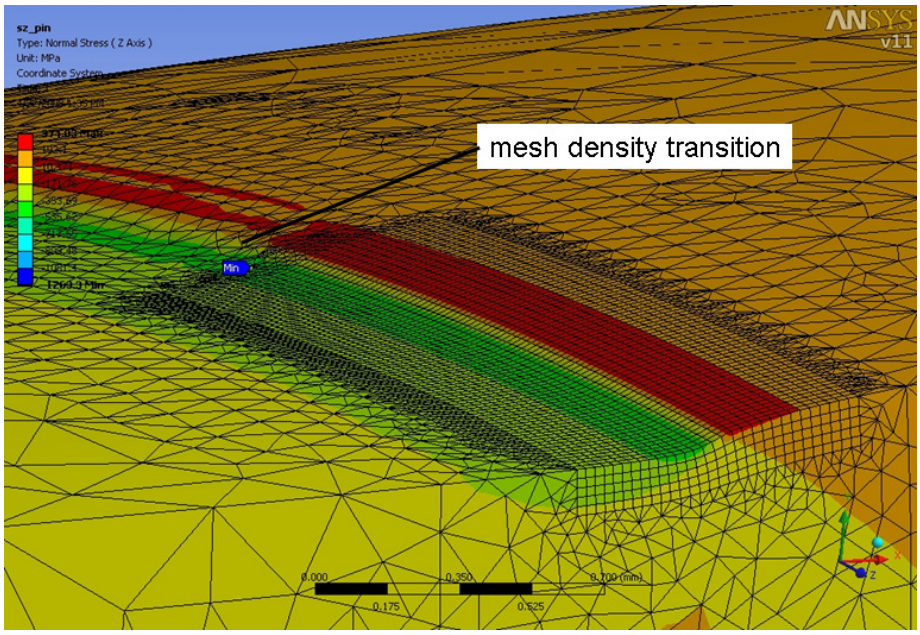

Figure A.3.2 Isometric view of axial stress on the pin at the SCA.

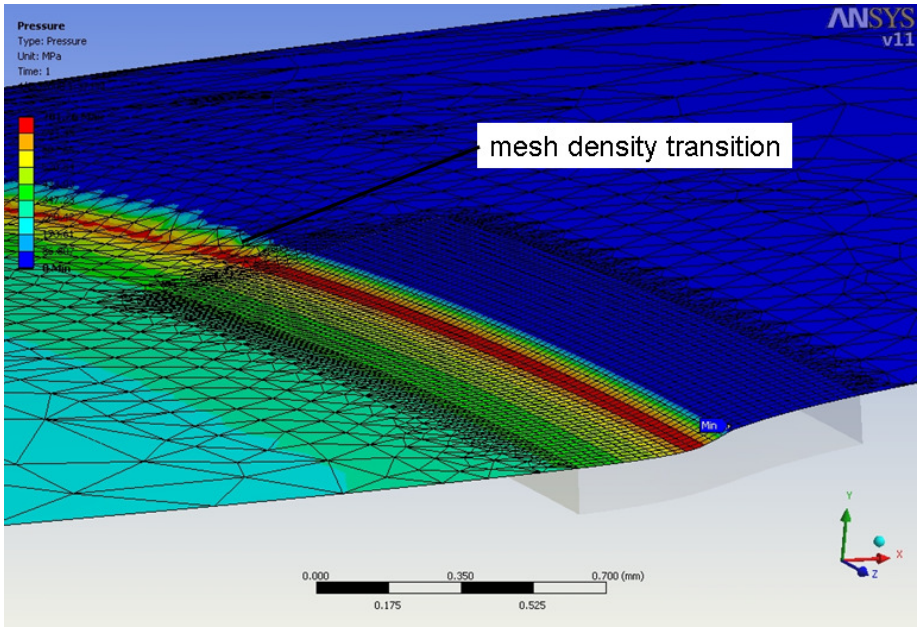

Figure A.3.3 Isometric view of surface contact pressure on the pin at location A

Appendix B: Full Geometry 3-D Crankshaft FEA Model Details

This appendix contains further information on the 3-D model details, in support of the model description in section 5.3.1. The pin and web are split in to volume segments to enhance the post-processing of results; also a thin cylindrical volume is used for good control of the mesh at the SCA. First note that the cylindrical volume is cut into 10^{o} segments, which is shown in Fig. B.1.

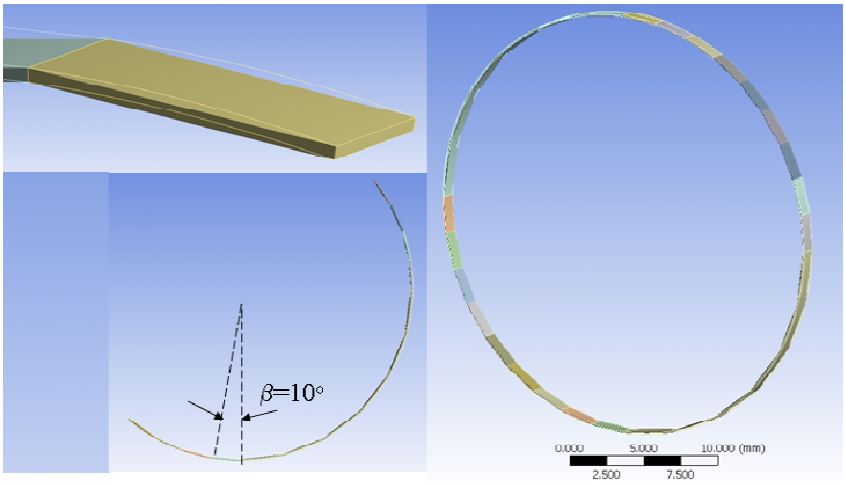

Figure B.1 A thin rectangular cylinder at the SCA is cut into pie shaped segments.

Next the PTO outer web is shown with a partial selection set in Fig. B.2. Since the wedge volumes center about the pin axis, the selection set chosen here is not symmetric about the main shaft. This same web volume selection set is shown in Fig. B.3 in an isometric view, both with and without the pin.

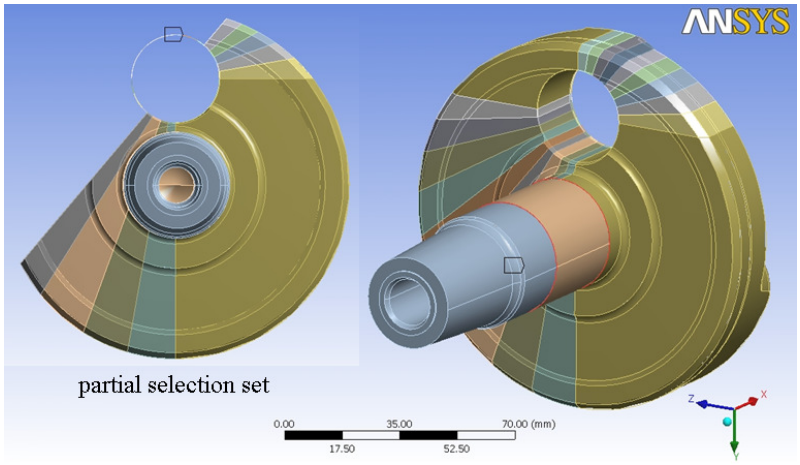

Figure B.2 The PTO outer web volume segments.

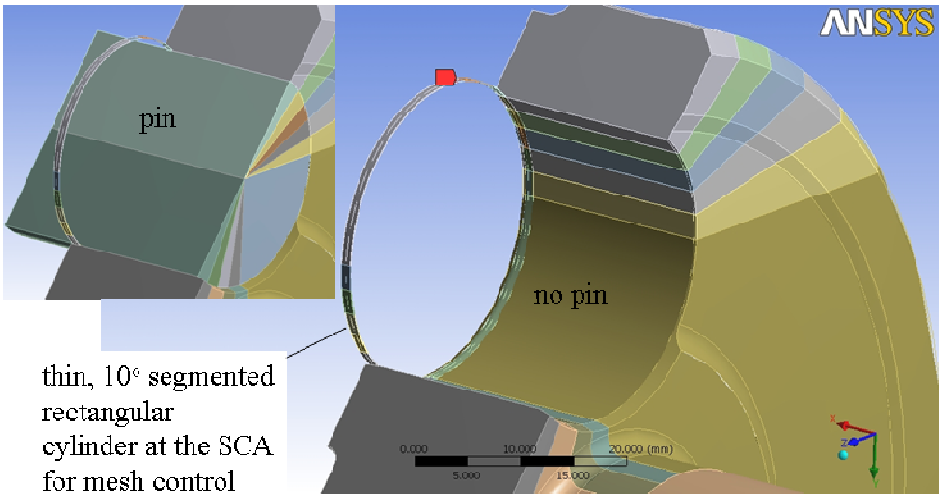

Figure B.3 The PTO outer web is cut into volume segments for post processing.

Now additional FEM mesh descriptions are provided in support of section 5.3.1. Some key fillet radii, which are shown on the crankshaft mesh in Fig. B.4, need to maintain adequate mesh refinement to predict accurate stress values around the curved surfaces.

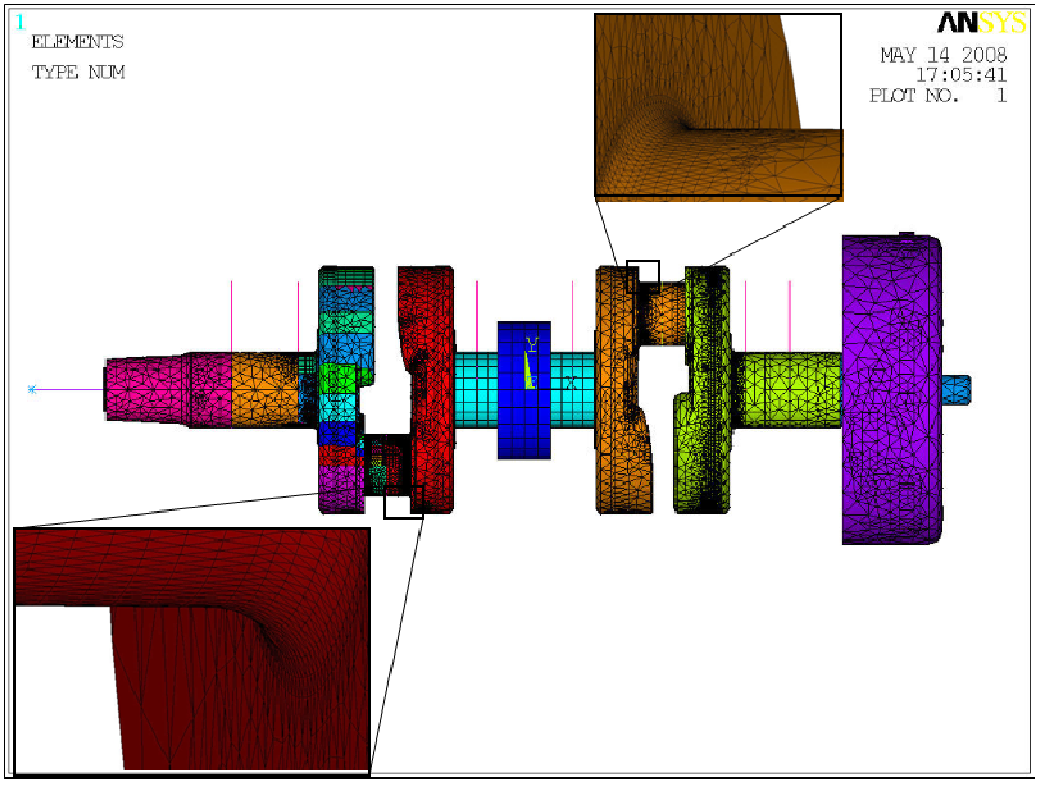

Figure B.4 Fillet regions on the crankshaft with good mesh refinement.

Next the brick element based mesh present in the thin cylindrical volume at the SCA is shown in Figure B.5. The element size is controlled in both volumes on the pin OD and the web ID so that stress sensitivity studies may be mapped relative to element size.

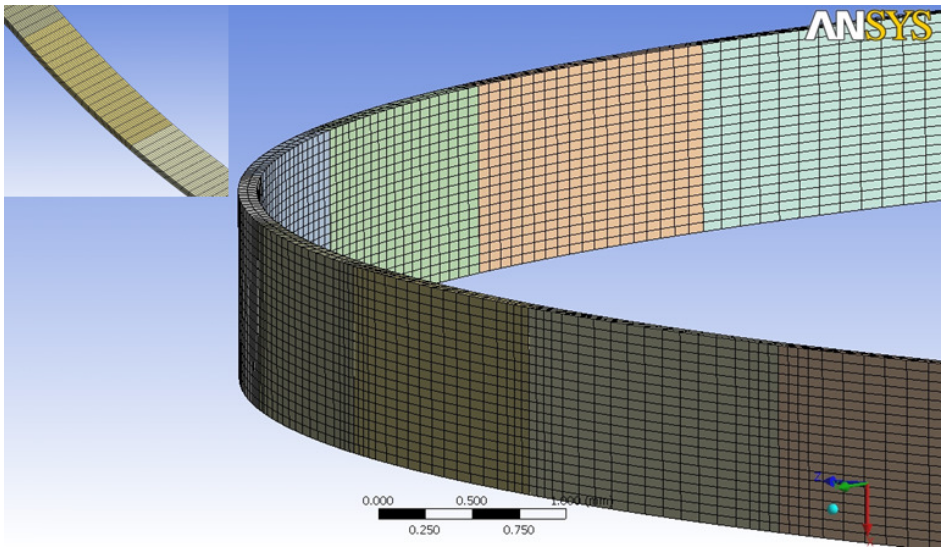

Figure B.5 The thin cylinder mesh at the SCA which is segmented by 10^{o} increments.

The solid mesh is a mixture of 20 node brick and 10 node tetrahedral quadratic elements, which require prism and wedge elements in the transition from the brick shape to the tetrahedral shape. The transition from brick to tetrahedral elements is shown in different views in Figs.B.6 and B.7.

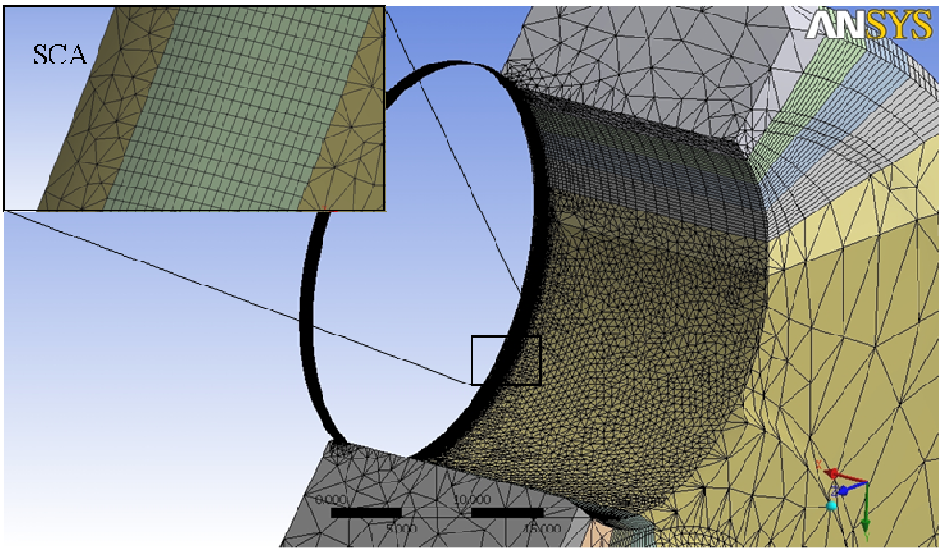

Figure B.6 Details of the mesh at the PTO outer web, including bore mesh details.

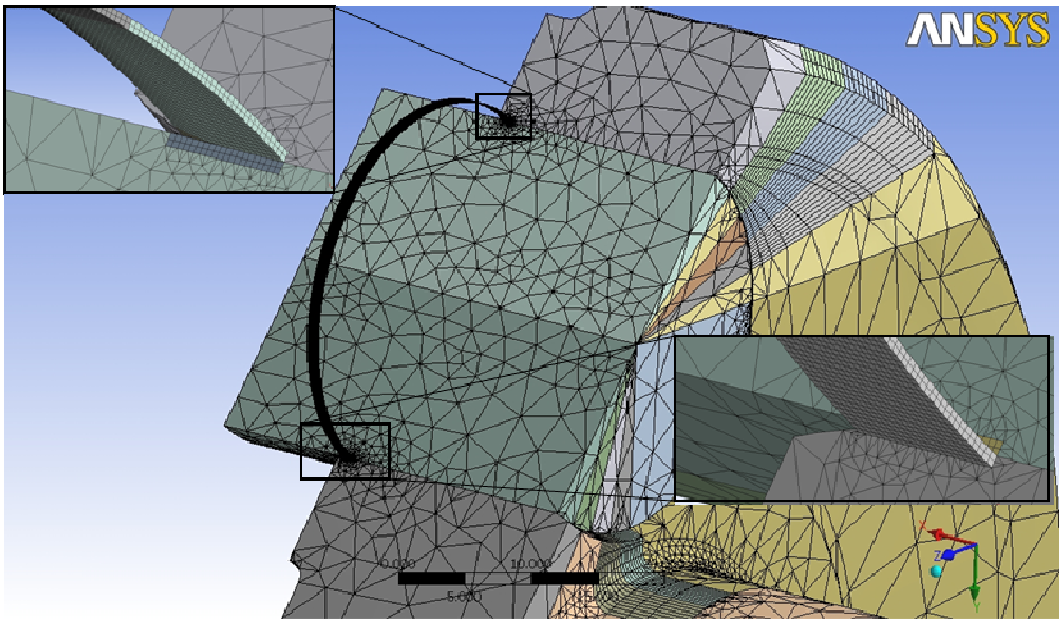

Figure B.7 A sectioned view of the PTO outer web and pin.

Appendix C: Full Geometry 3-D Crankshaft FEA Assembly Results

The information included in this Appendix contains FEM results from the full 3-D crankshaft model used to evaluate the press-fit assembly problem, time step 1. The assembly results are presented in great detail in Chapter 4, and in particular these results match closely to those for the one-quarter bench FEM model.

The equivalent stress on the PTO outer web is shown in Fig.C.1 for time step 1, assembly. Stress of any significance is limited to the local area around the press-fit joint, as the crankshaft main bearing boundary conditions are set such that the reactions there are zero for the assembled state. The stress contours and magnitudes match the previous results provide in chapter 4 for this same geometry and radial interference.

The contact pressure calculated at the SCA on the pin OD surface is very uniform for the meshing and contact approach used. Radial stress for the pin SCA cylindrical volume is plotted in Fig.C.2. A comparison of maximum radial stress to element size and the previous 3-D results is provided in section 5.4. A high compressive radial stress peaks at location *A* which has been the case for all previous 2-D and 3-D models.

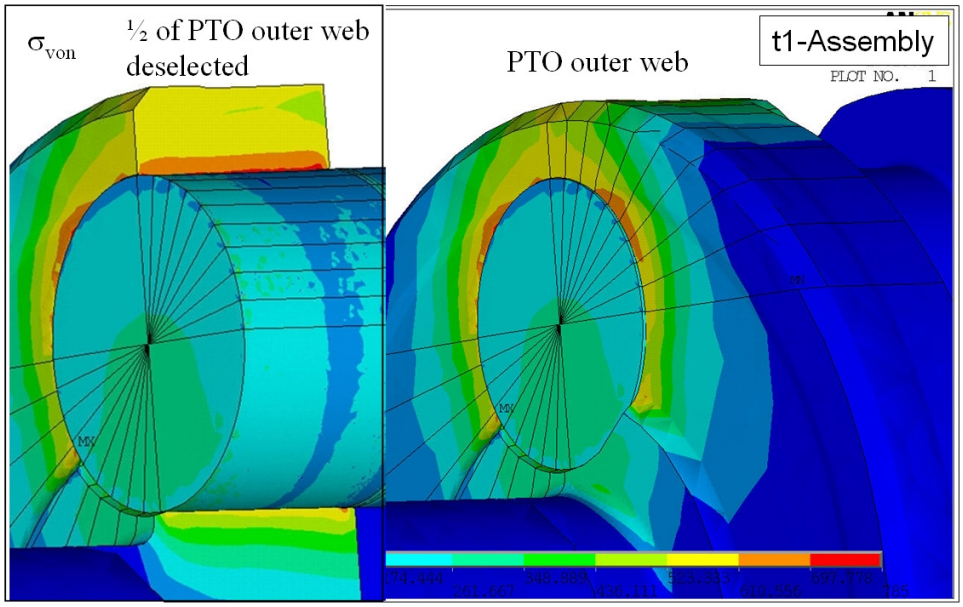

Figure C.1 End view of PTO outer web equivalent stress plot, LC1 (assembly).

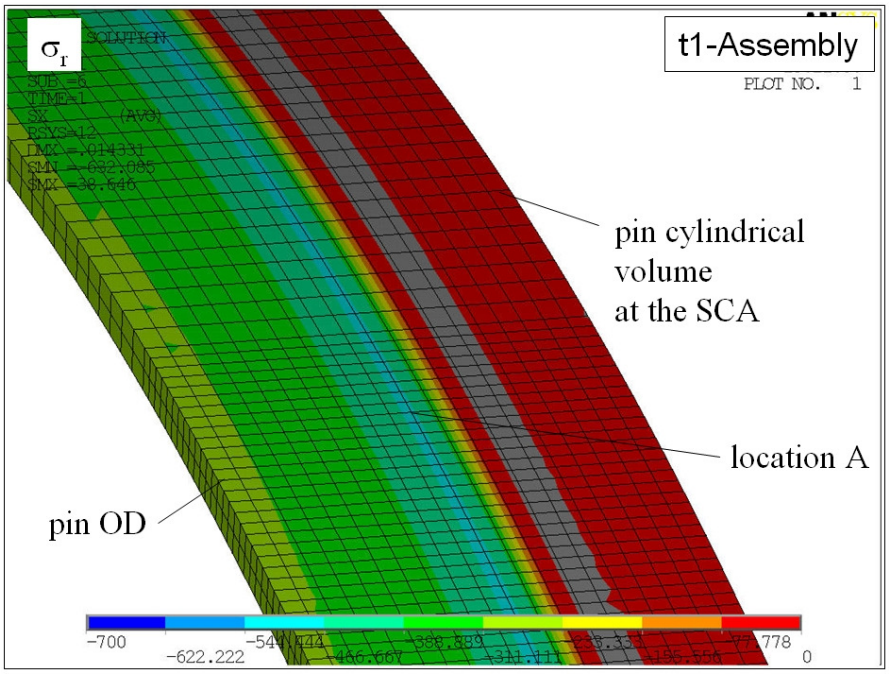

Figure C.2 Pin SCA cylindrical volume σ_r plot, LC1 assembly.

Axial stress is plotted considering the pin SCA cylindrical volume only in Fig.C.3. Tensile stress on the pin free surface is shown to occur just outside the contact region as previously demonstrated.

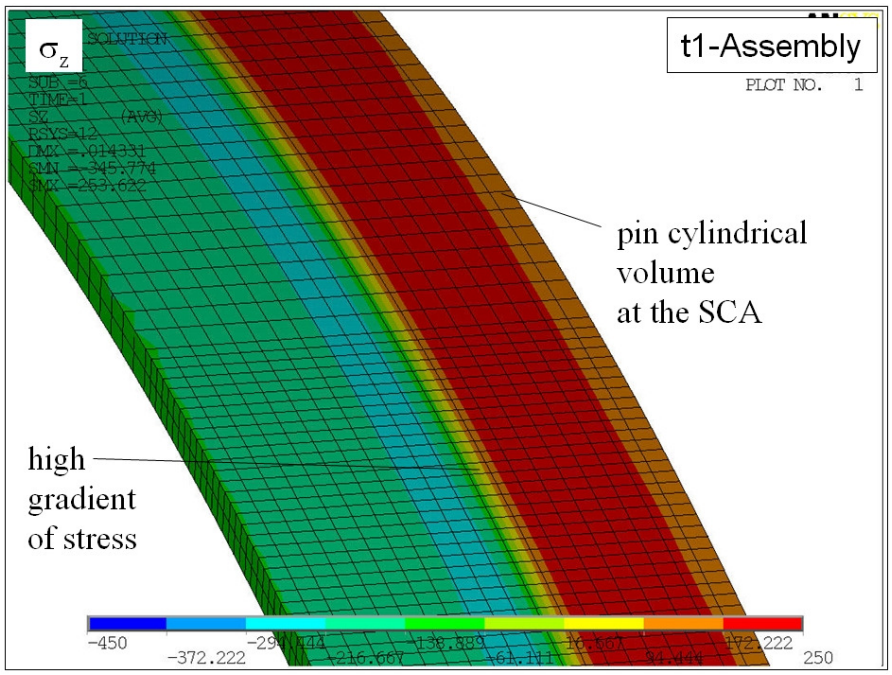

Figure C.3 Pin SCA cylindrical volume σ_z plot, LC1 assembly.

Next assembly radial stress is shown at the SCA area for the web only in Fig.C.4, on the bottom side of the pin. High compressive radial stress occurs at location A, and the stress drops quickly to zero at the point of no contact between the pin and the web. The stress contour is very uniform in the theta direction, which supports the earlier assessment of the press-fit problem as axisymmetric.

Figure C.5 shows a plot of radial stress on the pin and outer web plane of symmetry. High compressive radial stress is present at the interface as has been demonstrated throughout this research document. Note that the location of the SCA on the bottom of the pin is designated as the BDC (Bottom Dead Center) location.

Hoop stress is shown next in Fig.C.6 for a model cut along the plane of symmetry. High hoop stress in the web material above the pin dominates the plot, and again this is consistent with the previous data.

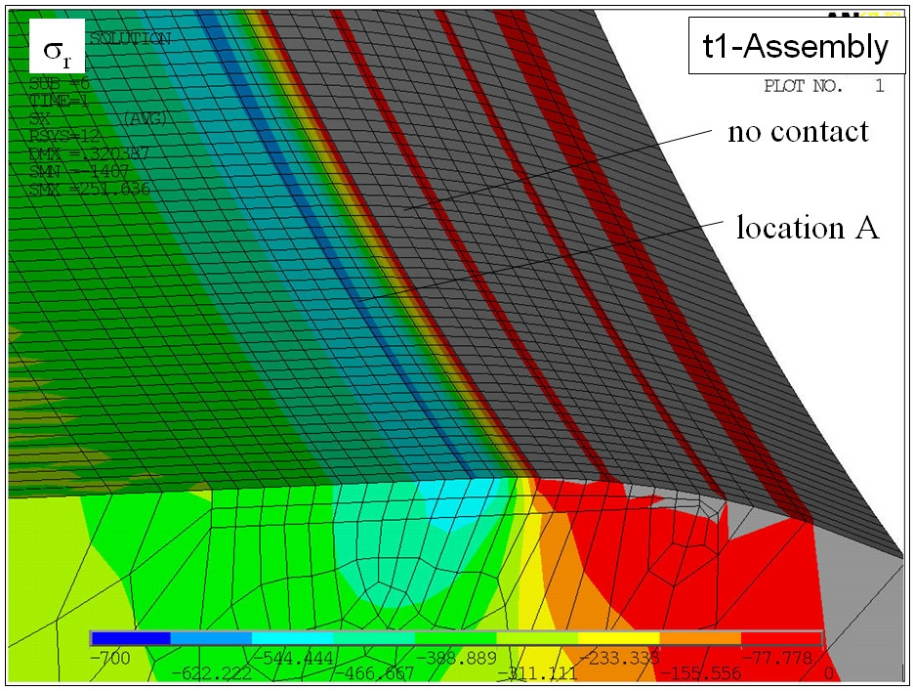

Figure C.4 Plot of σ_r on the web at the SCA, LC1 assembly.

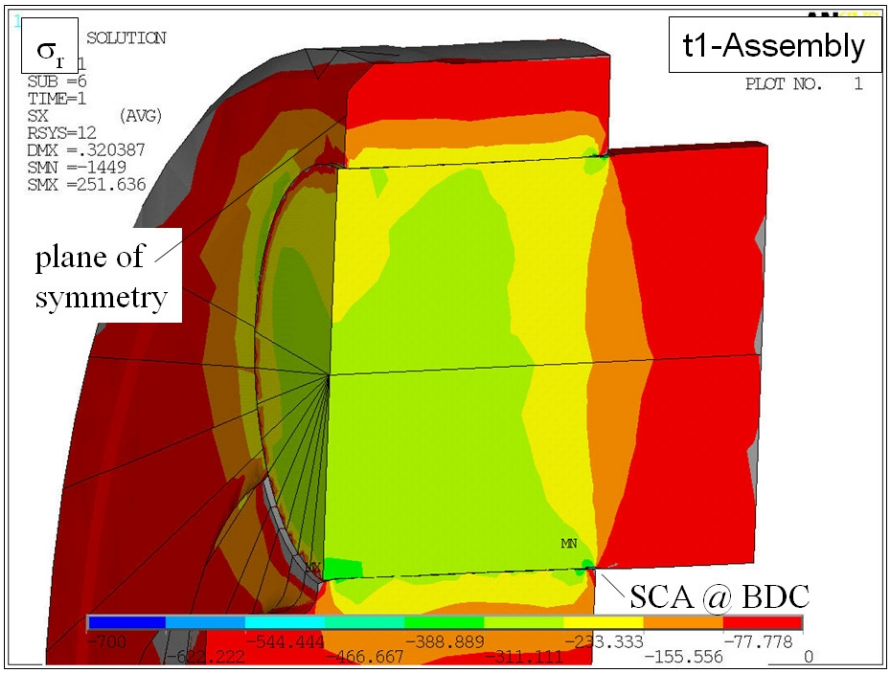

Figure C.5 Plot of σ_r on the PTO outer web plane of symmetry, LC1.

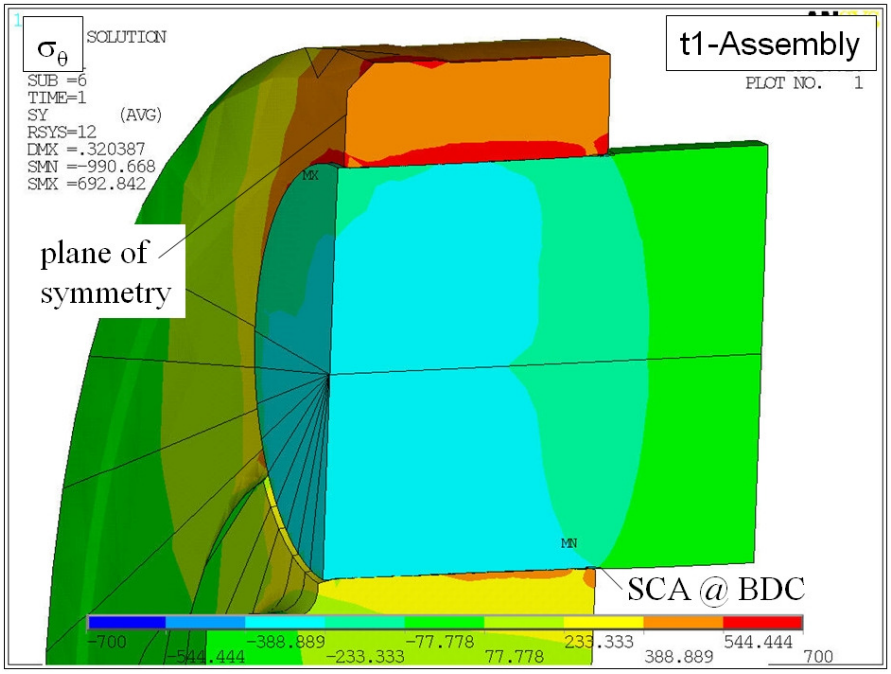

Figure C.6 Plot of σ_y on the PTO outer web plane of symmetry, LC1.

Axial stress is plotted next in Fig.C.7 on the plane of symmetry, and demonstrates the tensile stress is created on the free surface of the pin (OD) just beyond the SCA location.

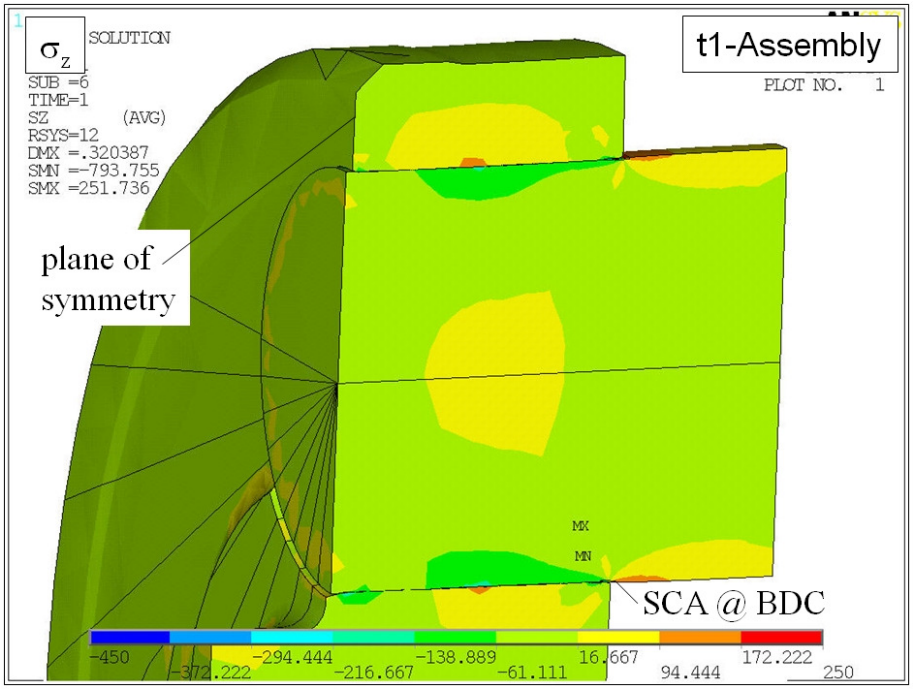

Figure C.7 Plot of σ_z on the PTO outer web plane of symmetry, LC1.

Appendix D: Full Geometry 3-D Crankshaft FEA Rotational Inertial Results

This appendix contains supporting FEM data from the full 3-D model for time step 2, the rotational inertia load case. A plot of equivalent stress on the PTO outer web is shown in Fig. D.1; the press-fit stresses captured in the assembly LC1 are the basis for most of the high stress area in LC2.

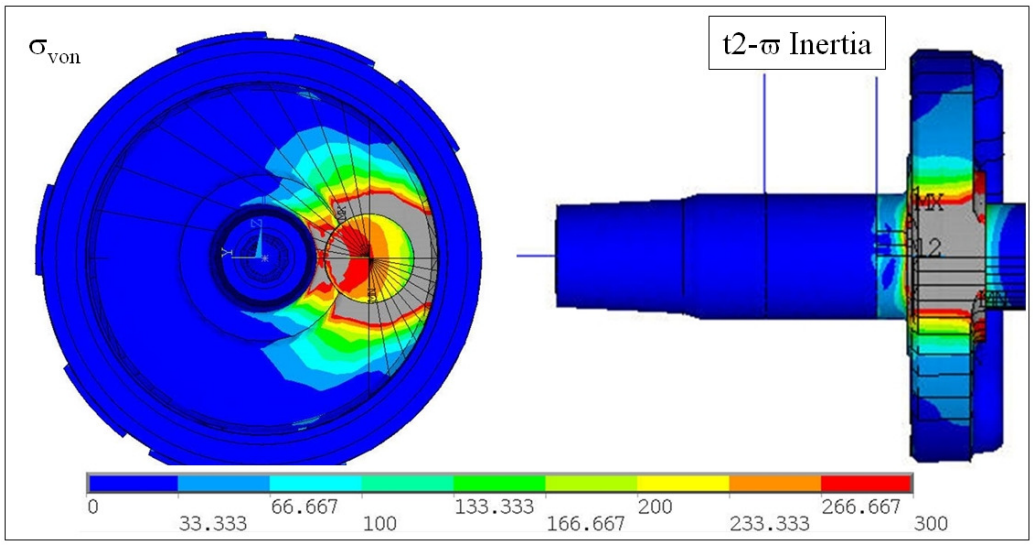

Figure D.1 PTO end equivalent stress plot for time step 2.

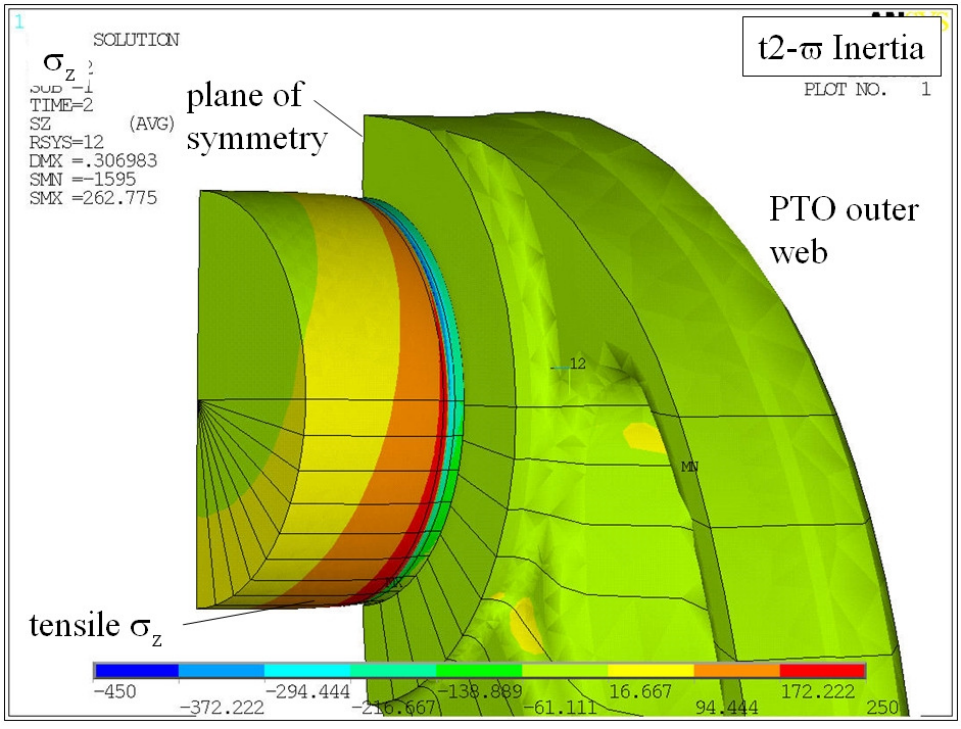

Figure D.2 PTO end web and pin axial stress plot for time step 2.

Next LC2 axial stress is plotted for the pin and web in Fig. D.2. As has been shown previously the rotational inertia load from the web counterweights creates pin bending. This creates a tensile stress at the bottom of the pin, which adds to the tensile stress already present on the pin surface just next to the SCA location.

Figure D.3 presents the same view as Fig. D.2 but plots equivalent stress; the high stress in the web that is created by the press-fit is shown to be significantly higher than the pin rotational inertia stresses.

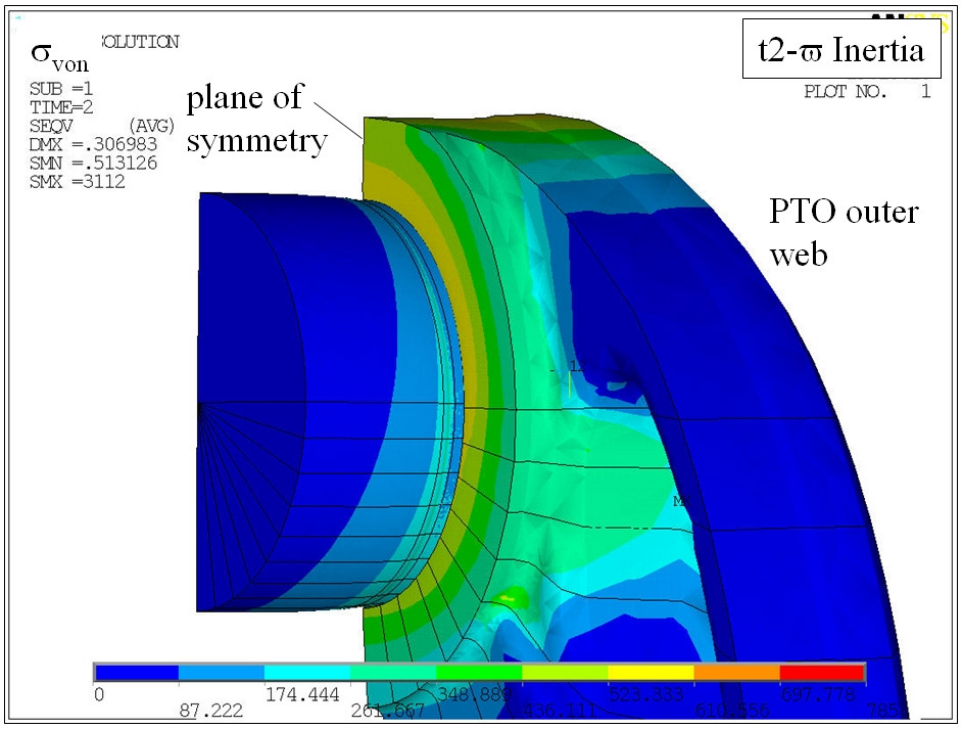

Figure D.3 PTO end web and pin equivalent stress plot for time step 2.

The next set of plots examines stress components on the global x-y plane of symmetry. A plot of radial stress on the pin and outer web plane of symmetry is shown in Fig. D.4. For time step 2, the radial stress increases at the SCA on top of the pin, and also on the opposite diagonal corner of the pin at the bottom (indicated by arrows in Fig. D.4). In section 5.2 it was demonstrated with the one-quarter model that this occurs as a result of the pin carrying the bending load created by the web counterweights.

Figure D.5 plots hoop stress for the model cut along the plane of symmetry, showing little change in stress overall from LC1 assembly to LC2 rotational inertia loading. Previous one-quarter symmetry results indicated that hoop stress levels and magnitudes are not very sensitive to inertia and crankpin loading.

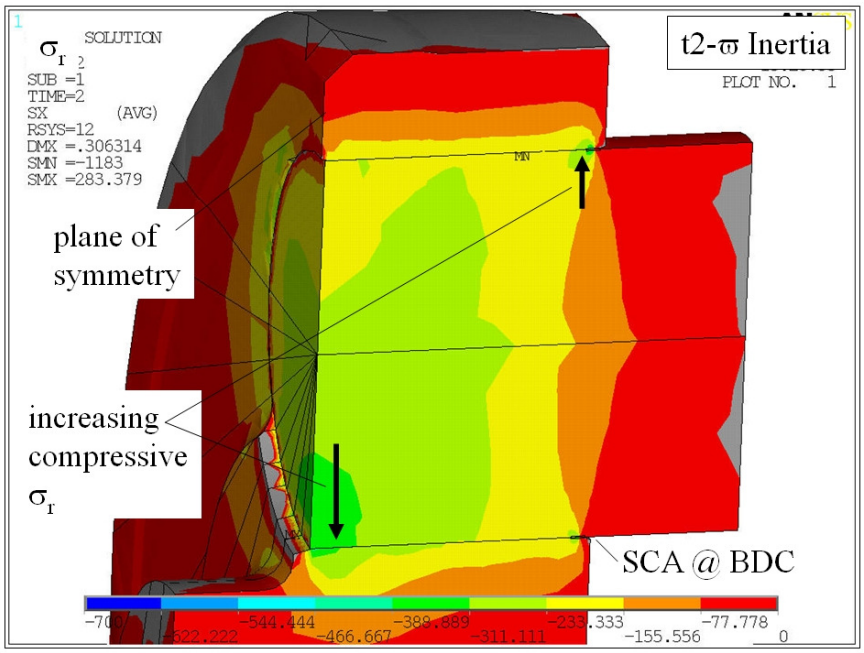

Figure D.4 Plot of σ_r on the PTO outer web plane of symmetry.

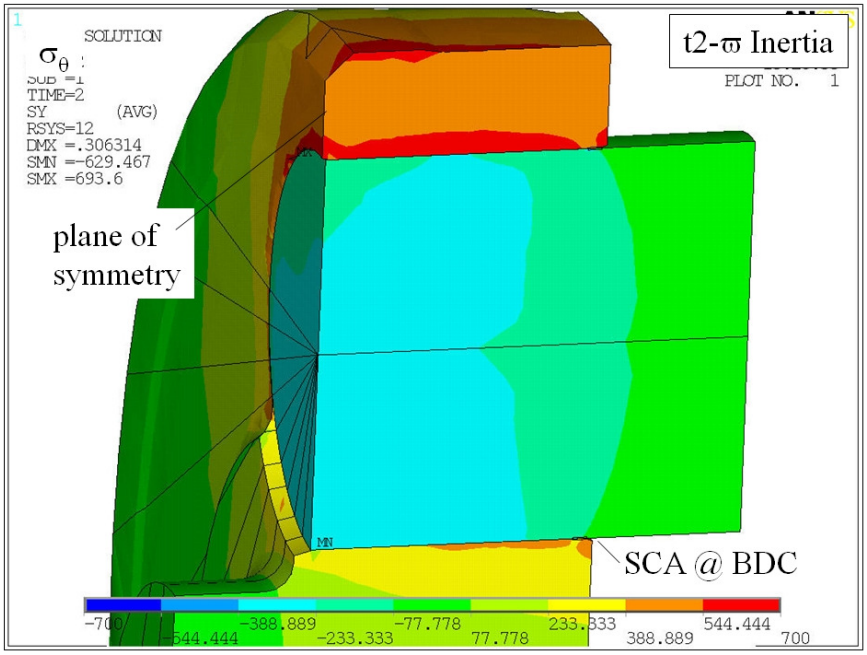

Figure D.5 Plot of σ_θ on the PTO outer web plane of symmetry.

Previously in Fig. D.2, a high tensile stress was demonstrated on the bottom of the pin, created by the inertia loading of the web counter-weight. Figure D.6 plots axial stress on the plane of symmetry, which also shows the tensile stress created at the bottom of the pin by the rotation inertia loading.

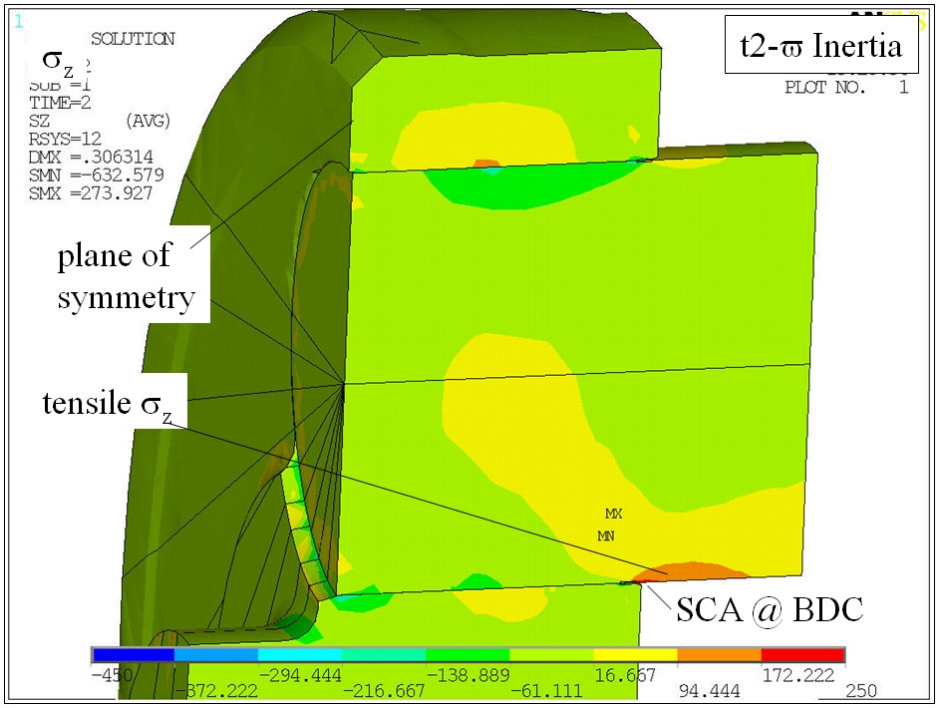

Figure D.6 Plot of σ_z on the PTO outer web plane of symmetry.

Appendix E: Full 3-D Model: PTO Crankpin Results On Cutting Plane B

This appendix contains summary operating load results for the full 3-D FEM model, with a focus on the stress condition on the PTO crankpin using cutting plane B which was identified in section 5.3.5. This data is presented in support of section 5.3.6, the full 3-D crankshaft FEM results summary.

The information in this section examines the stress fields on plane B for the PTO crankpin. As a reminder from earlier in this chapter, plane B was identified as the location of maximum axial stress on the pin for load case 4.

Figure E.1 plots radial stress across plane B for load cases 3 and 4. Note in Fig. E.1 that location B2 unloads for time step 3, this is due to the fact that location B2 is only 40 degrees offset from location A1 (see Fig. 5.3.6.2). Location A1 also unloads during time step 3 because of the combined effect of the combustion forces on the crankpin and the belt forces. Since cutting planes A and B shown in Fig.5.3.6.2 are similar in orientation, and locations A1 and B1 are on opposite sides of the pin, stress at these two locations will load and unload in an opposite manner for time steps 3 and 4.

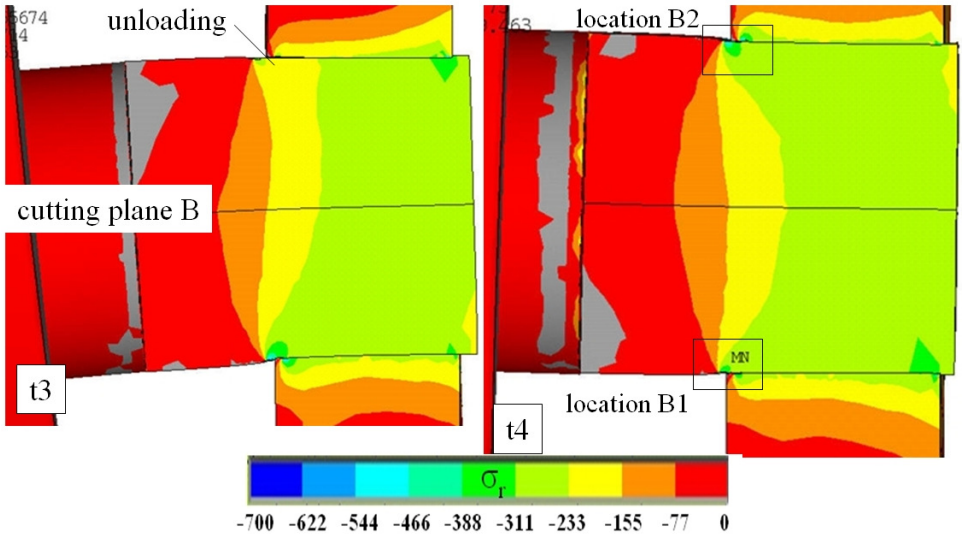

Figure E.1 Plot of σ_r on plane B for PTO crankpin.

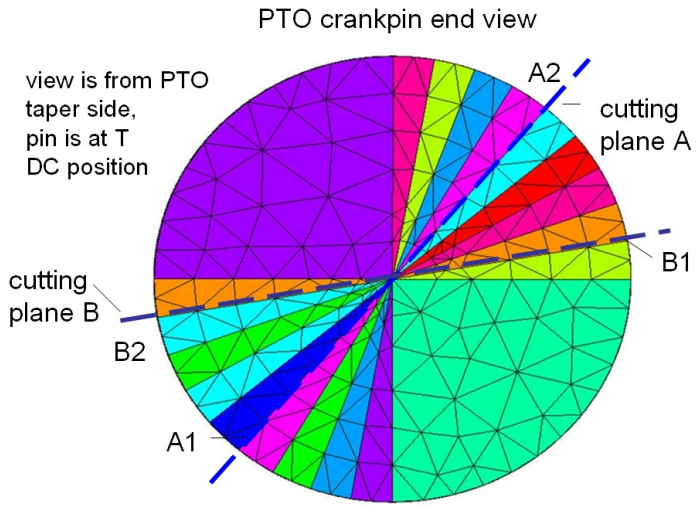

Figure E.2 Cutting plane locations on PTO crankpin end view.

Note that the location B1 in Fig. E.3 shows high axial stress for LC4, but it appears to be lower than axial stress at location B2 for LC3. This suggests that PTO crankpin bending is more significant for time step 3 than 4. Both time steps have significant belt forces which influence pin bending, but time step 3 crankpin loading should create higher pin distortion, which supports Fig. E.3. The combustion load applied to the PTO crankpin in LC3 adds to the rotational inertia bending on the pin, while the inertial loads applied in the opposite direction are opposed by the spin bending on the pin.

Finally the equivalent stress is plotted on plane B for LC3 and LC4 in Fig. E.4. The pin stress distribution does show minor sensitivity to loading on plane B.

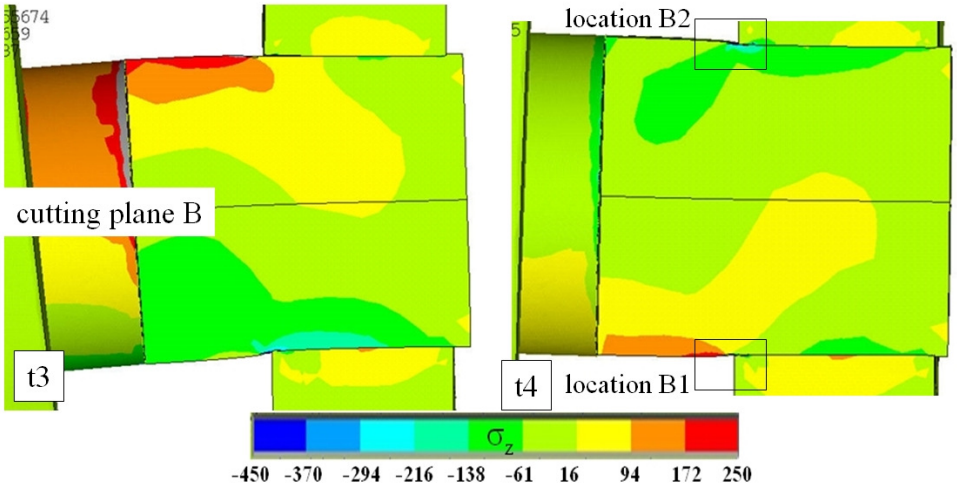

Figure E.3 Plot of σ_z on plane B for PTO crankpin.

The stress details at location B1 are now presented, first by examining the radial stress field. Figure E.5 shows some radial stress unloading at time step 2 at B1, but since it is close to the neutral axis of the crankshaft, it is not significant. Location B1 shows high radial stress loading for LC3 because of the location's position relative to the belt and crankpin combustion loads.

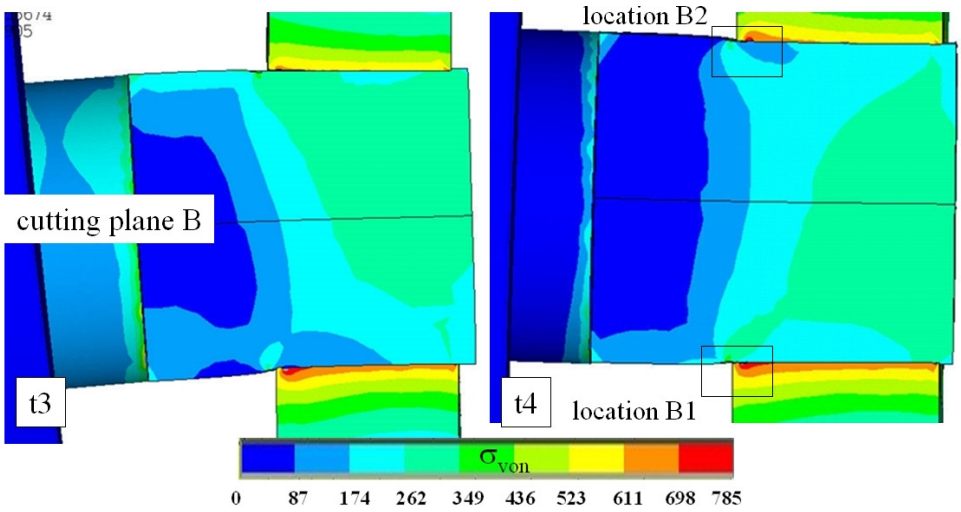

Figure E.4 Plot of σ_{VM} on plane B for PTO crankpin.

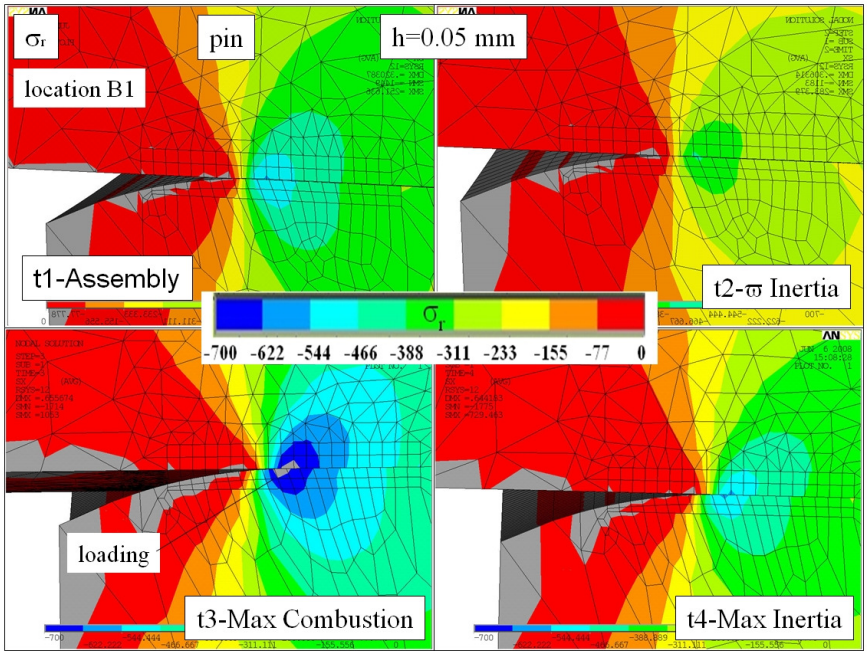

Figure E.5 Radial stress (σ_r) plot at location B1 for load steps 1 to 4.

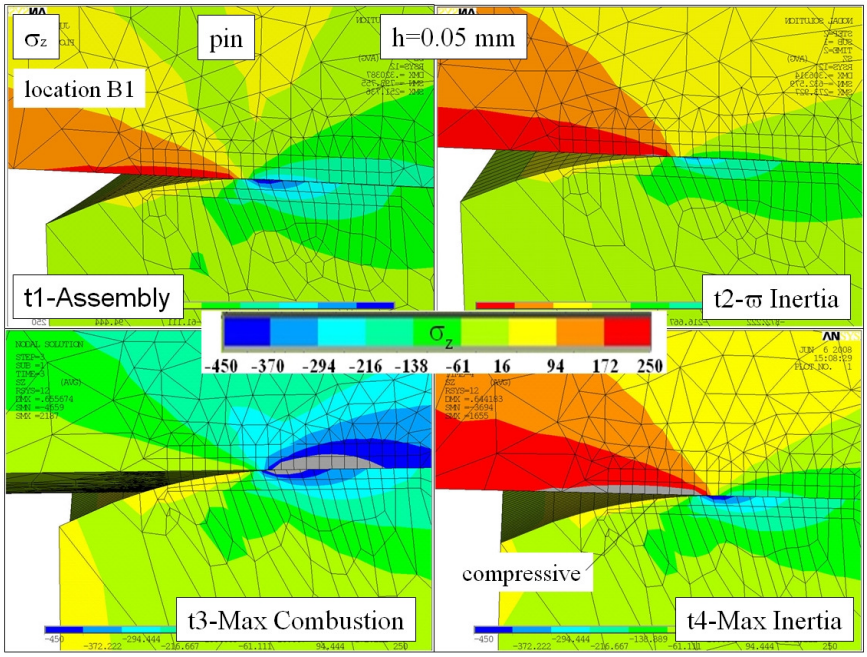

Figure E.6 Axial stress (σ_z) plot at location B1 for load steps 1 to 4.

Axial stress details for location B1 follow a trend opposite to location A1 on cutting plane A. Slightly compressive stresses are developed during time step 3 (see Fig. E.6) and tensile axial stresses follow in time step 4.

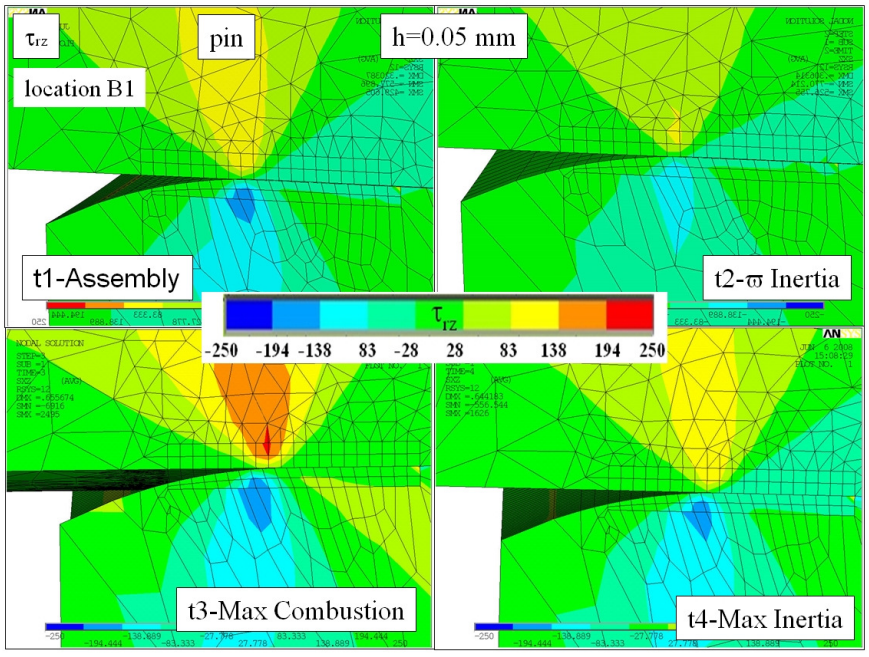

Figure E.7 Shear stress (τ_{rz}) plot at location B1 for load steps 1 to 4.

The shear stress plot in Fig.E.7 follows the radial stress magnitudes of Fig.E.5, a trend that has been consistent for all result sets. The highest shear stress τ_{rz} at location B1 occurs at time step 3, when the compressive radial stresses are greatest.

Next the equivalent stress at location B1 is plotted for load cases 1 thru 4 in Fig.E.8; variation in equivalent stress in the pin is shown to be very low. However, the web experiences significant variation for time steps 3 and 4, created by the thin section of the web at location B1 (a thin section exists because of the pockets in the web near to the pin interface is used for mass balance).

The equivalent stress is now examined at location B2 in Fig.5.3.6.9. Much of the same trend reported for equivalent stress at location B1 is shown to hold true for location B2 as well.

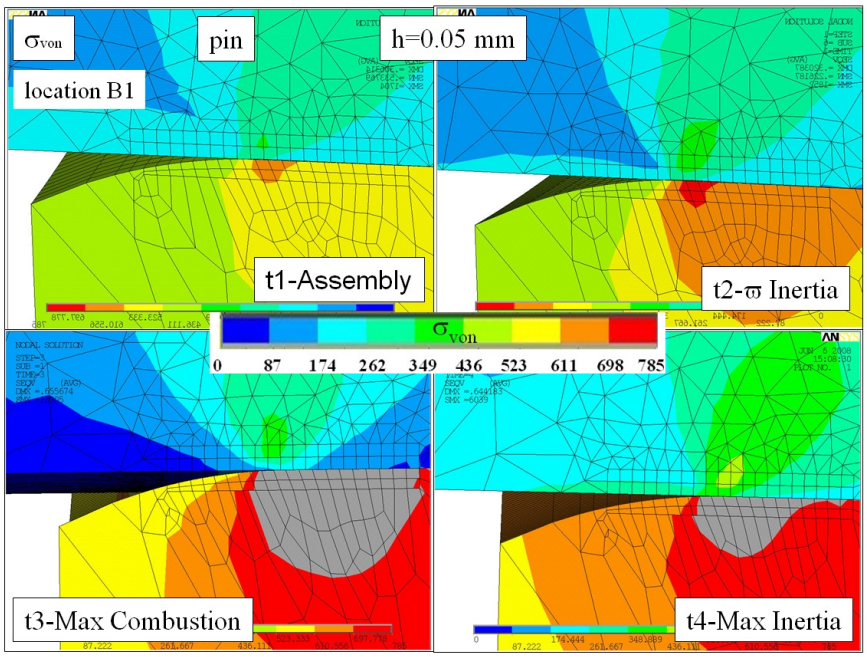

Figure E.8 Equivalent stress (σ_{VM}) plot at location B1 for load steps 1 to 4.

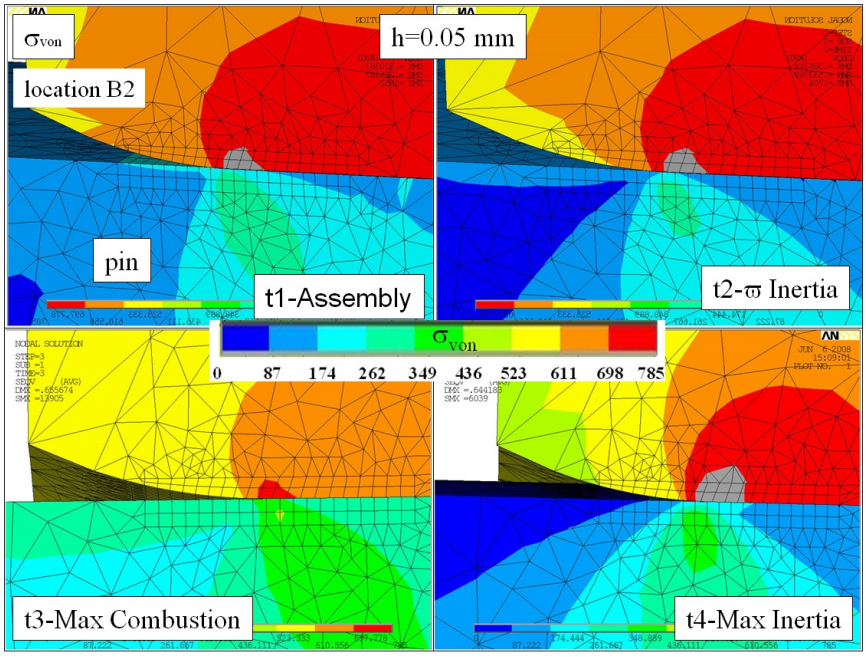

Figure E.9 Equivalent stress (σ_{VM}) plot at location B2 for load steps 1 to 4.

Finally, the axial stress plots along line fg for locations B1 and B2 are provided in Fig. E.10 and E. 11. Since location B1 is nearly opposite to A1 on the pin outer diameter, it is expected that the vertical shifting of the axial stress curve will trend oppositely. What is noteworthy is that the changes in axial stress from LC1 (assembly) to LC2 (spin inertia) are very slight, which is due to the fact that plane B is oriented very close the neutral axis of pin bending created by the crankshaft spinning in LC2.

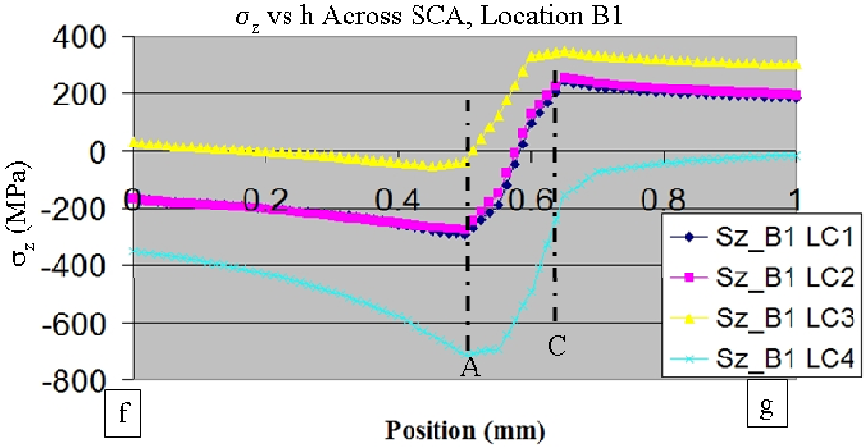

Figure E.10 Plot of σ_z along line fg for load cases 1 thru 4, location B1.

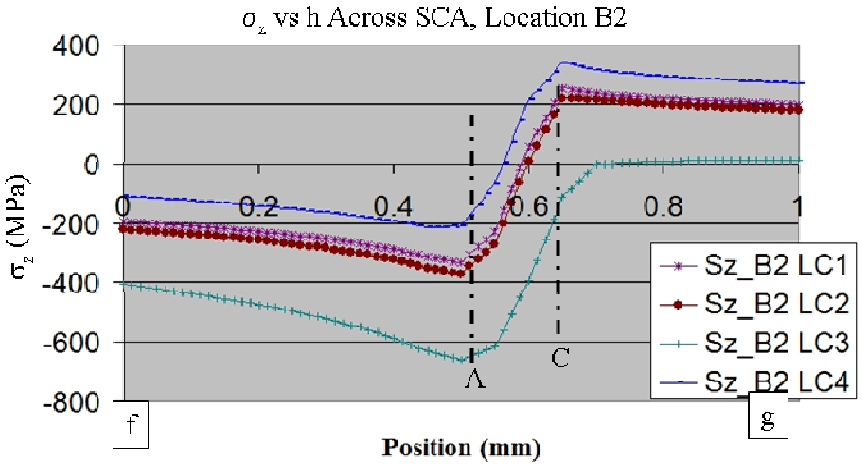

Figure E.11 Plot of σ_z along line fg for load cases 1 thru 4, location B2.

Appendix F: Example Experimental Verification Of Crankshaft Strain

In this appendix an example of a correlated FEA crankshaft model which uses the static load case approach and the general FEM methodology outlined in this research is presented in brief to gain confidence in the numerical methods. The FEM model of the full crankshaft uses the same overall approach deployed in chapter 5, specifically the static load cases and boundary conditions implemented.

Note that the strain measurements described in Chapter 6 reflect only the engine operating conditions. The strain gauges on a multi-piece crankshaft can be located only at some distance from the SCA and from the press-fit joint, in general.

It is also assumed that both a multi-piece or a one piece crankshaft will behave similarly when considering the general displacement and stress field away from the press-fit connection. For example, the fillet radius stress values tracked in chapter 5 (the full 3-D model) should be calculated as nearly identical values with the press-fit joint modeled either as continuous or non-continuous. The correlation data presented this appendix is taken from a crankshaft which is of one piece construction. If a one piece crankshaft FEM model shows good correlation to the

measured data, it can be assumed that a FEM model of a multi-piece crankshaft would also correlate well to the measured strain data, when both models use the same general FEM methodology outlined in the research.

First the degree of reliability of the input load data for the FEM full 3-D crankshaft model is discussed. A measured combustion curve in Fig.F.1 [37] is used as an input to the MBD model to calculate crankpin loads as well as the belt forces for the FEM model. The calculated MBD loads are thought to be of high quality with a measured combustion curve input; the crankpin loads will then be dependent on rotational speed, and part geometry, mass / inertia, all of which are known quantities.

After belt and crankpin loads were calculated with the MBD model, several static load cases were extracted based on engineering logic and experience (see Fig.F.2). Among the load cases extracted from the MBD force data is the 'maximum PTO end combustion' load case, which is used in the research also (LC3 in chapter 5). This load case is highlighted in the MBD crankpin force data provided in Fig.F.2.

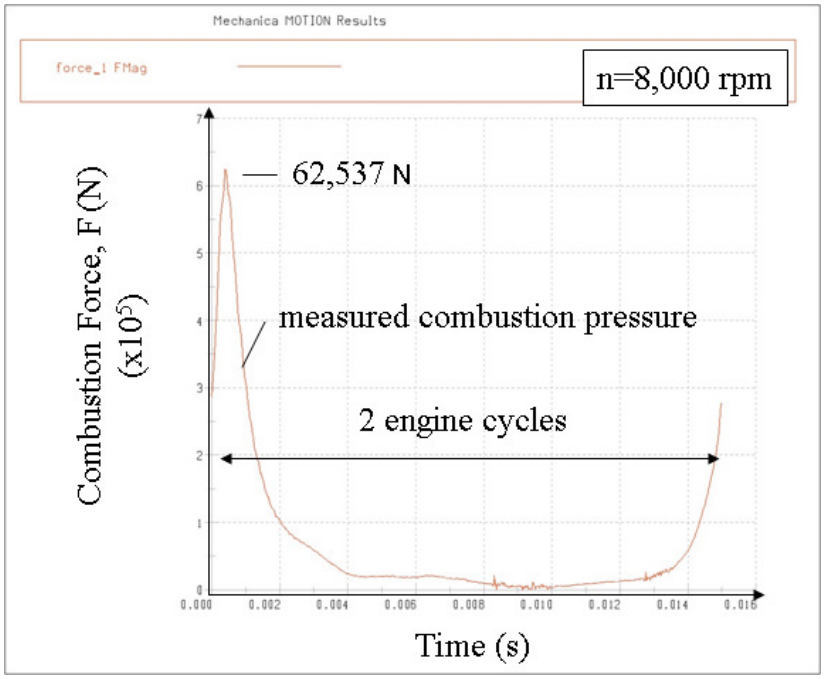

Figure F.1 The measured 'in-cylinder' combustion curve for a 4-stroke engine [37].

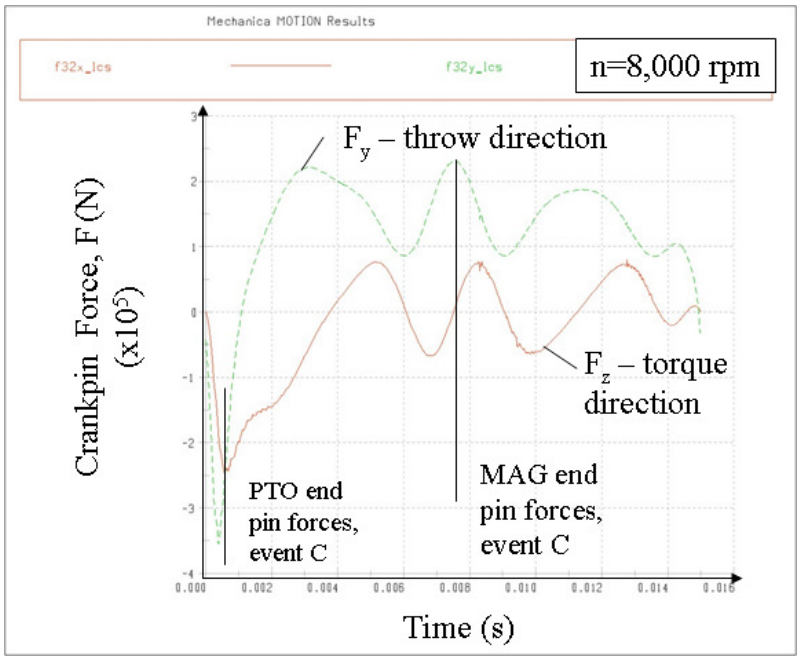

Figure F.2 Crankpin MBD loads calculated with the measured combustion pressure [37].

Next, in Fig. F.3 a general resultant displacement and equivalent stress plot are provided for the crankshaft design using the LC3 maximum PTO crankpin combustion load event. The crankshaft displacement and stress plot shows sensitivity to belt and crankpin loading.

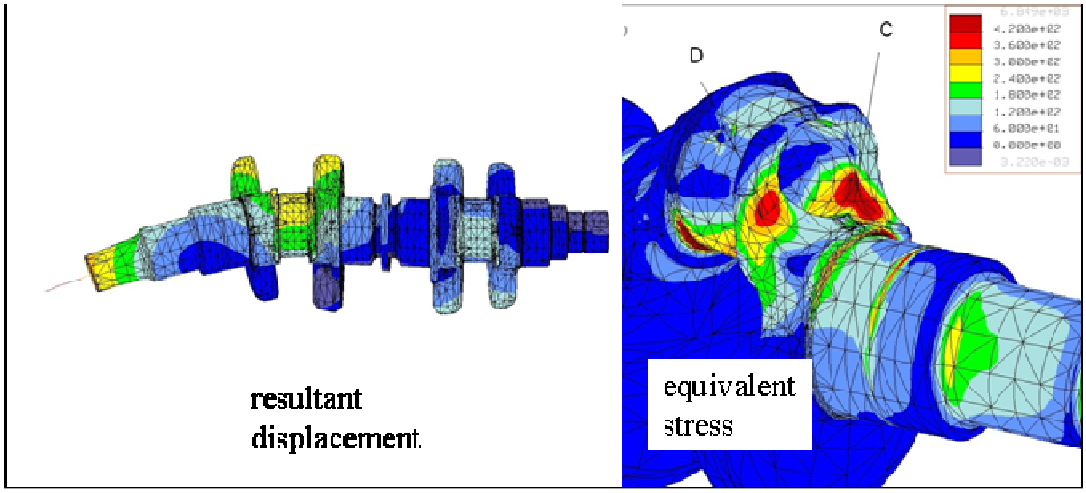

Figure F.3 FEA model results for the twin cylinder crankshaft combustion event load case [37].

Dynamic strain measurements were taken on the crankshaft for several operating conditions in the locations presented in Fig. F.4.

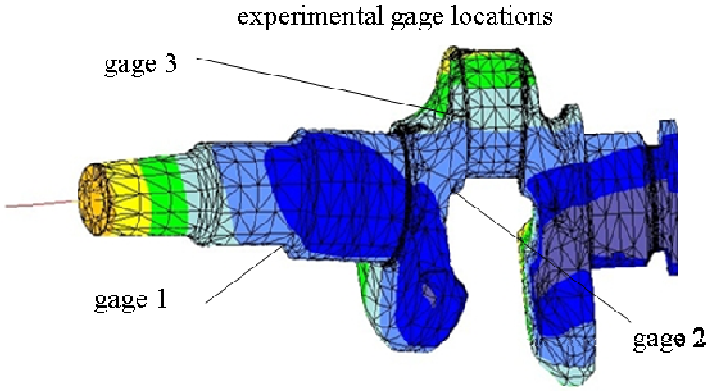

Figure F.4 Experimental strain measurements locations on the crankshaft [37].

Next, the time history strain data for gauges 1, 2, and 3 [38] are presented in Fig. F.5 for the high speed maximum load condition, the same operating condition that is used in the FEM model assumption (LC3 in chapter 5). The repetitive nature of the time history strain data is revealed, which is typical for data from an engine operating environment.

The finite element model shows good correlation with respect to experimental strain measured on the crankshaft in three locations, as is shown in Fig. F.6. The maximum bending strain on the PTO end web (gage 3) occurs during the PTO end combustion event, and the experimental and FEA values match within 5 % (the numerical answer is higher). The finite element model did not quite match the bending strain measured at gage 2 nearly as well, with predicted strains 16% higher than measured; but this should be still considered as acceptable correlation.

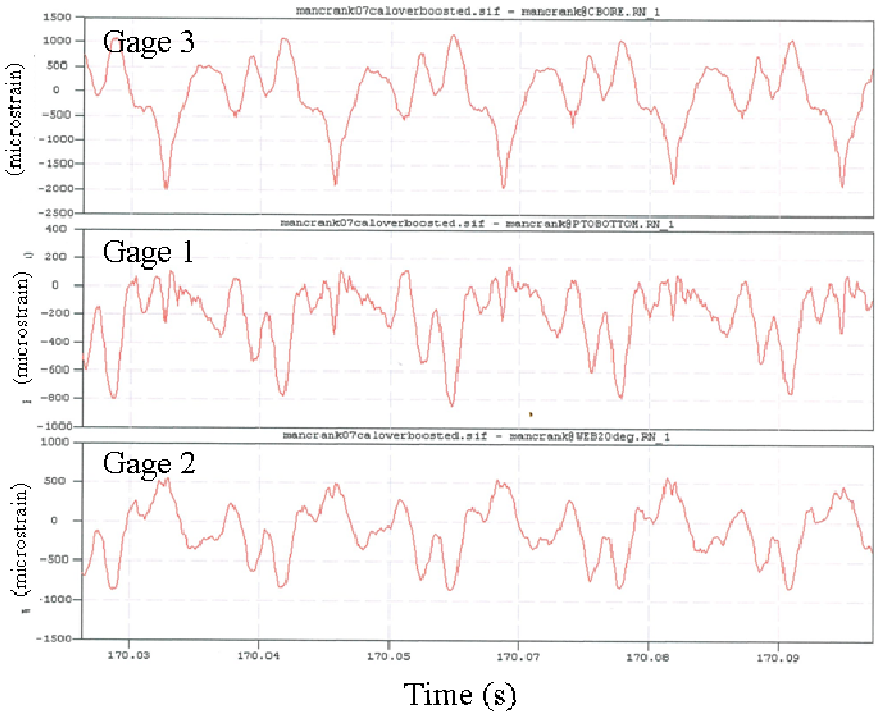

Figure F.5 Time history strain measured at gages 1, 2, and 3 [38].

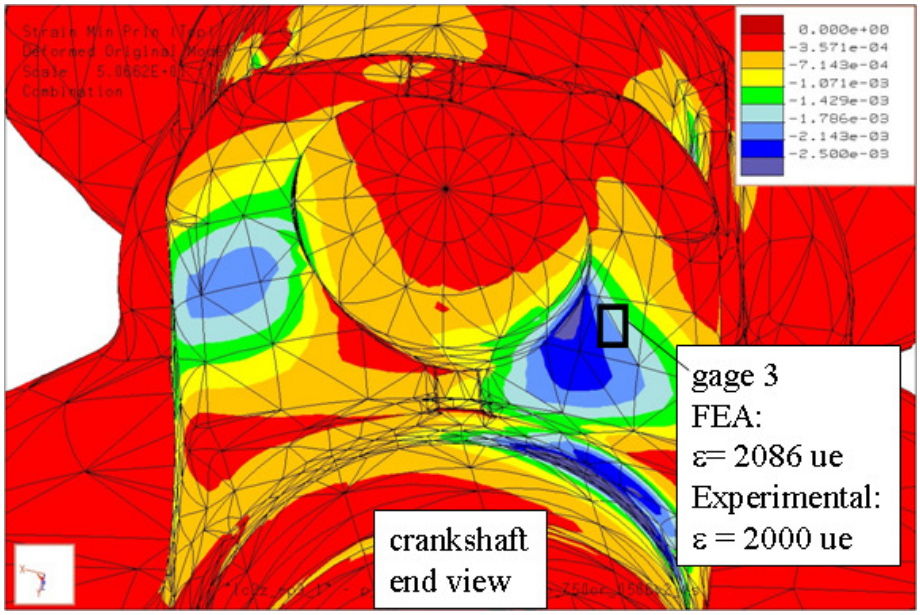

Figure F.6 FEA model results at gage 3 for the correlated combustion event. Note the high strain gradient in the area of measurement [37].

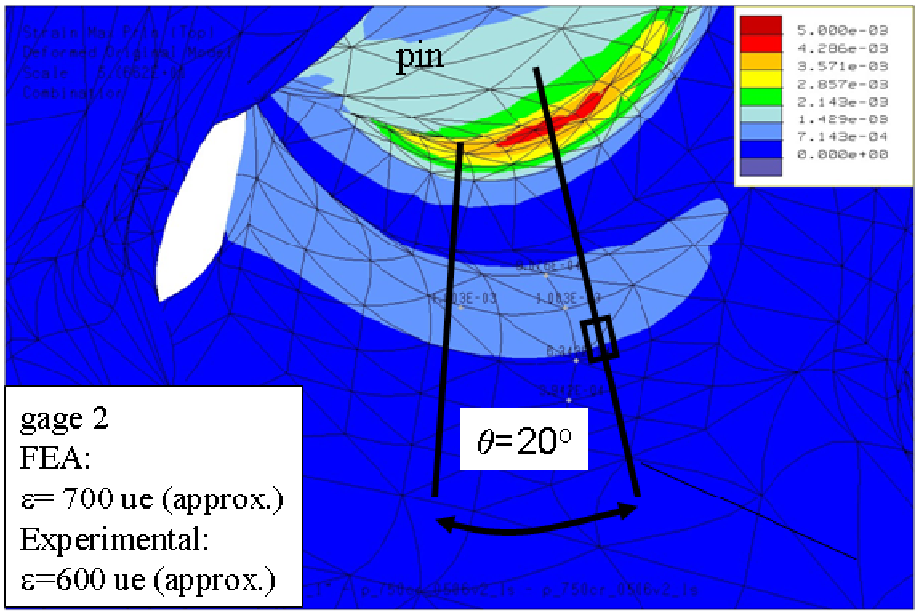

Figure F.7 FEA model results at gage 2 for the correlated combustion event [37].

Appendix G: Undercut Solution Optimization Results

The following results from the one-quarter bench test FEM model are presented as supporting data to that discussed for the optimized undercut solution in section 7.3.

Figures G.1 through G.4 demonstrates the general behavior of the press-fit joint with the undercut geometry. Equivalent stress, maximum and minimum principal stress plots are provided for load cases 1 to 4, which may be directly compared to similar plots in section 5.2. Because of the added undercut, the web has higher stretch than the baseline geometry, especially at the bottom of the pin (see Fig. G.1). As the joint is loaded by the rotational inertia (time step 2), the joint exhibits the same basic loading mechanics that are discussed in detail in Chapter 5. Radial stress increases at opposite diagonal corners of the pin to carry the counter weight bending load. Local stresses at the SCA are reduced when the combustion load is applied in load step 3 (Fig. G.3), and when the reciprocating mass load is applied in load step 4 (see Fig. G.4).

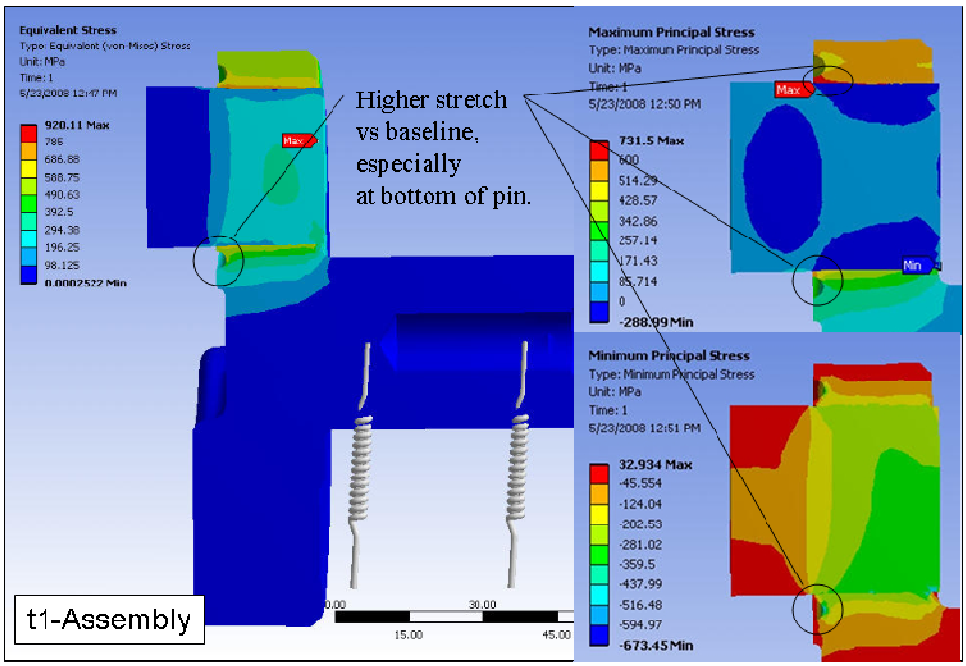

Figure G.1 Equivalent, maximum and minimum principal stress plots, time step 1.

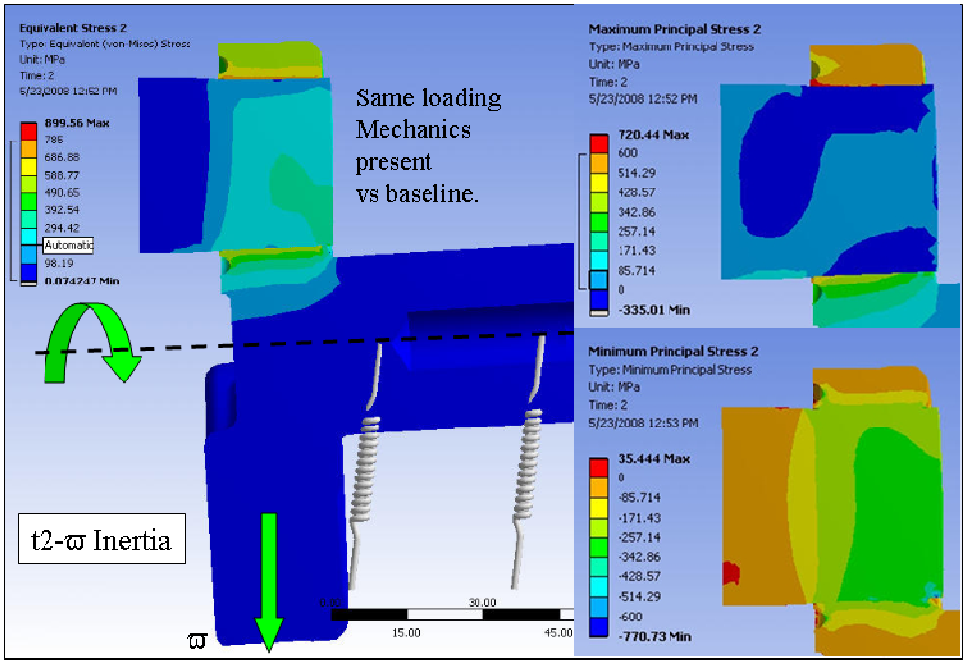

Figure G.2 Equivalent, maximum and minimum principal stress plots, time step 2.

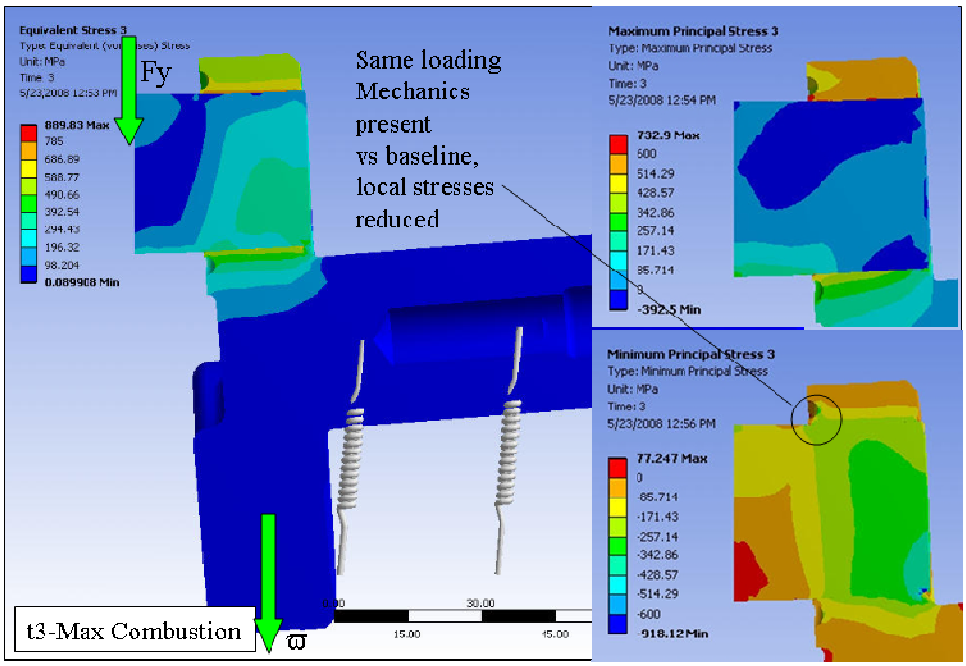

Figure G.3 Equivalent, maximum and minimum principal stress plots, time step 3.

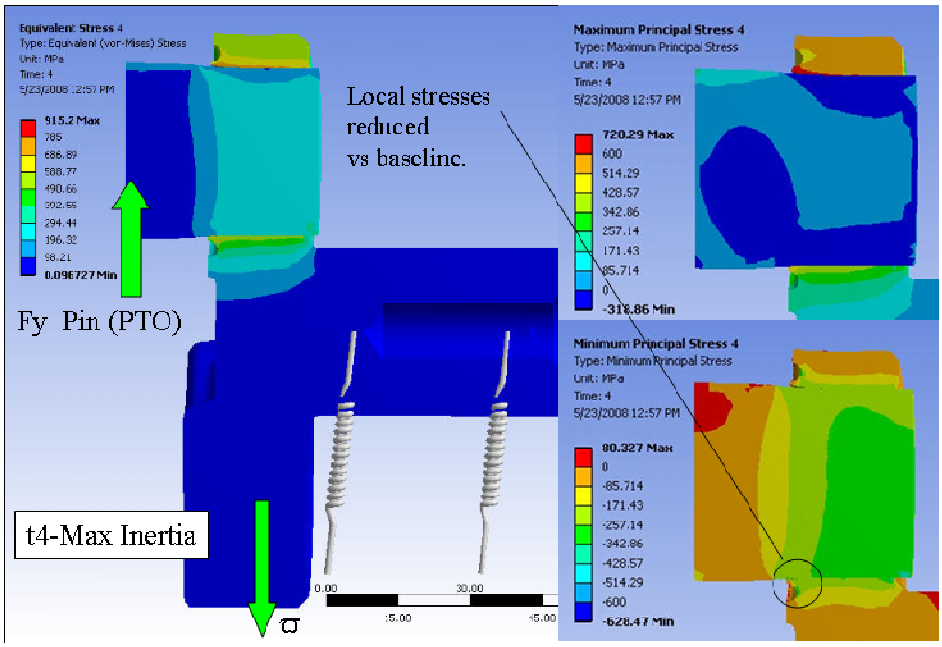

Figure G.4 Equivalent, maximum and minimum principal stress plots, time step 4.

Next the general stress behavior of the web at the undercut feature is outlined in Fig. G.5 through G.7 for load steps 1, 2, and 4 respectively. For each time step, the equivalent and maximum principal stress plots are given, as was provided for the baseline geometry in section 5.3.

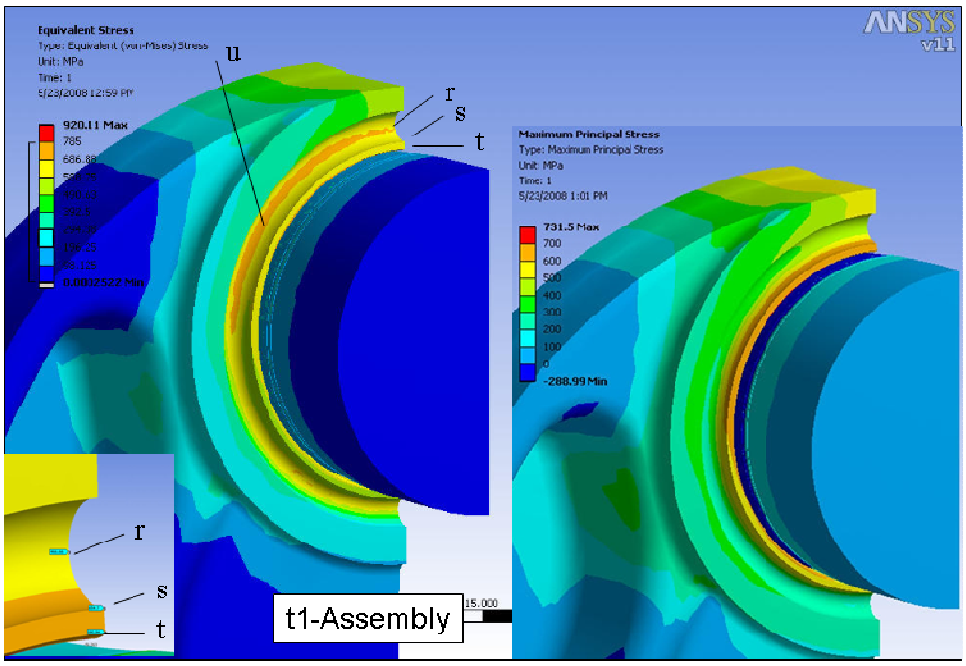

Figure G.5 Equivalent and maximum principal stress plot isometric view, time step 1.

Note each plot uses consistent stress range scales, 0 to 785 MPa for equivalent stress, and 0 to 700 MPa for maximum principal stress. This set of stress plots do not show a great deal of variation in stress in the undercut feature.

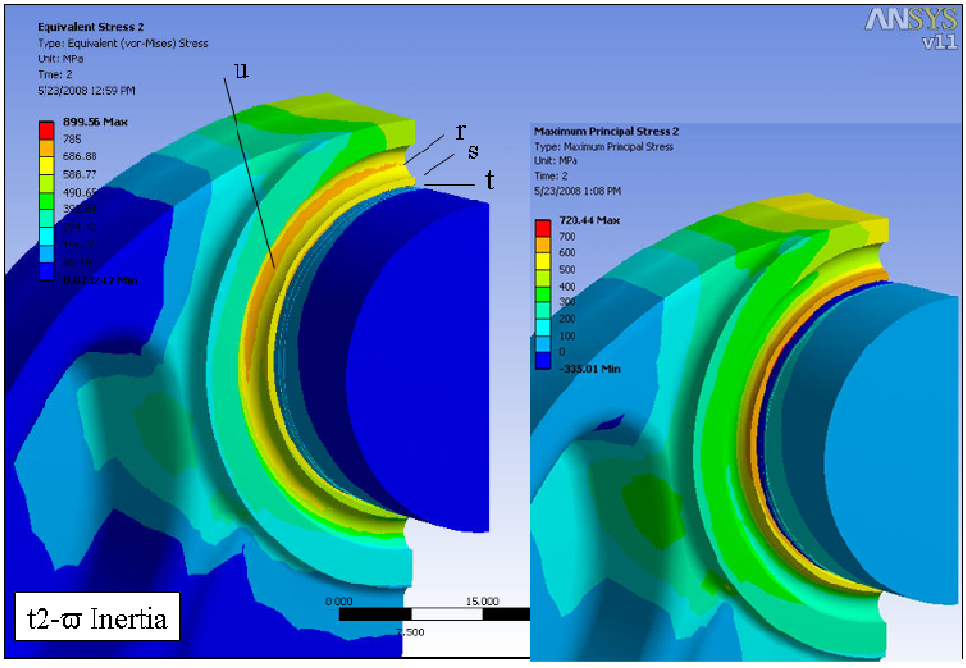

Figure G.6 Equivalent and maximum principal stress plot isometric view, time step 2.

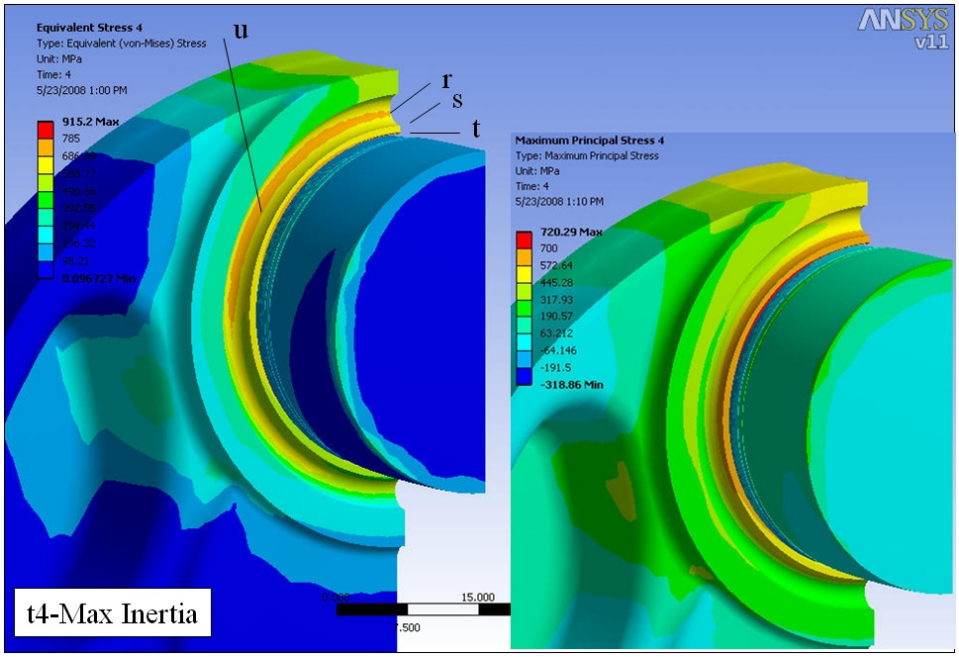

Figure G.7 Equivalent and maximum principal stress plot isometric view, time step 4.

The details of the stress field at the SCA are given next to describe fully the benefit of the undercut. The axial stress details at the SCA are examined at the bottom of the pin at line fg. Fig.G.8 plots pin surface axial stress across the SCA area for load steps 1 thru 4 for the undercut geometry. Note the stress gradient from location *A* to C appears to be reduced and also transitions over a longer distance, in comparison to similar plots in section 5.2 for the baseline geometry.

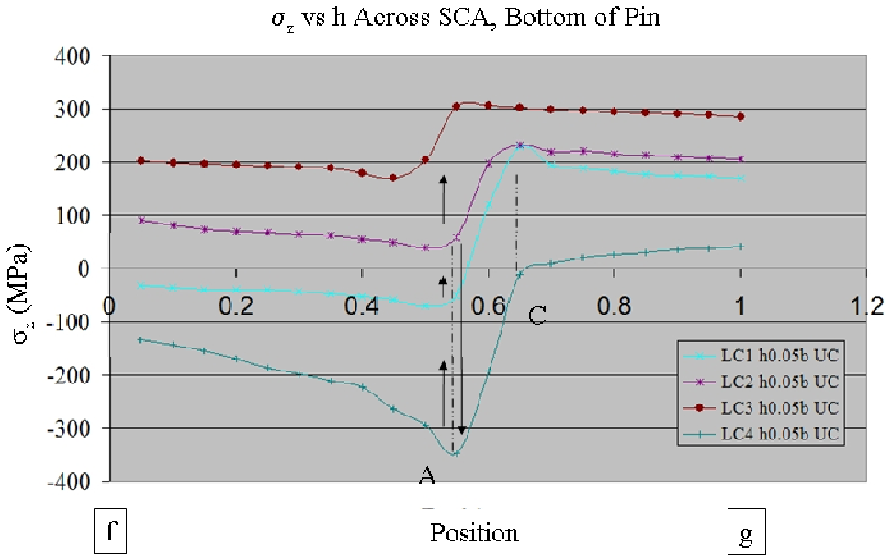

Figure G.8 Axial stress at the SCA along line fg for time steps 1 to 4, bottom of pin.

The baseline and undercut geometry are compared directly in Fig. G.9 for load step 1. Axial stress is significantly reduced (1/3 to 1/4 the value of the baseline) on the pin for the portion inserted into the web. Maximum axial stress at location *C* is reduced from 257 MPa (baseline) to 229 MPa (undercut) for the *h* equals 0.05 mm solution; it is felt this reduction will be greater with a refined mesh solution. The baseline solution will be more sensitive to mesh refinement than the undercut geometry.

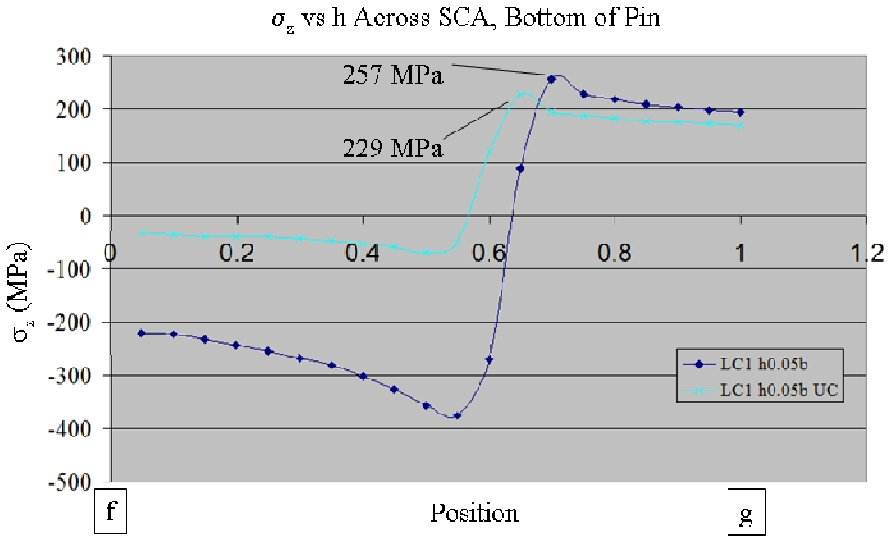

Figure G.9 Stress σ_z along line fg for LC1, for the baseline and undercut (UC) data.

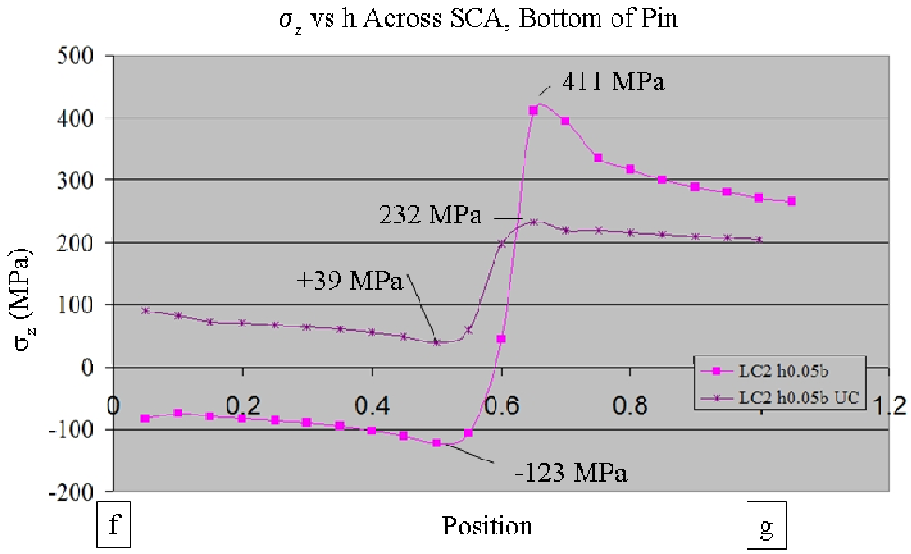

Figure G.10 Stress σ_z along line fg for LC2, for the baseline and undercut (UC) data.

A comparison of load step 2 and 4 is given in Fig. G.10 and Fig. G.11 respectively, with the undercut providing a significant reduction in stress.

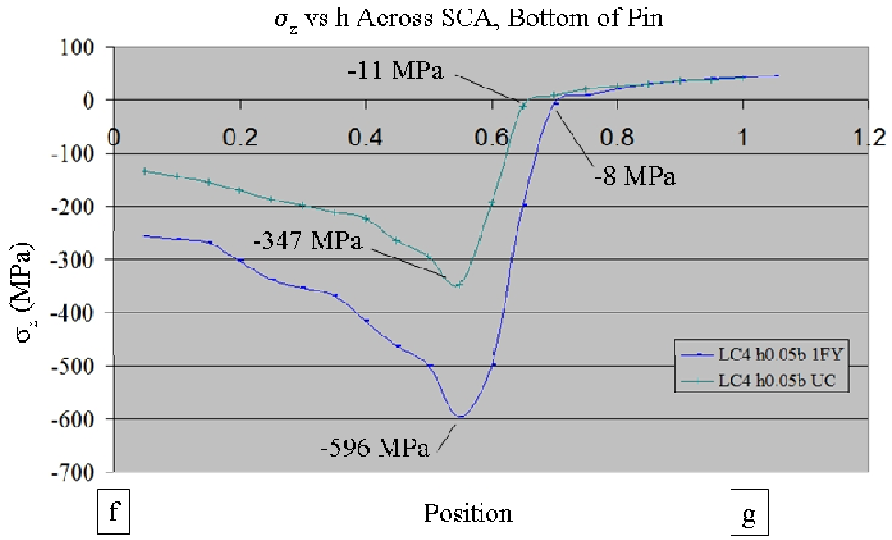

Figure G.11 Stress σ_z along line fg for LC4, for the baseline and undercut (UC) data.

Appendix H: 2-D Axisymmetric FEA Model Input Decks

The following input deck listing is used to create the parametric 2-D axisymmetric model:

```
/prep7
!*
!*
!*  Define Parameters
!*****************************************
!*  Geometric Parameters
!*        This file generates parametric
!*        geometry for a "true" radius,
!*        which has a tangent radius on the cylinder
!*        side, which is cut off.
!*
PIN_OD=(30.003/2)
WEB_L=12.35
!*
CRANK=X
PIN_OD=(29.000/2)
PIN2OD=2*PIN_OD
PIN_ID=0.25
PIN_L=36
WEB_ID=(29.000/2)
```

```
WEB_OD=(44.80/2)
WEB_L=17.68
TRUE_R=2.0
TRUE_T=0.9
IFER=(PIN_OD-WEB_ID)
UR_B=0.15     !* radial distance path B is in from pin surf
UR_C=0.25
UR_D=0.35
!*****************************************
!*  Mesh size parameters
!*
web_h1=0.005
web_h2=0.005
pin_h1=0.005
pin_h2=0.005
pin_h3=0.010  !* sets e size for areas 4, 5 next to SCA
pin_h4=0.020  !* sets l div for lines 20,23 (areas 4,5 above)
e_globe=0.5
!*****************************************
!*  Coefficient of Friction
fric1=0.13
!*
!*****************************************
!*
temp2=332
!*
!*****************************************
!*  solution substeps
!*
n_sbsteps=20
max_sbsteps=40
min_sbsteps=10
!*****************************************
!*
!*  /title, 72 alpha-numeric max w %parmeter%
/title,ELASTIC, %CRANK% crank, %PIN2OD% pin OD, %IFER% interfere, %pin_h1% h
!*
!*
!*****************************************
!*   Database
!*
ET,1,PLANE82
!* ET,1,PLANE42
!*
!*
!*
```

```
!*
KEYOPT,1,1,0
KEYOPT,1,2,0
KEYOPT,1,3,1
KEYOPT,1,5,0
KEYOPT,1,6,0
!*
!*
!*  Pin Material
!*
MP,EX,1,206000,
MP,NUXY,1,0.27,
MP,DENS,1,7.829e-9,
MP,ALPX,1,0.000012
MP,MU,1,fric1
!*
!*  Web Material
!*
MP,EX,2,206000,
MP,NUXY,2,0.27,
MP,DENS,2,7.829e-9,
MP,ALPX,2,0.000000012
MP,MU,2,fric1
!*
!*
TREF,22
TUNIF,temp2
!*
!*
!*
K,1,PIN_ID,0,0,
K,2,PIN_OD,0,0,
K,3,PIN_OD,PIN_L,0,
K,4,PIN_ID,PIN_L,0,
K,5,WEB_ID,0,0,
K,6,WEB_OD,0,0,
K,7,WEB_OD,WEB_L,0,
K,8,WEB_ID,WEB_L,0,
!*
!*      Define Points for True Radius Arc
!*
k,9,WEB_ID,WEB_L-TRUE_T,0
k,10,WEB_ID+TRUE_R,WEB_L-TRUE_T,0
k,11,WEB_ID+TRUE_R,WEB_L-TRUE_T+TRUE_R,0
!*
!*         Define points for mesh refinement at interface
```

```
!*
k,14,PIN_OD,WEB_L-TRUE_T-TRUE_T,0
k,15,PIN_OD,WEB_L,0
k,16,PIN_OD,WEB_L+TRUE_T,0
k,17,WEB_ID,WEB_L-TRUE_T-TRUE_T,0
!*
!*
!*      Create "true radius" arc
!*
larc,11,9,10,TRUE_R
!*      Create Lines.
!*
!*        Add v2 keypoints for creation of areas at SCA
!*
K,18,PIN_OD-UR_B,0,0,      !* keypoints for path definitions
K,19,PIN_OD-UR_C,0,0,
K,20,PIN_OD-UR_B,PIN_L,0
K,21,PIN_OD-UR_C,PIN_L,0
k,29,PIN_ID,WEB_L,0
!*
!* LSTR,       1,       2   !line 2
LSTR,       1,       19   !line 2
LSTR,       2,       14   !3
LSTR,       14,      15   !4
LSTR,       15,      16   !5
LSTR,       16,      3    !6
!*LSTR,      3,       4    !7
LSTR,       21,      4    !7
LSTR,       4,       29    !8
!*
!*
LSTR,       5,      6    !9
LSTR,       6,      7    !10
LSTR,       7,      8    !11
LSTR,       9,      17    !12
LSTR,       17,      5    !13
!*
!*        Divide the arc by the interface edge
!*
lsbl,1,11,0,keep,keep
!*
!*        Add line after intersection cut.
!*
LSTR,       7,      12    !14
!*
!*
```

```
LDELE,11
LDELE,1
LDELE,15
!*
!*        Add v2 keypoints for creation of areas at SCA
!*
!*
k,22,PIN_OD-UR_B,WEB_L-TRUE_T-TRUE_T,0 !* keypoints for
k,23,PIN_OD-UR_B,WEB_L,0                !* new areas at
k,24,PIN_OD-UR_C,WEB_L-TRUE_T-TRUE_T,0 !* the SCA
k,25,PIN_OD-UR_C,WEB_L,0
k,26,PIN_OD-UR_D,WEB_L-TRUE_T-TRUE_T,0
k,27,PIN_OD-UR_D,WEB_L,0
K,28,PIN_ID,WEB_L-TRUE_T-TRUE_T,0
!*
!*        DEFINE NODES ON KEYPOINTS FOR PLPATH
!*
!* NKPT,1,2
!* NKPT,2,3
!* NKPT,3,5
!* NKPT,4,8
!*
NKPT,1,2
NKPT,2,3
NKPT,3,5
NKPT,4,12
NKPT,5,9
!*        DEFINE NODES ON KEYPOINTS FOR PLPATH
NKPT,6,18     !* path UR_B in from pin OD
NKPT,7,20
NKPT,8,19
NKPT,9,21
NKPT,10,14
NKPT,11,15
NKPT,12,22
NKPT,13,23
NKPT,14,24
NKPT,15,25
NKPT,16,26
NKPT,17,27
!*        DEFINE NEW LINES
LSTR,       19,       18   !line 1
LSTR,       18,       2   !line 11
LSTR,       14,       22   !line 15
LSTR,       22,       23   !line 17
LSTR,       23,       15   !line 18
```

```
LSTR,      22,      24   !line 19
LSTR,      24,      25   !line 20
LSTR,      25,      23   !line 21
LSTR,      24,      26   !line 22
LSTR,      26,      27   !line 23
LSTR,      27,      25   !line 24
LSTR,      3,       20   !line 25
LSTR,      20,      21   !line 26
LSTR,      26,      28   !line 27
LSTR,      27,      29   !line 28
LSTR,      29,      28   !line 29
LSTR,     28,       1        !line 30
!*
!*        Add in keypoints and lines for web 2nd area
!*        get kepoint location for kp12
*get,kp12_xloc,kp,12,loc,x
k,30,kp12_xloc,WEB_L-TRUE_T-TRUE_T,0
LSTR, 12,  30 !line 31
LSTR, 30,  17   !line 32
!*
!*      DEFINE AREAS
!*
AL,2,1,11,3,15,19,22,27,30    !* Area 1
!*
AL,9,10,16,31,32,13   !* Area 2
!*
AL,15,4,18,17            !* Area 3
!*
AL,19,17,21,20                   !* Area 4
!*
AL,22,20,24,23                   !* Area 5
!*
AL,27,29,28,23                   !* Area 6
!*
AL,28,24,21,18,5,6,25,26,7,8  !* Area 7
!*
AL,32,31,14,12  !* Area 8, web 2nd area
TYPE,   1
MAT,       1
REAL,
ESYS,       0
SECNUM,
!*
!*
MSHAPE,0,2D
MSHKEY,0
```

```
!*****************************************************************
!*  Set up mesh controls on lines
!*****************************************************************
lesize,12,web_h1,,
lesize,14,web_h2,,
lesize,4,pin_h1,,
lesize,5,pin_h2,,
!*        Set up h size on Pin Areas
lesize,17,pin_h1,,
lesize,20,pin_h4,,
lesize,23,pin_h4,,
lesize,31,web_h1,,
!*
!*        Areas 2,8 on Web
!*
!*        Mesh areas 3,4,5.
esize,pin_h1,              !*  Set default element edge size.
!*  Areas 3 and 8 are at the SCA
AMESH,3
MAT, 2
AMESH,8
MAT, 1
!*  Areas 4 and 5 are next to the SCA on the Pin
esize,pin_h3,              !*  Set default element edge size.
AMESH,4
AMESH,5
!*
!*        Mesh areas 1 and 2.
esize,e_globe,             !*  Set default element edge size.
!*
AMESH,1
MAT, 2
AMESH,2
MAT, 1
AMESH,6
AMESH,7
!*
!*      APPLY CONSTRAINTS TO LINES
!*
!* DL,8, ,UX,0
DL,2, ,UY,0
DL,1,,UY,0
DL,11,,UY,0
DL,9, ,UY,0
!*
!*
```

```
!*
!*
!*************************************
!*        Generate the contact pair(s)
!*
/COM, CONTACT PAIR CREATION - START
!*
!*      CM Command is used to group entities into selection sets
!*
CM,_NODECM,NODE
CM,_ELEMCM,ELEM
CM,_LINECM,LINE
CM,_AREACM,AREA
!*
!*      GSAV command for output of graphics to file
!*
/GSAV,cwz,gsav,,temp
!*
!*      Set up coefficient of friction for material
MP,MU,1,FRIC1
MAT,1
R,4
REAL,4
!*      Define ET 169, the target element, and
!*      ET 172, the contact element (2-D).
ET,4,169
ET,5,172
RMODIF,4,1,,,1.0,0.1,,
RMODIF,4,7,,,1.0e20,0.0,1.0
KEYOPT,5,2,0
KEYOPT,5,3,0
KEYOPT,5,6,0
KEYOPT,5,7,0
KEYOPT,5,8,
KEYOPT,5,9,0
KEYOPT,5,11,
KEYOPT,5,12,0
! Generate the target surface
LSEL,S,,,3
LSEL,A,,,4
CM,_TARGET,LINE
TYPE,4
NSLL,S,1
ESLN,R,0
ESURF,ALL
CMSEL,S,_ELEMCM
```

```
! Generate the contact surface
LSEL,S,,,13
LSEL,A,,,12
LSEL,A,,,14
CM,_CONTACT,LINE
TYPE,5
NSLL,S,1
ESLN,R,0
ESURF,ALL
ALLSEL
ESEL,ALL
ESEL,S,TYPE,,4
ESEL,A,TYPE,,5
ESEL,R,REAL,,4
/PSYMB,ESYS,1
/PNUM,TYPE,1
/NUM,1
EPLOT
ESEL,ALL
ESEL,S,TYPE,,4
ESEL,A,TYPE,,5
ESEL,R,REAL,,4
CMSEL,A,_NODECM
CMDEL,_NODECM
CMSEL,A,_ELEMCM
CMDEL,_ELEMCM
CMSEL,S,_LINECM
CMDEL,_LINECM
CMSEL,S,_AREACM
CMDEL,_AREACM
/GRES,cwz,gsav
CMDEL,_TARGET
CMDEL,_CONTACT
/COM, CONTACT PAIR CREATION - END
*SET,_REALID,4
/GSAV,cwz,gsav,,temp
CM,_CWZ_EL,ELEM
ESEL,S,REAL,,4
ESEL,R,ENAME,,169,174
KEYW,CWZCNTC,1
KEYW,CWZTARG,1
/PSYMB,ESYS,0
/PNUM,TYPE,1
/NUM,1
EPLOT
*SET,_REALID,4
```

```
CMSEL,S,_CWZ_EL
CMDEL,_CWZ_EL
/GRES,cwz,gsav
FINISH
```

The following input deck listing is used to post-process the parametric 2-D axisymmetric model:

```
/POST1
!*****************************************
!*  Set no. of divisions for plot paths
!*
DIV_SEG=pin_h1/5
PATH_DIV_p=PIN_L/DIV_SEG
PATH_DIV_w=WEB_L/DIV_SEG
!*
/auto,1
PLDISP,0
*ask,n,next,plot
PLDISP,2
!*********************************
/SHOW,JPEG
JPEG,QUAL,75,       !* default quality
JPEG,ORIENT,HORIZ   !* default orientation
JPEG,COLOR,2            !* default color
JPEG,TMOD,1             !* default bitmap text
/GFILE,800,       !* default 800 pixel resolution
!*
/CMAP,_TEMPCMAP_,CMP,,SAVE  !* default color map, w 9 contours
/RGB,INDEX,100,100,100,0    !* specifies RGB color format
/RGB,INDEX,0,0,0,15
/REPLOT
/CMAP,_TEMPCMAP_,CMP
/DELETE,_TEMPCMAP_,CMP
/SHOW,CLOSE                     !* purges graphic buffer, needed every time output format
changes
/DEVICE,VECTOR,0    !* vector mode default 0 areas shown as shaded colors
!*********************************
!*
!* Plot nodal stress in radial direction
!*
plnsol,s,x,2,10
!*********************************
/SHOW,JPEG
!*
/CMAP,_TEMPCMAP_,CMP,,SAVE  !* default color map, w 9 contours
/RGB,INDEX,100,100,100,0    !* specifies RGB color format
```

```
/RGB,INDEX,0,0,0,15
/REPLOT
/CMAP,_TEMPCMAP_,CMP
/DELETE,_TEMPCMAP_,CMP
/SHOW,CLOSE
!*********************************
*ask,n,next,plot
!*
!* Plot nodal stress in axial direction
!*
plnsol,s,y,2,10
!*********************************
/SHOW,JPEG
!*
/CMAP,_TEMPCMAP_,CMP,,SAVE  !* default color map, w 9 contours
/RGB,INDEX,100,100,100,0    !* specifies RGB color format
/RGB,INDEX,0,0,0,15
/REPLOT
/CMAP,_TEMPCMAP_,CMP
/DELETE,_TEMPCMAP_,CMP
/SHOW,CLOSE
!*********************************
*ask,n,next,plot
!*
!* Plot nodal stress in theta direciton
!*
plnsol,s,z,2,10
!*********************************
/SHOW,JPEG
!*
/CMAP,_TEMPCMAP_,CMP,,SAVE  !* default color map, w 9 contours
/RGB,INDEX,100,100,100,0    !* specifies RGB color format
/RGB,INDEX,0,0,0,15
/REPLOT
/CMAP,_TEMPCMAP_,CMP
/DELETE,_TEMPCMAP_,CMP
/SHOW,CLOSE
!*********************************
*ask,n,next,plot
!*
!* Plot nodal stress, VonMises Equivalent
!*
plnsol,s,eqv,2,10
!*********************************
/SHOW,JPEG
!*
```

```
/CMAP,_TEMPCMAP_,CMP,,SAVE  !* default color map, w 9 contours
/RGB,INDEX,100,100,100,0    !* specifies RGB color format
/RGB,INDEX,0,0,0,15
/REPLOT
/CMAP,_TEMPCMAP_,CMP
/DELETE,_TEMPCMAP_,CMP
/SHOW,CLOSE
!*********************************
*ask,n,next,plot
!*
!* Plot nodal stress, Zoomed view Radial
!*
/ZOOM,1,SCRN,0.465342,-0.056204,0.503673,-0.145620
/ZOOM,1,RECT,0.0999029,0.309615 ,0.517314991678 ,-0.104999995232
PLNSOL, S,x, 1,1.0
!*********************************
/SHOW,JPEG
!*
/CMAP,_TEMPCMAP_,CMP,,SAVE  !* default color map, w 9 contours
/RGB,INDEX,100,100,100,0    !* specifies RGB color format
/RGB,INDEX,0,0,0,15
/REPLOT
/CMAP,_TEMPCMAP_,CMP
/DELETE,_TEMPCMAP_,CMP
/SHOW,CLOSE
!*********************************
*ask,n,next,plot
!*
!* Plot nodal stress, Zoomed view Axial
!*
PLNSOL, S,y, 1,1.0
!*********************************
/SHOW,JPEG
!*
/CMAP,_TEMPCMAP_,CMP,,SAVE  !* default color map, w 9 contours
/RGB,INDEX,100,100,100,0    !* specifies RGB color format
/RGB,INDEX,0,0,0,15
/REPLOT
/CMAP,_TEMPCMAP_,CMP
/DELETE,_TEMPCMAP_,CMP
/SHOW,CLOSE
!*
!*********************************
*ask,n,next,plot
!*
!* Plot nodal stress, Zoomed view Theta
```

```
!*
PLNSOL, S,z, 1,1.0
!***********************************
/SHOW,JPEG
!*
/CMAP,_TEMPCMAP_,CMP,,SAVE  !* default color map, w 9 contours
/RGB,INDEX,100,100,100,0    !* specifies RGB color format
/RGB,INDEX,0,0,0,15
/REPLOT
/CMAP,_TEMPCMAP_,CMP
/DELETE,_TEMPCMAP_,CMP
/SHOW,CLOSE
!*
!***********************************
*ask,n,next,plot
!*
!* Plot nodal stress, Zoomed view Von Mises
!*
PLNSOL, S,eqv, 1,1.0
!***********************************
/SHOW,JPEG
!*
/CMAP,_TEMPCMAP_,CMP,,SAVE  !* default color map, w 9 contours
/RGB,INDEX,100,100,100,0    !* specifies RGB color format
/RGB,INDEX,0,0,0,15
/REPLOT
/CMAP,_TEMPCMAP_,CMP
/DELETE,_TEMPCMAP_,CMP
/SHOW,CLOSE
!***********************************
asel,s,area,,1    !* select area 1 - pin
asel,a,area,,3,7,1          !* select area 3-7 pin
ALLSEL,BELOW,AREA      !* select all below area 1
!***********************************
*ask,n,next,plot
!*
!* Plot nodal stress, Zoomed view Von Mises, Pin Area Only
!*
PLNSOL, S,eqv, 1,1.0
!***********************************
/SHOW,JPEG
!*
/CMAP,_TEMPCMAP_,CMP,,SAVE  !* default color map, w 9 contours
/RGB,INDEX,100,100,100,0    !* specifies RGB color format
/RGB,INDEX,0,0,0,15
/REPLOT
```

```
/CMAP,_TEMPCMAP_,CMP
/DELETE,_TEMPCMAP_,CMP
/SHOW,CLOSE
allsel,all
!*
!*********************************
*ask,n,next,plot
!*********************************
!*      Generate plots along the Pin OD
!*
!*        Set path nodes for paths b and c
pathb_t=7
pathb_b=6
pathc_t=9
pathc_b=8
!*********************************
!*        Select Pin Elements only
asel,s,area,,1    !* select area 1 - pin
asel,a,area,,3,7,1          !* select area 3-5 pin
ALLSEL,BELOW,AREA      !* select all below area 1
NSEL,a,NODE,,1,2
!* ksel,s,kp,,2
!* allsel,below,kp
!*
path,pin_od,2,30,path_div_p   ! define path_name,no.points,no.sets,no.div.
!*
!*
ppath,1,1              ! path point 1 is node 1.
ppath,2,2              ! path point 2 is node 2.
!*
!*
pmap                  ! mapping of discontinuities.
!*
pdef,sx_PIN,s,x            ! interpret radial stress.
pdef,sz_PIN,s,z            ! interpret hoop stress.
pdef,sy_PIN,s,y            ! interpret axial stress.
pdef,seq_PIN,s,eqv         ! interpret equiv stress.
!*
!*
!*
plpath,sx_PIN,sy_PIN,sz_PIN         ! plot
!*********************************
/SHOW,JPEG
!*
/CMAP,_TEMPCMAP_,CMP,,SAVE  !* default color map, w 9 contours
/RGB,INDEX,100,100,100,0    !* specifies RGB color format
```

```
/RGB,INDEX,0,0,0,15
/REPLOT
/CMAP,_TEMPCMAP_,CMP
/DELETE,_TEMPCMAP_,CMP
/SHOW,CLOSE
*ask,n,next,plot
!*
!*
plpath,sx_PIN,sy_PIN,sz_PIN,seq_PIN         ! plot
!*********************************
/SHOW,JPEG
!*
/CMAP,_TEMPCMAP_,CMP,,SAVE  !* default color map, w 9 contours
/RGB,INDEX,100,100,100,0    !* specifies RGB color format
/RGB,INDEX,0,0,0,15
/REPLOT
/CMAP,_TEMPCMAP_,CMP
/DELETE,_TEMPCMAP_,CMP
/SHOW,CLOSE
*ask,n,next,plot
!*
plpath,seq_PIN                              !plot
!*********************************
/SHOW,JPEG
!*
/CMAP,_TEMPCMAP_,CMP,,SAVE  !* default color map, w 9 contours
/RGB,INDEX,100,100,100,0    !* specifies RGB color format
/RGB,INDEX,0,0,0,15
/REPLOT
/CMAP,_TEMPCMAP_,CMP
/DELETE,_TEMPCMAP_,CMP
/SHOW,CLOSE
*ask,n,next,plot
!*
plpath,sx_PIN         ! plot
!*********************************
/SHOW,JPEG
!*
/CMAP,_TEMPCMAP_,CMP,,SAVE  !* default color map, w 9 contours
/RGB,INDEX,100,100,100,0    !* specifies RGB color format
/RGB,INDEX,0,0,0,15
/REPLOT
/CMAP,_TEMPCMAP_,CMP
/DELETE,_TEMPCMAP_,CMP
/SHOW,CLOSE
*ask,n,next,plot
```

```
!*
plpath,sy_PIN        ! plot
!*********************************
/SHOW,JPEG
!*
/CMAP,_TEMPCMAP_,CMP,,SAVE  !* default color map, w 9 contours
/RGB,INDEX,100,100,100,0    !* specifies RGB color format
/RGB,INDEX,0,0,0,15
/REPLOT
/CMAP,_TEMPCMAP_,CMP
/DELETE,_TEMPCMAP_,CMP
/SHOW,CLOSE
*ask,n,next,plot
!*
plpath,sz_PIN
!*********************************
/SHOW,JPEG
!*
/CMAP,_TEMPCMAP_,CMP,,SAVE  !* default color map, w 9 contours
/RGB,INDEX,100,100,100,0    !* specifies RGB color format
/RGB,INDEX,0,0,0,15
/REPLOT
/CMAP,_TEMPCMAP_,CMP
/DELETE,_TEMPCMAP_,CMP
/SHOW,CLOSE
!*
!*********************************
allsel,all
!*
!*
!*
!*********************************
!*      Generate plots along the WEB ID
!*********************************
!*        Select Web Elements only
asel,s,area,,2    !* select area 2 - web
ALLSEL,BELOW,AREA      !* select all below area 2
NSEL,a,NODE,,3,4
!*
path,web_id,2,30,path_div_w   ! define path_name,no.points,no.sets,no.div.
!*
!*
ppath,1,3              ! path point 1 is node 1826.
ppath,2,4         ! path point 2 is node 1895.
!* ppath,1,1826           ! path point 1 is node 1826.
!* ppath,2,1895           ! path point 2 is node 1895.
```

```
!*
!*
pmap                ! mapping of discontinuities.
!*
pdef,sx_WEB,s,x          ! interpret radial stress.
pdef,sz_WEB,s,z          ! interpret hoop stress.
pdef,sy_WEB,s,y          ! interpret axial stress.
pdef,sxy_WEB,s,xy
pdef,syz_WEB,s,yz
pdef,sxz_WEB,s,xz
pdef,seq_WEB,s,eqv      ! interpret equiv stress.
!*
!*
plpath,sx_WEB,sy_WEB,sz_WEB        ! plot
!**********************************
/SHOW,JPEG
!*
/CMAP,_TEMPCMAP_,CMP,,SAVE  !* default color map, w 9 contours
/RGB,INDEX,100,100,100,0    !* specifies RGB color format
/RGB,INDEX,0,0,0,15
/REPLOT
/CMAP,_TEMPCMAP_,CMP
/DELETE,_TEMPCMAP_,CMP
/SHOW,CLOSE
*ask,n,next,plot
!*
plpath,sx_WEB,sy_WEB,sz_WEB,sxy_WEB,syz_WEB,sxz_WEB,seq_WEB  ! plot
!**********************************
/SHOW,JPEG
!*
/CMAP,_TEMPCMAP_,CMP,,SAVE  !* default color map, w 9 contours
/RGB,INDEX,100,100,100,0    !* specifies RGB color format
/RGB,INDEX,0,0,0,15
/REPLOT
/CMAP,_TEMPCMAP_,CMP
/DELETE,_TEMPCMAP_,CMP
/SHOW,CLOSE
*ask,n,next,plot
!*
plpath,seq_WEB                    !plot
!**********************************
/SHOW,JPEG
!*
/CMAP,_TEMPCMAP_,CMP,,SAVE  !* default color map, w 9 contours
/RGB,INDEX,100,100,100,0    !* specifies RGB color format
/RGB,INDEX,0,0,0,15
```

```
/REPLOT
/CMAP,_TEMPCMAP_,CMP
/DELETE,_TEMPCMAP_,CMP
/SHOW,CLOSE
*ask,n,next,plot
!*
plpath,sx_WEB        ! plot
!*********************************
/SHOW,JPEG
!*
/CMAP,_TEMPCMAP_,CMP,,SAVE  !* default color map, w 9 contours
/RGB,INDEX,100,100,100,0    !* specifies RGB color format
/RGB,INDEX,0,0,0,15
/REPLOT
/CMAP,_TEMPCMAP_,CMP
/DELETE,_TEMPCMAP_,CMP
/SHOW,CLOSE
*ask,n,next,plot
!*
plpath,sy_WEB        ! plot
!*********************************
/SHOW,JPEG
!*
/CMAP,_TEMPCMAP_,CMP,,SAVE  !* default color map, w 9 contours
/RGB,INDEX,100,100,100,0    !* specifies RGB color format
/RGB,INDEX,0,0,0,15
/REPLOT
/CMAP,_TEMPCMAP_,CMP
/DELETE,_TEMPCMAP_,CMP
/SHOW,CLOSE
*ask,n,next,plot
!*
plpath,sz_WEB
!*********************************
!*
allsel,all
!************************************************
!*        Plot stress along path x nodes in from OD
!************************************************
!*
!*  node 36, on symm plane
!* node 130, on end of pin
!*********************************
!!*      Generate plots along the Pin OD
!*********************************
!*        Select Pin Elements only
```

```
asel,s,area,,1    !* select area 1 - pin
asel,a,area,,3,7,1          !* select area 3-5 pin
ALLSEL,BELOW,AREA      !* select all below area 1
NSEL,a,NODE,,6,9,1
!* ksel,s,kp,,2
!* allsel,below,kp
!*
path,pin_od_b,2,30,path_div_p   ! define path_name,no.points,no.sets,no.div.
!*
!*
ppath,1,pathb_t         ! path point 1 is node 36.
ppath,2,pathb_b         ! path point 2 is node 130-h=0.25,134-h=0.2.
pmap                    ! mapping of discontinuities.
!*
pdef,sx_PINb,s,x             ! interpret radial stress.
pdef,sz_PINb,s,z             ! interpret hoop stress.
pdef,sy_PINb,s,y             ! interpret axial stress.
pdef,seq_PINb,s,eqv       ! interpret equiv stress.
!*
!*
!*
plpath,sx_PINb,sy_PINb,sz_PINb         ! plot
!*********************************
/SHOW,JPEG
!*
/CMAP,_TEMPCMAP_,CMP,,SAVE  !* default color map, w 9 contours
/RGB,INDEX,100,100,100,0    !* specifies RGB color format
/RGB,INDEX,0,0,0,15
/REPLOT
/CMAP,_TEMPCMAP_,CMP
/DELETE,_TEMPCMAP_,CMP
/SHOW,CLOSE
*ask,n,next,plot
!*
!*
plpath,sx_PINb,sy_PINb,sz_PINb,seq_PINb         ! plot
!*********************************
/SHOW,JPEG
!*
/CMAP,_TEMPCMAP_,CMP,,SAVE  !* default color map, w 9 contours
/RGB,INDEX,100,100,100,0    !* specifies RGB color format
/RGB,INDEX,0,0,0,15
/REPLOT
/CMAP,_TEMPCMAP_,CMP
/DELETE,_TEMPCMAP_,CMP
/SHOW,CLOSE
```

```
*ask,n,next,plot
!*
plpath,seq_PINb                    !plot
!*********************************
/SHOW,JPEG
!*
/CMAP,_TEMPCMAP_,CMP,,SAVE  !* default color map, w 9 contours
/RGB,INDEX,100,100,100,0    !* specifies RGB color format
/RGB,INDEX,0,0,0,15
/REPLOT
/CMAP,_TEMPCMAP_,CMP
/DELETE,_TEMPCMAP_,CMP
/SHOW,CLOSE
*ask,n,next,plot
!*
plpath,sx_PINb        ! plot
!*********************************
/SHOW,JPEG
!*
/CMAP,_TEMPCMAP_,CMP,,SAVE  !* default color map, w 9 contours
/RGB,INDEX,100,100,100,0    !* specifies RGB color format
/RGB,INDEX,0,0,0,15
/REPLOT
/CMAP,_TEMPCMAP_,CMP
/DELETE,_TEMPCMAP_,CMP
/SHOW,CLOSE
*ask,n,next,plot
!*
plpath,sy_PINb        ! plot
!*********************************
/SHOW,JPEG
!*
/CMAP,_TEMPCMAP_,CMP,,SAVE  !* default color map, w 9 contours
/RGB,INDEX,100,100,100,0    !* specifies RGB color format
/RGB,INDEX,0,0,0,15
/REPLOT
/CMAP,_TEMPCMAP_,CMP
/DELETE,_TEMPCMAP_,CMP
/SHOW,CLOSE
*ask,n,next,plot
!*
plpath,sz_PINb
!*********************************
allsel,all
!*
!*
```

```
!*  node 36, on symm plane
!* node 130, on end of pin
!*********************************
!!*      Generate plots along the Pin OD
!*********************************
!*        Select Pin Elements only
asel,s,area,,1    !* select area 1 - pin
asel,a,area,,3,7,1          !* select area 3-5 pin
ALLSEL,BELOW,AREA      !* select all below area 1
NSEL,a,NODE,,6,9,1
!* ksel,s,kp,,2
!* allsel,below,kp
!*
path,pin_od_b,2,30,path_div_p   ! define path_name,no.points,no.sets,no.div.
!*
!*
ppath,1,pathc_t          ! path point 1 is node 35.
ppath,2,pathc_b          ! path point 2 is node 130-h=0.25,n135-h=0.2.
pmap                   ! mapping of discontinuities.
!*
pdef,sx_PINc,s,x             ! interpret radial stress.
pdef,sz_PINc,s,z             ! interpret hoop stress.
pdef,sy_PINc,s,y             ! interpret axial stress.
pdef,seq_PINc,s,eqv       ! interpret equiv stress.
!*
!*
!*
plpath,sx_PINc,sy_PINc,sz_PINc         ! plot
!*********************************
/SHOW,JPEG
!*
/CMAP,_TEMPCMAP_,CMP,,SAVE  !* default color map, w 9 contours
/RGB,INDEX,100,100,100,0    !* specifies RGB color format
/RGB,INDEX,0,0,0,15
/REPLOT
/CMAP,_TEMPCMAP_,CMP
/DELETE,_TEMPCMAP_,CMP
/SHOW,CLOSE
*ask,n,next,plot
!*
!*
plpath,sx_PINc,sy_PINc,sz_PINc,seq_PINc         ! plot
!*********************************
/SHOW,JPEG
!*
/CMAP,_TEMPCMAP_,CMP,,SAVE  !* default color map, w 9 contours
```

```
/RGB,INDEX,100,100,100,0    !* specifies RGB color format
/RGB,INDEX,0,0,0,15
/REPLOT
/CMAP,_TEMPCMAP_,CMP
/DELETE,_TEMPCMAP_,CMP
/SHOW,CLOSE
*ask,n,next,plot
!*
plpath,seq_PINc                    !plot
!*********************************
/SHOW,JPEG
!*
/CMAP,_TEMPCMAP_,CMP,,SAVE  !* default color map, w 9 contours
/RGB,INDEX,100,100,100,0    !* specifies RGB color format
/RGB,INDEX,0,0,0,15
/REPLOT
/CMAP,_TEMPCMAP_,CMP
/DELETE,_TEMPCMAP_,CMP
/SHOW,CLOSE
*ask,n,next,plot
!*
plpath,sx_PINc         ! plot
!*********************************
/SHOW,JPEG
!*
/CMAP,_TEMPCMAP_,CMP,,SAVE  !* default color map, w 9 contours
/RGB,INDEX,100,100,100,0    !* specifies RGB color format
/RGB,INDEX,0,0,0,15
/REPLOT
/CMAP,_TEMPCMAP_,CMP
/DELETE,_TEMPCMAP_,CMP
/SHOW,CLOSE
*ask,n,next,plot
!*
plpath,sy_PINc         ! plot
!*********************************
/SHOW,JPEG
!*
/CMAP,_TEMPCMAP_,CMP,,SAVE  !* default color map, w 9 contours
/RGB,INDEX,100,100,100,0    !* specifies RGB color format
/RGB,INDEX,0,0,0,15
/REPLOT
/CMAP,_TEMPCMAP_,CMP
/DELETE,_TEMPCMAP_,CMP
/SHOW,CLOSE
*ask,n,next,plot
```

```
!*
plpath,sz_PINc
!*********************************
allsel,all
!*
```